Lecture Notes in Electrical Engineering 439

Jiadong Sun
Jingnan Liu
Yuanxi Yang
Shiwei Fan
Wenxian Yu
Editors

China Satellite Navigation Conference (CSNC) 2017 Proceedings: Volume III

Springer

Lecture Notes in Electrical Engineering

Volume 439

About this Series

"Lecture Notes in Electrical Engineering (LNEE)" is a book series which reports the latest research and developments in Electrical Engineering, namely:

- Communication, Networks, and Information Theory
- Computer Engineering
- Signal, Image, Speech and Information Processing
- Circuits and Systems
- Bioengineering

LNEE publishes authored monographs and contributed volumes which present cutting edge research information as well as new perspectives on classical fields, while maintaining Springer's high standards of academic excellence. Also considered for publication are lecture materials, proceedings, and other related materials of exceptionally high quality and interest. The subject matter should be original and timely, reporting the latest research and developments in all areas of electrical engineering.

The audience for the books in LNEE consists of advanced level students, researchers, and industry professionals working at the forefront of their fields. Much like Springer's other Lecture Notes series, LNEE will be distributed through Springer's print and electronic publishing channels.

More information about this series at http://www.springer.com/series/7818

Jiadong Sun · Jingnan Liu · Yuanxi Yang
Shiwei Fan · Wenxian Yu
Editors

China Satellite Navigation Conference (CSNC) 2017 Proceedings: Volume III

Springer

Editors
Jiadong Sun
Academician of CAS
China Aerospace Science and Technology Corporation
Beijing
China

Jingnan Liu
Wuhan University
Wuhan
China

Yuanxi Yang
National Administration of GNSS and Applications
Beijing
China

Shiwei Fan
China Satellite Navigation Office
Beijing
China

Wenxian Yu
Shanghai Jiao Tong University
Shanghai
China

ISSN 1876-1100 ISSN 1876-1119 (electronic)
Lecture Notes in Electrical Engineering
ISBN 978-981-10-4593-6 ISBN 978-981-10-4594-3 (eBook)
DOI 10.1007/978-981-10-4594-3

Library of Congress Control Number: 2017937524

Printed on acid-free paper

This Springer imprint is published by Springer Nature
The registered company is Springer Nature Singapore Pte Ltd.
The registered company address is: 152 Beach Road, #21-01/04 Gateway East, Singapore 189721, Singapore

Preface

BeiDou Navigation Satellite System (BDS) is China's global navigation satellite system which has been developed independently. BDS is similar in principle to global positioning system (GPS) and compatible with other global satellite navigation systems (GNSS) worldwide. The BDS will provide highly reliable and precise positioning, navigation and timing (PNT) services as well as short-message communication for all users under all-weather, all-time and worldwide conditions.

China Satellite Navigation Conference (CSNC) is an open platform for academic exchanges in the field of satellite navigation. It aims to encourage technological innovation, accelerate GNSS engineering and boost the development of the satellite navigation industry in China and in the world.

The 8th China Satellite Navigation Conference (CSNC 2017) is held during May 23–25, 2017, Shanghai, China. The theme of CSNC2017 is Positioning, Connecting All, including technical seminars, academic exchanges, forums, exhibitions and lectures. The main topics are as follows:

Conference Topics

S01 Satellite Navigation Technology
S02 Navigation and Location Service
S03 Satellite Navigation Signals and Signal Processing
S04 Satellite Orbit and Satellite Clock Error
S05 Precise Positioning Technology
S06 Atomic Clock and Time-frequency Technology
S07 Satellite Navigation Augmentation Technology
S08 Test and Assessment Technology
S09 User Terminal Technology
S10 Multi-source Fusion Navigation Technology
S11 PNT New Concept, New Methods and New Technology
S12 Policies and Regulations, Standards and Intellectual Properties

The proceedings (Lecture Notes in Electrical Engineering) have 188 papers in twelve topics of the conference, which were selected through a strict peer-review process from 599 papers presented at CSNC2017. In addition, another 272 papers were selected as the electronic proceedings of CSNC2017, which are also indexed by "China Proceedings of Conferences Full-text Database (CPCD)" of CNKI and Wan Fang Data.

We thank the contribution of each author and extend our gratitude to 249 referees and 48 session chairmen who are listed as members of editorial board. The assistance of CNSC2017 organizing committees and the Springer editorial office is highly appreciated.

Beijing, China — Jiadong Sun
Wuhan, China — Jingnan Liu
Beijing, China — Yuanxi Yang
Beijing, China — Shiwei Fan
Shanghai, China — Wenxian Yu

Editorial Board

Topic: S5: Precise Positioning Technology

Qile Zhao, Wuhan University
Jianwen Li, Information Engineering University
Songshu Li, Shanghai Astronomical Observatory, Chinese Academy of Sciences
Feng Yanming, Queensland University of Technology Brisbane, Australia

Topic: S6: Atomic Clock and Time-frequency Technology

Lianshan Gao, The 203th Research Institute of China Aerospace Science & Industry Corporation
Chunhao Han, Beijing Satellite Navigation Center
Xiaohui Li, National Time Service Center, Chinese Academy of Sciences
Rochat Pascal, Spectratime & T4Science

Topic: S7: Satellite Navigation Augmentation Technology

Junlin Zhang, OLinkStar Co., Ltd., China
Jinping Chen, Beijing Satellite Navigation Center
Rui Li, Beihang University
Shaojun Feng, Imperial College London

Topic: S8: Test and Assessment Technology

Xiaolin Jia, Xi'an Institute of Surveying and Mapping
Jun Yang, National University of Defense Technology
Jianping Cao, Air Force Equipment Research Institute
Yang Gao, University of Calgary, Canada

Topic: S9: User Terminal Technology

Haibo He, Beijing Satellite Navigation Center
Baowang Lian, Northwestern Polytechnical University
Hong Li, Tsinghua University
Yong Li, University of New South Wales, Australia

Topic: S10: Multi-source Fusion Navigation Technology

Zhongliang Deng, Beijing University of Posts and Telecommunications
Hong Yuan, Academy of Opto-electronics, Chinese Academy of Sciences
Yongbin Zhou, National University of Defense Technology
Jinling Wang, University of New South Wales, Australia

Topic: S11: PNT New Concept, New Methods and New Technology

Mingquan Lu, Tsinghua University
Wei Wang, The 20th Research Institute of China Electronics Technology Group Corporation
Yin Xu, Academy of Opto-Electronics, Chinese Academy of Sciences
Xiangzhen Li, Chungnam National University, Korea

Topic: S12: Policies and Regulations, Standards and Intellectual Properties

Scientific Committee and Organizing Committee

The 8th China Satellite Navigation Conference (CSNC 2017)

Scientific Committee

Chairman
Jiadong Sun, China Aerospace Science and Technology Corporation

Vice-Chairman
Rongjun Shen, China
Jisheng Li, China
Qisheng Sui, China
Changfei Yang, China
Zuhong Li, China Academy of Space Technology
Shusen Tan, Beijing Satellite Navigation Center, China

Executive Chairman
Jingnan Liu, Wuhan University
Yuanxi Yang, China National Administration of GNSS and Applications
Shiwei Fan, China

Committee Members: (By Surnames Stroke Order)
Xiancheng Ding, China Electronics Technology Group Corporation
Qingjun Bu, China
Liheng Wang, China Aerospace Science and Technology Corporation
Yuzhu Wang, Shanghai Institute of Optics and Fine Mechanics, Chinese Academy of Sciences
Guoxiang Ai, National Astronomical Observatories, Chinese Academy of Sciences
Shuhua Ye, Shanghai Astronomical Observatories, Chinese Academy of Sciences
Zhaowen Zhuang, National University of Defense Technology
Qifeng Xu, PLA Information Engineering University

Houze Xu, Institute of Geodesy and Geophysics, Chinese Academy of Sciences
Guirong Min, China Academy of Space Technology
Xixiang Zhang, China Electronics Technology Group Corporation
Lvqian Zhang, China Aerospace Science and Technology Corporation
Junyong Chen, National Administration of Surveying, Mapping and Geoinformation
Benyao Fan, China Academy of Space Technology
Dongjin Luo, China
Guohong Xia, China Aerospace Science & Industry Corporation
Chong Cao, China Research Institute of Radio Wave Propagation (CETC 22)
Faren Qi, China Academy of Space Technology
Sili Liang, China Aerospace Science and Technology Corporation
Shancheng Tu, China Academy of Space Technology
Rongsheng Su, China
Zhipeng Tong, China Electronics Technology Group Corporation
Ziqing Wei, Xi'an Institute of Surveying and Mapping

Organizing Committee

Secretary General
Haitao Wu, Navigation Headquarters, Chinese Academy of Sciences

Vice-Secretary General
Weina Hao, Navigation Headquarters, Chinese Academy of Sciences

Under Secretary
Wenhai Jiao, China Satellite Navigation Office Engineering Center
Zhao Wenjun, Beijing Satellite Navigation Center
Wenxian Yu, Shanghai Jiao Tong University
Wang Bo, Academic Exchange Center of China Satellite Navigation Office

Members: (In Surname Stroke Order)
Qun Ding, The 20th Research Institute of China Electronics Technology Group Corporation
Miao Yu, China Academy of Space Technology
Li Wang, International Cooperation Research Center, China Satellite Navigation Engineering Office
Liu Peiling, Shanghai Jiao tong University
Ying Liu, China Satellite Navigation Office Engineering Center
Lu Mingquan, Tsinghua University
Xiuwan Chen, Peking University
Ouyang Guangzhou, Academy of Opto-Electronics, Chinese Academy of Sciences
Zhao Qile, Wuhan University

Xiangan Zhao, China Defense Science and Technology Information Center
Gang Hu, Beijing Unicore Communications, Inc.
Min Shui, National Remote Sensing Centre of China

Contents

Part I
Satellite Orbit and Satellite Clock Error

Orbit Determination Based on Particle Filtering Algorithm

Daming Bai

Abstract Since the distribution of state variables of satellite orbit estimation is non-Gaussian, the particle filtering algorithm is put forward. Through the presentation of the particle filtering algorithm and the mechanism of satellite orbit estimation, the orbit determination model based on the particle filtering algorithm is established. The results of simulation show that the particle filtering algorithm can effectively solve the problem that the distribution of state variables of satellite orbit estimation is non-Gaussian.

Keywords Particle filter · Orbit determination · Non-Gaussian · Estimation value

1 Introduction

The method of autonomous orbit determination using magnetic measurement information generally uses the extended Kalman filter (Extended Kalman, Filter, EKF), in addition to the unscented Kalman filter (Unscented Kalman Filter, UKF) to confirm satellite position and velocity, and they are based on the assumption that the distribution of state variables is similar to the Gauss distribution, and estimate the mean and covariance of state variables [1]. When the distributions of the state variables were not Gauss distribution, the performance of the filter algorithm will be reduced, even if the initial position and velocity distribution are Gauss distribution, but the process noise and the measurement noise are white Gauss noise. At this time, because of the nonlinearity in the model, the actual distribution of position

D. Bai (✉)
Xi'an Satellite Control Center, Xi'an 710043, China
e-mail: 464864443@qq.com

D. Bai
Key Laboratory of Spacecraft in-Orbit Fault Diagnosis and Maintenance, Xi'an 710043, China

J. Sun et al. (eds.), *China Satellite Navigation Conference (CSNC) 2017 Proceedings: Volume III*, Lecture Notes in Electrical Engineering 439,
DOI 10.1007/978-981-10-4594-3_1

and velocity is not Gauss distribution. In order to solve the nonlinear model and the estimation of the initial deviation to the negative effects caused by the filtering, this paper uses particle filtering algorithm for satellite orbit, and its effectiveness is proved by mathematical simulation.

2 Particle Filter Algorithm and Orbit Estimation

The particle filter is used for target tracking, and its principle is that the particle filter (Particle Filter PF) is a kind of approximate Bayesian filtering algorithm [1, 4] based on Monte Carlo simulation; its core idea is to use some discrete random sampling points (particle) probability density function to approximate the system random variable, instead of integral to the sample mean to obtain estimation of the state minimum variance. A mathematical description for the stationary random process, assuming that $k-1$ moment system of the posterior probability density for $p(x_{k-1}|z_{k-1})$ random samples selected n according to certain principles, k time measurement information, through state prediction and time update process, n particle of the posterior probability density can be approximated as $p(x_k|z_k)$. As the number of particles increases, the probability density function of the particle is gradually approaching the probability density function of the state. Particle filter can be applied to any nonlinear stochastic system. With the improvement of computer performance, the method has been paid more and more attention to [4].

The basic problem of the orbit determination is as follows: The dynamic process of a differential equation is not exactly known, and the optimal estimation of the motion state of the satellite in a certain sense is solved using the observation value with error and the not accurate initial state. When the system can be described as a linear model, and the system and the measurement error are white noise, the unbiased optimal estimation in statistical sense can be obtained by Kalman filtering [5]. However, in practical applications, the target motion model and the measurement model are mostly nonlinear; the noise is non-Gauss; and the traditional Kalman filter application has been limited. Relative orbit determination problem is usually based on the Hill equation using extended Kalman filtering algorithm to estimate the state of the target aircraft. Because of the need to linearize the state equation and the Hill equation which is only applicable to the relative distance filtering calculation, when the relative distance or large initial errors are easy to cause filter divergence and its application scope has been greatly constrained, therefore, the application to the relative distance between the target orbit determination method will be an important direction for future research.

With the development of space technology, the requirement of spacecraft orbit precision becomes higher and higher. The data processing methods of satellite orbit determination can be divided into two categories: (1) batch processing. Using all data to get track and related parameter of the epoch is a method of post-processing, needs to store a large number of observation value, and demands high processing

ability of computer. (2) Sequential recursive method. When the observation value is reached, the corresponding processing is performed, and the next moment is no longer observed by the previous moment. The particle filter algorithm is a sequential recursive method; the data processing only uses the current value of observation data and the previous data storage, and requires lower capacity of the computer. The particle filter algorithm for solving nonlinear and non-Gauss problems has obvious theoretical advantages, such as the algorithm can be used to set orbit spacecraft, which is bound to improve the accuracy of orbit determination. However, no one shows any interest in the research model, algorithm, and application of the precise orbit of the spacecraft.

3 Satellite Orbit Determination Model Based on Particle Filter

3.1 Satellite Orbit Influence Factor Analysis

The satellite is subjected to various forces in the course of the movement around the earth; these forces can be divided into two categories: one is conservative forces; the other is the divergent force [6]. Conservative forces include earth gravity, day, month, the gravity of the planet to the satellite, and the gravitational field changes caused by the earth tide phenomenon. For conservative force systems, it can be described by the "bit function". The divergence force includes the atmospheric resistance, the earth infrared radiation, and the power of satellite attitude control. The divergence force does not have the position function, so the expression is directly used. The expressions of the above forces are very complex. Besides the two-body problem, it is difficult to obtain the analytical solution of the motion equation of the satellite, which is usually based on the approximate analytical solution.

On orbit determination, dynamic model is not very accurate. The main point is as follows: Under certain accuracy, dynamic model omits some perturbed factors, even without omission, it also made some simplifications and approximations. In the considered perturbation factors, the model parameters are approximate. The initial state of general satellite $\boldsymbol{r}_0$ and $\boldsymbol{v}_0$ could not be precisely known; only the reference value $\boldsymbol{r}_0^*$ and $\boldsymbol{v}_0^*$ needs to continue to refine the satellite observation reference value in order to obtain the initial motion state $\boldsymbol{r}_0$ and $\boldsymbol{v}_0$ of satellite. Measurement data itself are not very accurate; the equipment itself and a variety of factors affect measurement data with random error and system error. Therefore, the orbit estimation problem is a dynamic process which is not known exactly for the differential equation, and the best estimate of the satellite motion state is obtained using the observational data with random errors and the inaccurate initial state.

3.2 Establishing the State Equation and Observation Equation of Satellite Motion

The particle filter algorithm is used to calculate the satellite motion. The state of the next moment is calculated according to the current state of the moment. In addition, it is necessary to obtain the real observations by an observation equation

(1) Equation of state

Aircraft dynamics equation can be expressed as

$$\left.\begin{array}{l}\dot{x} = v_{\mathrm{x}} \\ \dot{y} = v_{\mathrm{y}} \\ \dot{z} = v_{\mathrm{z}} \\ \dot{x} = -\frac{u}{x^2+y^2+z^2}\frac{x}{\sqrt{x^2+y^2+z^2}} + f_{\mathrm{T}}a_{\mathrm{x}} + f_{\mathrm{px}} \\ \dot{y} = -\frac{u}{x^2+y^2+z^2}\frac{y}{\sqrt{x^2+y^2+z^2}} + f_{\mathrm{T}}a_{\mathrm{y}} + f_{\mathrm{py}} \\ \dot{z} = -\frac{u}{x^2+y^2+z^2}\frac{z}{\sqrt{x^2+y^2+z^2}} + f_{\mathrm{T}}a_{\mathrm{z}} + f_{\mathrm{pz}}\end{array}\right\} \quad (1)$$

In the formula, x, y, and z are the position vector components as the target in inertial system; v_{x}, v_{y}, and v_{z} are the velocity vector component of target in inertial coordinate system; u is the earth gravity parameters; f_{px}, f_{py}, and f_{pz} are the perturbation accelerations, and said f_{T} for thrust acceleration; a_{x}, a_{y}, and a_{z} for thrust acceleration vector components. Considering the impact of the J2 perturbation potential function for earth oblateness,

$$U_{\mathrm{J2}} = \frac{u}{r^3}R_{\mathrm{e}}^2 J_2 \frac{1}{2}(3\sin^2 f - 1). \quad ((2))$$

In the formula, R_{e} is for the equatorial radius; $\sin\phi = \frac{z}{r}$; J2 for the two-order harmonic coefficient; and ϕ for the spherical coordinate system defined position angle. J2 perturbation in Cartesian coordinates for the component, respectively:

$$f_{\mathrm{J2,x}} = -\frac{\partial U_{\mathrm{J2}}}{\partial x}, f_{\mathrm{J2,y}} = -\frac{\partial U_{\mathrm{J2}}}{\partial y}, f_{\mathrm{J2,z}} = -\frac{\partial U_{\mathrm{J2}}}{\partial z}.$$

The target state model can be divided into two types: non-maneuvering and maneuvering model. The difference is the influence of thrust acceleration.

(2) Observation equation analysis

Generally, the discrete time system filter is a mature linear estimation theory in mathematical theory and mathematical methods [5]. However, the orbit determination is exactly the state equation and observation equations are nonlinear, which is the main content of this paper.

The relationship between the measured observations and the state vector of the satellite is obtained by the tracking and measuring system, and the satellite observations are oblique distance, slant distance change rate, azimuth, and elevation angle. The determination of satellite orbit is the observation value obtained by real-time measurement, and the satellite position is estimated sequentially. The particle filter algorithm used in this paper is to solve the optimal estimation of satellite position. n-dimensional linear dynamic systems and m-dimensional linear observation system equations are described as follows:

$$\left.\begin{aligned} X_k &= \boldsymbol{f}_{k,k-1}X_{k-1} + W_{k-1} \\ Z_k &= \boldsymbol{H}_k X_k + V_k \end{aligned}\right\} \tag{3}$$

In the formula, X_k is for the n-dimensional state vector system in the moment k, $k = 1, 2, \ldots$; $\boldsymbol{f}_{k,k-1}$, called the state transition matrix; the reaction system sampling time state from $k-1$ to k is the sampling time state transform; $W_k - 1$ is for the random disturbances acting on the system at the time k, called the model for noise; Z_k is for the m-dimensional observation vector; $\boldsymbol{H}_k$ is for the observation the $m \times n$ order of the matrix, for the conversion from the state X_k to the measurements Z_k; V_k is for the m-dimensional measurement noise.

In the horizontal coordinate system of the TT&C station, the measured is slant distance R, slant distance change rate $\dot{R}$, azimuth angle A, and elevation angle E. The rectangular coordinate in the horizontal coordinate system of the TT&C station is $(x, y, z, \dot{x}, \dot{y}, \dot{z})$, in that way:

$$\left.\begin{aligned} R &= \sqrt{x^2+y^2+z^2} \\ \dot{R} &= \frac{x\dot{x}+y\dot{y}+z\dot{z}}{\sqrt{x^2+y^2+z^2}} \\ A &= \begin{cases} \arctan\left(\dfrac{y}{x}\right) & x > 0 \\ \arctan\left(\dfrac{y}{x}\right) + \pi & x < 0 \end{cases} \\ E &= \arcsin\left(\frac{z}{R}\right) \end{aligned}\right\}. \tag{4}$$

3.3 Build the Particle Filter Algorithm

Through the tracking and measuring system, the relationship between the measured observations and the state vector of the satellite is nonlinear, and the satellite observations are oblique distance, slant distance change rate, azimuth, and elevation angle. Satellite orbit determination means sequential estimation of the location of the satellite based on the observed value of a real-time measurement; the particle filter algorithm used in this paper is to solve the problem of the best estimation of satellite position.

Bias filtering provides a way to describe the tracking problem. The tracking problem can be considered as at the present time t, the state of the target is X_t. Given all observation states $Z^t\{Z_1, \ldots, Z_t\}$, the posterior probability distribution $p(x_t|z^t)$ of the target state is obtained. In the tracking process, the target is often divided into multiple regions (assuming for n) tracking, and this will describe the state of the target for a joint state $X_t \triangleq \{X_{it}\}_{i=1}^{n}$, and at the moment t, the target tracking of the posterior probability distribution formula is as follows:

$$P(X_t|Z^t) = cP(Z_t|X_t) \int P(X_t|X_{t-1})P\left(X_{t-1}|Z^{t-1}\right)\mathrm{d}X_{t-1}. \tag{5}$$

In the formula, $P(Z_t|X_t)$ is for the probability of the observed value Z_t at the given moment t state X_t; $P(X_t|X_{t-1})$ for the motion model represents the probability that the state X_{t-1} of the previous moment $t-1$ is predicted to the current moment t target state X_t.

In the actual calculation, obtaining the integral formula (5) is difficult, so this paper uses the sequential importance resampling (SIR) particle filter [7], to get the integral value by sampling. It is assumed that the moment $t-1$ of the posterior probability distribution $P(X_{t-1}|Z^{t-1})$ can be approximated as number for N-weighted particle, i.e., $P(X_{t-1}|Z^{t-1}) \approx \left\{X_{t-1}^{(r)}, \pi_{t-1}^{(r)}\right\}_{r=1}^{N}$, $\pi_{t-1}^{(r)}$ is the weight of the first r particle, and the integral value of the formula (5) can be approximated by the following Monte Carlo method:

$$P(X_t|Z^t) \approx cP(Z_t|X_t) \sum_r \pi_{t-1}^{(r)} P\left(X_t|X_{t-1}^{(r)}\right). \tag{6}$$

Then, the particle filter can be regarded as an important sampling $X_t^{(s)} \sim q(X_t) \triangleq \sum_r \pi_{t-1}^{(r)} P\left(X_t|X_{t-1}^{(r)}\right)$ of the proposed distribution $q(X_t)$, and posterior probability distribution formula for $P(X_t|Z^t) \approx \left\{X_t^{(s)}, \pi_t^{(s)}\right\}_{s=1}^{N}$, here $\pi_t^{(s)} = P\left(Z_t|X_t^{(s)}\right)$.

4 Algorithm Simulation and Analysis

4.1 Simulation Experiment of Satellite Orbit Determination Based on Particle Filter Model

It is necessary to construct a posteriori probability density function in the particle filter model, in principle it can be completed through two steps by prediction and updating. However, due to the complexity of the probability density function integration, it cannot be achieved in practice. To this end, the following three

methods are adopted: sequential importance sampling method, the preferred importance density function method, and resampling method.

This paper adopts the third method, resampling method. For the resampling method, it adopted three kinds of modeling method, namely the residue sampling method, the minimum variance sampling method, and sampling polymorphism.

Initialization: r = 1… N (N is the number of particles). Random samples are extracted according to prior probability density $p(X_0)$, which obey the normal distribution; Set the initial weights value of $\pi_0^{(r)} = 1/\mathrm{N}$.

4.2 Calculation and Analysis of Simulation Data

A precise orbit calculation program is used to consider the multiple perturbations, and only the gravitational field (4 order) and the solar gravity are taken into account in the orbit determination.

For near earth satellite, range increases random difference and systematic difference of each 20 m; angle measurement increases angular random error and systematic error of the 70″; and velocity measurement increases speed random error; and systematic error is 0.1 m/s, using 2 m data arc. Simulation results of near earth satellite are shown in Table 1 (contains GPS orbit results).

For launch of the synchronous satellite, range increases random difference and systematic difference of each 20 m, and angle measurement increases angular random error and systematic error of the 180″; speed random error and systematic error is 1.0 m/s, 80 s arc length. Simulation results of synchronous satellite launching section are shown in Table 2 (contains GPS orbit results).

Table 1 Perigee satellite simulation and GPS result

Orbit determination method	*a*/(km)	*e*	*i*/(°)	Ω/(°)	ω/(°)	*M*/(°)
Theoretical value	7102.193	0.00103166	98.49868	60.00098	67.34898	79.90475
Particle filter tracking	7101.877	0.00099869	98.52088	59.98408	65.52956	81.72396
Particle filter GPS	7102.171	0.00103098	98.49870	60.00095	67.17730	80.07644

Table 2 Synchronous satellite launch phase simulation and GPS result

Orbit determination method	*a*/(km)	*e*	*i*/(°)	Ω/(°)	ω/(°)	*M*/(°)
Theoretical value	24744.364	0.7339334	24.49899	79.99942	180.01355	1.74250
Particle filter tracking	24736.303	0.7338462	24.51730	80.00519	180.02767	1.74120
Particle filter GPS	24743.979	0.7339291	24.49898	79.99942	180.01406	1.74249

Through the LEO satellite and geosynchronous satellite launch phase tracking and GPS, the simulation data based on this model has shown that particle filter algorithm can be used to solve the nonlinear problem of satellite orbit determination, and will have a great effect on satellite orbit determination to raise the level of valuation.

5 Conclusions

The estimation of satellite orbit is usually based on the assumption that the distribution of state variables is approximated by Gauss distribution, so as to estimate the mean and covariance of the state variables. When the distribution of state variables is obviously not Gauss distribution, the performance of the usual estimation algorithm will be reduced (such as extended Kalman filtering algorithm). In addition, even though the initial distribution of position and velocity is Gauss distribution, the process noise and measurement noise are Gauss white noise. Because of the nonlinearity in the model, the actual distribution of position and velocity is not Gauss distribution. In order to solve the negative influence brought by the nonlinearity of the model and the large estimation of the initial bias on the rail estimation, this paper applies particle filtering algorithm to estimate satellite orbit, and its effectiveness is proved by simulation. At the same time, the algorithm will also have a profound impact on the estimation of the state of satellite fault diagnosis.

References

1. 胡士强, 敬忠良. 粒子滤波算法综述. 控制与决策 (2005) 20(4): 361–365
2. Fredrik G, Niclas B, Urban F, et al. (2002) Particle filters for positioning, navigation and tracking. IEEE Trans Sig Process 50(2): 425–437
3. Arulampalam MS, Maskell S, Gordon N et al (2002) Atutorial on particle filter for online nonlinear/non-gaussian Bayesian tracking. IEEE Trans Sig Process 50(2):174–188
4. Doucet A, Godsill S, Andrieu C (2000) On sequential Monte Carlo sampling methods for Bayesian filtering. Stat Comput 10(3):197–208
5. Steven MK. 统计信号处理基础: 估计与检测理论. 北京: 电子工业出版社 (2003) 11(2): 186–218
6. 章仁为. 卫星轨道姿态动力学与控制. 北京: 北京航空航天大学出版社 (1999) 10(4): 150–178
7. Belviken E, Acklam PJ (2001) Monte Carlo filter for non-linear state estimate. Automatica 37 (01):177–183

A Method for Predicting Satellite Clock Bias Based on EEMD

Zan Liu, Xihong Chen, Jin Liu and Chenlong Li

Abstract In order to improve the accuracy of satellite clock bias (SCB) prediction, a combined model is proposed. In combined model, polynomial model is used to extract the trend of SCB, which can enhance relevance of data and improve efficiency of ensemble empirical mode decomposition (EEMD). Simultaneously, residual data is decomposed into several intrinsic mode functions (IMFs) and a remainder term according to EEMD. Principal component analysis (PCA) is introduced to distinguish IMFs using frequency as a reference, and high-frequency sequence is the sum of IMFs with high frequency, low-frequency sequence is the sum of IMFs with low frequency and the remainder term. Meanwhile, LSSVM model is employed to predict the high-frequency sequence, and other sequence is predicted by GM(1,1) model. The final consequence is the combination of these two models and the SCB's trend. SCBs from four different satellites are selected to evaluate the performance of this combined model. Results show that combined model is superior to conventional model both in 6- and 24-h prediction. Especially, as for Cs clock, it achieves 6-h prediction error less than 3 ns, and 24-h prediction error less than 8 ns.

Keywords Clock bias prediction · EEMD · Principal component analysis · LSSVM · Gray model

1 Introduction

Atomic clock is one of core components in satellite navigation system, which affects the performance of satellite system service. In process of satellite service, satellite clock bias (SCB) between atomic clock of satellite and normal time in the system must be got, which can be used to improve performance of satellite service. As a fact, satellites orbit in space and their clocks cannot compare with time of

Z. Liu (✉) · X. Chen · J. Liu · C. Li
Air and Missile Defense College, Air Force Engineering University, Xi'an, Shannxi, China
e-mail: kgdliuzan@163.com

J. Sun et al. (eds.), *China Satellite Navigation Conference (CSNC) 2017 Proceedings: Volume III*, Lecture Notes in Electrical Engineering 439,
DOI 10.1007/978-981-10-4594-3_2

system continuously, namely SCB may not be acquired in real time. Therefore, predicting SCB plays a significant role in the service of satellite [1–4].

At present, for improving the performance of predicting SCB, several models have been proposed, such as gray model, least square support vector machine (LSSVM) model, autoregressive model, etc. In [1], Cui et al. proposed a prediction model based on gray theory, which had negative performance to predict the SCB with poor stability; and in [2], Liu et al. used LSSVM to predict SCB, which received higher precision. However, the optimal parameters of LSSVM cannot be certain. Autoregressive model was also used to the predict SCB, nevertheless, this model not only based on large-scale data, but also was sensitive to stability of original data.

In order to enhance the performance of SCB prediction model, a combined prediction model is proposed. In the combined model, polynomial model is used to extract the trend of SCB, which can improve not only relevance of data, but also efficiency of ensemble empirical mode decomposition (EEMD). Then, EEMD is used to decompose the residual data into several intrinsic mode functions (IMFs) and a remainder term. The two sequences with high and low frequencies are reconstructed according to principal component analysis (PCA). Finally, LSSVM model is employed to predict the high-frequency sequence. As well, the low-frequency sequence is predicted by the GM(1,1) model. The final consequence is the combination of these models.

2 Combined Clock Bias Prediction Model

In this paper, we use the EEMD combined with LSSVM model and GM(1,1) model to predict the SCB, and these three models are presented as follows, respectively.

2.1 EEMD Model

Empirical mode decomposition (EMD) can decompose the complicated signal into intrinsic mode functions (IMFs), which bases on the local characteristic timescales of a signal [5–7]. However, the problem of mode mixing exists in EMD. Mode mixing is defined as a single IMF including oscillations of dramatically disparate scales, or a component of a similar scale residing in different IMFs. So ensemble empirical mode decomposition (EEMD) is introduced to eliminate the mode mixing phenomenon and obtain the actual time–frequency distribution of seismic signal. EEMD adds white noise to the data, which distributes uniformly in the whole time–frequency space. The bits of signals of different scales can be automatically designed onto proper scales of reference established by the white noises. EEMD can decompose the signal $f(t)$ into the following style:

$$f(t) = \sum_{i=1}^{n} h_i(t) + r_n(t), \tag{1}$$

where $h_i(t)$ stands for different IMFs with different frequencies. Therefore, the different IMFs represent the natural oscillatory mode embedded in the signal.

SCB of satellite PRN09 during July 10–12 in 2012 is used to analyze the effect of EEMD. First, the trend removal is extracted from original data, and then, EEMD is used to manage the residual part, and consequence is shown in Fig. 1.

As shown in Fig. 1, EEMD can decompose the original into IMFs with different frequencies. For accurately distinguishing the frequency of IMFs, PCA is introduced. The concrete steps are described as follows:

Step 1 EEMD is used to decompose data into several IMFs and a remainder term.

Step 2 The consequence of EEMD is $\mathbf{X} = [\mathbf{x}_1, \mathbf{x}_2, \ldots, \mathbf{x}_n]$, here $\mathbf{x}_i = [x_1, x_2, \ldots, x_m]^{\mathrm{T}}$. Covariance can be acquired by the equation $\mathbf{\Omega}_{m\times m} = E\{\bar{\mathbf{X}}_{m\times n}\bar{\mathbf{X}}_{n\times m}^{\mathrm{T}}\}$, where $\bar{\mathbf{X}}_i = \mathbf{x}_i - E(\mathbf{x}_i)$.

Step 3 Singular value decomposing $\mathbf{\Omega}$ can be acquired by $\mathbf{\Omega} = \mathbf{\Phi}\mathbf{\Lambda}\mathbf{\Phi}^{\mathrm{T}}$, where $\mathbf{\Lambda} = \mathrm{diag}(\lambda_1, \lambda_2, \ldots, \lambda_m)$, $\Phi = (\boldsymbol{\varphi}_1, \boldsymbol{\varphi}_2, \ldots, \boldsymbol{\varphi}_m)$, respectively. Meanwhile, $\lambda_i(\lambda_1 > \lambda_2 > \cdots > \lambda_m)$ is the characteristic of $\mathbf{\Omega}$, and $\boldsymbol{\varphi}_i$ is the feature vector corresponding to evaluate λ_i, respectively.

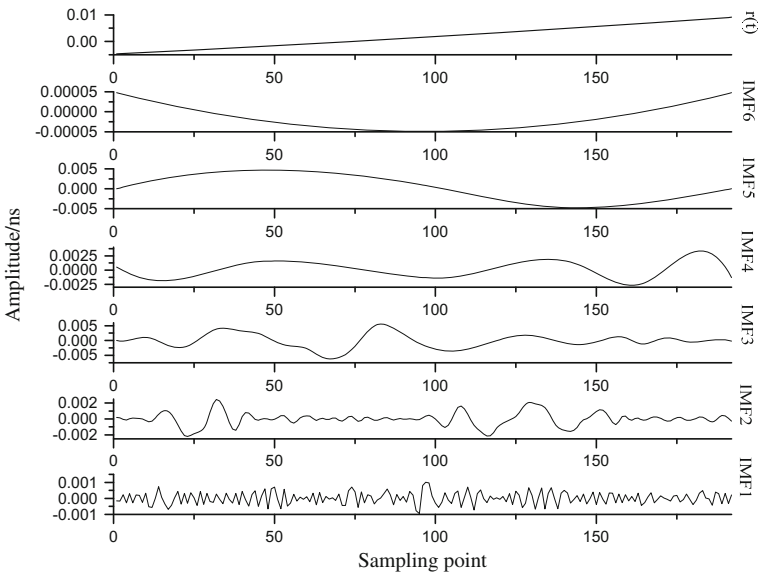

Fig. 1 Consequence of EEMD

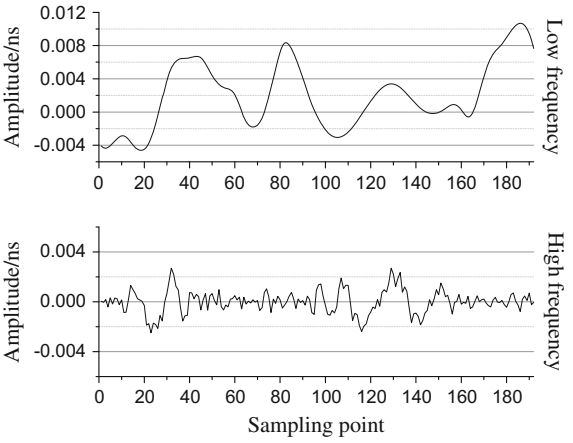

Fig. 2 Consequence of reconstruction

Step 4 Define $\mathbf{P} = \mathbf{\Phi}^{\mathbf{T}}\bar{\mathbf{X}}$, $\mathbf{P} = (\mathbf{p}_1^{\mathrm{T}}, \mathbf{p}_2^{\mathrm{T}}, \ldots, \mathbf{p}_m^{\mathrm{T}})^{\mathrm{T}}$, here $\mathbf{p}_i$ is the principal component of $\bar{\mathbf{X}}$. The value of $\lambda_i / \sum_{i=1}^{m} \lambda_i$ stands for contribution rate of $\mathbf{p}_i$, here λ_i is the characteristic value of $\mathbf{p}_i$.

Step 5 If parameter β meets $\Delta\lambda_\beta > \overline{\Delta\lambda}$, where $\Delta\lambda_i = \lambda_i - \lambda_{i+1}$, and

$$\overline{\Delta\lambda} = \frac{1}{n-1} \sum_{i=1}^{n-1} \Delta\lambda_i \tag{2}$$

The sequence with high frequency can be the sum of first β IMFs. As well, the sequence with low frequency is the sum of remainder sequences.

The data in Fig. 1 is also used to analyze this signal reconstruction algorithm, and result is exhibited as follows.

The consequence in Fig. 2 indicates that PCA is available to reconstruct the IMFs.

2.2 *LSSVM Model*

According to LSSVM model [8–10], $T = \{x_i, y_i\}_1^n$, where $x_i \in \mathbf{R^n}$ and $y_i \in \mathbf{R}$ are the input and output data, respectively. x_i is made for nonlinear mapping according to $F(x) = \omega^T \varphi(x) + b$, where φ denotes nonlinear mapping function, ω denotes weight vector, and b denotes mapping bias, respectively. The constraint condition and an optimization objective function of LSSVM are defined as

$$\begin{cases} \min\limits_{\omega,\xi} J = \frac{1}{2}\omega^T\omega + \frac{c}{2}\sum\limits_{i=1}^{l}\xi_i^2 \\ y_i = \omega^T\varphi(x_i) + b + \xi_i \end{cases}. \tag{3}$$

Lagrange function is introduced to solve Eq. 3, where ω, b, ξ, α can be expressed as

$$\begin{bmatrix} 0 & \mathbf{A}^T \\ \mathbf{A} & K + C^{-1}\boldsymbol{I} \end{bmatrix} \begin{bmatrix} b \\ \boldsymbol{\alpha} \end{bmatrix} = \begin{bmatrix} 0 \\ \boldsymbol{y} \end{bmatrix}, \tag{4}$$

where $\mathbf{A} = [1, 1, \ldots, 1]^T$, $\boldsymbol{\alpha} = [\alpha_1, \alpha_2, \ldots, \alpha_n]^T$, $\mathbf{Y} = [y_1, y_2, \ldots, y_n]^T$, $\boldsymbol{I}$ denotes identity matrix, C represents penalty factor, and $K = K(x_k, x_l)$ is the kernel function, respectively. $\boldsymbol{\alpha}, b$ can be acquired from Eq. 4. Therefore, the final LSSVM prediction model can be represented as

$$f(x) = \sum_{i=1}^{l} \alpha_i K(x, x_i) + b. \tag{5}$$

Parameters C and σ in LSSVM model can be acquired basing on the cross searching mechanism.

2.3 GM(1,1) Model

GM(1,1) model is one of conventional gray models, which has advantage on calculation speed. As well, building GM(1,1) model needs less data [8, 10, 11]. In GM(1,1) model, $\boldsymbol{x}^{\mathbf{1}}$ can be acquired using original data after their accumulation. Considering characteristic of $\boldsymbol{x}^{\mathbf{1}}$, differential equation is shown as follows:

$$\frac{d\boldsymbol{x}^1(t)}{dt} + a\boldsymbol{x}^1(t) = u, \tag{6}$$

where a and u are the parameters of GM(1,1) model, which can be acquired using least square criterion (LSC). The final GM(1,1) model can be expressed as

$$\hat{x}^0(k) = \mathrm{e}^{-a(k-1)} \cdot \left[x^0(1) - \frac{u}{a}\right] \cdot (1 - \mathrm{e}^a), \tag{7}$$

where $\boldsymbol{x}^{\mathbf{1}}(k)$ stands for the kth element in the primitive sequence. According to LSC, the estimated value of parameters can be acquired by the following:

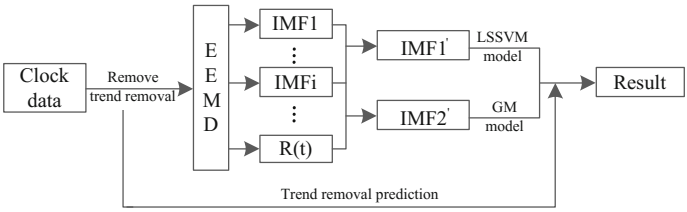

Fig. 3 The flow of the combined model

$$\begin{cases} [\hat{a},\hat{u}]^T = (G^T G)^{-1} Y_n \\ G = [-Z(K+1),1]_{(n-1)\times 2} \\ Z(K+1) = [x^1(k+1) + x^1(k)]/2 \\ Y_n = [x^1(2),\ldots,x^1(n)]^T \end{cases}. \tag{8}$$

2.4 Flow of Combined Model

The flow of the combined SCB prediction model proposed in this paper is shown in Fig. 3.

The particular flow of this combined SCB prediction model is described as follows:

Step 1 Trend removal of the clock bias is removed on the basis of polynomial model, which can increase the relevance of original clock bias data and enhance the efficiency of EEMD.

Step 2 EEMD is used to decompose residual data into several IMFs and a remainder term. As well, two sequences with high and low frequency are reconstructed according to PCA.

Step 3 LSSVM model is employed to predict the high-frequency sequence. Meanwhile, the low-frequency sequence is predicted by GM(1,1) model.

Step 4 The final consequence is the combination of these two models and a trend removal.

3 Accuracy of Combined Model

3.1 Selecting Clock Bias Data

For evaluating this combined model, satellite data announced by international GNSS service (IGS) are used. To be fair, we randomly select four satellites with different types of clock from July 10 to July 12, 2012. The selected satellites with different clocks are displayed in Table 1.

SCBs of different clocks are shown in Fig. 4.

Table 1 Satellites correspond to different clocks

Type	Rb clock	Cs clock
ID	PRN01,06	PRN09,10

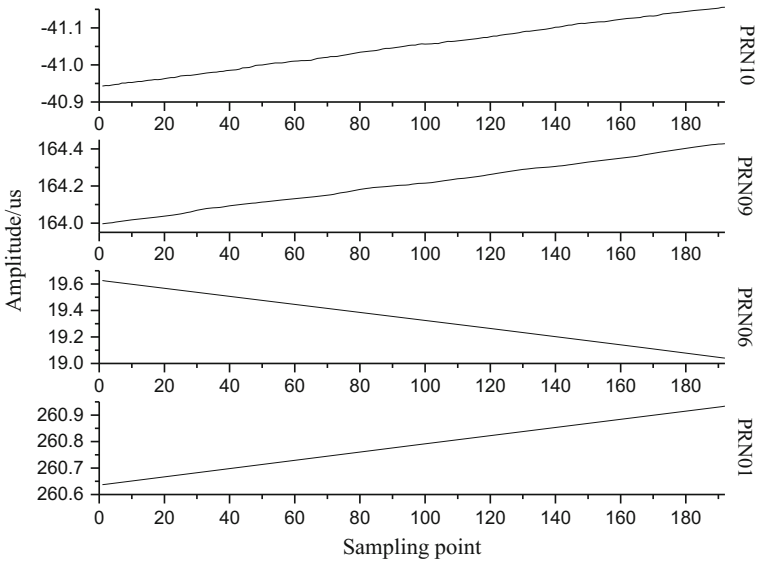

Fig. 4 Original SCB data

3.2 Results Analysis

Considering individual atomic clocks have different frequencies of offset characteristics, polynomials with different orders are used to precisely remove the trend removal of SCB. Relationship between order of polynomial and atomic clocks is defined as

$$x(t) = a + bt + \beta \cdot \frac{ct^2}{2}, \quad \beta = \begin{cases} 1, \text{ Rb} \\ 0, \text{ Cs} \end{cases}. \tag{9}$$

SCBs are used to establish polynomial model, GM(1,1) model and combined model proposed in this paper, respectively. At same time, for improving accuracy of GM(1,1) model, SCB with decreasing trend or minus amplitude must be managed.

First, SCBs of all four satellites during first 42 h are used to establish these models, and data during last 6 h are used to test consequences. Prediction errors are shown as follows.

Then, SCBs of PRN01 and PRN09 during first 24 h are selected to establish those three models, and SCBs during last 24 h are used to test these models. Prediction errors are shown in Fig. 6.

The absolute mean errors (ME) of different models are expressed as follows.

In Table 2, "PN" denotes polynomial model, "GM" denotes GM(1,1) model, and "Combined" denotes combined model, respectively.

As demonstrated in Figs. 5, 6, and Table 2, we can conclude that

1. SCB prediction in 6 h: max error of combined model is less than 3 ns, which is superior to GM(1,1) model and polynomial model.

Table 2 The mean error of prediction

Length (h)	ID	PN	GM	Combined
6	PRN01	0.25	0.46	0.07
	PRN06	2.49	4.07	0.18
	PRN09	11.14	6.55	0.04
	PRN10	1.57	2.49	0.61
24	PRN01	0.29	0.22	0.20
	PRN10	11.13	3.59	1.19

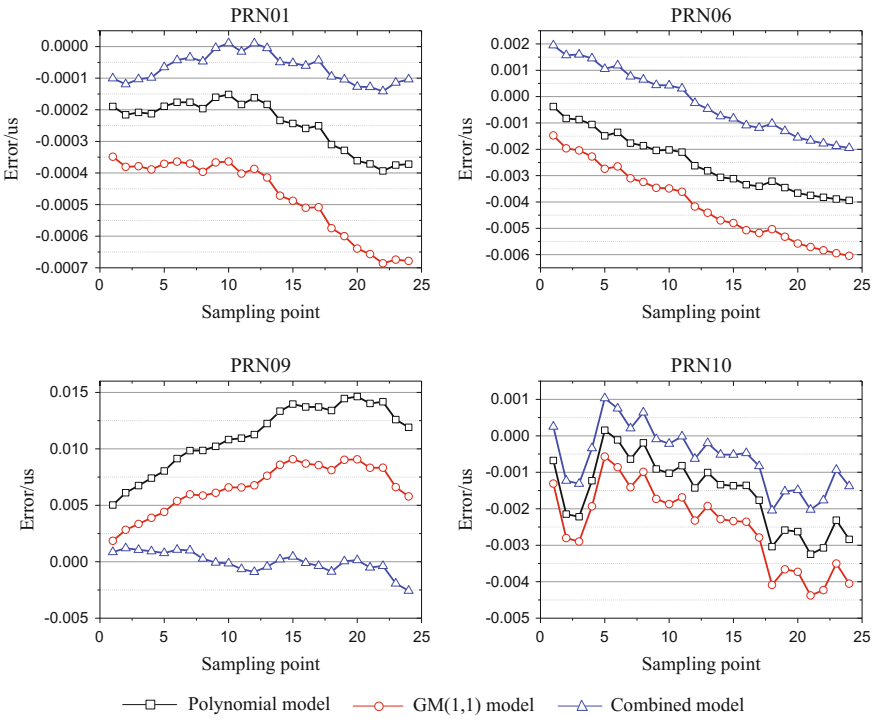

Fig. 5 Prediction errors of 6 h

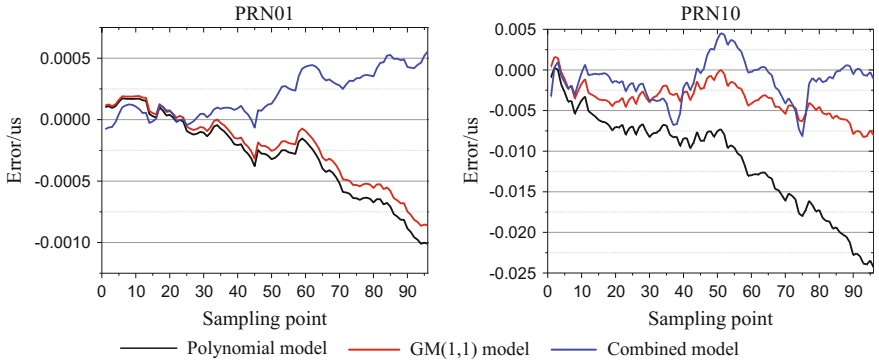

Fig. 6 Prediction errors of 24 h

2. SCB prediction in 24 h: max error of combined model is less than 8 ns, which is also superior to GM(1,1) model and polynomial model. Constant error compensation of the latter two models is obvious.
3. As for Rb clock, maximum ME is less than 0.6 ns during 6-h prediction, and ME is less than 0.9 ns during 24-h prediction. As for Cs clock, ME is less than 0.9 ns during 6-h prediction, and ME is less than 5.7 ns during 24-h prediction. The mean error of combined model is superior to other two models. Accuracy of mean error is improved to 0.18–6.51 ns for Rb clock and 0.02–9.04 ns for Cs clock, respectively.
4. Simulation also shows that the improved model has superior performance in predicting Rb atomic clock than Cs atomic clock. The relatively poor performance results from the negative stability of Cs atomic clock.

4 Conclusion

In this paper, we propose a combined SCB prediction model. In combined model, polynomial model is used to extract the trend of SCB, and then, EEMD is used to decompose the residual data into several IMFs and a remainder term. Two sequences with different frequencies are reconstructed using IMFs according to PCA. Finally, LSSVM model and GM(1,1) model are employed to predict these sequences, respectively. The different SCBs provided by IGS are used to evaluate this combined model. Results indicate that the improved model is superior to conventional models, and accuracy can meet the requirement of satellite service. Meanwhile, compared with traditional combined models, this new combined model does not need to set any parameters.

Acknowledgements The work was supported by the National Natural Science Foundation of China (No. 61671468). The authors are very grateful to the reviewers for their insightful and professional suggestions to this paper, and we also would like to thank IGS for granting access to SCB data.

References

1. Cui X, Jiao W (2005) Grey system model for the satellite clock error predicting. Geomatics Inf Sci Wuhan Univ 30(5):447–450
2. Liu Z, Chen X, Xue L et al (2015) Prediction of satellite clock errors based on GM-LSSVM improved by IPSO. Sci Surveying Mapp 40(9):115–119
3. Lou Y, Zhang W, Wang C et al (2014) The impact of orbital errors on the estimation of satellite clock errors and PPP. Adv Space Res 54(8):1571–1580
4. Huang G, Zhang Q (2012) Real-time estimation of satellite clock offset using adaptively robust Kalman filter with classified adaptive factors. GPS Solut 16:531–539
5. Wenbo W, Xiaodong Z, Xiangli W (2013) Empirical mode decomposition denoising method based on principal component analysis. Acta Electronica Sinica, 2013, 41(7): 1425–1430
6. Lei Y, He Z, Zi Y (2011) EEMD method and WNN for fault diagnosis of locomotive roller bearings. Expert Syst Appl 38(6):7334–7341
7. Jinde Z, Junsheng C, Yu Y (2014) Partly ensemble empirical mode decomposition: an improved noise-assisted method for eliminating mode mixing. Sig Process 96: 362–374
8. HongQiao W, FuChun S, YanNing C et al (2014) An unbiased LSSVM model for classification and regression. Soft Comput 14(2):171–180
9. Ahmadi MA, Rozyn J, Lee M et al (2016) Estimation of the silica solubility in the superheated steam using LSSVM modeling approach. Environ Progress Sustain Energy 35 (2):596–602
10. Silva DA, Neto ARR (2015) A genetic algorithms-based LSSVM classifier for fixed-size set of support vectors. Lect Notes Comput Sci 9095(1):127–141
11. Huang GW, Zhang Q, Xu GC (2014) Real-time clock offset prediction with an improved model. GPS Solut 18:95–104

Estimation, Validation, and Application of 30-s GNSS Clock Corrections

Rengui Ruan, Ziqing Wei and Xiaolin Jia

Abstract High-rate precise satellite clock corrections are essential for precise point positioning (PPP) with global navigation satellite system (GNSS), especially for kinematic PPP (KPPP) for low earth orbiting satellites or moving vehicles on the ground where positioning precision of a few centimeters is demanded. To estimate high-rate clock corrections in a full network solution using zero-difference observations from a large tracking network (e.g., 100 stations) is quite time-consuming which even goes worse with increasing satellites. An efficient approach with estimation of high-rate epoch-difference clocks and a densification procedure to compute high-rate zero-difference clocks based on lower rate zero-difference clocks is developed at Xi'an Research Institute of Surveying and Mapping (XISM) to routinely produce 30-s "rapid" and "final" satellite clocks for the existing GNSS: GPS, GLONASS, BDS, and Galileo. In this paper, basic principle and data processing procedure are described in detail. The GPS clocks at XISM are compared with IGS final clocks to validate their quality and it is demonstrated that both the XISM 30-s and 5-min clocks are in essence the same in quality as clocks provided by IGS analysis centers. When the XISM clocks are used to assess the frequency stability performance of GPS satellites, a good agreement with IGS final clocks is again demonstrated,which further confirms the good quality of clock products at XISM. With the 30-s clocks, the frequency stability performance of GPS, GLONASS, BDS, and Galileo satellites is assessed for a time interval ranging from 30 s to about 15,000 s, which demonstrate a pretty good stability performance of BDS satellites for short intervals, even superior to GPS Block IIR and GLONASS-M satellites. Finally, experiments for KPPP with individual GPS, GLONASS, or BDS are conducted with the XISM 30-s and 5-min clocks to evaluate the impact of clock

R. Ruan (✉)
Institute of Surveying and Mapping, Information Engineering University, Zhengzhou 450001, China
e-mail: rrg2002me@163.com

R. Ruan · Z. Wei · X. Jia
State Key Laboratory of Geo-Information Engineering, Xi'an 710054, China

R. Ruan · Z. Wei · X. Jia
Xi'an Research Institute of Surveying and Mapping, Xi'an 710054, China

J. Sun et al. (eds.), *China Satellite Navigation Conference (CSNC) 2017 Proceedings: Volume III*, Lecture Notes in Electrical Engineering 439,
DOI 10.1007/978-981-10-4594-3_3

sampling rate. The result shows that, compared with the result with 5-min clocks, 3D repeatability with 30-s clocks is improved by about 67, 72, and 24% for GPS-, GLONASS-, and BDS KPPP, respectively, and it is interesting that when using 5-min clocks, KPPP with BDS has better repeatability performance than using GPS or GLONASS, which may benefit from the comparative good stability performance of almost the whole BDS constellation for short time interval.

Keywords GNSS · Satellite clock · Epoch-difference · Clock densification · Frequency stability · Kinematic precise point positioning

1 Introduction

Precise satellite clock product is essential for precise point positioning (PPP) [17] applications using the global navigation satellite system, e.g., GPS, GLONASS, BDS, or Galileo. Previous research indicates the result of PPP, especially kinematic PPP (KPPP), is sensitive not only to the accuracy but also to the sampling rate of satellite clock corrections [2, 17, 10]. It has been suggested that, in order to achieve KPPP result at cm level, the GPS clock sampling interval should be smaller than 60 s [17], whereas for precise orbit determination (POD) for low earth orbiting satellites like the CHAMP, GRACE, and GOCE, GNSS satellite clocks with the same sampling rate as the observation are necessary [8].

Although the International GNSS Service (IGS) has start to provide precise GPS satellite orbit and clock product (15 min sampled in SP3 format) since their beginning in late 1993, it is not until GPS week number (WN) 0983 (Nov 8, 1998), GFZ (German Research Centre for Geosciences), one of the analysis centers (ACs) of the IGS, first start to provide their 5-min satellite and station clocks in RINEX format and not until GPS WN 1010 (May 16, 1999), JPL (Jet Propulsion Laboratory) start to contribute 30-s satellite clocks. The combined IGS clocks with 5-min and 30-s sampling are even later and not available until WN1085 (Oct 22, 2000) and WN1406 (Dec 17, 2006), respectively. Nowadays, along with the modernization of GPS, constellation reconstruction and modification of GLONASS, development of BDS, Galileo, and several regional navigation systems such as QZSS and NAVIC, people on the earth are stepping into the age of multi-GNSS. In order to support the applications of multi-GNSS, a project named Multi-GNSS Experiment (MGEX) [9] was set up by the IGS and five ACs start to provide GNSS products including satellite cocks. In order to monitor the status and assess the performance of GNSS, the International GNSS Monitoring and Assessment System (iGMAS) [4] was proposed and established and more than 13 institutions participate in as analysis centers and start to provide precise products for GNSS (till now only for GPS, GLONASS, Galileo and BDS). Since the estimation of high-rate clocks using zero-difference observation from a large tracking network (e.g., 100 stations) is quite time-consuming which even goes worse with increasing satellites, among the 13 iGMAS ACs, only three ACs, i.e., IGG (Institute of

Geodesy and Geophysics, Wuhan, China), TLC (Beijing Space Information Relay and Transmission Technology Research Center, Beijing, China), and XISM (Xi'an Research Institute of Surveying and Mapping, Xi'an, China, since DOY 162 2016), provide 30-s clocks for GPS, GLONASS, BDS, and Galileo satellites, while among the five IGS/MGEX ACs only two ACs, GFZ and CNES (Centre National d'Etudes Spatiales), contribute 30-s clocks for GPS, GLONASS, and Galileo, and only GFZ generate 30-s satellite clocks for BDS and QZSS.

In order to estimate 30-s satellite clocks for GPS, GLONASS, Galileo, and BDS simultaneously, an efficient approach similar to that used by CODE (Center for Orbit Determination in Europe) [2, 3] is developed at XISM. In this paper, basic principle and data processing procedure are introduced and summarized in Sect. 2. Then in Sect. 3 the clock product at XISM is validated by comparison with IGS clocks and applied to assess the frequency stability performance of GNSS satellites, and experiments are conducted to evaluate the influence of clock sampling rate on KPPP with individual GPS, GLONASS, and BDS. Finally, in Sect. 4, a brief summary is given.

2 Basic Principle and Data Processing Procedure

2.1 Estimation of Zero-Difference Clock

In order to eliminate the ionosphere delay, the ionosphere-free linear combination (IFLC) of code and carrier phase observation are usually used for orbit determination and clock estimation for GNSS satellites and many other geodetic applications. The IFLC for satellite s observed at station r can be expressed in meters (somewhat simplified and without error term) as [5]

$$\begin{aligned} \phi_r^s(i) &= \rho_r^s(i) + \delta_r(i) - \delta^s(i) + B_r^s + m_r^s(i) \cdot T_r(i) \\ p_r^s(i) &= \rho_r^s(i) + \delta_r(i) - \delta^s(i) + m_r^s(i) \cdot T_r(i) + \Delta_r, \end{aligned} \tag{1}$$

where

ϕ_r^s is the IFLC of observed code pseudorange,
p_r^s is the IFLC of observed carrier phase,
ρ_r^s is the slant distance,
δ_r is the station clock parameter,
δ^s is the satellite clock parameter,
B_r^s is the phase bias parameter (PBP), superposition of the phase ambiguity and the equipment delay on both satellite and receiver,
m_r^s is the mapping function for troposphere delay,
T_r is the zenith troposphere delay (ZTD), and
Δ_r is the inter-system bias (ISB) of multi-GNSS receiver.

The subscripts r refer to stations; the superscripts s refer to satellites; and i is the epoch number of the measurement.

After necessary model correction and linearization for the above IFLC observations, based on the least-square method, the station and satellite clocks can be estimated, together with other unknown parameters: the ZTDs, PBPs, ISBs, satellite orbits (ORBs), station coordinates (CRDs), earth rotation parameters (ERPs), and so on, if they are not precisely known in advance which is very the case in data processing for POD with software packages using zero-difference observation such as GIPSY, EPOS, etc. Nevertheless, for some software tools, e.g., GAMIT and Bernese, the double-difference observations are used for POD to estimate the ZTDs, double-difference PBPs, ORBs and ERPs, and a separate procedure must be conducted to estimate the zero-difference clocks with the following corrected observation:

$$\begin{aligned}\tilde{\phi}_r^s(i) &= \phi_r^s(i) - \hat{\rho}_r^s(i) - m_r^s(i)\cdot\hat{T}_r(i) = \delta_r(i) - \delta^s(i) + B_r^s \\ \tilde{p}_r^s(i) &= p_r^s(i) - \hat{\rho}_r^s(i) - m_r^s(i)\cdot\hat{T}_r(i) - \hat{\Delta}_r = \delta_r(i) - \delta^s(i),\end{aligned} \tag{2}$$

where $\tilde{\phi}_r^s$ and $\tilde{p}_r^s$ are the corrected phase and code observation for zero-difference clock estimation; $\hat{\rho}_r^s$ is the slant distance calculated with previously estimated ORBs, CRDs, and ERPs; $\hat{T}_r$ is the estimated ZTD; and $\hat{\Delta}_r$ is the estimated ISB if there is.

Regardless of using Eq. (1) or (2), the epoch-wise clock parameters are usually modeled as a process of white noise and can be pre-eliminated from the normal equation system (NES), which dramatically reduce the dimension of the NES. In order to avoid the NES to become singular due to lack of time datum, a satellite or station clock is set up as the reference clock. Other parameters, especially PBPs, in Eqs. (1) and (2), comprise the majority of the unknown parameters in the NES which greatly increase the dimension of the NES and make the estimation of zero-difference clock with (2) or (1) (simultaneously for POD) a time-consuming task. Therefore, the zero-difference clocks are usually estimated at a low sampling rate, e.g., 5 min.

2.2 *Estimation of Epoch-Difference Clock*

As mentioned above, due to the existence of PBPs, it is quite time-consuming to directly estimate the zero-difference clock parameters with Eq. (2) at a high sampling rate, e.g., 30 s, especially for large network and the situation goes even worse for multi-GNSS. A more reasonable and effective approach is to estimate epoch-difference clocks first and then the zero-difference clocks for each epoch can be obtained by a densification approach with the higher sampled epoch-difference clocks and the lower sampled zero-difference clocks estimated with zero-difference observations.

In order to estimate epoch-difference clocks, epoch-difference phase observations are constructed to eliminate the phase bias parameters [2]:

$$\Delta\tilde{\phi}_r^s(i) = \tilde{\phi}_r^s(i) - \tilde{\phi}_r^s(i-1) = \Delta\delta_r(i) - \Delta\delta^s(i); (i = 1, 2, \ldots n), \tag{3}$$

where Δ is the operator of epoch-difference, i.e., $\Delta x(i) = x(i) - x(i-1)$. With Eq. (3), neglecting the correlation between the consecutive epoch-difference observations, the epoch-difference station and satellite clocks, $\Delta\delta_r(i)$ and $\Delta\delta^s(i)$, can be effectively estimated with the classical least-square method. Just like the case for zero-difference clock estimation, in order to avoid the singularity of the NES, a satellite or station clock should be set up as the reference clock. Since the possible existence of cycle slip, quality control is quite essential in data processing for epoch-difference observation.

2.3 Clock Densification

In order to calculate high-sampled zero-difference clocks, the lower sampled zero-difference clock solution: $\tilde{\delta}_r(j \cdot k)$ and $\tilde{\delta}^s(j \cdot k)$ $(j = 0, 1, 2, \ldots;\ k$ is the resampling interval for determination of low sampled zero-difference clocks) and the high-sampled epoch-difference clock solution: $\Delta\tilde{\delta}_r(i)$ and $\Delta\tilde{\delta}^s(i)$ $(i = 1, 2, \ldots)$ should be combined in an approach of clock densification. The densification for satellite and station clocks is just the same. For a particular clock, omitting its subscript or superscript, the high-sampled zero-difference clocks for epoch i in the interval from $j \times k + 1$ to $j \times k + k - 1$ can be estimated by solving the following equations:

$$\begin{bmatrix} 1 & & & & & \\ -1 & 1 & & & & \\ & -1 & 1 & & & \\ & & \ddots & \ddots & & \\ & & & -1 & 1 & \\ & & & & & 1 \end{bmatrix} \cdot \begin{bmatrix} \delta(j \cdot k) \\ \delta(j \cdot k + 1) \\ \delta(j \cdot k + 2) \\ \vdots \\ \delta(j \cdot k + k) \end{bmatrix} = \begin{bmatrix} \tilde{\delta}(j \cdot k) \\ \Delta\tilde{\delta}(j \cdot k + 1) \\ \Delta\tilde{\delta}(j \cdot k + 2) \\ \vdots \\ \Delta\tilde{\delta}(j \cdot k + k) \\ \tilde{\delta}(j \cdot k + k) \end{bmatrix}. \tag{4}$$

The correlation between the consecutive epoch-difference clocks, as well as the correlation between the epoch-difference clocks and the zero-difference clocks with common zero-difference observation involved, is again neglected. The weights for the pseudo-observation $\Delta\tilde{\delta}(i)$ are taken from the a posteriori variance values of the epoch-difference clock solution:

$$p_{\Delta\tilde{\delta}(i)} = p_i = \frac{\sigma_0^2}{\sigma_{\Delta\tilde{\delta}(i)}^2}, \tag{5}$$

where σ_0^2 is the variance of the unit weight. In order to fix the endpoint values to the lower sampled zero-difference solution, the pseudo-observations $\tilde{\delta}(j \cdot k)$ are strongly constrained with heavy weight:

$$p_{\tilde{\delta}(j \times k)} \gg p_{\Delta\tilde{\delta}(i)}. \tag{6}$$

It is important to note that the zero-difference clocks and the epoch-difference clocks can be combined is preconditioned by that they are referenced to the same reference clock which is not yet guaranteed in their separated estimation procedures and therefore before being used to estimate the high-sampled zero-difference clocks, they must be realigned to the same reference clock, e.g., a reference station clock, with the following formulas:

$$\begin{aligned} \tilde{\delta}(j \cdot k) &:= \tilde{\delta}(j \cdot k) - \tilde{\delta}_{\text{ref}}(j \cdot k) \\ \Delta\tilde{\delta}(i) &: = \Delta\tilde{\delta}(i) - \Delta\tilde{\delta}_{\text{ref}}(i), \end{aligned}$$

where the subscript ref refers to the reference station.

2.4 Clock Estimation Procedure at XISM

Since Jan 2015, XISM starts to routinely process GNSS (GPS/GLONASS/BDS/Galileo) observation data collected from global distributed stations. A series of products including satellite orbits and clocks, CRDs, ERPs, ZTDs, global ionosphere maps (GIM), and differential code bias (DCB) are delivered to the iGMAS and all of the products except for the GIMs and FCBs are computed using the satellite positioning and orbit determination system (SPODS) developed at XISM [11, 15]. The key models, methods, and strategies applied were introduced in detail in [11, 15]. The GNSS clock determination is a part of a large number of daily processing tasks at XISM. Since DOY 162 2016, satellite clocks with 30-s sampling rate for GPS, GLONASS, BDS, and Galileo are routinely estimated with time latency of $\sim$12 h as the "rapid" product and 7 days as the "final" product, respectively. Regardless of the time delay, the clock estimation procedures for rapid and final products at XISM are the same and conducted in the following steps:

- **PREP**: Pre-processing of GNSS observation data,
- **POD**: Precise orbit determination with 5-min sampled data,
- **EEDC**: Estimation of epoch-difference clocks, and
- **CD**: Clock densification from 5 min to 30 s.

Figure 1 shows the flow chart for the rapid and final 30-s sampled GNSS satellite clocks at XISM. Dual-frequency observations with 30-s sampling rate from about 80 stations operated by IGS/MGEX and iGMAS are collected and, in the

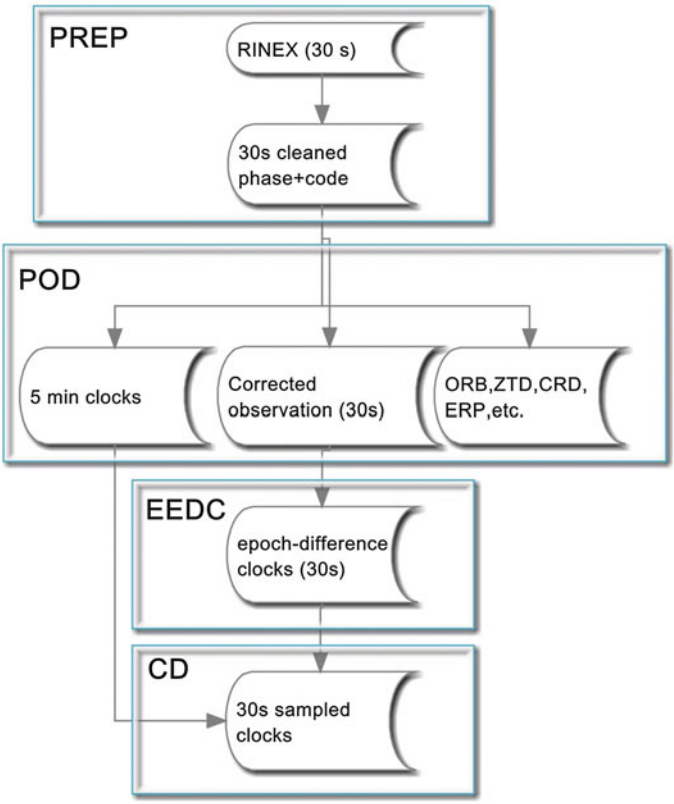

Fig. 1 Flow chart for 30-s clock estimation at XISM

PREP step, pre-processed to detect the cycle slips and outliers with a procedure similar to the TurboEdit [1] approach. In the **POD** step, the cleaned observation is precisely modeled with various corrections including PCO&PCV [12], the phase wind-up effect [16], site-displacement caused by the tidal effect (McCarthy and Petit [7]), etc. and then they are decimated to 5 min to estimate all the unknown parameters including station and satellite clocks, ORBs, CRDs, ZTDs, ERPs, and so on. In this step, the corrected observations with 30-s sampling rate containing information of clocks and PBPs are also generated as input to the **EEDC** step to estimate the epoch-difference clocks. In the **CD** step, the 5-min sampled zero-difference clocks and the 30-s sampled epoch-difference clocks from the previous two steps are combined and produced 30-s sampled zero-difference clock products. In this procedure, the 30-s clocks are just the external product of the **POD** step because all the necessary data are generated in the procedure for POD.

3 Validation and Application of Clocks at XISM

3.1 GPS Clock Comparison with IGS Clocks

The IGS final clocks, known having the highest quality, is combined based on high-quality clock products from its ACs, and are usually used to assess the performance of satellite clocks and to evaluate the quality of products from individual ACs. Since the IGS only provides combined GPS clocks, in this paper, the clock comparison method is only used to assess the quality of the GPS clocks generated at XISM. We calculate the differences between XISM clock products and the IGS final clocks and two statistic indicators: STD and RMS are used to measure the quality of the clocks. For the sake of comparison, the two indicators for the final clock products provided by IGS ACs are also computed. Figures 2 and 3, respectively, show the daily RMS and STD of final clock products from XISM and IGS ACs with respect to IGS final clock products during DOY 1–321 in 2016. It can be seen that the daily RMSs of XISM clock products are between 0.15 and 0.3 ns and is larger than most of the IGS ACs except for MIT, whereas the daily STDs are smaller than 0.05 ns and are as better as most of the IGS ACs. It should be emphasized that, since DOY 162 2016, the clocks at XISM are at a sampling rate of 30-s, and from the two figures, it is safe to conclude that the new 30-s clock products keep the same quality of the former 5-min products.

3.2 Allan Variance Analysis

An important application of precise satellite clocks is to assess the performance of GNSS satellite clocks and a number of specialized statistics have been developed for evaluating the performance of clocks (or clock products), including the Allan

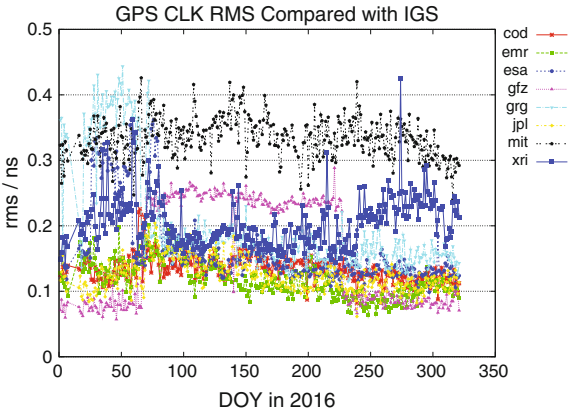

Fig. 2 Daily RMS of final clock products from XISM and IGS ACs with respect to IGS final clock products

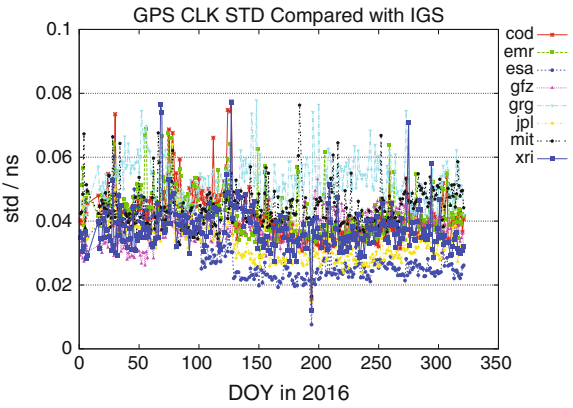

Fig. 3 Daily STD of final clock products from XISM and IGS ACs with respect to IGS final clock products

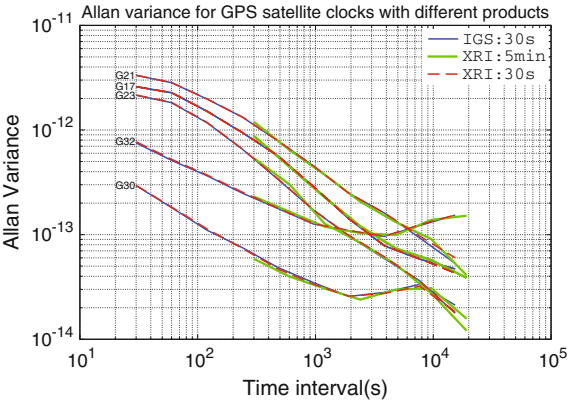

Fig. 4 Frequency instability (Allan variance) of five representative GPS satellites on DOY 234 2015 using IGS final 30-s clocks and XISM final 30-s and 5-min clocks

deviation, the modified Allan deviation, and the Hadamard deviation [6, 13]. Figure 4 shows the Allan variance (or square-root for Allan deviation) on DOY 234 2015 for five GPS satellite clocks (G32, G21, G23, G17, and G30), representing satellite groups of GPS Block IIA (Cesium), Block IIR-A (Rubidium), Block IIR-B (Rubidium), Block IIR-M (Rubidium), and Block IIF (Rubidium), respectively. In this figure, the Allan variances calculated with XISM final 30-s and 5-min clocks and IGS final 30-s clocks are plotted with different line types. It is easy to find that the instabilities of the newer Block IIR-A/B/M satellites are poorer than the older Block IIA satellite for intervals up to $\sim$1000 s. The performance of the newest Block IIF satellite is superior to Block IIR especially for intervals smaller than 5000 s. It is immediately evident that the lines with XISM clocks are nearly coincide with those using IGS clocks, which indicates XISM clocks are of the same quality as IGS clocks and, therefore, can be used to assess the clock performance of GNSS satellites.

Figure 5 shows the Allan variances calculated with XISM 30-s clocks for all BDS satellites (except for C11 and C13) and several representative GPS

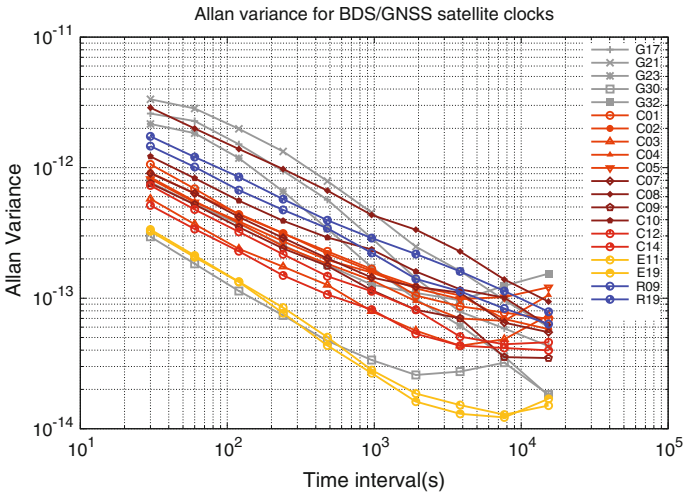

Fig. 5 Frequency instability (Allan variance) of BDS and representative GPS, GLONASS, and Galileo satellites on DOY 234 2015 using XISM final 30-s clocks

(G17/G21/G23/G30/G32), GLONASS-M (R09/R19) and Galileo (E11/E19) satellites. Cesium atomic clocks are employed by GLONASS satellites, while Rubidium is employed by BDS and Galileo (IOV) satellites [14]. For intervals smaller than 1000 s, the stability of the majority of BDS satellites except for C08 is better than the GPS Block IIR and GLONASS-M satellites and for intervals at ~10,000 s, the stability performance of BDS satellites is comparable with GPS IIR and GLONASS-M. For intervals smaller than 300 s, the GLONASS-M satellites have slightly better stability performance than Block IIR but worse than the majority of BDS satellites. Galileo satellites almost enjoy the best stability performance for all time intervals ranging from 30 to 15,360 s and are just a little worse than GPS IIF satellites for intervals smaller than 500 s.

3.3 Application for Kinematic PPP

To evaluate the influence of clock sampling rate on KPPP and the performance of the XISM final 30-s clocks for KPPP, observation with 30-s sampling rate from four stations equipped with multi-GNSS receiver are collected on DOY 234 2015. Among the four stations, PERT and MRO1 are operated by IGS/MGEX with receiver type of Trimble NETR9, while SHA1 and KUN1, with receivers, provide by UNICORE, belong to the iGMAS. With the SPODS software, experiments of KPPP are carried out separately for GPS, GLONASS, and BDS satellite using satellite orbits and 30-s/5-min clocks from XISM. When using 5-min clocks, the linear interpolation is used to calculate the satellite clock offsets at measurement.

The repeatability of epoch-wise station coordinates is calculated to measure the performance of KPPP with different constellation and clock products.

Figure 6 shows the coordinate repeatability of GPS KPPP in East, North, and Up directions for the four stations with 30-s and 5-min satellite clocks. It is demonstrated that the repeatability in East and North is reduced from about 0.025 m with 5-min clocks to about 0.010 m with 30-s clocks, while in Up direction from larger than 0.07 m to about 0.02 m with expectation of about 0.05 m for SHA1. The mean repeatability in East, North, and Up with 5-min clocks are 0.028, 0.026, and 0.076 m, respectively, while 0.008, 0.009, and 0.025 m when 30-s clocks are used. The 30-s clocks lead to improvements of 71.2, 65.5, and 67.3% in East, North, and Up directions, respectively.

Similarly, Fig. 7 shows the coordinate repeatability of GLONASS KPPP in East, North, and Up. It can be seen that, with 30-s GLONASS clocks, the repeatability in East is reduced from about 0.04 m to about 0.02 m, in North from about 0.07 m to about 0.04 m, and in Up from bigger than 0.22 m to smaller than 0.09 m. The mean repeatabilities of GLONASS KPPP in East, North, and Up with 5-min clocks are 0.041, 0.070, and 0.290 m, respectively, and 0.015, 0.032, and 0.074 m with 30-s clocks which result in improvements of 62.0, 52.4, and 73.3% in East, North, and Up directions, respectively.

The coordinate repeatability of BDS KPPP in East, North, and Up directions is shown in Fig. 8. Using 30-s clocks, a great improvement in East from bigger than

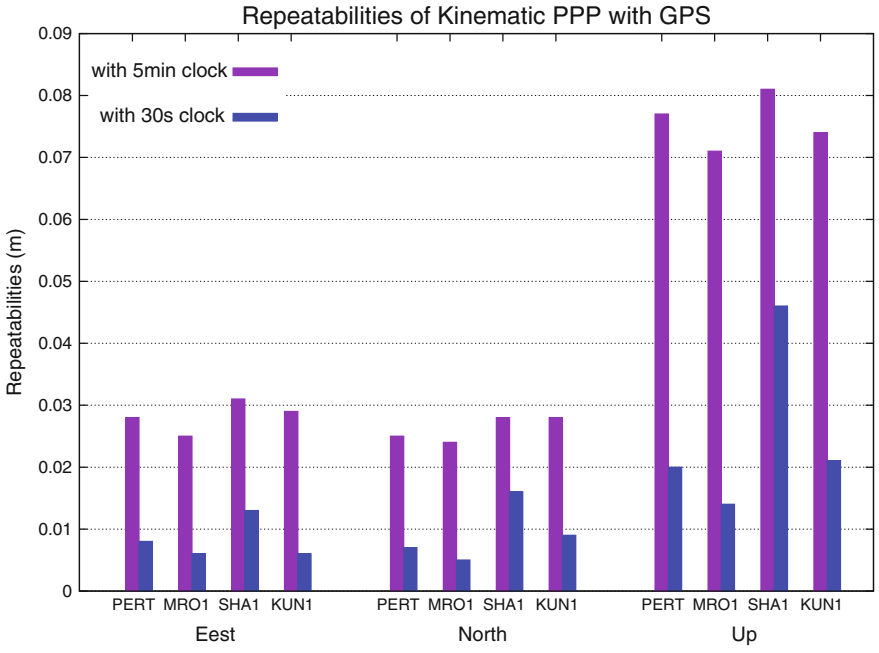

Fig. 6 Repeatability in East/North/Up for GPS KPPP with XISM 30-s and 5-min clocks

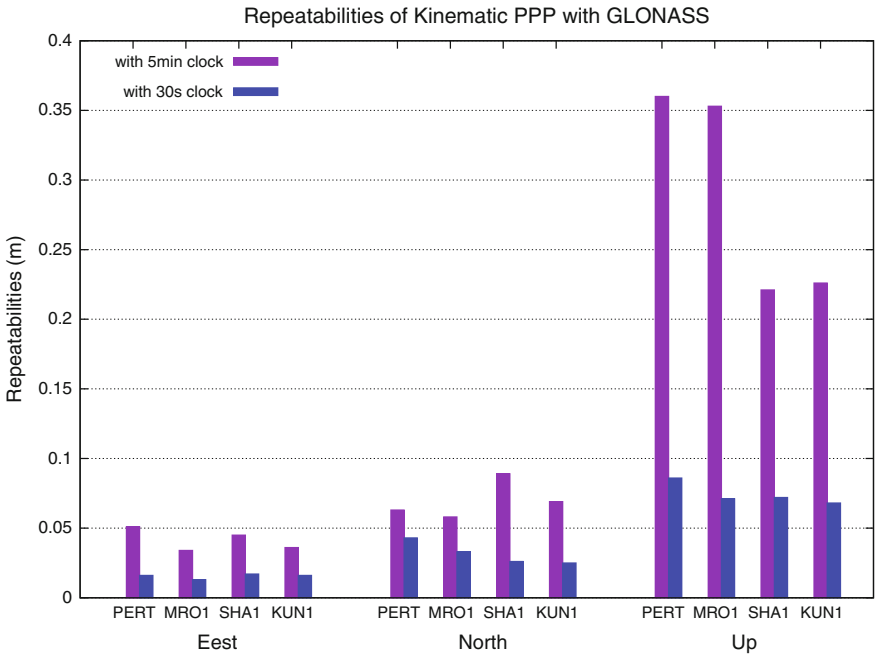

Fig. 7 Repeatability in East/North/Up for GLONASS KPPP with XISM 30-s and 5-min clocks

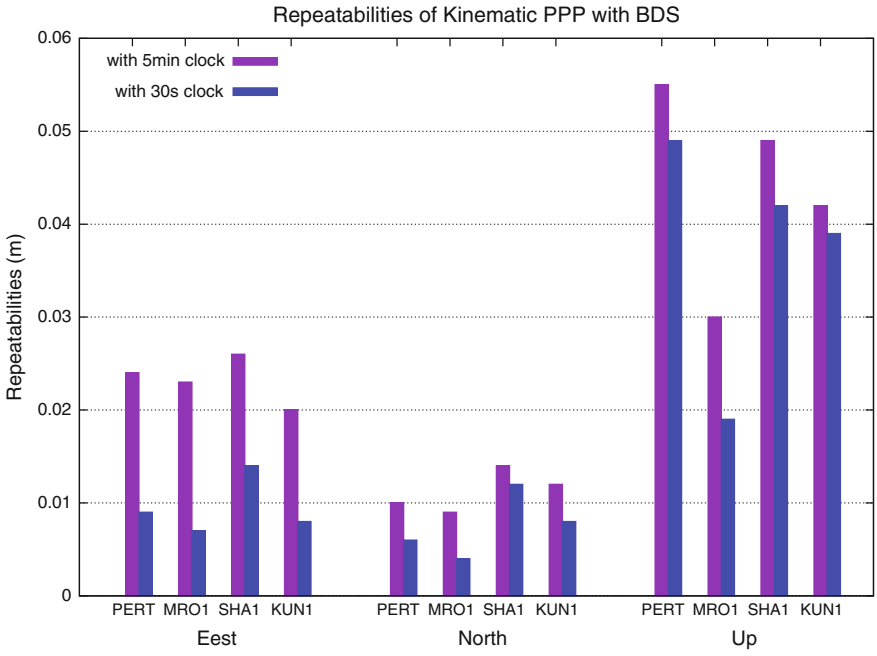

Fig. 8 Repeatability in East/North/Up for BDS KPPP with XISM 30-s and 5-min clocks

0.02 m to about 0.01 m and slight improvements in North and Up are shown. The mean repeatabilities are reduced by 59.6, 35.8, and 17.3%, from 0.023, 0.011, and 0.044 to 0.009, 0.008, and 0.037 m for E, N, and U components, respectively. The precisions of BDS KPPP are comparable to GPS KPPP in horizontal components.

Figure 9 shows the 3D position repeatability of individual GPS, GLONASS, or BDS KPPP with clocks of different sampling rates and improvements caused by 30-s clocks. As shown in the figure, with 5-min clocks, the mean 3D repeatability is 0.085 m for GPS KPPP, 0.303 m for GLONASS KPPP, and 0.051 m for BDS KPPP, while using 30-s clocks, the mean 3D repeatabilities are 0.028, 0.082, and 0.040 m, respectively. The improvements caused by the 30-s clocks are about 67, 72, and 24%, which means that the GPS/GLONASS KPPP are more sensitive to the sampling rate of clocks. It is interesting to find that when using 5-min clocks, BDS KPPP achieved the best KPPP repeatability, which can be explained with the comparative good stability performance of nearly all the BDS satellites clocks as shown in Fig. 5. The GLONASS KPPP is dramatically degraded with 5-min clocks due to the comparative poorer performance for the whole constellation. For GPS, although the newest Block IIF satellites enjoy the best performance especially for intervals smaller than 1000 s, the stability of Block IIR satellites which comprise 19 of the total 32 satellites is the poorest in short time interval and the superiority from BLOCK IIF satellites is canceled out.

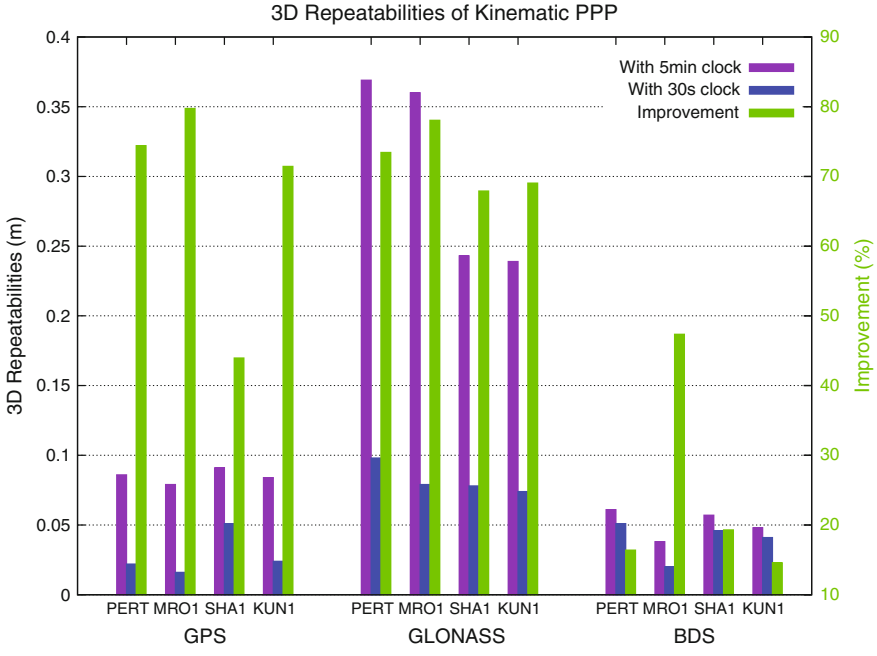

Fig. 9 3D repeatability of individual GPS, GLONASS or BDS KPPP with XISM 5-min and 30-s clocks with *bars* in *green* indicating the improvements by 30-s clocks (Color figure online)

In order to further explore the underlying reason and validate the former conclusions, the differences between interpolated values from the 5-min clocks and the estimated values from corresponding 30-s clocks are computed and plotted in Fig. 10 for several typical satellites in GPS, BDS, GLONASS, and Galileo constellations. Obviously, the differences of GPS IIR satellites (G17, G21, and G23) are much larger than IIA/IIF (G32/G30), GLONASS, Galileo, and BDS (except for C08) satellites in magnitude. The magnitude of the differences for most of the BDS satellites is also smaller than GLONASS satellites but a little bigger than Galileo and GPS IIF satellites. The root mean square (RMS) of the differences for each satellite is computed and shown in Fig. 11. The RMS differences for GPS IIR satellites are about 0.1 ns, while IIF is smaller than 0.02 ns with exception of about 0.1 ns for G24 and G08. The RMS for R17 is unusually large, about 0.35 ns, whereas RMSs for most of the other GLONASS satellites are smaller than 0.1 ns in RMS. The RMSs for Galileo satellites are smaller than 0.025 ns and are about 0.035 ns for most of the BDS satellites. In terms of the whole constellation, the mean RMS differences for GPS, GLONASS, BDS, and Galileo are 0.083, 0.098, 0.038, and 0.015 ns, which demonstrate that linear interpolation with 5-min clocks would cause more errors for GPS and GLONASS than BDS and Galileo. This also explains well the results of KPPP experiments and is consistent with the former conclusion of Allan variance analysis.

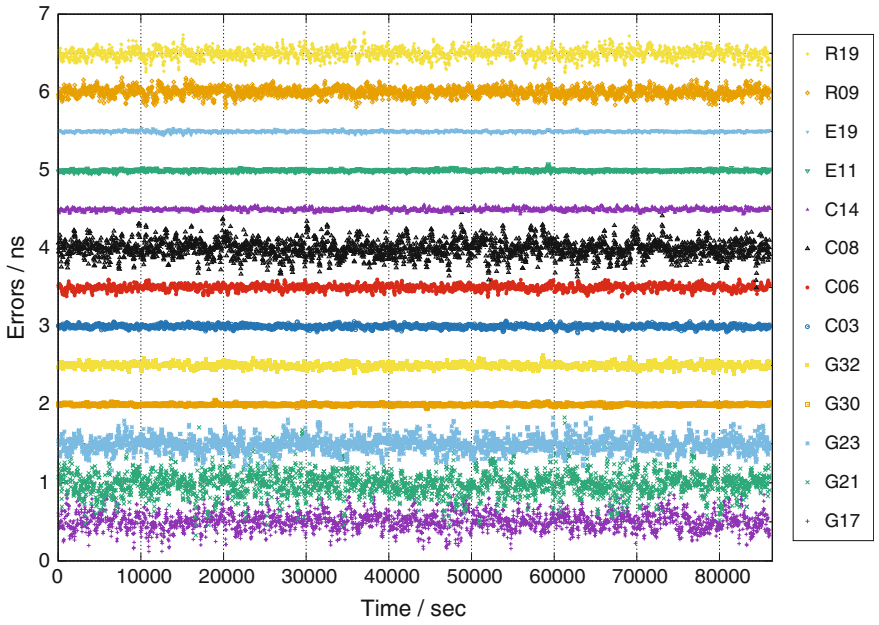

Fig. 10 Differences between interpolated values from the 5-min clocks and the estimated values from corresponding 30-s clocks for typical GPS, BDS, GLONASS, and Galileo satellites

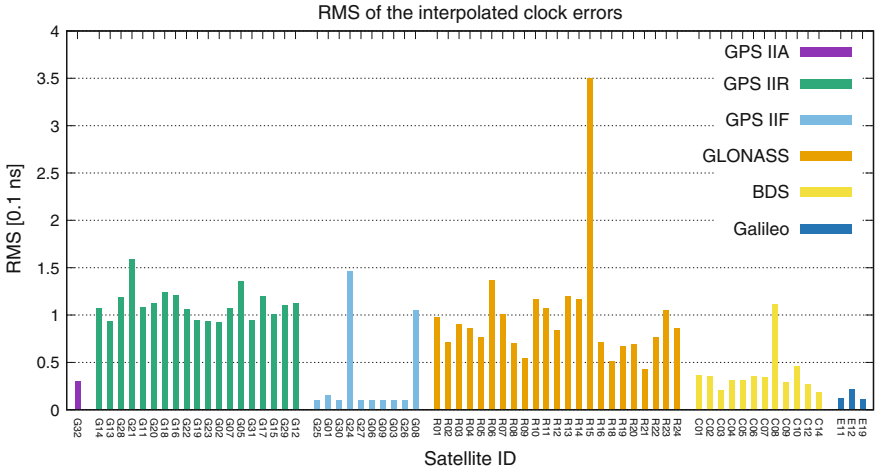

Fig. 11 The RMS differences between interpolated values from the 5-min clocks and the estimated values from corresponding 30-s clocks for each satellite

4 Summary and Conclusions

Since DOY 162 2016, the GNSS analysis center at XISM contributes to the iGMAS the "rapid" and "final" 30-s GNSS (GPS, GLONASS, BDS, and Galileo) clock product which are generated with the 5-min zero-difference clocks and 30-s corrected observation from POD procedure. The corrected observations are used to estimate the 30-s epoch-difference clocks which are then use to interpolate the 5-min zero-difference clocks to 30-s sampled clocks. The quality of the GPS clock products at XISM is validated by clock comparison with IGS final clocks, and it is demonstrated that the quality of XISM GPS clocks is in essence of the same as IGS ACs. A good agreement with IGS clocks is demonstrated when the 30-s clocks are used to assess the frequency stability performance of GPS satellites, which further confirm the good quality of XISM clock product. With the 30-s clocks, the frequency stability performance of GPS, GLONASS, BDS, and Galileo satellites were assessed for intervals ranging from 30 to 15360 s, which show pretty good stability performance of BDS satellites at short intervals. Finally, in order to evaluate the impact of the clock sampling rate on KPPP, KPPP with individual GPS GLONASS and BDS are conducted with 30-s and 5-min clocks at XISM. It is shown, with 30-s clocks, 3D repeatability is improved by about 67, 72, and 24%, respectively, for GPS, GLONASS, and BDS. And it is interesting to find that when using 5-min clocks, KPPP with BDS has better repeatability performance than with GPS or GLONASS.

References

1. Blewitt G (1990) An automatic editing algorithm for GPS data. Geophys Res Lett 17:199–202
2. Bock H, Dach R, Jggi A, Beutler G (2009) High-rate GPS clock corrections from CODE: support of 1 Hz applications. J Geodesy 83: 1083–1094
3. Chen J, Zhang Y, Zhou X, Pei X, Wang J, Wu B (2013) GNSS clock corrections densification at SHAO: from 5 min to 30 s Sci China-Phys Mech Astron 56: 1–10
4. Jiao W (2012) Architecture and current development of iGMAS CSNC 2012. Guangzhou, China
5. Kleusberg A, Teunissen PJG (eds) (1996) GPS for Geodesy. Springer, Berlin
6. Lichten SM, Border JS (1987) Strategies for high-precision global positioning system orbit determination. J Geophys Res 92:12751–12762
7. Mccarthy DD, Petit GE (2004) IERS conventions (2003). In: Mccarthy DD, Petit GE (eds) IERS technical note no. 32. Verlag des Bundesamtes für Kartographie und Geodäsie, Frankfurt am Main 2004
8. Montenbruck O, Gill E, Kroes R (2005) Rapid orbit determination of LEO satellites using IGS clock and ephemeris products. GPS Solutions 2005:226–235
9. Montenbruck O, Steigenberger P, Khachikyan R, Weber G, Langley RB, Mervart L, Hugentobler U (2014) IGS-MGEX: preparing the ground for multi-constellation GNSS science. InsideGNSS 9:42–49
10. Ruan R (2009) Study on GPS precise point positioning using un-differenced carrier phase. Zhengzhou, China, Information Engineering University
11. Ruan R, Jia X, Wu X, Feng L, Zhu Y (2014) SPODS software and its result of precise orbit determination for GNSS satellites. China Satellite Navigation Conference (CSNC) 2014 Proceedings, vol III. Nanjing
12. Schmid R, Dach R, Collilieux X, Jggi A, Schmitz M, Dilssner F (2016) Absolute IGS antenna phase center model igs08.atx: status and potential improvements. J Geodesy 90: 343–364
13. Senior KL, Ray JR, Beard RL (2008) Characterization of periodic variations in the GPS satellite clocks. GPS Solutions 12:211–225
14. Steigenberger P, Hugentobler U, Hauschild A, Montenbruck O (2013) Orbit and clock analysis of compass GEO and IGSO satellites. J Geodesy 87:515–525
15. Wei Z, Ruan R, Jia X, Wu X, Song X, Mao Y, Feng L, Zhu Y (2014) Satellite positioning and orbit determination system SPODS: theory and test. Acta Geodaetica Cartogr Sin 43:1–4
16. Wu JT, Wu SC, Hajj GA, Bertiger WI, Lichten SM (1993) Effects of antenna orientation on GPS carrier phase. Manuscripta Geodaetic: 91–98
17. Zumberge JF, Heftin MB, Jefferson DC, Watkins MM, Webb FH (1997) Precise point positioning for the efficient and robust analysis of GPS data from large networks. J Geophys Res 102:5005–5017

GNSS Performance Research for MEO, GEO, and HEO

Huicui Liu, Xiao Cheng, Geshi Tang and Jing Peng

Abstract GNSSs such as GPS, GLONASS, Galileo, and Beidou have demonstrated to be a valid and efficient system for various space applications in LEO. Since the 1990s precise GNSS-based positioning of GEO, MEO, HEO, and even deep space exploration satellites has also been considered feasible. This paper analyzes the GNSS satellite visibility and PDOP performances for 6 space users, including two GEO, one MEO, and three HEO satellites. The simulation results show that a single GNSS receiver with the sensitivity of about −180 to −188 dBW is enough for space user below 50,000 km while the receiver of a Lunar explorer must be able to process the received signal low to −202 ∼ −208 dBW. As for a multi-GNSS receiver, the sensitivity requirements decrease about 2–4 dBW compared with the single GNSS one. Viewed from the sensitivity standpoint, a GPS-only receiver and a BDS+GPS receiver are the best single GNSS and multi-GNSS choice for most of the six space users while a Beidou-only receiver performs the best for GEO1 satellite which is fixed above the Asia-Pacific area. It can be concluded that for the space users below 50,000 km, it is possible to attain an average PDOP of below 20 with a receiver sensitivity no higher than −184 dBW. An important conclusion drawn from the analysis is that the higher the space user flies, the more important role multi-GNSS application plays.

Keywords GNSS · MEO · GEO · HEO · Sensitivity · PDOP

H. Liu (✉) · X. Cheng · G. Tang
Beijing Aerospace Control Center, Beijing 100094, China
e-mail: liuhuicui@bacc.org.cn; vlcx26@gmail.com

J. Peng
School of Electronic Science and Engineering, National University of Defense Technology, Changsha, China

J. Sun et al. (eds.), *China Satellite Navigation Conference (CSNC) 2017 Proceedings: Volume III*, Lecture Notes in Electrical Engineering 439,
DOI 10.1007/978-981-10-4594-3_4

1 Introduction

Global Navigation Satellite System (GNSS) was originally designed as a Position, Velocity and Time (PVT) utility for land, maritime, and air applications [1]. However, GNSS service for space users is receiving increasing interest because of a range of foreseeable benefits [2], such as the significant improvement in navigation performance, large increase in autonomous operations, and remarkable reduces in the expensive on-board clocks needs. In fact, most Low Earth orbit (LEO) space users share similar performances (satellite visibility, geometry coverage, signal power, etc.) to tradition Earth users thanks to the Earth-directed transmitter antennas of GNSS [3–5]. But there are still great challenges for space users with a higher altitude especially above the GNSS constellations. Not until the 1990s has precise GNSS-based positioning of Geostationary Earth Orbit (GEO), Medium Earth Orbit (MEO), High Earth Orbit (HEO), and even deep space exploration satellites been considered feasible. This group of users primarily receives GNSS side lobe signals from the other side of the Earth [6]. The aggregate signal availability of mainlobes and sidelobes determines the level of performance for such space users. However, the sidelobe signals are not measured as thoroughly as the mainlobe signals because they are too weak to reach terrestrial users [7] and not reliable because they are not specified by the GNSS providers.

NASA has been advocated the concept of "GPS Space Service Volume (SSV)" since 2000 [8] to explicitly state the requirements of space user and protect the current performances. But only the volume of space between 3000 and 36,000 km altitude has been defined as the SSV, and signal availability and signal level was defined only for GEO users. Both Beidou system and Galileo system followed these definitions and published their current SSV performances in 2014 [9, 10].

As we have entered an era of "multi-GNSS", about 121 navigation satellites in operation are expected by 2020, which includes 32 GPS satellites, 24 GLONASS satellites, 35 Beidou satellites, as well as 30 Galileo ones. The increase in quantity of navigation satellites may be redundant for Earth users in some cases but brings better satellite availability for space users. Thus it is not enough to analyze the SSV performance of a single GNSS separately. Also, more and more GNSS applications have extended SSV to farer space: for example, about 40% of China's space missions will operate outside the domain of SSV over the following 5 years [9], and a GPS/GLONASS receiver mounted on China's CE-5T1 Lunar explorer in 2014 kept operational at the altitude up to 140,000 km [2, 11, 12]. Therefore, it is necessary to analyze the multi-GNSS performances for satellites in MEO, GEO, HEO, and even beyond. Several beneficial attempts have been done in this field [13, 14], but only GPS or GPS/Galileo combinations are considered in these works. This paper aims to provide a more comprehensive analysis: the four GNSSs, including GPS, GLONASS, Galileo and Beidou, with their complete constellations are all concluded and the performances [signal visibility, signal availability, Doppler, and Position Dilution of Precision (PDOP)] of different GNSSs and different combinations of multi-GNSSs are all provided for space users at the altitude from 32,000 km (MEO) to 380,000 km (HEO apogee).

2 Simulation Models

2.1 GNSS Satellites

There are going to be 121 GNSS satellites in operation in 2020 if the constellation constructions of Beidou and Galileo both go according to schedule. In this paper, the GNSS constellations applied are shown in Table 1. Although each GNSS satellite can transmit signals at more than one frequency, only L1/E1 for GPS/Galileo, B1 for Beidou, and G1 for GLONASS are analyzed in this paper.

The Equivalent Isotropic Radiated Power (EIRP) pattern of GNSS satellite antenna is an important factor for the signal visibility analysis. However, EIRP varies among different GNSSs and among satellites of different generations or different orbit types of the same GNSS. According to the correlated references [15–18], the EIRP models for Beidou GEO, Inclined Geosynchronous Satellite Orbit (IGSO) and MEO satellites, and GPS Block IIA, IIR and IIF satellites are shown in Fig. 1.

Table 1 The GNSS constellations

System	Constellation
GPS	32 MEO satellites, 6 planes, inclination 55°, altitude 20,180 km
GLONASS	24 MEO satellites, 3 planes, inclination 64.8°, altitude 19,100 km
Galileo	30 MEO satellites, 3 planes, inclination 56°, altitude 23,616 km
Beidou	5 GEO satellites, 58.75°E/80.3°E/110.5°E/139.9°E/160.0°E 3 IGSO satellites, inclination 55°, 118.0°E, Mean Anomaly 0°/120°/240° 27 MEO satellites, 3 planes, inclination 55°, altitude 21,500 km

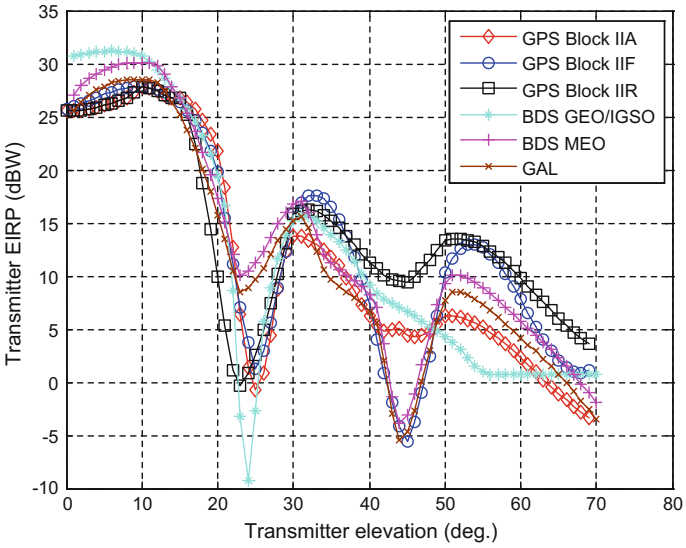

Fig. 1 The EIRP patterns of the GNSS satellite antennas

Significant similarities can be found in the EIRP results among GPS Block IIR, IIR-M, and GLONASS satellites based on the analysis of the CE-5T1 GNSS experiment in reference [10], and thus in this paper the three kinds of satellites are assumed to share the same EIRP pattern. In the absence of specific information about the Galileo antenna patterns, we use the modified EIRP model provided by reference [15] which can ensure the demanded Galileo Earth users' performance.

2.2 Space Users

In order to analyze GNSS performances of space users comprehensively and systematically, satellites of different orbit types and different orbit altitudes are concluded in this work. According to the orbit parameters listed in Table 2, the subastral points of the two GEO users are 180° apart on the equator; MEO1 and HEO1 are both in circular orbits, but MEO1 satellite orbits above the GNSS MEO satellites and below the Beidou GEO and IGSO satellites ,while HEO1 satellite orbits above all GNSS satellites; and the other two HEO satellites both flies across the GNSS constellations in high elliptical orbits. The apogee attitude of HEO3 satellite reaches near the Moon and then HEO3 can be also considered as a lunar explorer. All the receivers mounted on the space users are assumed to have zero-gain omni-directional antennas so that the analysis in this paper is more universally applicable. Hence, the receiver sensitivity mentioned in this paper includes both the receiver signal processing ability and the antenna gain.

3 Simulation Results and Analysis

3.1 Visibility and Sensitivity Requirements

Satellite visibility for this space application concerns two issues: (1) the light-of-sight is not obstructed by the Earth limb; and (2) the received signal power is sufficiently high for the receiver to carry out acquisition and tracking [6].

Table 2 The space user orbit parameters

Orbit types	No.	Orbit parameters
GEO	1	270°E
	2	90°E
MEO	1	Eccentricity 0°, inclination 0°, altitude 25,629 km
HEO	1	Eccentricity 0°, inclination 0°, altitude 43,621.9 km
	2	Inclination 5°, perigee altitude 1500 km, apogee altitude 50,000 km
	3	Inclination 5°, perigee altitude 1000 km, apogee altitude 38,4293 km

Thus, the word "visible" mentioned in this paper means not only "in view" but also "tracked". The space user received GNSS signal power of can be written as [2]

$$P_s = \mathrm{EIRP}(\theta_t) + L_p + G_r(\theta_r), \tag{1}$$

where the free space loss L_p can be calculated using the well-known equation $L_p = 20\log\left(\frac{\lambda}{4\pi d}\right)$ where λ is the wavelength of the GNSS signal and d is the propagation distance, θ_r and θ_t is the departure angle (off-boresight angle) and the incidence angle (off-boresight angle), respectively, and the receiver antenna gain G_r is zero as mentioned in Sect. 2.2. Losses due to tropospheric and ionospheric effects are neglected since all the space users in this paper flies well above the atmosphere.

To ensure the positioning calculation, at least four visible GNSS satellites are necessary for single GNSS application and the required receiver sensitivity values are plotted in Fig. 2. All the simulation results are calculated through at least one orbital period. It is clear to see that a single GNSS receiver with the sensitivity of about −180 to −188 dBW is enough for space user below 50,000 km while the receiver of the lunar explorer HEO3 must be able to process the received signal low to −202 ∼ −208 dBW. What's more, Fig. 2 also shows that for most of the space users except GEO1 the required sensitivity of a GPS-only receiver is the lowest. Meanwhile, the eight regional service satellites (5 GEOs and 3 IGSOs) help Beidou system become the first choice viewed from the sensitivity standpoint for GEO1 satellite which is fixed above the Asia-Pacific area.

More GNSSs might improve the visibility; thus it is easy to draw the conclusion arbitrarily that a multi-GNSS receiver definitely has the lower sensitivity

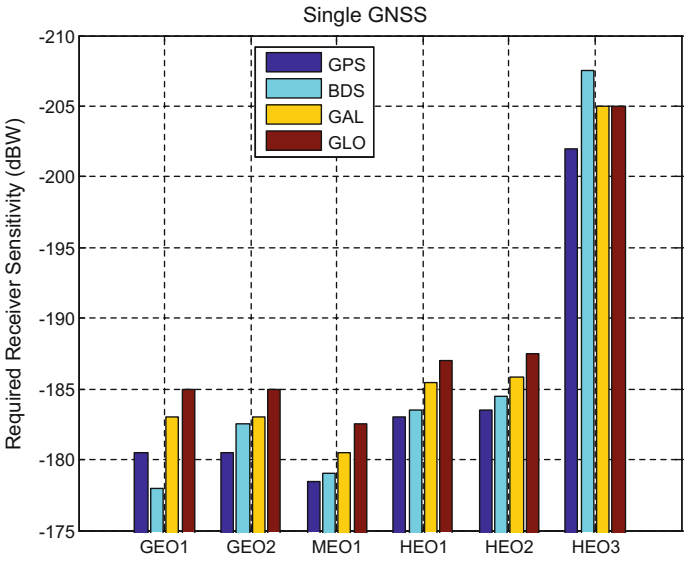

Fig. 2 The required receiver sensitivity for at least 4 GNSS satellites with single GNSS

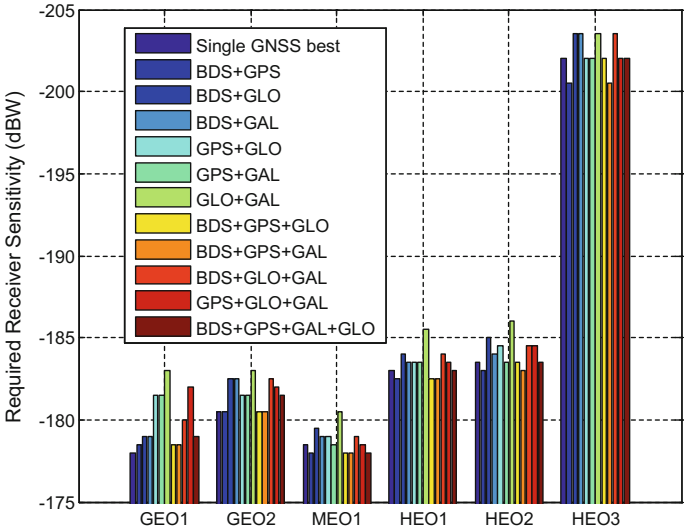

Fig. 3 The required receiver sensitivity for at least four GNSS satellites with dual and triple GNSS

requirement than a single GNSS one. However, each additional GNSS also brings one more unknown system bias into the positioning calculation, which demands one more visible GNSS satellite. Thus it is necessary to analyze carefully the receiver sensitivity required in multi-GNSS applications. According to the simulation results illustrated in Fig. 3, a multi-GNSS receiver with the sensitivity of about −178 to −186 dBW can serve all the space users below 50,000 km while the sensitivity requirement should be about −200 to −204 dBW for HEO2 satellite, which shows a slight improvement compared with the single GNSS results in Fig. 2. What's more, the required sensitivity value of the 'BDS+GPS' combination is the highest among all the GNSS (both single GNSS and multi-GNSS) combinations for all space users except GEO1 satellite. An interesting fact should be pointed out especially that multi-GNSS applications are not always better than single GNSS applications viewed from the sensitivity standpoint.

3.2 PDOP

The receiver sensitivity limits the satellite visibility and then affects the PDOP value. In this session, the lowest sensitivity requirements for positioning calculation in single GNSS, dual GNSS, triple GNSS, as well as quadruple GNSS applications are used. Since the sensitivity value and the corresponding PDOP statistics are listed in Table 3, several interesting facts should be noted. Please note that in single GNSS circumstance, Beidou system requires the lowest sensitivity for only GEO1 satellite, and then no results for those satellites except GEO1 in the first row.

Table 3 The lowest sensitivity requirements and corresponding PDOP statistics of all GNSS combinations

		GEO		MEO	HEO		
		1	2	1	1	2	3
BDS	Sensitivity requirement (dBW)	−178	/	/	/	/	/
	Average PDOP	36.9	/	/	/	/	/
	Max PDOP	268.4	/	/	/	/	/
	Min PDOP	11.5	/	/	/	/	/
GPS	Sensitivity requirement (dBW)	−180.5	−180.5	−178.5	−183	−183.5	−202
	Average PDOP	8.6	8.6	4.6	20.2	10.4	779.7
	Max PDOP	33.7	33.8	13.4	675.3	148.6	144,972.4
	Min PDOP	4.5	4.5	2.5	7.3	0.6	0.6
BDS+GPS	Sensitivity requirement (dBW)	−178.5	−180.5	−178	−182.5	−183	−200.5
	Average PDOP	7.8	6.6	2.4	8.9	6.5	396.4
	Max PDOP	18.9	19.2	5.6	24.2	32.1	4006.5
	Min PDOP	4.0	3.9	0.9	5.8	0.4	0.4
BDS+GPS+GAL	Sensitivity requirement (dBW)	−178.5	−180.5	−178	−182.5	−183	−200.5
	Average PDOP	7.2	6.1	2.2	8.2	5.9	323.9
	Max PDOP	15.8	18.9	5.1	17.5	27.7	1146.6
	Min PDOP	4.0	3.5	0.8	5.6	0.3	0.3
BDS+GPS+GAL+GLO	Sensitivity requirement (dBW)	−179	−181.5	−178	−183	−183.5	−202
	Average PDOP	6.1	4.5	2.1	7.2	5.1	254.4
	Max PDOP	12.6	8.4	4.9	16.6	14.7	670.2
	Min PDOP	3.7	3.1	0.8	5.1	0.3	0.3

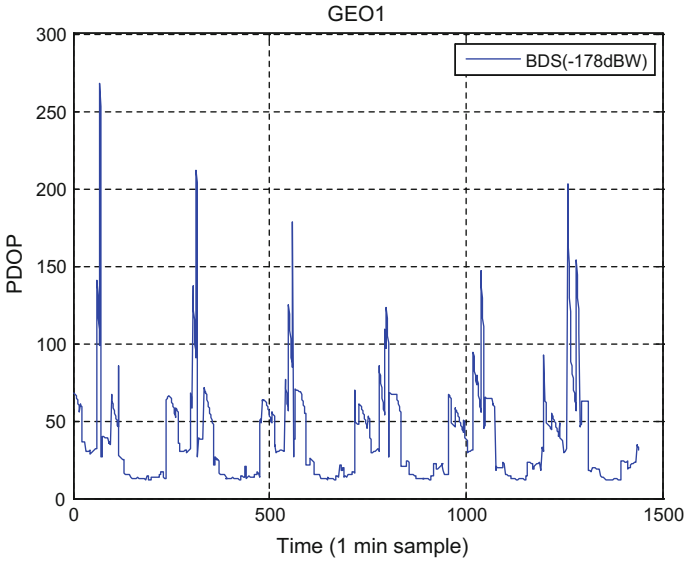

Fig. 4 The PDOP value of GEO1 satellite using Beidou system only

Although using Beidou system only requires the lowest sensitivity for GEO1 satellite, the large PDOP value up to 268.4 makes it less competitive than using GPS system only which needs a only 2.5 dBW higher sensitivity. Also, an approximately periodical variation can be found in the PDOP results of GEO1 using Beidou system only as shown in Fig. 4 and the period is about 4 h. This is corrected with the distribution of Beidou constellations. Compared with the single GNSS application, using a multi-GNSS receiver which can process both BDS and other GNSSs signals makes the low sensitivity requirement and low PDOP value achievable for GEO1 satellite. For the 5 space users below 50,000 km, it is possible to attain an average PDOP of below 20 with receiver sensitivity no higher than −184 dBW, but the PDOP difference between single GNSS and multi-GNSS applications is not as significant as that of HEO2. It is shown in Table 3 that multi-GNSS application plays an important role in reducing the PDOP values, especially the maximum PDOP values for HEO3.

4 Concluding Remarks

GNSS-based navigation for space users is receiving increasing interest because of a range of foreseeable economic and operational benefits. With the development of new GNSSs, such as Beidou, Galileo, there is going to be more than 100 GNSS satellites on operation by 2020. It is necessary and practical to analyze the multi-GNSS performances for space users, especially those flying above the GNSS

constellations. Based on the researches of six space users operating on various orbits, the lowest sensitivity requirements and the corresponding PDOP values of different GNSS combinations are attained. The numerical results of this paper can be beneficial to the future space GNSS applications.

Acknowledgements This work was supported by the National Natural Science Foundation of China (41304026).

References

1. Bauer F, Moreau M, Dahle-Melsaether M et al (2006) The GPS space service volume. In: Proceedings of ION GNSS 2006. Fort Worth, TX, USA
2. Liu H, Cao J, Cheng X et al (2016) The data processing and analysis for the CE-5T1 GNSS experiment. Adv Space Res. doi:10.1016/j.asr.2016.06.035
3. Capuano V, Botteron C, and Farine P (2013) GNSS performance for MEO, GEO and HEO. In: Proceedings of the 64th International Astronautical Congress, Beijing, China
4. Kaplan E, Hegarty C (2006) Understanding GPS: principles and applications, 2nd edn. Artech House, INC
5. Bock H, Jaggi A, Beutler G et al (2014) GOCE: precise orbit determination for the entire mission. J Geodesy 88(11):1047–1060
6. Moreau C (2001) GPS receiver architecture for autonomous navigation in high Earth orbits. University of Colorado
7. Ziedan N (2006) GNSS receivers for weak signals. Artech House, INC
8. Air Force Space Command/Air (2000) Combat Command Operational Requirements Document (ORD) AFSPC/ACC 003-92-I/II/III Global Positioning System (GPS)
9. Zhan X, Jing S, Yang H, Chang X (2014) Space service volume (SSV) characteristics of BDS. http://www.unoosa.org/pdf/icg/2014/wg/wgb03.pdf
10. Status of Galileo SSV Characterization, http://www.unoosa.org/pdf/icg/2014/wg/wgb05.pdf
11. Wang D, Dong Q, Wang M et al (2015) Results from the GNSS flight experiment on the circumlunar free return trajectory of China CE-5T1 spacecraft. In: Proceedings of the 66th international astronautical congress, Jerusalem, Israel
12. Fan M, Hu X, Dong G et al (2015) Orbit improvement for Chang'E-5T lunar returning probe with GNSS technique. Adv Space Res 56:2473–2482
13. Capuano V, Botteron C, Farine P (2013) GNSS performances for MEO, GEO and HEO. In: Proceedings of the 64th international astronautical congress, Beijing, China
14. Capuano V, Botteron C, Leclère J et al Feasibility study of GNSS as navigation system to reach the moon, Acta Astronautica. doi:10.1016/j.actaastro.2015.06.007
15. Liu H, Cheng X, Tang G et al (2015) The research on optimum space-borne antenna parameters for CE-5T1 autonomous navigation using GNSS. J Beijing Inst Technol (English Version) 24:141–146
16. Moreau M (2001) GPS receiver architecture for autonomous navigation in high Earth orbits. University of Colorado, 1800 Grant Street, Denver, CO
17. Lorga F, Silva P, Cintio A et al (2010) GNSS sensor for autonomous orbit determination. In: Proceedings of ION ITM 2010, Portland, OR, USA, pp 2717–2731
18. Czopek F (1993) Description and performance of the GPS Block I and II L-band antenna and link budget. In: Proceedings of institute of navigation GPS 93 conference, Salt Lake City, UT, pp 37–43

Research on the On-Orbit Precision Evaluation Method of Inter-Satellite Measurement Based on Geometry Configuration

Daoning Yang, Jun Yang, Gang Li, Haojie Wang and Ying Liu

Abstract Navigation constellation inter-satellite link (ISL) is one of the efficient ways to improve the service performance of global navigation satellite system (GNSS). The four major GNSSs have been equipped with ISLs or plan to equip in near future. Narrow beam inter-satellite link in a time-division multiple access (TDMA) system have advantages of fast beam switching, flexible networking, high communication speed, and good security. For navigation constellation to improve service performance, the measurement values have to transfer back to the ground facilities in a short time, at the same time, facilities have to transfer telecommand and uplink ephemeris to satellites which are invisible to ground facilities as soon as possible. These all made a request to shorter communication delay, and it is very important to improve the performance of ISLs by rapidly assessing the quality of the connection and adjusting the unreasonable connection in time. In this paper, a communication time delay model for ISLs based on directed graphs is studied. By abstracting the ISL timeslot table into a directed graph, and based on the shortest path algorithm, the communication time delay can be obtained quickly. Simulation verifications have been carried out for different scenes. Results show that the proposed model works well.

Keywords Inter-satellite links · Geometry · Precision evaluation · Inter-satellite measurement · GNSS

D. Yang (✉) · J. Yang · H. Wang
College of Mechatronics Engineering and Automation, National University of Defense Technology, Changsha 410073, China
e-mail: Yang_daoning@hotmail.com

G. Li · Y. Liu
Beijing Institute of Tracking and Telecommunications Technology, Beijing 100094, China

J. Sun et al. (eds.), *China Satellite Navigation Conference (CSNC) 2017 Proceedings: Volume III*, Lecture Notes in Electrical Engineering 439,
DOI 10.1007/978-981-10-4594-3_5

1 Introduction

The core function of the Global Navigation Satellite System (GNSS) is to provide users with location, navigation, and timing (PNT) service. In recent years, in order to improve the positioning accuracy of satellite navigation systems, a series of technical means have been adopted. Among the massive techniques used to improve the performance of GNSS, inter-satellite link technology has become a research hotspot. Inter-satellite links can greatly improve the accuracy of ephemeris prediction and enhance GNSS performance effectively, and it has become a sign of new-generation satellite navigation systems [1–3]. The establishment of inter-satellite links has become an important consensus of building the current global satellite navigation system.

Global satellite navigation systems rely on inter-satellite links to perform inter-satellite clock error and pseudorange measurements, enabling autonomous navigation. Autonomous navigation refers to process of GNSS utilizing inter-satellite measurements to generate ephemeris parameters and provide reliable service to users, without the support of ground stations. Autonomous navigation can significantly improve the warfare capacity of navigation constellation, while reducing the number of ground stations and the ephemeris upload frequency.

Both the conventional operation mode supported by the ground and the autonomous navigation mode without the ground station support rely on high precision measurements of inter-satellite links. Obviously, once the measurement errors, the ephemeris update will error, and the navigation system cannot provide reliable services [4]. Only ensuring the accuracy of inter-satellite measurements can ensure the quality of navigation system. Therefore, the accuracy of inter-satellite measurements should be effectively evaluated to avoid the use of erroneous measurement data. Because the satellite orbit in the navigation constellation is determined, the geometric configuration of multiple satellites is relatively determined. Using this constraint, the inter-satellite measurement quality can be verified and evaluated, and measurement value with large deviation can be excluded, ensuring the quality of inter-satellite measurement data.

In this paper, we focus on the accuracy of on-orbit measurement based on geometrical configuration. First, the evaluated method of the inter-satellite measurement accuracy based on geometry configuration is introduced. Then, the related simulation is presented. Simulation results show that the performance of inter-satellite measurement accuracy evaluation has greatly improved.

2 Evaluation Method

2.1 Overview of the Evaluation Method

For the navigation satellite, its position can be obtained through ephemeris. Real distance value can be calculated from the position of two satellites. Once the

difference between the inter-satellite pseudorange measurement and the theoretical value exceed a certain value, one can determine the measurement as a gross error. However, due to the fact that the satellite position of the ephemeris prediction is deviated, this method can only achieve a rough accuracy evaluation of the measured data [5].

The navigation constellation runs on a pre-defined satellite orbit, and the orbital information is predictable. It is found that, although the absolute position provided by ephemeris has a large error compared to inter-satellite measurements, it has a high accurate relative value when the time interval is small. In addition, although the accuracy of position information provided by ephemeris is low, it is more reliable. On the contrary, the precision of inter-satellite measurements is high, but once it exists deviation, the deviation can be much bigger.

Inter-satellite measurements require more than two satellites to participate. In image satellites as a point, the inter-satellite measurement is the edge linking two points. Then the navigation constellation can be abstracted into a definite geometry. According to geometric constraints of geometric configuration, adjustment operation can be obtained at the current time of the precise location of the satellite.

When the time interval is not large, the relative position change provided by the ephemeris has very small error, so we can calculate the satellite position at the next moment according to the present. We can evaluate the accuracy of inter-satellite measurement through the relative precise position. Figure 1 shows the flow chart for accuracy evaluation.

2.2 Accuracy Evaluation Method Based on Triangle

Inter-satellite measurements between each two satellites in three constitute a triangular configuration. According to the coordinate adjustment method of triangulation edge measurement, denote the position adjustment value $\hat{X}_1$, $\hat{Y}_1$, $\hat{Z}_1$, $\hat{X}_2$, $\hat{Y}_2$, $\hat{Z}_2$, $\hat{X}_3$, $\hat{Y}_3$, $\hat{Z}_3$ of the three satellites at time t as the parameter to be estimated, and let

$$\begin{cases} \hat{X}_{1,t} = X_{1,t}^0 + \hat{x}_{1,t} \\ \hat{Y}_{1,t} = Y_{1,t}^0 + \hat{y}_{1,t} \\ \hat{Z}_{1,t} = Z_{1,t}^0 + \hat{z}_{1,t} \end{cases} \tag{1}$$

$$\begin{cases} \hat{X}_{2,t} = X_{2,t}^0 + \hat{x}_{2,t} \\ \hat{Y}_{2,t} = Y_{2,t}^0 + \hat{y}_{2,t} \\ \hat{Z}_{2,t} = Z_{2,t}^0 + \hat{z}_{2,t} \end{cases} \tag{2}$$

$$\begin{cases} \hat{X}_{3,t} = X_{3,t}^0 + \hat{x}_{3,t} \\ \hat{Y}_{3,t} = Y_{3,t}^0 + \hat{y}_{3,t} \\ \hat{Z}_{3,t} = Z_{3,t}^0 + \hat{z}_{3,t} \end{cases}. \tag{3}$$

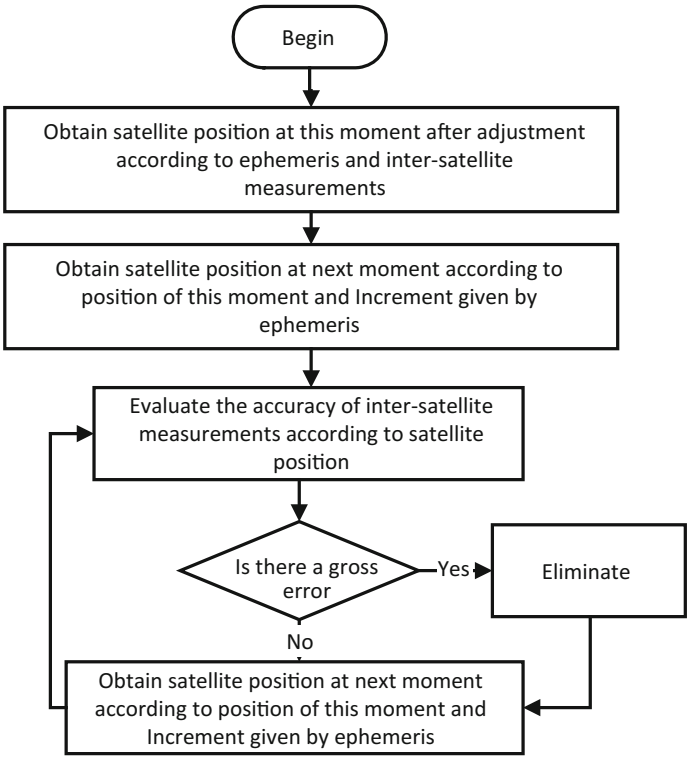

Fig. 1 Inter-satellite measurement accuracy evaluation method

Adjustment equations of inter-satellite measurement are

$$\hat{L}_{1-2,t} = L_{1-2,t} + v_{1-2,t} = \sqrt{(\hat{X}_{1,t} - \hat{X}_{2,t})^2 + (\hat{Y}_{1,t} - \hat{Y}_{2,t})^2 + (\hat{Z}_{1,t} - \hat{Z}_{2,t})^2} \quad (4)$$

$$\hat{L}_{1-3,t} = L_{1-3,t} + v_{1-3,t} = \sqrt{(\hat{X}_{1,t} - \hat{X}_{3,t})^2 + (\hat{Y}_{1,t} - \hat{Y}_{3,t})^2 + (\hat{Z}_{1,t} - \hat{Z}_{3,t})^2} \quad (5)$$

$$\hat{L}_{2-3,t} = L_{2-3,t} + v_{2-3,t} = \sqrt{(\hat{X}_{2,t} - \hat{X}_{3,t})^2 + (\hat{Y}_{2,t} - \hat{Y}_{3,t})^2 + (\hat{Z}_{2,t} - \hat{Z}_{3,t})^2}. \quad (6)$$

According to Taylor formula, we have

$$\begin{cases} L_{1-2,t} + v_{1-2,t} = S^0_{1-2,t} + \frac{\Delta X^0_{1-2,t}}{S^0_{1-2,t}}(\hat{x}_{1,t} - \hat{x}_{2,t}) + \frac{\Delta Y^0_{1-2,t}}{S^0_{1-2,t}}(\hat{y}_{1,t} - \hat{y}_{2,t}) + \frac{\Delta Z^0_{1-2,t}}{S^0_{1-2,t}}(\hat{z}_{1,t} - \hat{z}_{2,t}) \\ L_{1-3,t} + v_{1-3,t} = S^0_{1-3,t} + \frac{\Delta X^0_{1-3,t}}{S^0_{1-3,t}}(\hat{x}_{1,t} - \hat{x}_{3,t}) + \frac{\Delta Y^0_{1-3,t}}{S^0_{1-3,t}}(\hat{y}_{1,t} - \hat{y}_{3,t}) + \frac{\Delta Z^0_{1-3,t}}{S^0_{1-3,t}}(\hat{z}_{1,t} - \hat{z}_{3,t}) \\ L_{2-3,t} + v_{2-3,t} = S^0_{2-3,t} + \frac{\Delta X^0_{2-3,t}}{S^0_{2-3,t}}(\hat{x}_{2,t} - \hat{x}_{3,t}) + \frac{\Delta Y^0_{2-3,t}}{S^0_{2-3,t}}(\hat{y}_{2,t} - \hat{y}_{3,t}) + \frac{\Delta Z^0_{2-3,t}}{S^0_{2-3,t}}(\hat{z}_{2,t} - \hat{z}_{3,t}) \end{cases} \quad (7)$$

where

$$\begin{cases} \Delta X^0_{i-j,t} = X^0_{i,t} - X^0_{j,t} \\ \Delta Y^0_{i-j,t} = Y^0_{i,t} - Y^0_{j,t} \\ \Delta Z^0_{i-j,t} = Z^0_{i,t} - Z^0_{j,t} \end{cases} \tag{8}$$

$$S^0_{i-j,t} = \sqrt{\left(\Delta X^0_{i-j,t}\right)^2 + \left(\Delta Y^0_{i-j,t}\right)^2 + \left(\Delta Z^0_{i-j,t}\right)^2}. \tag{9}$$

Let

$$l_{i-j,t} = L_{i-j,t} - S^0_{i-j,t} \tag{10}$$

The error equation can be obtained as follows:

$$\begin{cases} v_{1-2,t} = \frac{\Delta X^0_{1-2,t}}{S^0_{1-2,t}}\left(\hat{x}_{1,t} - \hat{x}_{2,t}\right) + \frac{\Delta Y^0_{1-2,t}}{S^0_{1-2,t}}\left(\hat{y}_{1,t} - \hat{y}_{2,t}\right) + \frac{\Delta Z^0_{1-2,t}}{S^0_{1-2,t}}\left(\hat{z}_{1,t} - \hat{z}_{2,t}\right) - l_{1-2} \\ v_{1-3,t} = \frac{\Delta X^0_{1-3,t}}{S^0_{1-3,t}}\left(\hat{x}_{1,t} - \hat{x}_{3,t}\right) + \frac{\Delta Y^0_{1-3,t}}{S^0_{1-3,t}}\left(\hat{y}_{1,t} - \hat{y}_{3,t}\right) + \frac{\Delta Z^0_{1-3,t}}{S^0_{1-3,t}}\left(\hat{z}_{1,t} - \hat{z}_{3,t}\right) - l_{1-3} \\ v_{2-3,t} = \frac{\Delta X^0_{2-3,t}}{S^0_{2-3,t}}\left(\hat{x}_{2,t} - \hat{x}_{3,t}\right) + \frac{\Delta Y^0_{2-3,t}}{S^0_{2-3,t}}\left(\hat{y}_{2,t} - \hat{y}_{3,t}\right) + \frac{\Delta Z^0_{2-3,t}}{S^0_{2-3,t}}\left(\hat{z}_{2,t} - \hat{z}_{3,t}\right) - l_{2-3} \end{cases} \tag{11}$$

In the same manner, position provided by ephemeris can be also regarded as observation, and the error equation is as follows:

$$\begin{cases} v_{x1,t} = \hat{x}_{1,t} + X^0_{1,t} - X^e_{1,t} \\ v_{y1,t} = \hat{y}_{1,t} + Y^0_{1,t} - Y^e_{1,t} \\ \quad\quad\vdots \\ v_{z3,t} = \hat{z}_{3,t} + Z^0_{3,t} - Z^e_{3,t} \end{cases}, \tag{12}$$

where $X^e_{1,t}$, $Y^e_{1,t}$, …, $Z^e_{3,t}$, etc. are position parameters provided by the ephemeris. Considering (11) and (12) together, writing them in matrix form, we have the error equation as

$$\boldsymbol{v} = \boldsymbol{A}\hat{x} - \boldsymbol{l}, \tag{13}$$

where $\boldsymbol{A}$ is the coefficient matrix

$$\boldsymbol{v} = \left[v_{1,t}, v_{2,t}, v_{3,t}, v_{x1,t}, \ldots, v_{z3,t}\right]^{\mathrm{T}}_{12\times 1} \tag{14}$$

$$l = \begin{bmatrix} L_{1-2,t} - S^0_{1-2,t} \\ L_{1-3,t} - S^0_{1-3,t} \\ L_{2-3,t} - S^0_{2-3,t} \\ X^e_{1,t} - X^0_{1,t} \\ \vdots \\ Z^e_{3,t} - Z^0_{3,t} \end{bmatrix}_{12\times 1}. \tag{15}$$

And we can easily got that [6, 7]

$$\hat{x} = \left(\boldsymbol{A}^{\mathrm{T}}\boldsymbol{P}\boldsymbol{A}\right)^{-1}\boldsymbol{A}\boldsymbol{P}\boldsymbol{l}, \tag{16}$$

where $\boldsymbol{P}$ is the weight matrix, the satellite position after adjustment

$$\hat{\boldsymbol{X}}_t = \boldsymbol{X}_t^0 + \hat{\boldsymbol{x}}. \tag{17}$$

On the basis of this, and combining with the satellite position in next moment, which derived by ephemeris increment, satellite position at $t + 1$ is

$$\hat{\boldsymbol{X}}_{t+1} = \hat{\boldsymbol{X}}_t + (\boldsymbol{X}_{t+1}^{\boldsymbol{e}} - \boldsymbol{X}_t^{\boldsymbol{e}}). \tag{18}$$

The inter-satellite range reference at $t + 1$ is given by

$$\begin{cases} \hat{L}_{1-2,t+1} = \sqrt{(\hat{X}_{1,t+1} - \hat{X}_{2,t+1})^2 + (\hat{Y}_{1,t+1} - \hat{Y}_{2,t+1})^2 + (\hat{Z}_{1,t+1} - \hat{Z}_{2,t+1})^2} \\ \hat{L}_{1-3,t+1} = \sqrt{(\hat{X}_{1,t+1} - \hat{X}_{3,t+1})^2 + (\hat{Y}_{1,t+1} - \hat{Y}_{3,t+1})^2 + (\hat{Z}_{1,t+1} - \hat{Z}_{3,t+1})^2} \\ \hat{L}_{2-3,t+1} = \sqrt{(\hat{X}_{2,t+1} - \hat{X}_{3,t+1})^2 + (\hat{Y}_{2,t+1} - \hat{Y}_{3,t+1})^2 + (\hat{Z}_{2,t+1} - \hat{Z}_{3,t+1})^2} \end{cases}. \tag{19}$$

3 Simulation Results

Aiming at the accuracy evaluation method proposed in the second section, simulation results have been presented. In order to verify the effectiveness of the proposed method, the simulated results of accuracy evaluation, which uses the inter-satellite distances calculated by ephemeris, is utilized as a benchmark.

Set the normal ranging accuracy as 0.1 m, and set detection threshold to let the false alarm probability be 0.000007.

Figure 2 shows the error and detection threshold of three inter-satellite links without gross error: Blue for the detection threshold, and red, yellow and green lines are three measurement errors, respectively. It can be seen that the detection threshold and ranging error are all below 1 m, implying the proposed method can detect error larger than 1 m. Figure 3 shows the contrasted group which is evaluated by ephemeris only. Ranging error is at the meter level, and detection threshold is greater than 30 m.

Figures 4 and 5 show the measurement error after adding a gross error of 1 m to the first link at 1000th minute. As they show, after adding 1 m of error, the proposed accuracy evaluation method can obviously detect the error. On the other hand, in the case of which only relies on ephemeris, the error curve has no significant change, and cannot detect the deviation.

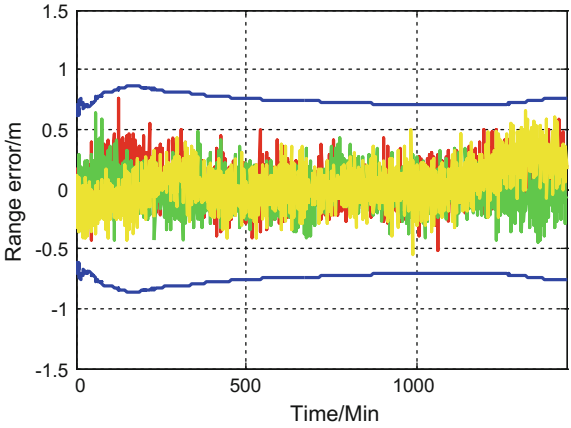

Fig. 2 The measurement error and detection threshold of the three links in normal circumstances

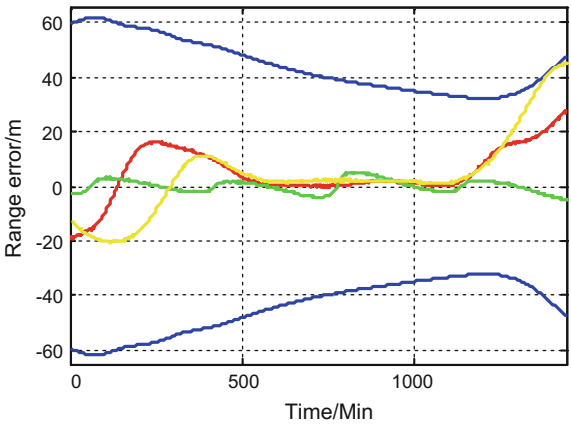

Fig. 3 The measurement error and detection threshold only rely on ephemeris in normal circumstances

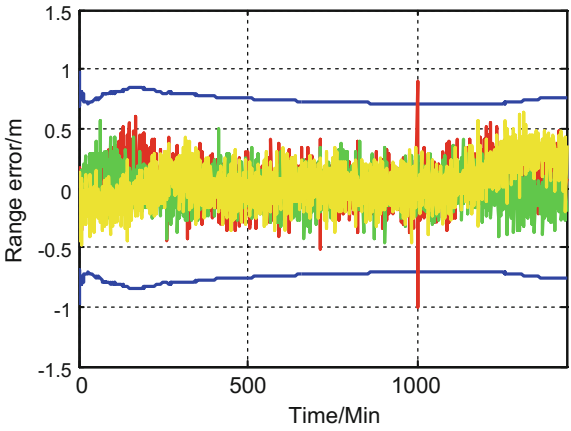

Fig. 4 The measurement error and detection threshold after adding gross error

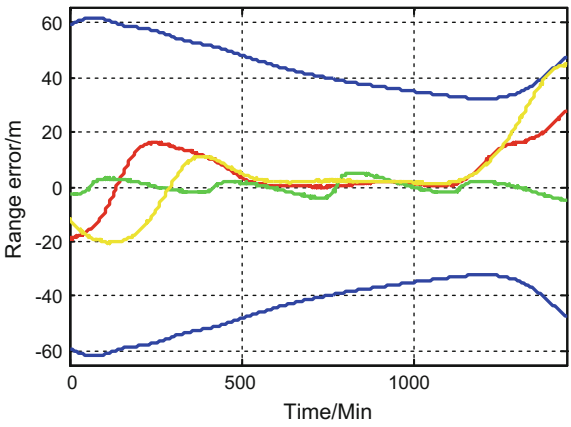

Fig. 5 The measurement error and detection threshold after adding gross error only rely on ephemeris

4 Conclusion

In this paper, a method for evaluating the accuracy of navigation constellation based on geometric configuration is proposed. The method utilizes the constraint of geometrical configuration of several satellites and the slowly varying characteristics of ephemeris errors to evaluate the accuracy of inter-satellite measurements. Simulation results show that the proposed method can effectively evaluate the accuracy of inter-satellite measurements, and can accurately distinguish gross error in the level of 1 m under 0.1 m of inter-satellite ranging accuracy.

References

1. Rajan JA (2002) Highlights of GPS IIR autonomous navigation. In: Proceedings of the ION 58th annual meeting and the CIGTF. The Institute of Navigation, Albuquerque, pp 354–363
2. Kristine PM, Paul A, John L (2003) Crosslinks for the next-generation GPS. IEEEAC 4: 1589–1595
3. Yang D, Yang J, Xu P (2016) GPS Solution. doi:10.1007/s10291-016-0587-0
4. Wang F, Gong X, Liu W (2015) A novel decimeter-level real-time orbit determination algorithm using space-borne GPS measurements with separation and absorption of broadcast ephemeris error. Geomatics Inform Sci Wuhan Univ 40(9):230–1236 (Ch)
5. Zhang X, Huang P, Yang L (2014) Satellite autonomous integrity research based on the satellite link ranging. China satellite navigation coference (Ch)
6. Wuhan university press (2014) The basis of error theory and surveying adjustment (Ch)
7. Zhang Y, Zhang YL (2006) Study of the robust estimation method of inter-satellite ranging network. XI Tong Gong Cheng Yu Dian Zi Ji Shu/Syst Eng Electron. 28(4):519–524 (Ch)

Research on Distributed Autonomous Time Reference Maintain Method of Navigation Constellation

Daoning Yang, Gang Li, Ying Liu, Jun Yang, Yinan Meng and Xianyu Zhang

Abstract Satellite navigation system to provide users with high-precision positioning, navigation, and timing services, requires a uniform high-precision time reference. When the navigation system is operating in the normal mode, this reference is maintained by the ground and measured through the satellite–ground link and modifies the onboard clock parameters to ensure the uniformity of the entire system time reference. In the autonomous navigation mode, the navigation constellation to leave the ground support, need to maintain the time reference autonomously. This paper analyzes the maintenance method of autonomous time reference based on inter-satellite observation and designs a distributed autonomous time reference maintenance algorithm. The satellite clock error is used as the basic observation to compose the system measurement equation. According to the system state equation, each satellite uses Kalman filter to estimate and update its own clock parameters to maintain the constellation time reference. Simulation results show that the proposed algorithm can maintain the uniform time reference of navigation constellations.

Keywords Inter-satellite link · Time reference · GNSS · Distributed method

D. Yang (✉) · J. Yang
College of Mechatronics Engineering and Automation, National University of Defense Technology, Changsha 410073, China
e-mail: Yang_daoning@hotmail.com

G. Li · Y. Liu · Y. Meng
Beijing Institute of Tracking and Telecommunications Technology, Beijing 100094, China

X. Zhang
Rocket Force Academy, Beijing 100000, China

J. Sun et al. (eds.), *China Satellite Navigation Conference (CSNC) 2017 Proceedings: Volume III*, Lecture Notes in Electrical Engineering 439,
DOI 10.1007/978-981-10-4594-3_6

1 Introduction

Satellite navigation system to provide users with high-precision positioning, navigation, and timing services, requires a uniform high-precision time reference. When the navigation system is operating in the normal mode, this reference is maintained by the ground and measured through the satellite–ground link and modifies the onboard clock parameters to ensure the uniformity of the entire system time reference. Autonomous navigation is a process that constellation autonomously generates ephemeris parameters and provides service to users by using the inter-satellite measurements without the ground support. Autonomous navigation can significantly improve the navigation warfare ability and has potential to reduce the number of ground stations and the frequency of ephemeris upload. However, in autonomous navigation mode, navigation constellation can only autonomously maintain the time reference due to unavailability of ground support [1–3].

Centralized method and distributed method are two different techniques of autonomous time reference maintain of navigation constellation. Centralized method is to gather the measurement data to a single satellite, this satellite compute the clock parameters of the whole constellation and then give out these parameters to all other satellites. The distributed method is satellites of the navigation constellation link with visible satellites and complete the measurements, respectively. Then each satellite computes the clock parameters itself. In the Centralized methods, there is a high requirement for compute ability for the master satellite. At the same time, it increases the inter-satellite communication pressure when collecting measurement data and delivering clock parameters. The whole navigation constellation cannot provide service when the master satellite failed. As for the distributed method, each satellite is equal and computes its own parameters independently. A single satellite failure will not affect the entire constellation. The distributed method can greatly improve the robustness of navigation system, and reducing the pressure of inter-satellite communication.

In this paper, we studied a distributed autonomous time reference maintain method. We introduced the framework of the method first, and then introduced the clock error model of the atomic clock, inter-satellite bidirectional measurement model and the Kalman filter method. At last, the simulation of the proposed method and the conclusion are given.

2 Distributed Time Reference Maintain Method

The core of the time reference maintain method is to accurately estimate the clock parameters of each satellite. Based on the Kalman filter, each satellite can estimate the clock parameters by acquiring the clock error between itself and the surrounding satellite.

2.1 Atomic Clock Error Model

The onboard atomic clock system model can be represented by the following linear discrete system

$$\boldsymbol{X}_k = \boldsymbol{\Phi}_{k,k-1}\boldsymbol{X}_{k-1} + \boldsymbol{W}_{k-1} \tag{1}$$

$$\boldsymbol{X}_k = \begin{bmatrix} x_k \\ y_k \\ z_k \end{bmatrix} \tag{2}$$

Where, x_k is the clock correction (phase correction) of the k epoch, y_k is the frequency correction, z_k is the frequency drift rate, and y_k is the time derivative of x_k, and z_k is the time derivative of y_k. $\boldsymbol{\Phi}_{k,k-1}$ is the state transition matrix [4, 5].

$$\boldsymbol{\Phi}_{k,k-1} = \begin{bmatrix} 1 & \tau & \tau^2/2 \\ 0 & 1 & \tau \\ 0 & 0 & 1 \end{bmatrix} \tag{3}$$

τ is the Filtering period.

$$\boldsymbol{W}_{k-1} = \begin{bmatrix} w_{x,k-1} \\ w_{y,k-1} \\ w_{z,k-1} \end{bmatrix} \tag{4}$$

$w_{x,k-1}$, $w_{y,k-1}$ and $w_{z,k-1}$ are phase noise, frequency noise, and frequency drift-rate noise independent of x_{k-1} , y_{k-1} and z_{k-1} in k-1 epochs, respectively. The statistical properties are determined by the selected atomic clock Hadamard variance. The covariance matrix can be expressed as

$$\begin{aligned} Q_{k-1} &= \Sigma_{\boldsymbol{W}_k} = E\left[\boldsymbol{W}_k \boldsymbol{W}_k^T\right] \\ &= \begin{bmatrix} q_1\tau + \frac{q_2\tau^3}{3} + \frac{q_3\tau^5}{20} & \frac{q_2\tau^2}{2} + \frac{q_3\tau^4}{8} & \frac{q_3\tau 3}{6} \\ \frac{q_2\tau^2}{2} + \frac{q_3\tau^4}{8} & q_2\tau + \frac{q_3\tau^3}{3} & \frac{q_3\tau^2}{2} \\ \frac{q_3\tau^3}{6} & \frac{q_3\tau^2}{2} & q_3\tau \end{bmatrix} \end{aligned} \tag{5}$$

Where q_1 is the process noise parameter corresponding to w_x, described by the phase random walk noise description, q_2 corresponds to the process noise parameter of w_y, described using the frequency modulation random walk noise, q_3 is the process noise parameter corresponding to w_z, described by the frequency modulation random running noise. These parameters are determined by atomic clock.

2.2 Inter-satellite Bidirectional Measurement Model

The inter-satellite links measure inter-satellite clock errors by bidirectional measurements. Inter-satellite bidirectional measurements can be expressed as follows.

$$\bar{\rho}_{ij} = \left|\vec{\boldsymbol{r}}_j(t) - \vec{\boldsymbol{r}}_i(t)\right| + c \cdot (\delta t_j - \delta t_i) + \varepsilon_{ij} \tag{6}$$

$$\bar{\rho}_{ij} = \left|\vec{\boldsymbol{r}}_j(t) - \vec{\boldsymbol{r}}_i(t)\right| + c \cdot (\delta t_j - \delta t_i) + \varepsilon_{ij} \tag{7}$$

$\bar{\rho}_{ij}$ and $\bar{\rho}_{ji}$ are bidirectional pseudoranges between satellite i and satellite j after epoch correction to time t. $\vec{\boldsymbol{r}}_i(t)$ and $\vec{\boldsymbol{r}}_j(t)$ are the position vectors of satellite i and satellite j at time t. δt_i and δt_j are the clock error of satellite i and the satellite j. ε_{ij} and ε_{ji} are the measurement noise.

Equation (6) minus (7), there is

$$\bar{\rho}_{ij} - \bar{\rho}_{ji} = 2c(\delta t_i - \delta t_j) + \varepsilon_{ij} - \varepsilon_{ji} \tag{8}$$

Equation (8) can be transformed as

$$\bar{\rho}_{ij} - \bar{\rho}_{ji} + 2c * \delta_{tj} = 2c * \delta_{ti} + \varepsilon_{ij} - \varepsilon_{ji} \tag{9}$$

This equation is the observation equation of inter-satellite clock error Kalman filter.

When a satellite i establish link with m satellites at time k, the observation equation can be written as

$$\boldsymbol{Z}_k = \boldsymbol{H}\boldsymbol{X} + \boldsymbol{V} \tag{10}$$

Where

$$\boldsymbol{Z}_k = \begin{bmatrix} \bar{\rho}_{i1} - \bar{\rho}_{1i} + 2c \times \delta_{t1} \\ \bar{\rho}_{i2} - \bar{\rho}_{2i} + 2c \times \delta_{t2} \\ \vdots \\ \bar{\rho}_{im} - \bar{\rho}_{mi} + 2c \times \delta_{tm} \end{bmatrix} \tag{11}$$

$$\boldsymbol{H} = \begin{bmatrix} 2c & 0 & 0 \\ 2c & 0 & 0 \\ \vdots & \vdots & \vdots \\ 2c & 0 & 0 \end{bmatrix}_{m \times 3} \tag{12}$$

$$V = \begin{bmatrix} \varepsilon_{i1} - \varepsilon_{1i} \\ \varepsilon_{i2} - \varepsilon_{2i} \\ \vdots \\ \varepsilon_{im} - \varepsilon_{mi} \end{bmatrix} \tag{13}$$

ε_{ij} and ε_{ji} are inter-satellite measurement noises which can be regarded as zero mean Gaussian white noise. The covariance matrix of measurement is

$$R = [VV^T] \tag{14}$$

2.3 Kalman Filter Method

Based on the above-mentioned atomic clock error model and inter-satellite observation model, the basic equation of Kalman filter can be expressed as follows:

$$\begin{cases} \hat{\boldsymbol{X}}_{k,k-1} = \boldsymbol{\Phi}_{k,k-1}\hat{\boldsymbol{X}}_{k-1} \\ \boldsymbol{P}_{k,k-1} = \boldsymbol{\Phi}_{k,k-1}\boldsymbol{P}_{k-1}\boldsymbol{\Phi}_{k,k-1}^T + \boldsymbol{Q}_{k-1} \\ \boldsymbol{K}_k = \boldsymbol{P}_{k,k-1}\boldsymbol{H}_k^T(\boldsymbol{H}_k\boldsymbol{P}_{k,k-1}\boldsymbol{H}_k^T + \boldsymbol{R}_k)^{-1} \\ \hat{\boldsymbol{X}}_k = \hat{\boldsymbol{X}}_{k,k-1} + \boldsymbol{K}_k(\boldsymbol{Z}_k - \boldsymbol{H}_k\hat{\boldsymbol{X}}_{k,k-1}) \\ \boldsymbol{P}_k = (\boldsymbol{I} - \boldsymbol{K}_k\boldsymbol{H}_k)\boldsymbol{P}_{k,k-1}(\boldsymbol{I} - \boldsymbol{K}_k\boldsymbol{H}_k)^T + \boldsymbol{K}_k\boldsymbol{R}_k\boldsymbol{K}_k^T \end{cases} \tag{15}$$

Where

$$\hat{\boldsymbol{X}}_k = \begin{bmatrix} \hat{x}_k \\ \hat{y}_k \\ \hat{z}_k \end{bmatrix}; \quad \boldsymbol{\Phi}_{k,k-1} = \begin{bmatrix} 1 & \tau & \tau^2/2 \\ 0 & 1 & \tau \\ 0 & 0 & 1 \end{bmatrix};$$

$$Q_{k-1} == \begin{bmatrix} q_1\tau + \frac{q_2\tau^3}{3} + \frac{q_3\tau^5}{20} & \frac{q_2\tau^2}{2} + \frac{q_3\tau^4}{8} & \frac{q_3\tau 3}{6} \\ \frac{q_2\tau^2}{2} + \frac{q_3\tau^4}{8} & q_2\tau + \frac{q_3\tau^3}{3} & \frac{q_3\tau^2}{2} \\ \frac{q_3\tau^3}{6} & \frac{q_3\tau^2}{2} & q_3\tau \end{bmatrix};$$

$$\boldsymbol{Z}_k = \begin{bmatrix} \bar{\rho}_{i1} - \bar{\rho}_{1i} + 2c \times \delta_{t1} \\ \bar{\rho}_{i2} - \bar{\rho}_{2i} + 2c \times \delta_{t2} \\ \vdots \\ \bar{\rho}_{im} - \bar{\rho}_{mi} + 2c \times \delta_{tm} \end{bmatrix}; \quad \boldsymbol{H} = \begin{bmatrix} 2c & 0 & 0 \\ 2c & 0 & 0 \\ \vdots & \vdots & \vdots \\ 2c & 0 & 0 \end{bmatrix}_{m\times 3};$$

$$\boldsymbol{R}_k = \begin{bmatrix} \sigma_{i1}^2 & 0 & \cdots & 0 \\ 0 & \sigma_{i2}^2 & \cdots & 0 \\ & & \vdots & \\ 0 & 0 & & \sigma_{im}^2 \end{bmatrix}$$

$\boldsymbol{K}_k$ is a $3 \times m$ filter gain matrix. $\boldsymbol{P}_k$ is a 3×3 error covariance matrix. $\boldsymbol{I}$ is a 3-order identity matrix. $\boldsymbol{R}_k$ is the covariance matrix of measurement.

3 Simulation Analysis

3.1 Simulation Scene

A typical navigation constellation Walker 24/3/1 is simulated [6–9].

The simulation scenario settings are as follows:

1. Orbit height of about 21,528 km, 55° inclination [6].
2. For the inter-satellite link, the antenna is narrow beam and the angle is ±70° [7].
3. The initial clock bias, frequency deviation and frequency drift rate are set to 0.
4. The clock coefficients q_1, q_2 and q_3 are set to $1 \times 10–22$, $2 \times 10–32$ and $6 \times 10–45$, respectively.
5. Inter-satellite bidirectional measurement accuracy is set to 0.0001–20 m.
6. The filter period is set to 5 min.

Based on the above scenario, at first we analyzed the inter-satellite visibility, and we found each satellite has eight continuous visible satellites in 60 days. Taking into account the robustness of autonomous navigation, each satellite is only considered establishing link with these eight continuous visible satellites.

3.2 Results and Analysis

The clock error variation of 24 satellites in 60 days is simulated and analyzed. First of all, the clock error parameters which are predicted only according to the model were simulated, the result as shown in Fig. 1. And then the result of the clock error

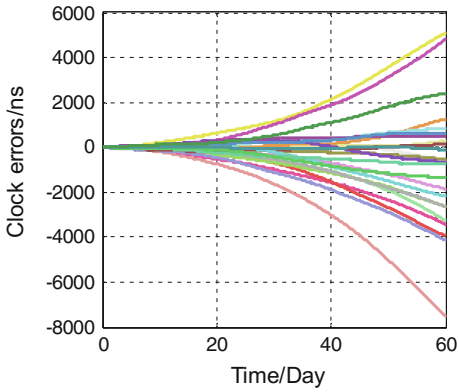

Fig. 1 Clock error of 24 satellites in 60 days predicted by clock error model

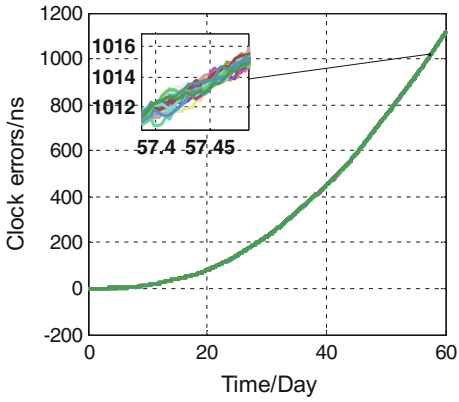

Fig. 2 Clock error of 24 satellites in 60 days predicted time reference maintain method (range error 0.1 m)

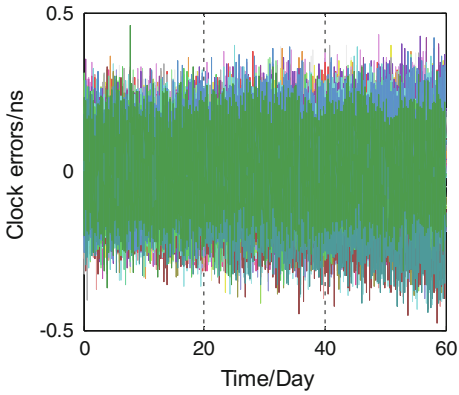

Fig. 3 Time synchronization accuracy of 24 satellites in 60 days (range error 0.1 m)

parameters are analyzed by distributed time reference maintain method under the conditions of 0.1 m range error, as shown in Fig. 2.

In Fig. 1, after 60 days, the satellite can only rely on the model estimated clock parameters in a long time without correction. The clock errors of 24 satellites become larger and divergence in 60 days, and the maximum of the clock error has been more than 10,000 ns. Although, the clock error corrected by distributed time reference maintain method is less than 1200 ns after 60 days, the variation trend of clock corrections of 24 satellites is consistent, that is to say the time is basically kept synchronous. For the satellite navigation system, as long as the time of each satellite in navigation constellation to maintain high-precision consistent, you can ensure the accuracy of navigation and positioning services.

Figure 3 shows the time synchronization accuracy obtained by subtracting the mean clock error from the 24 satellites shown in Fig. 2. It can be seen that the accuracy of time synchronization is basically the same within 60 days and is basically maintained within 0.4 ns.

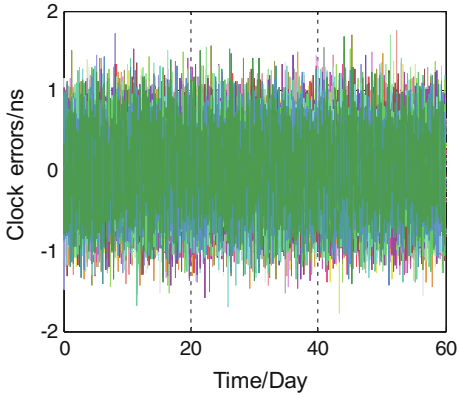

Fig. 4 Time synchronization accuracy of 24 satellites in 60 days (range error 1 m)

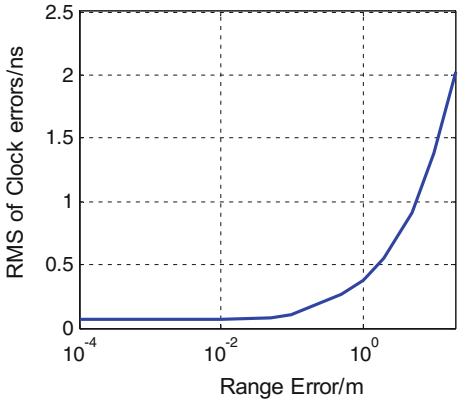

Fig. 5 The relationship between range error and time synchronization accuracy

Figure 4 shows the time synchronization accuracy of 1 m range error, compared to the accuracy of 0.1 m. As the range accuracy becomes worse, the time synchronization accuracy also becomes larger.

Figure 5 gives the relationship between inter-satellite range error and time synchronization accuracy. The abscissa is the range error and vertical axis is the time synchronization accuracy of the RMS value. We analyzed the accuracy of time synchronization for the range error varies from 0.0001 to 20 m. It can be found that the accuracy of time synchronization is improved with the decreasing of range error from 20 to 0.1 m, and the accuracy of time synchronization is almost no longer change after 0.1 m due to the presence of clock noise.

4 Conclusion

In this paper, we studied the Kalman filter-based distributed navigation constellation time reference maintain method. The simulation results show that under the condition of navigation constellation autonomous navigation, each satellite

establishes link with eight continuous visible satellites by inter-satellite link to carry out inter-satellite bidirectional measurement. And the clock errors estimated by Kalman filter is less than 1200 ns in 60 days for the range error is 0.1 m. However, the precision of synchronization between satellites is better than 0.4 ns, which can meet the needs of users' high-precision navigation and positioning applications.

When the noise level of the atomic clock is fixed, the accuracy of time synchronization is no longer improved with the decreasing of range error after the range accuracy reaches a certain level.

References

1. Rajan JA (2002) Highlights of GPS IIR autonomous navigation. In: Proceedings of the ION 58th annual meeting and the CIGTF. The Institute of Navigation, Albuquerque, pp 354–363
2. Kristine PM, Paul A, John L (2003) Crosslinks for the next-generation GPS. IEEEAC 4:1589–1595
3. Yang D, Yang J, Xu P (2016) GPS Solut. doi:10.1007/s10291-016-0587-0
4. Shuai P, Qu GJ (2005) Time synchronization techniques of the autonomous navigation of navigation constellation. J Astronaut
5. Gu Y, Chen Z, Shuai P (2010) Autonomous time synchronization algorithm on Hadamard variance among navigation satellites. Chin Space Sci Technol
6. BeiDou navigation satellite system signal in space interface control document open service signal (Version 2.0). China Satellite Navigation Office, December 2013
7. Wu G, Chen J, Guo X et al (2014) Design and simulation of time-slot allocation of inter-satellites links based on TDMA system. Comput Meas Control 22(12):4087–4090
8. Liu JY, Feng YU, Liang HE et al (2009) Autonomous positioning and timing for navigation constellation. J Astronaut 30(1):215–219
9. Xu P, Chen J, Tang Y et al (2016) Time-slot allocation of inter-satellite links with low communication delay simulation and analysis. In: China satellite navigation conference

A Study on the Orbit Accuracy Variation Characteristics and Yaw-Attitude Modes of Beidou Navigation Satellites

Guofeng Ji, Yuxi Liu, Zhiqiang Yang and Xiaolin Jia

Abstract Research on the orbit accuracy variation characteristics of Beidou navigation satellite can help to discover the deficiency of yaw-attitude modeling during eclipse season, which may further contribute to refine the functional models in precise orbit determination (POD). In this article, the broadcast orbit accuracy of Beidou Navigation Satellite System was evaluated firstly by Satellite Laser Ranging (SLR) residuals ranging from Jan 2015 to Nov 2016. For BDS GEO satellites, the orbit accuracy evaluated by SLR residuals is 0.6 m around with a systematic bias of about −0.6 m. The orbit accuracy of BDS IGSO and MEO satellites is about 0.5 m whereas the orbit quality would significantly reduced to 1.0–1.4 m level when the yaw-attitude mode switch happens. Based on the results above, this article also analyzed the broadcast orbit accuracy of BDS IGSO-6 satellite which was launched in March 2016 and adopt a modified yaw-attitude mode during its eclipse season, and found that the orbit accuracy of BDS IGSO-6 satellite is better than 0.25 m, no obvious orbit accuracy decrease can be observed, which is inconsistent with that of previous IGSO satellites. However, the performances of precise orbit product released by GFZ and iGMAS were still degraded during theoretical yaw maneuver periods. Finally, a POD experiment was carried out to analysis the orbit quality performance of BDS IGSO-6 satellite. The preliminary results show that benefiting from the modified yaw-attitude mode during its eclipse season, the orbit quality of BDS IGSO-6 satellite has high accuracy and stability, and special attention is needed in POD processing.

Keywords Beidou navigation satellite system · Broadcast ephemeris · SLR · Yaw-attitude mode · IGSO-6

G. Ji · Z. Yang (✉)
College of Geology Engineering and Geomantics, Chang'an University, Xi'an, China
e-mail: yang_gps@chd.edu.cn; changan_4440@163.com

Y. Liu · X. Jia
National Key Laboratory of Geographic Information Engineering, Xi'an, China

Y. Liu · X. Jia
Xi'an Research Institute of Surveying and Mapping, Xi'an, China

J. Sun et al. (eds.), *China Satellite Navigation Conference (CSNC) 2017 Proceedings: Volume III*, Lecture Notes in Electrical Engineering 439,
DOI 10.1007/978-981-10-4594-3_7

1 Introduction

BeiDou Navigation Satellite System (BDS) has been officially providing regional positioning,navigation and timing services for Asia-Pacific area since December 27, 2012 [1]. With the rapid development of BDS, five Beidou-3 satellites, each of which has a new navigation signal system, inter-satellite links, and other test features, has been launched, and a global navigation satellite system which consists of 5 GEO, 3 IGSO, and 27 MEO satellites will be completed in 2020 [2]. With the increasing quality requirement for civilian and scientific applications, several analysis centers (ACs), e.g., the Center for Orbit Determination in Europe (CODE), GeoForschungsZentrum (GFZ), and Wuhan University (WHU) have provided the precise ephemeris, clock, and bias products of BDS to MGEX. Besides IGS MGEX, the International GNSS Monitoring and Evaluation System (iGMAS) has been launched by China, to monitor and assess the performance as well as operational status and to promote compatibility and interoperability among different GNSS systems [3]. This project has planed to deploy 30 well-distributed stations (15 stations completed), and the combined products are also generated and could be downloaded by freely.

Different from the attitude control mechanism of GPS and GLONASS satellites, the BDS IGSO and MEO satellites adopt two attitude modes, namely Yaw-Steering (YS) and orbit-normal (ON) mode [4]. When the elevation angle β of sun above the satellite orbit plane is less than a critical value, e.g., when $|\beta|$ is closed to 4°, the yaw attitude will switch from YS mode to ON mode and vice versa [5]. The attitude mode has significant influence on POD. The orbit quality would reduce significantly during and after the attitude mode switch [6]. According to [7], the reason that one single set of orbital parameters is unsuitable for POD when attitude switch happens was figured out by the Box-wing model, and a piecewise linear solar radiation model was used to improve the orbit accuracy. The impacts of attitude, solar radiation and function model on POD for GNSS satellites was studied deeply by Guo [8], and the optimization POD strategy for GPS/GLONASS/Galileo/BDS quad-constellation at WUM was given in [9]. More recently, a preliminary attitude switch model of BDS IGSO and MEO satellites was established by Dai [10] based on a modified POD processing schema and the Reverse kinematic PPP technique proposed by Dilssner [11].

Although several studies on BDS yaw-attitude mode are already available as listed above, however, previous studies have only focused on the satellites that have been in service for many years. With the development of BDS, the attitude control mechanism of the new launched satellite may not be released in time. It would bring trouble to the data processing if the mistake experience mode of previous satellite was used. Broadcast ephemeris is important orbital information, which can roughly reflect the in-orbit attitude behavior of navigation satellite. Therefore, this article evaluates the BDS broadcast orbit accuracy firstly by the Satellite Laser Ranging (SLR) residuals starting from Jan 2015 to Nov 2016 in order to analyze and summarize the orbit accuracy variation characteristics of BDS GEO, IGSO, and MEO satellites. Based on the results described in previous step, we also analyzed

the broadcast orbit accuracy of BDS IGSO-6 satellite which was launched in March 2016 and adopt a modified yaw-attitude mode during its eclipse season [12]. After a short discussion, a POD experiment based on ground observations collected by MGEX and BETS networks was carried out to analysis the orbit quality performance of BDS IGSO-6 satellite. In the last section, this article was summarized.

2 The Orbit Accuracy Variation Characteristics of BDS Satellites

In order to analyze the orbit accuracy variation characteristics of BDS satellites based on broadcast ephemeris, the SLR tracking data of BDS satellites were collected from Jan 2015 to Nov 2016, and the orbit radial accuracy was evaluated. The broadcast ephemeris was derived from the multi-GNSS hybrid ephemeris published by MGEX. SLR is an optic technique providing independent validation of the satellite orbits. SLR residuals are computed in the sense observed versus computed range between satellite and SLR stations. Only four BDS satellites:C01 (GEO-1), C08 (IGSO-3), C10 (IGSO-5), and C11 (MEO-3) are tracked by the stations of the International Laser Ranging Service (ILRS) on a regular basis. It has been shown that the reference point of the Beidou broadcast ephemeris is at the center of satellite mass [13], therefore only the geometric center offsets of Laser Retroreflector Array (LRA) were corrected in this article. Figure 1a–d given the SLR residual series of the above four satellites (the residual was regarded as outliers and removed when the value greater than 5 m), and the red curves represent the elevation angle β of Sun above the satellite orbit plane. GEO and IGSO satellites enter into shadow when $|\beta| < 8.7°$, and the MEO satellites enter into shadow when $|\beta| < 13.2°$. The black dotted lines indicate the entering and exiting shadow times, regions between two green dotted lines indicate the ON mode period. BDS GEOs always maintain the ON mode, while IGSO and MEO satellites would switch their yaw-attitude mode when $|\beta| \approx 4°$, the switch times obtained from (ftp://igs.gnsswhu.cn/pub/BDS/bds_yaw) are used within this article.

As shown in Fig. 1a–d, BDS satellites will undergo two eclipse seasons each year. Around spring and autumn equinox, GEO satellite will enter the eclipse season, each lasting about 46 days. While the duration of IGSO and MEO satellites is short and with a long term change. In Fig. 1a, the SLR residuals of GEO satellites are less than 2 m. Although the orbit accuracy is slightly decreased during eclipse season, but the amplitude is not obviously. Which may be related to ON mode maintained by GEO satellites in the entire arc, and the impact of the eclipse season on orbit accuracy is difficult to reflect. Figure 1b–d show that the IGSO satellites have a better orbit accuracy than the MEO satellites. Possible explanations are issues with the uplink stations of Beidou ground segment are limited to the China mainland. However, in general, the orbit accuracy of IGSO and MEO satellites during yaw maneuvers is significantly reduced, with maximum SLR residuals

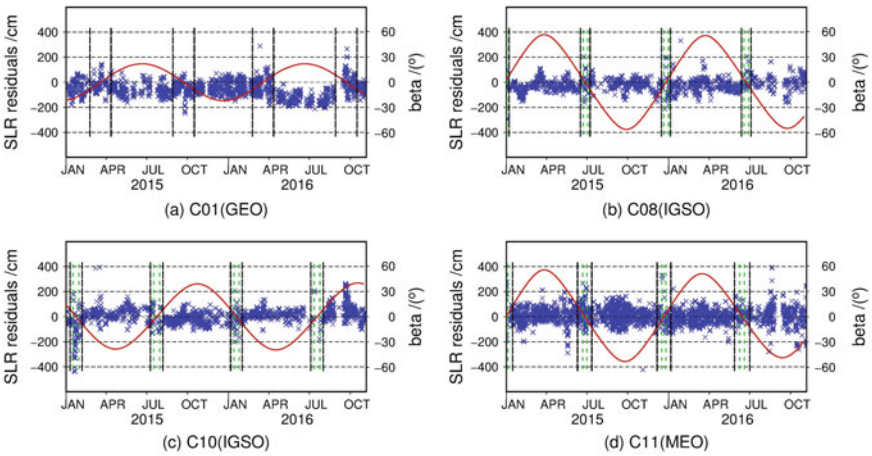

Fig. 1 SLR residual series of broadcast ephemerides against β angle

Table 1 Orbit accuracy statistics of BDS broadcast ephemerides against different periods

PRN	Mean			STD		
	No-esclipse	Esclipse season		No-esclipse	Esclipse season	
		YS	ON		YS	ON
C01	−60.7	−33.4	–	60.6	65.6	–
C08	−23.8	−24.6	−19.6	48.8	61.8	105.6
C10	5.7	−24.5	−85.3	50.8	60.8	140.2
C11	7.1	7.1	55.1	56.6	53.3	120.0

All values are given in cm

exceeding 4 m. The orbit accuracy decay times coincide with the switch times given by Wuhan University.

Table 1 shows the orbit accuracy statistics of the above four satellites in different cases (residual value greater than three times STD is not statistics). (1) The GEO satellites have a radial orbit accuracy of 0.6 m around with a systematic bias of about −0.6 m. (2) During non-eclipse periods, the orbit accuracy of BDS IGSOs and MEOs is about 0.5 m. (3) When entering the eclipse season, the orbit accuracy of IGSO and MEO satellite is slightly decreased, but not obvious; however, the orbit quality is significantly reduced to 1.0–1.4 m when yaw-attitude mode switch happens.

3 Analysis of BDS IGSO-6 Satellite Ephemeris

BDS IGSO-6 satellite was launched in March 30, 2016, and is in service recently. It is also tracked by the stations of ILRS since June 2016. Therefore, this article collected the broadcast ephemeris and SLR tracking data from June to November

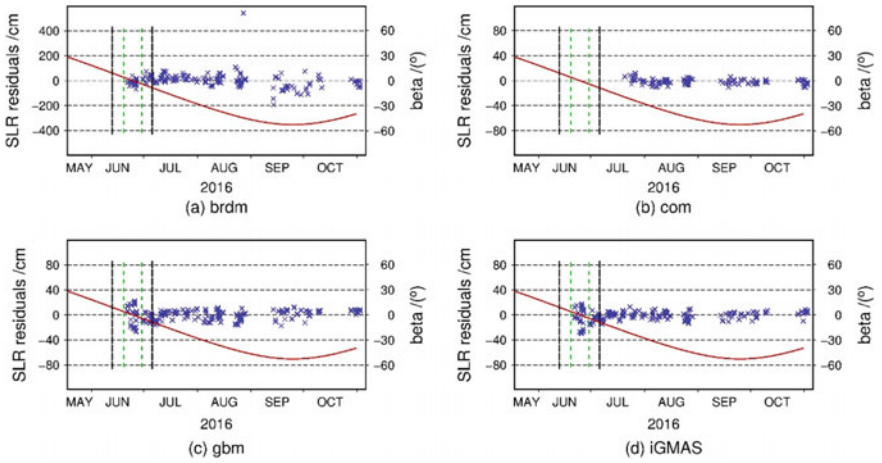

Fig. 2 SLR residual series of BDS IGSO-6 satellite against different products

Table 2 Orbit accuracy statistics of BDS IGSO-6 satellite in different cases

Ephemeris	Mean			STD		
	No-esclipse	Esclipse season		No-esclipse	Esclipse season	
		YS	ON			YS
BRDM	−2.1	26.2	−14.9	42.3	23.8	21.7
COM	−1.5	–	–	4.7	–	–
GBM	0.7	−4.9	−1.7	7.7	6.0	17.2
iGMAS	−0.2	−5.6	−3.9	6.0	6.2	15.6

All values are given in cm

2016, and analyzed its broadcast orbit accuracy in the same method as provided in Sect. 2. Figure 2a–d give SLR residuals of the broadcast ephemeris (brdm) as well as precise orbits from CODE, GFZ and iGMAS. Table 2 gives the orbit accuracy statistics of BDS IGSO-6 satellite against different products. From Fig. 2a, one can see that the broadcast orbit accuracy of BDS IGSO-6 satellite is stable, and no obvious orbit accuracy decrease can be observed. According to the results described in Sect. 2, the orbit accuracy of BDS IGSO satellites would significantly reduce during yaw maneuver, but the orbit accuracy variation charecteristics of BDS IGSO-6 satellite is inconsistent with that of the previous IGSO satellites.

However, as shown in Fig. 2c–d, the performances of precise orbit product released by GFZ and iGMAS are still degraded during theoretical yaw maneuver periods. We address the question that whether a mistake attitude mode was used by those ACs. Thus, some closer investigations will be carried out to analysis the orbit quality performance of BDS IGSO-6 in next section.

4 Experiment and Analysis

4.1 Data and Software

To clear the orbit accuracy variation characteristics of BDS IGSO-6, 41 well-distributed stations, spans from day 165 to 186, 2016, were selected from MGEX network and 13 stations distributed in China mainland are collected from BETS network which was established by the GNSS Research Center, Wuhan University [14–16]. Besides above, three stations with high quality hydrogen maser were collected from National Time Service Center (NTSC), Chinese Academy of Sciences. During the time period considered, the IGSO satellite C08 switched attitude from YS mode to ON mode and back to YS mode. The IGSO-6 (C15) satellite was in its eclipse season. The MEO satellite C11and C12 switched their attitude mode from ON mode to YS mode. The distribution of tracking stations and ground traces of Beidou constellation are shown in Fig. 3. The Satellite Positioning and Orbit Determination System (SPODS) software developed at Xi'an Institute of Surveying and Mapping was utilized in this experiment. SPODS software has high precision positioning and orbit determination capability [17].

4.2 Orbit Determination Strategy

The BDS data were processed together with GPS as only a limited amount of BDS satellite can be tracked beyond Asia-Pacific area currently. Dual-frequency code and carrier phase observations were used to form the ionosphere-free linear

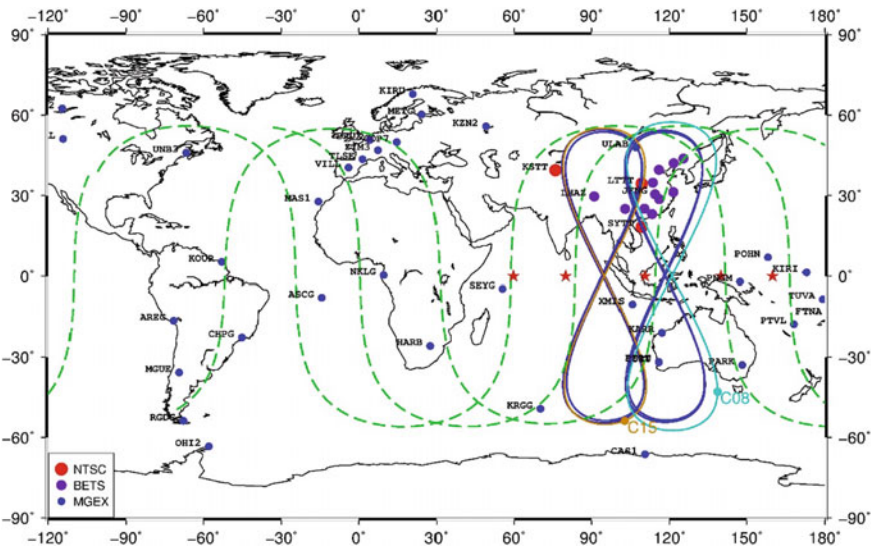

Fig. 3 Ground traces of Beidou constellation and tracking stations

combination (L1/L2 for GPS and B1/B2 for BDS). The reduced 5-parameter CODE SRP model without applying a priori model was employed for all GPS and BDS satellites. The five-parameter model consists of three constant terms in the direction of the Sun (D), in the direction of the solar panel axis (Y), and in the direction perpendicular to D and Y (B), as well as sine/cosine terms in B-direction, and the orbital parameters were estimated per 3-day interval. The PCO and PCV values were estimated by ESA [18] were used for BDS IGSOs and MEOs. In the absence of public satellite antenna phase center information, the PCO and PCV values of IGSO satellites C08 are used for the C15 satellite. BDS GEO satellites adopt the ON mode only, and the yaw-attitude of BDS IGSO and MEO satellites were calculated according to the model given in Dai et al. [10]. Since the attitude mode of the C15 satellite is not public, this article assumed that it would always maintain the nominal attitude which was reported by Bar-Sever [19]. A detailed list of processing options is given in Table 3. The orbit accuracy was evaluated by SLR residuals and orbit overlap difference, the illustration of overlap orbit comparison is shown in Fig. 4.

Table 3 Observation models and force models for multi-GNSS POD

Item	Applied models
Geopotential	EGM2008 model (12 × 12)
N-body gravity	Sun, Moon and planets
Tide forces	Solid Earth, pole, ocean tide IERS conventions 2010
Relative effects	IERS conventions 2010
Phase wind-up	WU et al. [20]
Solar radiation pressure	Reduced CODE 5-parameter with no initial value
Basic observables	Undifferenced ionosphere-free combination of code and phase based on GPS LI/L2, BDS B1/B2
Processing sampling	300 s
Cutoff elevation	7°
Satellite antenna phase center	PCOs and PCVs for GPS and BDS GEO from IGS08.ATX. PCO/PCV corrections estimated by ESA were used for BDS IGSOs and MEOs
Yaw-attitude model	A simplified Model from Kouba [21] for GPS, attitude switch model estimated by Dai et al. was used for BDS IGSOs and MEOs
Tropospheric delay	Saastamoinen model for wet and dry hydrostatic delay with GMF mapping function +2 h inteval PWC parameter
Satellite and receiver clock	Estimated as white noise for each epoch, a high quality hydrogen maser was selected as reference clock
Earth ratation parameters (ERP)	Fixed to values from IERS EOP 08 C04 series
Station coordnates	Estimated with tight constraint
Inter-system bias	Estimated as constant parameter, one station fixed
Ambiguity	Fixed for GPS/BDS (IGSO, MEO) separately

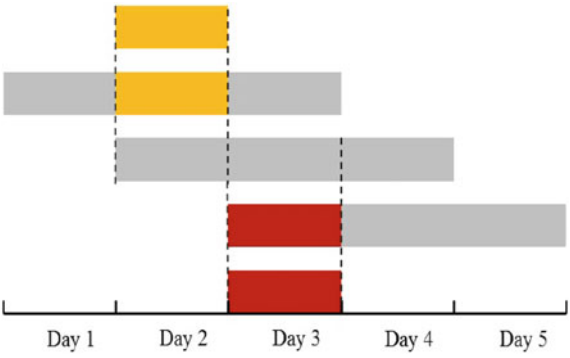

Fig. 4 Orbit arc and orbit overlap difference

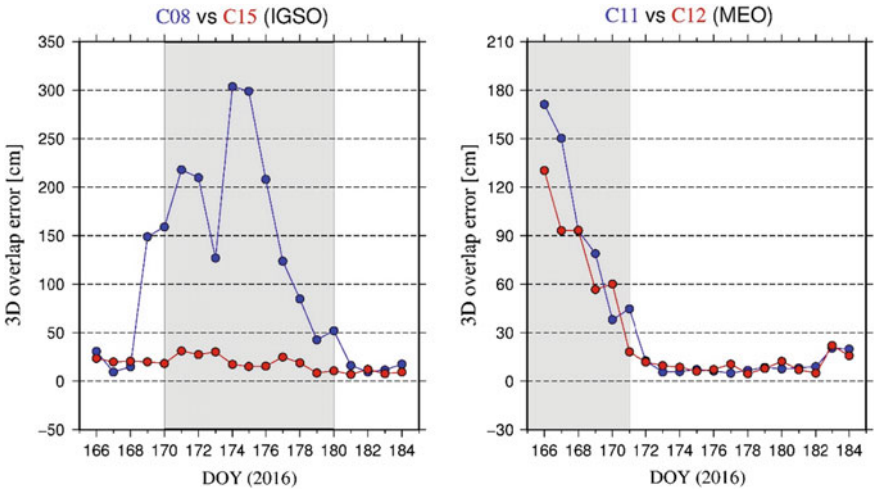

Fig. 5 Orbit overlap differences (3D) for C08/C15/C10/C11, the shaded areas illustrate the duration of the ON mode period

4.3 Results and Analysis

As already mentioned in the introduction, the attitude mode has significant influence on POD. Figure 5 shows 3D orbit overlap differences of the IGSO satellites (C08 and C15) and the MEO satellites (C11 and C12). The shaded areas illustrate the duration of ON mode period, while Fig. 6 shows the orbit overlap accuracy series in the along, cross-track and radial directions. One can be seen that: (1) when attitude switch happens and during the ON mode period, the orbital accuracy of C08 satellite is worse than that of the YS mode period, and the maximum overlap differences would reach up to 3 m; (2) However, as shown in Fig. 5 (lift) and Fig. 6, the orbit accuracy series of C15 satellite is very smooth, and no obvious orbit accuracy decrease can be observed; (3) Similar to C08 satellite, during the ON

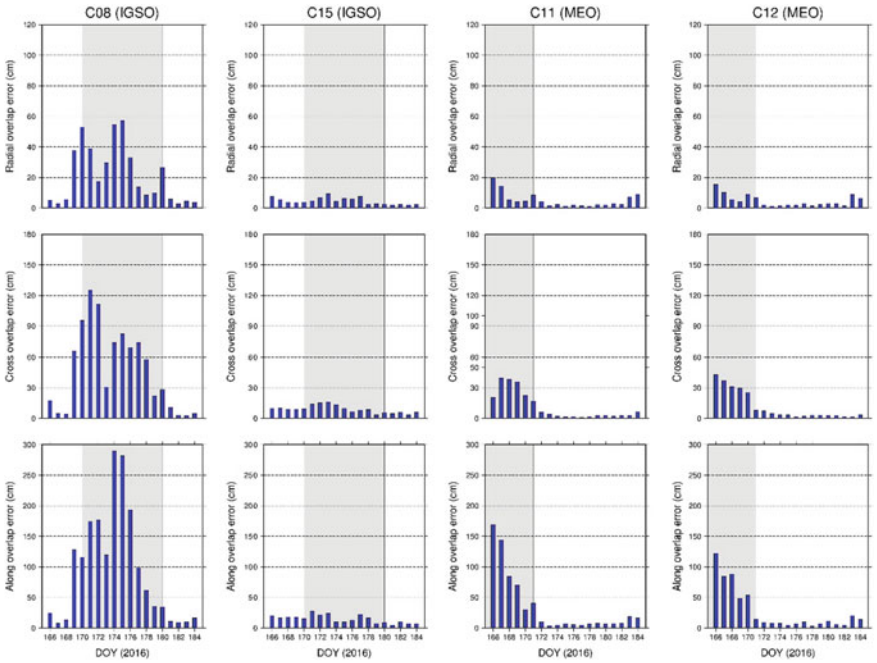

Fig. 6 Orbit overlap differences (in Along, Cross, Radial direction) for C08/C15/C10/C11, and the shaded areas illustrate the duration of the ON mode period

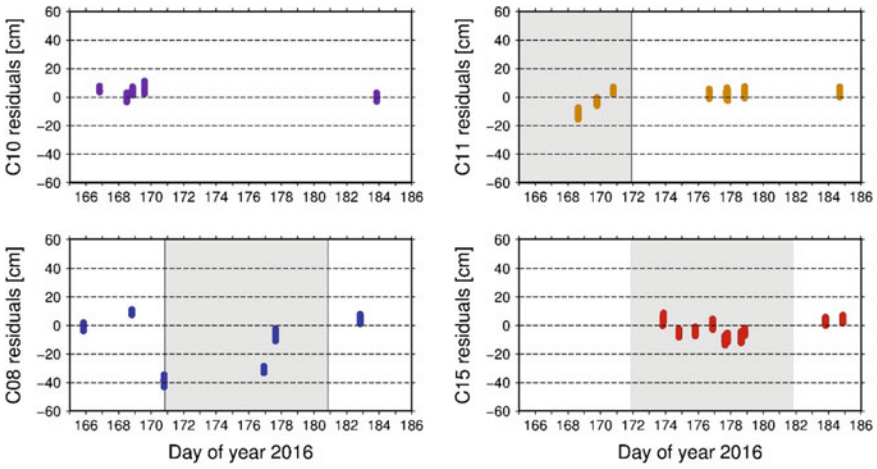

Fig. 7 SLR residuals series for C08/C15/C10/C11, the shaded areas illustrate the duration of ON mode period

mode period, the orbit accuracy of the C11 and C12 satellite is significantly lower than that of the YS mode period. In addition, Fig. 7 shows the SLR residual series for C08, C15, C10, and C11 satellites. It can be seen from Fig. 7 that the C08 and C11 satellites have lower orbit accuracy during the ON mode period (especially for C08 satellite when attitude mode switch happens), but the orbit quality of C15 has high accuracy and stability. In general, the orbit overlap accuracy and SLR results are in good agreement.

Although a proper yaw-attitude mode for BDS C08, C10 and C12 satellites was used in the article, but the orbit accuracy of those satellites is still not better than that of C15 (assuming that it would always maintain the nominal attitude) during eclipse season. Since measurement correction errors result from an improper modeling of the antenna phase center location and the antenna phase wind-up effect are generally less critical. However, the largest attitude-related error is the dynamic orbit errors due to improper modeling of the solar radiation pressure force which is a strong function of the attitude as well [10]. Obviously, the SRP of BDS IGSO and MEO satellites could not be well represented by CODE SRP model during eclipse season. Similar conclusions have earlier been presented by Guo [8]. However, it seems that the CODE SRP model is applicable for BDS IGSO-6 satellite during its eclipse season. Hence, a rough conclusion could be drawn that the BDS IGSO-6 satellite adopts a new yaw-attitude mode which is different from that of the previous BDS IGSO and MEO satellites, and the performance of this new yaw-attitude mode is superior. Further investigations are needed to understand the BDS IGSO-6 attitude control mechanism during shadow transits, i.e., using the Reverse Kinematic PPP technique to estimate the yaw-angle.

5 Conclusions

To simplify the attitude control in eclipse season, two attitude modes are used by BDS IGSO and MEO satellites. With the rapid development of BDS, the attitude control mode of the new launched satellite may not be released in time. Research on the orbit accuracy variation characteristics of navigation satellites can help to discover the deficiency of yaw-attitude modeling during eclipse season, and may further contribute to refine the functional models in precise orbit determination processing.

In this article, the orbit accuracy variation characteristics of BDS GEO, IGSO, and MEO satellites are analyzed and summarized firstly by SLR residuals spans two years. In general, the orbit accuracy evaluated by SLR residuals is 0.6 m around with a systematic bias of about −0.6 m for BDS GEO satellite. When entering the eclipse season, the orbit accuracy of IGSO and MEO satellite is slightly decreased, but not obvious; however, the orbit quality is significantly reduced to 1.0–1.4 m level when the yaw-attitude mode switch happens. In addition, the orbit accuracy of BDS IGSO-6 satellite is also evaluated by SLR residuals spans half a year, and the orbit accuracy better than 0.25 m could be found, which is different from that of

previous BDS IGSO satellites during theoretical yaw maneuver period. To clear the orbit accuracy variation characteristics of BDS IGSO-6 satellite, a 22-day POD experiment was carried out. The experimental results show that benefiting from the new yaw-attitude mode during its eclipse season, the orbit quality of BDS IGSO-6 satellite has high accuracy and stability.

Despite a rough conclusion is drawn in this article, but the attitude control mechanism during shadow transits and the PCOs and PCVs of BDS IGSO-6 satellite are unclear so far. A public release of relevant model is strongly encouraged and will greatly improve the orbit accuracy.

Acknowledgements The IGS MGEX and ILRS are greatly acknowledged for providing the multi-GNSS and SLR tracking data. We would also like to thank WHU, NTSC and iGMAS project for providing GNSS data and precise orbit products.

References

1. Yang YX, Jinlong LI, Wang AB, Junyi XU, Haibo HE, Guo HR et al (2014) Preliminary assessment of the navigation and positioning performance of beidou regional navigation satellite system. Sci China Earth Sci 57(1):144–152
2. CSNO (2013) BeiDou navigation satellite system signal in space interface control document open service signal (version 2.0)
3. Jiao W (2014) International GNSS monitoring and assessment system (iGMAS) and latest progress. Presented at China satellite navigation conference (CSNC) 2014, Nanjing, 20 May 2014
4. Montenbruck O, Schmid R, Mercier F, Steigenberger P, Noll C, Fatkulin R et al (2015) Gnss satellite geometry and attitude models. Adv Space Res 56(6):1015–1029
5. Guo J, Zhao Q, Geng T, Su X, Liu J (2013) Precise orbit determination for COMPASS IGSO satellites during Yaw Maneuvers. In: China satellite navigation conference (CSNC) 2013 proceedings. Springer, Berlin Heidelberg
6. Wang W, Chen G, Guo S, Song X, Zhao Q (2013) A study on the Beidou IGSO/MEO satellite orbit determination and prediction of the different Yaw control mode. In: China satellite navigation conference (CSNC) 2013 Proceedings. Springer, Berlin Heidelberg
7. Mao Y, Song X, Wang W, Jia X, Wu X (2014) Igso satellite orbit determining strategy analysis with the yaw-steering and orbit-normal attitude control mode switching. Wuhan Daxue Xuebao 39(11):1352–1356
8. Guo J (2014) The impacts of attitude, solar radiation and function model on precise Orbit determination for GNSS satellites. PhD Dissertation (in Chinese with English abstract), GNSS Research Center, Wuhan University, Wuhan, China
9. Guo J, Xu X, Zhao Q, Liu J (2016) Precise orbit determination for quad-constellation satellites at wuhan university: strategy, result validation, and comparison. J Geodesy 90(2): 1–17
10. Dai X, Ge M, Lou Y, Shi C, Wickert J, Schuh H (2015) Estimating the yaw-attitude of BDS IGSO and MEO satellites. J Geodesy 89(10):1005–1018
11. Dilssner F, Springer T, Gienger G, Dow J (2011) The glonass-m satellite yaw-attitude model. Adv Space Res 47(1):160–171
12. Pan C (2016) The twenty-second Beidou navigation satellite successfully launched. China Sci Technol Netw Sci Technol Daily. http://h.wokeji.com/jbsj/yb/201603/t20160331_2378755.shtml. Accessed 12 Oct 2016

13. Peng H, Yang Y, Gang W, Haibo HE (2016) Performance analysis of BDS satellite orbits during eclipse periods: results of satellite laser ranging validation. Acta Geodaetica Cartogr Sin 45(6):639–645
14. Zhao Q, Guo J, Li M, Qu L, Hu Z, Shi C et al (2013) Initial results of precise orbit and clock determination for compass navigation satellite system. J Geodesy 87(5):475–486
15. Lou Y, Liu Y, Shi C, Yao X, Zheng F (2014) Precise orbit determination of beidou constellation based on bets and mgex network. Sci Rep 4(8):1255–1264
16. Lou Y, Liu Y, Shi C, Wang B, Yao X, Zheng F (2016) Precise orbit determination of beidou constellation: method comparison. GPS Solutions 20(2):1–10
17. Wei Z, Ruan R, Jia X, Wu X, Song X, Mao Y et al (2014) Satellite satellite positioning and orbit determination system spods: theory and test. Acta Geod Cartogr Sin 724:312–317
18. Dilssner F, Springer T, Schönemann E, Enderle W (2014) Estimation of satellite antenna phase center corrections for BeiDou. In: Proceedings of IGS workshop 2014, 23–27 June 2014, Pasadena, USA
19. Bar-Sever YE (1996) A new model for GPS Yaw attitude. J Geodesy 70(11):714–723
20. Wu JT, Wu SC, Hajj GA, Bertiger WI, Lichten SM (1992) Effects of antenna orientation on GPS carrier phase. Astrodynamics 18:1647–1660. (Astrodynamics 1991)
21. Kouba J (2009) A simplified Yaw-attitude model for eclipsing GPS satellites. GPS Solutions 13(1):1–12

A Method for Polar Motion Prediction Based on LS Model of Error Compensation

Zhiwen Wang, Hui Xu, Qianxin Wang and Yilei He

Abstract Polar motion is an important component of the Earth Rotation Parameter (ERP). Not only is it one of the necessary transformation parameters between International Celestial Reference Frame (ICRF) and International Terrestrial Reference Frame (ITRF), but it is also essential for deep space exploration mission and satellite ultra-fast precise orbit determination. Polar motion is usually available with a delay of hours to days, thus polar motion prediction is needed to meet the growing demands for spacecraft navigation and physical geography science research. The least square model (LS) is a kind of mature polar motion forecasting model, but it has the problem that, though, the inner residual value of LS fitting is reasonable, the residual value of LS extrapolation, however, is poor, which will cause prediction errors to accumulate greatly. This paper proposes a LS model of error compensation (ECLS model) to solve this problem with the LS model, and hence improve the accuracy of predictions. Restrictions are first added to the two endpoints of LS fitting data to place them on the fitting curve of LS. If the LS interpolation residual sequence and the extrapolation of the residual sequence have a good correlation, then the LS interpolation errors can be used to correct the LS extrapolation value and to make the adjustment to the prediction errors of LS model. Feasibility and effectiveness of the ECLS model can be proved for predicting polar motion by comparing CELS with EOP_PCC, RLS + AR, RLS + ARIMA and LS + ANN. In addition, for the short term (30 days) prediction, examples show that the ECLS model can effectively improve prediction accuracy of polar motion, and the results show prediction accuracy equal to that achieved/observed at International level.

This paper was funded by The Natural Science Foundation of China (41404033) Supported, State Key Laboratory Lake Science and Environment (SKLGIE2014-Z-1-1) and the Fundamental Research Funds for the Central Universities (2015QNA31).

Z. Wang · H. Xu (✉) · Q. Wang · Y. He
Department of Computer Science and Technology, China University of Mining and Technology, Xuzhou 221116, China
e-mail: xuhui@cumt.edu.cn; 1162574974@qq.com

J. Sun et al. (eds.), *China Satellite Navigation Conference (CSNC) 2017 Proceedings: Volume III*, Lecture Notes in Electrical Engineering 439,
DOI 10.1007/978-981-10-4594-3_8

Keywords LS model · ECLS model · Polar motion prediction · Error compensation

1 Introduction

Movement of the earth's axis of rotation in the earth body is called the polar motion (PMX, PMY). polar motion is one of the necessary transformation parameters between International Celestial Reference Frame (ICRF) and International Terrestrial Reference Frame (ITRF) [5], and high accuracy in polar motion prediction is essential for deep space exploration missions, Satellite ultra-fast precise orbit determination and, especially, for the real-time and high-accuracy navigation missions. A large number of space-geodetic techniques can obtain polar motion of high accuracy but these techniques involve post processing of data, so the polar motion parameters' availability is delayed by hours (and even days) which makes it difficult to obtain in real time [2, 6]. Thus, polar motion prediction is adapted to meet the demands of scientific research.

At present, many methods have been developed and applied to polar motion prediction across the world, such as Kalman filter [3, 4], the least square extrapolation (LS) model [1], the least square extrapolation of a harmonic model and autoregressive (AR) prediction [8], the least square extrapolation of a harmonic model and artificial neural network (ANN) [7] and so on. In order to compare the predicted results of various prediction models, Schuh et al. Launched an Earth Orientation Parameter Prediction Competition (EOP_PCC) in 2005 [5]. The EOP_PCC has shown that there is no particular prediction technique superior to the others for polar motion in all prediction intervals.

Errors in LS extrapolation values is a well-known problem, and in order to solve this problem, we usually combine both LS model and other models to reduce LS prediction errors, e.g., (1) LS + AR model, (2) LS + ANN model. However, there are some problems to be solved in these combination models, such as LS fitting residual sequence is nonlinear, so it is unsuitable to establish AR model for the residual sequence. For ANN, the network model and the training network are very important for the predicted results, but there is no a standard for selecting network models and training network. In this paper, we try for the first time to propose a prediction model, which is LS model based on error compensation (ECLS). It can correct the LS model itself to improve the prediction accuracy and avoids the problem of LS model's incompatibility with other models.

2 LS Model

LS model is a complex natural phenomenon is shown in formula (3) and it contains liner term and periodic term that contains Chandler wobbles, annual, half of a year, etc. [9].

$$P(t) = A + Bt + C^1 \cos\left(\frac{2\pi t}{P_{\mathrm{SA}}}\right) + C^2 \sin\left(\frac{2\pi t}{P_{\mathrm{SA}}}\right) + D^1 \cos\left(\frac{2\pi t}{P_A}\right) + D^2 \sin\left(\frac{2\pi t}{P_A}\right) + E^1 \cos\left(\frac{2\pi t}{P_S}\right) + E^2 \sin\left(\frac{2\pi t}{P_S}\right) \tag{1}$$

Where t is the UTC time, and A, B, C^1, C^2, D^1, D^2, E^1, E^2 are the fitting parameters, In the case of polar motion, $P_{\mathrm{SA}} = 0.5$, $P_A = 1$, $P_{\mathrm{s}} = 1.183$ (unit is year).

LS model parameters can be solved by the least square principle, and the following are calculated sequentially to obtain the LS model parameters estimations.

$$X = \begin{bmatrix} A & B & C^1 & C^2 & D^1 & D^2 & E^1 & E^2 \end{bmatrix} \tag{2}$$

$$L = \begin{bmatrix} \hat{X}(t_1) & \hat{X}(t_2) & \ldots\ldots & \hat{X}(t_n) \end{bmatrix} \tag{3}$$

$$H = \begin{bmatrix} 1 & t_1 & \cos\left(\frac{2\pi t_1}{P_{\mathrm{SA}}}\right) & \sin\left(\frac{2\pi t_1}{P_{\mathrm{SA}}}\right) & \cos\left(\frac{2\pi t_1}{P_A}\right) & \sin\left(\frac{2\pi t_1}{P_A}\right) & \cos\left(\frac{2\pi t_1}{P_S}\right) & \sin\left(\frac{2\pi t_1}{P_S}\right) \\ 1 & t_2 & \cos\left(\frac{2\pi t_2}{P_{\mathrm{SA}}}\right) & \sin\left(\frac{2\pi t_2}{P_{\mathrm{SA}}}\right) & \cos\left(\frac{2\pi t_2}{P_A}\right) & \sin\left(\frac{2\pi t_2}{P_A}\right) & \cos\left(\frac{2\pi t_2}{P_S}\right) & \sin\left(\frac{2\pi t_2}{P_S}\right) \\ \vdots & \vdots & \vdots & \vdots & \vdots & \vdots & \vdots & \vdots \\ 1 & t_n & \cos\left(\frac{2\pi t_n}{P_{\mathrm{SA}}}\right) & \sin\left(\frac{2\pi t_n}{P_{\mathrm{SA}}}\right) & \cos\left(\frac{2\pi t_n}{P_A}\right) & \sin\left(\frac{2\pi t_n}{P_A}\right) & \cos\left(\frac{2\pi t_n}{P_S}\right) & \sin\left(\frac{2\pi t_n}{P_S}\right) \end{bmatrix} \tag{4}$$

$$X = (H^T H)^{-1} H^T L \tag{5}$$

Note that X denotes the fitting parameter, where L is observed value of the polar motion and B is coefficient matrix of fitting parameters.

3 Problems and Analysis of LS Model

The internal residual of LS fitting is reasonable but the residual value of LS extrapolation is unreasonable, which is a well-known problem; the following methods are used to solve the problem in case the LS extrapolation errors are too large. Restrictions are added to the two endpoints of LS fitting data to place them on fitting curve of LS. Taking the PMX direction of polar motion as an example, residual sequences are graphically shown in Fig. 1a, b. The LS extrapolation residual is very big without the constraints, but it improves greatly after additional constraint. In addition, additional constraints on the LS can make the fitting value next to the two endpoints close to the observed value as well as the prediction errors

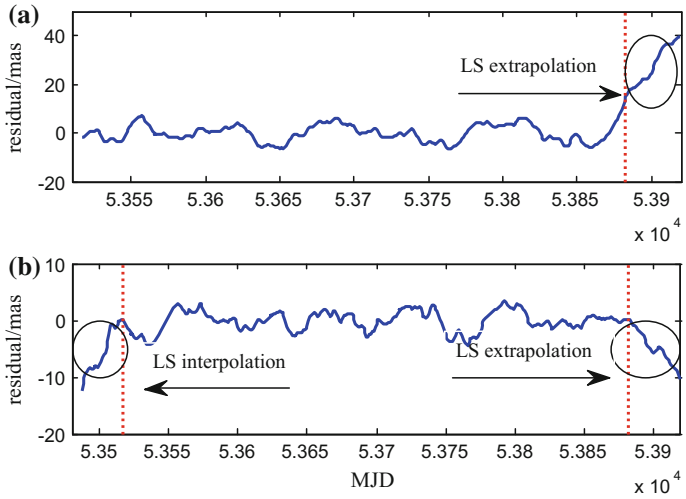

Fig. 1 The variation of residual series of LS model after adding constraints. The **a** represents residual sequence of LS model, and **b** denotes the residual sequence of LS model with constraint

are zero at the two endpoints. At the same time, the value of the extrapolation residual series of LS fitting curve as well as the interpolation residual series are increased from zero. As is shown in Fig. 1b, the trend of the LS interpolated residual sequence is similar to that of the LS extrapolated residual sequence in the short term. If the LS extrapolation residual sequence has good correlation with the internal residual error sequence, we use LS interpolation errors to correct the LS extrapolation errors to adjust to the prediction errors.

The following experiments are done to test the correlation between LS interpolated residual sequence and LS extrapolated residual sequence after adding constraints on LS model. It is considered that the pole shift has time-varying and periodic characteristics, so we use the LS model with the basic sequence of 432 days (1.183 year, one cycle) to make the short term (30 days) prediction, from January 1, 2008 rolling prediction to December 31, 2011 (1461points), as well as the correlation statistics are shown in Fig. 2. This investigation employs the International Earth Rotation Service (IERS) EOP 08 C04 of polar motion data. In Fig. 3, at first sight it can be seen that most of the correlation coefficients are greater than 0.5. In the direction of PMX, the correlation coefficient greater than 0.5 accounts for 70%, and, in the PMY, the ratio of correlation coefficient larger than 0.5 reaches 68%, which shows that the LS interpolated residual sequence has a strong correlation with the LS extrapolated residual sequence, therefore LS interpolation errors can be used to correct the LS extrapolation errors and to improve the prediction accuracy.

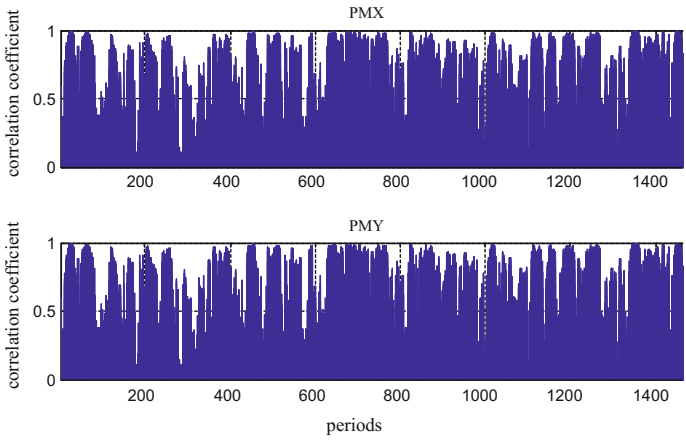

Fig. 2 Chart of correlation coefficient

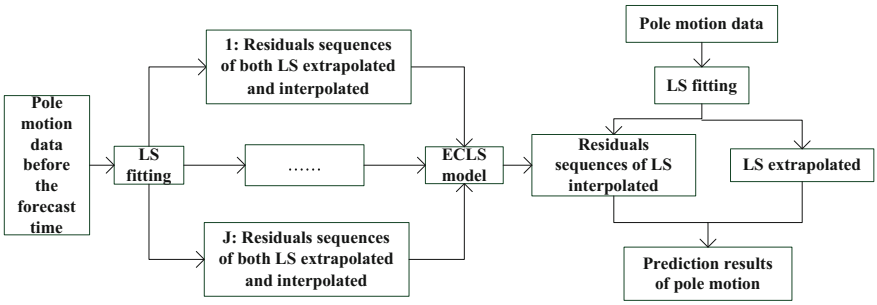

Fig. 3 Forecast flow of ECLS model

4 LS Model of Error Compensation (ECLS Model)

The polar motion sequence is periodic and time-varying, which increases the difficulty of polar motion prediction and it is one of the reasons for the serious accumulation of prediction errors. From the first section we know that LS interpolated residual sequence has a strong correlation with LS extrapolated residual sequence, so we use LS interpolation errors to correct the LS extrapolation value. In this article, the main formulae of polar motion prediction are as follows:

$$\begin{cases} \hat{Y}_{\mathrm{k}} = Y'_k + \Delta\varphi_k \\ \Delta\varphi_{\mathrm{k}} = A_k + B_k \Delta\phi_{\,k} \end{cases} \tag{6}$$

Where $\hat{Y}_k$ is the final polar shift forecast sequence when the forecast time span is K days, Y'_k is the LS extrapolation forecast sequence when the forecast time span is

K days, $\Delta\varphi_k$ is the error correction value sequence of LS extrapolation forecast while the forecast time span is K days, $\Delta\phi_k$ is the error sequence of LS interpolated value while the forecast time span is K days, A_k is a diagonal matrix of $K \times 1$ dimensions which is constant term $(a_1\ a_2 \cdots a_k)$ in error compensation model, and B_k is a diagonal matrix of $K \times K$ dimension and is coefficient term $(b_1\ b_2 \cdots b_k)$ in error compensation model. Parameters in error compensation model which are both A_k and B_k can be solved by the least square principle, and the following are calculated sequentially to obtain those parameters estimations.

$$\alpha = [\,a_1 \quad a_2 \cdots a_k \quad b_1 \quad b_2 \cdots b_k\,]^T \tag{7}$$

$$W = \left[\,\Delta\varphi_{1,k} \quad \Delta\varphi_{2,k} \quad \cdots \quad \Delta\varphi_{j,k}\,\right]^T \tag{8}$$

$$\beta = \begin{bmatrix} E_\mathrm{k} & E_k & \cdots & E_k \\ \Delta\phi_{1,k} & \Delta\phi_{2,k} & \cdots & \Delta\phi_{j,k} \end{bmatrix}^T \tag{9}$$

$$\alpha = (\beta^T\beta)^{-1}W \tag{10}$$

Note that $\Delta\varphi_{j,k}$ represents the true value sequence of the LS extrapolated error in the j periods while forecast time span is K days, $\Delta\phi_{j,k}$ is the error sequence of LS interpolated value in the j periods while forecast time span is K days, and E_k is the unit matrix of K dimension. The prediction process of ECLS model is as follows: First, the LS model with constraint is used to predict polar motion. In the next part, we use the data of polar motion before the prediction time to calculate the unknown parameters in the error compensation model according to the formula (6)–(10), and finally we use the error compensation model to correct the prediction value of LS to obtain the final result of the prediction. The forecast flow chart is shown in Fig. 3.

5 Calculation and Analysis

5.1 Comparison of the Results of ECLS and EOP_PCC

This investigation employs the International Earth Rotation Service (IERS) EOP 08 C04 of polar motion data, from January 1, 1980 to March 8, 2008. The sampling interval is one day. In order to compare our results with EOP_PCC results in ultra-short term prediction (1–10 days) and short term prediction (30 days), we choose the data from October 1, 2005 to March 8, 2008 as the test sequence (almost 889 points), and selected 432 days as the length of the base sequence. For each prediction interval (1–30 days), 889 predictions are made using ECLS model, and mean absolute error (MAE) is utilized as the prediction accuracy index as shown:

$$\mathrm{MAE}_i = \frac{1}{M}\sum_{m=1}^{M}\left|\varepsilon_{i,m}\right| \tag{11}$$

Where i is prediction day, M and $\varepsilon_{i,m}$ are the prediction number and the difference between the predicted values and the observed values.

The prediction results of EOP_PCC are given in the form of graphs, so we can only compare with the prediction accuracy map of EOP_PCC. Figure 4 upper shows the prediction results of ECLS model, while the prediction results of EOP_PCC can be seen in Fig. 4 middle and lower. In the prediction accuracy chart of EOP_PCC, curves of different colors indicate the prediction results of the different participants. In the case of polar motion prediction, Kalrus (orange solid line), EOP product center (pink solid line), and the combined forecasting method of different participants (black circle line) are the best in the EOP_PCC. By comparison, in the direction of PMX, the prediction accuracy of the ECLS model is only inferior to both Kalrus (rank first in EOP_PCC) and combined forecasting method (rank second in EOP_PCC) in ultra-short term prediction, and it is equivalent to prediction accuracy of results of EOP product center in short term prediction which reaches to fourth in the results of EOP_PCC. In addition, in the direction of PMY, the prediction accuracy of the ECLS model in ultra-short term prediction or short term prediction is only second to both Kalarus (rank second in EOP_PCC) and the combined forecasting method (rank first in EOP_PCC).

From the above analysis, ECLS prediction results of polar motion are at the same level as EOP_PCC and are also superior to prediction results of most EOP_PCC participants, so prediction accuracy of ECLS model can reach the international level.

5.2 Comparison of the Results of ECLS and Other Models

The ECLS model can obtain a good prediction result of polar motion, which is proved in the previous sections. In order to further verify the feasibility of the ECLS model, the prediction results of CELS model are compared with prediction results of other models including RLS + AR, RLS + ARIMA by Xu [8] as well as LS + ANN by Schuh et al. [7], which are found to be comparable with those of other models (Table 1). In order to make the comparison with above models, the prediction time period is the same as the above models, so we choose the data from January 1, 2000 to January 20, 2002 as the test sequence (almost 750 points). From January 1, 2000 to carry out prediction of the polar motion, and each predictions interval (1–30 days), 750 predictions are made using ECLS model. Note that the prediction results of Schuh are given in the form of comprehensive prediction accuracy, and it is shown as follows:

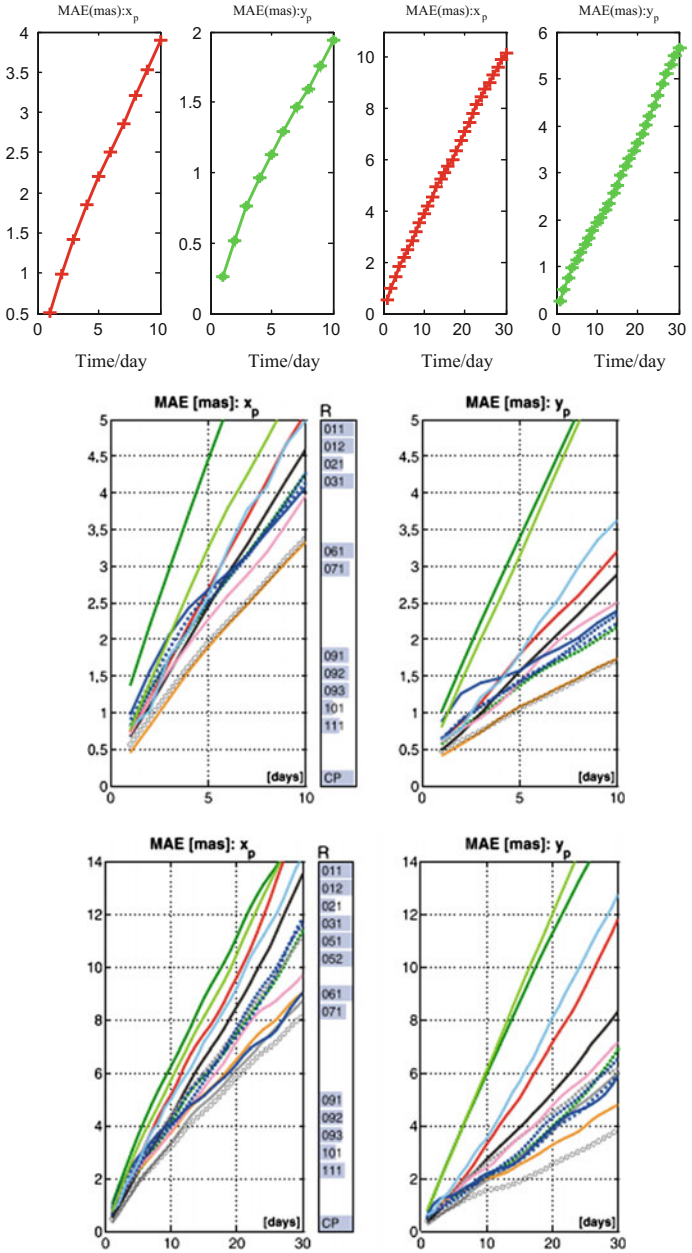

Fig. 4 Comparison of prediction results both ECLS model and EOP_PCC. The *upper* represents the prediction results of ECLS model, and the *lower* denotes forecast results of EOP_PCC

Table 1 Accuracy statistic of both ECLS and other models

Day	RMSE			
	Mas			
	ECLS	RLS + AR	RLS + ARIMA	LS + ANN
1	0.50	0.364	0.25	0.29
2	0.95	0.88	0.74	0.57
3	1.26	1.45	1.26	0.95
4	1.75	2.01	1.79	1.3
5	2.07	2.57	2.31	1.79
6	2.32	3.08	2.81	2.1
7	2.64	3.57	3.26	2.39
8	2.88	4.01	3.74	2.67
9	3.21	4.46	4.19	2.95
10	3.43	4.90	4.65	3.25
20	5.90	9.28	9.41	6.28
30	8.43	14.23	14.66	8.89

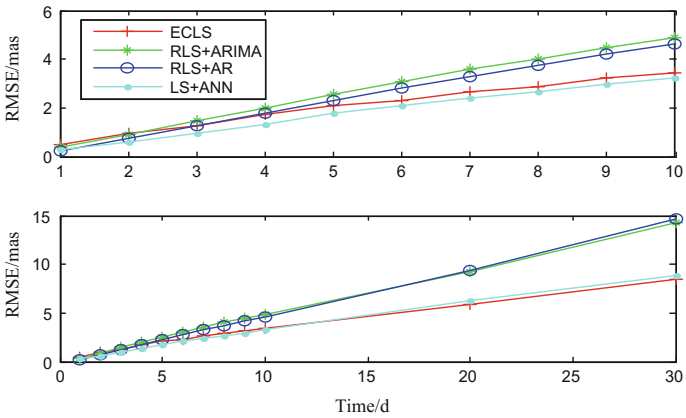

Fig. 5 Comparison of prediction results of both ECLS and other models

$$\mathrm{RMSE} = \sqrt{\frac{\sum_{j=1}^{M} \varepsilon_i^2}{M}} \tag{12}$$

$$\mathrm{RMSE_{PM}} = \frac{\sqrt{\mathrm{RMSE_{PMX}^2} + \mathrm{RMSE_{PMY}^2}}}{2} \tag{13}$$

Note that M is prediction day, where ε_i are the difference between the predicted values of pole motion and the observed values.

As can be seen in Fig. 5 and Table 1, for the ultra-short term prediction or short term prediction, prediction results of ECLS model is are superior to both RLS + AR

and RLS + ARIMA in addition to the first day and second days prediction results, and the advantage of ECLS model is more obvious with the increase of the time span, so the ECLS model has some advantages compared to other models which are combined with LS model. Furthermore, it is found that the ECLS model is equal to or slightly better than Schuh in the prediction results of 10–30 day. Therefore, the feasibility of ECLS model is further proved in short term polar motion prediction, and high accuracy prediction results can be obtained by ECLS model.

6 Conclusion

In this study, we analyzed and solved the problems existing in LS prediction model. We improved LS model prediction accuracy by constructing error compensation model. Comparing the prediction results of ECLS with EOP_PCC, RLS + AR, RLS + ARIMA and LS + ANN, the results show that the ECLS model proposed in this paper is equal to or better than other models which are combined with LS model. In addition, it is also proved that the ECLS model can obtain prediction results of the international level in the short term polar motion prediction.

The method proposed in this paper is only suitable for short term forecasting. For the improvement of long term polar motion prediction accuracy, we need to find other methods, which is the focus of the next work.

Acknowledgements We would like to thank the International GNSS Monitoring Assessment System (IGMAS) for their support for this paper, and the International Earth Rotation Service (IERS) for providing us the polar motion data.

References

1. Akulenko LD, Kumakshev SA, Markov YG (2002) Motion of the Earth's pole. In: Doklady physics. MAIK Nauka/Interperiodica, vol 47, no 1, pp 78–84
2. Behrend D, Baver KD (2009) International VLBI service for Geodesy and astrometry 2008 annual report
3. Freedman AP, Steppe JA, Dickey JO, Eubanks TM, Sung LY (1994) The short-term prediction of universal time and length of day using atmospheric angular momentum. J Geophys Res-All Ser 99:6981–6981
4. Gross RS, Eubanks TM, Steppe JA, Freedman AP, Dickey JO, Runge TF (1998) A Kalman-filter-based approach to combining independent Earth-orientation series. J Geodesy 72 (4):215–235
5. Kalarus M, Schuh H, Kosek W, Akyilmaz O, Bizouard C, Gambis D, Cerveira PM (2010) Achievements of the Earth orientation parameters prediction comparison campaign. J Geodesy 84(10):587–596
6. Ratcliff JT, Gross RS (2010) Combinations of Earth orientation measurements: space 2009, COMB2009, and POLE 2009. JPL Publication, Pasadena, CA, pp 10–22
7. Schuh H, Ulrich M, Egger D, Müller J, Schwegmann W (2002) Prediction of Earth orientation parameters by artificial neural networks. J Geodesy 76(5):247–258

8. Xu J (2010) Researches on the theories and algorithms of Earth orientation parameters prediction. The PLA Information Engineering University
9. Xu XQ, Zhou YH (2010) High precision prediction method of earth orientation parameters. J Spacecr TT&C Technol 29:70–76

Research on Autonomous Orbit Determination Test Based on BDS Inter-Satellite-Link on-Orbit Data

Haiong Wang, Qiuli Chen, Weisong Jia and Chengpan Tang

Abstract Autonomous orbit determination and time synchronization based on inter-satellite-link is core of autonomous navigation for navigation constellation. On the basis of the on-orbit Data of inter-satellite links system of test satellites of BD global navigation satellite system, autonomous orbit determination test had been carried out using space-borne autonomous navigation prototype software in this paper. The test work consisted of analysis for inter-satellite ranging and satellite-ground ranging, precision analysis of autonomous orbit prediction which grounded long-term forecast reference ephemeris, and analysis for autonomous orbit determination which based on on-orbit data of inter-satellite system. The precise orbit determined by both inter-satellite and satellite-ground ranging had been used as standard, which offered by master control station of operational control system. The result proved that, SIS-URE of autonomous orbit determination of four test satellites are all better than 5 m (1σ).

Keywords BDS · Inter-satellite-link · Autonomous orbit determination

1 Introduction

Following the development of global satellite navigation system, the autonomous navigation technology has been improved also. As early as 80s in the twentieth century, the conception that autonomous operation for 180 days had been proposed in design scheme of GPS Block IIA satellite in the United States GPS engineering test phase. The main technical feature of autonomous operation was that broadcasting directly navigation message for 180 days stored on the satellite. The user ranging error (URE) is approximately 5 km for 180 days. Form the beginning of 90s to the

H. Wang (✉) · Q. Chen · W. Jia
Beijing Institute of Spacecraft System Engineering, Beijing 100094, China
e-mail: 5585737@qq.com

C. Tang
Shanghai Astronomical Observatory, Shanghai 200030, China

J. Sun et al. (eds.), *China Satellite Navigation Conference (CSNC) 2017 Proceedings: Volume III*, Lecture Notes in Electrical Engineering 439,
DOI 10.1007/978-981-10-4594-3_9

present, UHF wide beam inter satellite link device had been equip on the GPS Block IIR satellite, Block IIM satellite, and Block IIF satellite. The main technical feature of that upgraded to distributed autonomous orbit determination and time synchronization based on inter satellite ranging. And the URE was better than 6 and 3 m for 180 and 60 days [1–3]. The design of second generation Galileo System (G2G) has been started by European Union, inter satellite link will also be configured on Galileo satellite in order to reduce dependence on the ground system [4].

In China, a wide and deep research had been carried out for autonomous navigation technology of navigation constellation. All of them included that constellation autonomous navigation system design, algorithm research and simulation for navigation satellite autonomous orbit determination and time synchronization, and research on constraint and correction algorithms of inter satellite orientation constraint parameter [5]. All of these have laid a solid technical reserve for design of BD system autonomous navigation of China.

In March 2015, China had launched the first test satellite of BD global system. This satellite runs on inclined geosynchronous orbit (IGSO). Novel inter satellite link device on the satellite could carry out two-way ranging named satellite-ground ranging with three inter satellite link ground station. Chang Jiachao [6] carried out the autonomous orbit determination test using measured data. The result showed that URE is kept in 5 m approximately for 9 days. He also pointed out that, the precision of orbit determination fail rapidly in the absence of an effective ranging link. Maximum of URE is up to 15 m.

From July 2015 to March 2016, China had launched another four test satellites of BD global system. Three of them run on medium earth orbit (MEO), and the other runs on IGSO. Inter satellite two-way ranging and satellite-ground two-way ranging with a inter satellite link ground station had been carried out between all of these five test satellites. On the basis of inter satellite and satellite-ground ranging data of newly launched four test satellites, autonomous orbit determination has been tested in this paper depending on prototype software for satellite autonomous navigation [7, 8].

2 Inter Satellite and Satellite-Ground Ranging

2.1 Steric Configuration Between Test Satellite and Inter Satellite Link Ground Station

The two MEO test satellites, namely, BD-18 and BD-19, run on the same medium earth orbit, which is the first orbit of Walker 24/3/1 with orbital altitude 21,528 km and inclination 55°. The positions of them are the first and the sixth phase. The phase of BD-18 leads BD-19 135°. The two IGSO test satellites, namely, BD-17 and BD-20, run on two different inclined geosynchronous orbits, longitude of ascending node of which both are 95° E. The phase of BD-17 is backward BD-20 40°. Inter satellite link ground station locates in Beijing, namely BJ station.

Table 1 Orbital roots of four teat satellites in J2000.0

	BD-17	BD-20	BD-18	BD-19
a (km)	42166.91	42159.00	27906.35	27904.26
e	0.004321	0.004491	0.000413	0.000299
i (deg.)	54.659	54.638	55.315	55.311
Ω (deg.)	337.513	300.362	65.137	65.151
w (deg.)	176.682	165.514	297.434	279.396
M (deg.)	46.268	96.984	287.164	166.542

BD time 547 week 475200.0 s

The orbital roots number of four test satellites on 548 week 475200.0 s of BD time, that is also 11:59:57 in July 8, 2016 of coordinated universal time (UTC), is shown in Table 1.

2.2 *Analysis of on-Orbit Measured Ranging Data of Inter Satellites Link*

On the basis of on-orbit measured ranging data of inter satellite device of test satellites and BJ station, simulation analysis has been done for 14.2 days, from 548 week 474,465 s to 550 week 602,000 s in this paper. On-orbit measured ranging data consists of one-way ranging and inter satellite pointing information recording by inter satellite link device terminal for every 1.5 s, which had been transferred to central station through satellite telemetry channel. All of the on-orbit measured ranging data from all the test satellites and BJ station has been collected by central station. According to the principle of that two one-way ranging can be composed of two-way ranging in every 3 s with inter satellite pointing information at the same time, the measured ranging data has been made a pair, which is the original measurement data for this paper.

Satellite number of constellation is little. And ground telemetry receiving station distributes being restricted. Because of these, even if inter satellite link has been used, satellite telemetry information for full time period could not be transferred to central station. On the basis of measured ranging data, the actual number of ranging link of four test satellites and the constellation has been proposed in Fig. 1.

As shown in Table 2, the actual number of ranging link is three at most for IGSO test satellite and MEO satellite. Four satellites constellation has six ranging links at most, which had been shown in Fig. 2.

To the sparsity of original ranging data, on the one hand, space-borne autonomous navigation software design demand to predigest calculating process to reducing computing workload. A doable simplified scheme is that, every five minutes was chosen as a processing period. And the first minute bidirectional ranging data of each processing period was used in autonomous navigation computability. On the other hand, in the test satellite project moment, there is a small

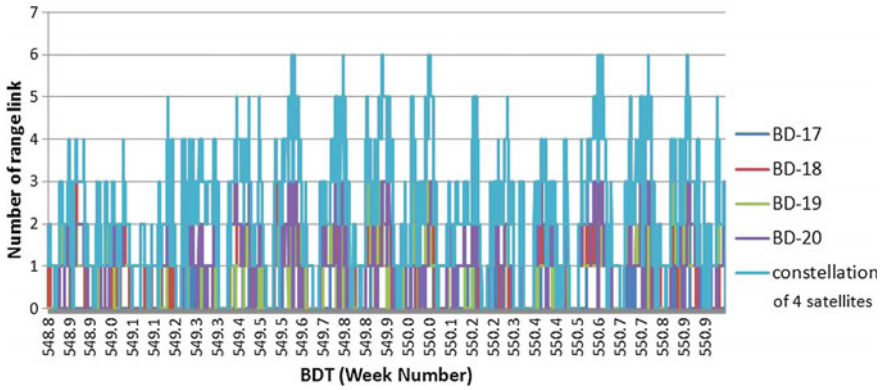

Fig. 1 The actual number of ranging link of four test satellites and the constellation

Table 2 The actual number of ranging link of four test satellites and the constellation

	BD-17	BD-20	BD-18	BD-19	Constellation of 4 satellites
Max.	3	3	3	3	6
Min.	0	0	0	0	0
Mean	0.5	0.9	0.8	1.1	2.2

BDT: 548 week 475200.0 s–550 week 602,000 s

quantity of theoretic link which could be constructed. And the link programming table is short. The measured data show that, it could repeat link constructing for every 18 s. It means that, every satellite circular construct ranging and communication link with six constructing link object.

On the basis of original ranging data, every five minutes was chosen as a processing period. And the first 18 s bidirectional ranging data of each processing period was used in autonomous orbit determination.

3 Accuracy Analysis for Ground Upload Long-term Ephemeris Prediction and Autonomous Orbit Prediction

The method of autonomous orbit determination had been detailed bewrite in [7]. The main character is that, autonomous orbit prediction [9] basis on ground upload long-term ephemeris prediction parameters and expandable Kalman filter [10] with the format of UD square root decomposable. Concrete method hadn't been noticed in this paper. Accuracy analysis for ground upload long-term ephemeris prediction parameters which had been used in autonomous orbit determination test and autonomous orbit prediction based on the aboved prediction parameters in this section.

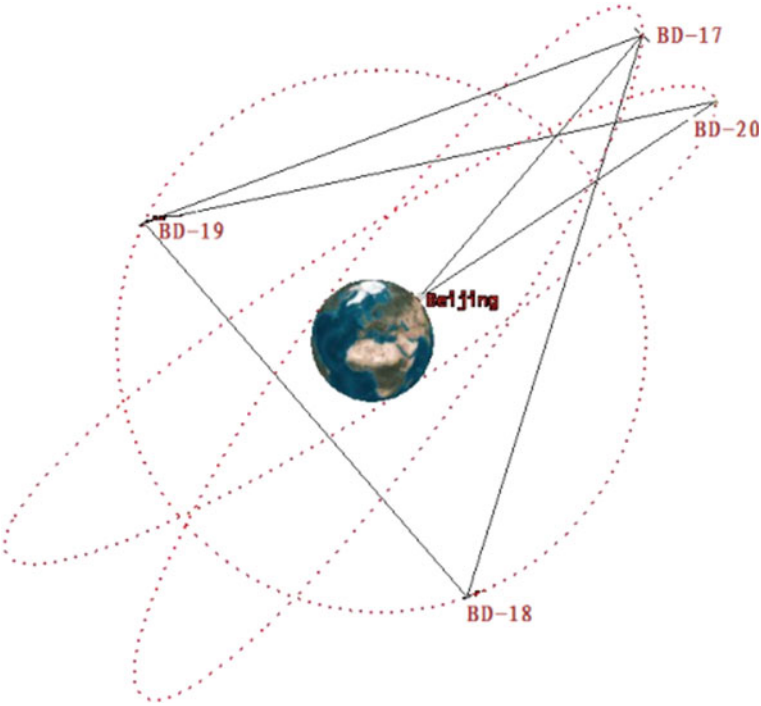

Fig. 2 Six range link scenarios for four satellites constellation and BJ station (BDT: 550 week 527820.0 s)

3.1 Accuracy Analysis for Ground Upload Long-term Ephemeris Prediction Parameters

Ground upload long-term ephemeris prediction parameter is crested by ground operation control system. In order to keep the high precision of long-term ephemeris prediction parameters, the precise orbit of navigation satellite usually used as initial orbit. At the same time, elaborate dynamic model and numeric integrator were used in operation. The long-term ephemeris prediction parameters used in autonomous orbit determination test is 86.2 days, which is from 538 week 413,100 s to 550 week 604,500 s of BD time.

Inter satellite and ground-satellite precise orbit of navigation satellite offered by master control station of operation control system was chosen as criterion. Taking BD-17 and BD-18 as example, the result of accuracy analysis has been shown in Fig. 3. Error of long-term ephemeris prediction of BD-17 and BD-18 in Earth-Centered Earth Fixed (ECEF) were respectively shown in the upper two parts. URE of long-term ephemeris prediction of two test satellites was shown in the three parts.

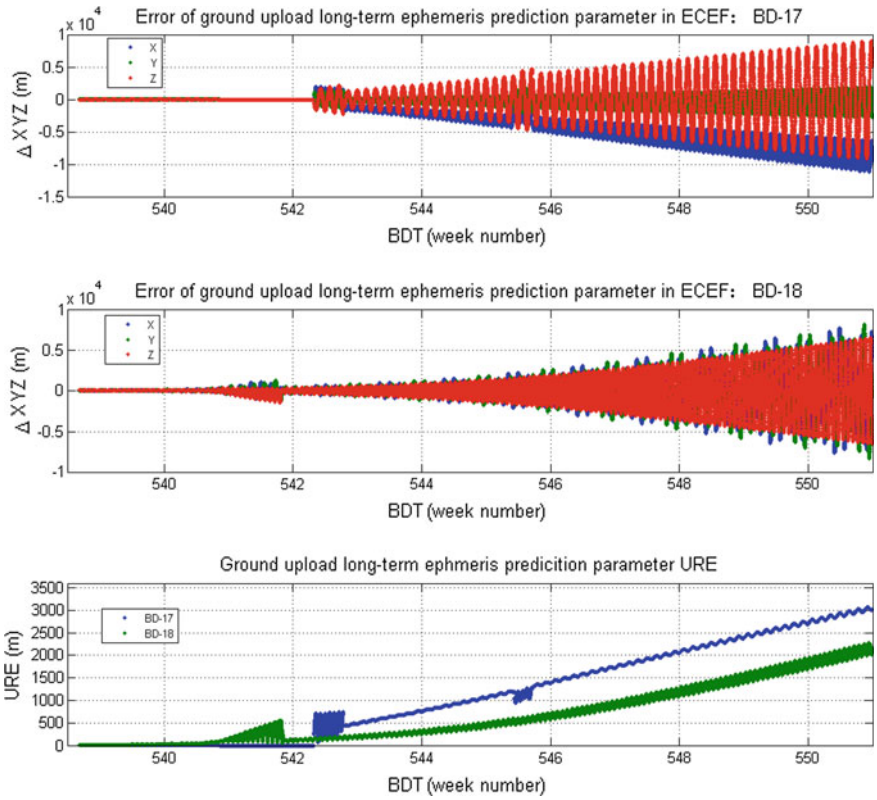

Fig. 3 The precision of ground upload long-term ephemeris prediction parameter (BDT: 538 week 413,100 s–550 week 604,500 s)

In Fig. 3, the curve of prediction error of two test satellites has obvious leap. Considering dynamics flowingness of long-term orbit prediction, the possible reason is that precise ephemeris which had been chosen as standard is non-flowing. It's also determined by diversity of on-orbit test. For example, orbit phasing of test satellite was adjusted.

3.2 Accuracy Analysis for Autonomous Orbit Prediction Based on Ground Upload Long-term Ephemeris Prediction Parameters

On the basis of long-term ephemeris precision parameter, which had been proposed in the last chapter, autonomous orbit prediction and accuracy analysis has been studied. The prediction arc was according to on-orbit range data of inter satellite link device from 548 week 474,465 s to 550 week 602,000 s of BD time,

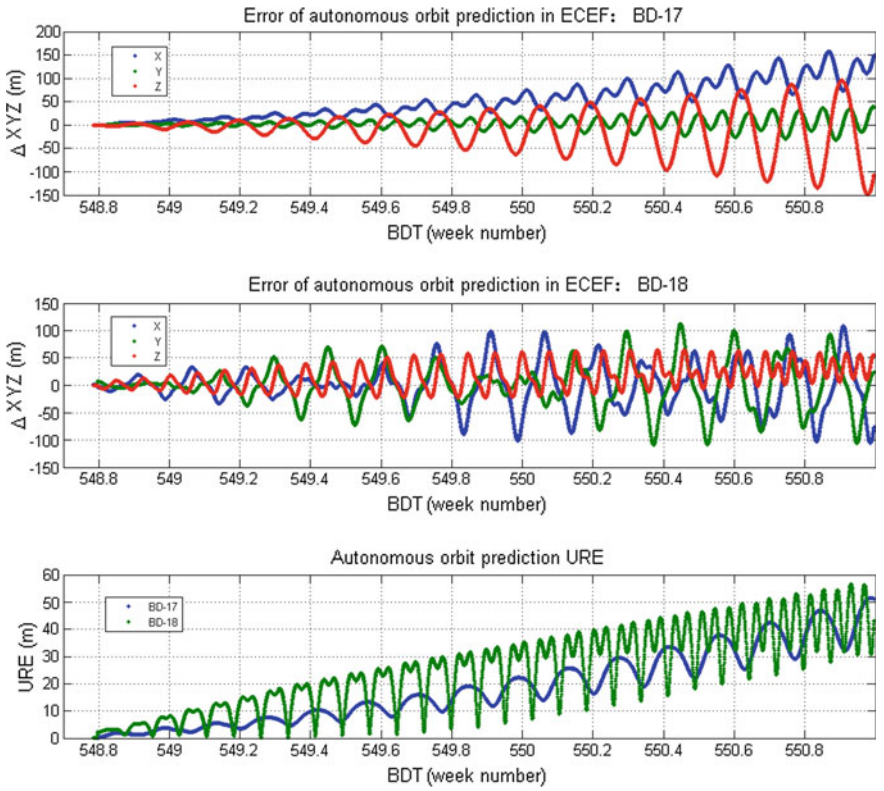

Fig. 4 The precision of autonomous orbit prediction (14.2 days) (BDT: 548 week 474,465 s–550 week 602,000 s)

which also was homologous with the last 14.2 days' prediction data showing in Fig. 3. It should be pointed out that, the step of autonomous orbit prediction was 5 min. It's the same with on-orbit simplified scheme of autonomous navigation data handling period (Fig. 4).

To the error of autonomous orbit prediction, there was a detailed theoretical analysis in [9]. The connection between autonomous orbit prediction error and error of long-term ephemeris prediction parameter has been shown as follow.

$$\Delta x = \Delta \Phi \times x \tag{1}$$

Where, x is long-term ephemeris prediction parameter error. $\Delta\Phi$ is error of state transition matrix. And Δx is autonomous orbit prediction error. In the autonomous orbit determination of this paper, the maximum error of long-term ephemeris prediction parameter was 10 km. On the other hand, only geodynamics oblateness perturbation had been calculated in state transition matrix. The error of state transition matrix was existed due to lack of Sun and Moon gravitation in calculation. To IGSO

satellite, the error of Sun and Moon gravitation was about 3×10^{-5}, length dimension unit of which is Earth equator radius Ae (6378,137 m). To MEO satellite, the error of Sun and Moon gravitation was about 1.5×10^{-5}. Hence, the error of autonomous orbit prediction dynamic model has been estimated as following.

- To IGSO satellite, $\Delta x = 4.71 \times 10^{-8}$.
- To MEO satellite, $\Delta x = 2.36 \times 10^{-8}$.

Solar radiation pressure of navigation satellite is about $1–2 \times 10^{-7}$ m/s^2 [11]. Hence, the calculation method of state transition matrix with geodynamics oblateness perturbation had only bring in a dynamic model error, which was equal to 12–23% error of solar radiation pressure model.

4 Analysis for Autonomous Orbit Determination

As mentioned in the 2.2 chapter, the central station collected the original measurement data, which had been used as input of on-orbit measurement of autonomous navigation prototype software after thinning. Autonomous orbit determination data processing analysis has been carried out. To the measurement system with four satellites constellation and BJ station, there was nine range combinations. Inter satellite and ground-satellite distance corresponding to precise ephemeris had been chosen as comparison standard. Measurement variance of the nine range combinations had been computed for 14.2 days from 548 week 474,465 s to 550 week 602,000 s of BD time, which has been shown in Table 3.

Autonomous orbit determination result has been proposed in Fig. 5 using both inter satellite and ground-satellite ranging data. The mean URE of four test satellites were respectively 3.07, 3.40, 3.51, 3.06 m. The variance of them were respectively 1.47, 1.74, 1.75, 1.55 m. To four satellites constellation, the mean URE and variance were 3.26 m and 1.63 m respectively. That is to say, URE of autonomous orbit determination for four satellites constellation was 4.89 m (1σ).

It should be noted that, there is no available actual ranging data due to the measurement suspend. There were 21 times interruptions, each of which persisted for more than 1 h. The total length of time was 71.5 h accounting for 21% of the 14.2 days. The average outage time was 3.4 h. There were 4 interruptions for more than 6 h. The longest interruption time was 6.7 h. In the autonomous orbit determination test, autonomous orbit prediction had been used while measuring data being interrupted. In order to ensure the continuity of the output trajectory of the

Table 3 The measurement variance statistics of inter satellite link with four satellites constellation and BJ station (m)

	BD-18	BD-19	Beijing
BD-17	0.33	0.52	0.25
BD-20	0.43	0.54	0.33
BD-18	\	0.81	0.17
BD-19	\	\	0.39

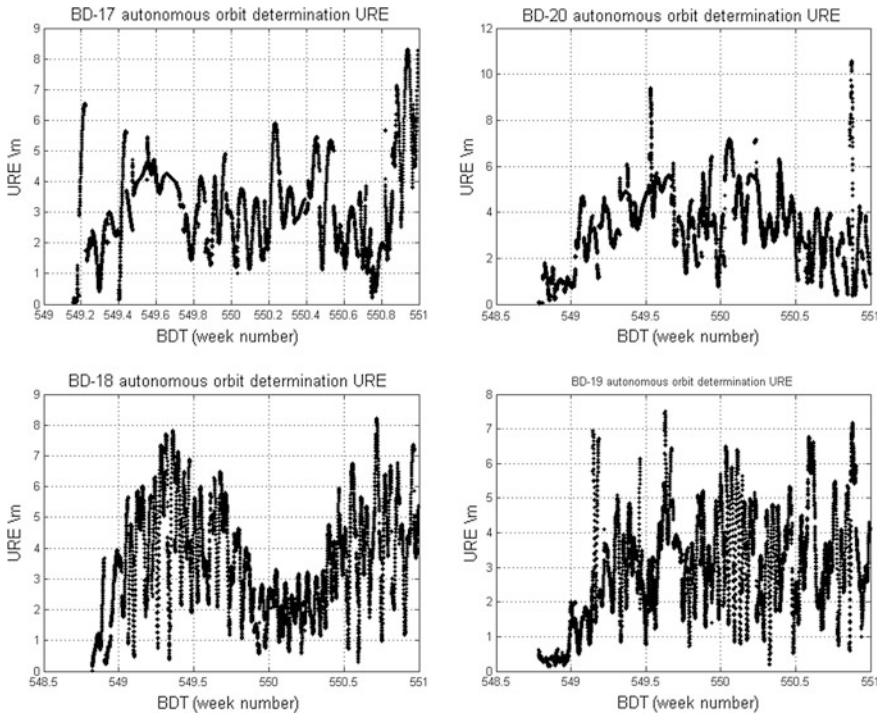

Fig. 5 URE of autonomous orbit determination for four satellites constellation (with inter satellite and ground-satellite ranging)

autonomous navigation software, forecast step size was 5 min, which was the same with data processing period of on-orbit autonomous navigation. Figure 5 proved that, the result of autonomous orbit determination of four test satellites showed a better stable feature when lack of available ranging data for constellation.

On the basis of ground-satellite ranging data, autonomous orbit determination test of IGSO test satellite has also been proposed as shown in the following figure. The mean URE of two IGSO test satellites were respectively 1.10, 0.75 m. The variance of them were respectively 0.45, 0.33 m. It means that, URE of autonomous orbit determination for two IGSO test satellites was 1.31 m (1σ) with ground-satellite ranging data only. The result of autonomous orbit determination of IGSO test satellites showed a better stable feature also when lack of available ranging data. Compared with [6], the autonomous orbit determination and stability had been improved for IGSO test satellite (Fig. 6).

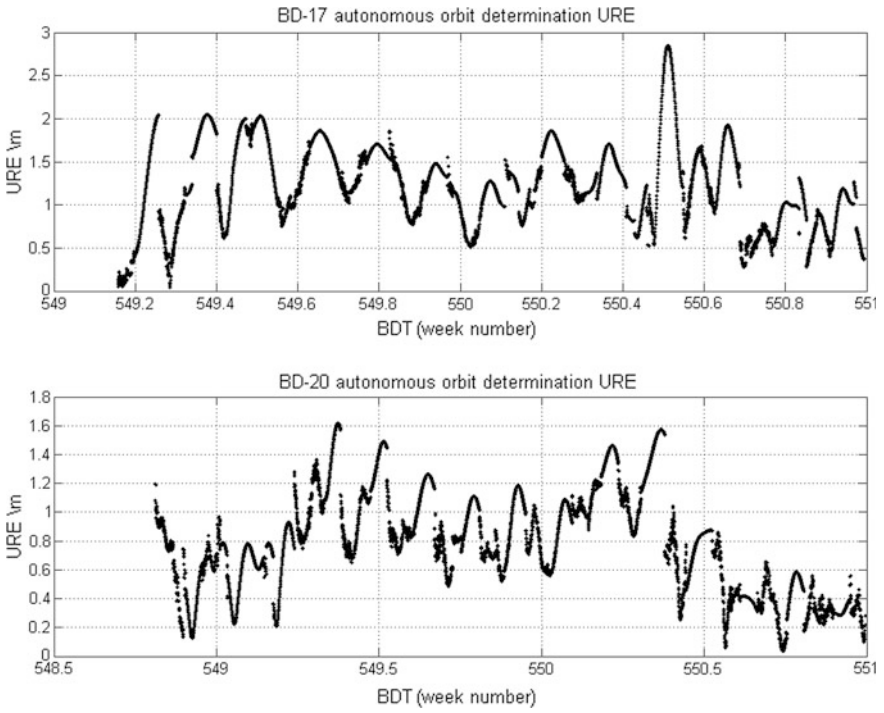

Fig. 6 URE of autonomous orbit determination for IGSO test satellite (with ground-satellite ranging data)

5 Conclusion

Basing on of 14.2 days' measured data of inter satellite link device between BD test satellite and ground station, ranging data was sparse according to the working period of the autonomous navigation software. There was 80% of the time to establish a ranging link for four satellites constellation including BD-17, BD-20, BD-18, and BD-19. Average ranging link was 2.2. Random difference was between 0.17 and 0.81 m of inter satellite and ground-satellite range after calculating. On this basis, URE of autonomous orbit determination for four satellites constellation was 4.89 m (1σ). URE of autonomous orbit determination for two test IGSO satellites constellation was 1.31 m (1σ). The autonomous orbit determination hadn't diverged when lacking of available ranging data.

References

1. Abusali PAM, Tapley BD, Schutz BE (1998) Autonomous navigation of global positioning system satellites using crossing-link measurements. J Guid Control Dyn 21(2):321–327
2. Rajan JA Dr (2002) Highlights of GPS II-R autonomous navigation. In: ION 58th annual meeting/CIGTF 21th guidance test symposium, 24–26 June 2002, Albuquerque, NM
3. Fisher SC, Ghassemi K (1999) GPS IIF—the next generation. Proc IEEE 1, 87(1):24–47
4. Saks N, Baldesarra M, Kieffer R (2016) Developing the future galileo space segment. In: 67th International astronautical congress 2016, space communications and navigation symposium (B2), space-based navigation systems and services
5. Wang H, Han X, He S et al (2012) The correction method of overall pseudo-rotation on autonomous navigation of navigation constellation. In: CSNC2012 Proceedings, Lecture notes in electrical engineering, vol 160, pp 289–300
6. Chang J, Shang L, Li G (2016) The accuracy analysis of autonomous orbit determination based on onboard observation data of inter-satellite link. In: CSNC 2016 proceedings, vol III, pp 213–222
7. Wang H, Chen Z, Zheng J et al (2011) A new algorithm for on-board autonomous orbit determination of navigation satellite. J Navig 64:S162–S179
8. Wang H, Zheng J, He S et al (2011) Distributed autonomous orbit determination system of navigation satellite based on upload ephemeris. CSNC2011
9. Wang H, Chen Z, Chu H et al (2012) On-board autonomous orbit prediction algorithm for navigation satellites. J Astronaut 33(8):1019–1026
10. Lin Y, Qin Z, Chu H et al (2010) A satellite cross link-based GNSS distributed autonomous orbit determination algorithm. J Astronaut 31(9):2088–2094
11. Chen Q, Wang H, Yang H et al (2015) Parametric study of solar radiation pressure model applying to navigation satellite orbit determination for long arc. CSNC2015

GNSS Satellite Observations with Interference Measurement Technology

Li Li, Geshi Tang, Tianpeng Ren, Jing Sun, Ming Shi and Junwei Wang

Abstract Interference measurement Technology has been proved as a very good space geodetic technique used to determine the Earth Orientation Parameters (EOP), the Terrestrial Reference Frame (TRF), and the Celestial Reference Frame (CRF). For the rigorous determination of the entire system of TRF-EOP-CRF, there is an urgent need for alternative methods for connecting various spatial geodetic techniques. Using Very Long Baseline Interferometry (VLBI) to observe the GNSS satellites is a promising solution. This paper analyzes the importance and key issues of GNSS satellite observations with Interference measurement technology. This work studies the tracking of interferometric measurements of GEO satellites, tracks the Beidou satellite to verify the tracking measurement technology, and obtains the time-delay measurement of ns level. The orbit determination is completed by processing the measured data, we use single baseline and double baseline data for the orbit determination. The maximum orbit deviation of the single—baseline orbit determination is nearly 40 km, the accuracy of the orbit determination is significantly improved by using the double baseline data. The maximum orbital deviation is less than 1.5 km.

Keywords Interference measurement · Time delay · BeiDou

1 Introduction

Very Long Baseline Interferometry (VLBI) is a well-probed space geodetic technique used to determine the Celestial Reference Frame (CRF), the Terrestrial Interpretation and comparison of geodetic measurements have to be made in one common reference system in order to achieve correct and reliable results. In geodetic practice, coordinates are usually provided either in the kinematical International Terrestrial Reference Frame (ITRF) or in the quasi-inertial

L. Li (✉) · G. Tang · T. Ren · J. Sun · M. Shi · J. Wang
Beijing Aerospace Control Center, Beijing 100094, China
e-mail: lynnsee720@163.com; 13810205290@163.com

J. Sun et al. (eds.), *China Satellite Navigation Conference (CSNC) 2017 Proceedings: Volume III*, Lecture Notes in Electrical Engineering 439,
DOI 10.1007/978-981-10-4594-3_10

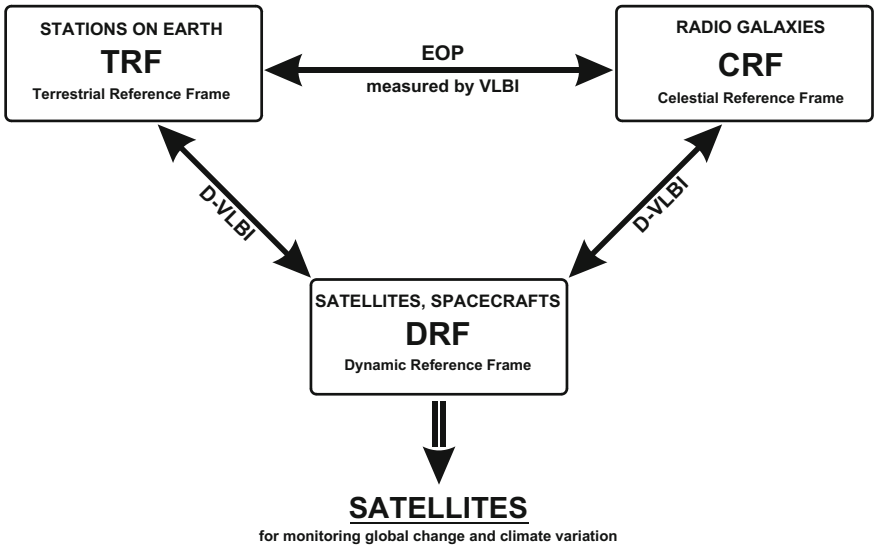

Fig. 1 The importance of reference frames for monitoring global change and climate variation

International Celestial Reference Frame (ICRF), whereas measurements of space probes such as satellites, spacecrafts, or planetary ephemerides rest upon dynamical theories. To avoid inconsistencies and errors during measurement and calculation procedures, exact frame ties between kinematic and dynamic reference frames have to be secured. By observing space probes alternately to radio sources with the differential Very Long Baseline Interferometry (D-VLBI) method, the relative position of the targets to each other can be determined. As the positions of the radio sources are well known in the ICRF, it is possible with such observational configurations to link the bodies of the solar system with the ICRF. While the Earth Orientation Parameters (EOP), which are regularly provided by the International Earth Rotation and Reference Systems Service (IERS) link the ICRF to the ITRF, the ties between the terrestrial and the dynamic frames will be established by D-VLBI observations (Fig. 1).

2 Observations to BeiDou Satellite

2.1 Purpose of the Observation

We use a single baseline interferometric system to track the calibration satellite and the satellite to be measured. The equipment delay, clock error of the equipment is obtained by the calibration satellite. The geometrical delay of the measured satellite is obtained by deducting the equipment delay of the measured satellite from the

interferometric delay. The geometric time delay is used as the orbit determination input to complete the orbit determination.

We take the Beidou GEO satellite C03 (110.5 E) as a calibration satellite, Beidou GEO satellite C02 (80E) as the measured satellite, as shown in Fig. 2.

The observation is based on the interference measurement system composed of two antennas of HangTianCheng and Changping Shahe. The baseline length is about 5.5 km. The observation plan is:

Phase1: Day1, 22:00:00 start to observe the calibration satellite C03, for 2 h
Phase2: Day2, 03:10:00 start to observe the measured satellite C02, for 8 h
Phase3: Day2, 13:20:00 start to observe the calibration satellite C03, for 2 h

Because the interference baseline is short, the ionosphere and neutral atmosphere delay of the same target signal arriving at different station propagation paths are basically the same, so the propagation delay is not considered. The theoretical geometric time delay is obtained by using C03 precision ephemeris, and the difference between C03 interferometric measurement delay and theoretical geometric time delay is taken as device delay. The C02 geometry delay is deducted from the C02 interferometric measurement delay and the device delay. The geometric time delay of C02 is taken as the input of orbit determination, and the solution ephemeris is obtained.

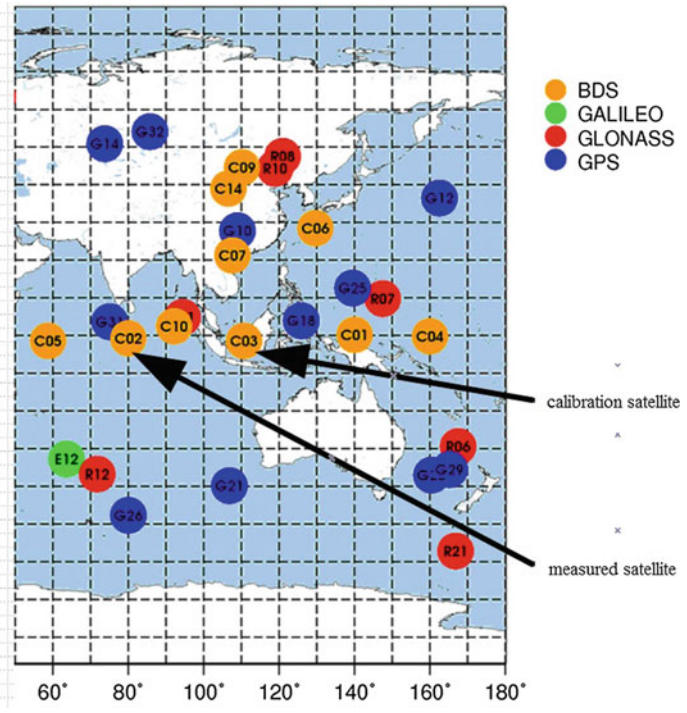

Fig. 2 Targets of the differential interferometry observation

After the observation, the theoretical geometric time delay can be obtained by C02 precise ephemeris, and the difference between the theoretical geometric time delay and the actual geometric time delay is regarded as the measurement precision. The difference between the solution ephemeris of C02 and the precision ephemeris is regarded as the orbit determination precision.

2.2 Satellite Signal Spectrum

In the observation, the spectrum of C03 and C02 downlink signals collected by the interferometric system are shown in Fig. 4. The signal with a higher signal-to-noise ratio is selected as the interference object. (As shown in "o" in Fig. 3a and "+" in Fig. 3b). Interference bandwidth is about 250 kHz. The interference fringe is obtained as shown in Fig. 4.

2.3 Analysis of Interference Delay and Error

We interfered with the original data of C03 and C02 collected by interferometric system, and the integration time is 2 s. We obtain the group delay, phase delay and theoretical geometric delay based on the precise ephemeris of C03 in observation

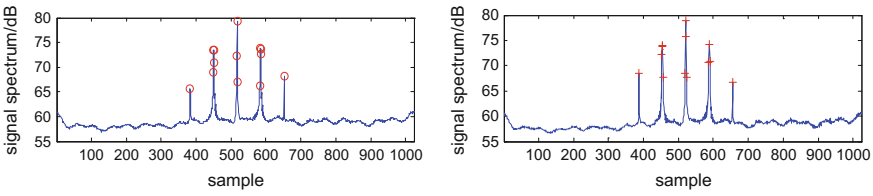

(a) Signal Spectrum of C03 (b) Signal Spectrum of C02

Fig. 3 Downlink signal spectrum of Beidou satellite C03 and C02 (Sampling rate, fs = 1.0 MHz)

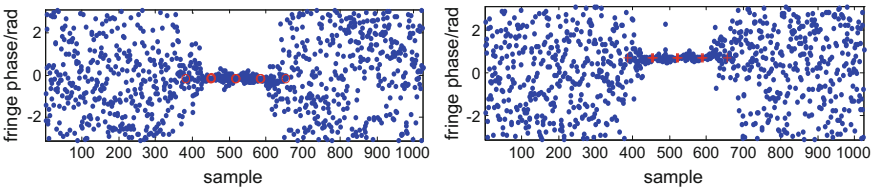

(a) Interference fringes of C03 (b) Interference fringes of C02

Fig. 4 Interference fringes of Beidou satellite C03 and C02 (Sampling rate, fs = 1.0 MHz)

phase 1 and observation phase 3, and take the phase delay as the interference measurement delay, as shown in Fig. 5.

We obtain the group delay and phase delay of C02 in observation phase 2, where the group delay measurement noise is about 4.01 ns (the residual effective value of the group delay minus the phase delay), the phase delay measurement noise is about 9.4 ps (a 300-second linear fit residual RMS value). We consider the phase delay as the interferometric delay, as shown in Fig. 6.

We use the C03 interferometric measurement delay to subtract its theoretical geometric delay to obtain the interferometric measurement device delay during the C03 observation period. We linearly interpolate the device delays of observation phase 1 and observation phase 3 to obtain the interpolation device delay of

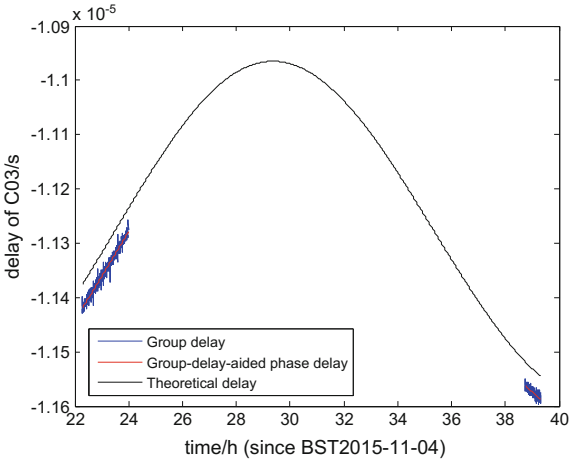

Fig. 5 Interference delay and theoretical geometric delay of C03

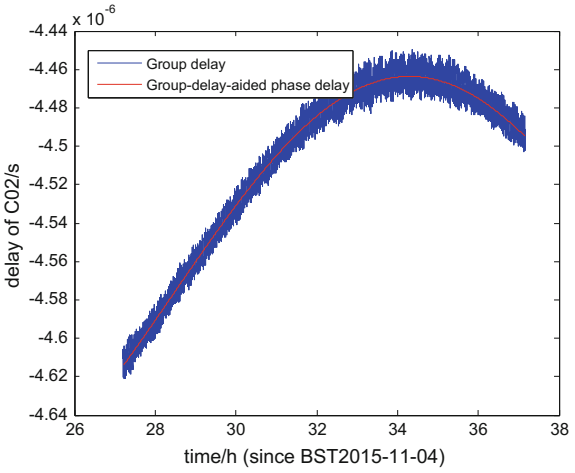

Fig. 6 The interferometric delay of C02

observation phase 2 for calibrating the measurement results of C02, as shown in Fig. 7. We subtract the interpolated device delay from the interferometric measurement delay of C02 in the observation phase 2 to obtain the geometric time delay of C02 for subsequent trajectory determination.

To estimate the interferometric error (ie, the difference between the geometric delay of C02 and the theoretical geometric time delay), the theoretical geometric time delay is derived using the C02 precision ephemeris, as shown in Fig. 8. It can be seen that the interferometric error is about 0.267 ns (rms) and 0.536 ns (max).

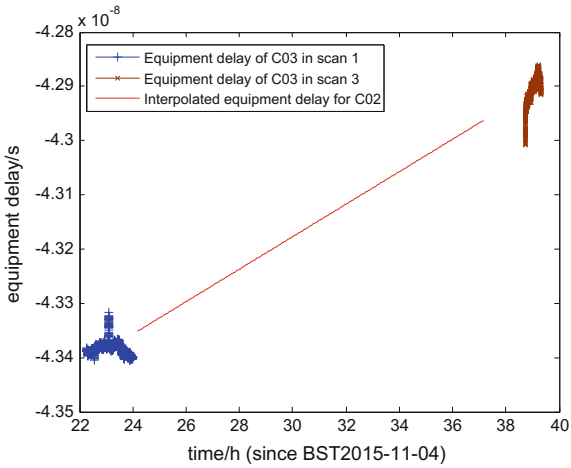

Fig. 7 Device delay, and interpolation device latency of C03

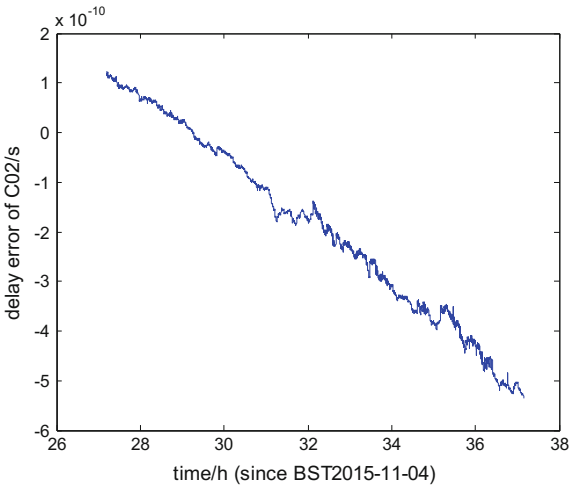

Fig. 8 Interference measurement error of C02

2.4 The Result and Accuracy of Orbit Determines

The interpolation delay is subtracted equipment delay from the C02 interferometric measurement delay to obtain the geometric time delay as the input to the orbit determination solution. The resolution of ephemeris is compared with the precision ephemeris to evaluate the orbit determination accuracy.

After solving, the orbit determination based on C02 geometric delay is convergent. Figure 9 shows the comparison between the calculated trajectories and the precision ephemeris. It can be seen that the maximum error of the calculated trajectory in the *X*, *Y*, and *Z* directions in the CGCS2000 coordinate system is 26.8 km (shown as Fig. 9a), 12.4 km (shown as Fig. 9b), 23.5 km (shown as Fig. 9c). The orbital accuracy is limited due to single baseline measurements, if double baselines are used for measurement, the orbital precision will be greatly improved.

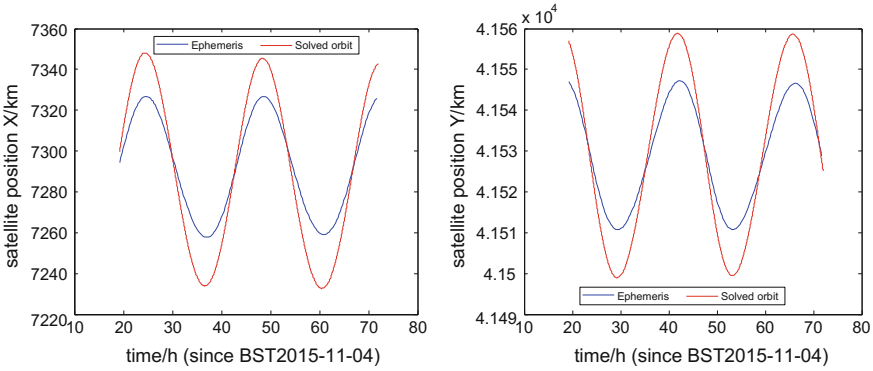

(a) X axis: max error 26.8km

(b) Y axis: max error 12.4km

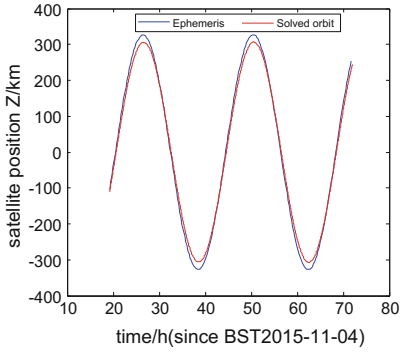

(c) Z axis: max error 23.5km

Fig. 9 Determination of GEO satellite orbit based on single baseline interferometry

2.5 Simulation of Double Baseline Data

Taking into account the current conditions cannot be achieved fiber optic connection dual baseline test, the use of simulation analysis for orbital calculation. Specific steps are: (1) The ephemeris integration is performed using the initial orbits as the benchmark for the validation of orbit determination. (2) The observed data are simulated using the reference orbit and the extracted data errors are added to the simulated data as the observed data. (3) Based on the simulation observed data, orbit determination is performed using single baseline and double baseline, and compare the orbit determination accuracy.

Initial simulation orbit:
Initial orbit epoch: 2016 10 01 00 00 00.000 (UTC)
Initial position:

41846493.638676	−5085894.663318	−116157.996570
370.374555	3053.016449	−1.853515

Orbit Determination of Single Baseline
See Figs. 10 and 11.

Orbit Determination of Double Baseline
See Figs 12 and 13.

We use single baseline and double baseline data for the orbit determination. The maximum orbit deviation of the single—baseline orbit determination is nearly 40 km, the accuracy of the orbit determination is significantly improved by using the double baseline data. The maximum orbital deviation is less than 1.5 km.

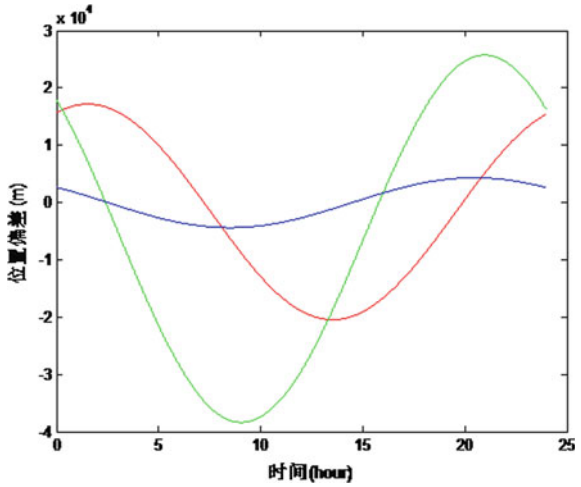

Fig. 10 Deviation of orbit determination

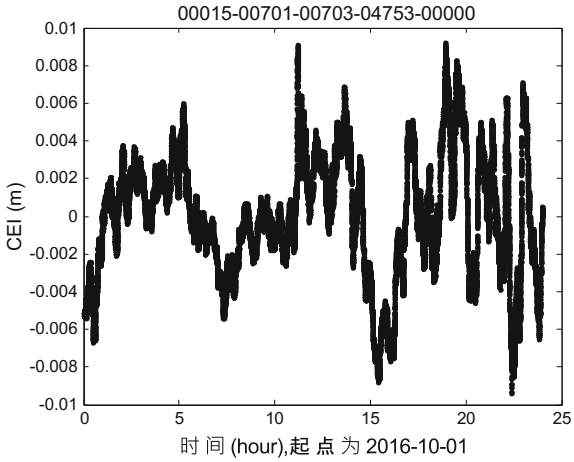

Fig. 11 Residuals of orbit determination

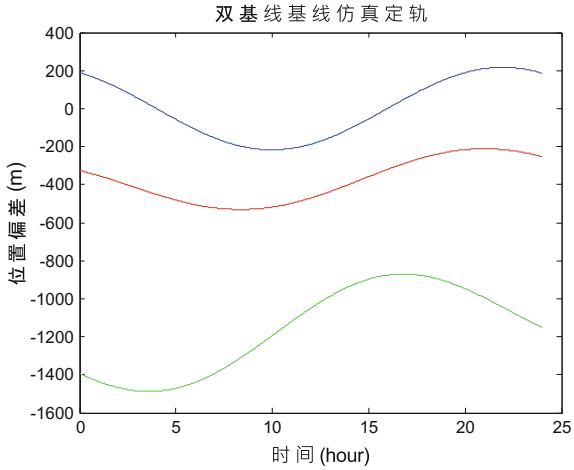

Fig. 12 Deviation of orbit determination

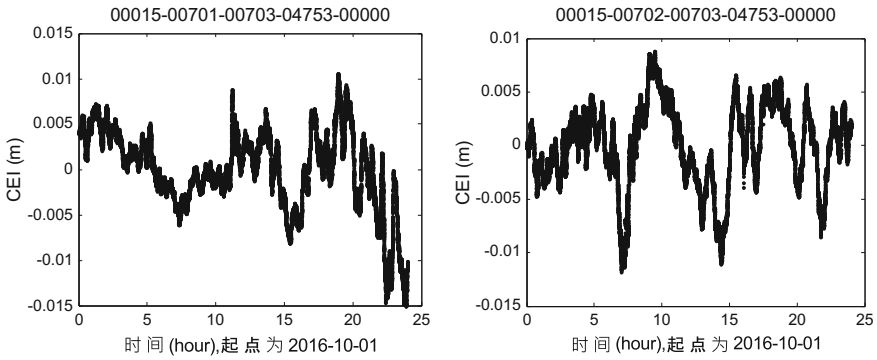

Fig. 13 Residuals of Orbit determination

3 Conclusions

Simulation results show that the double baseline tracking satellite is not only beneficial to the improvement of accuracy, but also can reduce the required observation arc length. The orbit accuracy of the order of 1 km can be achieved by approximately 6 h observation. Thus, the orbit accuracy of this tracking experiment is largely limited by the single baseline constraint. If double baseline tracking is used, orbit accuracy will be greatly improved.

Based on the short baseline interferometry system tracking GNSS satellites, is the first attempt of the county, this test successfully obtains the measurement data and the solution track. Although the data obtained in this experiment have certain systematic deviation, the accuracy of orbit determination is restricted, but this systematic deviations can be calibrated by other technical means. Therefore, we believe that this test has good engineering significance and application prospects.

Acknowledgements This work is sponsored by the National Natural Science Foundation of China (No. 11403001).

References

1. Briess K, Konemann G, Wickert J (2009) MicroGEM – microsatellites for GNSS earth monitoring, Abschlussbericht Phase 0/A. 15. September 2009, Helmholtz-Zentrum Potsdam Deutsches GeoForschungsZentrum GFZ and Technische Universität Berlin
2. CCSDS (2011) Delta-differential one way ranging (Delta-DOR) operations. Recommendation for space data system practices, Magenta Book, CCSDS 506.0-M-1-
3. King RW, Counselman CC, Shapiro II (1976) Lunar dynamics and selenodesy: results from analysis of vlbi and laser data. J Geoph Res 84(35):6251–6256
4. Sekido M, Fukushima T (2006) A VLBI delay model for radio sources at a finite distance. J Geod 80:137–149

5. Tornatore V, Haas R, Maccaferri G, Casey S, Pogrebenko SV, Molera G, Duev D (2010) Tracking of GLONASS satellites by VLBI radio telescopes
6. Lambert SB, Poncin-Lafitte CL (2011) Improved determination of γ by VLBI (Research Note). Astron Astrophys 529:A70
7. Moyer TD (2003) Formulation for observed and computed values of deep space network data types for navigation. In: Yuen JH (ed) JPL JPL deep space communications and navigation series, Wiley, ISBN: 0-471-44535-5
8. Plank L (2013) VLBI satellite tracking for the realization of frame ties. PhD thesis
9. Li P, Hu X, Huang Y, Wang G, Jiang D, Zhang X, Cao J, Xin N (2012) Orbit determination for Chang'E-2 lunar probe and evaluation of lunar gravity models. Sci China – Phys Mech Astron 55:222–514
10. Sun J (2013) VLBI scheduling strategies with respect to VLBI2010. ISSN 1811–8380

Experiment Research on GEO Satellite Orbit Measurement by Using CEI

Zejun Liu, Chunlin Shi, Lan Du, Lili Wu and Ruopu Wang

Abstract Measurement of GEO satellite orbit by using passively Connected Element Interferometry (CEI) has obvious advantages in measurement accuracy and optimization of satellite resource utilization, etc. In this paper, the downlink signal of TV satellite was received and recorded by using the CEI measurement system. Clear interference fringes were obtained by processing downlink signals. The results showed that the RMS of phase fluctuation is less than 2° at night. In the daytime, the RMS of phase fluctuation increases significantly. After using calibration of signals, the RMS of the phase fluctuation during the day is significantly reduced to the same level as the nighttime. It is indicated that the phase fluctuation is caused by the variation of the temperature during the day, especially the direct sunlight. It also highlighted the necessity of signal calibration. Phase delay was compared with the precise-ephemeris-based delay, and the systematic error was analyzed. Our work lay a foundation for future GEO satellite precise orbit determination with the passively connected element interferometry.

Keywords CEI measurement · GEO satellite · Orbit determination

1 Introduction

In recent years, with the rapid development of satellite technology, especially, the Geosynchronous Earth Orbit (GEO) is easy to track, measure and control because of its unique characteristics of high and static orbit. It has been widely used in communication, data transmission, television broadcasting, meteorology, ocean exploration, navigation and so on [1]. But the orbit of GEO resources are limited, in order to make full use of valuable orbit resources, we use multiple juxtapositions of technology, leading to more and smaller intervals on the track. In order to avoid the

Z. Liu (✉) · C. Shi · L. Du · L. Wu · R. Wang
Institute of Navigation and Aerospace Engineering, Information Engineering University, No. 62 Kexue Street, Zhengzhou 450001, Henan, China
e-mail: liuzejun7994@126.com

J. Sun et al. (eds.), *China Satellite Navigation Conference (CSNC) 2017 Proceedings: Volume III*, Lecture Notes in Electrical Engineering 439,
DOI 10.1007/978-981-10-4594-3_11

common satellite elegant window and collision, we need very fine orbit control to ensure satellite safety. At present, the high accurate absolute position measurement for GEO satellite mainly uses the multi-station ranging and the velocity measurement. However, due to the high and static orbit of the GEO satellite, the satellite has poor accuracy along the tangential and normal directions, which cannot meet the requirements of orbit accuracy [2].

The radio-interferometry technology is of high precision, not affected by the weather changes, which can be competent for all-weather measurement [3–5]. The radio-interferometry can track cooperative and non-cooperative space object, and provide new means to determine the orbit. Therefore, the radio-interferometry technology can be used to improve the accuracy of GEO satellite orbit along the tangential and normal direction.

According to the differences of baseline length, there is very long baseline interferometry (VLBI) and connected element interferometry (CEI) of the radio interference measuring technology [1, 6, 7]. The VLBI has higher precision for orbit determination, but the equipment and data processing are very complex, which usually used for deep space exploration beyond the moon. However, the CEI using the same frequency standard were connected by the optical fibre that provided high-speed data transfer between the sites together with time and frequency synchronization. The resulting measurement was the time difference of arrival of the radio frequency phase difference between the two sites. This measurement, in turn, was converted to the differential range. The high precision and high sensitivity angle measurement signal can be used to enhance and supplement the existing measurement and control of the geostationary satellite [2].

At present, the CEI measurement technology with low investment and low cost, we can make full use of the existing infrastructure, such as radar station, establish CEI tracking measurement station network with 10–100 km baseline length, and transform and upgrade frequency facilities, ground data transfer and calibration stations, and so on. We can achieve experimental research on space object orbit measurement by using CEI. Xiaojie et al. [1, 7] has analyzed the influence of observation length, CEI baseline length, direction and baseline location on the precision orbit determination of GEO by using simulation method. Tianpeng [8] has carried out single-baseline-interferometry-based orbit measurement and determination test of GEO Satellite, the results show that the single-baseline interferometry can converge to the solution of GEO satellite orbit, which would bring a high-accuracy orbit even as passive monitoring. Lei et al. [9] have investigated the impact of frequency characteristics on the accuracy of connected element interferometry, it show a good rubidium frequency reference is enough for measurement in CEI mode. Songtao [10] has carried out experiment analysis on Chang' e-2 satellite using CEI.

Overall, the current experiment test on the CEI measurement technology is comparatively rare, especially on the effect of GEO satellite orbit determination accuracy. In this paper, we observe a TV satellite to investigate the law of the measured phase change and analyze the main influencing factors by using 75 m 35 m baseline, which will establish the foundation for future GEO satellite orbit determination missions.

2 Measurement Principle and Measurement Model

2.1 CEI Measurement Principle

In order to get a direction of angular information, a real-time CEI measurement system needs two stations at least. Therefore a complete CEI measurement system requires at least three stations, which form two baselines perpendicular to each other. Each site includes receiving antennae, low-noise amplifier, frequency synthesizer, down converter, data receiving, recording system, data transmission system and data processing centre. The relation of CEI interferometry is shown in Fig. 1.

The delay is related to the angle, between the baseline and the direction to the radio source:

$$\tau = \frac{1}{c} B \cos\theta \tag{1}$$

In the formula, τ is a signal delay between two measurement stations, c is the speed of light, B is the baseline length, θ is the angle between the target and the

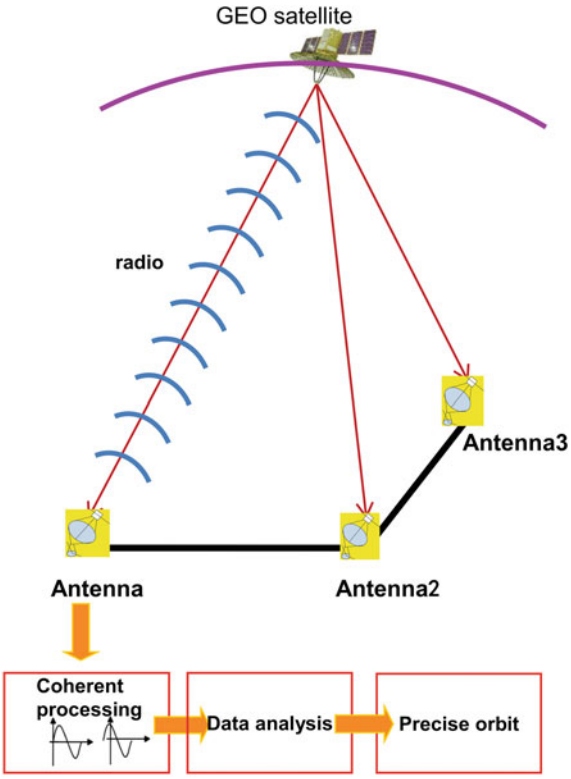

Fig. 1 Schematic diagram of CEI measuring principle

baseline. By calculating the formula (1), the angle precision expression can be obtained.

It is obvious that the angular accuracy is inversely proportional to the length of B. in order to obtain high precision angle measurements, we can use a longer baseline (i.e. increasing the length of the B) or improve the measurement accuracy of the interferometer delay (i.e. reducing $\delta\tau$).

2.2 Measurement Model

The resulting measurement is the phase difference of arrival of the radio frequency (RF) signals between the two sites. In another word, the basic observable of any interferometer is the relative phase (the fractional part of less than a wavelength) of a received signal at two spatially separated antennas, As shown in Fig. 1, for the 10–100 km baseline, the measurement equation can be established according to the signal transmitted by the spherical wave, namely:

$$\begin{aligned}\phi + \lambda N &= \rho_A - \rho_B \\ &= \left|\vec{R}_A(t_1) - \vec{r}(t_0)\right| - \left|\vec{R}_B(t_2) - \vec{r}(t_0)\right| + C\Delta t_{\text{clock}} + \Delta\rho_{\text{atm}} + \Delta\rho_{\text{ins}} + \varepsilon\end{aligned} \tag{2}$$

where ϕ and N are measurement phase and cycle ambiguity. λ is the signal wavelength of satellite, $\vec{r}$, $\vec{R}_A$ and $\vec{R}_B$ are the position vector of A and B for both satellite and baseline stations; Δt_{clock} is the difference between the two stations clock; $\Delta\rho_{\text{atm}}$ is the residual error of atmospheric propagation delay between stations, including the propagation error of troposphere and ionosphere; $\Delta\rho_{\text{ins}}$ is the distance error caused by instrument delay; ε is the observation noise.

3 The Measurement System

The CEI experimental system consists of two parts: outdoor and indoor equipment. Outdoor equipment includes receiving antenna, while indoor consist of data receiver and processing, and the corresponding hardware and software.

3.1 Outdoor Receiving Antenna Equipment

Outdoor antenna equipment includes three 2.4 m antennas (east–west distance 75 m, north-south distance 35 m), and low-noise amplifier (with first order frequency conversion capability). The antenna is connected by the 100 m long coaxial

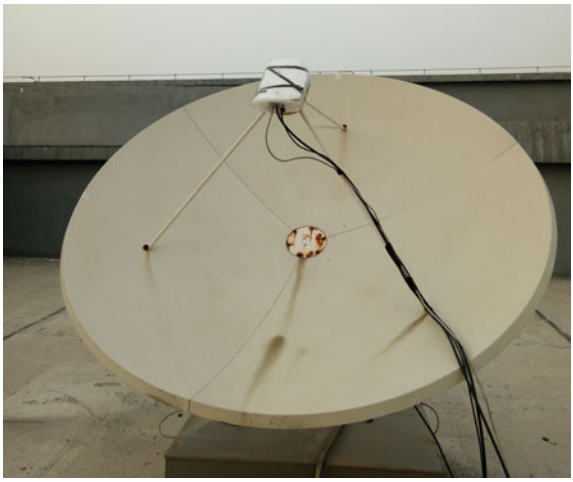

Fig. 2 C band measurement antenna

cable (including low-noise amplifier power cable, local oscillator uplink cable, and intermediate frequency down cable), and connected to the indoor signal acquisition equipment, as shown in Fig. 2.

3.2 Indoor Data Collection and Processing

The data collection and processing equipment comprise a power supply, signal distributor, baseband frequency converter, rubidium atomic clock and the computer, data collection card and data visualization and storage software. The precise phase measurement of GEO satellite can be realized by data processing, then the precise orbit of the satellite can be obtained, as shown in Fig. 3.

4 Measured Data Processing Result

4.1 Observation Conditions

The observation conditions are as follow.

(1) Start observation time: Beijing time on December 5, 2016 at 9 a.m. Note that the starting point of the horizontal coordinate in the following figure is UTC on December 5, 2016, at 0 am.
(2) The observation satellite: ChinaSat 10;
(3) The observation frequency point is 3817 MHz;
(4) The signal generator: output frequency is 3815 MHz.

Fig. 3 Indoor measuring equipment

Fig. 4 Layout of measuring antenna

(5) The layout of the outdoor antenna is shown in Fig. 4, 1–2 antenna is composed of the east–west baseline and the length of 75 m, and the 2–3 antenna consists of the north-south baselines, with a length of 35 m.

Calibration measures of calibration system use antennae to receive three standard indoor signal sources simultaneously. The principle is: the signal source generates C-band calibration signal is sent to the 3 antennae, turning into the tuner with the satellite signal, and finally it is sent to the acquisition and storage terminal. In the process of data processing, the phase change of satellite signal is different from the signal phase of calibration (In this paper, the phase change is the change of phase delay).

4.2 Observation Results of Satellite Signals

we can see from Fig. 5 that the satellite signal phase jump position generally appear in the Beijing time 10 points to 11 points; we also can find that although the phase

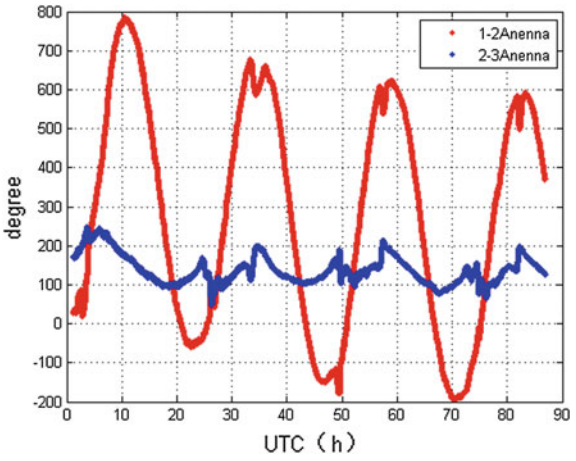

Fig. 5 Phase change of satellite signal

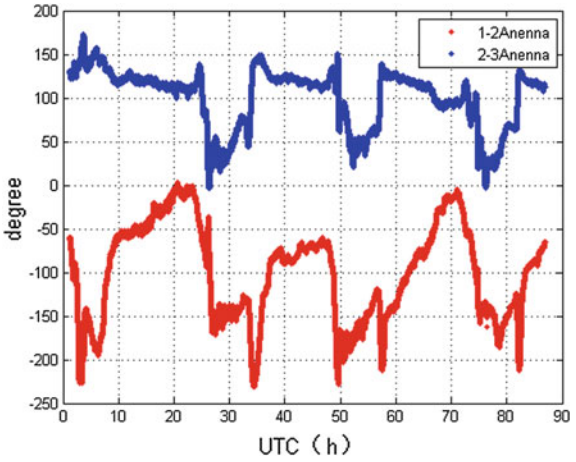

Fig. 6 Calibration signal phase change

jumps for the east–west antenna, but the overall trend remains unchanged. However, for the north-south baseline, satellite signal phase not only jumps but also affect the overall phase change trend.

4.3 Observation Results of Calibration Signal

Figure 6 shows the phase change of calibration signal. It can be seen that the jump time of the calibration signal is almost the same as that of the satellite signal. This shows that the signal jump is the problem of the measurement system, and the satellite signal in the space transmission path has little relationship with the factors. It also shows that the system difference can be eliminated by using calibration signal.

4.4 Comparison of Calibration and Satellite Signal

Figure 7 compares the variation of the phase of the satellite signal with the calibration signal for the two baselines. It can be seen clearly that the jump of the satellite signal and the jump trend of the calibration signal are basically the same, subsequently, the phase jump phenomenon can be eliminated by making the difference method.

Figure 8 shows the making difference between the phase of the satellite signal and the calibration signal. By comparing Fig. 7, it is obvious that the phase jump phenomenon is eliminated basically after the making difference, which greatly improves the quality of observed data, adding calibration signal in system design is necessary. In addition, the cables of the satellite signal and calibration signal cable

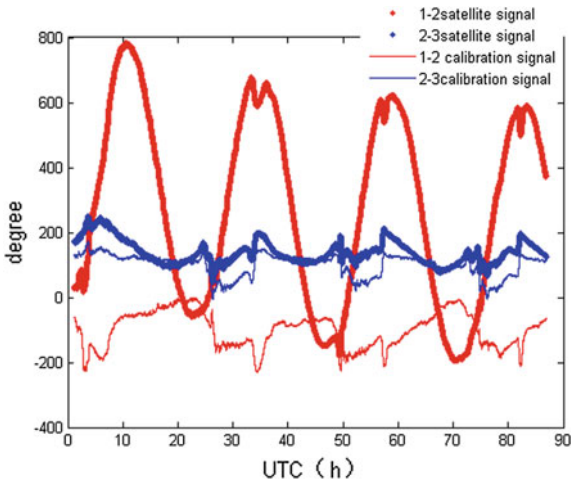

Fig. 7 Comparison of satellite signal and calibration signal phase

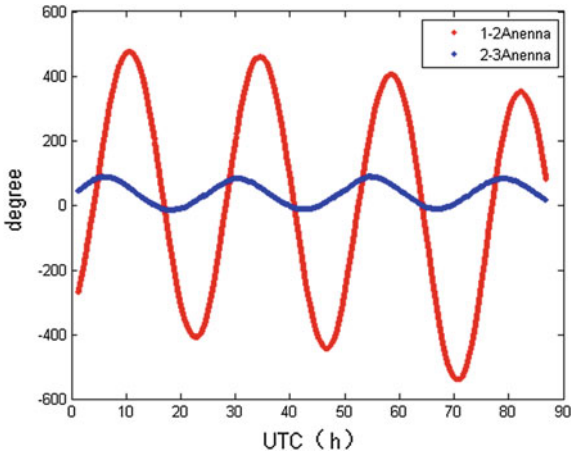

Fig. 8 Variation of phase difference between satellite and calibration signal

are not completely together, so the cable environment of the satellite signal and calibration signal are not completely consistent. Therefore, it needs to be improved further.

The comparison without calibration and with calibration shows this calibration method is effective for the ultra-short baseline. Previous observations show that daytime solar irradiation has great influence on interferometry phase. As a result of the north-south baseline is short for 35 m, which has smaller range of phase change than east–west baseline, phase change because of air temperature and phase change of satellite motion is same order of magnitude, resulting in daytime observation data cannot be used for orbit determination, only the data at night can be used. In order to eliminate this effect, adding calibration signal can eliminate the most of the phase changes caused by air temperature, the quality of the data during the daytime and the quality of the evening data is almost the same, so that the observation arc increased greatly.

4.5 *Comparison of Measurement Results with Precision Orbit*

Figures 9 and 10 gives a comparison between the measured phase values and the phase values calculated by the precise trajectory.

Figure 11 shows the difference between measured phase values and calculated phase values, the difference is less than 0.15 wavelength for 1–2 baseline, however, the difference of 2–3 baseline is less than 0.05 wavelength. It can also be seen that the change trend is same as the temperature change, and also shows that the temperature change caused by the temperature of the cable has great influence on the observation phase. It can be seen from the figure, the residual error of measured

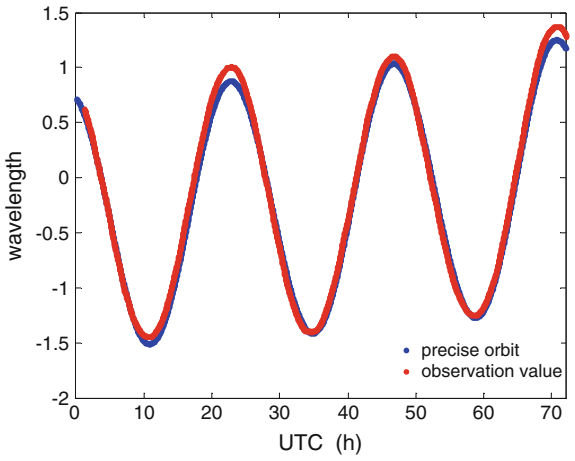

Fig. 9 Measured phase and theoretical phase change (1–2 baseline)

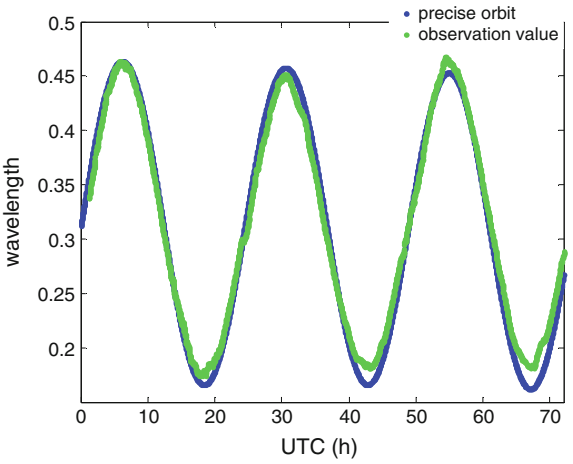

Fig. 10 Measured phase and theoretical phase change (2–3 baseline)

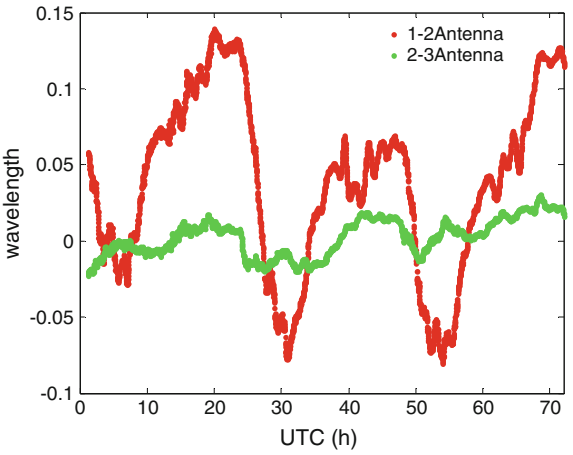

Fig. 11 Phase residual error between observation phase and precise orbit

phase values and calculated phase values at the daytime is larger than that of the evening, it further illustrates that the cable temperature variation because of the sun shining during the daytime is the main cause of phase change.

5 Conclusions

In this paper, the orbit measurement experiment of a GEO satellite is carried out by using the L-type 75 m × 35 m interferometer system:

(1) Although the east–west antenna phase jumps, the overall trend remains unchanged. The signal phase of north–south baseline not only jumps but also affects the trend of the whole phase.

(2) After making phase difference between the satellite signal and the calibrated signal, the phase jump phenomenon is eliminated, and the quality of the observed data is improved greatly. Adding calibrated signals in system design is very essential.
(3) The residual error variation of the measured phase is basically the same as the temperature change, and it also shows that the cable temperature variations caused by the air temperature change has a great influence on the observation phase.

Acknowledgements This work was supported partially by State Key Laboratory of Geo-Information Engineering Laboratory fund No. SKLGIE2016-Z-2-4 and the National Science Foundation of China under Grant No. 41604011. The authors also give great acknowledges and thanks to the Qian Zhihan and Wang Jinqing of the Shanghai Astronomical Observatory for support of our work, and National Time Service Centre for providing precise ephemeris of GEO Satellite.

References

1. Lan D, Xiaojie L, Ruopu W (2012) Relative orbit monitoring of GEO co-lactated geostationary satellites by using same beam CEI. J Geodesy Geodyn 32(3):50–54
2. Zhugen T, Yongqiang C (2015) Study on VLBI tracking measurement technology. Electron Sci Technol 02(02):134–137
3. Thurman SW (1990) Galileo earth approach navigation using connected-element interferometer phase-delay tracking. TDA Prog Rep 42–100:34–47
4. Edwards CJ, Rogstad D, Fort D et al (1992) The goldstone real-time connected element interferometer. Telecommun Data Acquis Prog Rep 110:52–62
5. Thurman SW (1990) Information content of a single pass of phase-delay data from a short baseline connected element interferometer. Telecommun Data Acquis Prog Rep 101
6. Weiren W, Qinghui L, Yong H et al (2015) Design and realization of same-beam interferometry measurement of CE-3. J Deep Space Explor 2(1):34–42
7. Xiaojie L, Jin H, Ling P (2010) The method of improving single group CEI baselines orbit determination for geostationary satellite. Hydrogr Surv chart 30(4):5–7
8. Tianpeng R, Geshi T, Jianfeng C et al. (2016) Correction modeling of tropospheric delay and clock error in real-time interferometry. Manned Spaceflight 22(4):483–487
9. Lei H, Haitao L, Wanhong H (2014) Impact of frequency characteristics on the accuracy of connected-element interferometry. J Spacecraft TT&C Technol 33(5):371–376
10. Songtao H, Geshi T, Lue C (2012) Connected element interferometry and experiment analysis on Chang'e-2 satellite. Spacecraft Eng 21(5):135–138

Real Time Precise Satellite Clock Estimation for Quad-System GPS/GLONASS/GALILEO/BDS

Xiaotao Li, Hua Chang, Shaoming Xin and Jianghui Geng

Abstract With the fast-pacing development of the GNSS, the number of satellites in orbit is increasing, and the accuracy of the multi-GNSS orbits is gradually improved, which makes it possible to use the GPS/GLONASS/BDS/Galileo quad-system model to achieve real-time precise point positioning (PPP). Usually, predicted orbits can be considered known because of its high accuracy. The high precision real-time satellite clock is a prerequisite for real-time PPP. In this paper, the estimation model and strategy of the quad-system satellite clock errors are studied, and the quad-system satellite clock errors are calculated based on the square root information filter method. Compared with the final GFZ 30 s precise clock products, the accuracy of real-time quad-system clock was about 0.06 ns which shows a high agreement. The kinematic PPP solutions based on the real-time quad-system clocks were with the solutions based on GFZ clock products, which verifies the correctness of the model and strategy.

Keywords Real-time clock error · Quad-System · Kinematic PPP · Epoch-differenced

1 Introduction

Nowadays, there is a great demand for real-time precise point positioning (PPP), such as disaster early warning, weather forecasting and deformation monitoring [1, 2]. Real-time precision satellite clock errors are the key to real-time PPP applications. The accuracy and stability of real-time precise satellite clock errors will directly decide the real-time PPP performance. With the establishment and improvement of the four global satellite navigation systems (GNSS) and the steady improvement of the accuracy of all systems, the integration of four systems for real-time PPP has been recognized as an inevitable architecture for both hardware

X. Li (✉) · H. Chang · S. Xin · J. Geng
GNSS Research Center, Wuhan University, Wuhan, China
e-mail: lixiaotao@whu.edu.cn

J. Sun et al. (eds.), *China Satellite Navigation Conference (CSNC) 2017 Proceedings: Volume III*, Lecture Notes in Electrical Engineering 439,
DOI 10.1007/978-981-10-4594-3_12

and algorithm designs, and so quad-system real-time precision satellite clocks also naturally become a major problem to be solved nowadays. There are many research results in the field of satellite clock error estimation [3–6]. Zhang et al. [4] present a joint estimation model for GPS/BDS real-time clocks and produce 1-Hz clock updates for real-time applications efficiently. Then, a method of real-time precise satellite clock estimation for combined BDS/GPS was investigated by Zhao et al. [5] and Chen et al. [6].

We build a joint estimation model for GPS/GLONASS/BDS/Galileo to estimate the quad-system combined satellite clock errors by the method, which combines epoch-differenced phases observations and un-differenced range observations so that it can ensure the precision and the efficiency [3]. We use 31 days of data in 2015 of 128 MGEX stations globally to estimate the real-time quad-system combined satellite clock errors, and then the estimated precise clock errors are used in real-time PPP. The results shows that the clock errors can reach a good level corresponding to the analysis center (GFZ) and the kinematic PPP results also achieve high consistency with the results from GFZ final precise product. In addition, the influence of the inter-frequency biases of GLONASS and the inter-system biases are discussed in this paper. The computational efficiency is also reported, which is important to real-time application.

2 Method

We use the method proposed by Ge et al. [3] to estimate satellite clocks. This method combines epoch-differenced phase observations and un-differenced range observations so that it can ensure the precision and the efficiency.

2.1 The Un-Differenced Method

Commonly, we use the ionosphere-free phase and range combinations method to reduce the influence of the ionosphere and improve the process procedure. The observation equations of the multi-system un-differenced method can be expressed as

$$\begin{aligned} v_{\mathrm{Lc}}^{\Gamma}(i) &= \delta t_r^{\Gamma}(i) - \delta t_s^{\Gamma}(i) + m(i)\delta T^{\Gamma}(i) + B^{\Gamma} + l_{\mathrm{Lc}}^{\Gamma}(i) \\ v_{\mathrm{Pc}}^{\Gamma}(i) &= \delta t_r^{\Gamma}(i) - \delta t_s^{\Gamma}(i) + m(i)\delta T^{\Gamma}(i) + l_{\mathrm{Pc}}^{\Gamma}(i) \end{aligned} \tag{1}$$

where i is the number of epoch; $\delta t_r(i)$ and $\delta t_s(i)$ are the receiver and satellite clock parameters; δT and $m(i)$ represent the ZTD parameter and its mapping function. B represents the ambiguity of the ionosphere-free phase observations. The post-fit and pre-fit residuals of the phase and range observations are v_{Lc}, l_{Lc} and v_{Pc}, l_{Pc},

respectively. The symbol Γ represents the four systems: GPS (G), BDS (C), Galileo (E) and GLONASS (R).

The number of ambiguities will be rapidly increasing with the number of stations and satellites increasing. A large number of ambiguities will degrade the calculation efficiency, which hinder the application in real-time positioning.

2.2 The Epoch-Differenced Method

Using the difference between two adjacent epochs, we can get the epoch-differenced method. The method can be expressed as

$$\begin{aligned} v^{\Gamma}_{\Delta \mathrm{Lc}}(i) &= \triangle \delta t^{\Gamma}_{r}(i) - \triangle \delta t^{\Gamma}_{s}(i) + \triangle m(i) \delta T^{\Gamma}(i) + \triangle l^{\Gamma}_{\mathrm{Lc}}(i) \\ v^{\Gamma}_{\Delta \mathrm{Pc}}(i) &= \triangle \delta t^{\Gamma}_{r}(i) - \triangle \delta t^{\Gamma}_{s}(i) + \triangle m(i) \delta T^{\Gamma}(i) + \triangle l^{\Gamma}_{\mathrm{Pc}}(i) \end{aligned} \tag{2}$$

The differenced clock $\triangle \delta t(i) = \delta t(i) - \delta t(i-1)$ is expressed by symbol $\triangle$. When we use this method, the ambiguity parameters are removed from the observations. This method avoids the large number ambiguity parameters and has high computation efficiency, but will introduce a constant clock biases. This will prolong the convergence time of PPP and lead to residual mean is nonzero.

2.3 The Mixed Method

The approach combines epoch-differenced phase observations and un-differenced range observations to estimate clocks proposed by Ge et al. [3]. This method uses epoch-differenced phase observation to eliminate ambiguity parameters, and un-differenced range observation to determine a precise constant clock biases, so that it can ensure the precision and the efficiency.

$$\begin{aligned} v^{\Gamma}_{\Delta \mathrm{Lc}}(i) &= \triangle \delta t^{\Gamma}_{r}(i) - \triangle \delta t^{\Gamma}_{s}(i) + \triangle m(i) \delta T^{\Gamma}(i) + \triangle l^{\Gamma}_{\mathrm{Lc}}(i) \\ v^{\Gamma}_{\mathrm{Pc}}(i) &= \delta t^{\Gamma}_{r}(i_{r0}) - \delta t^{\Gamma}_{s}(i_{s0}) + \overline{l}^{\Gamma}_{\mathrm{Pc}}(i) \end{aligned} \tag{3}$$

where $\overline{l}_{\mathrm{Pc}}(i)$ means:

$$\overline{l}_{\mathrm{Pc}}(i) = \sum_{j=i_{r0}+1}^{i} \triangle \delta t_{r}(j) - \sum_{j=i_{s0}+1}^{i} \triangle \delta t_{s}(j) - m(i) \delta T(i) \tag{4}$$

With the reformulations, we can describe each epoch's data processing with two steps. This method can be carried out in parallel so that it will reduce the process time:

(a) The estimations of the differenced clock and ZTD parameters using epoch-differenced phase equations.
(b) The estimations of the initial clock biases using un-differenced ranges equations.

The significance of multi-system real-time clock estimation is that it can provide high quality clock results in real time. The method adopted in this paper improves the operation efficiency by using the idea of epoch-differenced and two estimators, and to improve the precision of the results by the combination of the un-differenced method and the multi-system data.

In addition, it is worth noting that we use some measures to improve the efficiency. Computing efficiency is very important for real-time data process. For example, the number of the inter-frequency bias of GLONASS parameters is 2880 if we estimate 24 satellites' clock products for 120 stations. Apparently, so many parameters which needed to be estimated will greatly reduce the computational efficiency. So we do not take that into account, and meanwhile, we also do not consider the inter-system bias. Using this measure will greatly reduce the number of parameters to be estimated and improve the procedure of data process. As a result, the computational efficiency can meet the need of the real-time clock errors' process.

On the other hand, it does not affect the usage of clock product if we do not consider the inter-frequency bias and the inter-system bias. Because we generally set the parameters to be estimate about of the inter-frequency bias and the inter-system bias in PPP, and these parameters can be absorbed into these parameters. In this paper, there is no impact for positioning and we will introduce the problems in details in our PPP experiment.

3 Data and Process Strategy

To investigate the accuracy and availability of real-time satellite clock errors, we use the RINEX data (30 s) collected from 128 MGEX stations at doy 300- doy 330 in 2015 in the simulated real-time mode, which is shown in Fig. 1. The data pre-processing is necessary. We use combined observations to detect blunders and correct the cycle slips. The process of repairing cycle slips involves detecting the slips, estimating its exact integer and correcting the phase measurement with the integer estimate. We use the approach of quadric difference [7] to evaluate satellite clock products. The satellite G02 is selected to be the reference satellites. The GFZ satellite clock products are used as a reference. Processing strategy used in this paper is showed in Table 1.

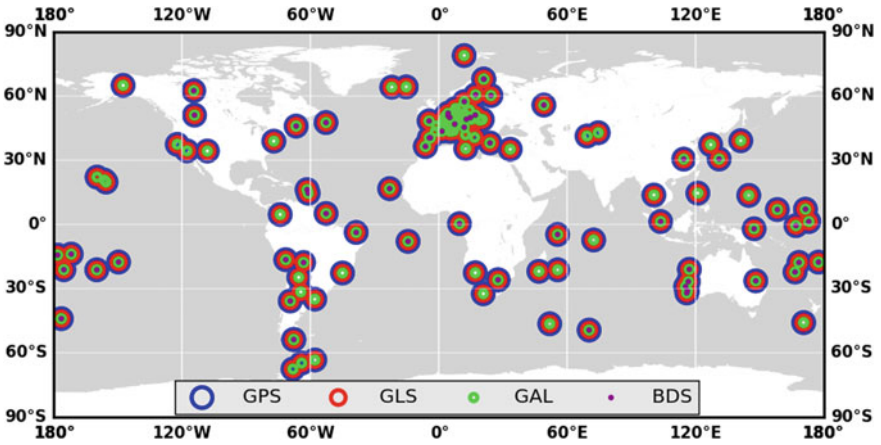

Fig. 1 The distribution of the MGEX stations for determining satellite clock

Table 1 Data processing strategy

	Parameters	Processing strategies
Observations data	Observations' types	Epoch-differenced phase observations and un-differenced range observations
	Elevation cutoff angle	10°
	Weights of observations	$p = 1, e > 30°$; $p = 2\sin(e), e \leq 30°$
Error corrections	Earth tides	Model corrected: FES2004
	Satellites orbit	GBM orbit by GFZ, 15 min interval
	EOP	GFZ products
	DCB	DCB products provided by CODE for GPS
	Relativistic effects and earth rotation	Model corrected
	Receiver PCO	GPS/GLONASS by igs08_1869.atx; BDS/GAL use GPS value
	Satellite PCO	igs08_1869.atx
	Phase windup	Corrected
	Clock of satellite	Estimated: Gaussian noise
	Clock of receiver	Estimated: Gaussian noise
Parameters estimation	ZTD (Zenith tropospheric delay)	The priori meteorological parameters were modeled by GPT2; priori troposphere: Saastamoinen; Mapping function: GMF. A priori model+Parameter estimation model, Random walk, the spectral density is $2\,\mathrm{cm}/\sqrt{h}$
	Ambiguity	Estimated: section constant parameters
	ISB (system inter bias)	Estimated: constant parameters
	Positions of stations	Static: a priori constraint of 10 m Dynamic: a priori constraint of 10 m, dynamic noise of 1 m/s

4 Discussion and Analysis

4.1 Satellite Clocks

We evaluate the estimated quad-system satellite clocks by selecting GFZ satellites clock products as a reference. The result of DOY 300 in 2015 as examples is shown in Fig. 2. There are no statistical results of the PRNs because they do not work. Then we count the average STDs of different systems on DOY 300/310/320/330 in 2015, which is shown in Table 2. Compared with the final GFZ 30 s precise clock product, the accuracy of real-time quad-system clock was about 0.06 ns and shows high agreement. The precision of the estimated quad-system clock is stable with time.

The estimated initial satellite clock biases are largely related to the convergence time, so the RMS of quad-system satellite clock biases on DOY 300 in 2015 is shown in Fig. 3. From Fig. 3, we can get some conclusions. First, the RMS values of GPS are small, which are less than 1 ns. Second, the RMS values of GLONASS are irregular due to the influence of inter-frequency bias (IFB). Third, owing to select GPS satellite as a reference, there are inter-system time differences existed in other system, such as BDS and GALILEO. If we remove the mean value of RMS of GALILEO satellite as inter-system time difference, the remaining RMS values of

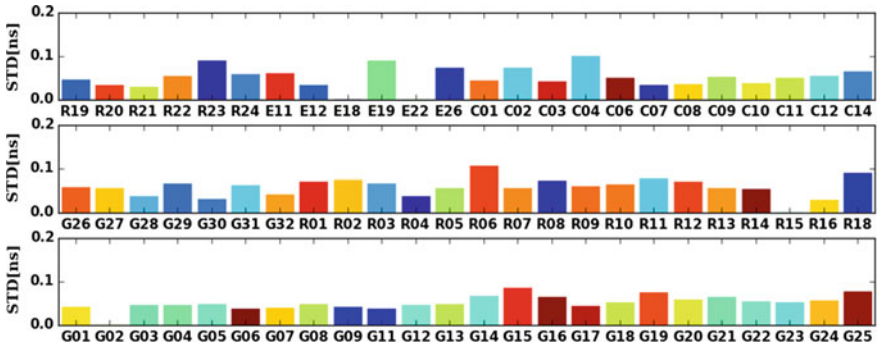

Fig. 2 The STDs of clock estimates compared with the clocks of GFZ final products on DOY 300 in 2015

Table 2 The average STD of estimated quad-system clock versus GFZ final clock products

mean STD (ns)	2,015,300	2,015,310	2,015,320	2,015,330
GPS	0.052	0.062	0.060	0.054
GLONASS	0.060	0.066	0.056	0.062
Galileo	0.064	0.087	0.068	0.084
BDS	0.053	0.057	0.056	0.063
All system	0.055	0.064	0.059	0.060

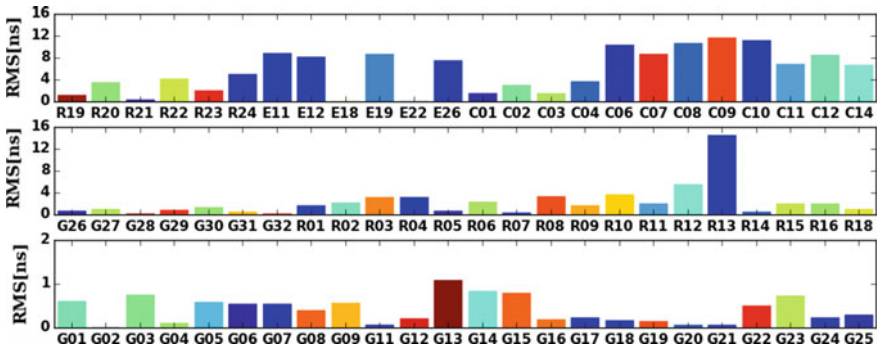

Fig. 3 The RMS of clock estimates compared with the clocks of GFZ final products on DOY 300 in 2015

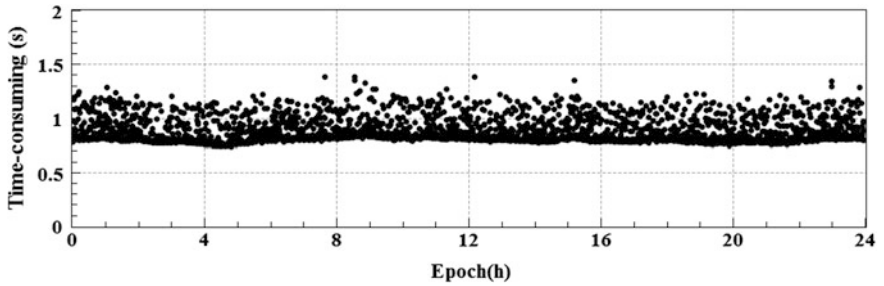

Fig. 4 The computational efficiency

GALILEO is very small. Inter-system time difference also existed in BDS. The RMS of BDS satellites clock is related to the type of satellites. PRN C01-C05 are GEO satellites, and C06-C10 are IGSO satellites while other BDS satellites are MEO satellites. The RMS in Fig. 3 reaches good consistency with the BDS satellite types.

In addition, the time series of time-consuming of an epoch is shown in Fig. 4. The statistical result is generated from a laptop equipment with INTEL i5-4300 M and 4 GB memory. Data involved is 128 stations and 72 satellites from quad-system. According to Fig. 4, we can see time-consuming of most epoch is below 0.8 s and all epochs lower than 1.5 s, which can meet the need of real-time high-frequency processing. All in all, our study shows that the quad-system combined satellite clocks can be well estimated and next we use the clock into the precise point positioning.

4.2 Positioning Results

In order to analyze the performance of estimated real-time clock, both estimated real-time clock products and GFZ final precise clock products are used to perform the kinematic PPP respectively. In kinematic PPP mode, the station position is modeled as white noise. If the kinematic PPP can get perfect performance, the static PPP also can get good performance. So we just do the experiment of the kinematic PPP in this paper. CUT0, GMSD, JFNG and MRO1 are used to test kinematic PPP from DOY 300 to 306 in 2015. Figure 5 give the distribution of these stations. Taking CUT0 station for example, the kinematic PPP time series based on different satellite clock product on DOY 300 in 2015 is shown in Fig. 6. According to Fig. 6,

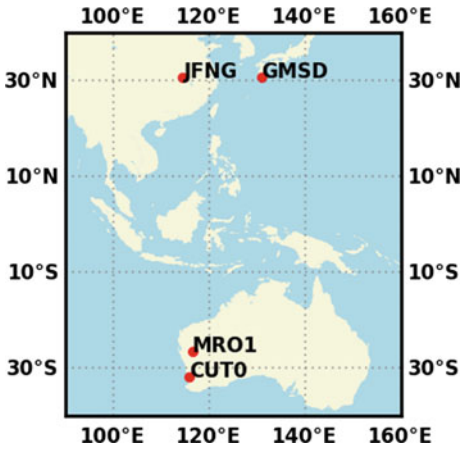

Fig. 5 The distribution of the stations for kinematic PPP

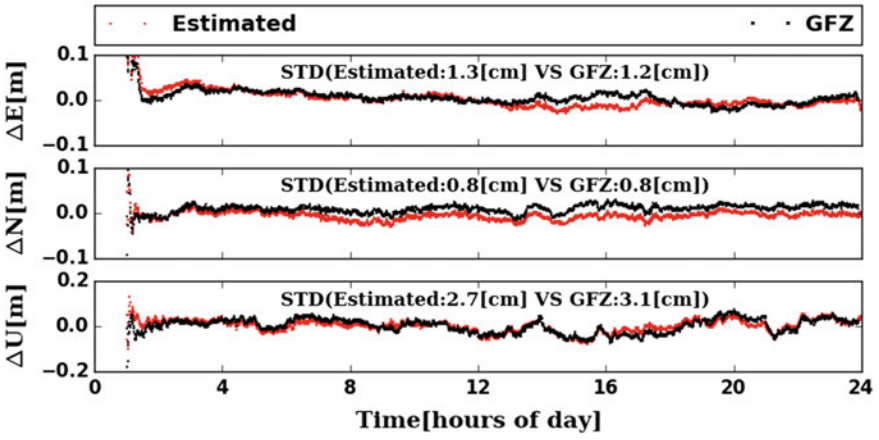

Fig. 6 Kinematic positioning time series based on different satellite clock product on DOY 300 in 2015

we can find that the performance of PPP based on estimated quad-system clock is consistent with the result from GFZ final clock, and the time series of PPP based on estimated satellite clock is more smoothness in U direction. Figure 7 gives STD of positioning error from 4 stations' kinematic PPP over one week, The black bar reflects the result with GFZ's final clock product (GBM) and the red bar reflects the result with our estimated clock product. From Fig. 7, we can see the PPP results with estimated real-time clock products can reach the perfect precision which is similar to the results with GFZ's clock. The STD of the east direction can reach 1.5 cm. The STD of the north direction can reach 1 cm. The STD of the up direction can reach 3 cm. From clock products used in kinematic PPP standpoint, estimated clock product based on the method used in this paper is approximately consistent with the GFZ final clock products.

Inter-frequency bias of GLONASS and the inter-system bias are not considered in the determining the satellite clock. The impact of these biases in PPP can be analyzed by residual distribution of code and phase measurements. Residual histogram of code and phase measurement is shown in Fig. 8. According to Fig. 8, we can see residual mean of code observation from different is closed to 0. These results show that though we do not consider the inter-frequency bias and the inter-system bias in estimating the satellites clock, these biases can be absorbed into the parameters of inter-frequency bias and inter-system bias setup in PPP.

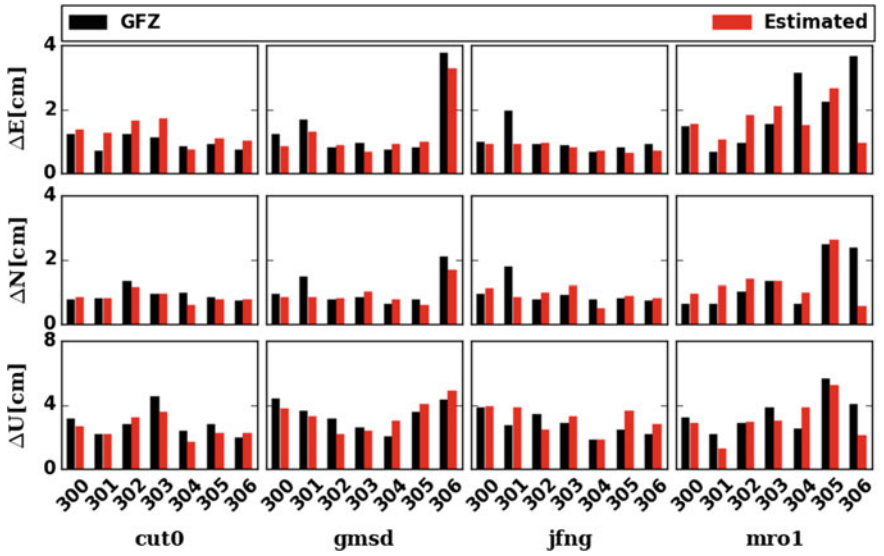

Fig. 7 STD of position error from kinematic PPP based on different clock product over DOY 300–306 in 2015

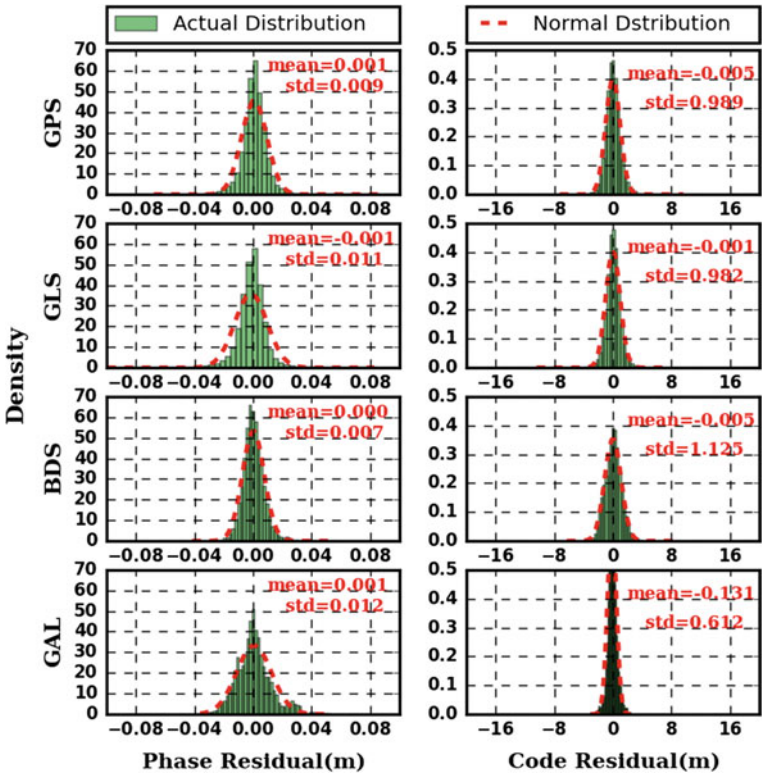

Fig. 8 Residual distribution of kinematic quad-system PPP at JFNG on DOY 300 in 2015

5 Conclusion

With data on DOY 300–330 in 2015 from about 128 stations on global scale, the performance of the estimated quad-system clock products is investigated. According to the content above, this paper mainly studies the method of quad-system satellite clock estimation using the approach proposed by Ge et al. [3]. The estimated satellites clock results are compared with GFZ's final clock products, and we can see that they are in good agreement.

According our experiments, we can address that:

(a) The accuracy of real-time quad-system clocks was about 0.06 ns and shows high agreement with GFZ final clock products.
(b) The RMS of GPS clock difference are small, which are less than 1 ns. The RMS of GLONASS counterparts are irregular due to the influence of inter-frequency bias (IFB). The RMS of BDS satellites clock are related to the type of satellites.

(c) The computational efficiency of the method can meet the need of real-time high-frequency PPP.
(d) The inter-frequency biases and the inter-system biases can be ignored when we estimate the satellites clocks to improve the computational efficiency and that will not affect the PPP results.

References

1. Zumberge JF, Heflin MB, Jefferson DC et al (1997) Precise point positioning for the efficient and robust analysis of GPS data from large networks. J Geophys Res: Solid Earth 102 (B3):5005–5017
2. Bar-Sever YE, Kroger PM, Borjesson JA (1998) Estimating horizontal gradients of tropospheric path delay with a single GPS receiver. J Geophys Res: Solid Earth 103 (B3):5019–5035
3. Ge MR, Chen JP, Dousa J et al (2012) A computationally efficient approach for estimating high-rate satellite clock corrections in realtime. GPS Solutions 16(1):9–17
4. Zhang W, Lou Y, Gu S et al (2015) Joint estimation of GPS/BDS real-time clocks and initial results. GPS Solutions 20(4):665–676
5. Zhao Q, Dai Z, Wang G et al (2016) Real-Time precise BDS clock estimation with the undifferenced obervation. Geomat Inf Sci Wuhan Univ 41(5):686–691
6. Chen L, Geng C, Zhou Q (2016) Estimation model and accuracy analysis of BeiDou/GPS real-time precise satellite clock error integrated resolving. Acta Geodaetica Cartogr Sin 09:1028–1034
7. Lou YD, Shi C, Zhou X et al (2009) Realization and analysis of GPS precise clock products. Geomat Info Sci Wuhan Univ 01:88–91

The Analysis and Modeling of Intersystem Biases Between GPS and BDS

Dongwei Zhu, Dingfa Huang, Abubakr Hassan and Bolin Xiong

Abstract Receiver hardware delay is one of the error sources which affect ambiguity resolution and positioning. In this contribution, differential receiver hardware delay between GPS and BDS, namely differential phase and code intersystem bias (ISB), are estimated together with other parameters using single differential (SD) observation, and analyzed by Fast Fourier Transform (FFT). The experiment shows that the differential ISBs are close to zero for the baseline using two identical receivers, and can be neglected when taking the measurement noise of phase and code into account. However they become significant for receivers which are of different types. According to FFT, the ISB time series only contains the constant term, and no trend and periodic terms are included. The model can be established on the basis of the characteristics of ISB and is used for prediction and calibration. Taking into account the ISBs correction, the success rate of ambiguity resolution is up to 99%. The mean values are −0.3, 0.6, −1.7 mm and standard deviations are 2.9, 3.4, 6.3 mm for baseline component in North, East, and Up directions, respectively. The result shows that the prediction and calibration for ISB are feasible.

Keywords BDS · GPS · Single differential · Intersystem bias · Fast fourier transform

D. Zhu · D. Huang (✉) · A. Hassan · B. Xiong
Faculty of Geosciences and Environmental Engineering, Southwest Jiaotong University, Chengdu 611756, Sichuan, China
e-mail: dfhuang@swjtu.edu.cn

D. Zhu
e-mail: mn.401@163.com

J. Sun et al. (eds.), *China Satellite Navigation Conference (CSNC) 2017 Proceedings: Volume III*, Lecture Notes in Electrical Engineering 439,
DOI 10.1007/978-981-10-4594-3_13

1 Introduction

The instrument hardware delay is an important error source especially coming from receiver. Since it depends on the correlation inside the instrument, we cannot know the value of hardware delay. It will be assimilated by other parameters, for example, receiver clock error, when we process solo GNSS data. However, for multi-GNSS data processing, we have to take into account the differential hardware delay, namely the differential intersystem bias (ISB), if we use undifferential or single differential (SD) observation, because the hardware delay is a system-dependent parameter [6, 9] and the signals come from different constellations. Montenbruck et al. [5] point out the GPS-to-Galileo ISB may reach up to several hundreds of nanoseconds. Odijk et al. [6] analyze the characteristic of between-receiver GPS-Galileo intersystem biases. The result shows that the differential ISB is only significant for different types and manufacturers of receivers, but they have not shown up for baseline consisting of identical receiver types. Torre and Caporali [8] analyze the ISB for GPS/BDS/GLONASS/Galileo/QZSS with different receivers. Jiang et al. [3] estimate GPS/BDS short-term ISB by precision point positioning first, and then model and predict ISB. The model consisting of a quadratic polynomial in time and two or three periodic functions with diurnal and semi-diurnal periods is used for ISB prediction. The convergence time can be shortened by 19.6, 16.1, and 2.4% in N, E and U component with a priori ISB constraint. Gioga and Borio [2] estimate ISB with different approaches and evaluate the stability of ISB. Besides, the impact of ISB on Position Velocity Time solution is also considered. The result shows that the ISB is very stable and the performance of multi-constellation navigation can be significantly improved by using of ISB. Khodabandeh and Teunissen [4] apply *S*-system theory to estimate parameters. An ISB look-up table is constructed. Users can search the table for a network receiver of their own type and select the corresponding ISBs.

In this paper, we estimate the differential phase and code ISB between GPS and BDS using single differential (SD) observation. Then the characteristics of ISB are analyzed by Fast Fourier Transform (FFT). According to the characteristics of ISB, the model is established. Finally, the models of differential phase and code ISB as priori values are used to correct the phase and code observation in the purpose of verifying the feasibility of calibration.

2 ISB Estimation Model

2.1 Single-Difference Observation Model for GPS and BDS with Unknown ISBs

If we track the GPS (G) and BDS (C) satellites on L1 and B1 frequency, respectively, at the same time by receiver r and b. For short baseline, we can get the single-frequency (SF) and SD observation equation between receiver r and receiver b for phase and code observation

$$\begin{aligned} P_{r,b}^{G} &= \rho_{r,b}^{G} + \mathrm{d}t_{r,b} + d_{r,b}^{G} + \varepsilon_{P}^{G} \\ \varphi_{r,b}^{G} &= \rho_{r,b}^{G} + \mathrm{d}t_{r,b} + \delta_{r,b}^{G} + \lambda^{G} N_{r,b}^{G} + \varepsilon_{\varphi}^{G} \\ P_{r,b}^{C} &= \rho_{r,b}^{C} + \mathrm{d}t_{r,b} + d_{r,b}^{C} + \varepsilon_{P}^{C} \\ \varphi_{r,b}^{C} &= \rho_{r,b}^{C} + \mathrm{d}t_{r,b} + \delta_{r,b}^{C} + \lambda^{C} N_{r,b}^{C} + \varepsilon_{\varphi}^{C} \end{aligned} \tag{1}$$

with $P_{r,b}, \varphi_{r,b}$ the SD code and phase observation, $\rho_{r,b}$ the SD range between receiver r and receiver b with a common satellite, $dt_{r,b}$ the difference of receiver clock error, $d_{r,b}, \delta_{r,b}$ the hardware delay for code and phase, λ the wavelength, $N_{r,b}$ the SD integer ambiguity between receivers, $\varepsilon_P, \varepsilon_\varphi$ the measurement noise and the other unmodeled errors.

However the linear combination of the design matrix column vectors may produce zero vector, so the observation Eq. (1) is not of full-rank. But we can use *S*-system theory [7] for the purpose of eliminating the rank defect. In this procedure, a GPS satellite (R_G) and a BDS satellite (R_C) are chosen as the pivot satellite for GPS and BDS system, respectively. Then the transformed observation equation can be obtained

$$\begin{aligned} P_{r,b}^{G} &= \rho_{r,b}^{G} + \mathrm{d}\tilde{t}_{r,b} + \varepsilon_{P}^{G} \\ \varphi_{r,b}^{G} &= \rho_{r,b}^{G} + \mathrm{d}\tilde{t}_{r,b} + \tilde{\delta}_{r,b}^{G} + \lambda^{G} N_{r,b}^{GR_G} + \varepsilon_{\varphi}^{G} \\ P_{r,b}^{C} &= \rho_{r,b}^{C} + \mathrm{d}\tilde{t}_{r,b} + \mathrm{d}t_{r,b}^{CG} + \varepsilon_{P}^{C} \\ \varphi_{r,b}^{C} &= \rho_{r,b}^{C} + \mathrm{d}\tilde{t}_{r,b} + \tilde{\delta}_{r,b}^{G} + \lambda^{C} N_{r,b}^{CR_C} + \tilde{\delta}_{r,b}^{CG} + \varepsilon_{\varphi}^{C} \end{aligned} \tag{2}$$

where $N_{r,b}^{GR_G}, N_{r,b}^{CR_C}$ represent the double-difference (DD) integer ambiguity for GPS and BDS satellite respectively, $N_{r,b}^{R_C}, N_{r,b}^{R_G}$ are SD ambiguity of BDS and GPS pivot satellite respectively, $\mathrm{d}\tilde{t}_{r,b} = \mathrm{d}t_{r,b} + d_{r,b}^{G}$, $\mathrm{d}t_{r,b}^{CG} = \mathrm{d}t_{r,b}^{C} - \mathrm{d}t_{r,b}^{G}$, $\tilde{\delta}_{r,b}^{G} = \delta_{r,b}^{G} - d_{r,b}^{G} + \lambda^{G} N_{r,b}^{R_G}$, $\tilde{\delta}_{r,b}^{CG} = \delta_{r,b}^{C} - \delta_{r,b}^{G} + \lambda^{C} N_{r,b}^{R_C} - \lambda^{G} N_{r,b}^{R_G}$, and the other terms are as defined in (1).

Due to different solo GNSS, the time system and reference frame are not same for GPS and BDS. For GPS, the time system is GPS time (GPST), and for BDS, that is BDS time (BDST). So the transform should be done when processing GPS and BDS data. Although there exist differences in the reference frame, the discrepancy is small. So it can be safely ignored for short baseline [10].

2.2 *The Differential Intersystem Biases Between GPS and BDS*

Though the rank defect is eliminated by introducing a pivot satellite for each system, and seeing GPS code hardware delay as part of receiver clock error in (2),

the ISB cannot be obtained directly. So the further calculation must be made to get the differential code and phase ISB

$$\begin{aligned} \mathrm{ISB}_P &= \mathrm{d}t_{r,b}^{C} - \mathrm{d}t_{r,b}^{G} \\ &= \mathrm{d}t_{r,b}^{CG} \end{aligned} \tag{3}$$

where ISB_P denotes the code ISB, and the other terms are same to above.

$$\begin{aligned} \mathrm{ISB}_\varphi &= \mathrm{Frac}((\delta_{r,b}^{C} - \delta_{r,b}^{G})/\lambda^{C}) \\ &= \mathrm{Frac}((\tilde{\delta}_{r,b}^{CG} - \lambda^{C} N_{r,b}^{R_C} + \lambda^{G} N_{r,b}^{R_G})/\lambda^{C}) \end{aligned} \tag{4}$$

where ISB_ϕ denotes the phase ISB, $\mathrm{Frac}(\cdot)$ represents fractional part, and the other terms are same to above.

The code ISB can be achieved immediately by (2), but the phase ISB cannot. We must obtain SD integer ambiguity value of pivot satellite of GPS and BDS in the first place and treat the fractional part as the phase ISB at the same time. The SD integer ambiguity value can be obtained by way of calculating the average of multi-epoch SD ambiguity and rounding the average. Since the estimation of ISB is based on epoch-by-epoch processing, there is no link between epochs. It should be pointed out that the ISB for code and phase in (3) and (4) is not the true delay, but is the differential values between receiver r and b.

2.3 Single-Difference Observation Model for GPS and BDS with Known ISBs

If ISBs can be neglected or calibrated, the differential hardware delay will be equal. That is to say, $d_{r,b}^{G} = d_{r,b}^{C}$ and $\delta_{r,b}^{G} = \delta_{r,b}^{C}$ after calibration in (1). So the (1) can be written as

$$\begin{aligned} P_{r,b}^{G} &= \rho_{r,b}^{G} + \mathrm{d}t_{r,b} + d_{r,b} + \varepsilon_{P}^{G} \\ \varphi_{r,b}^{G} &= \rho_{r,b}^{G} + \mathrm{d}t_{r,b} + \delta_{r,b} + \lambda^{G} N_{r,b}^{G} + \varepsilon_{\varphi}^{G} \\ P_{r,b}^{C} - \mathrm{ISB}_P &= \rho_{r,b}^{C} + \mathrm{d}t_{r,b} + d_{r,b} + \varepsilon_{P}^{C} \\ \varphi_{r,b}^{C} - \mathrm{ISB}_\varphi &= \rho_{r,b}^{C} + \mathrm{d}t_{r,b} + \delta_{r,b} + \lambda^{C} N_{r,b}^{C} + \varepsilon_{\varphi}^{C} \end{aligned} \tag{5}$$

where $d_{r,b}, \delta_{r,b}$ are the hardware delay for code and phase, and the other terms are same as in (1), (3), and (4).

The same point to (1), observation Eq. (5) is also not of full-rank. So we must change the observation equation to eliminate the rank defect. Due to different wavelength for BDS and GPS and the need to retain integer character for DD

integer ambiguity, a GPS satellite and a BDS satellite are also chosen as pivot satellites

$$\begin{aligned} P_{r,b}^{G} &= \rho_{r,b}^{G} + \mathrm{d}\tilde{t}_{r,b} + \varepsilon_{P}^{G} \\ \varphi_{r,b}^{G} &= \rho_{r,b}^{G} + \mathrm{d}\tilde{t}_{r,b} + \eta_{r,b}^{G} + \lambda^{G} N_{r,b}^{\mathrm{GR}_G} + \varepsilon_{\varphi}^{G} \\ P_{r,b}^{C} - \mathrm{ISB}_{P} &= \rho_{r,b}^{C} + \mathrm{d}\tilde{t}_{r,b} + \varepsilon_{P}^{C} \\ \varphi_{r,b}^{C} - \mathrm{ISB}_{\phi} &= \rho_{r,b}^{C} + \mathrm{d}\tilde{t}_{r,b} + \eta_{r,b}^{C} + \lambda^{C} N_{r,b}^{\mathrm{CR}_C} + \varepsilon_{\varphi}^{C} \end{aligned} \tag{6}$$

where $\eta_{r,b}^{G} = \delta_{r,b} - d_{r,b} + \lambda^{G} N_{r,b}^{R_G}$, $\eta_{r,b}^{C} = \delta_{r,b} - d_{r,b} + \lambda^{C} N_{r,b}^{R_C}$, and the other terms are same as in (2), (3) and (4).

As can be seen in (2) and (6), the number of unknown parameters decreases from 7 to 6, except for DD integer ambiguity. So the redundancy of the observation equation will increase, and this is a favorable factor to ambiguity resolution and positioning.

3 The Characteristics of Differential ISB and the Modeling

In this section, we will estimate and analyze the differential code and phase ISB using GPS/BDS datasets based on the formulas (2), (3), and (4). Two short-baseline cases are adopted, and one baseline (#1) employs different types of receivers, and the other (#2) employs identical receivers. The datasets were collected over three days. First, for the purpose of analyzing the characteristics and stability of ISB, the data of the first and the second day were used to estimate the code and phase ISB of all epochs, and the DD integer ambiguity acted as known value. Then we model the ISB according to the characteristics. Finally, the data of the third day was applied in order to investigate the feasibility of prediction and calibration using the model as a priori correction.

3.1 The Characteristics of ISB

Two cases were carried out with different and identical types of receivers, respectively. The two baselines are short, so some error items are not taken into account when processing data, for example, atmosphere delay. Broadcast ephemeris is used to calculate satellite position and clock error. The measurement sampling interval is 1s, and the cutoff elevation is 15°.

Figure 1 shows the differential ISBs for baseline occupied by two different types of receivers, and Fig. 2 is contrary. As can be intuitively seen, the variety of phase and code ISB are stable, and there are not trend terms in Figs. 1 and 2. However,

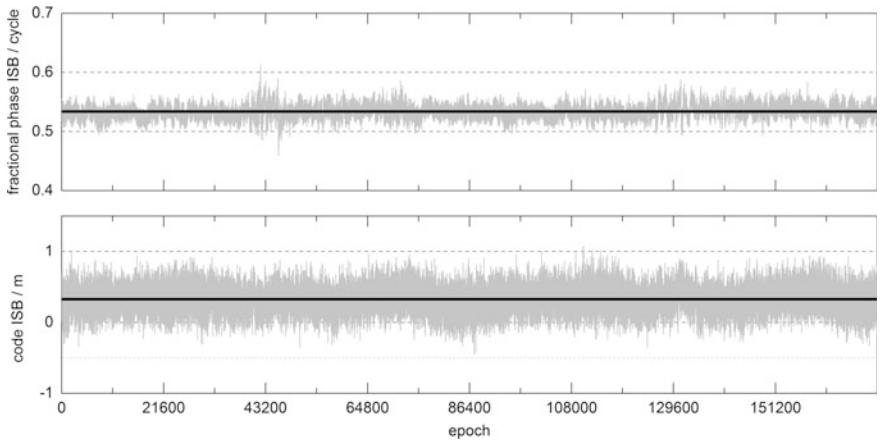

Fig. 1 Estimated differential ISBs time series for baseline #1. The *up panel* is fractional phase ISB, and the *down* is code ISB. The *gray lines* represent ISB. The *black line* represents the mean value of corresponding ISB

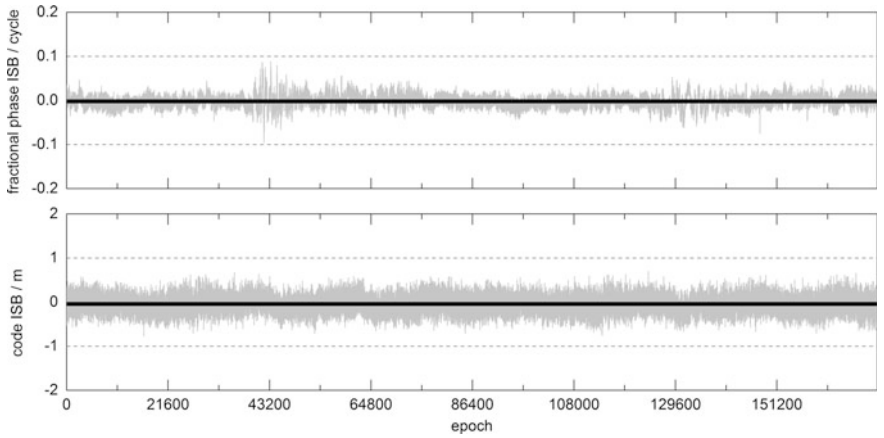

Fig. 2 Estimated differential ISBs time series for baseline #2. The *up panel* is fractional phase ISB, and the *down* is code ISB. The *gray lines* represent ISB. The *black line* represents the mean value of corresponding ISB

the size of values is different between Figs. 1 and 2. The former is bigger than the latter obviously.

To further analyze the characteristic of ISB, the Fast Fourier Transformation (FFT) is used. FFT can convert time to frequency and vice versa [1], so we can obtain the frequency spectrum of ISB time series. Figures 3 and 4 are power spectral density (PSD) for baseline #1 and #2, respectively. As shown in figures, only one signal is clear, and the frequency of this signal is zero. The other signals are so weak that they can be considered as noise and can be neglected. The analysis

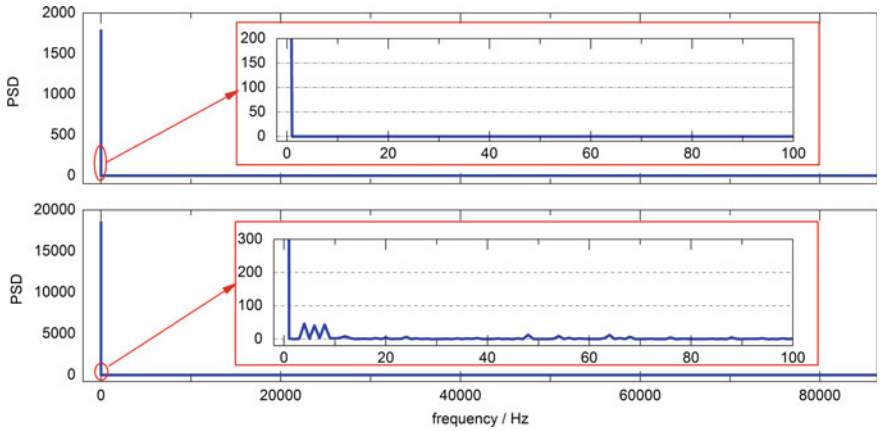

Fig. 3 Power spectral density of the fractional phase ISB (*up*) and code ISB (*down*) for baseline #1

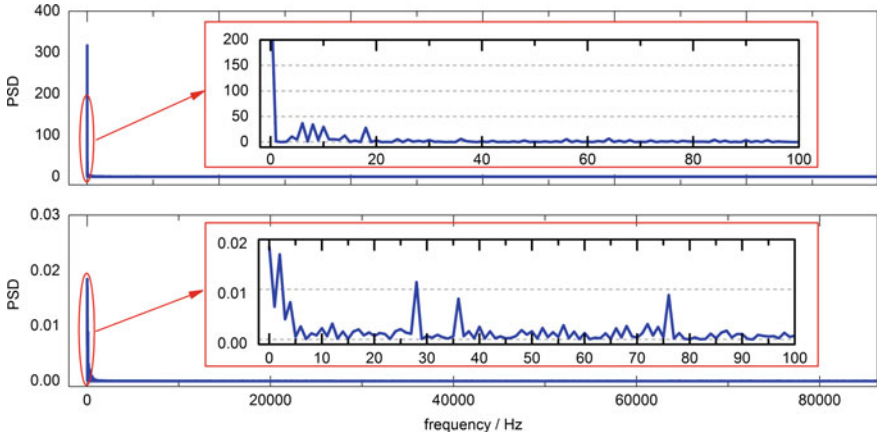

Fig. 4 Power spectral density of the fractional phase ISB (*up*) and code ISB (*down*) for baseline #2

about PSD implies that the time series of phase or code ISB only consists of a signal, and do not contain periodic terms definitely so that the ISB can be seen as a constant.

3.2 The Model of ISB

The characteristics and stability of ISB were analyzed in Sect. 3.1. In this section, we will model for ISB according to its characteristics. As we have known, the differential ISB does not contain trend and periodic terms, and it is only a constant. So we will search the constant in the next step, and establish the model of ISB.

Table 1 Statistic of differential phase and code ISB of all epochs

Baseline	Total epochs	Fractional phase ISB (cycle)		Code ISB (m)	
		Mean	STD	Mean	STD
#1	172,798	0.534	0.011	0.327	0.161
#2	172,589	−0.002	0.013	−0.043	0.166

Table 1 is the mean and standard deviation (STD) of ISBs. The estimated ISBs for baseline #1 have a mean of 0.534 cycles for phase ISB and a mean of 0.327 m for code ISB. The baseline #2 has a mean of −0.002 cycles for phase ISB and a mean of −0.043 m for code ISB. Taking the measurement noise into account, which is at the level of few millimeters for phase and a few decimeters for code [6], the differential phase and code ISB of baseline #2 drop into the range of measurement noise. So we can neglect the influence of ISB. That is to say; there is no disadvantage effect if we do not estimate ISB. For baseline #1, the differential ISBs seem to be very significant. However, it is gratifying that the STDs of ISBs are much lower than the measurement noise of phase and code. This implies that the variety is stable, and the estimated differential ISBs can be used to calibration for other datasets. Besides, the mean values agree with the amplitude of FFT when the frequency is 0 Hz. We also draw black lines which stand for the mean value in Figs. 1 and 2. According to above-mentioned analysis, the model of ISB can be built

$$\mathrm{ISB}_{\mathrm{correction}} = \mathrm{ISB}_{\mathrm{mean}} \tag{7}$$

with $\mathrm{ISB}_{\mathrm{correction}}$ the correction value of code or phase ISB for code or phase observation, $\mathrm{ISB}_{\mathrm{mean}}$ the average value of estimated ISB.

3.3 The Calibration of ISB for Other Datasets

The model has been established for ISB in Sect. 3.2. As a result of the mean value is so close to zero, the ISBs have no effect on baseline occupied by two identical receivers. So, in this section, the emphasis of our work is on analyzing the effect of ISBs on baseline occupied by two different types of receivers. Datasets of the third day of the baseline #1 are used. Moreover the models of differential phase and code ISB as priori values are used to correct the phase and code observation, respectively. Besides, the method of processing data that DD integer ambiguity is estimated with ISBs at the same time and is different from above.

Figure 5 is the estimated differential ISBs time series with or without ISBs correction. Table 2 is the statistic result of ISBs with or without ISBs correction. The estimated differential ISBs without correction are consistent with ISBs in Table 1. Due to the benefit of ISBs correction, the estimated differential ISBs are

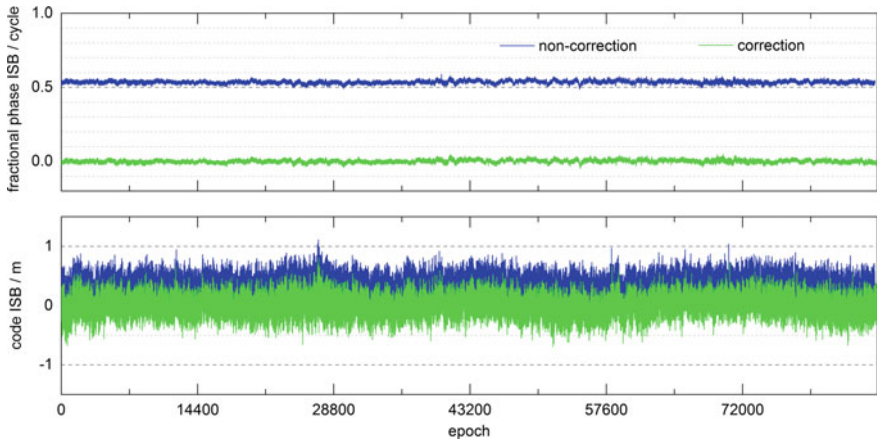

Fig. 5 Estimated differential ISBs time series of the third day with or without ISBs correction for baseline #1. The *up panel* is fractional phase ISB, and the *down* is code ISB

Table 2 Statistic of differential phase and code ISB of the third day for fixed epoch with or without ISBs correction

	Fractional phase ISB (cycle)		Code ISB (m)	
	Mean	STD	Mean	STD
Non-correction	0.535	0.010	0.329	0.159
Correction	0.001	0.011	0.003	0.159

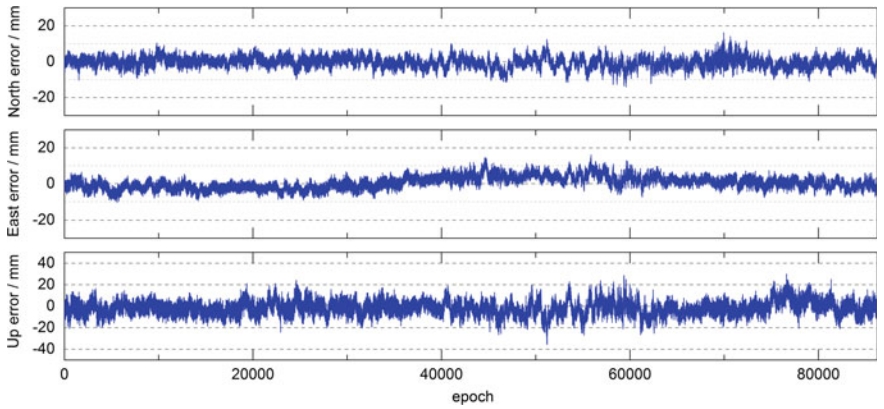

Fig. 6 The time series of errors for baseline #1 in North, East and Up directions

close to zero which is similar to baseline #2. So they have no effect on ambiguity resolution and relative positioning.

Figure 6 is the time series of errors for baseline component with ISBs correction. The errors are in the range of −20 to 20, −20 to 20, −30 to 30 mm in North, East,

Table 3 Statistic of ambiguity resolution success rate of the third day with or without correction

	Total epochs	Fixed epochs	Success rate (%)
Non-correction	86,400	85,977	99.5
Correction	86,400	86,239	99.8

Table 4 Statistic of positioning accuracy of the third day with or without correction

		Baseline components (mm)		
		North	East	Up
Non-correction	Mean	−0.4	0.7	−1.0
	STD	2.9	3.5	6.3
Correction	Mean	−0.3	0.6	−1.7
	STD	2.9	3.4	6.3

Up directions, respectively. Table 3 depicts the ambiguity resolution success rate and Table 4 depicts the mean and standard deviation (STD) of baseline components. As shown in Table 3, the success rate of ambiguity resolution exceeds 99% with or without correction. However, the fixed epochs increase by 262 when the correction models are used because we can get higher precision SD code observation and it is beneficial for ambiguity resolution. We can see that the mean values are −0.4, 0.7, −1.0 mm and −0.3, 0.6, −1.7 mm and STDs are 2.9, 3.5, 6.3 mm, and 2.9, 3.4, 6.3 mm in North, East, and Up directions without and with correction, respectively. According to the baseline length and the epoch-by-epoch processing way, the errors can be accepted. The ambiguity resolution success rate and relative positioning accuracy demonstrate that calibrating for receivers is feasible on account of the differential phase and code ISB obtained by earlier datasets.

4 Conclusion

ISB is an important error source and effects ambiguity resolution and positioning. In this contribution, we use SD observation to estimate differential phase and code ISB, which is considered to be unknown parameters and estimated with baseline components. Due to the phase ISB is mixed with SD ambiguity of pivot satellite of BDS and GPS, so the SD ambiguity must be fixed by multi-epochs first, and the fractional part appears to be the phase ISB.

The result of FFT shows that there are not trend and periodic terms in the ISB time series, and the STD of ISB is at the level of the measurement noise of phase and code, so ISB can be set as a constant. However, the constant are different for the two baselines. The constant is close to zero, and can be safely neglected for the baseline occupied by two identical receivers. The constant becomes so significant that cannot be neglected for the baseline occupied by different types of receivers. As a result of the differential fractional phase ISB for baseline #1 is about 0.5 cycles, it

is impossible to fix ambiguity without considering the effect of ISBs. So according to the characteristics of ISB, the model of ISB can be established.

The models of differential phase and code ISB as priori values are used to correct the phase and code observation, respectively. Taking into account the ISBs correction, the success rate of ambiguity resolution exceeds 99%. The mean values of baseline components in North, East, and Up directions are −0.3, 0.6, −1.7 mm and the standard deviations are 2.9, 3.4, 6.3 mm respectively. The result is in agreement with the situation that the ISBs are not corrected but estimated. So the modeling and correction for ISB are significantly useful, and the calibrating is feasible.

Acknowledgements This work is supported by the National Natural Science Foundation of China (No. 41374032), and a grant from National key Research Program of China "Collaborative Precision Positioning Project" (No. 2016YFB0501900).

References

1. Bergland GD (1969) A guided tour of the fast Fourier transform. IEEE Spectr 6(7):41–52
2. Gioia C, Borio D (2016) A statistical characterization of the Galileo-to-GPS inter-system bias. J Geodesy 1–13
3. Jiang N, Xu Y, Xu T, et al (2016) GPS/BDS short-term ISB modelling and prediction. Gps Solutions 1–13
4. Khodabandeh A, Teunissen PJG (2016) PPP-RTK and inter-system biases: the ISB look-up table as a means to support multi-system PPP-RTK. J Geodesy 1–15
5. Montenbruck O, Hauschild A, Hessels U (2011) Characterization of GPS/GIOVE sensor stations in the CONGO network. GPS Solutions 15(3):193–205
6. Odijk D, Teunissen PJG (2013) Characterization of between-receiver GPS-Galileo inter-system biases and their effect on mixed ambiguity resolution. GPS Solutions 17 (4):521–533
7. Teunissen P (1985) Zero Order Design: Generalized Inverses, Adjustment, the Datum Problem and S-Transformations. Optimization and design of geodetic networks. Springer, Berlin, Heidelberg, pp 11–55
8. Torre AD, Caporali A (2014) An analysis of intersystem biases for multi-GNSS positioning. GPS Solutions 19(2):297–307
9. Wanninger L (2011) Carrier-phase inter-frequency biases of GLONASS receivers. J Geodesy 86(2):1–10
10. Ziqing W (2008) China geodetic coordinate system 2000 and its comparison with WGS84. J Geodesy Geodyn 28(5):1–5

Research on Dependability of Navigation Satellite Precise Orbit Determination Based on Regional Monitoring Network

Zhuopeng Yang, Shanshi Zhou, Heng Zheng and Xiaogong Hu

Abstract For characteristics of satellite-ground operation, complex relationship, reliability, maintainability, and supportability, Petri net (PN) and Bayesian network (BN) are applied integrated to dependability modeling and analysis of precise orbit determination in this paper. The hardware fault, software fault, and coupling fault are considered for availability of monitor stations based on PN, and the state transition of a monitor station can be obtained. The orbit determination algorithm, outage analysis, stress intensity algorithm are taken into account for dependability of precise orbit determination based on BN, and the transition of performance and reliability can be researched. The weakness of monitor stations is confirmed and improved schemes are given. The regional monitoring network results show, this method can be used for dependability analysis and design improved, and extended to upload mission, integrity monitoring mission, and so on.

Keywords Dependability · Precise orbit determination · Petri net · Bayesian network

1 Introduction

The navigation satellite precise orbit determination is a key technology for construction and operation of satellite navigation system. The accuracy, availability, continuity, and integrity are decided by precise orbit determination. The orbit determination algorithm, monitoring network configuration, and state (operation or

Z. Yang (✉) · H. Zheng
China Academy of Aerospace Standardization and Product Assurance, Beijing 100071, China
e-mail: yangzhuopeng88@163.com

S. Zhou · X. Hu
Shanghai Astronomical Observatory, Chinese Academy of Sciences, Shanghai 200030, China

J. Sun et al. (eds.), *China Satellite Navigation Conference (CSNC) 2017 Proceedings: Volume III*, Lecture Notes in Electrical Engineering 439,
DOI 10.1007/978-981-10-4594-3_14

outage) of monitor stations are major factors of precise orbit determination. Due to the national territorial area, monitoring network configuration is restrained, so optimized orbit determination algorithm, stable and reliable operation of monitor stations are required.

There exist some interesting papers about precise orbit determination based on regional monitoring network. The three days track segment pseudorange and carrier phase observable, or three normal equations for improving orbit accuracy are proposed in [1–3]. The prior information of kinetic parameters is constrained in [4]. Based on parameters or orbit prediction of global monitoring network, the orbit accuracy is improved by a priori constraint or virtual observed value in [5]. The relationship of monitor stations distribution and satellite orbit determination are described, and orbit determination is optimized by adding observation data in [6]. The orbit determination is improved by ambiguity resolution [7]. The theory research and engineering application are discussed successfully in above papers. On the other hand, the state of monitoring network, hardware fault, software fault, coupling fault, and repair time of monitor stations take important roles in dependability of precise orbit determination, and the research about those are scarce.

Considering the precise orbit determination algorithm, state of monitoring network, and monitor stations, the dependability of precise orbit determination is analyzed by applying PN and BN, fault diagnose and improved schemes are proposed in this paper.

2 The Organization of Modeling and Analysis

The dependability is taken as representative of precise orbit determination. Dependability is a measure of the degree to which an item is operable and capable of performing its required function at any (random) time during a specified mission profile, given that the item is available at mission start. And the state of the mission can be described as user range error (URE). The steps of modeling and analysis are shown as

(1) Considering operation, outage (fault detect, hardware fault, software fault, and coupling fault), the availability of a monitor station is modeled by PN. (2) The state probability of monitoring network is confirmed by considering the core monitor station as common cause. (3) Considering URE under different outage of monitor stations, the dependability of orbit determination mission is analyzed by BN. (4) The improved schemes are put forward by fault diagnose. The organization of modeling and analysis is shown in Fig. 1.

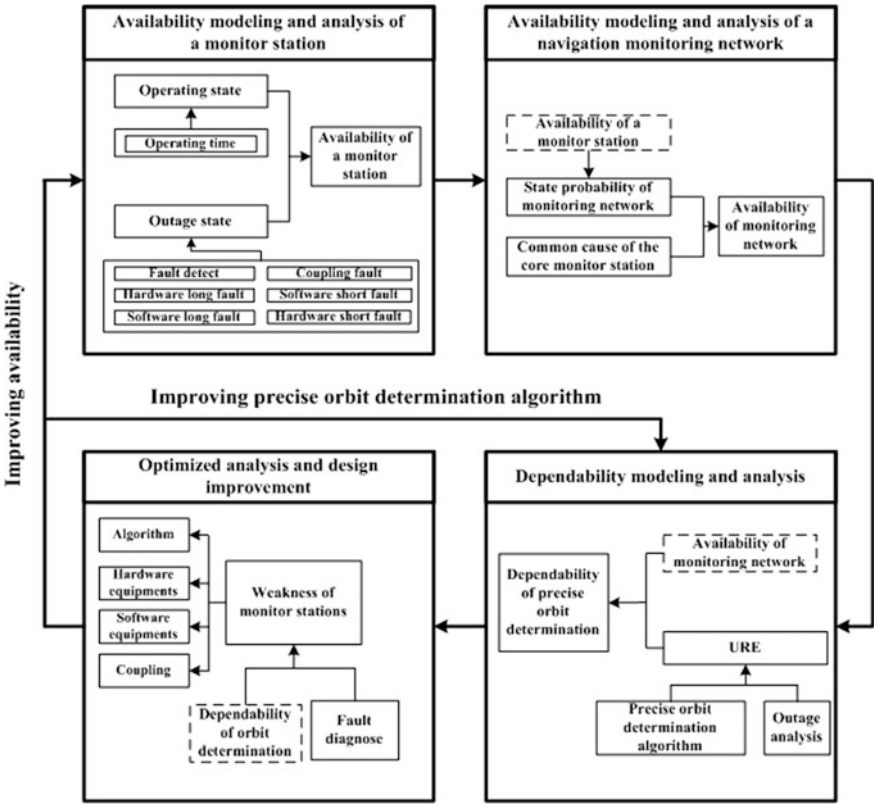

Fig. 1 The flow chart of modeling and analysis for dependability of precise orbit determination

3 Dependability Modeling and Optimizing of Precise Orbit Determination

3.1 Availability Modeling and Analysis of a Monitor Station

The state of a monitor station can be divided into operation and outage. The operation state is mean time between faults, the outage state include fault detect time, hardware short fault, hardware long fault, software short fault, software long fault, and coupling fault. The state parameters of a monitor station are shown as Table 1.

(1) Hardware and software availability of a monitor station

The hardware and software availability of a monitor station based on PN is shown in Figs. 2 and 3.

In Fig. 2, P_{H} is operational state of hardware. $\mathrm{MTBF_H} = 1/\lambda_{\mathrm{MTBF_H}}$ is mean time between faults of hardware. P_{SOLH} is select state about hardware long or short fault.

Table 1 Parameters of a monitor station

State	Parameters
Operation	Mean time between faults (MTBF)
Fault detect	Fault detect time (FD)
Fault detect	Fault probability of hardware (f_H)
Fault detect	Fault probability of software (f_S)
Hardware short fault	Hardware short fault probability (f_{SH})
Hardware short fault	Mean time to repair of hardware short fault ($MTTR_{SH}$)
Hardware long fault	Hardware long fault probability (f_{LH})
Hardware long fault	Mean administrative delay time ($MADT_{LH}$)
Hardware long fault	Probability of spares sufficiency (f_{SPH})
Hardware long fault	Mean supply response time (SRT_{LH})
Hardware long fault	Mean time to repair of hardware long fault ($MTTR_{LH}$)
Software short fault	Software short fault probability (f_{SS})
Software short fault	Restart fault probability of software (f_{RS})
Software short fault	Self repairing fault probability of software (f_{IS})
Software short fault	Mean time to restart ($MTTR_{SRS}$)
Software short fault	Mean time to self repairing ($MTTR_{SIS}$)
Software long fault	Software long fault probability (f_{LS})
Software long fault	Mean time to repair of software long fault ($MTTR_{LS}$)
Coupling fault	Coupling fault probability (f_{STH})
Coupling fault	Time of coupling fault (T_{STH})

f_{SH} and f_{LH} are hardware short and long fault probability, and $f_{SH} + f_{LH} = 1$. P_{SH} and P_{LH} are hardware short and long fault state. $MTTR_{SH} = 1/\mu_{MTTR_{SH}}$ and $MTTR_{LH} = 1/\mu_{MTTR_{LH}}$ are mean time of repair of hardware short fault and long fault. $MADT_{LH} == 1/\lambda_{MADT_{LH}}$ is mean administrative delay time. P_{SONH} is select state of spares. f_{SPH} is probability of spares sufficiency, and $f_{SPH} + f_{NSPH} = 1$. P_{SWH} is waiting state of spares. $MSRT_{LH} = 1/\lambda_{MSRT_{LT}}$ is mean supply response time. P_{RWH} is waiting state of repair.

In Fig. 3, P_S is operational state of software. $MTBF_S = 1/\lambda_{MTBF_S}$ is mean time between faults of software. P_{SOLS} is select state about short or long fault. f_{LS} and f_{SS} are software short and long fault probability, and $f_{LS} + f_{SS} = 1$. P_{LS} is software long fault state. $MTTR_{LS} = 1/\mu_{MTTR_{LS}}$ is mean time to repair of software long fault. P_{ROIS} is select state of software short fault. f_{RS} and f_{IS} are restart and self-repairing fault probability of software, and $f_{RS} + f_{IS} = 1$. P_{RS} and P_{IS} are restart and self-repairing state of software. $MTTR_{RS} = 1/\mu_{MTTR_{RS}}$ and $MTTR_{IS} = 1/\mu_{MTTR_{IS}}$ are mean time to restart and mean time to self-repairing.

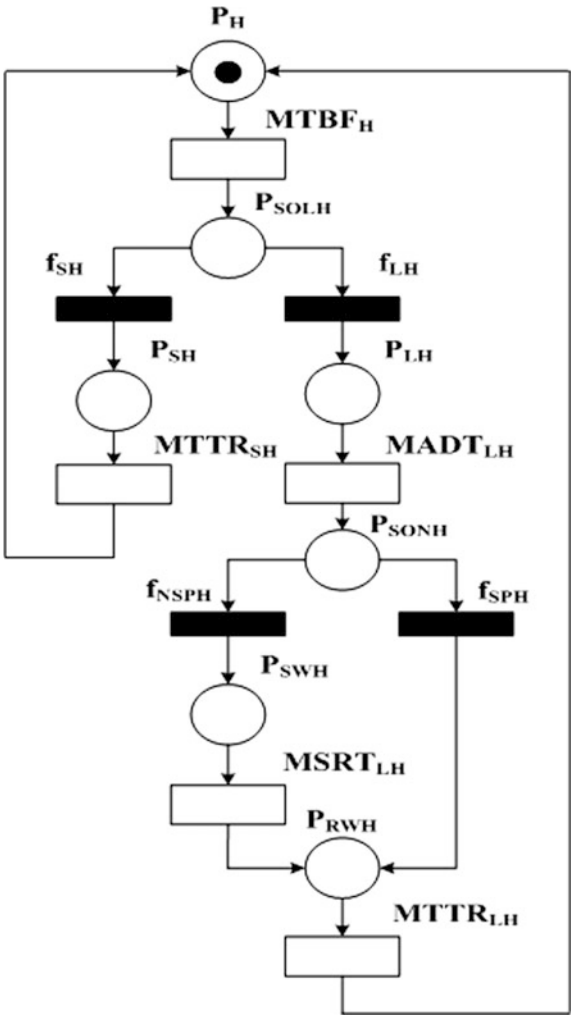

Fig. 2 Availability of monitor station hardware

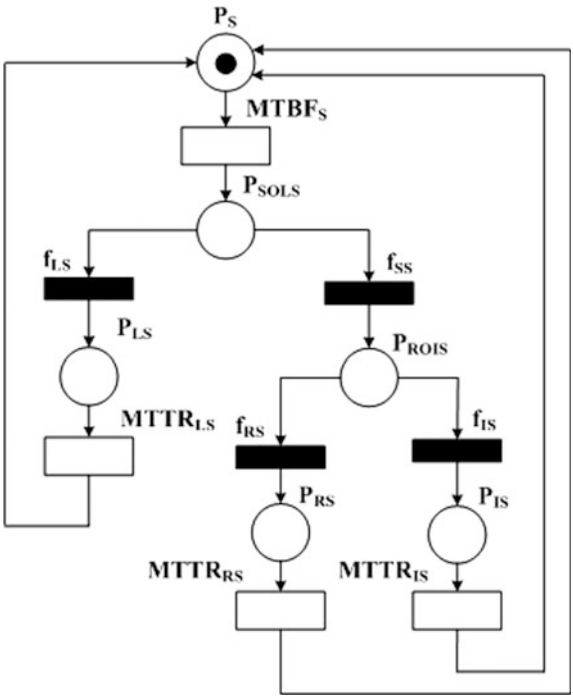

Fig. 3 Availability of monitor station software

The states transformation equation of hardware is

$$\begin{bmatrix} \dot{p}_{\mathrm{H}}(t) \\ \dot{p}_{\mathrm{SH}}(t) \\ \dot{p}_{\mathrm{LH}}(t) \\ \dot{p}_{\mathrm{SWH}}(t) \\ \dot{p}_{\mathrm{RWH}}(t) \end{bmatrix} = \begin{bmatrix} -\lambda_{\mathrm{MTBF_H}} & \mu_{\mathrm{MTTR_{SH}}} & 0 & 0 & \mu_{\mathrm{MTTR_{LH}}} \\ \lambda_{\mathrm{MTBF_H}} \cdot f_{\mathrm{SH}} & -\mu_{\mathrm{MTTR_{SH}}} & 0 & 0 & 0 \\ \lambda_{\mathrm{MTBF_H}} \cdot f_{\mathrm{LH}} & 0 & -\lambda_{\mathrm{MADT_{LH}}} & 0 & 0 \\ 0 & 0 & \lambda_{\mathrm{MADT_{LH}}} \cdot f_{\mathrm{NSPH}} & -\lambda_{\mathrm{MSRT_{LH}}} & 0 \\ 0 & 0 & \lambda_{\mathrm{MADT_{LH}}} \cdot f_{\mathrm{SPH}} & \lambda_{\mathrm{MSRT_{LH}}} & -\mu_{\mathrm{MTTR_{LH}}} \end{bmatrix} \cdot \begin{bmatrix} p_{\mathrm{H}}(t) \\ p_{\mathrm{SH}}(t) \\ p_{\mathrm{LH}}(t) \\ p_{\mathrm{SWH}}(t) \\ p_{\mathrm{RWH}}(t) \end{bmatrix} \tag{1}$$

$$P_{\mathrm{H}}(t) + P_{\mathrm{SH}}(t) + P_{\mathrm{LH}}(t) + P_{\mathrm{SWH}}(t) + P_{\mathrm{RWH}}(t) = 1 \tag{2}$$

and the steady availability of hardware is

$$p_{\mathrm{H}} = \frac{\mu_{\mathrm{MTTR_{SH}}} \cdot \lambda_{\mathrm{MADT_{LH}}} \cdot \lambda_{\mathrm{MSRT_{LH}}} \cdot \mu_{\mathrm{MTTR_{LH}}}}{A_{\mathrm{H}} + B_{\mathrm{H}} + C_{\mathrm{H}} + D_{\mathrm{H}} + E_{\mathrm{H}}} \tag{3}$$

where

$$\begin{aligned}
A_{\mathrm{H}} &= \mu_{\mathrm{MTTR_{SH}}} \cdot \lambda_{\mathrm{MADT_{LH}}} \cdot \lambda_{\mathrm{MSRT_{LH}}} \cdot \mu_{\mathrm{MTTR_{LH}}},\\
B_{\mathrm{H}} &= \lambda_{\mathrm{MTBF_H}} \cdot \lambda_{\mathrm{MADT_{LH}}} \cdot \lambda_{\mathrm{MSRT_{LH}}} \cdot \mu_{\mathrm{MTTR_{LH}}} \cdot f_{\mathrm{SH}},\\
C_{\mathrm{H}} &= \lambda_{\mathrm{MTBF_H}} \cdot \mu_{\mathrm{MTTR_{SH}}} \cdot \lambda_{\mathrm{MSRT_{LH}}} \cdot \mu_{\mathrm{MTTR_{LH}}} \cdot f_{\mathrm{LH}},\\
D_{\mathrm{H}} &= \lambda_{\mathrm{MTBF_H}} \cdot \mu_{\mathrm{MTTR_{SH}}} \cdot \lambda_{\mathrm{MADT_{LH}}} \cdot \mu_{\mathrm{MTTR_{LH}}} \cdot f_{\mathrm{LH}} \cdot f_{\mathrm{NSPH}},\\
E_{\mathrm{H}} &= \lambda_{\mathrm{MTBF_H}} \cdot \mu_{\mathrm{MTTR_{SH}}} \cdot \lambda_{\mathrm{MADT_{LH}}} \cdot \lambda_{\mathrm{MSRT_{LH}}}(1 - f_{\mathrm{SH}}).
\end{aligned}$$

The states transformation equation of software is

$$\begin{bmatrix} \dot{P}_{\mathrm{S}}(t) \\ \dot{P}_{\mathrm{LS}}(t) \\ \dot{P}_{\mathrm{RS}}(t) \\ \dot{P}_{\mathrm{IS}}(t) \end{bmatrix} = \begin{bmatrix} -\lambda_{\mathrm{MTBF_S}} & \mu_{\mathrm{MTTR_{LS}}} & \mu_{\mathrm{MTTR_{RS}}} & \mu_{\mathrm{MTTR_{IS}}} \\ \lambda_{\mathrm{MTBF_S}} \cdot f_{\mathrm{LS}} & -\mu_{\mathrm{MTTR_{LS}}} & 0 & 0 \\ \lambda_{\mathrm{MTBF_S}} \cdot f_{\mathrm{SS}} \cdot f_{\mathrm{RS}} & 0 & -\mu_{\mathrm{MTTR_{RS}}} & 0 \\ \lambda_{\mathrm{MTBF_S}} \cdot f_{\mathrm{SS}} \cdot f_{\mathrm{IS}} & 0 & 0 & -\mu_{\mathrm{MTTR_{IS}}} \end{bmatrix} \cdot \begin{bmatrix} P_{\mathrm{S}}(t) \\ P_{\mathrm{LS}}(t) \\ P_{\mathrm{RS}}(t) \\ P_{\mathrm{IS}}(t) \end{bmatrix} \tag{4}$$

$$P_{\mathrm{S}}(t) + P_{\mathrm{LS}}(t) + P_{\mathrm{RS}}(t) + P_{\mathrm{IS}}(t) = 1 \tag{5}$$

and the steady availability of software is

$$P_{\mathrm{S}} = \frac{\mu_{\mathrm{MTTR_{LS}}} \cdot \mu_{\mathrm{MTTR_{RS}}} \cdot \mu_{\mathrm{MTTR_{IS}}}}{A_{\mathrm{S}} + B_{\mathrm{S}} + C_{\mathrm{S}} + D_{\mathrm{S}}} \tag{6}$$

where

$$\begin{aligned}
A_{\mathrm{S}} &= \mu_{\mathrm{MTTR_{LS}}} \cdot \mu_{\mathrm{MTTR_{RS}}} \cdot \mu_{\mathrm{MTTR_{IS}}},\\
B_{\mathrm{S}} &= \lambda_{\mathrm{MTBF_S}} \cdot \mu_{\mathrm{MTTR_{RS}}} \cdot \mu_{\mathrm{MTTR_{IS}}} \cdot f_{\mathrm{LS}},\\
C_{\mathrm{S}} &= \lambda_{\mathrm{MTBF_S}} \cdot \mu_{\mathrm{MTTR_{LS}}} \cdot \mu_{\mathrm{MTTR_{IS}}} \cdot f_{\mathrm{SS}} \cdot f_{\mathrm{RS}},\\
D_{\mathrm{S}} &= \lambda_{\mathrm{MTBF_S}} \cdot \mu_{\mathrm{MTTR_{LS}}} \cdot \mu_{\mathrm{MTTR_{RS}}}(1 - f_{\mathrm{LS}} - f_{\mathrm{SS}} \cdot f_{\mathrm{RS}}).
\end{aligned}$$

(2) Coupling availability of a monitor station

Considering some situations, the probability of transform from software long fault to hardware fault is f_{STH}, and the time is T_{STH}, as shown in Fig. 4.

Where imaginary line is transform from software to hardware. Considering Figs. 2, 3 and 4, the availability of a monitor station can be modeled. Due to the complex process, Monte-Carlo is applied, and the availability is $A_{\mathrm{M}} = P_{\mathrm{M}}$.

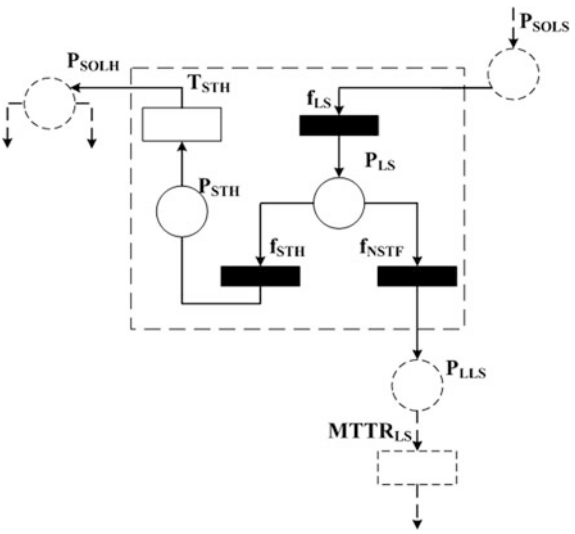

Fig. 4 Coupling model of hardware and software

3.2 State Probability of Monitoring Network

Considering the monitoring network (N) and n numbers monitor stations, there are $n+1$ status, set $S_k\,(k = 0, 1, 2, \ldots, n)$ is state of monitoring network, and S_0 is operation state of a monitor station, S_1 is outage state of a monitor station, and so on. The probability value P_k, which states probability of outage of k monitor stations, represents the state of S_k, thus $\sum P_k = 1$, so P_k is

$$P_k = \sum_{l=1}^{C_n^k} P_{k,l} = \sum_{l=1}^{C_n^k} \left(\prod_{m=1}^{n-k} P_{Ml,m} \right) \left(\prod_{i=n-k+1}^{n} (1 - P_{Ml,i}) \right) \tag{7}$$

where C_n^k is combination of k (outage) in n monitor stations, $P_{k,l}(t)$ is the state probability of the lth combination under outage of k monitor stations, $P_{Ml,m}$ is steady availability of $n-k$ monitor stations of the lth combination, and $(1 - P_{Ml,i})$ is steady nonavailability.

Considering common cause of the core monitor station, it cannot be considered when computing state probability of monitoring network.

3.3 Modeling and Analysis of Precise Orbit Determination

3.3.1 Orbit Determination Algorithm

The kinetic equation is

$$\begin{cases} \dot{X} = F(X,t) \\ X(t_0) = X_0 \end{cases}, \tag{8}$$

where X is state vector including 3D location, 3D velocity, parameters of kinetic model, and geometrical parameters beyond kinetic equation. The partial derivative $\dot{X}$ is function of X at t, represents as $F(X,t) \cdot X(t_0)$ is state of satellite at t, represents as X_0.

The observation equation is

$$Y_i = G(X_i, t_i) + \varepsilon_i \tag{9}$$

where: Y_i is the ith observation value, $G(X_i, t_i)$ is state function at t_i, and ε_i is observation noise.

Taking linearization of (8) and (9), and comparing standard orbit, the error of radial direction (dR), tangential direction (dT) and normal direction (dN) about MEO, GEO, IGSO can be given

$$\begin{cases} \mathrm{URE_{MEO}} = \sqrt{(0.9989\,\mathrm{d}R)^2 + (0.2997\,\mathrm{d}T)^2 + (0.3018\,\mathrm{d}N)^2} \\ \mathrm{URE_{GEO}} = \sqrt{(1.013\,\mathrm{d}R)^2 + (0.2895\,\mathrm{d}T)^2 + (0.3041\,\mathrm{d}N)^2} \\ \mathrm{URE_{IGSO}} = \sqrt{(0.584\,\mathrm{d}R)^2 + (0.3878\,\mathrm{d}T)^2 + (0.3059\,\mathrm{d}N)^2} \end{cases} \tag{10}$$

Consider URE under different outage combinations of $n-1$ monitor stations. Due to practical reality actual, all the monitor stations are operational, any one monitor station is outage, and any two stations are outage considered.

3.3.2 Normalization of URE

Normalizing URE, as

$$\begin{aligned} C_{\mathrm{URE}}(t) &= P(\delta_{\mathrm{in}} > \sigma_{\mathrm{st}}) = 1 - P(\delta_{\mathrm{in}} < \sigma_{\mathrm{st}}) \\ &= 1 - \int_0^{\infty} \left[\int_0^{\infty} g(\delta_{\mathrm{in}})\,\mathrm{d}\delta_{\mathrm{in}} \right] f(\sigma_{\mathrm{st}})\,\mathrm{d}\sigma_{\mathrm{st}} \end{aligned} \tag{11}$$

where C_{URE} is normalization, $f(\sigma_{\mathrm{st}})$ is actual URE, σ_{st} is stress. $g(\delta_{\mathrm{in}})$ is required URE, δ_{in} is strength.

3.3.3 Modeling and Prediction of Precise Orbit Determination

Modeling and prediction of precise orbit determination by BN. The qualitative part of BN can be representing as topological structure, which describes relationship of variables. The quantitative part of BN can be representing as CPT, which describes conditional probability under state of father nodes and variable. The root nodes are the nodes without father nodes, and their value is prior probability. The rule of BN can be describes as [8, 9]

$$P[X_1, X_2, \ldots, X_n] = \prod_{i=1}^{n} p[X_i | \text{Parent}(X_i)] \tag{12}$$

where $[X_1, X_2, \ldots, X_n]$ is BN, $P[X_1, X_2, \ldots, X_n]$ is joint probability distribution, Parent (X_i) is father nodes set. The dependability model of precise orbit determination is shown in Fig. 5:

where the inputs of root nodes $M_1, \ldots, M_n$ are availability and nonavailability, the input of center node dependability is normalization of URE. The output of center node is P_D

$$\begin{aligned} P_D &= P(P_D = 1) = \sum_{P_{M_i}} P(P_{M_1}, P_{M_2}, \ldots, P_{M_n}, P_D) \\ &= \sum_{P_{M_i}} P(P_D = 1 | P_{M_1}, P_{M_2}, \ldots, P_{M_n}) P(P_{M_1}) \ldots P(P_{M_n}). \end{aligned} \tag{13}$$

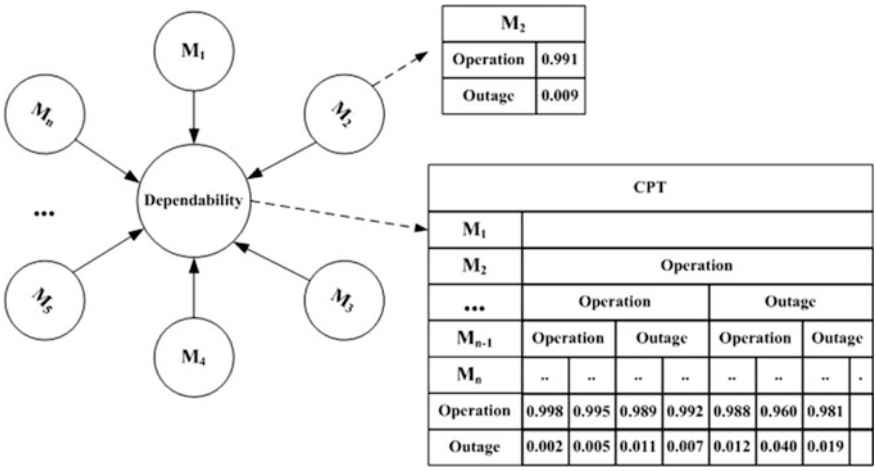

Fig. 5 Dependability model of precise orbit determination based on BN

3.4 Optimization and Design Improvement

Taking fault diagnose of orbit determination by BN. By setting parameters, the probability importance (Pi) and structure importance (Si) can be given. The availability of monitor stations can be reflected by probability importance, and the distribution of monitor stations can be reflected by structure importance. Furthermore, compositive importance can be given by probability importance and structure importance. Supposing there is a fault of dependability, then the state probability of monitor stations can be given, where 1 represents success, and 0 represent fault. The fault state probability of M_i is

$$P(M_i = 0|P_D = 0) = \frac{P(M_i = 0)P(P_D = 0|M_i = 0)}{P(P_D = 0)} \tag{14}$$

where $i = 1, 2, \ldots, n$.

4 Case Study

Supposing a regional monitoring network and a MEO satellite. Considering seven monitor stations $(M_i,\ i = 1, 2, \ldots 7)$ distribute among China area, where M_1 is a core monitor station, shown in Fig. 6.

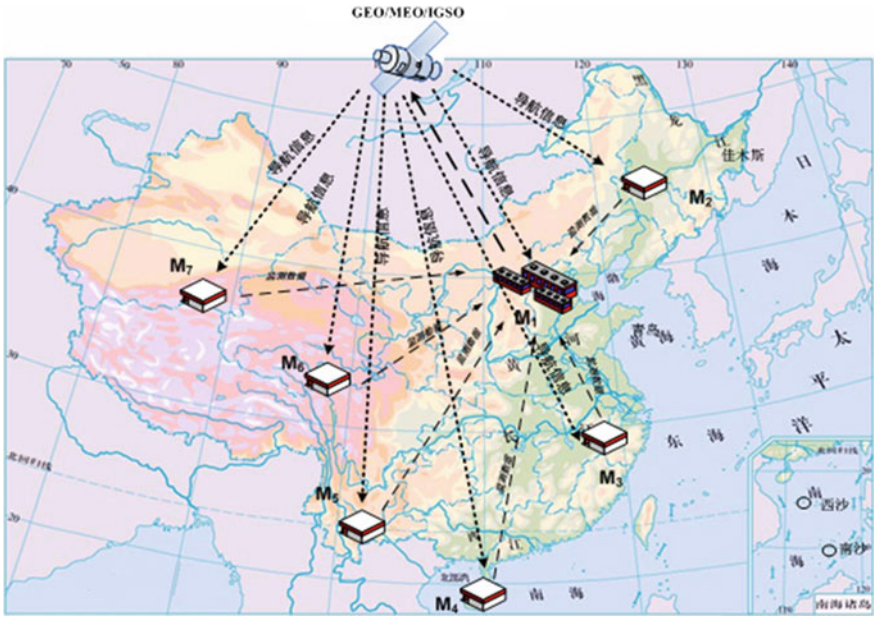

Fig. 6 The distribution of monitor stations

(1) **The availability of a monitor station**

According operational data of monitor stations, the parameters of M_1 can be shown as Table 2.

Then, the hardware and software steady availability of M_1 are $P_{M_1\mathrm{H}} = 0.9989$, $P_{M_1\mathrm{S}} = 0.997$, $P_{M_1} = 0.9979$. Similarly, the steady availability of $M_2 \sim M_7$ can be calculated as Table 3.

(2) **The state probability of monitoring network**

Considering all the monitor stations are operational, any one monitor station is outage, any two monitor stations are outage, thus there are 29 situations, as shown in Table 4.

Considering the common cause of core monitor station, calculate different probability $P_{\mathrm{Ng}} = 0.97978$, $P_{\mathrm{No}} = 0.01799$.

Table 2 Value of M_1

Parameter	Value	Parameter	Value
MTBF[a]	5000 h	$\mathrm{MTTR_{LH}}$	1 h
FD	0.5 h	f_{SS}	0.7
f_{H}	0.3	f_{RS}	0.5
f_{S}	0.7	f_{IS}	0.5
f_{SH}	0.8	$\mathrm{MTTR_{SRS}}$	0.05 h
$\mathrm{MTTR_{SH}}$	1 h	$\mathrm{MTTR_{SIS}}$	0.05 h
f_{LH}	0.2	f_{LS}	0.3
$\mathrm{MADT_{LH}}$	1.5 h	$\mathrm{MTTR_{LS}}$	50
f_{SPH}	0.8	f_{STH}	0.1
$\mathrm{MSRT_{LH}}$	100 h	T_{STH}	3 h

[a]The MTBF of hardware and software is 5000 h

Table 3 Steady availability of monitor stations

No.	Availability
M_1	0.9979
M_2	0.9969
M_3	0.9971
M_4	0.9967
M_5	0.9973
M_6	0.9972
M_7	0.9965

Table 4 Simulation condition of monitor stations

No.	State	Number
1	7 monitor stations are operation	1
2	Any one monitor station is outage	7
3	Any two monitor station are outage	21

Table 5 Normalization of URE

No.	M_1	M_2	M_3	M_4	M_5	M_6	M_7	URE (m)	C_{URE}
1	1[a]	1	1	1	1	1	1	0.391	0.997
2	1	0	1	1	1	1	1	0.422	0.714
3	1	1	0	1	1	1	1	0.395	0.993
4	1	1	1	0	1	1	1	0.421	0.738
5	1	1	1	1	0	1	1	0.397	0.990
6	1	1	1	1	1	0	1	0.399	0.986
7	1	1	1	1	1	1	0	0.423	0.690

[a]0 and 1 represent outage and operation of monitor stations

(3) **Modeling and prediction of precise orbit determination**

Simulation URE of MEO under different outage of monitor stations, set requirement value as strength, and normalizing as Table 5.

Considering the common cause of M_1, the dependability of precise orbit determination based on BN can be given

$$\begin{aligned} P_D = P(P_D = 1) &= \sum_{P_{M_i}} P(P_{M_1}, P_{M_2}, \ldots, P_{M_7}, P_D) \\ &= \sum_{P_{M_i}} P(P_D = 1 | P_{M_1}, P_{M_2}, \ldots, P_{M_7}) P(P_{M_1}) \ldots P(P_{M_7}) \\ &= 0.9920 \end{aligned}$$

(4) **Optimization and design improvement**

Taking fault diagnose as following: probability importance, structure importance, compositive importance.

(a) Probability importance

Considering the influence between dependability and the state of monitor stations, then the probability importance can be given as Fig. 7.

According to Fig. 7 the probability importance of monitor stations is $P_i(M_1) > P_i(M_7) > P_i(M_2) > P_i(M_4) > P_i(M_6) > P_i(M_5) > P_i(M_3)$.

(b) Structure importance

Set the same availability of all monitor stations, and considering the influence between dependability and the state of monitor stations, then the structure importance can be given as Fig. 8.

According to Fig. 8 the structure importance of monitor stations is $P_i(M_1) > P_i(M_7) > P_i(M_2) > P_i(M_4) > P_i(M_6) > P_i(M_5) > P_i(M_3)$. Because of the common cause, M_1 is the most important of structure importance. M_7, M_2 and M_4 are more important than other monitor stations due to distribution.

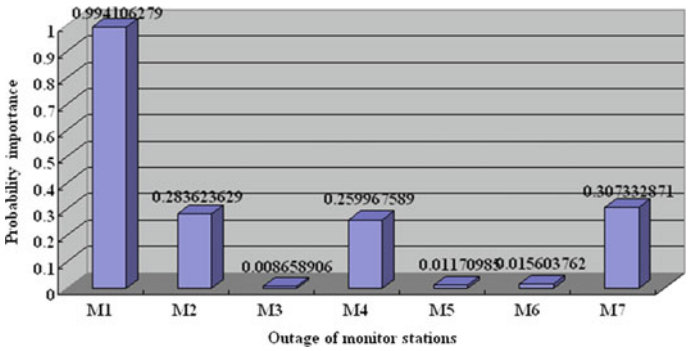

Fig. 7 Probability importance of outage monitor stations

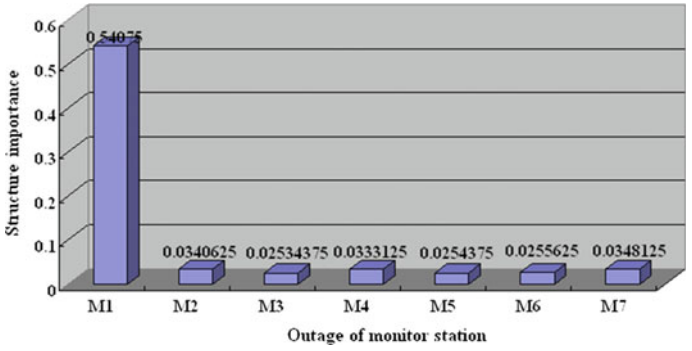

Fig. 8 Structure importance of outage monitor stations

(c) Compositive importance

The compositive importance can be given as Fig. 9.

According to Fig. 9, the compositive importance is same as structure importance, and it is different from the availability rank of monitor stations. Since the availability of monitor stations are almost same, thus distribution plays a more important role than the value of availability.

Taking design improvement, considering the following situations:

(1) Scheme 1: Improving the availability of M_7 by optimizing MTBF and MTTR, making $P_{M_7} = P_{M_1}$.
(2) Scheme 2: Optimizing relationship of monitor stations, set M_6 as a spare core monitor station.

Recalculating the dependability as Table 6.

According to Table 6, optimizing relationship of monitor stations plays a more important role than availability of a monitor.

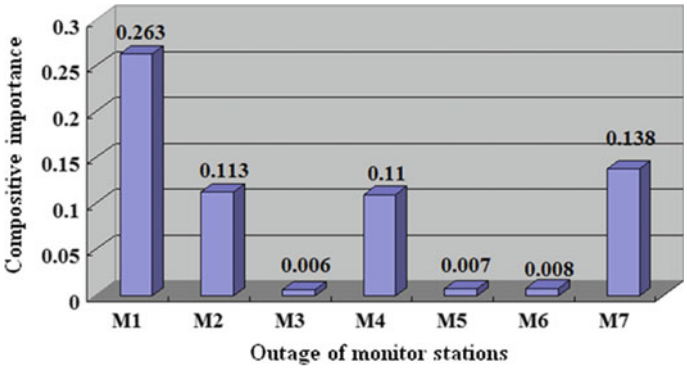

Fig. 9 Compositive importance of outage monitor stations

Table 6 Schemes comparison of dependability

Scheme	Dependability	Percent (%)
Original scheme	0.9920	–
Scheme 1	0.9924	0.04
Scheme 2	0.9941	0.21

5 Conclusions

The dependability of precise orbit determination is modeled and analyzed by PN and BN as follows:

(1) Dependability quantitative analysis. Considering the operation time, fault detect time, hardware fault (long and short), software fault (long and short), coupling fault of hardware and software, and other probability, the availability of a monitor station is analyzed by PN. Considering URE, common cause of a core monitor station, and transform performance to reliability, the dependability of precise orbit determination is analyzed by BN, and the value is 0.9920.

(2) Recognising the weakness by fault diagnose. The probability importance, structure importance, and compositive importance can be given by BN, and it is shown that distribution plays a more important role than the value of availability in regional area system.

(3) Optimization and design improvement. Two schemes (Scheme 1: improving the availability of M_7, Scheme 2: set M_6 as a spare of M_1) are proposed for optimization. The results shown, by comparing the Scheme 1, Scheme 2 plays a more major role.

References

1. Chuang S, Mon L, Yidong L et al (2008) Near realtime orbit determination of navigation satellite using regional tracking network. Geomat Inform Sci Wuhan Univ 33(7):697–700
2. Qile Z, Tao G, Junyi L et al (2009) Regional orbit determination of navigation satellite based on priori orbit constraint information. J Geodesy Geodyn 28(5):81–84
3. Jianwen I, Liucheng C (2009) Single navigation satellite orbit determination and evaluation by SLR. Geomat Inform Sci Wuhan Univ 34(11):1276–1279
4. Shanshi Z, Xiaogong H, Bin W et al (2010) Analysis of precise orbit determination and prediction accuracy based on regional tracking network. Sci China Phys Mech Astron 40:800
5. Tao G, Qile Z, Jingnan L et al (2010) Regional orbit determination of navigation satellite based on global priori information. Geomat Inform Sci Wuhan Univ 35(4):491–494
6. Longpeng Z, Yamin D, Changhui X et al (2015) Research on the influence of monitoring stations distribution on precise orbit determination of BeiDou constellation. Sci Survey Mapp 40(12):68–72
7. Yidong L, Xiuguang Y, Yang L et al (2016) Impact of ambiguity resolution and arc length on regional precise orbit determination. Geomat Inform Sci Wuhan Univ 41(2):249–254
8. Jesen FV (2001) Bayesian networks and decision graphs. Springer, New York, p 18–28
9. Van der Gaag LC (1996) Bayesian belief networks: odds and ends. Comput J 97–113

Combined Precise Orbit Determination for High-, Medium-, and Low-Orbit Navigation Satellites

Haibo Ge, Bofeng Li, Maorong Ge, Yunzhong Shen, Liangwei Nie and Harald Schuh

Abstract The bottleneck of Precise Point Positioning (PPP) is the long convergence time for achieving the centimeter accuracy. Some researchers put forward to improve the diversity of available satellites' geometric distribution and reduce the correlation of observation data by deploying the Low Earth Orbit (LEO) constellations in addition to the medium and high-orbit satellites. The prerequisite is to get the precise orbit products of all these orbiting satellites. This paper studies the combined precise orbit determination for high-, medium-, and low-orbit navigation satellite systems. In order to investigate the theory and algorithms of the high–medium–low POD and to study the effect of LEO to the POD of high-orbit satellites and the influence of ground data from LEO to its own POD, we simulate all the data, including high orbit to low orbit, medium orbit to low orbit, high orbit to ground stations, medium orbit to ground stations, and low orbit to ground stations. The results show that the combined POD can improve the precision of high-orbit satellites significantly, especially for the along-track component, which can reach to sub-decimeter even centimeter level. Also, the precision of LEO POD can be improved with the data from ground stations.

Keywords High, medium, and low orbit · Navigation satellite · Combined precise orbit determination · Geometric distribution

H. Ge · B. Li (✉) · Y. Shen · L. Nie
College of Surveying and Geo-Informatics, Tongji University,
Shanghai 200092, China
e-mail: bofeng_li@tongji.edu.cn

H. Ge
e-mail: haibo_Ge@163.com

H. Ge · M. Ge · H. Schuh
Department of Geodesy, GeoForschungsZentrum (GFZ), 14473 Potsdam, Germany

J. Sun et al. (eds.), *China Satellite Navigation Conference (CSNC) 2017 Proceedings: Volume III*, Lecture Notes in Electrical Engineering 439,
DOI 10.1007/978-981-10-4594-3_15

1 Introduction

Nowadays, besides USA GPS and Russian GLONASS, the European Galileo and Chinese BeiDou are developing rapidly. The Galileo constellation will consist of 30 satellites in three orbital planes [10]. By the end of 2020, BeiDou system will be completed for global service, consisting of 5 Geostationary Earth Orbit (GEO) satellites, 27 Medium Earth Orbit (MEO) satellites, and 3 Inclined Geosynchronous Satellite Orbit (IGSO) satellites [4]. At that time, there will be over 100 satellites providing Positioning, Navigation, and Timing (PNT) service. Since the slow variation of GNSS satellites' geometry with respect to a ground station, it takes nearly several minutes or even hours to achieve centimeter accuracy of PPP. Due to the poor geometry, there are some challenges for the POD of different constellations of GNSS satellites. Taking BDS IGSO and GEO satellites for example, they operate in higher orbits than MEO satellites and their geometric variations are less sensitive to the ground stations, especially for GEO satellites because of its geostationary characteristic, which leads to the great challenge for GEO POD. In recent years, some commercial companies, such as SpaceX and OneWeb, put forward a new idea to build global LEO constellations to deliver the Internet to the whole world by providing truly global and robust broadband coverage [13]. The largest constellation today is Iridium consisting of 66 LEO satellites [9]. The sheer number of satellites, along with the global coverage, gives rise to the opportunities not only for the broadband but also as a platform for providing navigation services. Some researchers make a thorough investigation on this topic. The results showed that the LEO constellations can provide better geometry and stronger signals compared to the GNSS constellations [8, 12]. LEO satellites have much faster motion in the space, passing overhead over minutes instead of hours in MEO. This gives rise to more multi-path mitigation, as reflections are no longer static over short averaging times. Meanwhile, initial PPP convergence time can be shortened [8].

The precise orbit and clock products are the prerequisites of all the precise PNT service. It brings huge challenges for POD with tens to hundreds of satellites with different orbits. The present GNSS orbits are determined by the observation data from well-distributed global-tracking network, while the LEO orbits are determined by the onboard GNSS observations [2]. However, as the fast-moving platform, the onboard observations can also be acted as the important data source of the GNSS POD [7, 17], especially for the GEO and IGSO satellites, which can provide the better geometry to improve the precision of GEO orbits [18]. When the LEO satellites are able to transmit GNSS signals to the ground stations, not only the onboard GNSS observations but also the ground-tracking observations can be used for its POD. So it is of great interest to investigate the effect of this information on the LEO POD.

Above all, the multi-source data brings the challenge for POD. All relevant observations will be simulated, including GEO/IGSO to LEO, MEO to LEO, GEO/IGSO to ground, MEO to ground, and LEO to ground. Using the simulated

data, we will investigate the methods of combined POD of high-medium-low earth orbit satellites, analyzing the effects of LEO satellites on the high-orbiting satellite POD. In addition, by using the data from the LEO satellites to ground-tracking stations, the POD improvements of LEO and GNSS satellites are investigated.

2 Data Simulation

Since there is no public onboard BDS data and no LEO satellites sending navigation signals to the ground, we simulate all the data. We first simulate the GPS constellation [14] and current BDS constellation [4] shown in Figs. 1 and 2. The Iridium system constellation [16] is used as LEO constellation shown in Fig. 2. Meanwhile, 76 well-distributed global-tracking stations which can track GNSS and LEO signals are selected, shown in Fig. 3.

With the constellations and stations mentioned above, all the observations can be simulated according to

$$\begin{aligned} P^s_{r,i,j} &= \rho^s_{r,i} + c(\mathrm{d}t_{r,i} - \mathrm{d}t^s_i) + \iota^s_{r,i,j} + \tau^s_{r,i} + \delta_{\mathrm{PCO},r,j} + \gamma^s_{\mathrm{PCO},j} + \varepsilon^s_{P,r,i,j} \\ \Phi^s_{r,i,j} &= \rho^s_{r,i} + c(\mathrm{d}t_{r,i} - \mathrm{d}t^s_i) - \iota^s_{r,i,j} + \tau^s_{r,i} + \delta_{\mathrm{PCO},r,j} + \gamma^s_{\mathrm{PCO},j} + \lambda_j N^s_{r,i,j} + \varepsilon^s_{\Phi,r,i,j} \end{aligned} \tag{1}$$

where the subscripts i and j denote epoch and frequency, respectively. The subscripts r and s denote receiver and satellite indices, respectively. $P^s_{r,i,j}$ and $\Phi^s_{r,i,j}$ are code and phase range which need to be simulated. $\rho^s_{r,i}$ denotes the satellite-to-receiver distance. $\mathrm{d}t_{r,i}$ and $\mathrm{d}t^s_i$ denote receiver and satellite clock. $\iota^s_{r,i,j}$ and $\tau^s_{r,i}$ denote ionospheric and tropospheric delay. $\delta_{\mathrm{PCO},r,j}$ and $\gamma^s_{\mathrm{PCO},j}$ are the Phase Centre Offset (PCO) of receiver

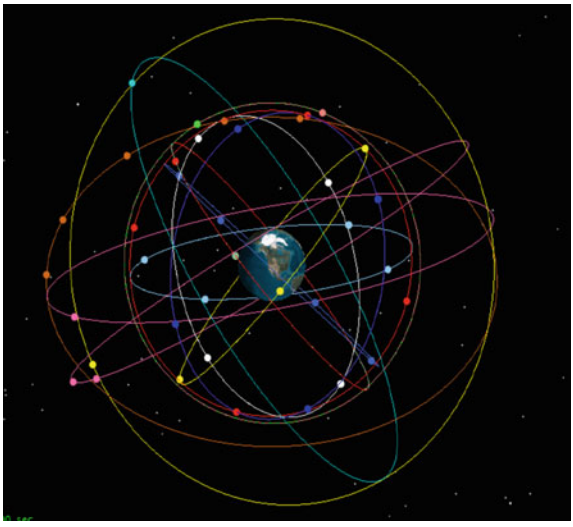

Fig. 1 GPS and BDS constellations

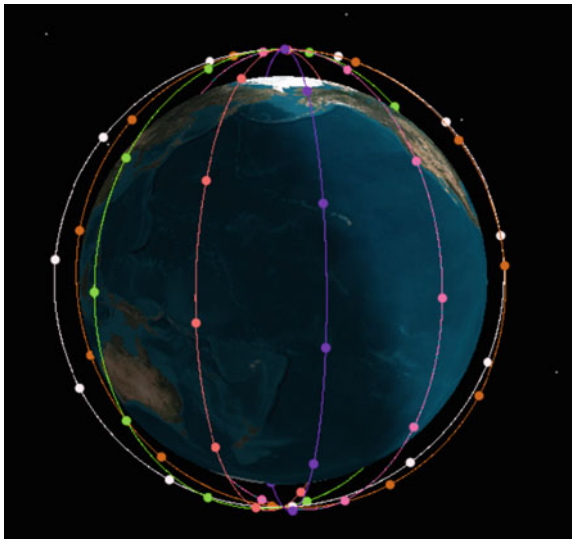

Fig. 2 LEO constellation

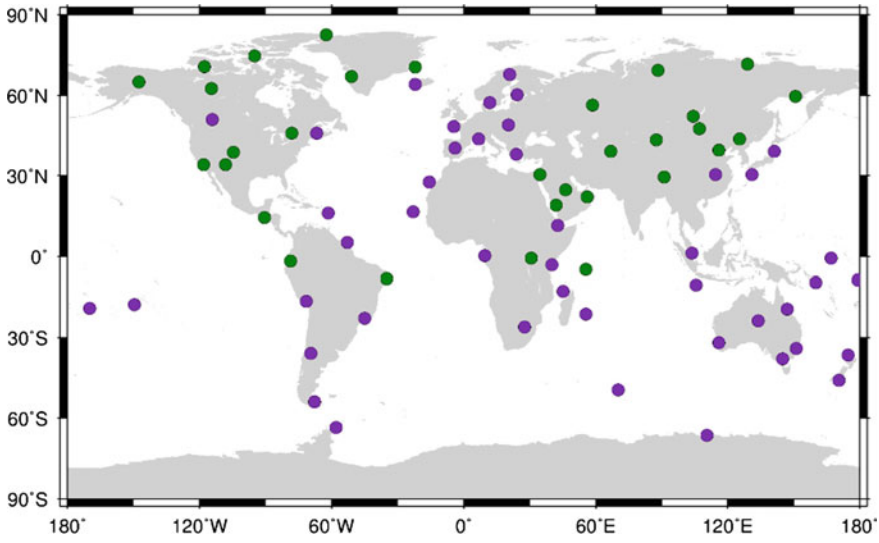

Fig. 3 Ground BDS/GPS/LEO (*purple*) and GPS/LEO (*green*) tracking stations (Color online)

and satellite. The term λ_j denotes wavelength and $N^s_{r,i,j}$ means integer ambiguity. The term $\varepsilon^s_{P,r,i,j}$ and $\varepsilon^s_{\Phi,r,i,j}$ denote the code and phase observation errors, respectively.

In summary, the parameter configurations are shown in Table 1 for simulations. As the altitude of LEO satellites is much higher than that of the troposphere layer, we do not simulate the tropospheric delay of onboard observations. For another,

Table 1 Parameter configuration for simulated data

	Ground network	Onboard LEO stations
Sampling rate	30 s	30 s
Cutoff elevation	1°	1°
Tropospheric delay	SAAS/GMF	No
Ionospheric delay	No	No
Phase wind up	Yes	Yes
Precision of code	1.0 m	1.0 m
Precision of phase	5 mm	5 mm

since we use the ionosphere-free combination and the second and third ionospheric delays are too small to consider in the POD process, the ionospheric delay do not consider in the simulation, either. In addition, according to the orbit height of Iridium, approximately 781 km, we set the angular range of Iridium from boresight 65°, while the angular range of GPS [14] is 14.3° and BDS GEO 10°, IGSO 10°, and MEO 15°, respectively [4].

3 Mathematic Model and Schemes of Combined POD of High-Medium-Low Navigation Satellites

3.1 Mathematic Model

The initial reference orbit and the state transition matrix can be obtained by integrating the GNSS and LEO motion and variation equations, which satisfy with the following equations

$$\begin{cases} \boldsymbol{X}_{G_i}^* = \boldsymbol{\Psi}_G(\boldsymbol{X}_{t_i}\, \boldsymbol{X}_{t_0})\boldsymbol{X}_{G_0}^* \\ \boldsymbol{X}_{L_i}^* = \boldsymbol{\Psi}_L(\boldsymbol{X}_{t_i}\, \boldsymbol{X}_{t_0})\boldsymbol{X}_{L_0}^* \end{cases}, \tag{2}$$

where $\boldsymbol{X}_{G_i}^*$ and $\boldsymbol{X}_{L_i}^*$ denote the correction state vectors of GNSS and LEO at time t_i; $\boldsymbol{\Psi}_G(\boldsymbol{X}_{t_i}\, \boldsymbol{X}_{t_0})$ and $\boldsymbol{\Psi}_L(\boldsymbol{X}_{t_i}\, \boldsymbol{X}_{t_0})$ denote the state transition matrices of GNSS and LEO, respectively. $\boldsymbol{X}_{G_0}^*$ and $\boldsymbol{X}_{L_0}^*$ are the state corrections of GNSS and LEO at initial epoch.

The observation equations for ground-tracking station and LEO satellites are as follows:

$$\boldsymbol{Y}_{G_i} = \boldsymbol{G}(\boldsymbol{X}_{G_i}, \boldsymbol{X}_{o_i}, t_i) + \boldsymbol{\varepsilon}_{G_i} \tag{3}$$

$$\boldsymbol{Y}_{\mathrm{LG}_i} = \boldsymbol{L}_{\boldsymbol{G}}(\boldsymbol{X}_{L_i}, \boldsymbol{X}_{n_i}, t_i) + \boldsymbol{\varepsilon}_{\mathrm{LG}_i} \tag{4}$$

$$\boldsymbol{Y}_{L_i} = \boldsymbol{L}(\boldsymbol{X}_{G_i}, \boldsymbol{X}_{L_i}, \boldsymbol{X}_{O_i}, t_i) + \boldsymbol{\varepsilon}_{L_i} \tag{5}$$

where $\boldsymbol{Y}_{G_i}, \boldsymbol{Y}_{\mathrm{LG}_i}$, and $\boldsymbol{Y}_{L_i}$ are the ground station of GNSS, the ground station of LEO, and onboard GNSS observations, respectively. $\boldsymbol{X}_{o_i}, \boldsymbol{X}_{n_i}$, and $\boldsymbol{X}_{O_i}$ are the parameters except $\boldsymbol{X}_{G_i}$ and $\boldsymbol{X}_{L_i}$ at t_i, such as clock error, ambiguity and so on. $\boldsymbol{\varepsilon}_{G_i}, \boldsymbol{\varepsilon}_{LG_i}$, and $\boldsymbol{\varepsilon}_{L_i}$ are observations errors for these three types observations. Then the observation equations are linearized at the reference orbit

$$\begin{cases} \boldsymbol{V}_{G_i} = \frac{\partial \boldsymbol{G}}{\partial \boldsymbol{X}_{G_i}} \boldsymbol{X}^*_{G_i} + \frac{\partial \boldsymbol{G}}{\partial \boldsymbol{X}_{o_i}} \boldsymbol{X}^*_{o_i} - \mathrm{omc}_{G_i} \\ \boldsymbol{V}_{LG_i} = \frac{\partial \boldsymbol{L_G}}{\partial \boldsymbol{X}_{L_i}} \boldsymbol{X}^*_{L_i} + \frac{\partial \boldsymbol{L_G}}{\partial \boldsymbol{X}_{n_i}} \boldsymbol{X}^*_{n_i} - \mathrm{omc}_{\mathrm{LG}_i} \\ \boldsymbol{V}_{L_i} = \frac{\partial \boldsymbol{L}}{\partial \boldsymbol{X}_{G_i}} \boldsymbol{X}^*_{G_i} + \frac{\partial \boldsymbol{L}}{\partial \boldsymbol{X}_{L_i}} \boldsymbol{X}^*_{L_i} + \frac{\partial \boldsymbol{L}}{\partial \boldsymbol{X}_{O_i}} \boldsymbol{X}^*_{O_i} - \mathrm{omc}_{L_i} \end{cases}, \tag{6}$$

where $\boldsymbol{X}^*_{o_i}$, $\boldsymbol{X}^*_{n_i}$, and $\boldsymbol{X}^*_{O_i}$ are the corrections for the parameters, omc denotes observation minus computed. With (2) and (6), Eq. 7 can be obtained, which is the error equations of combined POD with LEO observation data from ground-tracking stations.

$$\begin{cases} \boldsymbol{V}_{G_i} = \frac{\partial \boldsymbol{G}}{\partial \boldsymbol{X}_{G_i}} \boldsymbol{\Psi}_G(\boldsymbol{X}_{t_i}\, \boldsymbol{X}_{t_0}) \boldsymbol{X}^*_{G0} + \frac{\partial \boldsymbol{G}}{\partial \boldsymbol{X}_{o_i}} \boldsymbol{X}^*_{o_i} - \mathrm{omc}_{G_i} \\ \boldsymbol{V}_{\mathrm{LG}_i} = \frac{\partial \boldsymbol{L_G}}{\partial \boldsymbol{X}_{L_i}} \boldsymbol{\Psi}_L(\boldsymbol{X}_{t_i}\, \boldsymbol{X}_{t_0}) \boldsymbol{X}^*_{L0} + \frac{\partial \boldsymbol{L_G}}{\partial \boldsymbol{X}_{n_i}} \boldsymbol{X}^*_{n_i} - \mathrm{omc}_{\mathrm{LG}_i} \\ \boldsymbol{V}_{L_i} = \frac{\partial \boldsymbol{L}}{\partial \boldsymbol{X}_{G_i}} \boldsymbol{\Psi}_G(\boldsymbol{X}_{t_i}\, \boldsymbol{X}_{t_0}) \boldsymbol{X}^*_{G0} + \frac{\partial \boldsymbol{L}}{\partial \boldsymbol{X}_{L_i}} \boldsymbol{\Psi}_L(\boldsymbol{X}_{t_i}\, \boldsymbol{X}_{t_0}) \boldsymbol{X}^*_{L0} + \frac{\partial \boldsymbol{L}}{\partial \boldsymbol{X}_{O_i}} \boldsymbol{X}^*_{O_i} - \mathrm{omc}_{L_i} \end{cases} \tag{7}$$

In this paper, the un-differenced ionospheric-free model is used to estimate parameters with the least square principle.

3.2 The Schemes of POD

In this paper, dynamic orbit determination is used for GNSS and LEO satellites. The schemes of POD are as follows:

Scheme 1 (S1): Firstly, GNSS POD is processed, then do the LEO POD with the fixed GNSS orbit and clock (without the ground data with LEO). (So-called "two-step method").
Scheme 2 (S2): POD of combined GNSS and LEO (without the ground data with LEO). (So-called "one-step method"), where the error equations of this scheme will ignore the second equation of Eq. 7.
Scheme 3 (S3): POD of combined GNSS and LEO (with the ground data with LEO). (We call it "synthetical method").

In the method of combined POD of GNSS and LEO, the increasing number of LEO can improve the satellite geometric distribution, which results in the orbit improvement of GNSS. However, this also increase the number of parameters to be estimated, whether the strength of solution will decrease or not and how precise of the orbit can be reached needs further investigation. In order to investigate the

Table 2 Force models and parameters

Force model	LEO	GNSS
Earth gravity	EIGEN6C (120 × 120) [6]	EIGEN6C (12 × 12) [6]
N-body	JPL DE405 [15]	JPL DE405 [15]
Tide displacement	IERS Convention 2010 [11]	IERS Convention 2010 [11]
Ocean model	CSR 3.0 [5]	CSR 3.0 [5]
Relativity	IERS Convention 2010 [11]	IERS Convention 2010 [11]
Solar radiation	Based on the surface of LEO	ECOM model [3]
Atmosphere drag	DTM94 [1]	None
Estimated parameter		
Initial state	3D position and velocity	3D position and velocity
Phase ambiguity	One per combination per pass	One per combination per pass
Troposphere zenith delay	No	One per station in a 2 h arc
Receiver clock	White noise	White noise
Drag coefficient	Every 6 h	No
Solar radiation	No	ECOM 5 parameters
Empirical force	Every revolution 6 parameters	No

influence of the number of LEO, we conduct the experiment by adding a different number (6, 12, 18, …, 66) of LEO satellites in different orbit planes in S2 and S3, respectively.

The important options of force models and parameters for the POD are listed in Table 2.

4 Results and Discussions

According to the schemes mentioned above, we simulated all the data and analyze all the schemes. The S1 results of BDS and GPS POD are shown in Figs. 4 and 5, respectively.

From the figures, we can easily see that the results of BDS GEO satellites are much worse than those of other satellites. For example of C01, the precision of along-track component is about 34 cm and C04 is the worst of about 57 cm. The main reason is that the geometry of GEO satellites is nearly unchanged. The precision of along-track component is decimeter, while the cross-track and the radial-track components are much better than along-track component, reaching centimeter level. For GPS, the precision of POD is centimeter which matches the current POD techniques. Then we conduct the LEO POD by fixing the GNSS orbit and clock. The results are shown in Fig. 6.

From Fig. 6, we can see that the precision of LEO is at the centimeter level. Among the three components, the cross-track component is the best, which is around 1–2 cm, while the along-track component is the worst, which is about

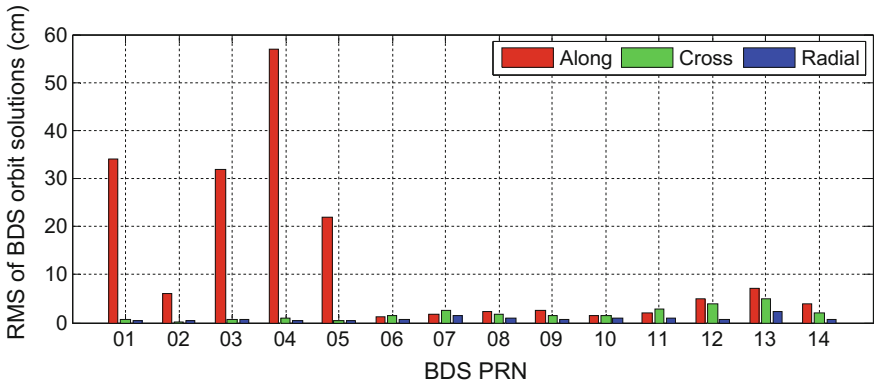

Fig. 4 POD results of BDS (Scheme 1)

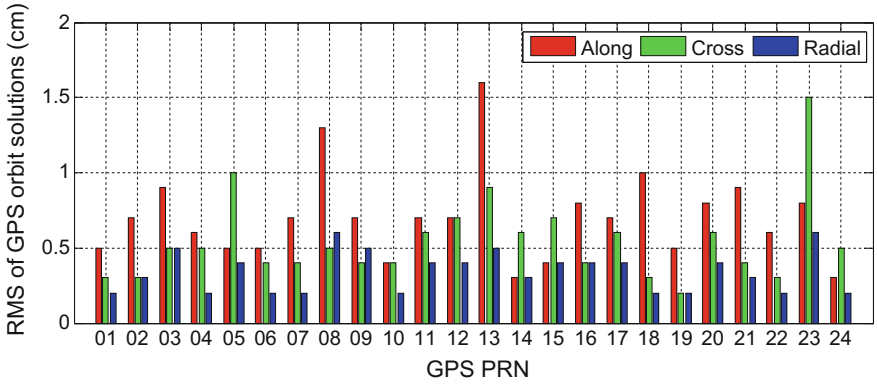

Fig. 5 POD results of GPS (Scheme 1)

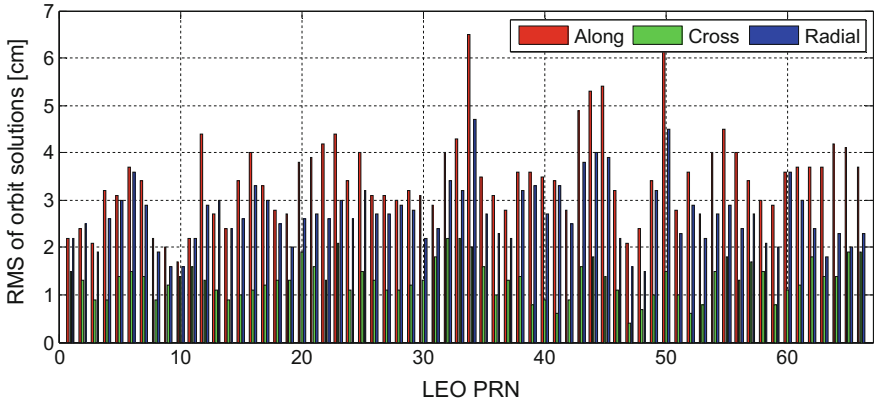

Fig. 6 POD results of LEO (Scheme 1)

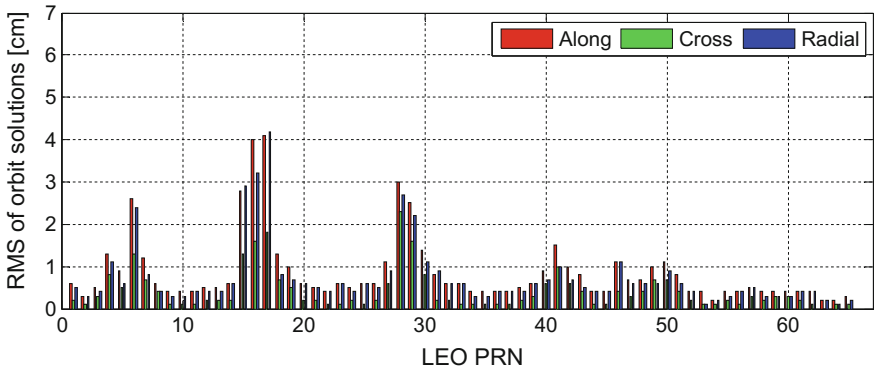

Fig. 7 POD results of LEO (Scheme 2)

4–5 cm. Since the GNSS orbits are fixed, the GNSS orbit error will be introduced into the LEO orbits, which will contaminate the precision of LEO orbits. POD results indicate that the simulation data is close to the real situation. Then we can use these results as the reference of the scheme 2 and scheme 3.

In scheme 2, the POD of LEO and GNSS satellites are processed together. Compared to the scheme 1, the POD results of LEO and GNSS have better consistence because of the combined solution. The precision of LEO satellites has a great improvement, as shown in Fig. 7. However, we can find some periodicity in the LEO results. This periodicity has some relationship with the orbit plane of LEO, which needs further investigation in the future.

LEO orbits can be determined by the onboard GNSS observations with the GNSS orbit fixed or estimated simultaneously. The latter one can have the better consistence in GNSS orbits, LEO orbits, and geodetic coordinate frame. It is important to highlight that since the significant geometry improvement when adding 66 LEO, the results of GNSS satellites, especially for the GEO, are much better than those in scheme 1. The POD results of BDS and GPS are shown in Figs. 8 and 9.

Compared to scheme 1, the precision of all three types of BDS satellites are better than that of scheme 1. Especially for the along-track component of GEO satellites, the precision increases from decimeter in scheme 1 to centimeter in scheme 2. This improvement attributes to the high kinematic of LEO satellites for improving the geometry of GEO POD. To be more clearly, the comparisons of all the satellites are shown in Fig. 10 where the relative improvements are on the right *y*-axis.

We can easily see that all the satellites have better results when adding LEO satellites, especially for the GEO satellites. The GEO precision is improved from decimeter to centimeter. For C01, the orbit precision of C01 increases from 34 to 2.2 cm, that is about 15 times better than that of scheme 1; while for C04, it has even much more improvement from 21.9 to 2.07 cm, that is nearly 21.5 times better

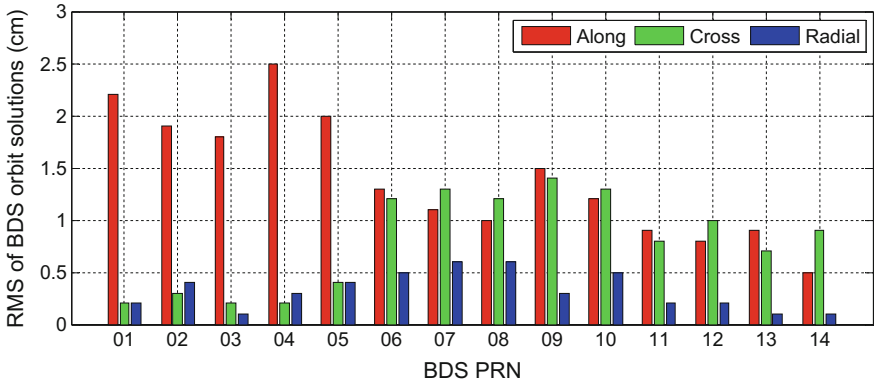

Fig. 8 POD results of BDS (Scheme 2)

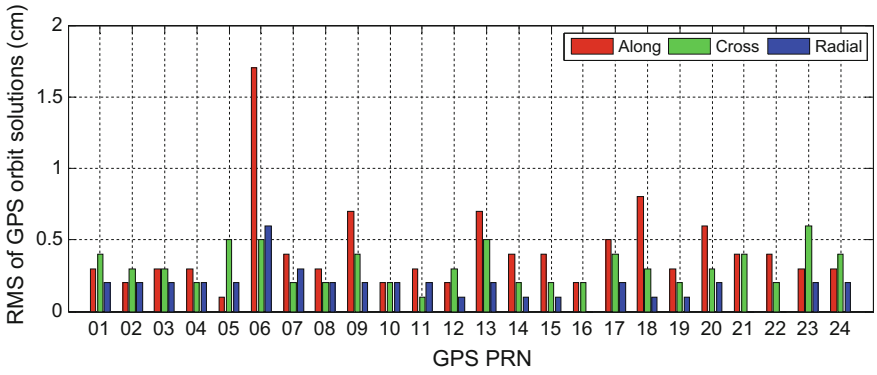

Fig. 9 POD results of GPS (Scheme 2)

than that of scheme 1. Though the improvements are not as significant as GEO satellites, IGSO satellites still have better performance. The orbit precision of C07 increases from 3.4 to 1.8 cm, i.e., improved by 92%. Though the precisions of BDS MEO and GPS are already very high in scheme 1, they can still be improved by the combined solution of scheme 2, especially for the BDS MEO satellites. The orbit precision of C13 in scheme 2 is 7 times better than that in scheme 1 and all other BDS MEO can improve more than 1 times. For GPS, all the satellites can be improved from 0.2 to 3 times, except G06, the orbit precision decreased from 1 to 1.87 cm, which need to be further investigation.

In order to investigate the contribution of the number of LEO satellites to the GNSS POD, we conduct a set of combined GNSS and LEO POD experiment with increasing the number of LEO in each orbit plane (such as 0, 1, 6, 12, 18, …, 66). All the POD results of different satellites are shown in Fig. 11.

It is clear that the GPS orbits are improved for all three components with the increase of LEO satellites. Though the precision of GPS is already high without

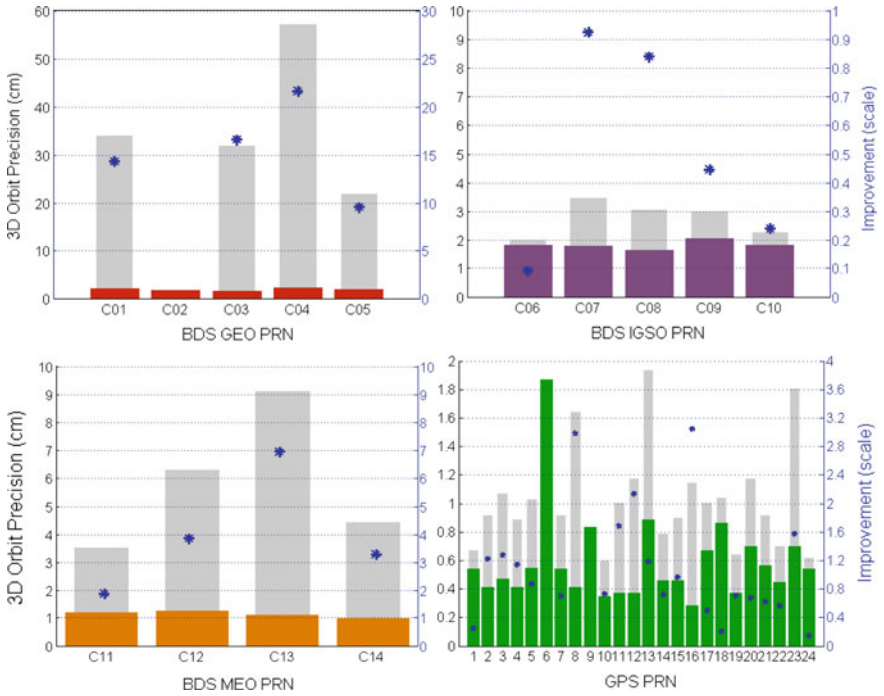

Fig. 10 Comparison of Scheme 1 (*gray*) and Scheme 2 (Color online)

LEO, the 3D RMS still can be improved from 1 to about 0.6 cm. For GEO of BDS, the precision of along-track component can be significantly improved when adding just one LEO satellite, increasing from decimeter to about 2 cm, while cross-track and radial-track components improve not so much. With the increasing number of LEO, the precision of GEO satellites stabilizes at the centimeter accuracy. The IGSO satellites have some improvement but not so obvious compared to the GEO satellites. The 3D RMS of the orbit is about 2 cm. For the BDS MEO satellites, with the number of LEO satellites increasing to six, there is a great improvement in orbit determination, increasing from about 6 cm to nearly 1.4 cm. Then, it remains stable at 1 cm.

Based on all above results, we conclude that combined POD of GNSS and LEO can improve the orbit precisions of all types of satellites. LEO satellites can strengthen the geometry of GNSS orbit, especially for the GEO satellites with the characteristic of geostationary. As for the effect of the number of LEO satellites, the precision of all satellites remain stable with the increasing number of LEO.

In the future, LEO satellites may carry the signal transmitter like GNSS satellites to have the navigation function. In scheme 3, we also use these data (observation data from LEO satellites to ground-tracking stations) to conduct the combined LEO and GNSS orbit determination. Figures 12, 13 and 14 show the RMS of three components of BDS, GPS, and LEO, respectively.

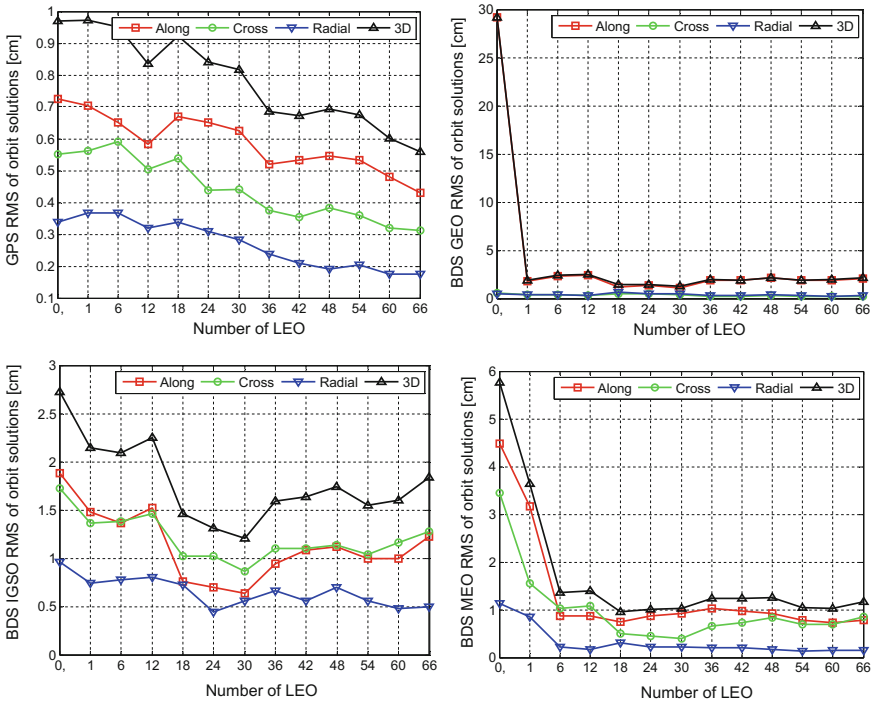

Fig. 11 GNSS POD results with different number of LEO

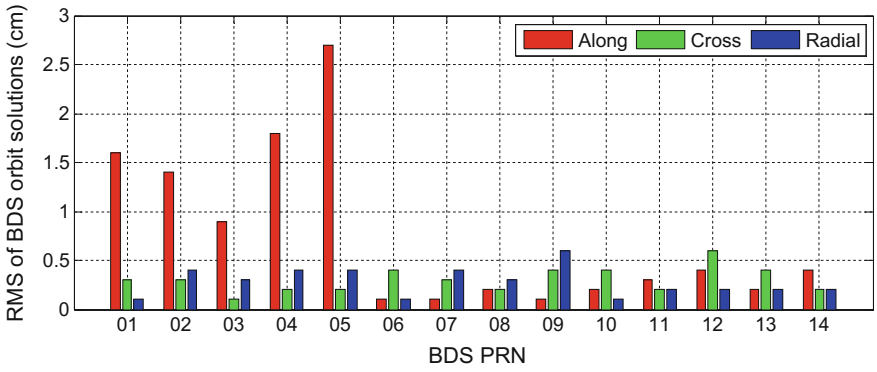

Fig. 12 POD results of BDS (Scheme 3)

From the figures, we can see that the orbits of BDS, GPS, and LEO satellites have further improvement. The ground-tracking observations deeply strengthen the geometry of LEO, resulting in better LEO orbits than those of Scheme 2. It is important to highlight that the periodicity of LEO POD in this scheme disappears compared to scheme 2. What's more, the orbit precision of GNSS satellites also

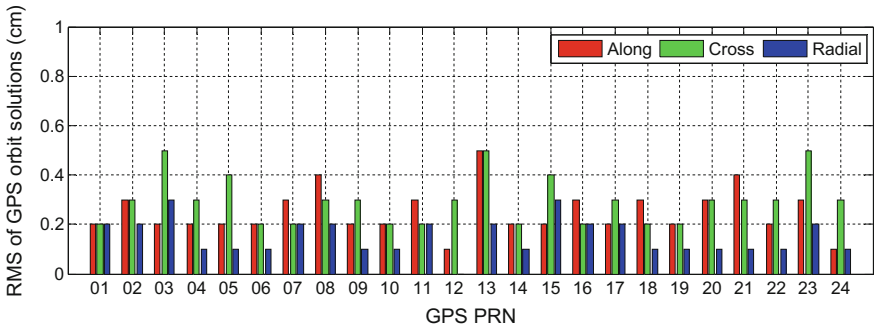

Fig. 13 POD results of GPS (Scheme 3)

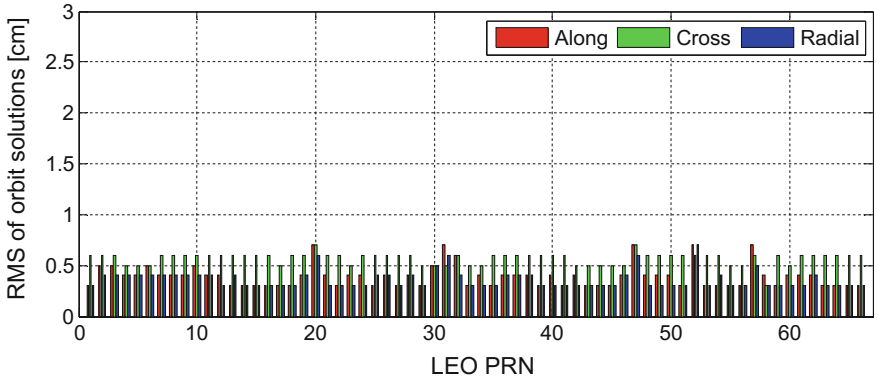

Fig. 14 POD results of LEO (Scheme 3)

improves with the better orbit of LEO. Figure 15 shows the comparison of every type of satellites between scheme 2 and scheme 3.

As shown in Fig. 15, the orbits of all types of satellites are improved when doing POD with the ground observations of LEO satellites. The orbit 3D RMS of GPS decreased by 25.7%, while the 3D RMS of BDS GEO satellites can be decreased from 2.11 cm in scheme 2 to 1.72 cm in scheme 3. IGSO have the greatest improvement from 2.11 cm in scheme 2 to 0.24 cm. The precision of MEO satellites can still be improved from 1.34 cm to 0.56 cm. In scheme 3, we can find that the orbit precision of IGSO is better than that of MEO satellites. The reason may be as follows. The main factor of MEO orbit precision is the distribution of ground-tracking stations since MEO satellites run around the earth. In our case, the distribution of Asia-Pacific (especially in China) ground stations are not so good for the MEO satellites. For IGSO satellites, though the ground tracking is of great importance, the orbit geometry is improved so much that the POD perfumes much better than that of MEO satellites. The trend of all satellites remains stable when having more LEO satellites which just like the scheme 2.

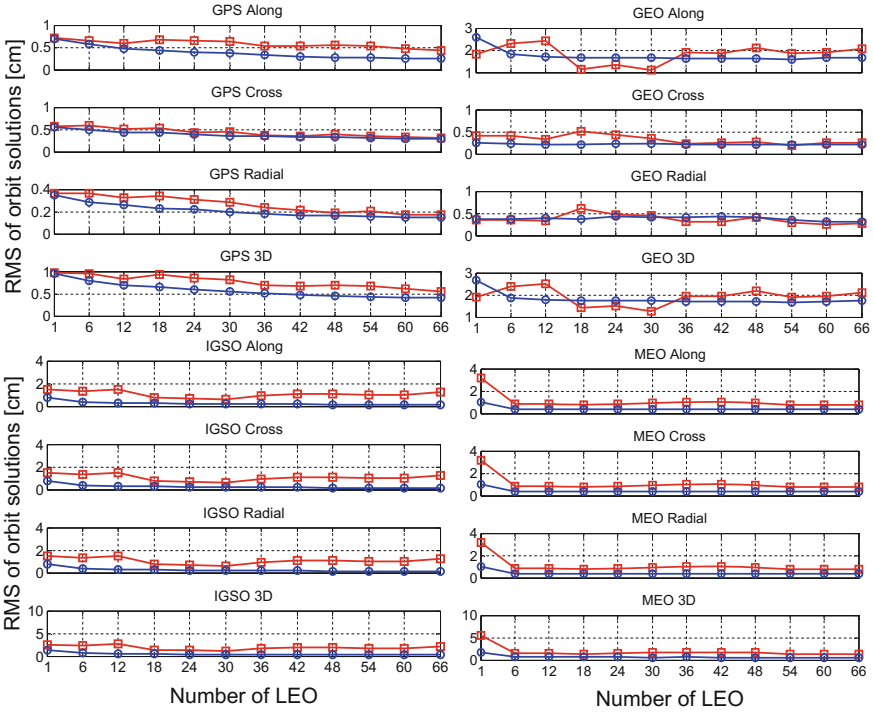

Fig. 15 Comparison of scheme 2 (*red*) and scheme 3 (*blue*) (GPS, BDS GEO, BDS IGSO, and BDS MEO) (Color online)

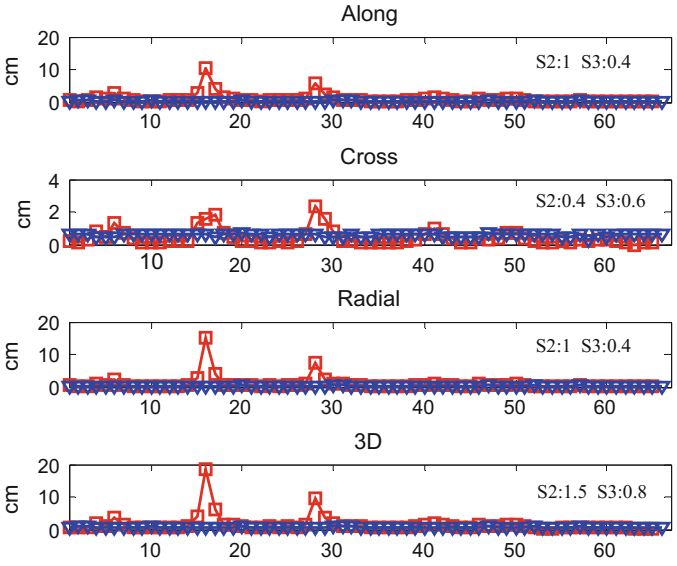

Fig. 16 Comparison between scheme 2 and 3 of LEO POD results

Figure 16 shows the LEO orbit comparison between scheme 2 and scheme 3. The along-track and radial-track components have great improvement with the ground observation of LEO satellites. For some LEO satellites, the ground observation makes a great contribution to the POD, such as LEO 16. To conclude all, with the ground observation of LEO satellites, the geometry of LEO is much more complete and can have a better orbit, which in turn, improves the GNSS orbit determination.

5 Conclusions

In this paper, with the thinking that the future LEO may carry GNSS transmitter, we simulate all the observations from space to ground (including high orbit to low orbit, medium orbit to low orbit, high orbit to ground stations, medium orbit to ground stations, and low orbit to ground stations). After that, three schemes of POD are conducted, the conclusions are as follows:

1. The "two-step method" has its limits. One the one hand, the precision of GEO of GNSS satellites are much worse than that of MEO satellites, especially for the along-track component because of the characteristic of geostationary, which cause the bad geometry of the orbit. On the other hand, since the GNSS orbits are fixed when doing LEO POD, the orbit error of GNSS satellites will be introduced into the LEO satellites, which contaminate the LEO orbit.
2. Compared to the "two-step method", "One-step method" has its advantages. For one thing, since the high kinematic characteristic of LEO satellites, the bad geometry of GEO satellites can be improved. For another, the orbits of GNSS, LEO, and the geodetic coordinate frame can have a good consistency. The results show that the orbit precision of GEO satellites can reach to centimeters and that of IGSO can be improved by 50%.
3. When LEO have the capability of sending GNSS signals and do the combined GNSS and LEO POD, more precise LEO orbit can be obtained since a complete geometry. In return, the GNSS orbit can also be improved.
4. The orbit cannot be improved infinitely. So how to choose the LEO satellites to strengthen the geometry of GNSS may have further investigations.

Acknowledgements The study is sponsored by the National Natural Science Funds of China (41622401, 41574023, 41374031) and the State Key Laboratory of Geodesy and Earth's Dynamics (Institute of Geodesy and Geophysics, CAS) (SKLGED2016-3-1-EZ).

References

1. Barlier F, Berger C, Falin J, Kockarts G, Thuillier G (1978) A thermospheric model based on satellite drag data. Annales de Geophysique, pp 9–24
2. Bertiger WI et al (1994) GPS precise tracking of TOPEX/POSEIDON: Results and implications. J Geophys Res 99:24449–24464. doi:10.1029/94jc01171
3. Beutler G, Brockmann E, Gurtner W, Hugentobler U, Mervart L, Rothacher M, Verdun A (1994) Extended orbit modeling techniques at the CODE processing center of the international GPS service for geodynamics (IGS): theory and initial results. Manuscr Geod 19:367–386
4. CSNO (2012) BeiDou navigation satellite system signal in space interface control document
5. Eanes RJ, Bettadpur S (1996) The CSR3. 0 global ocean tide model: diurnal and semi-diurnal ocean tides from TOPEX/POSEIDON altimetry. The University of Texas Center for Space Research
6. Förste C et al (2012) A new release of EIGEN-6: The latest combined global gravity field model including LAGEOS, GRACE and GOCE data from the collaboration of GFZ Potsdam and GRGS Toulouse. In: EGU General Assembly Conference Abstracts, p 2821
7. König R, Reigber C, Zhu SY (2005) Dynamic model orbits and earth system parameters from combined GPS and LEO data. Adv Space Res 36:431–437. doi:10.1016/j.asr.2005.03.064
8. Ke M, Lv J, Chang J, Dai W, Tong K, Zhu M (2015) Integrating GPS and LEO to accelerate convergence time of precise point positioning. In: International Conference on Wireless communications and signal processing (WCSP), IEEE, pp 1–5
9. Maine K, Devieux C, Swan P (1995) Overview of IRIDIUM satellite network. In: WESCON/ ’95. Conference record microelectronics communications technology producing quality products mobile and portable power emerging technologies, IEEE, p 483
10. Montenbruck O, Steigenberger P, Khachikyan R, Weber G, Langley RB, Mervart L, Hugentobler U (2014) IGS-MGEX: preparing the ground for multi-constellation GNSS science Inside GNSS 9:42–49
11. Petit G, Luzum B (2010) IERS conventions (2010). DTIC Document
12. Reid TG, Neish AM, Walter TF, Enge PK (2016) Leveraging commercial broadband LEO constellations for navigation. In: Paper presented at the 29th international technical meeting of the satellite division of the Institute of Navigation (ION GNSS+ 2016), Portland
13. Selding PBd (2015) SpaceX to build 4000 Broadband satellites in Seattle. http://spacenews.com/spacex-opening-seattle-plant-to-build-4000-broadband-satellites/
14. SMC/GP (2004) Navstar global positioning system interface specification
15. Standish E (1998) JPL planetary and lunar ephemerides. DE405/LE405//Interoffice Memorandum 312. F-98-048
16. Wikipedia (2016) Iridium satellite constellation
17. Zhu S, Reigber C, Koenig R (2004) Integrated adjustment of CHAMP, GRACE, and GPS data. J Geodesy 78 doi:10.1007/s00190-004-0379-0
18. Zhao J, Yu X, Feng S, Deng L (2013) Design and performance analysis of LEO satellites enhanced COMPASS system. Telecommun Eng 53(2):131–135

Design of Deorbit Parameters for BEIDOU MEO and IGSO Satellites Based on Long-Term Eccentricity Evolution

Chen Xingyi, Zhang Wei and Xie Chen

Abstract Useless satellites permanently stay in operational orbit occupy valuable orbital resources, and that increase the collision risk of other active satellites. If the useless satellites breakup, the massive new space debris will have catastrophic effect on running circumstance of active satellites. Therefore it is important to take deorbit maneuver if the satellites are in the end of lifetime. Setting up reasonable deorbit parameters and avoiding secondary disasters is very crucial. The paper studies the long-term evolution of eccentricity and semi-major axis that result from a resonance of the third body and the nonspherical gravitational perturbation. On the basis of the phenomenon, analysis and calculates the biggest change in perigee attitude. According to the long-term variation of eccentricity, the MEO (Medium Earth Orbit) and IGSO (Inclined Geosynchronous Satellite Orbit) satellites in the BEIDOU navigation constellation studied. Designing the deorbit parameters to reduce their orbital lifetime or make sure that the perigee of disposal orbit is not below the protected region in 100 years. The simulation results show that the deorbit parameters are reasonable and meet the requirements of IADC (Inter-Agency Space Debris Coordination Committee). It can provide reference for the deorbit strategy of the BEIDOU navigation satellites and the other MEO or IGSO Satellites at the end of life.

Keywords Long-term eccentricity evolution · Deorbit · BEIDOU MEO · IGSO satellites

1 Introduction

It is not only a waste of precious orbit resources post-operational spacecraft's long time stay in orbit, but also increasing the collision probabilities with other spacecraft in mission, worse more, it is a catastrophes to space once breaks up Fig. 1 is the

C. Xingyi (✉) · Z. Wei · X. Chen
Xi'an Satellites Control Center, Xi'an 710043, China
e-mail: xingyio0o@126.com; 512853206@qq.com

J. Sun et al. (eds.), *China Satellite Navigation Conference (CSNC) 2017 Proceedings: Volume III*, Lecture Notes in Electrical Engineering 439,
DOI 10.1007/978-981-10-4594-3_16

collision threats statistics with spatial distance less than 5 km for BEIDOU Navigation Satellite (BDS) from January to August in 2015. It is observed that there are big collision risks for BDS IGSO and MEO as well as GEO. So it is significant to imply deorbit disposal in the end of their lifetime to reduce the post-operational spacecraft in orbit.

Inter-Agency Space Debris Coordination Committee (IADC) issued the 《IADC Space Debris Mitigation Guide》 clearly requesting for GEO satellite post-operational deorbit disposal [1]. BDS include three orbits-GEO, MEO and IGSO's, making deorbit disposal much more difficult, in which the outstanding one is the increase of eccentricity due to inclined orbit's long-term evolution [2]. The dissertation studies these on MEO and IGSO evolution characteristics of BDS and projects their deorbit parameters respectively.

2 Long-Term Eccentricity Evolution of MEO and IGSO Satellites Based on

Equation (1): Eccentricity periodic variation caused by lunisolar gravitation when the orbit inclination is not 0° [3],

$$\frac{de}{dt} = -\frac{15}{32}\beta n a^3 e\left[\begin{array}{l}\frac{1}{2}(1-\cos i)^2 K_1 + \frac{1}{2}(1+\cos i)^2 K_2 + \sin^2 iK_3 + 2\sin i(1-\cos i)K_4 \\ +2\sin i(1+\cos i)K_5\end{array}\right] \tag{1}$$

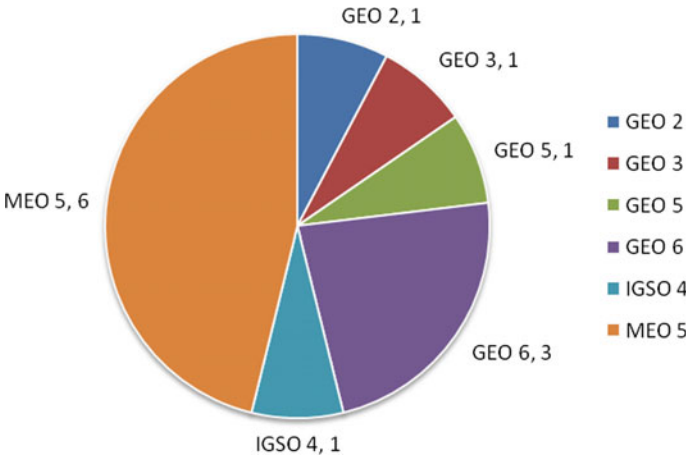

Fig. 1 BDS collision threats 2015/01–2015/08

Among which, $K_m\,(m = 1-5)$ relates to lunisolar inclination, lunisolar location, argument of perigee ω, longitude of ascending node Ω and first-order variability $\dot{\Omega}$, $\dot{\omega}$ Its amplitude depends on items below

$$\frac{1}{2\dot{\omega} + l\dot{\Omega}} \quad (l = -2, -1, 0, 1, 2) \tag{2}$$

$\dot{\Omega}$, $\dot{\omega}$ are first-order variability for long-term cause by the nonspherical gravity of earth.

$$\begin{aligned} \dot{\omega} &= \frac{J_2 n}{p^2}\left(3 - \frac{15}{4}\sin^2 i\right) \\ \dot{\Omega} &= -\frac{3J_2 n}{p^2}\cos i \end{aligned} \tag{3}$$

It is observed that $\dot{\Omega}$, $\dot{\omega}$ relate to semi-major axis of satellites, inclination angle, and the earth oblateness. When the inclination is a constant value, $2\dot{\omega} + l\dot{\omega} \approx 0$, the eccentricity will increase seriously. Bibliography [4] describes the maximum of eccentricity changes with inclination for MEO orbit in long term. Refer Fig. 2.

Orbital inclination of BDS MEO and IGSO $i \approx 55°$, which is close to critical value 56 of $2\dot{\omega} + \dot{\Omega}$. We can see from Fig. 2 that inclination of GPS and GALILEO is 55 or so; and inclination of GLONASS closes to 64.8 and $2\dot{\omega}$ approaches to 0, thus leading to the seriously increase of eccentricity. The result makes no difference

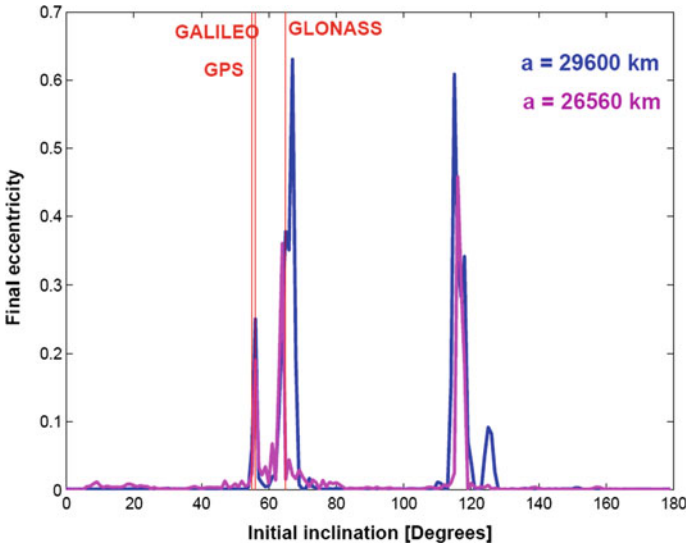

Fig. 2 Relations between maximum value of eccentricity and initial orbital inclination

Table 1 Critical inclinations corresponding to each resonance item

Resonance term	Critical inclination
$2\dot{\omega} - 2\dot{\Omega}$	73.1
$2\dot{\omega} - \dot{\Omega}$	69.0
$2\dot{\omega}$	63.4
$2\dot{\omega} + \dot{\Omega}$	56.0
$2\dot{\omega} + 2\dot{\Omega}$	46.4

from previous analysis. Table 1 lists critical inclinations corresponding to each resonant item.

It is the resonance among nonspherical of Earth, solar and lunar that makes the deorbit parameters stricter for those inclined orbital satellite. Considering the much too propellent consumption and mission lifetime influence by changing the inclination and right ascension of ascending node, the dissertation will choose proper deorbit parameters for BDS under the premise of not changing these two parameters.

3 BDS MEO Satellite Deorbit Parameters

The second section of the dissertation analyzes the eccentricity's instability for inclined orbital satellite. The orbital inclination for BDS MEO satellite is 55° or so, but the eccentricity will probably increase ten or hundred times under the influence of resonance among the Earth's nonsphere, solar and lunar, so phase have to be limited to control the perigee descending altitude.

There are many phase elements caused by lunisolar gravitation that leading to the long periodic variation of eccentricity, the main elements among of which can be summarized as $2\dot{\omega} + l\dot{\Omega}\,(l = -2. -1, 0, 1, 2)$. There are three orbital planes for BDS MEO satellite constellations, their right ascensions of ascending note are about 15°, 103°, and 222°, respectively. The dissertation analyzes the perigee altitude variation of the disposal orbits in these three planes under different arguments of perigee. Perigee ascending altitude for MEO satellite disposal orbit is set

$$\Delta H = 200\text{km} + 300\text{km} + 600 \times C_R \frac{A}{m}, \quad e < 0.005 \tag{4}$$

Among it, 200 km is the protection altitude. The maximum variation of perigee altitude for MEO satellite caused by solar radiation pressure is about $510 \times C_R \frac{A}{m}$ Km, while $600 \times C_R \frac{A}{m}$ is used for simulation verification; mechanical model has considered the earth nonspherical gravitation (3×3), solar gravitation, lunar gravitation, solar radiation pressure, and other initial parameters (see Table 2), the result can be seen from Fig. 3.

Judging by above results, BDS MEO satellite deorbit parameters are set as below Table 3.

Table 2 BDS MEO satellite initial parameter of disposal orbit 2

Time (UTC)	2015–01–01 00:00:00
A	28,543 km
E	0.005
Ω	15°/103°/222°
I	55°

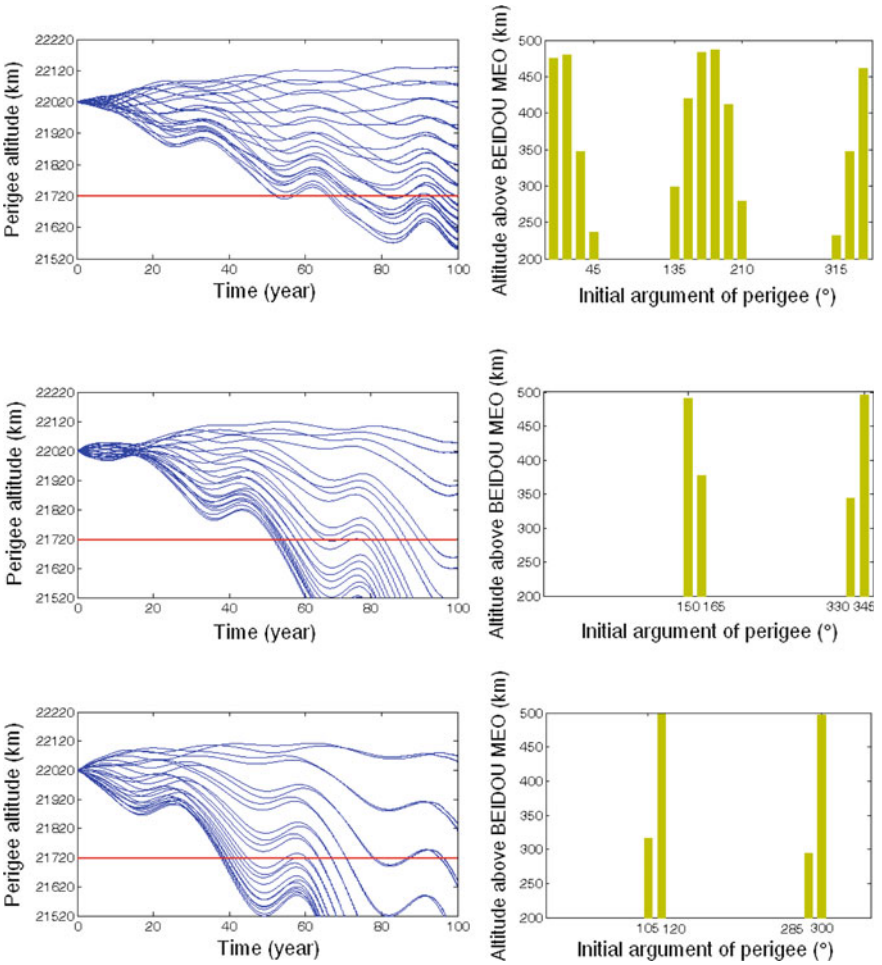

Fig. 3 BDS MEO perigee altitude variation of disposal orbit

Table 3 BDS MEO satellite deorbit parameters

Orbit plane	ΔH	E	ω_0
$i = 55^\circ\ \Omega = 15^\circ$	$500\,\text{km} + 600 \times C_R \frac{A}{m}$	<0.005	$[-45^\circ, 45^\circ][135^\circ, 210^\circ]$,
$i = 55^\circ\ \Omega = 103^\circ$	$500\,\text{km} + 600 \times C_R \frac{A}{m}$	<0.005	$[150^\circ, 165^\circ]\ [330^\circ, 345^\circ]$
$i = 55^\circ\ \Omega = 222^\circ$	$500\,\text{km} + 600 \times C_R \frac{A}{m}$	<0.005	$[105^\circ, 120^\circ]\ [285^\circ, 300^\circ]$

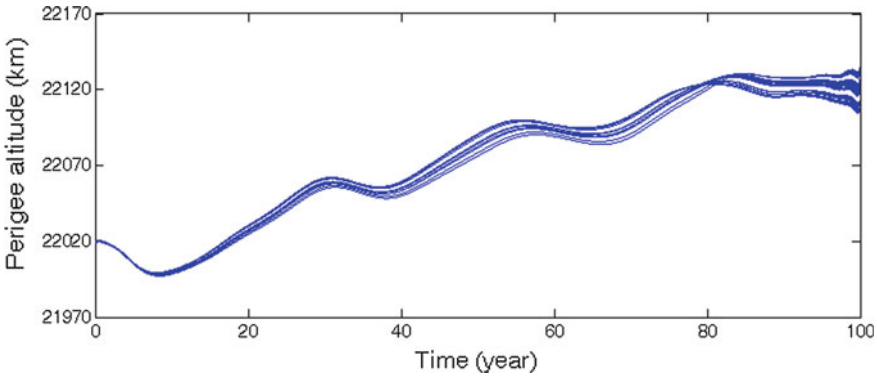

Fig. 4 Perigee altitude influenced by initial EPOC

Initial epoch has a little influence on the perigee altitude, which minimum value is about 10 km. To illustrate this issue, we set $i = 55^\circ, \Omega = 15^\circ, \omega_0 = 0^\circ$ as initial vales and analyzed the variation of perigee altitude under condition that initial epochs are different months in 2015. The consequence can be seen from Fig. 4. The main reason for this consequence is that the amplitudes including of lunisolar locations are smaller than amplitudes only including of $2\dot{\omega} + l\dot{\Omega}$.

4 BDS IGSO Satellite Deorbit Parameters

Characteristics of long-term variation for orbit are distinctive between BDS IGSO and MEO satellites, mainly because the elongate semi-major axis amplifies the influence of resonance. Under influence of resonance among Earth's nonsphere, solar and lunar, proper disposal orbit probably will not be found [10]. The increase of eccentricity for inclined synchronous orbits could help to design proper deorbit parameters for BDS IGSO satellite, thus enabling the eccentricity reach a certain value within minimum duration so that the satellite gradually falls on earth. The dissertation studies on the variation of eccentricity within 200 years for three orbital planes with different arguments of perigee (Table 4).

Table 4 BDS IGSO initial parameters of disposal orbit

Time (UTC)	2015–01–01 00:00:00
A	42,164 km
E	0.005
I	55°
Ω	88°/210°/328°

Figure 5a, when initial argument of perigee ω_0 is about 292°, the earliest time for "eccentricity >0.83" is about 184 years. Figure 5b, When initial argument of perigee ω_0 is 300° or so, the earliest time for "eccentricity >0.83" is about 138 years. Figure 5c No initial argument of angle is available to get "eccentricity >0.83" within 200 years. It is observed that under the influence of lunisolar resonance, eccentricity of BDS IGSO satellites will be increased by leaps. But not all the orbital planes have proper argument of perigee to let the satellite, after long-term evolution in orbits while eccentricity bigger enough, fall on ground. According to this, the literature [11] studies on the maximum eccentricity for different initial right ascensions of ascending note Ω_0. It points out that when Ω_0's variation are within about [90°, 180°] and [210°, 250°], 600 years are necessary for the satellite to fall on the ground (intervals 30°) when eccentricity >0.83 (minimum altitude <200 km). From the point of debris mitigation, the launching directions Ω_0 could be tried choosing within ranges of [90°, 180°] and [210°, 250°] for subsequent BDS IGSO satellites.

According to consequences above, we set the deorbit parameters for BDS IGSO satellites orbital

Planes I and II are as below:

(1) Orbital plane I, $(i = 55°, \Omega = 88°)$: $\omega_0 \approx 292°$, $e_0 \approx 0.005$;
(2) Orbital plane II, $(i = 55°, \Omega = 210°)$: $\omega_0 \approx 292°$, $e_0 \approx 0.005$;

For orbits plane III$(i = 55°, \Omega = 328°)$, concluding the deorbit parameters as MEO deorbit parameters to make the perigee altitude of IGSO satellite higher than its protection altitude within 100 years (Maximum perigee descending altitude caused by solar radiation pressure of BEIDOU IGSO satellite is $930 \times C_R \frac{A}{m}$, the dissertation uses $1000 \times C_R \frac{A}{m}$). Deorbit parameters are set as below.

$$\Delta H = 200km + 300km + 1000 \times C_R \frac{A}{m}, \quad \omega_0 \in [64°, 70°] \text{or} [243°, 249°] \tag{5}$$

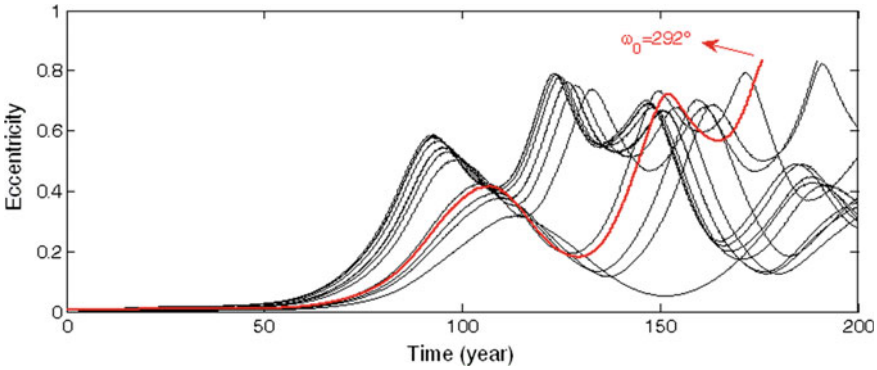

(a) Orbital plane I, ($i = 55^0, \Omega = 88^0$), $\omega_0 \in [0^0, 360^0)$, intervals 30°

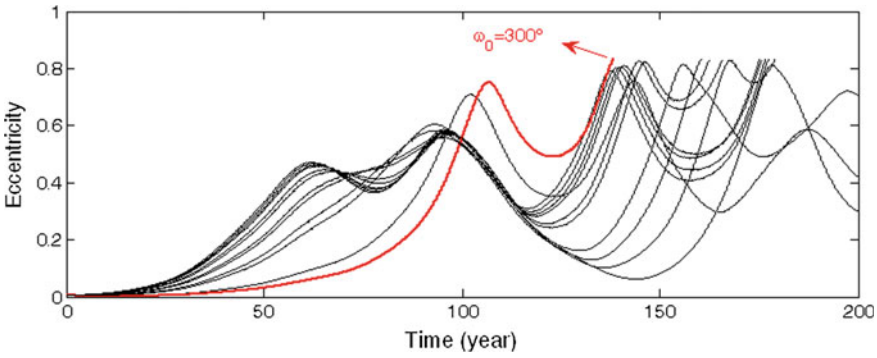

(b) Orbital plane II ($i = 55^0, \Omega = 210^0$), $\omega_0 \in [0^0, 360^0)$, intervals 30°

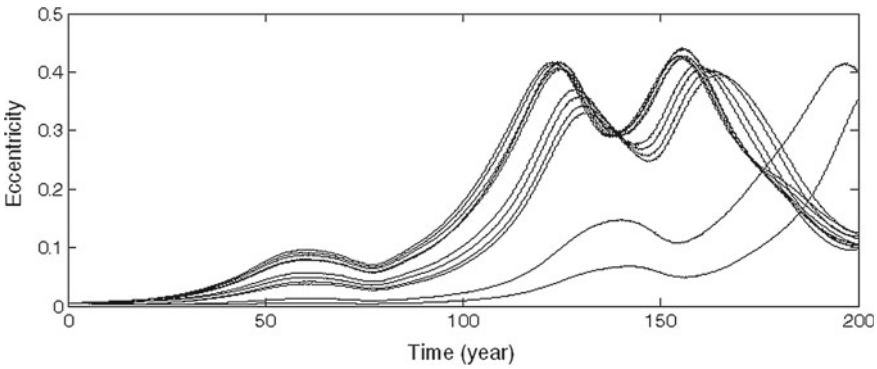

(c) Orbital plane II ($i = 55^0, \Omega = 328^0$), $\omega_0 \in [0^0, 360^0)$, intervals 30°

Fig. 5 BDS IGSO satellite eccentricity's long-term evolution

Table 5 Deorbits parameters of BDS satellite

Orbit type		Deorbit parameters
BEIDOU MEO	$i = 55°$, $\Omega = 15°$[a]	$\Delta H = 500\,\text{km} + 600 \times C_R \frac{A}{m}, e < 0.005$ $\omega_0 \in [-45°, 45°], [135°, 210°]$
	$i = 55°$, $\Omega = 103°$[a]	$\Delta H = 500\,\text{km} + 600 \times C_R \frac{A}{m}, e < 0.005$ $\omega_0 \in [150°, 165°], [330°, 345°]$
	$i = 55°$, $\Omega = 222°$[a]	$\Delta H = 500\,\text{km} + 600 \times C_R \frac{A}{m}, e < 0.005$ $\omega_0 \in [285°, 300°], [105°, 120°]$
BEIDOU IGSO	$i = 55°$, $\Omega = 328°$[a]	$\Delta H = 500\,\text{km} + 1000 \times C_R \frac{A}{m}, e < 0.005$ $\omega_0 \in [64°, 70°], [243°, 249°]$
	$i = 55°$, $\Omega = 88°$[b]	$\omega_0 \approx 292°, e > 0.005$
	$i = 55°$, $\Omega = 210°$[b]	$\omega_0 \approx 300°, e > 0.005$

[a]The deorbit purpose is to make perigee altitude of the satellites higher than the protection areas for satellites in miss within 100 years

[b]The deorbit purpose is to make satellite fall on the earth in minimum duration

5 Conclusion

According to analysis summary for deorbit parameters of BEIDOU satellite are as below (Table 5).

The paper analyses the long-term variation of eccentricity, designing the deorbit parameters of BDS. The simulation results show that the deorbit parameters are reasonable and meet the requirements.

References

1. Inter-Agency Space Debris Coordination Committee (2002). IADC space debris mitigation guidelines. IADC-02–01. revised 2007
2. He-Feng Li (2013) Development. Advantages and suggestions of BeiDou navigation satellite system. J Navig Positioning, Vol.1
3. LiuLin (1992).Orbit Theory of Spacecraft. National Defence Industry Press, PeKing
4. Rossi A, Anselmo L (2009) Effectiveness of the de-orbiting practices in the MEO region. Acta Astronaution, 65
5. Nian LH (2010) Geostationary Satellite Orbital Analysis and Collocation Strategies. National Defence Industry Press, PeKing
6. Lewisa HG, Swinerda GG (2004) The stability of disposal orbits at super-synchronous altitudes. Acta Astronaution, 55
7. Gopinath NS, Ganeshan AS (2005) Long term evolution of objects in GEO-disposal orbit. In: Proceedings of the fourth European conference on space debris
8. Chao CC (2000) MEO disposal orbit stability and direct reentry strategy. Advances in the Astronautical Sciences, Vol 105

9. Gick RA, Chao CC (2001) GPS disposal orbit stability and sensitivity study. Adv astronaut sci, 108
10. Jenkin AB, Gick RA (2005) Dilution of disposal orbit collision risk for the medium earth orbit constellations. Aerospace. Report NO. TR-2005(8506)-2, 2005
11. Zhao C-Y (2015) Analysis on the long-term dynamical evolution of the inclined geosynchronous orbits in the Chinese BEIDOU navigation system. Adv Space Res., 56

A New Method and Strategy for Precise Ultra-Rapid Orbit Determination

Hongyang Ma, Qile Zhao and Xiaolong Xu

Abstract A new processing approach is proposed for the ultra-orbit orbit product of International GNSS Monitoring and Assessment System (iGMAS) Analysis Center. With this approach, a length of 22 h normal equation matrix and 3 h normal equation matrix are combined into a complete one to determinate the satellite orbits, which can satisfy the 2 h submit delay required by ultra-rapid products. In addition, one more hour observed data can be used compared with the traditional method with 24 h determination and 24 h prediction. Meanwhile the user available part in predicted orbit decreases from 2nd–8th to 1st–7th h. Details and procedures of this method are introduced in this paper, as well as the connection of orbit parameters when combining the normal matrices, especially the ambiguity parameters. To assess the impact of this new approach, the user available part in predicted orbit generated from the new and the old methods for 9 consecutive days is compared to the reference orbits. The results show that compared with the traditional method, the new method can improve the accuracy of quad-constellation predicted part of satellite orbit. This method is applicable to IGS analysis center equally.

Keywords iGMAS · Ultra-rapid orbit · GNSS · Normal matrices combine · Orbit predict

1 Introduction

The International GNSS Monitoring and Assessment System (iGMAS) is an open technology platform for collecting, storing, analysing and managing GNSS observation data, generating and publishing products related to GNSS satellites, monitoring and evaluating performance of all global satellite navigation systems [1]. As an important component of iGMAS, analysis centre undertakes the task of processing high-precision products, including precise orbits, clock offsets, tracking

H. Ma (✉) · Q. Zhao · X. Xu
GNSS Research Center, Wuhan University, Wuhan, Hubei, China
e-mail: mahy@whu.edu.cn

J. Sun et al. (eds.), *China Satellite Navigation Conference (CSNC) 2017 Proceedings: Volume III*, Lecture Notes in Electrical Engineering 439,
DOI 10.1007/978-981-10-4594-3_17

station coordinates, earth rotation parameters, zenith troposphere delay, global ionosphere delay, etc. Among these products, with the advantage of quick renewal and high accuracy, the ultra-rapid orbit products are widely used in high real-time applications [2–4]. Currently, numerical integration is often used to generate satellites predicted orbits [5]. However, the accuracy of the predicted orbit drops rapidly as time passes since there is no observed data in predicted part. Moreover, to satisfy the real-time performance, there is a strict time limit for generating and publishing ultra-rapid products, i.e. a 2-h delay. That means lead to the user available part in predicted orbit is actually the 2nd–8th h.

For the purpose of improving computation efficiency and calculation accuracy, the method of combining normal equation matrices has been applied in fields where large amounts of data need to be processed. Beutler proposed to combine three normal matrices generated by single-day observations to one complete normal matrix to calculate satellite orbits [6]. According to his research, each single-day orbit is described as three initial position parameters, three initial velocity parameters and n dynamic parameters. This method has the advantage of high efficiency and flexibility, and as for the accuracy, the orbit parameters have the calculation result as that of the 3-days solution. Brockmann applied this method to the field of geodesy and geodynamic to generate high-precision products of orbit, clock offsets, tracking station coordinates and earth rotation parameters [7]. Dong calculated and analysed earth deformation through different data length and different types of observation [8]. Andersen researched the combination of random parameters in multi-level observation arcs and proposed a new least-squares information filtering and smoothing method [9]. With the application of this method, parameters and covariance matrices of all arcs can be combined, no matter they are constant parameters, white noise parameters or coloured noise parameters. This method can improve efficiency without sacrificing the accuracy of parameters as well. Yao smoothed the combination of 3-day solution through using dynamic models and found out that the combined solution can significantly improve the accuracy of orbit parameters and track control in regional orbit determination [10]. Lou combined consecutive short normal matrices into a long matrix through a sliding window [11]. This method can help reach the accuracy of IGS rapid orbit products through one-day slide solution, and it also has the advantage of strong numerical stability and high data processing speed. Lutz researched the different accuracy between one-day solution and multi-day solution and emphatically analysed the impact of data with different lengths on the accuracy of the earth rotation parameters [12]. Liu researched the influence of pseudo-random parameters on combining normal matrices resolution and found out that the orbit jump can be effectively eliminated through adding pseudo-random parameters in the connection point of two arcs [13].

Currently, the 24-h observation length is generally used to generate ultra-rapid orbit products, while this paper proposes a new "22 + 3"-h processing method which can reach the same degree of accuracy as that of 25-h solution through combining two consecutive normal matrices formed by an observation length of

22 h and length of 3 h, respectively. Compared with the traditional method with 24-h determination and 24-h predication, this method can not only use one more hour observed data, but also reduce user available part in predicted orbit from 2nd–8th to 1st–7th h.

2 Method and Strategy for Processing Ultra-Rapid Orbit

2.1 Principle of Precise Orbit Determination

The basic code pseudo-range observations P and the carrier phase observations Φ can be written by distance as follows:

$$\begin{aligned} P^s_{r,i} &= \rho^s_r + T_r + c\delta t_r - c\delta t^s + \alpha_i I^s_r + \varepsilon_{P^s_{r,i}}, \\ \Phi^s_{r,i} &= \rho^s_r + T_r + c\delta t_r - c\delta t^s - \alpha_i I^s_r + \lambda_i N^s_{r,\,i} + \varepsilon_{\Phi^s_{r,i}}, \end{aligned} \tag{1}$$

where s, r and i ($i = 1, 2$) denote satellites, receivers and frequencies, respectively. ρ^s_r is the geometrical distance between the satellite and the receiver, T_r is the influence on the observation caused by zenith troposphere delay, δt_r and δt^s are satellite and receiver clock offsets, respectively, c denotes light speed, $\alpha_i I^s_r$ is the ionospheric delay, and $\alpha_i = f_1^2/f_i^2$, f_i denotes the frequencies of the carriers, $N^s_{r,\,i}$ is integer ambiguity and λ_i is wavelength of frequency f_i, $\varepsilon_{P^s_{r,i}}$ and $\varepsilon_{\Phi^s_{r,i}}$ are the remaining errors of these two observations, including multipath effect, observation noise, uncalibrated hardware delay of satellite and receiver, etc.

Based on the above observation equations, the function model and the random model of orbit determination can be expressed as:

$$\begin{aligned} E\{y_{m\times 1}\} &= A_{m\times n} x_{n\times 1}, \\ Q_y &= E\{(y_{m\times 1} - A_{m\times n} x_{n\times 1})(y_{m\times 1} - A_{m\times n} x_{n\times 1})^{\mathrm{T}}\}, \end{aligned} \tag{2}$$

where $E\{\cdot\}$ denotes mathematical expectation, y is the $m \times 1$ dimension observation vectors, x is the $n \times 1$ dimension parameters vectors, generally $m > n$ which indicates redundant observations exist, A is the $m \times n$ dimension design matrix which is usually full column rank. A is the concrete representation of the function model which represents the functional relationship between observations and parameters. Q_y is the covariance matrix of the observation vectors and indicates the stochastic characteristics of observations. Q_y is the concrete representation of the random model.

The parameter vector x includes constant parameters (initial position, initial velocity and force models of the satellites), process parameters (clock offsets of satellite and receiver, zenith troposphere delay) and ambiguity parameters.

According to the optimal robust estimating principle, the objective function and constraints are established to obtain the optimal unbiased estimation and covariance matrix of the parameters:

$$\begin{aligned} \hat{x} &= (A^{\mathrm{T}} Q_y^{-1} A)^{-1} A^{\mathrm{T}} Q_y^{-1} y \\ Q_{\hat{x}} &= (A^{\mathrm{T}} Q_y^{-1} A)^{-1} \end{aligned} \tag{3}$$

2.2 Strategy of Generating Ultra-Rapid Orbit

For now, the determined orbits in ultra-rapid products are usually generated through data with the observation length 24 or 45 h [14]. Take the process of generating ultra-rapid orbit product at 00 o'clock with 24 h determination and 24 h prediction as an example, Fig. 1 illustrates the difference between the traditional method and the method proposed in this paper.

The upper figure in Fig. 1 describes the traditional method with 24 h determination and 24 h prediction. It starts from 00 o'clock to process data observed during the 24 h in the previous day and publishes its orbit product at 2 o'clock. Since the ultra-rapid products update four times per day, the user available part is 2nd–8th h in predicted orbit every time after users get the latest ultra-rapid orbit product. The lower figure in Fig. 1 illustrates the method proposed in this paper. The complete process is divided into two processes: the first process starts from 22 o'clock and processed data observed during 22 h from 0 o'clock in the same day, and the whole information of normal matrix is stored in this process. The second process starts from 1 o'clock and processed data observed during 3 h from 22 o'clock in the previous day to 1 o'clock the next day. The prior information of orbit and normal matrix in the first process can help resolve orbit parameters in the second process quickly. Finally, two matrices of processes are combined into a complete normal

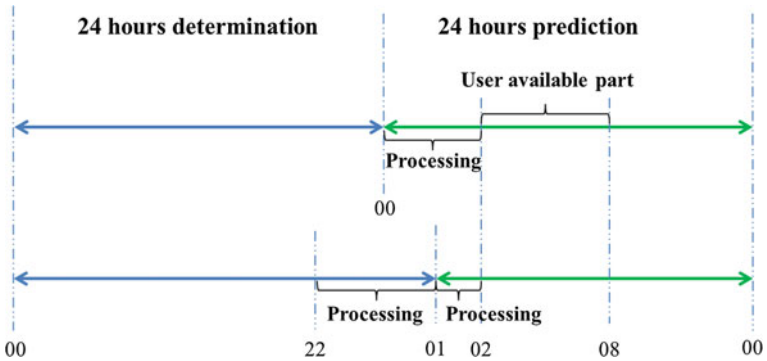

Fig. 1 The comparison between traditional method and method proposed in this paper

matrix to achieve the results of 25 h observations. In this case, user available part reduces from 2nd–8th to 1st–7th h in the predicted orbit. Therefore, compared with the traditional method, the proposed method can use one more observed data and reduce one hour interval between the start time of predicted orbit and the user available part.

2.3 Connection of Parameters

Based on the theory of reduced dynamic precision orbit determination introduced in Sect. 2.1, orbit parameters are divided into three types: constant parameters, process parameters and ambiguity parameters. Each type of orbit parameters has to be connected correctly for the consistency and continuity of resolution after combining two processes.

2.3.1 Connection of Constant Parameters

The constant parameters include three initial position parameters, three initial velocity parameters and n force model parameters. Satellite initial status is described by these parameters and they do not change over time, so each of the two processes has the same constant parameters and there is no need for them to be connected. Due to the big difference between two processes' observation length (22 and 3 h, respectively), the issue of data saturation has to be avoided [15, 16]. The weight of constant parameters in the normal matrix of first process has to be reduced properly. Let the normal matrix of the first process be

$$\begin{bmatrix} N11 & N12 \\ N21 & N22 \end{bmatrix} \begin{bmatrix} X1 \\ Y \end{bmatrix} = \begin{bmatrix} W1 \\ W2 \end{bmatrix}, \tag{4}$$

where $X1$ is the constant parameters and Y refers to other parameters. N denotes normal equation matrix and $N = A^{\mathrm{T}} Q_y^{-1} A$. $W = A^{\mathrm{T}} Q_y^{-1} y$. Introducing the following virtual observation equation

$$X1 - X2 = 0 \quad P \tag{5}$$

Forming formula (5) into normal matrix and substituting it into formula (4)

$$\begin{bmatrix} N11 + P & -P & N12 \\ -P & P & 0 \\ N21 & 0 & N22 \end{bmatrix} \begin{bmatrix} X1 \\ X2 \\ Y \end{bmatrix} = \begin{bmatrix} W1 \\ 0 \\ W2 \end{bmatrix} \tag{6}$$

Eliminating $X1$, a new normal matrix after reducing, the weight of constant parameters can be written as

$$\begin{bmatrix} \tilde{N}11 & \tilde{N}12 \\ \tilde{N}21 & \tilde{N}22 \end{bmatrix} \begin{bmatrix} X2 \\ Y \end{bmatrix} = \begin{bmatrix} \tilde{W}1 \\ \tilde{W}2 \end{bmatrix} \tag{7}$$

2.3.2 Connection of Process Parameters

Ionosphere-free combination is used in the process of orbit determination, so the process parameters include satellite and receiver clock offsets and zenith troposphere delay. Since the operational time of clock offset parameters is only one epoch and is eliminated as obsolete information, there is no need to consider connection. Since the operational time of troposphere delay can be set as arbitrary length, there is also no need to consider the connection of troposphere delay parameters when the operational time of the parameters is set as integer hours.

2.3.3 Connection of Ambiguity Parameters

Correctly connecting the ambiguity parameters is the critical issue for forming the complete normal matrix, reducing the number of ambiguity parameters and increasing the observation length. It is also a preparation for fixing ambiguity in the next phase. However, the number of satellites and stations participating in the process of orbit determination is very large, so different numbers of ambiguity parameters and operational time might be obtained through using different data processing methods, even for the same observed data. To solve the complex issue, MW combination and geometry-free combination are used for making the decision whether two divided ambiguity parameters at the joint point can be connected or not.

Let the mean and variance MW combination values of observed data relating to two divided ambiguities be $\bar{N}_1$, $\bar{N}_2$, σ_1 and σ_2, respectively. The judgement condition can be given as

$$\begin{aligned} |\bar{N}_1 - \bar{N}_2| &< 3\sigma \\ \sigma &= \sqrt{\sigma_1^2 + \sigma_2^2} \end{aligned} \tag{8}$$

Cycle-slips and gross errors are considered not to exist between two ambiguities joint point if formula (5) is satisfied. However, when two carrier phase observations occur of the same cycle at the same time, MW combination fails to detect these cycle-slips. So the continuity of geometry-free combination has to be taken into account in the following steps. [17, 18].

First, geometry-free observations L_g related to the first ambiguity are fitted by an n-order polynomial, and extrapolated to the epochs in the observations of second

ambiguity. Then the difference values between extrapolated values and observed values are calculated to decide whether these two ambiguity parameters can be connected or not. Since the geometry-free observations are influenced by the ionosphere delay, these differences reflect the changes of ionosphere and cycle-slip [19]. As the ionosphere is smooth and steady in a short period of time [20], the average of several differences can find out cycle-slips or errors at the joint point through using the condition following

$$\left|\bar{L}_{\mathrm{g}} - \bar{P}_{\mathrm{g}}\right| < \varepsilon, \tag{9}$$

where $\bar{L}_{\mathrm{g}}$ is the average of geometry-free observations during a period of time. $\bar{P}_g$ is the average in the same time extrapolated by previous observations. ε is the given threshold. Two ambiguity parameters can be connected if formula (8) and (9) are satisfied simultaneously.

After connecting all potential ambiguity parameters, the float ambiguities should be fixed to integer value. However, due to the existing uncalibrated hardware delays in the satellites and receivers, the ambiguities in the raw observations have no integer nature [21]. Therefore, double difference between satellites and receivers is used in integer ambiguity resolution. This is a mature method widely used in GPS ambiguity fixing and detailed descript can be found in reference [22–24]. They are not involved in this paper.

3 Experiment and Analysis

3.1 Process of Orbit Determination

Considering the optimized observation stations chosen by each satellite system and their different situations of development, the two-step orbit determination is adopted in this paper [25, 26]. First, IGS observation stations are used to generate GPS and GLONASS orbits and clock offsets, as well as to fix earth rotation parameters. Then, the GPS orbits determined in the first step are used to obtain station coordinates, station clock offsets and zenith troposphere delay of MGEX and iGMAS stations through PPP method. Finally, the observed data of MGEX and iGMAS stations are used to process BDS and GALILEO orbits and clock offsets, together with earth rotation parameters generated in the first step and station coordinates, station clock offsets and zenith troposphere delay generated in PPP. Since the number of satellites and stations can be decreased in each step, the process time required by adding observations and solving normal matrix can be thusly reduced. With most of the parameters having been calculated in the first step and PPP, only BDS and GALILEO satellite orbits and clock offsets have to be estimated in the second step. The stability and accuracy of solutions can be improved due to the few parameters. Since the same earth rotation parameters are used in both steps, the coordinate frame can be kept consistent. The flowchart of the process is shown in Fig. 2.

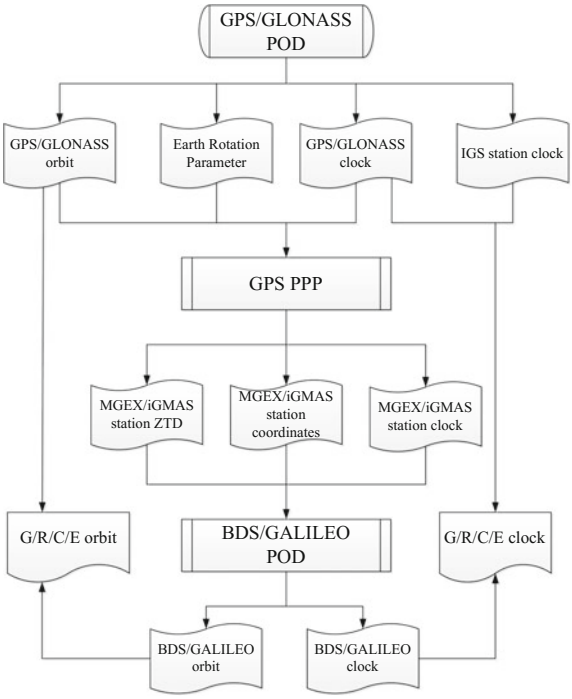

Fig. 2 The strategy of two steps orbit determination

3.2 The Results and Analysis

The new approach is implemented based on the routine data processing platform PANDA for the iGMAS analysis centre at Wuhan University [27–29]. To assess the impact of the new strategy, the user available parts in predicted orbit generated from the new and the old methods are compared. The old method is traditional 24-h determination and 24-h prediction; the new is proposed by this paper, i.e. "22 + 3"-h determination and 23-h prediction. The IGS observation stations are used to process GPS and GLONASS orbit, while MGEX and iGMAS observation stations are used to process BDS and GALILEO orbit. The distribution of the stations is shown in Fig. 3. User available part in predicted orbit of each system is compared with their reference orbit, respectively: the reference orbit of GPS is the final orbit product published by IGS, the reference orbit of GLONASS is the IGL orbit published by IGS, the reference orbit of BDS is the GMB orbit published by GFZ, and the reference orbit of GALILEO is the TUM orbit published by TUM. Four times per day at 00, 06, 12, 18 o'clock ultra-rapid orbit products are generated from days 310 to 318 in 2016 continuously, and the statistic of 3D RMS of each satellite system is shown in Table 1.

The RMS of all satellites in each system between the calculated orbit and reference orbit both generated through using two strategies is shown in Fig. 4.

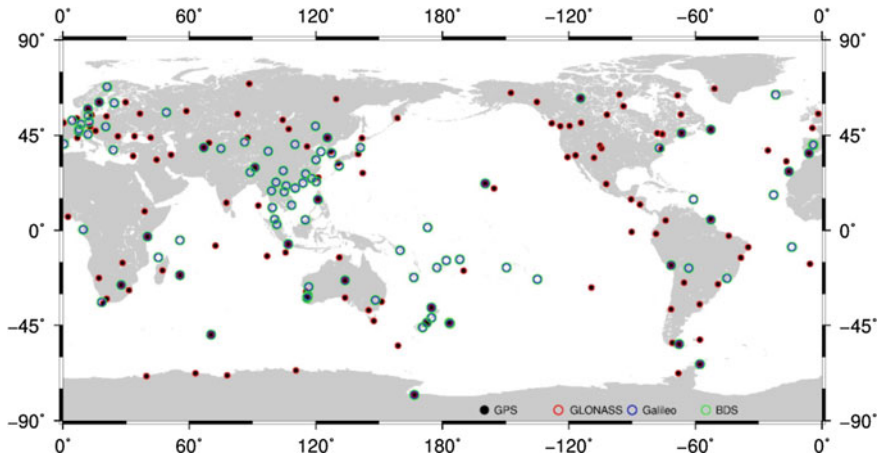

Fig. 3 The distribution of observation stations

The accuracy of all satellites in each system has improved through using the new approach proposed by this paper. The accuracy of GPS, GLONASS and GALILEO orbits has improved by 6.5, 8.9, and 14.5 %, respectively, while that of BDS GEO and IGSO/MEO orbits has improved by 14.2 and 30.2 %, respectively. Due to the well-distributed IGS observation stations all over the world, the orbit of GPS and GLONASS can be determined at a high precision. Therefore, the accuracy of GPS and GLONASS orbits did not improve significantly as BDS and GALILEO, which use MGEX and iGMAS stations concentrated in Asia and Europe region. Moreover, after having developed for a longer period of time, the force models and attitude control of the GPS and GLONASS satellites have been well researched. On the contrary, BDS and GALILEO are still in the phase of building global navigation system, the new satellites and new signals remain to be further studied. All the factors mentioned above may cause a lower accuracy of BDS and GALILEO determined orbits compared with that of GPS and GALONASS, so the accuracy of predicted orbits decreases more rapidly over time. It seems especially important to have one more hour observation values in this case. Furthermore, strict threshold is adopted in the process of connecting ambiguity parameters in case mistakes occurred. Therefore, it is inevitable to keep some two ambiguities divided which should have been connected into one. Such situation interrupts the continuity of observation, and influences the ambiguity fixing. Therefore the accuracy of GPS orbits is affected by these divided ambiguity parameters.

3D RMS of all epoch in user available part of predicted orbit in each system is shown in Fig. 5. No matter which method is used, the accuracy of predicted orbit decreases over time. Thusly big jump occurred at the joint of two consecutive orbits, leading to the discontinuity. However, compared with the traditional method with 24-h determination and 24-h prediction, one more hour observation values are used in proposed approach and the interval between the starting time of prediction

Table 1 The 3D RMS of the satellites (unit: mm)

		GPS		GLS		BDS				GAL	
						G		I/M			
DOY	Hour	24	22 + 3	24	22 + 3	24	22 + 3	24	22 + 3	24	22 + 3
310	00	55.0	53.4	95.7	92.1	1857.5	1731.8	483.9	438.2	282.5	259.3
	06	58.8	55.9	102.5	96.5	1956.2	1733.5	395.1	332.7	431.2	368.2
	12	58.8	55.1	123.2	106.0	2167.0	1728.2	567.3	498.7	400.2	321.1
	18	63.6	60.5	132.0	128.6	2285.5	1965.5	549.8	303.3	348.7	309.5
311	00	59.9	56.3	116.5	105.2	2468.0	2323.8	530.0	420.3	350.1	314.5
	06	64.9	57.5	131.1	115.6	3144.8	2397.2	307.9	271.8	275.5	297.2
	12	78.6	69.8	127.3	119.0	2433.2	2154.8	654.0	490.2	374.1	296.3
	18	110.3	102.5	161.8	155.7	2690.8	2340.8	665.6	287.4	322.0	292.0
312	00	110.2	102.7	103.2	110.9	1741.0	1398.5	475.6	403.8	341.5	325.2
	06	67.4	64.0	141.8	152.4	2379.0	1715.5	386.8	408.6	297.7	280.9
	12	65.2	65.8	140.2	120.5	2506.2	1559.3	617.0	515.4	358.8	307.6
	18	54.5	49.8	124.6	103.9	2235.2	1972.8	368.0	324.0	296.3	264.0
313	00	60.9	56.1	123.0	115.9	2771.0	2291.2	442.3	340.7	310.2	250.8
	06	63.5	60.8	150.6	138.5	1708.5	1856.0	396.7	453.0	347.7	325.1
	12	68.5	59.6	114.2	102.2	2315.3	1885.7	612.7	432.8	363.7	376.8
	18	58.1	58.6	125.7	118.0	1581.0	1636.5	456.2	313.3	303.3	277.5
314	00	63.7	57.6	125.1	121.0	5031.2	4700.2	370.6	278.0	359.4	333.8
	06	63.1	61.0	129.9	119.3	4013.6	4427.4	475.2	457.8	589.0	254.2
	12	83.4	75.0	129.8	109.6	4540.8	4101.8	949.8	732.9	414.2	355.7
	18	78.2	76.8	121.6	111.9	3072.0	3212.6	283.6	298.6	459.8	371.7
315	00	84.6	76.8	116.0	104.5	2264.6	2201.2	386.4	328.2	314.3	288.9
	06	81.7	79.9	131.5	115.3	2257.8	1553.8	644.6	515.9	350.5	288.5
	12	84.8	78.6	136.6	117.8	2259.8	1772.6	589.4	441.6	394.3	360.1
	18	71.4	68.1	124.5	117.3	2614.0	2282.4	456.2	394.0	506.8	457.1
316	00	91.6	84.5	103.5	88.4	1457.6	1337.8	453.0	323.1	327.6	316.6
	06	82.4	80.8	131.2	130.0	2855.8	2259.0	503.3	411.9	326.3	309.7
	12	90.4	94.1	146.9	136.2	2059.4	1611.6	403.2	354.6	356.7	327.8
	18	70.8	64.8	136.8	122.9	2020.0	1731.7	565.7	317.7	298.7	240.9
317	00	90.1	75.5	121.9	109.6	2703.4	2659.8	485.8	291.3	353.8	345.1
	06	88.3	86.2	140.0	131.4	2408.2	2000.4	750.1	526.0	337.2	281.3
	12	84.5	78.7	165.7	141.3	3055.4	2987.4	347.9	509.8	426.9	371.5
	18	93.9	88.8	115.3	100.1	4664.8	4642.0	800.4	358.2	463.6	391.6
318	00	63.6	57.7	113.1	106.0	1041.5	1072.5	588.3	324.2	303.8	311.2
	06	77.1	73.6	132.3	124.9	2706.0	1964.5	772.0	502.9	317.3	289.6
	12	71.6	62.1	135.5	119.1	1713.5	617.0	638.9	486.0	327.6	281.5
	18	73.9	70.9	130.3	119.8	2183.5	1978.5	495.2	401.2	327.8	277.6
Average		74.6	70.0	127.8	117.4	2532.3	2216.8	524.1	402.4	360.0	314.5

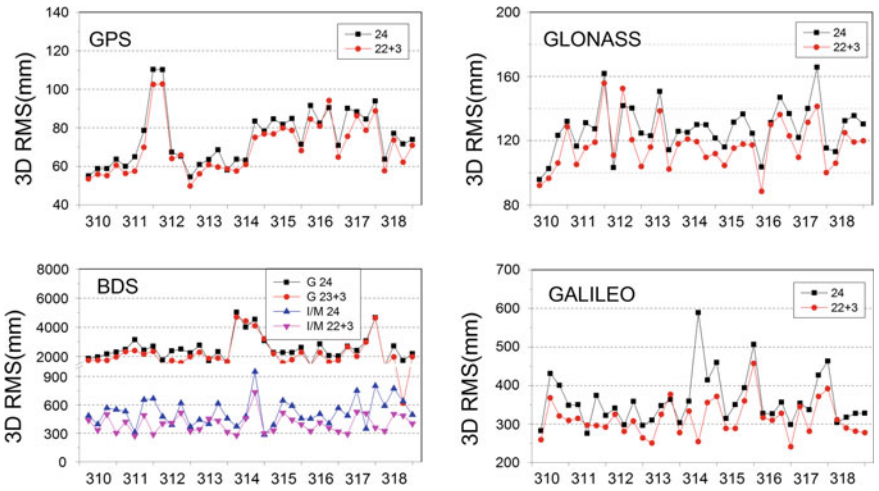

Fig. 4 The orbit precision of each navigation satellite system (processing 00, 06, 12, 18 ultra-orbit products on each single day)

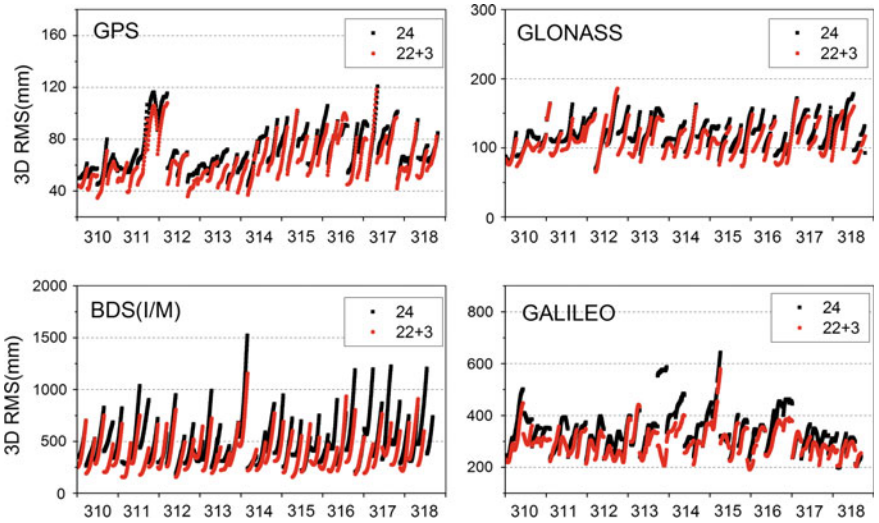

Fig. 5 All epoch precision in each navigation satellite system

and user available part decreases one hour accordingly. Therefore, the proposed approach has a better performance than the traditional method.

Figure 6 shows the statistical RMS of all satellites in each system. The accuracy of all satellites can be improved during user available part in predicted orbit through using the new approach. The accuracy of GPS satellites in user available part is

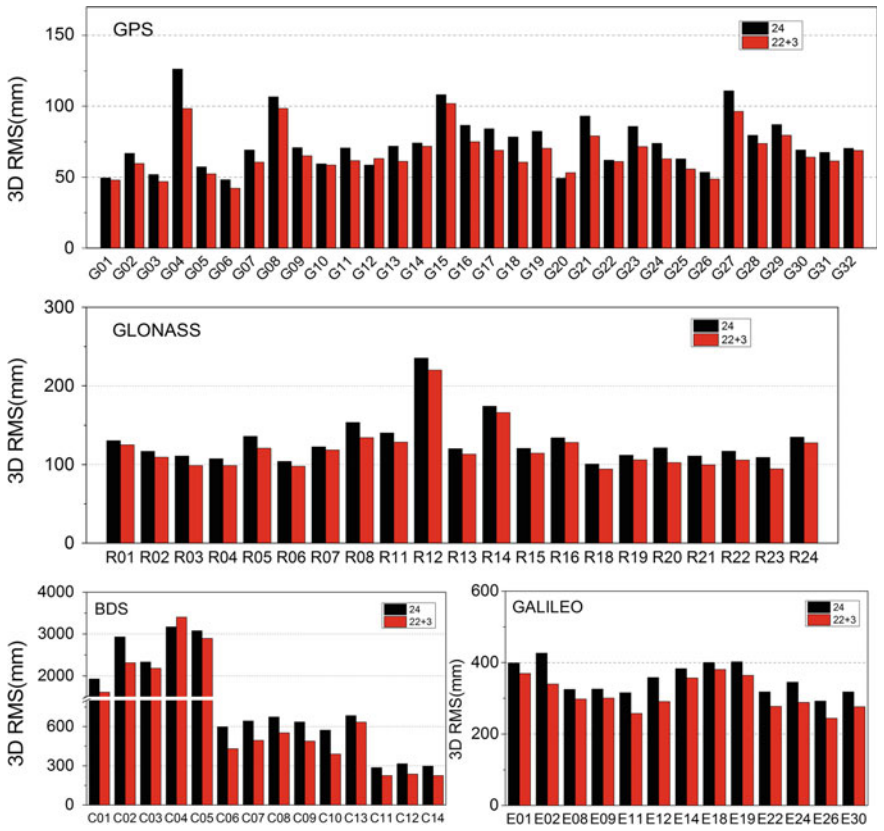

Fig. 6 Mean RMS of every satellite in each navigation system on 310–318

almost less than 80 mm. Because the only satellite belongs to BLOCK IIA, G04 has a bad performance compared with other GPS satellites, which have a better attitude control than G04, especially in the shadow period. Figure 7 shows that the accuracy of G04 in user available part has a bad performance in all epoch on 310–318. The accuracy of G08 and G27 is affected by the period from 311 20 o'clock to 312 8 o'clock, and both of the two satellites accuracy have the same trend of variability. These two satellites are likely to manoeuvre their attitudes at the midnight of 311. G15 has a bad performance because of the sudden change from 317 20 o'clock to 318 14 o'clock. The accuracy of GLONASS satellites in user available is almost less than 150 mm. Due to the motionless character to the observation stations position, the determination of GEO satellites is a challenge now. User available part is influenced by its bad determination. The accuracy of BDS MEO during user available part is less than 300 mm, better than GALILEO's 400 mm. But the

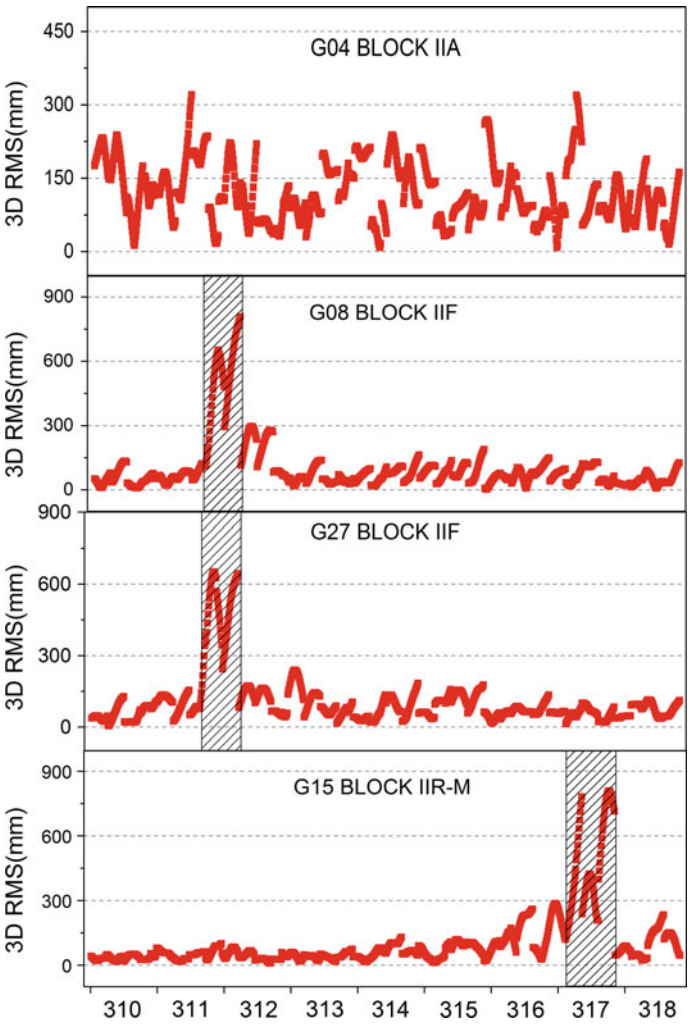

Fig. 7 RMS of one satellite in GPS system

accuracy of BDS IGSO is 600 mm. As shown in Table 1, the accuracy of BDS IGSO/MEO during user available part has improved quite a lot than any other system. This means that the accuracy of BDS IGSO/MEO decreases more rapidly in predicted orbit. Its dynamical models, attitude controls and the theory of integration need to be further studied.

4 Conclusion

A new approach to generate ultra-rapid orbit products is proposed in this paper which is suitable for iGMAS and IGS analysis center. Compared to the traditional method with 24-h determination and 24-h prediction, the new approach can use 25 h observed data through the strategy "22 + 3". The user available part in predicted orbit decreases from 2nd–8th to 1st–7th h. Processing the ultra-rapid orbit products through using the new and the old approaches from days 310 to 318, and comparing the user available part in predicted orbit with reference orbits and the results show that:

(1) The accuracy of all satellites in each system during user available part has improved through using new approach proposed by this paper. The accuracy of GPS improves has improved by 6.5%, GLONASS 8.9%, BDS GEO and IGSO/MEO 14.2% and 30.2%, respectively, and GALILEO 14.5%.
(2) With the application of the new approach, the accuracy of GPS during user available part is almost less than 80 mm, GLONASS 150 mm, BDS IGMO and MEO 600 mm and 300 mm, respectively, and GALILEO 400 mm.

Acknowledgements This work was supported by iGMAS analysis center at Wuhan University.

References

1. Cai H, Chen K, Xu T et al (2015) The iGMAS combined products and the analysis of their consistency. China satellite navigation conference (CSNC) 2015 proceedings: Vol III. Springer, Berlin, pp 213–226
2. Rodger SH, Genkins J, Mcmahon I et al (2009) Ambiguity resolution in precise point positioning with hourly data. GPS Solutions 13(4):263–270
3. Sobolev SV, Babeyko AY, Wang R et al (2007) Tsunami early warning using GPS-Shield arrays. J Geophys Res: Solid Earth 112 (B8)
4. Chen Junping, Li Haojun, Bin Wu et al (2013) Performance of real-time precise point positioning. Mar Geodesy 36(1):98–108
5. Yibin (2008) Theory and realization of GPS orbit integration. Geo-spatial Inform Sci 11(1): 1–5
6. Beutler G, Brockmann E, Hugentobler U et al (1996) Combining consecutive short arcs into long arcs for precise and efficient GPS orbit determination. J Geodesy 70(5):287–299
7. Brockmann E (1997) Combination of solutions for geodetic and geodynamic applications of the Global positioning system (GPS). Geod-Geophys Arb Schweiz Vol. 55:55
8. Dong D, Herring TA, King RW (1998) Estimating regional deformation from a combination of space and terrestrial geodetic data. J Geodesy 72(4):200–214
9. Andersen PH (2000) Multi-level arc combination with stochastic parameters. J Geodesy 74(7):531–551
10. Yibin Yao (2007) Theory and realization of GPS orbit integration. Geomatics Inf Sci Wuhan Univ 32(6):510–514
11. Yidong Lou, Chuang Shi, Maorong Ge (2008) GPS real time orbit determination and initial results analysis. Geomatics Inf Sci Wuhan Univ 33(8):815–817

12. Lutz S, Meindl M, Steigenberger P et al (2016) Impact of the arc length on GNSS analysis results. J Geodesy 90(4):1
13. Liu Weiping, Hao Jinming, Yu Heli (2016) Solution method and precision analysis of multi-days orbit combination of BeiDou satellites. Acta Geodaetica et Cartographic Sinica. 45(10):1157–1164
14. Choi KK, Ray J, Griffiths J et al (2013) Evaluation of GPS orbit prediction strategies for the IGS Ultra-rapid products. GPS Solutions 17(3):403–412
15. Duan B, Chen J (2016) Extended filter for real-time Multi-GNSS orbit determination. Igs Workshop
16. Mervart L, Weber G (2011) Real-time combination of GNSS orbit and clock correction streams using a Kalman filter approach. In: proceedings of international technical meeting of the satellite division of the institute of navigation. pp 707–711
17. Cai C, Liu Z, Xia P et al (2013) Cycle slip detection and repair for undifferenced GPS observations under high ionospheric activity. GPS Solutions 17(2):247–260
18. Zhao Q, Sun B, Dai Z et al (2015) Real-time detection and repair of cycle slips in triple-frequency GNSS measurements. GPS Solutions 19(3):381–391
19. Feng Y (2008) GNSS three carrier ambiguity resolution using ionosphere-reduced virtual signals. J Geodesy 82(12):847–862
20. Fritsche M, Dietrich R, Knöfel C et al (2005) Impact of higher-order ionospheric terms on GPS estimates. Geophys Res Lett 32(23):113–133
21. Li X, Ge M, Zhang H et al (2013) A method for improving uncalibrated phase delay estimation and ambiguity-fixing in real-time precise point positioning. J Geodesy 87(5): 405–416
22. Dong D-N, Bock Y (1989) Global positioning system network analysis with phase ambiguity resolution applied to crustal deformation studies in California. J Geophys Res Atmos 94 (B4):3949–3966
23. Ge M, Gendt G, Dick G et al (2005) Improving carrier-phase ambiguity resolution in global GPS network solutions. J Geodesy 79(1):103–110
24. Ge M, Gendt G, Rothacher M et al (2008) Resolution of GPS carrier-phase ambiguities in precise point positioning (PPP) with daily observations. J Geodesy 82(7):389–399
25. Li Min (2011) Research on multi-GNSS precise orbit determination theory and application. Wuhan University
26. Guo J, Xu X, Zhao Q et al (2016) Precise orbit determination for quad-constellation satellites at Wuhan University: strategy, result validation, and comparison. J Geodesy 90(2):1–17
27. Liu JN, Mao-Rong GE (2003) PANDA software and its preliminary result of positioning and orbit determination. Wuhan Univ J Nat Sci 8(2):603–609
28. Shi C, Zhao Q, Hu Z et al (2013) Precise relative positioning using real tracking data from COMPASS GEO and IGSO satellites. GPS Solutions 17(1):103–119
29. Shi C, Zhao QL, Li M et al (2012) Precise orbit determination of Beidou Satellites with precise positioning. Sci China: Earth Sci 55(7):1079–1086

Annual Variation Analysis and Forecasting Model of DCB Parameters for BDS Satellites

Xiaoli Wu, Xiao liu, Shuai Gao, Feng Zhou, Li Gu and Enqiang Dong

Abstract The accuracy and stability of differential code bias (DCB) parameters are important to the timing and positioning service performance. According to the actual observation data of Beidou navigation satellite system (BDS) from 2013 to 2015, DCB_{12} parameters and DCB_{13} parameters of BDS satellites are analyzed, and the long-term statistical results of DCB parameters of different types of satellites are given. The annual standard deviation of the DCB parameters of GEO satellites with good observation conditions is 0.3 ns. The statistical standard deviation of most IGSO satellites DCB parameters are less than 0.4 ns, and the statistical standard deviation of MEO satellite's DCB are about 0.5 ns. The annual statistical results show that the average DCB parameter of the BDS satellites has an annual slow change of 0.3 ns. The polynomial fitting method was used to forecast the long-term trend of DCB parameters. The results show that the mean annual variation trend of DCB parameters of BDS satellites is similar to that of GPS satellites, but the BDS satellite DCB parameter stability is 0.5 ns, which is affected by the regional distribution of the measurement stations and the poor data quality of some receivers, which has a large gap with the GPS satellite DCB parameters provided by the IGS ionosphere center (30-days stability better than 0.1 ns).

Keywords BDS · DCB · Forecasting model · Stability

1 Introduction

Pseudorange observations of global navigation satellite system (GNSS) are well known to be affected by the differential code biases (DCBs), which need to be precisely calibrated for pseudorange-based positioning, timing, and ionospheric modeling. Generally, DCBs can be classified into two categories: intra-frequency

X. Wu (✉) · X. liu · S. Gao · F. Zhou · L. Gu · E. Dong
Beijing Satellite Navigation Center, 100094 Beijing, China
e-mail: jasminework@163.com

J. Sun et al. (eds.), *China Satellite Navigation Conference (CSNC) 2017 Proceedings: Volume III*, Lecture Notes in Electrical Engineering 439,
DOI 10.1007/978-981-10-4594-3_18

bias and inter-frequency bias. The first one is the bias between two code observations at the same frequency, and the second one is the bias between code observations at two different frequencies [12]. The differential code deviation of different frequencies of the satellite is usually transmitted in the form of TGD (timing Group Delay) parameters in the navigation message for users. The GPS TGD parameter means the time delay between L1 phase and L1 L2 non-ionosphere combination reference point, which is equal to DCB between L1 and L2 frequencies multiplied by a frequency-dependent factor. Beidou navigation satellite system (BDS) broadcast tri-band navigation signals, and two TGD parameters are broadcasted in the navigation message. TGD1 is the differential code biases between B1 and B3 frequencies, TGD2 is the differential code biases between B2 and B3 frequencies [1, 10].

Before the launch of the satellite, its DCB parameters will be calibrated by the corresponding manufacturers in the laboratory. When the satellite is in orbit, due to the change of environment, the satellite DCB parameters do not match with the initial values. Because the DCB parameters are coupled with ionospheric delay corrections, the accuracy of DCB parameters depends largely on the ionospheric modeling accuracy [5, 7]. At present, DCB parameter calculation methods are mainly divided into two kinds. One is to calculate the single station/region/global ionospheric model and DCB parameters altogether, the other is to deduct ionospheric delays according to GIM (Global Ionosphere Map) from the without geometric combination observation [10]. A method is proposed to use the nonintegrated Precise Point Positioning (PPP) to make full use of the phase data to obtain high-precision ionospheric delay extraction accuracy [5, 12]. Multi-GNSS observations are used to determine differential code biases of multi-system [7].

At present, the research on the DCB parameters of GPS and Beidou satellites are mostly concentrated in the solution method and the accuracy evaluation in short time. The accuracy of DCB parameters of GPS satellites calculated by regional observation data is better than 0.2 ns [2, 9]. The accuracy of the BDS satellite DCB parameters is better than 0.5 ns [1, 5]. The IGS ionospheric team independently analyzed the long-term variation of GPS satellite DCB by four independent ionospheric Association Analysis Centers (IAACs) [4]. The results showed that the GPS satellite DCB parameters had a slow annual change of 0.3 ns, and the 30-days calculated DCB stability is better than 0.1 ns [4].

In this paper, the DCB parameters of the Beidou satellites are solved by using the regional low-order spherical harmonic function modeling and DCB parameter modeling, and the DCB parameters of different types of satellites of GEO, IGSO, and MEO are calculated by using the actual observation data of Beidou from 2013 to 2015. Long-term variation characteristics analysis is listed then, and GPS synchronization results are compared. Finally, the linear prediction model of Beidou satellite DCB parameters is analyzed.

2 DCB Determination Method of BDS Satellites

According to the GNSS observation equation, the two-frequency pseudorange without geometric combination is calculated as Eq. 1

$$P_4 = P_1 - P_2 \tag{1}$$

P_1 and P_2 are respectively pseudorange observations of Beidou system at B1 and B2 frequencies. The without geometric combination eliminates all geometric-related error terms except the ionospheric delay and the DCB parameters of the satellite and receiver. In the case of neglecting multipath and measurement errors, the without geometric combination can be described as Eq. 2:

$$P_4 = -\left(\frac{f_1^2 - f_2^2}{f_2^2}\right) F(z) \cdot I + c \cdot \Delta b^s + c \cdot \Delta b_r \tag{2}$$

f_1 and f_2 are the B1 and B2 frequencies of the BDS satellite, Δb^s is the satellite DCB, Δb_r is the receiver DCB, c is the speed of light, and I is the zenith ionospheric delay for the receiver to the satellite puncture site, $F(\cdot)$ is the ionospheric projection function, and z is the zenith angle.

$$I = \frac{40.28}{f_1^2} \cdot \mathrm{VTEC} \tag{3}$$

Since the DCB parameters of the satellite and receiver are relatively stable in the short term, they are usually treated as constants [5]. Suppose we use the spherical harmonic function to calculate the VTEC at each puncture point of each epoch.

$$\mathrm{VTEC} = \sum_{n=0}^{n_{\max}} \sum_{m=0}^{n} P_{\mathrm{nm}}(\sin \varphi) \cdot (C_{\mathrm{nm}} \cos(m\lambda) + S_{\mathrm{nm}} \sin(m\lambda)) \tag{4}$$

Where φ is the latitude at the puncture site, λ is the location at the puncture site, $n_{\max}$ is the order of the spherical harmonic function, P_{nm} is the normalized Legendre function, and C_{nm} and S_{nm} are the spherical harmonic coefficients to be determined.

PRN1 satellite DCB parameters are fixed as calibration, and $n_{\max}$ is set 6. With 24 h of Beidou actual observation data, we can get a group spherical harmonic coefficients and the DCB parameters of both satellites and receivers using the least squares method.

3 Analysis of Long-Term Variation Characteristics of BDS Satellite DCB Parameters

According to the actual observation data of the BDS ground monitoring station from 2013 to 2015, the DCB parameters of the BDS satellites and the receivers are calculated using the compound solution of the regional spherical harmonic function model and the satellite and receiver DCB parameters. In the process of calculation, the gross error is removed from the observation data, and the receiver observation data with the receiver DCB parameter RMS exceeding the threshold value (1–2 ns) is also removed after the first round of calculation. The RMS of the satellite DCB parameters calculated using 24 h data is better than 0.5 ns.

Tables 1 and 2 show the statistical results for the years from 2013 to 2015. Table 1 shows the annual statistical results of DCB_{12} parameter, which describe the code deviation between B1 and B2 frequency of BDS satellites. Table 2 shows the annual statistical results of DCB_{13} parameter, which describe the code deviation between B1 and B3 frequency of BDS satellites. As an example, Fig. 1 shows the results of the calculation of DCB_{12} parameters of BDS satellites in 2014.

From Table 1, the statistical standard deviation of the DCB parameters of two GEO satellites (Sat3 and Sat4) with good observation conditions is 0.3 ns in the whole year of 2013. The statistical standard deviation of the IGSO satellite (Sat6–Sat9) DCB parameters are less than 0.4 ns, and the stability of DCB parameter of satellite PRN 10 (IGSO satellite) is slightly worse, reaching 0.45 ns. The statistical standard deviation of MEO satellites (Sat11–Sat14) DCB are about 0.5 ns.

It can be seen from Fig. 1 that the DCB_{12} parameter of Sat3 gradually jumped 2 ns within a week since September 23 in 2014. On the same time, the DCB_{13} parameter of Sat3 jumped in the same direction with the order of magnitude changes.

Table 1 Statistic results of BDS satellites' DCB_{12} parameters (unit:ns)

PRN	2013		2014		2015	
	Mean	Std	Mean	Std	Mean	Std
Sat1	24.590	0.000	24.590	0.000	24.590	0.000
Sat2	19.632	0.476	19.492	0.499	18.954	0.452
Sat3	14.424	0.309	14.725	0.794	15.869	0.296
Sat4	14.334	0.318	14.261	0.367	13.759	0.308
Sat5	11.581	0.524	11.406	0.489	11.197	0.482
Sat6	11.249	0.405	11.222	0.401	10.824	0.397
Sat7	15.768	0.376	15.690	0.426	15.278	0.425
Sat8	14.451	0.380	14.311	0.401	14.150	0.319
Sat9	5.289	0.391	5.183	0.421	4.899	0.371
Sat10	5.809	0.446	5.603	0.413	5.198	0.425
Sat11	5.805	0.459	5.671	0.454	5.226	0.501
Sat12	7.934	0.485	7.494	0.462	7.115	0.528
Sat13	5.738	0.466	5.537	0.457	–	–
Sat14	9.345	0.484	9.001	0.450	8.629	0.530

Table 2 Statistic results of BDS satellites' DCB_{13} parameters (unit:ns)

PRN	2013		2014		2015	
	Mean	Std	Mean	Std	Mean	Std
Sat1	14.190	0.000	14.190	0.000	14.190	0.000
Sat2	5.843	0.410	5.758	0.363	4.922	0.304
Sat3	5.288	0.295	5.597	0.768	6.625	0.213
Sat4	6.323	0.311	6.313	0.287	5.696	0.271
Sat5	2.918	0.506	2.865	0.394	2.561	0.344
Sat6	9.955	0.389	9.938	0.343	9.754	0.268
Sat7	17.054	0.372	16.993	0.329	16.603	0.391
Sat8	14.712	0.349	14.573	0.311	14.174	0.401
Sat9	9.394	0.438	9.323	0.419	8.820	0.374
Sat10	9.013	0.432	8.895	0.491	8.473	0.472
Sat11	8.331	0.469	8.167	0.540	7.632	0.534
Sat12	8.541	0.478	8.287	0.586	7.754	0.585
Sat13	8.757	0.557	8.640	0.498	–	–
Sat14	11.886	0.542	11.738	0.539	10.985	0.610

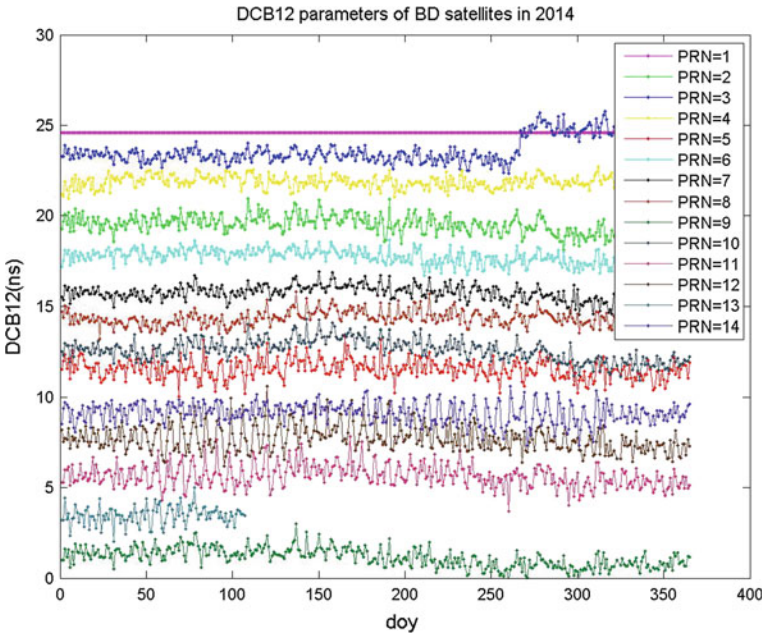

Fig. 1 DCB_{12} parameters of BD satellites in 2014

Investigation result shows that Sat3 occurred a recovery from failure on September 23 in 2014, after that the hardware delay at B1 frequency changes 2 ns, so the DCB_{12} and DCB_{13} parameters of Sat2 both changed 2 ns. Sat13 was not available for long periods of time since April 18, 2014, so the annual statistic results of the DCB parameters of Sat13 just counted from 1 to 138 days.

The 30-days statistical analysis results show that the standard deviation of BDS satellite DCB parameters is about 0.3–0.5 ns. From the annual statistical results, the average DCB parameters of each type of BDS satellites have a slowly changing tendency of 0.3 ns year by year.

According to the DCB parameters of GPS satellites provided by CODE (European Orbit Determination Center), the annual variation of DCB parameters of GPS satellites in 2014 was analyzed. Four GPS satellites (G03, G06, G09, G30) were replaced by GPS in 2014, Original BLOCK IIA satellites were substituted by BLOCK IIF satellites. After the replacement, the DCB parameters of the new satellites are 5–10 ns. In the initial stage, the DCB of the new satellite is slightly hopped, and the subsequent DCB is stable (the standard deviation is less than 0.1 ns in 30 days). The rest of the satellite DCB parameters are slightly jumped after the new satellite is launched. Because the constrained condition of GPS satellite DCB parameter calculation is that all satellites DCB parameters are zero, when the number of satellites participating in the calculation is changed from 32 to 31, or the number of satellites involved in solving is 32, the DCB value of the new replacement satellites will affect the DCB parameters of the original satellites in orbit.

4 Prediction Analysis

The physical characteristics of the satellite DCB parameter determines that it varies slowly, so we use polynomial fitting method to analyze the prediction characteristic of DCB parameters. Taking the DCB_{12} parameter in 2013 as an example, we get the second-order polynomial fitting coefficients using the first 200-days DCB_{12} results, then we can get the predict DCB_{12} results using these fitting coefficients. The prediction results are compared with the calculated DCB_{12} parameters with real observation. The fitting coefficients and the predict results are shown in Table 3. As can be seen from Table 3, the second-order polynomial fitting accuracy is slightly higher than the linear fitting. The first-order fitting coefficient is 10^{-3}, and the second-order fitting coefficient is 10^{-5}, indicating that there is a slow linear trend for BDS DCB parameters. Because the annual change and the calculation error of DCB parameters for BDS satellites are in the same order of magnitude, there is no significant difference among 30,60,90 days forecasting results.

Table 3 Fitting RMS and prediction accuracy of BDS satellites DCB_{12} parameters (unit:ns)

PRN	Std	Fitting coefficient			Fit RMS		Prediction accuracy			
		Constant	First order	Second order	Linear	Quadratic	7 days	30 days	60 days	90 days
Sat2	0.48	19.53	3.86E-03	−1.34E-05	0.48	0.44	0.43	0.38	0.41	0.56
Sat3	0.31	14.37	1.90E-03	−6.52E-06	0.31	0.30	0.21	0.23	0.34	0.35
Sat4	0.32	14.34	5.54E-04	−2.50E-06	0.32	0.32	0.39	0.31	0.36	0.26
Sat5	0.52	11.45	3.27E-03	−1.05E-05	0.52	0.51	0.37	0.60	0.50	0.58
Sat6	0.40	11.15	4.88E-03	−1.77E-05	0.40	0.32	0.25	0.23	0.46	0.39
Sat7	0.38	15.35	7.61E-03	−2.18E-05	0.38	0.30	0.16	0.28	0.31	0.38
Sat8	0.34	14.06	5.17E-03	−1.23E-05	0.34	0.31	0.22	0.28	0.30	0.36
Sat9	0.39	5.27	3.39E-03	−1.33E-05	0.39	0.33	0.25	0.38	0.29	0.42
Sat10	0.45	5.25	1.06E-02	−3.11E-05	0.47	0.34	0.21	0.29	0.28	0.47
Sat11	0.46	5.65	3.79E-03	−1.21E-05	0.46	0.44	0.48	0.46	0.36	0.42
Sat12	0.49	7.71	4.77E-03	−1.46E-05	0.49	0.46	0.35	0.33	0.53	0.46
Sat13	0.47	5.56	5.14E-03	−1.71E-05	0.47	0.42	0.44	0.52	0.46	0.38
Sat14	0.48	9.42	1.86E-03	−9.26E-06	0.48	0.45	0.36	0.51	0.39	0.43

5 Conclusion

Based on the actual observation data of the BDS monitoring stations, the DCB parameters of BDS satellites are calculated by the compound determination method for regional low-order spherical harmonic function model and the satellite and receiver DCB parameters. The long-term variation and prediction characteristics of the DCB parameters of the 14 orbiting satellites are analyzed. The results show

1. The calculation stability of DCB satellite DCB parameters is related to the number of observable stations, and the standard deviation of DCB parameters of PRN3 and PRN4 satellites (GEO satellites) with good observation condition is better than 0.3 ns.
2. The stability of the DCB parameters of BDS GEO satellite is the best, the IGSO satellite is the second, and the MEO satellite is the worst.
3. The standard deviation of DCB_{12} and DCB_{13} parameters of BDS satellites are 0.3–0.6 ns for the whole year and 0.3–0.5 ns for 30 days, which is different from the stability of DCB parameters in GPS satellites (the standard deviation is less than 0.1 ns in 30 days). The poor data quality of some monitoring receivers and the distribution of regional observational data may be the reason for poor stability of DCB parameters for BDS satellites.
4. Since the annual change and the calculation error of DCB parameters for BDS satellites are in the same order of magnitude, there is no significant difference among 30,60,90 days forecasting results.

References

1. Fan J, Wu X, Li Y, Wei G (2013) COMPASS satellites DCB parameter accuracy assessment based on tri-frequency data. Chin Space Sci Technol 33(4):62–70
2. Fan L, Zhong S, Li Z, Ou J (2016) Effect of tracking stations distribution on the estimation of differential code biases by GPS satellites based on uncombined precise point positioning. Geomatics Inf Sci Wuhan Univ 41(3):316–321
3. Guo F, Zhang X, Wang J (2015) Timing group delay and differential code bias corrections for BeiDou positioning. J Geod 89(5):427–445
4. Hernández-Pajares M, Juan JM, Sanz J, Orus R, Garcia-Rigo A, Feltens J, Komjathy A, Schaer SC, Krankowski A (2009) The IGS VTEC maps: a reliable source of ionospheric information since 1998. J Geod 83(3–4):263–275
5. Li Z, Yuan Y, Li H et al (2012) Two-step method for the determination of the differential code biases of COMPASS satellites. J Geodesy 86(11):1059–1076.
6. Li Z, Yuan Y, Fan L, Huo X, Hsu H (2014) Determination of the Differential. Code bias curr BDS satell. IEEE trans geosci remote sens 52(7):3968–3979
7. Montenbruck O, Hauschild A, Steigenberger P (2014) Differential code bias estimation using multi-GNSS observations and global ionosphere maps. Navig 61(3):191–201
8. Xing N, Wu X, Hu X, Su R (2012) Secular changes in differential code bias of COMPASS system. In: China Satell Navig Conf (CSNC) 2012 Proceedings, Springer, Heidelberg, 243–251

9. Wang N, Yuan Y, Li Z, Montenbruck O, Tan B (2016) Determination of differential code biases with multi-GNSS observations. J Geod 90:209–228
10. Wu X, Ping J, Liu L (2011) Estimation of differential code bias for regional satellite navigation. Geomatics Inf Sci Wuhan Univ 10:1218–1221
11. Zhang Q, Zhao Q, Zhang H (2014) BDS satellites and receivers DCB resolution, China Satell Navig Conf (CSNC) 2014 Proceedings. Springer Berlin Heidelberg, Nanjing, vol 3, pp 187–197
12. Zhang B, OU J, Yuan Y, LI Z (2011) Calibration of slant total electron content and satellite receiver's differential code biases with uncombined precise point positioning techniq. Acta Geodaet Cartographica Sinica 40(4):447–453 (CH)

Real-Time GPS Satellite Clock Estimation Based on OpenMP

Kang Gao, Shoujian Zhang, Jiancheng Li, Xinyun Cao and Kaifa Kuang

Abstract The undifferenced method is the usual way to estimate GPS satellite clock corrections by dealing with globally distributed reference stations. However, the task is very time consuming when estimating a lot of ambiguity parameters, so it is difficult to generate high-rate real-time GPS clock corrections. In order to obtain 1 Hz GPS clock corrections based on intensive reference stations, the analysis center of IGS, namely GFZ, CODE uses the epoch difference approach to remove ambiguity parameters. And yet, the satellite orbit must be known in advance, because the models for orbit determination and for clock corrections estimation are different. According to this paper, the most time-consuming two parts are gain matrix computation and covariance matrix update. Therefore, the single observable Kalman filter is involved directly to speed up gain matrix computation and OpenMP technique is also used to accelerate the covariance matrix update. In order to analyze the accuracy of GPS satellite clock corrections and computing efficiency of GPS satellite clock estimation, the global 49 IGS reference stations distributed uniformly are chosen to compute satellite clock corrections between 2015-10-7 and 2015-10-7 and interval of estimated clock corrections is 60 s. In experiment, the result shows that using 16 cores in server to estimate satellite clock needs 1 s every epoch and compared to IGS 30 s clock products, the difference is smaller than 0.5 ns. So, the approach proposed in this paper can satisfy the 1 Hz GPS satellite clock real-time estimation.

Keywords Real-time GPS satellite clock · Kalman filter · OpenMP

K. Gao · S. Zhang (✉) · J. Li · X. Cao · K. Kuang
School of Geodesy and Geomatics, Wuhan University, Wuhan 430079, China
e-mail: shjzhang@sgg.whu.edu.cn

K. Gao
e-mail: gaokang@whu.edu.cn; whurinex@163.com

J. Sun et al. (eds.), *China Satellite Navigation Conference (CSNC) 2017 Proceedings: Volume III*, Lecture Notes in Electrical Engineering 439,
DOI 10.1007/978-981-10-4594-3_19

1 Introduction

Real-time precise orbit and satellite clock products are the prerequisites for real-time precise point positioning. Currently, the predicted part of ultra-rapid orbit product provided by IGS meets the accuracy of 5 cm, which satisfies the Real-Time Precise Point Positioning (RT-PPP). However, the predicted clock corrections cannot be applied to it for the poor accuracy of 3 ns. Therefore, determining the real-time satellite clock corrections has become a research focus in the international. In order to provide the real-time precise satellite clock corrections service, the IGS Real-Time Working Group (RTWG) was established in 2001 [1] and the IGS announced the "Call for Participation in the IGS Real-time Pilot Project" in 2007 (http://www.rtigs.net).

Currently, the usual way to estimate real-time satellite clock corrections with Kalman filter is using ionosphere-free combination to eliminate the first order of ionospheric delay [2]. The parameters estimated in this model include clock offset of station, the tropospheric zenith delay, phase ambiguity, and satellite clock offset. Because the number of the ambiguity parameters is directly proportional to the number of stations, it is very time consuming to determine the real-time satellite clock offset with intensive reference stations and is also difficult to satisfy the real-time applications [3].

In recent years, with the extensive application of precise point positioning (PPP), especially the area of the earthquake monitoring and tsunami warning, how to realize the RT-PPP using the high-rate raw data becomes a new development trend [4]. So, it puts forward a new requirement to estimate high-rate real-time satellite clock corrections.

In order to generate the high-rate real-time satellite clock corrections, a lot of researchers in the world (Ge etc.; Li etc.) adopt the epoch difference model to remove the ambiguity parameters to generate high precision relative clock offset between epochs and then combine the pseudorange observable to determine the absolute clock offset. Some experiments have shown that it is effective to generate 1 Hz satellite clock corrections.

Although the epoch difference model can avoid to estimate the ambiguity parameters and improve the computing efficiency, it makes the software design complicated. This model is difficult to simultaneously estimate satellite and orbit in only one filter because the orbit need to be known in advance. Besides, after years of research, the undifferenced ambiguity can be fixed to integer, so the combination of satellite clock estimation and orbit determination based on undifferenced ambiguity fixing has become a new trend, for example, the model and software PPP-Wizard developed by CNES [5].

During the process of realizing fast satellite clock estimation with Kalman filter based on undifferenced model, it has found that the computation of gain matrix and covariance update are time-consuming. Therefore, the single observable Kalman filter was proposed to speed up the gain matrix computation. At the same time, OpenMP technique was also used to accelerate the covariance matrix update.

2 Mathematic Model and Error Corrections for Real-Time Satellite Clock Estimation

The ionosphere-free combination for real-time GPS satellite clock estimation as follows:

$$\begin{aligned} PC &= \rho + cdt_{\mathrm{r}} - cdt^{\mathrm{s}} + M(\theta) \cdot T_w + \varepsilon_{PC}, \\ LC &= \rho + cdt_{\mathrm{r}} - cdt^{\mathrm{s}} + M(\theta) \cdot T_w + \lambda_{LC} B_{LC} + \varepsilon_{LC}. \end{aligned} \tag{1}$$

In Eq. (1), PC is ionosphere-free pseudo-range combination, LC is ionosphere-free carrier phase combination, ρ is the distance between satellite phase center and receiver phase center, dt_{r} is receiver clock offset, dt^{s} is satellite clock offset, $M(\theta)$ is mapping function of tropospheric wet delay, T_w is tropospheric zenith wet delay, λ_{LC} is the wave length of ionosphere-free combination, B_{LC} is the float ionosphere-free ambiguity, ε_{PC}, ε_{LC} is respectively unmodeled errors (including multi-path effects) in pseudorange and carrier phase.

The ρ distance also contains some error, such as satellite antenna phase center offset and variation, receiver antenna phase center offset and variation, solid tide, ocean tide, gravitational delay, relativistic effects, earth rotation, phase wind up, tropospheric dry delay, and hardware delay of receiver and satellite. All kind of errors are listed below (Table 1).

Because of inconsistency between precise satellite orbit (mass center) and observables (antenna phase center), antenna phase center offset should be corrected. At the same time, the mean phase center and instantaneous phase center is also changed with satellite elevation and/or azimuth. Similarly, correction of receiver phase center variation and offset is also need for the inconsistency between receiver antenna reference point and receiver antenna phase center. Also, the difference of instantaneous phase center and mean phase center of receiver signal is changed with satellite elevation and/or azimuth. All of this correction can be corrected by antenna file provided by IGS.

Table 1 Error corrections for real-time GPS clock corrections estimation

Error type	Correction model
Antenna phase center offset and variation	igs08.atx file model
Tide	Solid tide, ocean loading model
Gravitational delay	Model
Relativistic effects	Model
Earth rotation	Model
Phase wind up	Model
Tropospheric dry delay	Neill model
Code bias	DCB product

Solid tide, ocean tide, gravitational delay, relativistic effects, earth rotation, and phase wind up can be corrected by the standard model recommended by IGS Conversion 2010. The tropospheric delay can be divided into two components, the one is tropospheric dry delay, which can be corrected precisely by empirical model, the other is tropospheric wet delay, which is very complicated and dependent on complex atmospheric environment. Therefore, in the procedure of real-time satellite clock estimation, the Neill tropospheric model is used to correct dry delay and then apply the random walk model to represent wet delay.

It is import to note that the products provided by IGS are compatible with ionosphere-free combination of raw P1/P2 observables. Therefore, DCB must be corrected to keep consistent with IGS products when C1/X2 observables are used. C1 and X2 observables should be corrected for cross-correlation receivers and C1 observables should be corrected for non-cross-correlation receivers. The specific method and its impact on different combinations can be found in the DCB file provided by CODE [6].

According to the equation of (1), it is difficult to estimate satellite clock offset and receiver clock offset at same time because of rank defect of normal equation [2]. In order to avoid defect, one clock datum should be defined, for example, fixing the clock offset of a satellite/receiver or their combination. If the accuracy of clock datum is higher than 10^{-6} s, it is equal to use relative clock offset or absolute clock offset, because the systematic bias contained in relative clock offset can be absolutely absorbed into receiver clock offset in the process of positioning.

3 Single Observable Kalman Filter

Kalman filter is efficient to deal with dynamic real-time applications, therefore, it was chosen to estimate precise satellite clock in this paper. It needs to know the dynamic model and the observation equation. The formation can be described as:

$$\begin{cases} X_k = \Phi_{k,k-1} X_{k-1} + W_{k-1} \\ L_k = H_k X_k + V_k \end{cases}. \tag{2}$$

In Eq. (2), X_k is state vector of $t(k)$, $\Phi_{k,k-1}$ is transition matrix from $t(k-1)$ to $t(k)$, W_k is process noise matrix, L_k is observable matrix, H_k is design matrix, V_k is measurement noise matrix. W_k and V_k need to meet with zero mean Gaussian white noise characteristics.

$$\begin{cases} E(W_i) = 0, \mathrm{Cov}(W_i, W_j) = \delta_{ij} Q_i \\ E(V_i) = 0, \mathrm{Cov}(V_i, V_j) = \delta_{ij} R_i \\ \mathrm{Cov}(W_i, V_j) = 0 \end{cases} \quad \delta_{ij} = \begin{cases} 1, & i = j \\ 0, & i \neq j \end{cases} \tag{3}$$

R is covariance matrix of measurement noise and Q is covariance matrix of process noise.

The state vector for precise satellite clock estimation is as follows:

$$X = \left[(cdt_{\mathrm{r}})_{1\times m}, (cdt^{\mathrm{s}})_{1\times n}, (T_w)_{1\times m}, BLC_{1\times mn}\right]^T \tag{4}$$

m is the number of stations and n is the number of satellites.

Because of the complicated variation of receiver/satellite clock, the stochastic model of both should be set as Gaussian white noise. Tropospheric wet component, whose stochastic model can be set as random walk model, usually changes slowly in most case. When there's no cycle slip, float ambiguity can be seen as constant, on the contrary, it should be treated as Gaussian white noise. Therefore, the mathematic formations are as follows:

$$\Phi_{k,k-1} = \begin{bmatrix} 0_{1\times m} & 0_{1\times n} & 0_{1\times m} & 0_{1\times mn} \\ 0_{1\times m} & 0_{1\times n} & 0_{1\times m} & 0_{1\times mn} \\ 0_{1\times m} & 0_{1\times n} & I_{1\times m} & 0_{1\times mn} \\ 0_{1\times m} & 0_{1\times n} & 0_{1\times m} & \delta_{1\times mn} \end{bmatrix} \tag{5}$$

$$Q_k = \begin{bmatrix} \sigma^2_{dt_{\mathrm{r}}} \cdot I_{1\times m} & 0_{1\times n} & 0_{1\times m} & 0_{1\times mn} \\ 0_{1\times m} & \sigma^2_{dt^{\mathrm{s}}} \cdot I_{1\times n} & 0_{1\times m} & 0_{1\times mn} \\ 0_{1\times m} & 0_{1\times n} & \sigma^2_{T_w} \cdot \Delta t \cdot I_{1\times m} & 0_{1\times mn} \\ 0_{1\times m} & 0_{1\times n} & 0_{1\times m} & \sigma^2_{\mathrm{BLC}} \cdot \delta'_{1\times mn} \end{bmatrix} \tag{6}$$

and

$$\begin{aligned} \delta &= \begin{cases} 0, & \mathrm{cs} \\ I, & \mathrm{non-cs} \end{cases} \\ \delta' &= I - \delta \end{aligned} \tag{7}$$

Then the procedure of Kalman filter can be divided into two steps:

(1) Time update

$$\begin{cases} X_k^- = \Phi_{k,k-1} X_{k-1} \\ P_k^- = \Phi_{k,k-1} P_{k-1} \Phi_{k,k-1}^T + Q_k \end{cases} \tag{8}$$

(2) Measurement update

$$\begin{cases} X_k = X_k^- + K(L_k - H_k X_{k-1}) \\ P_k = (I - KH_k) P_k^- \end{cases}. \tag{9}$$

In Eq. (9), K is gain matrix and set matrix G_k as:

$$G_k = R_k^{-1} + H_k P_k^- H_k^T \tag{10}$$

then

$$K = P_k^- H_k^T G_k^{-1} \tag{11}$$

In the whole procedure of filter, it is time consuming to inverse the matrix of G_k, because its dimension equals the number of observables which is proportional to the number of stations. At the same time, it looks like sparse matrix with a lot of zero elements in its off-diagonal position.

The core idea of the single observable Kalman filter is that processing a single observable recursively is equivalent to batch process all observables, when the observables are non-correlation [7]. In this situation, the observable vector L_k will be a scalar $\bar{l}_k$ and the design matrix H_k will transfer from two-dimensional matrix to one-dimensional vector. Therefore, the whole procedure of measurement update is:

$$\begin{cases} K = \bar{g}_k P_k^- H_k^T \\ X_k = X_k^- + K(\bar{l}_k - H_k X_{k-1}) \\ P_k = (I - KH_k) P_k^- \end{cases} \tag{12}$$

$\bar{g}_k$ is also a scalar and can be described as follow:

$$\bar{g}_k = \frac{1}{\bar{r}_k} + H_k P_k^- H_k^T \tag{13}$$

$\bar{r}_k$ is the variance of observable.

Compared with the process of inversing matrix of G_k, the single observable Kalman filter only has to process a single observable recursively and many matrices are reduced to vector. So, single epoch processing time is drastically reduced. However, the process of covariance matrix update is still time-consuming.

4 OpenMP Parallel Computation

OpenMP is s set of guiding compile processing scheme for shared memory parallel multiprocessor programming system and firstly proposed by OpenMP Architecture Review Board. It consists of a set of guiding compile statements, runtime library function, and environment variables (http://www.openmp.org).

OpenMP is a kind of parallel programming model based on thread and working in the Fork–Join way. In this way, the program starts with a main thread. When a parallel region appears, the code will be executed in the queue of threads, which are created immediately, and it will interrupt or synchronize to the main thread if it finishes. The whole work flow can be abstracted as below (Fig. 1).

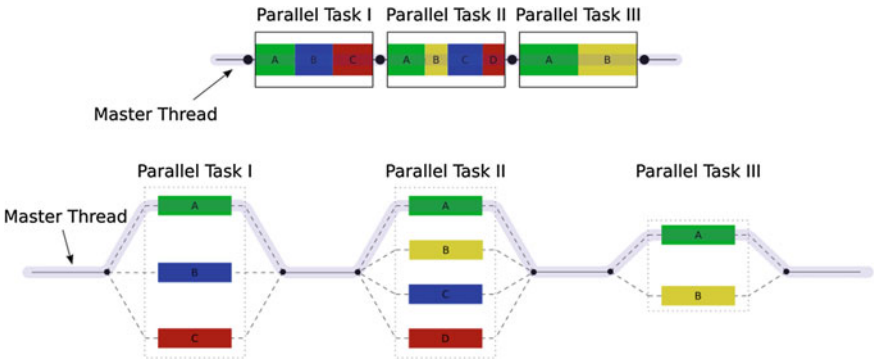

Fig. 1 The work flow of OpenMP (from Wikipedia https://en.wikipedia.org/wiki/OpenMP)

The parallelization of OpenMP is implemented by the guiding compile statements embedded in the source code of c/c++ and Fortran. The basic formation is:

$$\text{Flag of guiding compile} \quad \text{guiding name} \quad [\text{Clause},]$$

For example, in c/c++, the flag of guiding compile is "#pragma omp" and name of guiding has "parallel, for, section", etc. the Clause is used to explain the extra information of region, such as "privated, shared, reduction, copyin" etc.

Taking the independence of each element update procedure of covariance into consideration, the OpenMP can update a series of elements at same time to accelerate it. The pseudocode can be described as below.

```
#pragma omp parallel for
for(i = 0; i < n; i ++)
 {
 P(i,i) = P(i,i) − K(i)*M(i);
 for(j = i+1; j < n; j ++)
  {
 P(i,j) = P(j,i) = P(i,j) − K(i)*M(j);
  }
}
```

5 Analysis of Experiment Result

In order to analyze the accuracy of the estimated real-time satellite clock corrections, 49 IGS global reference stations were selected as shown in Fig. 2. Then, compute satellite clock corrections using the method described above from 2015-10-1 to 2015-10-7 and decimate sample rate to 60 s. At last, compared with 30 s IGS rapid satellite clock product by making double difference (between satellite and epoch) to remove inconsistency caused by different datum. In order to

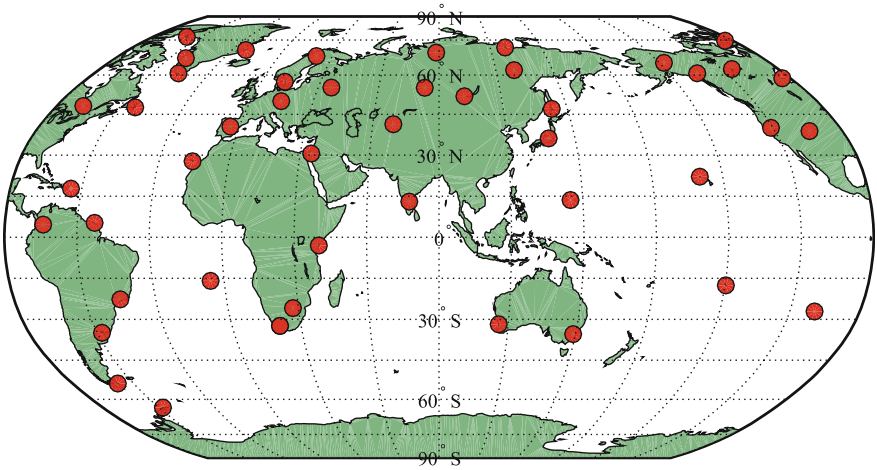

Fig. 2 The distribution of 49 global reference stations

make the result more clear, only the result of one day and part satellites after converged was showed in Fig. 3.

According to the Fig. 3, the clock offset difference of all satellites converges to the range of ±0.5 ns, which satisfies the requirement of RT-PPP. Only the clock offset difference of satellite G31 has an apparent fluctuation around epoch 1500, may be caused by poor quality of observables or lost to cause the ambiguity to reinitialize again. With the time goes by, the ambiguity will converge to the range of ±0.5 ns in the end.

In order to compare with the time cost before and after using single observable filter and OpenMP, different type of servers were applied to compute real-time satellite clock corrections. The server 1 is a workstation while the server 2 is super-computing center. The serial mode only used single observable filter without OpenMP. The result was shown in Fig. 4.

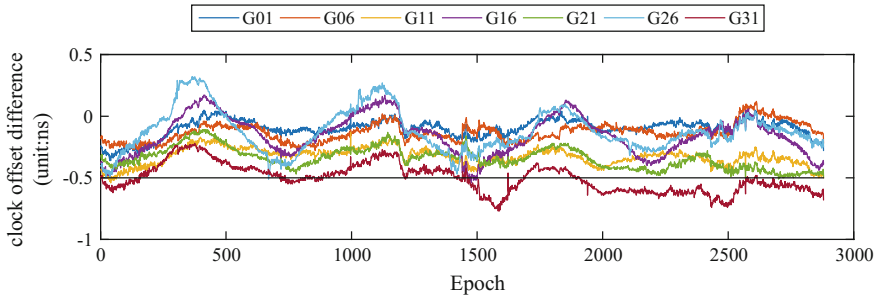

Fig. 3 The clock offset difference of 2015—275 to 276

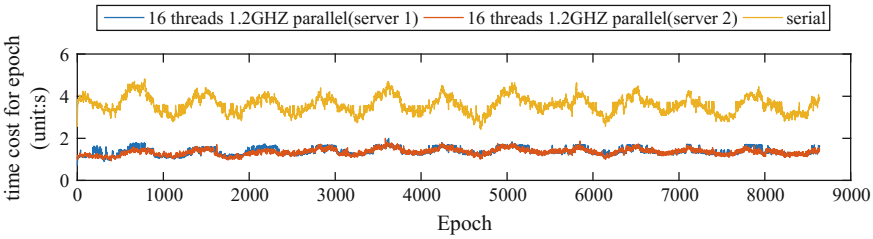

Fig. 4 The time cost for an epoch before and after using OpenMP

According to Fig. 4, the mean time cost for serial model was about 4 s and the maximum can be up to 5 s, while the minimum down to 3 s. After using OpenMP, no matter server 1 or server 2, the time cost for an epoch was dramatically reduced to 1 s, decreased by about 60%. Compared to the server 2, server 1 obviously needed more computing time at same epochs. Because the computing time was related to the stability of the computing environment and independent parallel threads at some time node provided by a small workstation may be lower than preset value. At the same time, it is apparently found that there is a great relationship between the time cost and number of parameters. Compared to serial mode, parallel model is less sensitive to the number of parameters, which showed a great advantage when dense stations were used.

6 Conclusion

It is different to use epoch difference approach to remove a large number of ambiguity parameters and introduce initialize satellite clock offset, in this paper, single observable Kalman filter is applied and using OpenMP to speed up the procedure of covariance update. The experiment results show that the accuracy of real-time satellite clock corrections is in range of $\pm$ 0.5 ns compared to IGS final clock products and the time cost for an epoch is reduced from 4 s in serial model to 1 s in parallel model.

The GPS satellite clock corrections estimation approach based on OpenMP proposed in this paper is very suitable for undifferenced observation model and is benefit to realize to estimate GPS satellite clock corrections and orbit at same time, can also effectively reduce the complexity of software design. Besides, this approach has a great scalability, such as introducing the fixed undifferenced ambiguity parameter to observation model.

References

1. Caissy M, Agrotis L (2011) Real-time working group and real-time pilot project. Int GNSS Serv Tech Rep 2011:183–190
2. Hauschild A, Montenbruck O (2008) Real-time clock estimation for precise orbit determination of LEO-satellites. ION GNSS, Savannah, Georgia
3. Ge M, Chen J, Jan D, Gerd G, Jens W (2012) A computationally efficient approach for estimating high-rate satellite clock corrections in realtime. GPS Solut 16:9–17
4. Miyazaki S, Laeson K, Choi K et al (2004) Modeling the rupture process of the 2003 September 25 Tokachi-Oki (Hokkaido) earthquake using 1 Hz GPS data. Geophys Res Lett 31:L21603
5. Laurichesse D, Cerri L, Berthias JP, Mercier F (2013) Real time precise GPS constellation and clocks estimation by means of a Kalman filter. In: Proceedings of ION-GNSS-2013, Institute of Navigation, 16–20 Sept, Nashville, TN, USA, pp 1155–1163
6. Schaer S (2008) Differential code biases (DCB) in GNSS analysis. IGS Workshop Presentation
7. Montenbruck O (2005) Satellite orbits models, methods and applications. Springer, Germany
8. Hauschild A (2010) Precise GNSS clock-estimation for real-time navigation and precise point positioning. TechnischeUniversittMünchen, München
9. Hauschild A, Montenbruck O (2009) Kalman-filter-based GPS clock estimation for near real-time positioning. GPS Solut (13):173–182
10. Xiaohong Z, Li X, Geo F (2011) Satellite clock estimation at 1 Hz for realtime kinematic PPP applications. GPS Solut 15:315–324
11. Li X (2013) Rapid ambiguity resolution in GNSS precise point positioning. WuHan University, WuHan

Part II
Precise Positioning Technology

A New RTK Ambiguity Resolution Method

Bingquan Dong and Huan Liu

Abstract This paper presents a new ambiguity resolution method, which differs with traditional method that includes all observations and searches the whole float ambiguities. The core is to use partial ambiguity fixing algorithm, which is counting on the satellite elevation angle to search the right ambiguity, and iterative deleting calculated observations depending on satellite continued tracking time is also included. Experiment proves that new method can increase the success rate of fixing to 99.8%, and the position precision is in the same level with traditional method.

Keywords RTK · Complex environment · Ambiguity resolution · Fixing rate

1 Introduction

RTK technology has been widely used in many fields for its high accuracy, real-time and high reliability property [9]. In order to obtain high accuracy positioning result, the carrier observation is included for the high-precision, and which introduces a big problem: fixing the inter ambiguities. In the conventional method, pseudo-range and carrier observations are simultaneously involved in adjustment calculations, and using the appropriate ambiguity search algorithm to fix them. With the fixed ambiguities, high precise positioning result can be got [2].

Correctly fixing the ambiguity parameter is a very important part in realizing the high accuracy positioning of RTK technology. The traditional processing method is generally to deal with all the satellites observations which meet the satellite elevation threshold [1, 5]. However, the complex observation environment will lead to more cycle slips in carrier and also increase the multipath effect. The observation accuracy will be reduced accordingly, some of them even bring gross error. The float ambiguities obtained from the lower quality observations deviate from the correct values, which will lead to the failure of ambiguity fixing. In this paper, we

B. Dong (✉) · H. Liu
Shanghai High Gain Information Technology Corp., Ltd, Shanghai 201702, China
e-mail: dongbingquan@highgain.com.cn; dong20081991@163.com

J. Sun et al. (eds.), *China Satellite Navigation Conference (CSNC) 2017 Proceedings: Volume III*, Lecture Notes in Electrical Engineering 439,
DOI 10.1007/978-981-10-4594-3_20

propose a strategy to improve the success rate of fixing ambiguity, the core idea is to control the number of satellites involved in the adjustment based on their continuous tracking time.

By controlling the number of satellites involved in the adjustment one can improve the success rate of ambiguity resolution. However, for the single system RTK, the deletion of more observations will lead to the reduction of the satellite geometric strength, the positioning accuracy and reliability will also be reduced accordingly. To use more observations efficiently, another new method based on step by step deletion algorithm is also introduced. Through gradually reducing the ambiguity searching set accounting on the elevation, the rate of fixing ambiguity can be improved again [4].

2 New Method of Ambiguity Resolution

2.1 Traditional RTK Algorithm

High-precision positioning usually requires more precise carrier observation, which is differed with pseudo-range for the ambiguity and it is necessary to fix the ambiguity parameters. The traditional method of fixing ambiguity is divided into the following processes: Firstly, the float ambiguity is obtained by combining the pseudo-range and the carrier observations; Secondly, the LAMBDA algorithm is used to search the float ambiguity to get integer ambiguity [2]. Detailed flow is as follows.

Firstly, the pseudo-range and carrier observations which throw the double difference between stations and satellites are combined to get the float ambiguity. The double difference observation equation is as follows:

$$\begin{pmatrix} l_P \\ l_L \end{pmatrix} = \begin{pmatrix} A & 0 \\ A & B \end{pmatrix} \begin{pmatrix} \Delta x \\ \Delta N \end{pmatrix} + \begin{pmatrix} \varepsilon_P \\ \varepsilon_L \end{pmatrix} \tag{1}$$

where: l_P and l_L are the prefit-residual of double difference pseudo-range and carrier observation, Δx and ΔN are position corrections and double difference float ambiguity respectively, ε_P and ε_L are the white noise of double difference pseudo-range and carrier observation, A and B are the design matrix of position corrections and ambiguity parameters.

The weight matrix:

$$P = \begin{pmatrix} P_P & 0 \\ 0 & P_L \end{pmatrix} \tag{2}$$

where, P_P and P_L are the weight matrix of double difference pseudo-range and carrier observation, respectively.

Introducing the least square principle:

$$\begin{pmatrix} A^T P_P A + A^T P_L A & A^T P_L B \\ B^T P_L A & B^T P_L B \end{pmatrix} \times \begin{pmatrix} \Delta x \\ \Delta N \end{pmatrix} = \begin{pmatrix} A^T P_P l_P + A^T P_L l_L \\ B^T P_L l_L \end{pmatrix} \tag{3}$$

And

$$\Delta N = N_{nn}^{-1} \cdot \left(B^T P_L l_L - B^T P_L A \cdot N_{aa}^{-1} \cdot (A^T P_P l_P + A^T P_L l_L) \right) \tag{4}$$

$$\Delta x = N_{aa}^{-1} \cdot \left(A^T P_P l_P + A^T P_L l_L - A^T P_L B \cdot \Delta N \right) \tag{5}$$

where, $N_{aa} = A^T P_P A + A^T P_L A$, $N_{nn} = B^T P_L B - B^T P_L A \cdot N_{aa}^{-1} \cdot A^T P_L B$.

ΔN is the double difference float ambiguity, N_{nn}^{-1} is the corresponding covariance matrix. The fixed ambiguity can be got by searching the float ambiguity with LAMBDA algorithm [8].

The LAMBDA search algorithm solves the following least-squares equation

$$\breve{N} = \arg\min \left((N - \hat{N})^T Q_N^{-1} (N - \hat{N}) \right) \tag{6}$$

where, N is float ambiguity, $\hat{N}$ is integer ambiguity, Q_N is the covariance matrix of N. The meaning of the formula is to select the minimal set of the objective function from the combination as the final ambiguity integer ambiguities. And whether the ambiguities is fixed or not is checked by the likelihood ratio test (ratio test)

$$\text{ratio} = \frac{(\breve{N}_{\text{sec}} - \hat{N}) Q_N^{-1} (\breve{N}_{\text{sec}} - \hat{N})}{(\breve{N}_{\min} - \hat{N}) Q_N^{-1} (\breve{N}_{\min} - \hat{N})} > k \tag{7}$$

where, k is the threshold of ratio test, $\breve{N}_{\min}$ and $\breve{N}_{\text{sec}}$ are optimal and suboptimal solution which can meet the Eq. (6). The threshold k is generally 2 or 3, and passing the ratio test is considered fixing successful.

2.2 *Improved Ambiguity Resolution Algorithm*

When searching the integer ambiguity with Eq. (6), sometimes passing the ratio test is relatively difficult with the complete ambiguity set. So we can narrow the search range of ambiguity, that is, partial ambiguity resolution algorithm [3, 4].

Firstly, sort the ambiguities set counting on the satellite elevation.

$$N = \begin{bmatrix} N_1 \\ N_2 \\ \vdots \\ N_i \\ \vdots \\ N_n \end{bmatrix}, \quad \sigma_N^2 = \begin{bmatrix} \sigma_{N_1}^2 & \sigma_{N_1N_2}^2 & \cdots & \sigma_{N_1N_i}^2 & \cdots & \sigma_{N_1N_n}^2 \\ & \sigma_{N_2}^2 & \cdots & \sigma_{N_2N_i}^2 & \cdots & \sigma_{N_2N_n}^2 \\ & & \ddots & \vdots & \vdots & \vdots \\ & & & \sigma_{N_i}^2 & \vdots & \sigma_{N_iN_n}^2 \\ & & & & \ddots & \vdots \\ & & & & & \sigma_{N_n}^2 \end{bmatrix} \tag{8}$$

Secondly, search the integer ambiguity by LAMBDA and check whether pass the ratio test. If through the test, the process is done and fixed ambiguities are got. Otherwise, go to the next step to reduce the ambiguities dimension.

Thirdly, eliminate the satellite ambiguity whose elevation is minimum and repeat second step to fix the residual ambiguities until the dimension less than four. If the dimension of the ambiguity subset is less than four, all ambiguities of the epoch adopt the floating result.

Some epochs are still unable to pass the ratio test even though using the partial ambiguity resolution technique described above. The reason may be that there is a gross error in the observations or the method of weighting according to the satellite elevation cannot truly reflect the quality of the observations. Aiming at this phenomenon, the strategy of stepwise satellite deletion strategy is proposed.

First, the observations of the satellites are arranged in ascending order according to the continuous tracking time.

Second, use the formula (1)–(5) to calculate float ambiguities and corresponding covariance matrix, and apply the partial ambiguity fixing algorithm mentioned above. If it gets through the test, the process is done and fixed ambiguities are obtained. Otherwise, go to the next step.

Third, remove the satellite observations with the shortest continuous tracking time and carry out the adjustment calculation again. And repeat second step until the ambiguity is fixed or the number of satellite is less than five. If the final test cannot pass the ratio test, use the float ambiguity as the final result. Detailed processing flow shown in Fig. 1.

3 Experiment and Analysis

In order to verify the effectiveness of the proposed ambiguity resolution algorithm, this paper uses the open source software platform RTKLIB for real-time relative positioning solution [6, 7]. The real-time data stream comes from five static stations, and the detailed information of the board used in the stations and baselines is shown in Table 1. Among them, HighGain G100 and G200 are high-precision positioning and orientation product developed by Shanghai HighGain Information Technology Corp., Ltd., and can receive GPS L1/L2 and BDS B1/B2 dual-mode quad-band satellite signals. They have high accuracy RTK positioning,

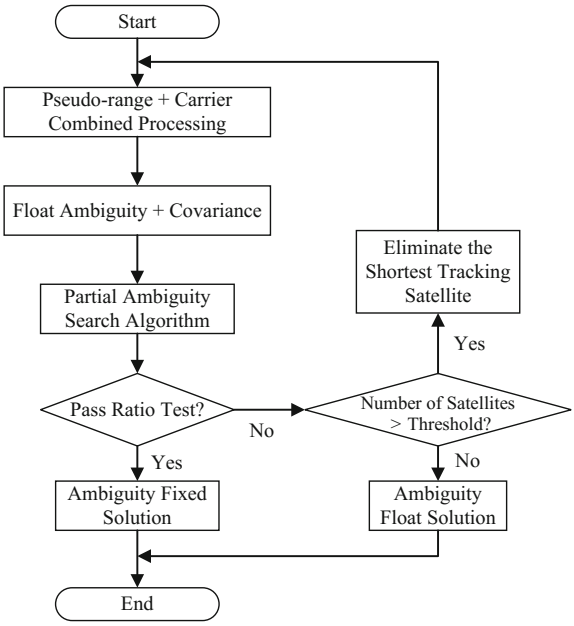

Fig. 1 Flowchart of new ambiguity resolution method

Table 1 Station information

Number	Board type	Description	Baseline length
B1	NovAtel 617	Base	–
R1	HighGain G200	Rover	≈3 km
R2	Hemisphere UN237C	Rover	≈3 km
R3	HighGain G100	Rover	≈10 m
R4	Hemisphere UN237C	Rover	≈10 m

high-precision attitude measurement, high-quality original observation collection and other features. The hardware size, interface, data command of G100 and G200 is compatible with the mainstream board at home and abroad.

Experiment was carried out for seven days, and the statistical results are shown in Table 2. The observation duration is the observed time of the station, the data efficiency is the ratio of the duration displayed by actual received data to the observation duration. Affected by the environment, if network transmission and other factors, real-time received data and expected data have a certain amount of difference, the data efficiency cannot reach 100%. The fixed rate is the ratio of epoch count which passes the ratio test to total epoch count, positioning accuracy is the three-dimensional STD statistic for all fixed solutions.

By analyzing the statistical results in Table 2, it can be found that the new method is better than or equal to the conventional method in terms of the fixed rate

Table 2 Statistical results

Date	Station	Observation duration	Data efficient (%)	Conventional method				New method			
				Fixed rate (%)	Positioning accuracy(mm)			Fixed rate (%)	Positioning accuracy(mm)		
					E	N	U		E	N	U
10.14	R1	8.0	99.9	99.5	8.7	6.3	21.9	99.9	7.9	5.6	18.8
	R2	14.4	99.5	98.2	7.6	5.3	17.7	99.6	7.8	5.4	18.1
	R3	14.4	99.8	99.9	2.1	1.7	5.9	100.0	2.2	1.7	6.2
	R4	14.4	99.9	100.0	1.6	1.4	4.5	100.0	1.6	1.4	4.5
10.15	R1	13.8	99.7	100.0	6.1	3.6	11.9	100.0	5.7	3.6	11.1
	R2	24.0	99.7	99.3	5.6	3.6	11.0	99.7	5.6	3.6	11.2
	R3	24.0	99.8	99.9	2.1	1.6	5.6	100.0	2.1	1.6	5.6
	R4	24.0	99.8	99.8	1.9	1.5	4.0	99.8	1.9	1.5	4.0
10.16	R1	24.0	99.9	93.4	8.1	4.3	13.7	99.9	11.4	4.5	15.7
	R2	24.0	99.9	91.9	7.2	4.2	13.1	97.8	9.5	4.4	13.4
	R3	24.0	99.4	99.2	2.2	1.8	6.1	99.9	2.2	1.9	6.2
	R4	24.0	100.0	99.4	1.7	1.6	4.5	99.8	1.7	1.7	5.0
10.17	R1	24.0	99.6	95.6	5.0	3.4	9.9	99.8	5.5	3.7	11.8
	R2	23.9	99.7	92.0	5.4	3.4	9.2	99.6	6.5	3.9	10.8
	R3	24.0	99.7	98.8	2.0	1.6	5.7	100.0	2.1	1.6	6.0
	R4	24.0	99.7	99.8	1.5	1.2	4.1	99.8	1.5	1.3	4.1
10.18	R1	24.0	99.9	95.2	5.6	3.4	11.2	100.0	6.3	3.9	14.6
	R2	24.0	99.7	93.0	6.1	3.9	13.4	100.0	7.3	4.3	16.9
	R3	24.0	98.2	100.0	2.0	1.6	5.5	100.0	2.0	1.6	5.5
	R4	24.0	100.0	100.0	1.4	1.2	3.9	100.0	1.4	1.2	3.9

(continued)

Table 2 (continued)

Date	Station	Observation duration	Data efficient (%)	Conventional method				New method			
				Fixed rate (%)	Positioning accuracy(mm)			Fixed rate (%)	Positioning accuracy(mm)		
					E	N	U		E	N	U
10.19	R1	24.0	99.8	99.9	4.4	3.2	8.9	100.0	4.4	3.2	8.9
	R2	24.0	98.0	99.5	4.1	3.1	8.2	99.8	4.1	3.1	8.3
	R3	24.0	99.7	99.9	2.0	1.6	5.7	100.0	2.0	1.6	5.8
	R4	24.0	99.7	99.9	1.4	1.3	3.9	99.9	1.4	1.3	3.9
10.20	R1	24.0	99.9	94.8	6.3	3.6	12.3	99.6	7.4	3.7	13.5
	R2	24.0	98.6	93.8	6.7	3.6	11.0	99.6	7.4	3.7	11.7
	R3	24.0	99.2	100.0	2.0	1.6	5.4	100.0	2.0	1.6	5.4
	R4	24.0	99.4	99.7	1.5	1.3	3.9	99.7	1.5	1.3	3.9
Average	–	–	96.6	97.9	4.0	2.7	8.6	99.8	4.4	2.8	9.1

of all the stations in seven days. The average fixed rate is increased from 97.9 to 99.8%, and the newly proposed method success rate is close to 100%.

For the accuracy of the fixed epoch, the statistical results of most stations show that the new ambiguity resolution method leads to a decrease in positioning accuracy. Since the new algorithm improves the fixed success rate by reducing the number of satellites involved in the adjustment and searching the subset of ambiguities, available satellites and fixed ambiguities are both less than those of the conventional method, and the reliability and accuracy of the positioning results will be reduced to a certain extent. The statistical results show that the three-dimensional average positioning precision is reduced from 4.0, 2.7 and 8.6 mm to 4.4, 2.8 and 9.1 mm, respectively. Positioning accuracy reduction is very small; the accuracy of the new algorithm is still on the same level with the traditional.

4 Conclusion

In this paper, a new ambiguity resolution method is proposed to break the fixed thinking of traditional algorithms which use the complete set of satellite observations and search the complete ambiguity set. The proposed algorithm uses the continuous tracking time of each satellite as the basis to control the number of observations involved in the adjustment calculation, and at the same time improves the ambiguity fixed success rate by searching the float ambiguity subset. Conclusions are as follows.

1. The new ambiguity resolution method can effectively improve the fixed success rate of ambiguity, and the average fixed success rate is improved from 97.9 to 99.8%. The fixed rate of new proposed method is closed to 100%.
2. The accuracy of the conventional method and the new algorithm are 4.0, 2.7, 8.6 mm and 4.4, 2.8 and 9.1 mm, respectively. The new algorithm has the same level accuracy as the traditional algorithm.

Acknowledgements We thank Tomoji Takasu of Tokyo University of Marine Science and Technology for the RTKLIB source code.

References

1. Duan J, Shen Y (2012) An algorithm of combined GPS/GLONASS static relative positioning. Acta Geodaetica Cartogr Sin 41(6):825–830
2. Liu G (2001) Real-time positioning algorithm with single frequency gps phase and pseudo-range and detection of cycle slip. Crustal Deformation Earthq
3. Pan Z (2015) Real-time precise point positioning and ambiguity resolution. PLA Information Engineering University, Zhengzhou

4. Pan Z, Chai H, Liu J, Dong B, Liu M, Wang H (2015) GPS partial ambiguity resolution method for zero-difference precise point positioning. Acta Geodaetica et Cartographica Sinica 44(11):1210–1218
5. Song Z, Gao X, Shi Q, Nie L (2016) Instantaneous single-frequency rtk positioning using combined GPS/ BDS/ GALILEO system. J Geomatics Sci Technol
6. Takasu T, Kubo N, Yasuda A (2009) RTKLIB: open source program package for RTK-GPS. Available from: http://gpspp.sakura.ne.jp/paper2005/foss4g_2009_rtklib.pdf
7. Takasu T, Yasuda A (2009) Development of the low-cost RTK-GPS receiver with an open source program package RTKLIB. In: International symposium on Gps/gnss Jeju South Korea
8. Teunissen PJG (1995) The least-squares ambiguity decorrelation adjustment: a method for fast GPS integer ambiguity estimation. J Geodesy 70(1):65–82
9. Wang L (2015) A study on key technology of high precision gps monitoring for geological hazard. Chang'an University, Xi'an

Algorithm and Experimental Analysis of Medium-Long Baseline Static Positioning Based on BeiDou Dual-Frequency Observations

Junjun Ying, Fengbo Wu and Wanke Liu

Abstract Medium-long baseline static positioning algorithm based on BeiDou dual-frequency observations is proposed first. In this paper, we concentrate on the processing strategy of atmosphere errors. We form four baselines in different days using data of B1 and B2 from HongKong CORS and Wuhan CORS (each CORS forming two baselines). In the experiment, we analyze the fix rate and positioning accuracy in different time periods (2, 3, 4 and 6 h). The results indicate that the poor geometry condition and slow variation of geometry in BDS constellation contribute to the poor performance than that of GPS, which drives us need more time(at least 4 h) to ensure reliable fixed solution and centimeter level positioning using BeiDou dual-frequency observations in medium-long baseline static positioning.

Keywords BDS (BeiDou navigation satellite system) · Medium-long baseline · Static positioning · Tropospheric delay · Ionosphere-free combination · Dual-frequency observation

1 Introduction

GPS baseline static positioning plays a significant role in the applications such as layout of geodetic control network and densification of geodetic control point. Thus, many researchers and institutions domestic and overseas are investing comprehensive

J. Ying (✉)
State Key Laboratory of Satellite Navigation System and Equipment Technology,
NO.589 West Zhongshan Road, Shijiazhuang
50081, Hebei Province, China
e-mail: yingjjcetc@163.com

J. Ying
The 54th Research Institute of China Electronics Technology Group Corporation,
Shijiazhuang, Hebei Province, China

F. Wu · W. Liu
School of Geodesy and Geomatics, Wuhan University,
129 Luoyu Road, Wuhan 30079, China

J. Sun et al. (eds.), *China Satellite Navigation Conference (CSNC) 2017 Proceedings: Volume III*, Lecture Notes in Electrical Engineering 439,
DOI 10.1007/978-981-10-4594-3_21

methods on the theory of GPS baseline static positioning algorithm significantly, which achieves much fruitful breakthrough [1, 2]. In the end of 2012, regional system of BeiDou Navigation Satellite System in China officially releases, providing effectual services including positioning, navigation and timing in Asian-Pacific region. The constellation of this regional system is constituted of 15 satellites, which consists of five satellites of GEO, five satellites of IGSO and five satellites of MEO [3].

Generally speaking, the principle of BDS baseline static positioning is similar to that of GPS. While we should also consider the fact that BeiDou system is composed of mixed constellation, i.e. GEO/IGSO/MEO, which provides poor geometry condition (PDOP is usually more than 2.5 with bigger fluctuation range [4]) and slow variation resulted in strong relevance in the measurements when we conduct on the carrier phase observations. Above concerns lead to serious morbidity of normal equation [5, 6], difficulty in separating systematic errors, location parameters and ambiguity parameters, which influence the algorithm performance of medium-long baseline principally.

Presently, many scholars are engaged in the theoretical algorithms and wide applications of BDS short baseline (less than 15 km) [7–9], while few pay close attention to its algorithm and performance analysis. In the meanwhile, considering the fact that many stations of current BeiDou receivers can only capture and track signals from B1I and B2I, we concentrate on describing the medium-long baseline static positioning algorithm based on BeiDou dual-frequency observations of B1 and B2 and evaluating the proposed algorithm and practical performance with real BeiDou data.

2 Static Algorithm Realization Based on Medium-Long Baseline

Static baseline resolution is achieved by double difference combination of receiver carrier phase, i.e. single difference between observation station and then double difference among visible satellites. Thus, the receiver clock bias and satellite clock bias are eliminated and the double difference observation equation is shown as follows:

$$\mathrm{DD}_L = \mathrm{DD}_\rho + \lambda_i \mathrm{DD}_N - \Delta I^s_{r,b} + \Delta T_{r,b} + \mathrm{DD}_\varepsilon \tag{1}$$

$$\mathrm{DD}_P = \mathrm{DD}_\rho + \Delta \mathrm{I}^s_{r,i} + \Delta \mathrm{T}_{r,b} + \mathrm{DD}_\delta \tag{2}$$

where DD_L and DD_P are double difference carrier phase, i.e., carrier phase pseudorange (unit: meter) and C/A code observation. DD_ρ is the double difference between satellite and the receiver. λ_i is the wavelength of corresponding frequency. $\mathrm{DD_N}$ is the integer ambiguity of double difference. $\Delta I^s_{r,b}$ and $\Delta T^s_{r,b}$ are ionospheric and tropospheric delay respectively. DD_ε is the residual noise of carrier phase and so is DD_ε of C/A pseudorange.

For the case of medium-long Baseline, the spatial correlation between ionosphere and troposphere delay will be weakened, which contributes to the ionosphere and troposphere delay error and has an influence on the accuracy of floating point ambiguity. In turn, it will enhance the fixed difficulty of ambiguity [1, 2]. In order to achieve the correct ambiguity integer, we should take the ionosphere and troposphere delay into consideration in the medium-long baseline, which will be detailed in the next section. It should be noted that the precision of BDS broadcast ephemeris is within Several meters order of magnitudes and the GEO (geostationary orbit) satellites may be larger than that of 10 m in some special cases [10, 11]. In addition, the influence on the medium-long baseline is usually millimeters and may be larger than 1 cm in special situation.

2.1 The Process of Ionosphere Delay in the Medium-Long Baseline

Considering the medium-long baseline, i.e. 15–100 km, we may achieve the weak correlation on the ionosphere delay above two receivers, which still includes large residual ionosphere delay bias by double difference and should be concerned significantly. On the other hand, there occurs closed relationship between ionosphere delay and corresponding frequency. We could eliminate the ionosphere delay by dual navigation signal frequency while we cannot obtain the integer characteristic by above combination. Hence, we could calculate the integer ambiguity by traditional LAMBDA searching algorithm. However, we could achieve the solution by the mode of dual-frequency elimination ionosphere [1, 2]. Based on Eq. 1, the observation equation of dual-frequency elimination ionosphere combination is shown as follows:

$$\begin{aligned}
\mathrm{DD}_{L3} &= \frac{f_1^2\mathrm{DD}_{L1} - f_2^2\mathrm{DD}_{L2}}{f_1^2 - f_2^2} = \mathrm{DD}_\rho - \frac{f_1^2\lambda_1\mathrm{DD}_{N1} - f_2^2\lambda_2\mathrm{DD}_{N2}}{f_1^2 - f_2^2} + \mathrm{DD}_{\mathrm{trop}} + \mathrm{DD}_\varepsilon \\
&= \mathrm{DD}_\rho - \frac{f_1^2\lambda_1 \times (\mathrm{DD}_{N1} - \mathrm{DD}_{N2}) + \mathrm{DD}_{N2} \times \left(f_1^2\lambda_1 - f_2^2\lambda_2\right)}{f_1^2 - f_2^2} + \mathrm{DD}_{\mathrm{trop}} + \mathrm{DD}_\varepsilon \\
&= \mathrm{DD}_\rho - \left(\frac{v\mathrm{light} \times f_1 \times \mathrm{DD}_{N5}}{f_1^2 - f_2^2} + \frac{DD_{N2} \times v\mathrm{light}}{f_1 + f_2}\right) + \mathrm{DD}_{\mathrm{trop}} + \mathrm{DD}_\varepsilon
\end{aligned}$$

or

$$\begin{aligned}
\mathrm{DD}_{L3} &= \frac{f_1^2\mathrm{DD}_{L1} - f_2^2\mathrm{DD}_{L2}}{f_1^2 - f_2^2} = \mathrm{DD}_\rho - \frac{f_1^2\lambda_1\mathrm{DD}_{N1} - f_2^2\lambda_2\mathrm{DD}_{N2}}{f_1^2 - f_2^2} + \mathrm{DD}_{\mathrm{trop}} + \mathrm{DD}_\varepsilon \\
&= \mathrm{DD}_\rho - \frac{f_1^2\lambda_1\mathrm{DD}_{N1} - f_2^2\lambda_2\mathrm{DD}_{N2} + f_2^2\lambda_2\mathrm{DD}_{N1} - f_2^2\lambda_2\mathrm{DD}_{N1}}{f_1^2 - f_2^2} + \mathrm{DD}_{\mathrm{trop}} + \mathrm{DD}_\varepsilon \\
&= \mathrm{DD}_\rho - \left(\frac{v\mathrm{light} \times f_2 \times \mathrm{DD}_{N5}}{f_1^2 - f_2^2} + \frac{\mathrm{DD}_{N1} \times v\mathrm{light}}{f_1 + f_2}\right) + \mathrm{DD}_{\mathrm{trop}} + \mathrm{DD}_\varepsilon
\end{aligned} \tag{3}$$

where DD_{L3}, DD_{L1}, DD_{L2} are carrier phase dual difference of ionosphere elimination, carrier phase dual difference of B1 and carrier phase double difference of B2 respectively. f_1 is the frequency of B1 and so is f_2 of B2. DD_{N1} and DD_{N2} are double difference ambiguity of B1 and B2. DD_{N5} is the ambiguity of wide-lane. DD_ρ is the distance double difference between the satellite and the receiver. $\Delta T^s_{r,b}$ is the tropospheric delay, DD_ε is the residual noise and $v$light is the speed of navigation signal transmission.

2.2 The Process of Troposphere Delay in the Medium-Long Baseline

Concerning the middle and long static baseline, we could realize that the troposphere delay is the largest observation error excluding ionospheric delay. The troposphere delay includes dry and wet delay, which could be eliminated about 90% dry delay by the classic tropospheric model and the left 10% of wet delay could not be eliminated by the mode l [1]. Generally speaking, we could estimate the wet delay of zenith troposphere delay by approximate evaluation on the medium-long baseline.

The estimation of tropospheric wet delay is shown as follows:

$$\Delta T_{r,b} = \Delta M^{i,j}_{w,b} T_{w,b} - \Delta M^{i,j}_{w,r} T_{w,r} \tag{4}$$

where $\Delta T_{r,b}$ is the oblique path projection of tropospheric wet delay. $\Delta M^{i,j}_{w,b}$ and $\Delta M^{i,j}_{w,r}$ are the single difference wet delay projection of observation station, $T_{w,b}$ and $T_{w,r}$ are zenith tropospheric wet delay of observation station and respectively.

In this paper, the tropospheric delay is estimated by Saastamoinen model and tropospheric wet delay is estimated by piecewise linear estimation. The mapping function of tropospheric dry and wet delay is adopted by NMF model [1].

2.3 The Algorithm Processing of Medium-Long Static Baseline

The algorithm resolution of the medium-long baseline is achieved by the above ionospheric delay elimination of dual-frequency observation equation. Based on long time observation source data, we conduct the observation equation by B1 and B2 wide-lane carrier phase double difference and C/A pseudorange double difference. After achieving the float resolution of DD_{N5}, we continue to calculate the wide-lane integer ambiguity DD_{N5} by LAMBDA algorithm. Then, the determinate wide-lane integer ambiguity DD_{N5} is brought into the dual-frequency ionospheric

delay elimination equation, which could compute the float resolution of DD_{N1} or DD_{N2}, the baseline coordinate connotative in DD_{ρ}, the zenith tropospheric wet delay of observation station. What is more, we will conduct immobilization on the float resolution of DD_{N1} or DD_{N2} by LAMBDA searching algorithm. Finally, we take the integer of DD_{N1} or DD_{N2} into above equation and achieve the accurate baseline coordinate and zenith tropospheric wet delay of observation station, which are achieved by the least square algorithm.

It should be noted that we could efficiently achieve the wide-lane integer ambiguity by the MW algorithm based on dual-frequency C/A code when concerning GPS observation. While according to the present research, there occurs obvious system bias in BDS code pseudorange, which has an influence on the resolution of dual-frequency wide-lane ambiguity. It will not only enhance the calculation time of wide-lane ambiguity but also increase the fixed error probability [12]. In order to conduct above concerns, some researchers set up bias correct model [13, 14], which is utilized in this paper for the model bias correction. In fact, the enhancement of MW wide-lane ambiguity resolution does not show obvious improvement. Thus, we take the above wide-lane ambiguity searching algorithm (LAMBDA searching algorithm) into consideration for the realization of medum-long static baseline. From the results of Teunissen et.al the proposed algorithm could achieve better performance on the efficiency of fixation and correction [15].

3 Analysis of Simulation Results

3.1 Source Data and Processing Algorithm

In order to estimate the actual performance of proposed BDS static long baseline dual-frequency resolution, we acquire two baselines in single day from Hong Kong CORS (HKC) and Wuhan CORS (WHC), shown in Table 1.

During data processing, we adopt the BDS broadcast ephemeris and take B1 and B2 into consideration. The dual-frequency of ionospheric delay elimination is introduced and tropospheric dry delay is eliminated by model correction, while the residual tropospheric wet delay is estimated by the unknown parameter. The cut-off

Table 1 Information of baseline

Name of baseline	Source	Length of baseline (km)	Receiver	Observation time
hklm_hktk	HKC	38	TRIMBLE NETR9	2016.5.16
hknp_hkws	HKC	50	LEICA GRX1200	2015.8.26
whcd_whhp	WHC	47	Trimble NetR9	2013.3.24
whcd_whxz	WHC	80	Trimble NetR9	2013.3.21

height angle is set. The sampling interval is set 30 s and LAMBDA algorithm is adopted by ambiguity resolution. The ratio threshold is set 3.0 [16].

To achieve the resolution of different processing time, we bring the 24 h observation date into 2, 3, 4 and 6 h sections, which are processed by above algorithm, including the analysis of fixation time and positioning precision of the medium-long baseline.

3.2 Analysis of Fixation Time

We estimate the resolution performance of above 4 baseline times and the fixation calculation is shown in Table 2. The column of 2–5 is the period fixed ratio, i.e. fixed time section/total time section. From Table 2, we could realize that the baseline of fixation has low performance when conducting by 2 h of one section, the two shorter baselines, i.e. hklm_hktk and whcd_whhp could only reach 59%. With the enhancement of time section, we could achieve higher baseline fixation and 3 h is larger than that of 2 h. During 4 h time section, the two short baselines could be completely fixed while the other two is still not ideal. Moreover, with the enhancement of time section to 6 h, the four baseline could be fixed completely, which implies that it needs long time to ensure the high rate of fixation and we could achieve the basic fixation in 4 h and could achieve the 100% fixation in 6 h.

From Table 2, we could realize that the medium-long baseline need long time to conduct good fixation. Thus, in order to estimate the proposed algorithm, we take the same baseline time section by corresponding GPS dual-frequency observation data of 2 h. The results of baseline fixation show that single GPS could be correctly fixed by all the time period of baseline, which implies that the reason of long time to fixation in BDS is the factors, which are mentioned in the introduction section.

The average ratio of different baseline in different section is shown in Fig. 1, where the 2 h_GPS stands for the 2 h time section of average ration in GPS and others stand for average ratio of BDS. We could realize that the long three baselines are inferior to the shorter hklm_hktk baseline in total. The longer the baseline, the lower the ratio value. And it illustrates that the ratio value will decrease with the enhancement of baseline distance. The reason may be that the residual bias of dual-frequency will improve with the enhancement of distance. Concerning all the

Table 2 Different period fixed ratio (fixed time section/total time section)

Name of baseline	Length of baseline (km)	Length of section			
		2 h	3 h	4 h	6 h
hklm_hktk	38	5/12	7/8	6/6	4/4
hknp_hkws	50	4/12	5/8	4/6	4/4
whcd_whhp	47	6/12	5/8	6/6	4/4
whcd_whxz	80	2/12	5/8	4/6	4/4

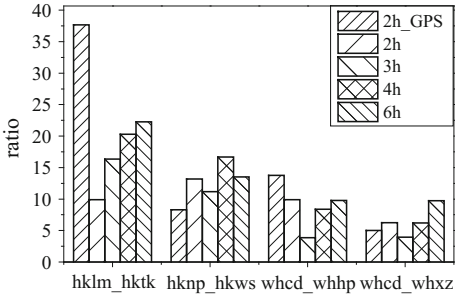

Fig. 1 Four baseline of average ratio in different period

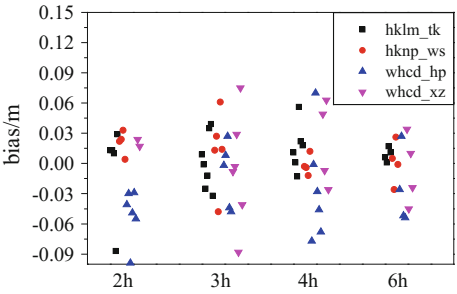

Fig. 2 The scatter diagram of E bias in different periods

baseline, with the time flies, the ratio value does not increase all through, but shows larger gradually in total, which shows that we could improve the performance of fixation accordingly to enhance the observation time of spatial distribution of BDS, lowly processed at the same time.

3.3 Analysis of Baseline Accuracy

When concerning the performance of baseline resolution, we take the ENU baseline component as reference from the CORS station of Hong Kong and Wuhan respectively. The baseline component bias and criterion of statistic accuracy are shown as follows:

$$\begin{aligned} v &= x - \tilde{x} \\ \text{rms} &= \sqrt{\frac{\sum_{i=1}^{n} v_i^2}{n}} \end{aligned} \tag{5}$$

where x stands for the baseline component of ENU, $\tilde{x}$ stands for the real value of baseline component. v is the single baseline bias in single period, n is the sampling numbers of accuracy analysis.

Figures 2, 3 and 4 illustrate the different time period fixation of ENU bias in total baseline. It should be noted that the x-axis stands for the time, which could be used

to distinguish baseline resolution accuracy in different time period. From the figures, we could realize that no matter how long it takes, the baseline component bias is about 1 cm + 1 ppm in horizontal orientation and 2 cm + 2 ppm in height orientation after fixation accomplished with most cases. It also shows that in the Medium-long Baseline, the accuracy of BDS ambiguity could be cm level after fixation. And the abnormal values usually concentrate on the short time period (2 or 3 h) or larger baseline, which indicates that the time period is shorter, the reliability is lower compared with longer time period. The longer the baseline, the lower the accuracy after baseline fixation. With the development of time period, there occurs the enhancement of baseline resolution. Thus, in order to ensure the high reliability and accuracy, we strongly suggest that the resolution time is larger than 4 h when conducting the middle and long period baseline resolution in BDS dual-frequency observation.

The different baseline time periods and average accuracy of ENU direction is shown in Table 3. We could realize that the baseline component is cm level after ambiguity fixation. The longer the time, the higher the accuracy. Comparing the accuracy between two longer baselines and shorter baselines, we could achieve that the longer baseline, the larger residual error. Although we could obtain the ambiguity, it still shows low accuracy of baseline component. Table 4 conducts the statistics of 2 h based on GPS dual-frequency observation, which shows superior performance than BDS of proposed algorithm in this paper, especially in height orientation. The above reason is that the geometric distribution of BDS is weaker

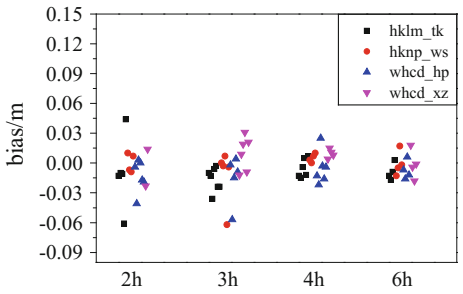

Fig. 3 The scatter diagram of N bias in different periods

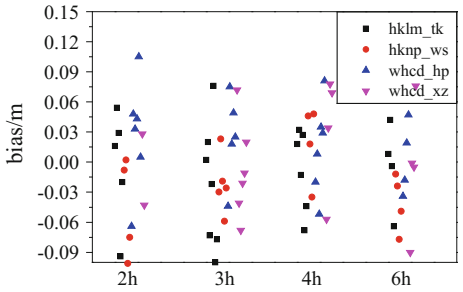

Fig. 4 The scatter diagram of U bias in different periods

Table 3 The RMS of different baseline component in different periods

Accuracy of baseline component		2 h			3 h			4 h		6 h	
	E/m	N/m	U/m	E/m	N/m	U/m	E/m	N/m	E/m	N/m	U/m
hklm_hktk	0.041	0.034	0.087	0.026	0.02	0.063	0.026	0.01	0.011	0.012	0.038
hknp_hkws	0.027	0.008	0.098	0.035	0.025	0.036	0.009	0.007	0.018	0.01	0.047
whcd_whhp	0.052	0.018	0.088	0.056	0.029	0.05	0.055	0.016	0.042	0.011	0.032
whcd_whxz	0.08	0.036	0.064	0.056	0.02	0.038	0.042	0.01	0.031	0.013	0.059
Average	0.05	0.024	0.084	0.043	0.024	0.047	0.033	0.011	0.026	0.012	0.044

Table 4 The accuracy of baseline component during 2 h in single GPS

Accuracy of baseline component	E/m	N/m	U/m
hklm hktk	0.019	0.010	0.031
hkws hknp	0.036	0.018	0.045
whcd_whhp	0.048	0.017	0.055
whcd_whxz	0.041	0.020	0.054
Average	0.036	0.016	0.046

than that of GPS [4]. In summarize of Tables 3 and 4, it takes 4 h at least when BDS wants to achieve the same accuracy with GPS.

4 Conclusion

Algorithm of medium-long baseline static positioning based on BeiDou dual-frequency observations is proposed in this paper. Moreover, we form four baselines in different days using data from Hong Kong CORS and Wuhan CORS, testing and analyzing actual results of the referred algorithm in different time period (2, 3, 4, 6 h). The results indicate the following aspects:

(1) Due to the poor geometry condition and slow variation of geometry of BDS constellation compared to that of GPS, we need more time to fix ambiguity and achieve centimeter level positioning accuracy;
(2) As for present BDS regional constellation, we need more time (at least 4 h) to ensure reliable fixed solution and higher positioning accuracy.

Further researches such as using triple-frequency observations, accurate ephemeris more reliability on how to reduce the ambiguity fix rate of BDS medium-long baseline static positioning and improve positioning accuracy are still required ambiguity fix attempts. Besides, China has started the invention of BDS global constellation since March of 2015 [17]. With the accuracy of service performance of BDS signals and the relevant error models, position accuracy of medium-long baseline based on BeiDou dual-frequency observations is doomed to improve momentously.

Acknowledgements This research were supported by National Natural Science Foundation of China(41204030) and Cooperative funded projects in Colleges and Universities of The 54th Research Institute of China Electronics Technology Group Corporation(KX132600031).

References

1. Li Z, Huang J (2005) GPS measurement and data processing. Wuhan University Press, Wuhan
2. Li Z, Zhang X (2009) Satellite navigation and positioning technology and high precision data processing method. Wuhan University Press, Wuhan

3. BeiDou satellite navigation system open service performance specification (1.0edition) [S/OL] (2013) China Satellite Navigation System Management Office, Beijing
4. Yang Y, Li J, Wang A et al (2014) Primary navigation and positioning performance of BeiDou satellite navigation system. SCIENTIA SINICA·Earth Sci 44:72–81
5. Wang S, Wang Q, Nie W et al (2013) The analysis and improvement of the high precision positioning model of BeiDou satellite system. J Navig Positioning 1(3):31–32
6. Qiu X, Liu G, Duan P, Wang B, Sha W (2015) Comparison analysis of Ill-condition for GPS and BeiDou carrier phase positioning. Sci Surv Mapp 40(7)
7. He J, Liu W, Zhang X et al (2015) The measured data of short baseline BeiDou triple band single epoch ambiguity fixed. J Wuhan Univ Inf Sci Ed 30(3):361–365
8. Gao M, Xu A, Zhu H et al (2015) Data processing method of short baseline solution for BeiDou system. Sci Surveying Mapp 40(4):28–33
9. Deng C, Tang W, Liu J, Shi C (2014) Reliable single-epoch ambiguity resolution for short baselines using combined GPS/BeiDou system. GPS Solut 18(3):375–386
10. Montenbruck O, Steigenberger P, Hauschild A (2015) Broadcast versus precise ephemerides: a multi-GNSS perspective. GPS Solut 19(2):321–333
11. Liu W, Ren J, Zeng Q et al (2016) Accuracy evaluation of BeiDou space signal ranging error in 2013–2015. J Nat Univ Defense Technol 38(3)
12. Zhang X, He X, Liu W (2016) Characteristics of systematic errors in BDS Hatch-Melbourne-Wübbena combination and its influence on wide-lane ambiguity resolution. GPS Solut. doi:10.1007/s10291-016-0520-6
13. Wanninger L, Beer S (2015) BeiDou satellite-induced code pseudorange variations: diagnosis and therapy. GPS Solut 19:639–648
14. Guo F, Li X, Liu W(2016) Mitigating BeiDou satellite-induced code bias: taking into account the stochastic model of corrections. Sensor 16, 909; doi:10.3390/s16060909
15. Teunissen PJG, Joosten P, Tiberius CCTM (2002) A comparison of TCAR, CIR and LAMBDA GNSS ambiguity resolution. In: ION GPS 2002, Portland, OR, pp 2799–2808
16. Verhagen S, Teunissen PJG (2013) The ratio-test for future GNSS ambiguity resolution. GPS Solut 17(4):535–548
17. http://www.BeiDou.gov.cn

A New Method of the Real-Time Precise Point Positioning Based on Epoch Difference of Satellite Clock Offset

Taogao Dai, Chen Chen, Jianwen Li, Peng Pang and Yongtao Li

Abstract The traditional real-time precise point positioning (PPP) model uses the satellite absolute clock offset products to achieve high accurate positioning. Precise satellite clock offset can be calculated by non-difference observation model and by epoch difference observation model. Non-difference observation model can directly solve the absolute satellite clock offset. While there are too many ambiguity parameters in the non-difference model which causing the dimensions of normal equation matrix are too large so that the calculation efficiency is lower. The epoch difference observation model eliminates the ambiguity parameters. Although the efficiency is much higher, while it solves the epoch difference of the satellite clock, and when restoring, the absolute clock offset of each epoch must require the initial clock offset. In this paper, a new real-time PPP method is proposed by using the epoch differential observation model, and this method can directly use the satellite clock offset products between epochs to positioning. The experimental results show that the positioning accuracy in both horizontal and elevation direction are better than 3.5 cm.

Keywords Real-time · PPP · Satellite clock offset · Epoch differential model · Carrier phase · Filter

1 Introduction

International GNSS Service Organization (IGS) which is intended to provide users with more accurate and faster services of positioning, issues satellite orbit, clock offset, ionospheric, and other precise products. Taking advantage of these products, the positioning accuracy can be raised from the meter to the centimeter or to millimeter level. The satellite clock offset is one of the important factors in the error

T. Dai (✉) · C. Chen · J. Li · P. Pang · Y. Li
Institute of Navigation and Aerospace Engineering, Information Engineering University, Zhengzhou 450001, China
e-mail: 18530948776@163.com; 1187611462@qq.com

J. Sun et al. (eds.), *China Satellite Navigation Conference (CSNC) 2017 Proceedings: Volume III*, Lecture Notes in Electrical Engineering 439,
DOI 10.1007/978-981-10-4594-3_22

sources which affect the accuracy of positioning [1]. Because the satellite clock offset is difficult to describe accurately by the model, the accurate prediction ability of the satellite clock offset is weaker than that of the satellite orbit, especially in the long-term prediction. A better method to solve this problem is to calculate the satellite clock offset in real time. And there are two common methods: non-difference method and epoch differential method. Non-difference method can directly calculate the value of the satellite clock offset of each epoch, but the epoch differential method works out the difference between epochs. And it needs to accumulate these epoch differences of satellite clock offset to restore the value at each epoch. The great advantage of the epoch differential method is that the calculation is of high efficiency and only the carrier phase would calculate the high-precision satellite clock offset between epochs. However, if the epoch difference value has jumped in result of the inaccurate cycle skip flag, the jump value could be passed to the subsequent epoch value. So there is a certain risk to calculate the satellite clock offset only by using the epoch differential method. Instead, it needs the non-difference method to adjust the initial satellite clock offset. Usually the PPP based on non-difference model uses the epoch value of the precise satellite clock offset, instead of the epoch difference value. Besides, the epoch differential model is also suitable for positioning. This paper makes a new adjustment in the positioning mathematic model based on the epoch differential observation model so that it can directly use the products of satellite clock offset between epochs. The experimental results show that this new PPP method is feasible and is more high efficient.

2 The Principle of Satellite Clock Offset Determination Based on Epoch Differential Model

The carrier phase observation has an initial ambiguity parameter, which does not change when no cycle slip occurs. The epoch differential observation is the difference between epochs of non-difference observations. If the cycle slip of adjacent epoch does not occur, the epoch differential observation of carrier phase will eliminate ambiguity parameters, so that the number of parameters to be estimated in the equation could be decreased. In order to reduce the influence of ionospheric delay, the ionospheric free combination is treated as the non-difference observation. The basic observation model can be expressed as follows.

$$\begin{cases} P_c(t) = \rho_0(t) + \mathrm{dtr}(t) - \mathrm{dts}(t) + m_h(t) \cdot \mathrm{zhd} + m_w(t) \cdot \mathrm{zwd} + \varepsilon_{P_c}(t) \\ L_c(t) = \rho_0(t) + \mathrm{dtr}(t) - \mathrm{dts}(t) + m_h(t) \cdot \mathrm{zhd} + m_w(t) \cdot \mathrm{zwd} + \lambda_c \cdot N + \varepsilon_{L_c}(t) \end{cases} \tag{1}$$

In the equation, t is an epoch, P_c and L_c are pseudo-range and carrier phase of the ionospheric free combination observation, respectively. ρ_0 is the distance from

satellite to tracking station. dtr is receiver clock offset. dts is satellite clock offset. zhd and zwd, respectively, are the zenith tropospheric dry and wet delay. m_h and m_w are the corresponding zenith mapping function [2]. N is the ambiguity parameter. λ_c is the wavelength of the ionospheric free combination observation. ε_{P_c} and ε_{L_c} are pseudo-range and carrier phase noise, respectively. For the construction method of the ionospheric free combination, see the literature [3, 4].

It can be seen from Eq. (1) that a carrier phase observation corresponds to an ambiguity parameter. When the number of carrier phase observations is large, the ambiguity parameter occupies a large proportion in all parameter lists.

The epoch differential mathematical model below can be obtained by the difference between epoch t and $t+1$ in the Eq. (1).

$$\begin{cases} \Delta P_c(t,t+1) = \Delta\rho_0(t,t+1) + \Delta\mathrm{dtr}(t,t+1) - \Delta\mathrm{dts}(t,t+1) \\ \qquad\qquad + \Delta m_h(t,t+1)\cdot\mathrm{zhd} + \Delta m_w(t,t+1)\cdot\mathrm{zwd} + \varepsilon_{\Delta P_c}(t+1) \\ \Delta L_c(t,t+1) = \Delta\rho_0(t,t+1) + \Delta\mathrm{dtr}(t,t+1) - \Delta\mathrm{dts}(t,t+1) \\ \qquad\qquad + \Delta m_h(t,t+1)\cdot\mathrm{zhd} + \Delta m_w(t,t+1)\cdot\mathrm{zwd} + \varepsilon_{\Delta L_c}(t+1) \end{cases} \tag{2}$$

In the equation, Δ is the difference operator between epoch t and $t+1$. In order to simplify representation of the formula, the following usage is the same.

The tropospheric dry delay can be corrected to the centimeter level by model correction [5], while wet delay model correction is poor. So tropospheric wet delay is treated as a parameter to estimate here. From Eq. (2), we can derive the error equation of satellite clock offset based on epoch differential model given below.

$$\begin{cases} V_{P_c}(t+1) = \Delta\mathrm{dtr} - \Delta\mathrm{dts} + \Delta m_w\cdot\mathrm{zwd} + \varepsilon_{\Delta P_c}(t+1) \\ V_{L_c}(t+1) = \Delta\mathrm{dtr} - \Delta\mathrm{dts} + \Delta m_w\cdot\mathrm{zwd} + \varepsilon_{\Delta L_c}(t+1) \end{cases} \tag{3}$$

In the equation,

$$\begin{cases} V_{P_c}(t+1) = \Delta P_c - \Delta\rho_0 - \Delta m_h\cdot\mathrm{zhd} \\ V_{L_c}(t+1) = \Delta P_L - \Delta\rho_0 - \Delta m_h\cdot\mathrm{zhd} \end{cases} \tag{4}$$

In the error Eq. (3), the coefficient design vectors of the two equations are identical. If both are involved in calculating, the coefficient matrix is correlative so that cannot get the solution. Instead, it only chooses the high measurement carrier phase observation to participate in calculation. In addition, the satellite clock offset parameter directly calculated by this model is $\Delta\mathrm{dts}(t,t+1)$, which is the epoch difference value.

In this paper, the satellite orbit is fixed to the prediction arc of ultra-fast ephemeris, and the coordinates of the tracking station are fixed to the weekly solution coordinates in SINEX file (also by PPP method, daily change value of the tracking station coordinates is so small that can be ignored in satellite clock offset estimation).

3 A New Precise Point Positioning Method Based on Epoch Differential Model

PPP often uses non-difference model for solution. If with epoch differential model for PPP, it is commonly used to solve the difference of position between epochs. Besides, the precise satellite clock offset products used in the above positioning modes are the epoch value of the satellite clock offset, instead of directly utilizing the epoch difference of it. If it is only to accumulate epoch differences of satellite clock offset for restoring the required epoch value of satellite clock offset, some anomalies differences between epochs will be passed to the subsequent restored satellite clock offsets, thus will bring influence in the follow-up positioning accuracy. Therefore, it is a risk to only utilize the product of satellite clock offset between epochs to work out epoch value of satellite clock offset.

In this paper, a new PPP model is designed to directly make use of the satellite clock offset products between epochs. It is supposed that the non-difference observation model of positioning at epoch t is as given below.

$$\begin{cases} P_c(t) = \rho_{X_0}(t) + (l(t), m(t), n(t)) \cdot \begin{pmatrix} dX \\ dY \\ dZ \end{pmatrix} + \mathrm{dtr}(t) - \mathrm{dts}(t) + m_h(t) \cdot \mathrm{zhd} \\ \qquad + m_w(t) \cdot \mathrm{zwd} + \varepsilon_{P_c}(t) \\ L_c(t) = \rho_{X_0}(t) + (l(t), m(t), n(t)) \cdot \begin{pmatrix} dX \\ dY \\ dZ \end{pmatrix} + \mathrm{dtr}(t) - \mathrm{dts}(t) + m_h(t) \cdot \mathrm{zhd} \\ \qquad + m_w(t) \cdot \mathrm{zwd} + \lambda_c \cdot N + \varepsilon_{L_c}(t) \end{cases} \tag{5}$$

In the equation, ρ_{X_0} is the distance from the satellite to sketchy coordinates X_0 of the tracking station, (dX, dY, dZ) is the three-dimensional deviation of the relative sketchy coordinates, and the remaining parameters are the same as Eq. (1).

Based on Eq. (5), and assuming it is static positioning mode, the new epoch differential model between t and $t+1$ is as follows.

$$\begin{cases} \Delta P_c = \Delta\rho_{X_0} + (\Delta l, \Delta m, \Delta n) \cdot \begin{pmatrix} dX \\ dY \\ dZ \end{pmatrix} + \Delta\mathrm{dtr} - \Delta\mathrm{dts} + \Delta m_h \cdot \mathrm{zhd} + \Delta m_w \cdot \mathrm{zwd} + \varepsilon_{\Delta P_c} \\ \Delta L_c = \Delta\rho_{X_0} + (\Delta l, \Delta m, \Delta n) \cdot \begin{pmatrix} dX \\ dY \\ dZ \end{pmatrix} + \Delta\mathrm{dtr} - \Delta\mathrm{dts} + \Delta m_h \cdot \mathrm{zhd} + \Delta m_w \cdot \mathrm{zwd} + \varepsilon_{\Delta L_c} \end{cases} \tag{6}$$

And the new model error equation of the PPP can be derived from the shift of Eq. (6), which is shown as below.

$$\begin{cases} V_{P_c}(t+1) = (\Delta l, \Delta m, \Delta n) \cdot \begin{pmatrix} dX \\ dY \\ dZ \end{pmatrix} + \Delta\text{dtr} - \Delta\text{dts} + \Delta m_w \cdot \text{zwd} + \varepsilon_{\Delta P_c}(t+1) \\ V_{L_c}(t+1) = (\Delta l, \Delta m, \Delta n) \cdot \begin{pmatrix} dX \\ dY \\ dZ \end{pmatrix} + \Delta\text{dtr} - \Delta\text{dts} + \Delta m_w \cdot \text{zwd} + \varepsilon_{\Delta L_c}(t+1) \end{cases} \tag{7}$$

In the above equation,

$$\begin{cases} V_{P_c}(t+1) = \Delta P_c - \Delta\rho_0 - \Delta m_h \cdot \text{zhd} \\ V_{L_c}(t+1) = \Delta P_L - \Delta\rho_0 - \Delta m_h \cdot \text{zhd} \end{cases} \tag{8}$$

It can be seen from Eq. (7) that the new epoch differential model eliminates the ambiguity parameters, and the clock offset parameters are the epoch difference. Meanwhile, the position parameters are the epoch values of tracking station coordinates. In Eq. (7), both parameters design vector are the same, so that it can just use the difference observations of carrier phase to positioning. In order to speed up the convergence, the initial probability coordinates should be given by standard point positioning with pseudo-range observation.

Because the products of satellite clock offset between epochs are directly used in the new precision positioning method, the jumping of epoch difference does not affect the subsequent positioning accuracy.

4 Date Processing Strategy

In this paper, GPS is taken as an example. In order to get all of the GPS satellite clock offsets, observations of 40 tracking stations evenly selected in the whole world are used to simulate the real-time processing. The distribution of the selected tracking stations is shown in Fig. 1.

In the use of epoch differential model to calculate the satellite clock offsets, the corresponding model and parameters configuration [6, 7] are shown in Table 1.

Combined with the above satellite clock offset calculation model and parameters configuration, the data processing flow chart of real-time satellite clock offset determination by epoch differential model is shown in Fig. 2.

The products of satellite clock offsets between epochs are directly used to realize the new real-time PPP by epoch differential model. The model and parameters configuration [7, 8] of the positioning are shown in Table 2.

Besides, the data processing flow chart of the new real-time PPP by epoch differential model is shown in Fig. 3.

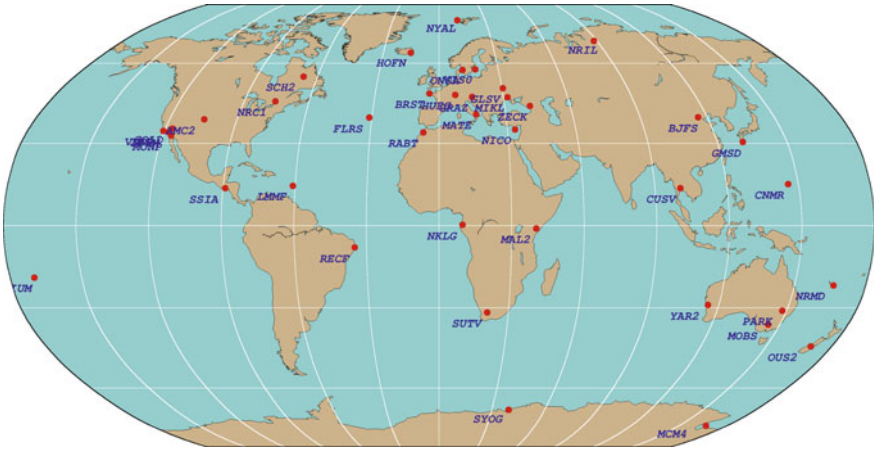

Fig. 1 Distribution map of selected tracking stations

Table 1 Models and parameters of satellite clock offset determination

Category	Model and parameters
Cutoff angle of height	10°
Observation	Ionospheric free combination
Antenna phase center	igs08.atx
Phase windup	Model correction
Tide correction	Solid, ocean, pole
EOP	Fixed to the prediction of the IGS
Satellite orbit	Fixed to the prediction arc of ultra-fast ephemeris
Tracking station position	Fixed to the coordinate of SINEX file
Tropospheric delay	SaaS model correction + estimating wet weight
Satellite clock offset	Broadcast ephemeris clock offset correction + parameter estimation + white noise
Receiver clock offset	Parameter estimation + white noise

5 Examples and Analysis

Due to the limited real-time data streams, this paper conducts the real-time test with the after-observation data. The satellite clock offsets are real-time calculated based on the epoch differential model with the selected tracking stations' observation data on the 333rd day of 2016. Meanwhile three tracking stations are selected to simulate the real-time PPP.

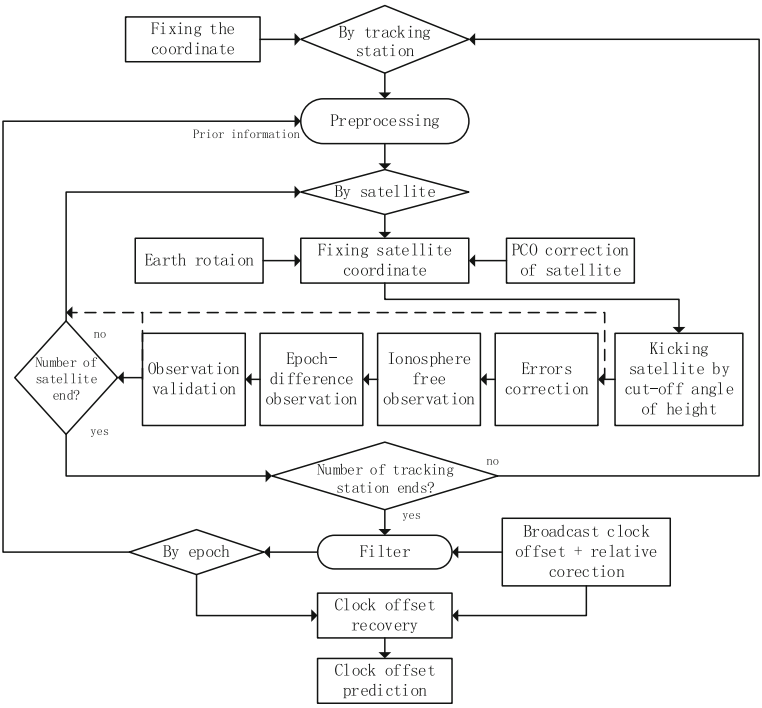

Fig. 2 Data processing flow chart of real-time satellite clock offset determination by epoch difference model

Table 2 Models and parameters of the new real-time PPP

Category	Model and parameters
Cutoff angle of height	10°
Observation	Ionospheric free combination
Antenna phase center	igs08.atx
Windup	Model correction
Tide correction	Solid, ocean, pole
EOP	Fast EOP product of IGS
Satellite orbit	Ultra-fast ephemeris prediction arc
Satellite clock	Real-time satellite clock offset between epochs
Tropospheric delay	SaaS model + estimating wet weight
Receiver clock offset	Parameter estimation + white noise
Position parameters	Parameter estimation

In order to evaluate the accuracy of satellite clock offset between epochs, the precise clock products of GFZ Analysis Center are chosen as the reference, and by means of root mean square (rms) as well as standard deviation (std). Because of the

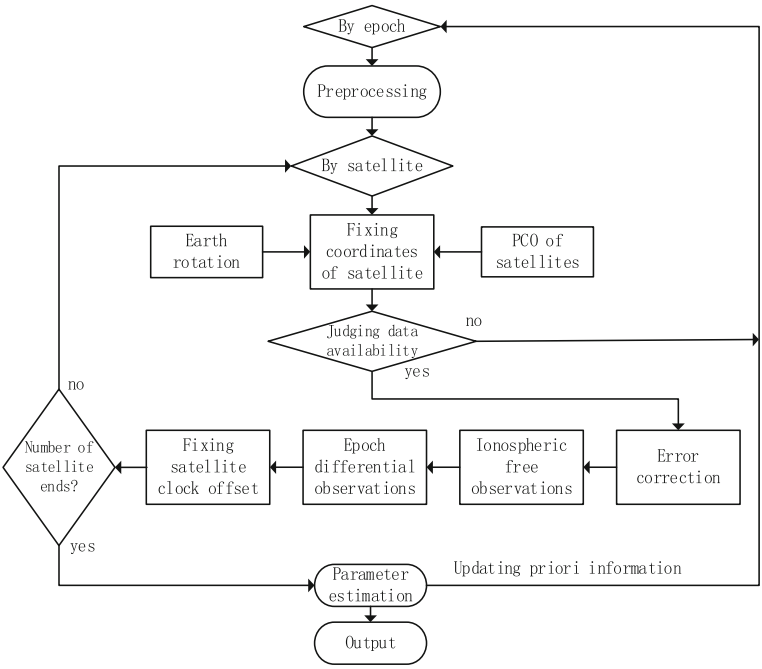

Fig. 3 Data processing flow chart of new real-time PPP

difference between the two reference clocks, it should first unify the reference clock, and then seek difference for comparison, called as "second difference" method [9, 10].

The accuracy of satellite clock offsets between epochs based on the epoch differential model is shown in Fig. 4 (G01 is the reference satellite, and the following is the same).

The accuracy of the single epoch satellite clock offset restored by that between epochs is shown in Fig. 5.

It can be seen that rms and std of the satellite clock offset between epochs are both better than 0.014 ns from Fig. 4. After recovery, rms of the epoch satellite clock offset is better than 0.35 ns, while std of that is better than 0.25 ns.

Using above products of satellite clock offsets between epochs to conduct real-time PPP, the program is designed as follows (Table 3).

Taking the BUCU tracking station as an example, the positioning accuracy of each program is shown in Figs. 6 and 7, and the positioning efficiency of the non-difference and epoch differential model is shown in Fig. 8.

It can be seen that the tendency of bias variation has no significant differences for each program, which shows that the satellite clock offset calculated by epoch differential model is self-consistent with the orbit. The results also show that the

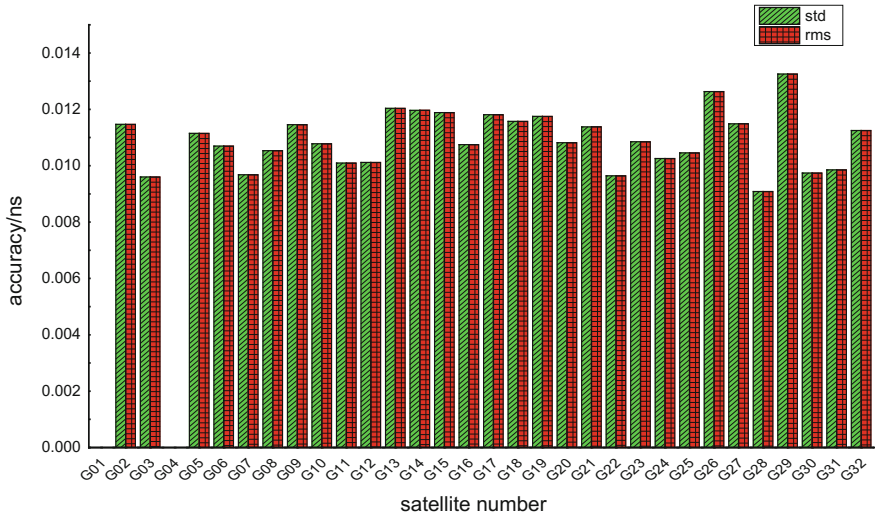

Fig. 4 Accuracy of satellite clock offset between epochs

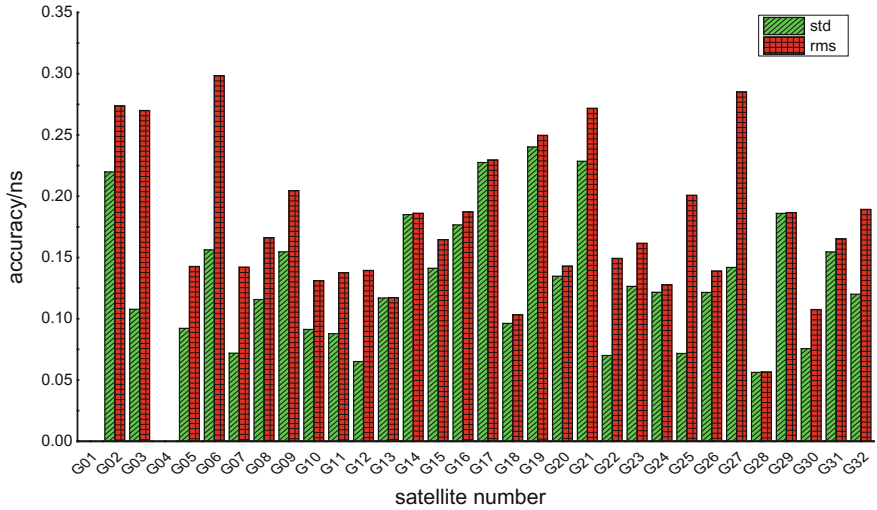

Fig. 5 Accuracy of satellite clock offset after recovery

Table 3 Program design of real-time PPP

Positioning mode	GBM clock offset products	Clock offset products by epoch differential model
Non-difference	1	2
Epoch difference	3	4

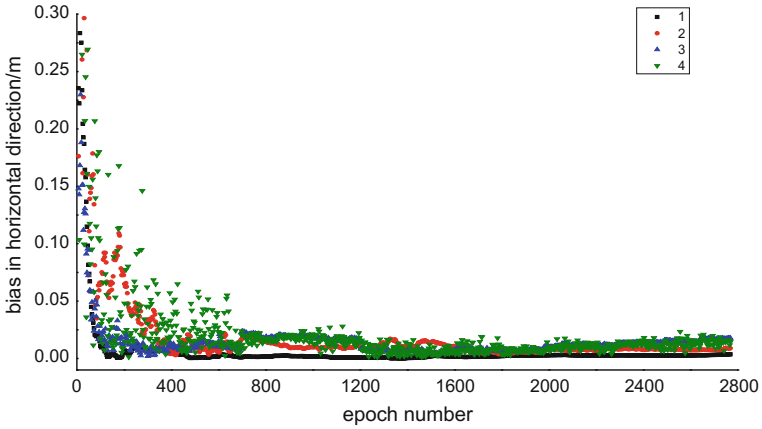

Fig. 6 Bias of every program in horizontal direction

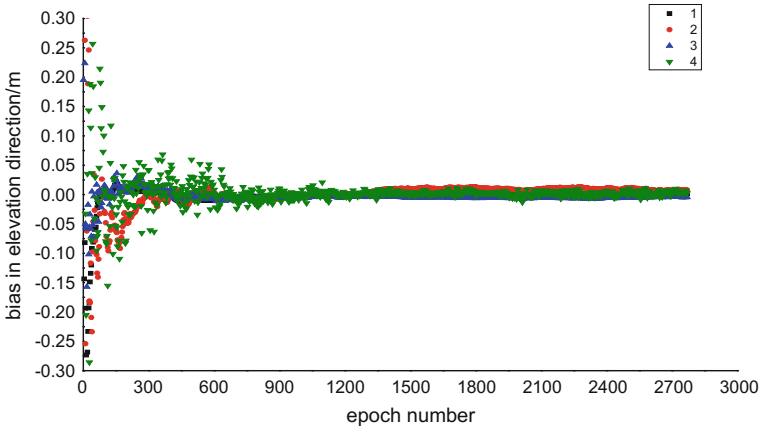

Fig. 7 Bias of every program in elevation direction

non-difference model converges faster than the epoch differential model, and the positioning accuracy is slightly better than that of the epoch differential model.

The accuracy differences of four positioning strategies are shown in table as follows.

It can be concluded from Tables 4 and 5 that the positioning accuracy of non-difference model is better than that of the new epoch differential model. With use of the restored satellite clock offsets based on the epoch differential model, the positioning accuracy in horizontal direction is better than 1.2 cm, and that is better than 0.9 cm in elevation direction. However, with use of the products between epochs, the accuracy in horizontal direction is better than 3.5 cm, and that is better than 2.5 cm in elevation direction. The reasons may be shown in the following. On

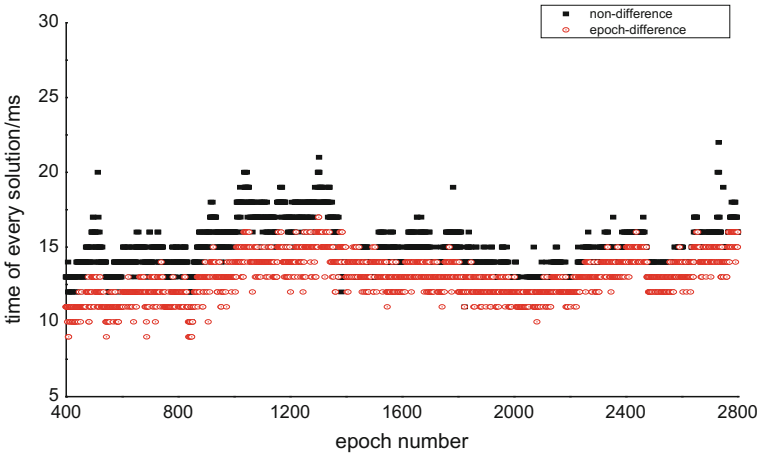

Fig. 8 Positioning efficiency of the non-difference and epoch differential model

Table 4 Accuracy of every program in horizontal direction

Tracking station	(cm)	1	2	3	4
BUCU	STD	0.09	0.32	0.48	0.58
	RMS	0.23	1.01	1.35	1.33
DRAG	STD	0.15	0.38	0.55	0.72
	RMS	0.40	0.57	2.88	3.26
GLSV	STD	0.19	0.25	0.76	0.92
	RMS	0.58	1.13	3.50	3.35

Table 5 Accuracy of every program in elevation direction

Tracking station	(cm)	1	2	3	4
BUCU	STD	0.22	0.66	0.16	0.59
	RMS	0.22	0.89	0.49	0.60
DRAG	STD	0.26	0.61	0.89	1.58
	RMS	0.56	0.68	1.11	2.44
GLSV	STD	0.21	0.46	0.28	1.13
	RMS	1.01	0.47	0.28	1.57

the one hand, the observation noise is amplified when making difference between observations. On the other hand, since the ambiguity parameters are removed by epoch differential model, Kalman filter mainly deals with random noise so that it is less easy to fix the position parameters. It can be seen from the positioning accuracy in horizontal and elevation direction that the satellite clock offset has a greater influence on the horizontal direction.

6 Conclusion

Satellite clock offset is one of the most important error sources which affect the accuracy of the PPP, so the high precision of it is the basis of the high precision of positioning. The satellite clock offset between epochs can be calculated in high precision based on epoch differential model, while it is not able to satisfy the PPP based on the non-difference model. In this paper, a new positioning method whose observation mathematical model is reconstructed is proposed to directly utilize the clock products between epochs. Although its positioning accuracy is not as good as the non-difference model, it will remove the ambiguity parameters and improve the calculation efficiency. So it could provide a new solution for the real-time PPP.

Acknowledgements Thanks to the data support provided by LSN iGMAS Analysis Center of the Information Engineering University.

References

1. Huang G (2009) Research on GPS precise point positioning and adjustment of high precision GPS baseline network and the realization of its software. Chang'an University, Xian, p 6
2. Ren K, Wu X, Jia X (2014) Realtime satellite clock estimation using undifferenced method. In: The 5th China satellite navigation conference—S4 atomic clock technology and time-frequency system
3. Chang Z, Hu R, Su X (2014) The positioning precision analysis with ionnsphere free combination of regional satellite navigation system. J Geomatics Sci Technol 6(31):557–558
4. Wan J (2016) Research on fusion algorithm of cycle slip detection and correction for GNSS. Chinese Academy of Surveying and Mapping, Beijing, p 6
5. Shi Z, Meng X, Guo J (2009) Comparison between modeling method and parameter estimation method in tropospheric delay correction of GPS precise point positioning. Bull Surveying Mapp 6:9–11
6. He M, Li X, Li P (2011) Comparison and analysis of estimations of precise satellite clock error based on non-difference model and epoch differential model. J Geodesy Geodyn 1 (31):95–99
7. Pan Z, Cai H, Dong B (2015) Real-time GPS precise satellite clock error estimation and precise point positioning. Hydrogr Surveying Charting 5(35):12–15
8. Song W (2011) Research on real-time clock offset determination and real-time precise point positioning. Wuhan University, Hubei, p 4
9. Li X, Xu Y, Wang L (2010) Undifferenced precise satellite clock error estimation and precision analysis. Geomatics Inf Sci Wuhan Univ 6(35):661–664
10. Lou Y, Shi C, Zhou X (2009) Realization and analysis of GPS precise clock products. Geomatics Inf Sci Wuhan Univ 1(34):88–91

Epoch-Differenced Cycle Slip Resolution Technique Considering Velocity Constraint

Yuanjun Chen, Xiang Zuo, Xiaoyu Shi and Chenggang Li

Abstract Carrier phase cycle slip detection and repair technology is one of the key technologies of high precision GNSS positioning. Carrier phase cycle slip cause the discontinuity of carrier phase observations. If the cycle slip can not be detected, which would draw an extra bias into positioning model with a minimum level of decimeter. Although, using a single epoch RTK algorithm can avoid the influence of carrier phase cycle slip, the method relies on high precision pseudorange observations or priori coordinates and it does not apply to the general high precision RTK positioning, especially for the single-frequency receivers. No doubt, the cycle slip detection and repair technology is vital for high precision carrier phase positioning. In order to satisfy the precision of sub-meter even centimeter RTK positioning with a low-cost single-frequency GNSS receiver, this paper proposes a cycle slip resolution method, which used velocity constraint information based on the carrier phase epoch-differenced model. First, we use Doppler observations to estimate the velocity of the current epoch, using the last epoch computed velocity, we can get the mean velocity between epochs, and multiply the mean velocity by the time difference between adjacent epochs, we can obtain epoch-differenced position increments vector. Then we can use the position increments as virtual observations, detect cycle slip with a modified data snooping method combined with the carrier phase epoch-differenced observations. Compared with the method only use the carrier phase epoch-differenced observations, more observation information is used with the velocity constraint information, and the accuracy and reliability of the detection result would also be improved. Experimental results show that the proposed epoch-differenced cycle slip resolution method can be effectively used in low-cost single-frequency RTK positioning.

Keywords Single-frequency · Low cost · Kinematic positioning · Cycle slip detection · Velocity constraint

Y. Chen (✉) · X. Zuo · X. Shi · C. Li
R&D Center, Guangzhou Hi-Target GNSS Navigation Technology Co., Ltd, Guangzhou 511400, China
e-mail: yjchen218@163.com

J. Sun et al. (eds.), *China Satellite Navigation Conference (CSNC) 2017 Proceedings: Volume III*, Lecture Notes in Electrical Engineering 439,
DOI 10.1007/978-981-10-4594-3_23

1 Introduction

Carrier phase cycle slip detection and repair technology is one of the key technology of high precision GNSS positioning, which directly influences the efficiency, availability, and reliability of RTK positioning. The carrier phase epoch-differenced model-based cycle slip detection method has a high detection accuracy without considering the receiver movement. Kirkko-Jaakkola M, etc., utilized a RAIM (Receiver Autonomous Integrity Monitoring) approach to detect GNSS outlier and cycle slip based on L1 carrier phase epoch-differenced mode [1]. A more efficient data snooping method with the same cycle slip detection model used to detect carrier phase cycle slip in [2]. YI Zhonghai, etc., developed a new cycle slip resolution algorithm suitable for real-time precise point positioning combination M-W method and phase–phase ionosphere residual method with carrier phase epoch-differenced cycle slip detection model [3]. In the field of RTK, Yuan-Hong, etc., illustrated a cycle slip method to handing cycle slip problem in ambiguity resolution on-the-fly based on triple differences solution [4]. Another study in [5] fusing the inertial data with the triple differences solution, can resolve the cycle slip problem even in the challenging environment. To avoid the problem of selecting a clear reference satellite in the triple differences solution based method, the research in [6] proposed a method based on double differenced model between receivers and epochs. Compared with triple differences solution based method, applicability and reliability of the double-difference model-based method has a certain increase. When using the epoch-differenced model-based cycle slip resolution method, more than four satellites need observed. The detection ability and reliability of the method affected by the model's redundant observation number and the geometric distribution of the observed satellites. Currently, with the rapid developing multi-GNSS, much more satellites could be observed, which enhanced the availability and reliability of epoch-differenced model-based cycle slip resolution method significantly, but still exist the problem that sometimes cycle slip is difficult to distinguish between satellite observations just using epoch-differenced carrier phase observations.

In this work, a new epoch-differenced model-based method was proposed, which introduced a velocity constraint. First, we use Doppler observations to estimate the velocity of the current epoch, using the last epoch computed velocity, we can get the mean velocity between epochs, and multiply the mean velocity by the time difference between adjacent epochs, we can obtain epoch-differenced position increments vector. Then we can use the position increments as virtual observations, detect cycle slip with a modified data snooping method combined with the carrier phase epoch-differenced observations. Experimental results show that the proposed epoch-differenced cycle slip resolution method can be effectively used in low-cost single-frequency RTK positioning.

2 Measurement Model

2.1 Double-Differenced (DD) Model Between Receivers and Epochs

The linearised single differences (SD) phase measurement equation between rover and base station can be written as

$$\lambda\Delta\varphi_t^p = \Delta\rho_t^p + l_{x,t}^p x_t + l_{x,t}^p x_t + l_{x,t}^p x_t + \Delta c\delta t_t - \Delta\delta\mathrm{ion}_t^p + \Delta\delta\mathrm{trop}_t^p + \lambda\Delta N^p + \varepsilon \quad (1)$$

where Δ is the station single differences operator, superscript t denotes the epoch time, and subscript p denotes the satellite. φ is the carrier phase measurement in cycle and λ is its wavelength. ρ is the geometric range, $\Delta\delta$ion and $\Delta\delta$trop denotes the ionospheric delay and tropospheric delay, respectively. $c\delta t$ is the receive clock error in meter, and N is the phase ambiguity which is constant during continuous phase lock. ε accounts for the phase noise and other remaining error. $l_{x,t}^p$, $l_{y,t}^p$, $l_{z,t}^p$ is the coefficient of the three coordinate parameters respectively, and $l_{x,t}^p = \left(\mathrm{X}_t^0 - \mathrm{X}_t^p\right)/\rho_t^p$, $l_{y,t}^p = \left(\mathrm{Y}_t^0 - \mathrm{Y}_t^p\right)/\rho_t^p$, $l_{z,t}^p = \left(\mathrm{Z}_t^0 - \mathrm{Z}_t^p\right)/\rho_t^p$, where $\begin{pmatrix}\mathrm{X}_t^0 & \mathrm{Y}_t^0 & \mathrm{Z}_t^0\end{pmatrix}^T$ represent the initial approximate coordinates vector of the rover station at epoch t. $\begin{pmatrix}\mathrm{X}_t^p & \mathrm{Y}_t^p & \mathrm{Z}_t^p\end{pmatrix}^T$ is the coordinate vector of satellite p at epoch t. $\begin{pmatrix}x_t & y_t & z_t\end{pmatrix}^T$ is the receiver position corrective value vector at epoch t.

For a short baseline under 15 km, atmospheric errors could be neglect in SD above. Then the double differences (DD) equation between two single differences related to the same satellite at adjacent epochs can be written as

$$v_p = l_{x,t2}^p dx + l_{y,t2}^p dy + l_{z,t2}^p dz + \Delta T - l_p + \gamma_{t1,t2}^p \quad (2)$$

where $t1$ and $t2$ denote two adjacent epochs, v_p is the DD residual of satellite p. $dx = x_{t2} - x_{t1}$, $dy = x_{t2} - x_{t1}$, $dz = z_{t2} - z_{t1}$, $l_p = (\lambda\Delta\varphi_{t2}^p - \lambda\Delta\varphi_{t1}^p) - (\Delta\rho_{t2}^p - \Delta\rho_{t1}^p)$, $\Delta T = \mathrm{c}\delta\mathrm{t}_{t2} - \mathrm{c}\delta\mathrm{t}_{t1}$, $\gamma_{t1,t2}^p = (l_{x,t2}^p - l_{x,t1}^p)x_{t1} + (l_{y,t2}^p - l_{y,t1}^p)y_{t1} + (l_{z,t2}^p - l_{z,t1}^p)z_{t1}$. $\gamma_{t1,t2}^p$ term is so small relative to the carrier phase length, so we can neglect its effect [6]. Neglecting $\gamma_{t1,t2}^p$ term, Eq. (2) can be transformed into

$$v_p = l_{x,t2}^p dx + l_{y,t2}^p dy + l_{z,t2}^p dz + \Delta T - l_p \quad (3)$$

the matrix form of total DD equations related to one epoch can be described as

$$V_\varphi = A_\varphi dX1 + I_{m\times 1}\Delta T - l_\varphi,\ P_\varphi \quad (4)$$

where

V_φ DD residual vector of dimension m,
A_φ DD coefficient matrix of dimension $m \times 3$,
$I_{m\times 1}$ vector of dimension m, whose elements all are 1,
$dX1$ unknown coordinate parameter vector of dimension 3, $dX1 = (\,dx \quad dy \quad dz\,)^T$,
ΔT unknown clock bias rate parameter vector of dimension 1,
l_φ DD observation minus compute vector of dimension m,
P_φ symmetric and definite weight matrix of dimension $m \times m$, which can be derived from the elevation angle based stochastic model,
m number of the DD equations.

For a short baseline under 15 km, double differences (DD) between rover station and base station at two adjacent epochs are extremely effective for eliminating common mode orbital, satellite clock errors, and atmospheric errors. When the velocity of rover receiver is less than 250 m/s, and the accuracy of the initial approximate receiver coordinates would be better than 10 m, for sampling interval of 0.2, 1.0 s observation data, give a limit error caused by neglecting $\gamma^p_{t1,t2}$ term, in turn, is 0.84, 4.2 mm, which is far smaller than the wavelength of the GNSS carrier phase [6]. Once cycle slip occurrence in the carrier phase observation, equivalent to introduced an extra bias with a minimum level of decimeter into the DD-based cycle slip detection model. Equation (4) contains only four parameters, so only need two adjacent epochs observed phase observation, can realize carrier phase cycle slip detection.

2.2 Velocity Constraint Equations

The velocity of receiver could be estimated by Doppler observations based on least square method when four or more satellites observed, the detail mathematic model and process can be find in reference [7]. At present, the sampling data rate of RTK general is 1 or 5 Hz, part of some receivers support 20 Hz, so the time difference between two adjacent epochs is so small that the receiver can be thought of moving in a uniform variable motion. Denoting the receiver velocity vector at epoch t as $\dot{X}1_t$, the position increments between the two adjacent epochs could be obtained by:

$$\Delta X1_{t1,t2} = \frac{1}{2}\left(\dot{X}1_{t1} + \dot{X}1_{t2}\right) \cdot \Delta t_{t1,t2} \tag{5}$$

where $t1$ and $t2$ are two adjacent epochs, $\Delta X1_{t1,t2}$ is epoch-differenced position increments vector of dimension 3, $\Delta t_{t1,t2}$ denote the time difference, there is $\Delta t_{t1,t2} = t_2 - t_1$. Putting $\Delta X1_{t1,t2}$ as virtual observations, the virtual equations could be built as

$$\Delta X1_{t1,t2} = X1_{t2} - X1_{t1} \tag{6}$$

where $X1_{t1}$ and $X1_{t2}$ denote the receiver position vector at epoch $t1$ and $t2$, respectively. Substituting the initial approximate coordinates vector of the receiver $\begin{pmatrix} X_t^0 & Y_t^0 & Z_t^0 \end{pmatrix}^T$ into Eq. (6), the velocity constraint virtual observation system could be easily derived as

$$V_{\Delta X1} = dX1 - l_{\Delta X1} \tag{7}$$

where

$V_{\Delta X1}$ velocity constraint virtual observation residual vector of dimension 3,

$dX1$ unknown coordinate parameter vector of dimension 3, $dX1 = \begin{pmatrix} dx & dy & dz \end{pmatrix}^T$, the same as in Eq. (4),

$l_{\Delta X1}$ observation minus compute vector, $l_{\Delta X1} = \Delta X1_{t1,t2} - \left(X1_{t2}^0 - X1_{t1}^0\right)$, $X1_{t2}^0$ and $X1_{t1}^0$ is the initial approximate coordinates vector of the receiver at epoch $t1$ and $t2$, respectively.

The corresponding prior-variance could be given by

$$\sigma^2_{(\Delta X1)_i} = \frac{1}{2}\sigma^2_{(\dot{X}1)_i} \cdot \Delta t^2_{t1,t2}, \quad (i = 1, 2, 3) \tag{8}$$

where $\sigma^2_{(\Delta X1)_i}$ is the prior-variance of the virtual observation, $\sigma^2_{(\dot{X}1)_i}$ denotes the variance of the velocity estimated by Doppler observations, which may be set according to the performance of the GNSS receiver used, in this paper the value is set to 0.1 m/s. $\Delta t_{t1,t2}$ is the time difference between epoch $t1$ and $t2$.

3 Cycle Slip Detection and Repair

There are two observation equation systems represented by Eqs. (4) and (7), and these two equation systems are independent and have the common unknown coordinate vector $dX1$. The combined problem can be represented as

$$\begin{bmatrix} V_\varphi \\ V_{\Delta X1} \end{bmatrix} = \begin{bmatrix} A_\varphi & I_{m\times 1} \\ E_{3\times 3} & 0 \end{bmatrix} \begin{bmatrix} dX1 \\ \Delta T \end{bmatrix} - \begin{bmatrix} l_\varphi \\ l_{\Delta X1} \end{bmatrix} \tag{9}$$

where $E_{3\times 3}$ is identity matrix of dimension 3×3, other symbols are the same as in Eqs. (4) and (7).

The posteriori residuals of Eq. (9) could be estimated with least square method, and a residuals test is performed to check if any cycle slip occurred. If the RMS (Root-Mean-Square) of the residuals is less than the setting threshold, the carrier phase would be free from cycle slip, otherwise, cycle slip detection need to take

carefully, and a iterative data snooping method used to detect cycle slip. In the case no cycle slip occurs, residuals are normally distributed and the corresponding standardized residuals are standard normally distributed, there are

$$v_i \sim N(0, \delta_0^2 Q_{v_i v_i}) \tag{10}$$

$$\overline{v_i} \sim N(0, 1) \tag{11}$$

$$\overline{v_i} = \frac{v_i}{\delta_0 \sqrt{Q_{v_i v_i}}} \tag{12}$$

where v_i denotes the posteriori residual of the ith DD observation in Eq. (9), δ_0 denotes the priori standard deviation, $Q_{v_i v_i}$ is the ith diagonal element of residual covariance matrix. If the maximum of $|\overline{v_i}|$ larger than $u_{\alpha/2}$, indicate at least one observation corrupt by outlier, $u_{\alpha/2}$ is the u-test critical value, in this paper set to 2.0.

The velocity estimated by Doppler observations is of high accuracy, whose nominal precision generally reached 0.05 m/s, but in the actual cases, due to the influence of the environment and receiver moving state, the estimated velocity precision is not stable, sometimes lower than the setting priori precision, causing velocity constraint observations detected as a outlier by the data snooping method, result in the corresponding velocity constraint observation removed in the next adjustment process, which lead to useful observation information loss. To handing this problem, some data snooping strategy modified. Once velocity constraint equation detected as a outlier, to adjust the weight of the corresponding velocity constraint virtual observation rather than removed directly, this make the data snooping more robust. The weight of the detected virtual observation could be adjusted as

$$P_{(\Delta X1)_i}^{k+1} = 0.25 \cdot P_{(\Delta X1)_i}^{k}, \quad (i = 1, 2, 3) \tag{13}$$

where $P_{(\Delta X1)_i}^{k}$ and $P_{(\Delta X1)_i}^{k+1}$ denotes the weight of the detected virtual velocity observation in the kth and $k + 1$th iteration, respectively 0.25 in Eq. (13) means that the setting priori variance of the ith component of the estimated velocity amplified to twice the original.

Specific cycle slip detection and repair processes are as follows:

Step 1: Form observation equations as Eq. (9), and solve the equations by least square method. If the RMS value of the carrier phase posteriori residuals satisfy the condition RMS $\leq$ RMS0 (RMS0 take 0.02 m in this paper), means that no cycle slip occurred in current epoch carrier phase observations, and end current epoch cycle slip detection.

Step 2: Calculate the absolute value of each observation posteriori standardized residual $|\overline{v_i}|$, and obtain the maximum $\max(|\overline{v_i}|)$.

Step 3: Check if $\max(|\overline{v_i}|)$ less than the threshold value of 2.0, if so, end current epoch cycle slip detection, otherwise enter the next step.

Step 4: If the corresponding observation of $\max(|\overline{v_i}|)$ is one of the virtual velocity observations, then adjust the observation weight as Eq. (13) in the next iteration, otherwise mark the corresponding satellite cycle slip flag, and remove the observation in next iteration.

Step 5: Solve the equations by least square method after velocity constraint virtual observation weight adjusted or cycle slip marked DD observation removed.

Step 6: Repeat steps (2) (3) (4) (5) until the step (3) to meet $\max(|\overline{v_i}|) < 2.0$, than end current epoch cycle slip detection process.

Step 7: Repair cycle slip with an empirical strategy that the outlier rate of the total carrier phase observations should be less than 20%, and only carrier phase observations that the corresponding DD residual error is less than 3 cm after cycle slip repaired by rounding could be repaired. Cycle slip repair is an open difficult problem for a low-cost receiver, especially when using a low-cost antenna in moving positioning, because of low-cost receiver and antenna susceptible to multipath effect. Furthermore, real-time computing efficiency is another important consideration in RTK positioning. So we adopt a conservative and simple strategy to deal with the cycle slip repair problem.

4 Experiment and Analysis

4.1 Case 1: Road Vehicle-Mounted 5 Hz Data Rate Test

The data was collected in December 2, 2016 on a rural road. Except for some shade trees on both sides of the road, there is no serious barrier around the test field. A affordable Hi-target single-frequency GNSS board named BX220 and a Hi-target double frequency helix antenna named AH-3232 were used in this test. The BX220 GNSS board can track GPS L1 and Beidou B1 signals, and the data sampling rate could be set to 1 or 5 Hz. In this test we used the 5 Hz data rate. The reference station data was collected by a double frequency geodetic-grade receiver, the baseline length is about 1.0 km. The cutoff angle is 12°, and 14 satellites could be observed, that is G12, G15, G18, G20, G21, G25, G32, C01, C02, C03, C07, C10, C13, C14. A –5 cycle slip occurs both in the carrier phase of G15 and G32 at epoch 08:10:23. 0 (GPST), which can be confirmed by comparing the double difference float ambiguitys between adjacent epochs related to the same satellite. The float ambiguity is derived by the receiver-differenced and satellite-differenced double difference carrier phase and the fixed baseline solution estimated by partial ambiguity resolution technology, and the baseline fixed solution of BX220 is similar to a RTK result of a OEM617 board receiver, whose antenna installed

beside the antenna of BX220. Deducting the antenna installation deviation, the solution difference between BX220 and OEM617 is in cm, which ensures the accuracy of the float ambiguities to check whether cycle slip occurs and determine the value of cycle slip if needed.

To evaluate the performance of the new method proposed in this paper, two schemes are designed to detect cycle slip with the collected data: (1) DD model-based cycle slip detection method (original method: no velocity constraint); (2) DD model-based cycle slip detection method considering velocity constraint (new method: with velocity constraint). G18, G02, G25, G10, and G03 is detected as cycle slip satellite in sequence when using the original method, obviously that is not the correct result. While G15 and G32 can be correctly detected as the cycle slip occurrence satellites with the new method. The related calculation information as shown in Table 1. Comparing the epoch-differenced position increments derived by the fixed baseline solution with those calculated by Doppler estimated velocity, we can find that the accuracy of the epoch-differenced position increments calculated by Doppler estimated velocity is in cm level, that means the accuracy of the velocity constraint virtual observations is in cm, such a high accurate prior constraint value ensures the accuracy of the cycle slip detection in the new method.

In the least square system, the relation between residual error V and true error Δ is given by

$$-V = R\Delta \tag{14}$$

$$R = I - B\left(B^T PB\right)^{-1} B^T P \tag{15}$$

where R is the model reliability matrix, B is the design matrix, P is the weight matrix. Denoting R as $R = [F_1 \quad F_2 \quad \cdots \quad F_n]$, where n is number of the observations, F_i (i = 1, 2, .., n) is the ith column vector, which is defined as the influence vector of measurement true error on the residual vector in reference [8]. For two measurements Li and Lj, the ability to distinguish their outlier from each other can be evaluated by the correlation coefficient ρ_{ij} between the corresponding influence vecotrs of Li and Lj. The more absolute value of ρ_{ij} closer to 1, the more difficult to

Table 1 Related calculation information

Variable information		X(m)	Y(m)	Z(m)
Epoch-differenced position increments	(1) By Fixed solution	−0.624	0.047	−0.678
	(2) By estimated velocity	−0.608	0.018	−0.668
	(3) By initial position	−0.708	0.039	−0.707
DD model coordinate parameter	(1)–(3)	0.084	0.008	0.029
	(2)–(3)	0.100	−0.021	0.039
	New method solution	0.100	−0.019	0.036
	Original method solution	0.335	−0.298	1.054

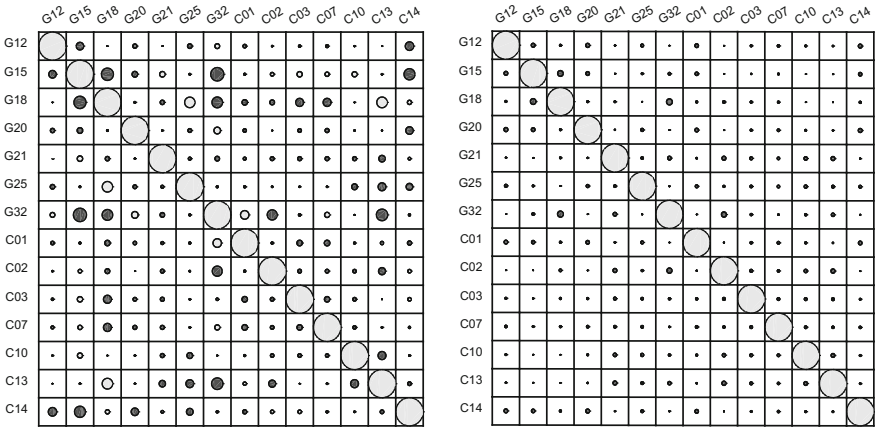

Fig. 1 Model reliability matrix R column vector correlation coefficient contrast (*Left* no velocity constraints *Right* with velocity constraint)

distinguish outlier between Li and Lj [8, 9]. Denoting the ith influence vector F_i as $F_i=[\,r_{i1}\quad r_{i2}\quad \cdots\quad r_{in}\,]^T$, the calculation formula of ρ_{ij} is given by

$$\rho_{ij}=\frac{\sum_{k=1}^{n}(r_{ki}-\overline{r}_i)(r_{kj}-\overline{r}_j)}{\sum_{k=1}^{n}(r_{ki}-\overline{r}_i)^2\sum_{k=1}^{n}(r_{kj}-\overline{r}_j)^2} \tag{16}$$

where

$$\overline{r}_i=\sum_{k=1}^{n}r_{ki},\ \overline{r}_j=\sum_{k=1}^{n}r_{kj}.$$

The correlation coefficients of the model reliability matrix R column vector were calculated at epoch 08:10:23. 0 (GPST), as shown in Fig. 1. Black color represents the correlation coefficient of the corresponding satellite influence vector is negative, while gray represents positive. Assume the side length of square in the figure is 1, then the area of the circle inside the square represents the absolute value of the correlation coefficient, and the length of the cycle diameter is equals to $|\rho_{ij}|$. The left subgraph illustrate correlation coefficients of the reliability matrix R column vectors when using the original method to detect cycle slip, while the right subgraph illustrate the result when using the new method. In the left subgraph, the correlation coefficient of the influence vector related to G15 and G32 is −0.48, and the correlation coefficient of the influence vector related to G18 and G15, G18

and32, is −0.44 and −0.38 respectively, means that it is tough to distinguish outliers between them, which is the reason that G18 is the first one detected as cycle slip satellite in original method. Compared to the left subgraph, the area of the non-diagonal cycles are significantly smaller in the right subgraph, that means the correlation coefficients of the influence vectors is much smaller when using the new method, its maximum value is 0.22. The correlation coefficient absolute value of the influence vectors related to G15 and G32 down to 0.09, and the new method can detect the cycle slip directly and correctly. Based on the analysis above, one can draw a conclusion that benefit of the velocity constraint, the robustness and accuracy of the DD model-based cycle slip detection method are developed.

4.2 Case 2: Road Vehicle-Mounted 1 Hz Data Rate Test

A RTK test was carried out in Tian' an Technology Park, Guangzhou on September 8, 2016 in the afternoon. A Hi-target built-in BX220 board UAV RTK module named U21R was used as the test platform, and the antenna was used a AH-3232 helix antenna. The data sampling rate was set to 1 Hz. The reference station used a Hi-target geodetic-grade receiver named Ubase, a RTCM data stream was transmitted via radio. The baseline length is about 0.7 km. RTK solution of a built-in Trimble BD970 board receiver named iRTK2 is regard as the reference solution. iRTK2 received the reference corrections information from Qiaonan station of Hi-target GuanZhou CORS Network via GPRS/3G, and the baseline is about 6.7 km. For comparison purpose, the AH-3232 helix antenna is attached to the center of iRTK2, which makes the horizontal position difference of the carrier phase center between the AH-3232 helix antenna and the antenna of iRTK2 is smaller than 2 cm. The test environment is shown in Fig. 2, Which covering areas of open sky, building block, shade trees. We make a RTK static initialization first, after the RTK of U21R fixed, began to move and collect the positioning data for about 9 min. The RTK fixed rate of U21R is 100% and the horizontal positioning difference between U21R and iRTK2 for most of the epochs is smaller than 5 cm as shown in Fig. 3, which indicated the RTK fixed solution of U21R is reliable.

Table 2 shows the statistics of cycle slip detection and repair. 525 epochs is collected in this test, and 204 epochs is detected as cycle slip occurs, the cycle slip epoch rate is up to 38.9%. The rate of the cycle slips whose absolute value smaller than 3 cycle to the total cycle slip number is 29.4%. Even there are a lot of cycle slips in the process of RTK positioning with such a low-cost GNSS board and antenna, the RTK solution is encouraging in this test, which shows that the new method can effectively deal with the cycle slip problem in RTK positioning.

Fig. 2 Trajectory

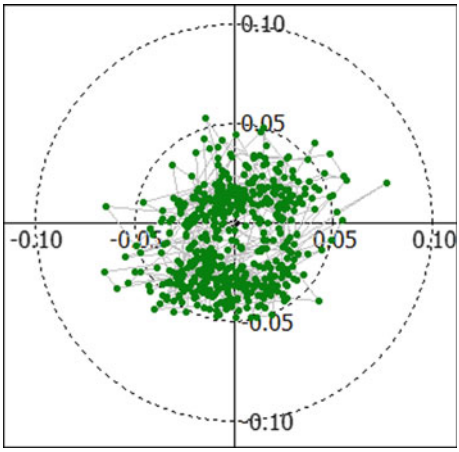

Fig. 3 Horizontal positioning errors (unit: m)

Table 2 Cycle-slip detection and repair statistics

Statistical variables	Slip epochs/total epochs	Repaired slips/total slips	<3 cycle slips/total slips
Number of cycle slip	204/525	122/350	103/350
Ratio	38.9%	34.9%	29.4%

5 Conclusion

A new epoch-differenced model-based cycle slip resolution method was proposed in this paper. Different from the previous methods, velocity constraint information derived by Doppler observations was used in this method. Benefit of the velocity constraint, the correlation coefficient absolute value of the influence vectors are significantly smaller than the method without the velocity constraint, which means it is easier to distinguish outlier in the cycle slip detection model, so that the robustness and accuracy of the DD model-based cycle slip detection method are developed. Experimental results show that the proposed epoch-differenced cycle slip resolution technique can be effectively used in low-cost single-frequency RTK positioning.

Acknowledgements This work was supported by the "Collaborative Precision Positioning Project" (No.2016YFB0501900) of National key Research Program of China.

References

1. Kirkko-Jaakkola M, Traugott J, Odijk D et al (2009) A RAIM approach to GNSS outlier and cycle slip detection using L1 carrier phase time-differences. In: IEEE workshop on signal processing systems. SiPS 2009. IEEE
2. Liu X, Song L, Huang L (2011) Outlier detection in detecting cycle slips based on epoch-difference location model. Sci Surveying Mapp 36(06):58–60
3. Yi Z, Zhu J, Chen Y, Dai W (211) Cycle-slip detection and correction algorithm for real-time PPP. Geomatics Inf Sci Wuhan Univ 36(11):1314–1319
4. Yuan H, Wan W, Ning B, Li J (1998) A new cycle slip detection and correction method using triple differences solution. Acta Geodaetica et Cartographica Sinica 27(03):189–194
5. He X, Liu Z, Hu X (2003) An algorithm of detecting and recoverying cycle slips based on triple differences solution and inertial data in single-frequency GPS. Navig Control 2(2):10–13
6. Chen Y, Yi Z (2016) A New method to detect and repair cycle-slip based on double-differenced model between receivers and epochs. Geomatics Inf Sci Wuhan Univ. http://www.cnki.net/kcms/detail/42.1676.TN.20161028.1138.001.html
7. Xu G (2011) GPS Theory. Algorithms and applications, 2nd ed. Tsinghua University Press, Beijing
8. Shi C, Liu J (1998) Correspondence based outlier analysis. J Wuhan Tech Univ Surveying Mapp 23(1):5–9
9. Tao B, Yao Y, Shi C (2004) Distinguishability of outlier based on correlative analysis. Geomatics Inf Sci Wuhan Univ 29(10):881–884

The Application of Instrumental Bias Estimation to Single Point Positioning

Weijun Lu and Guanyi Ma

Abstract The current GPS clock products are based on P_1–P_2 ionosphere-free (IF) observation combinations. Upon conducting single point positioning (SPP) by C_1 and P_2 observations, C_1–P_1 instrumental biases should be eliminated from the clock products. The BDS offers triple frequency signals with I_2–I_6 and I_7–I_6 instrumental biases. The current BDS clock products are based on I_6 observations, but some receivers can only get the I_2–I_6 instrumental biases. Upon conducting SPP by I_2 and I_7 observations, I_2–I_7 instrumental biases should be eliminated. We study a single station based method for instrumental bias estimation, and proceed to analyze the effect on SPP. Compared with the IGG products, the average accuracy of the estimated instrumental biases is 0.30 ns for C_1–P_1 and 0.86 ns for I_2–I_7. With the C_1–P_1 instrumental biases eliminated for GPS, the accuracy of SPP improves by 34% and the middle error of unit weight declines by 37%. With the I_2–I_7 instrumental biases eliminated for BDS, the accuracy of SPP improves by 33% and the middle error of unit weight declines by 50%.

Keywords Instrumental bias · Single station · Clock error · Accuracy · Single point positioning

1 Introduction

As for a GNSS satellite, distinct frequency signals are produced by different channels. Before being transmitted, those signals spend unequal time in the hardware. The bias between the delays of distinct frequency signals in a satellite is called instrumental bias [1]. The instrumental biases contribute to the system errors for ranging and ought to be eliminated upon conducting single point positioning

W. Lu (✉)
National Astronomical Observatories, Chinese Academy of Sciences, Beijing 100012, China
e-mail: luweijun14@mails.ucas.ac.cn

G. Ma
University of Chinese Academy of Sciences, Beijing 100049, China

J. Sun et al. (eds.), *China Satellite Navigation Conference (CSNC) 2017 Proceedings: Volume III*, Lecture Notes in Electrical Engineering 439,
DOI 10.1007/978-981-10-4594-3_24

(SPP) [2]. The current GPS and BDS clock products are based on P_1–P_2 ionosphere-free (IF) observation combinations and I_6 observations respectively [3, 4]. Upon conducting SPP by C_1–P_2 or I_2–I_7, the instrumental biases should be eliminated. But C_1–P_2 instrumental biases are absent from GPS broadcast ephemeris. For BDS, I_2–I_6 and I_7–I_6 instrumental biases should be given, but some receivers can only get the I_2–I_6 instrumental biases. So it is important to find a method to estimate C_1–P_1 and I_2–I_7 instrumental biases. On instrumental bias estimation, a lot of scholars have conducted massive researches and proposed some effective methods.

Some methods are based on derivation of total electron content (TEC). Representatives of the methods are grid method, Kalman filtering method and polynomial method. Polynomial method was primarily proposed for instrumental bias estimation with a single station [5, 6], and later it was applied to multiple stations [7]. Kalman filter as a tool for state estimation in real time was also applied to instrumental bias estimation [8]. Initially grid method was proposed for multiple stations [9], and several years later the grid-based algorithm was applied to instrumental bias estimation with a single station [10]. Some other methods are based on epoch-differenced and undifferenced algorithm. Gao [11] got C_1–P_1 instrumental biases via C_1–P_1 epoch-difference combinations. Zhang [12] applied a combined dual-thread algorithm consisting of an epoch-differenced and an undifferenced engine to estimate instrumental biases. Fan [13] conducted instrumental bias estimation based on uncombined precise point positioning with triple frequency observations. With increasing GPS receivers being set up all over the world, multiple stations are usually used for instrumental bias estimation, but as a flexible and convenient regional estimation pattern, single station still deserves research.

Based on the researches above, we study a single station based instrumental bias estimation method, and proceed to apply to SPP. The method of instrumental bias estimation and corresponding correction are introduced in Sect. 2. In Sect. 3 with SPP results through instrumental biases corrected data and uncorrected data, we analyze the effect of estimation. Finally, the summary is presented in Sect. 4.

2 Mathematical Models

2.1 Estimation of Instrumental Bias

The instrumental bias can be estimated by a single station-based method. GPS and BDS satellites broadcast information on at least two frequency carrier signals. Because the ionosphere is a dispersive medium which causes a group delay and a phase advance to a satellite signal, the slant total electron content (STEC) along the propagation path of a GPS signal can be extracted from pseudoranges and carrier phases.

$$\mathrm{TEC}_{\mathrm{sp}} = \frac{2(f_1 f_2)^2}{k(f_1^2 - f_2^2)}(P_2 - P_1) \tag{1.1}$$

$$\mathrm{TEC}_{\mathrm{sl}} = \frac{2(f_1 f_2)^2}{k(f_1^2 - f_2^2)}(\frac{cL_1}{f_1} - \frac{cL_2}{f_2} + \frac{cN_1}{f_1} - \frac{cN_2}{f_2}) \tag{1.2}$$

where $k = 80.62\ m^3 \cdot s^{-2}$ stands for the ionospheric refraction. f is the signal frequency of GPS or BDS. P and L are pseudorange and carrier phase corresponding to f. N is the integer ambiguity of L.

Through carrier phase smoothing over pseudorange, the STEC with high precision can be obtained [14]. In order to get vertical total electron content (VTEC) from STEC, the ionospheric single layer model [15] can be brought in, which assumes all electrons in the ionosphere concentrate on an infinitely thin single layer. The model is shown in Fig. 1:

The zenith angle can be computed based on the geometry relation among satellite, receiver and geocentre:

$$Z' = \arcsin(\frac{R \cdot \cos E}{R + H}) \tag{1.3}$$

where R is the mean radius of the earth. H is the height of single layer. E is the elevation angle of the satellite.

Instrumental biases of the satellites and the receivers must be eliminated. Hence, VTEC at the ionospheric piercing point (IPP) can be demonstrated as:

$$\mathrm{VTEC} = (\mathrm{TEC}_{\mathrm{s}} - b_{\mathrm{s}} - b_{\mathrm{r}}) \cdot \cos Z' \tag{1.4}$$

where b_{s} and b_{r} represent the instrumental biases of the satellite and the receiver, respectively.

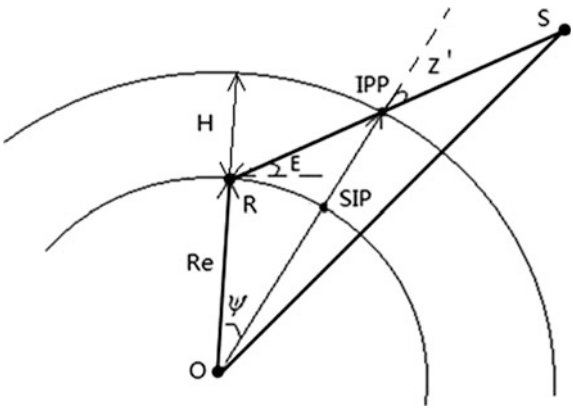

Fig. 1 Geometry of ionosphere, Satellite (*S*), Receiver (*R*) and Geocentre (*O*)

Polynomial based algorithm can adapt to single station well. The algorithm regards VTEC as a function of latitude difference and solar hour angle difference, and applies fitting method to observation data to get the coefficients of polynomial model [5, 6].

$$\mathrm{VTEC} = \sum_{i=0}^{n}\sum_{j=0}^{m} a_{ij}(\varphi - \varphi_o)^i (S - S_o)^j \tag{1.5}$$

where m and n are orders of polynomial, usually set to 2 for regional estimation. (φ, λ) is the coordinate of IPP. S_0 is the hour angle of central point (φ_0, λ_0) in observation area at time t_0. Difference of hour angles is $S{-}S_0 = (\lambda{-}\lambda_0) + (t{-}t_0)$, t is the observation time. a_{ij} stands for the coefficient of polynomial.

The observation equation can be listed as below:

$$\sec Z^{'} \cdot \sum_{i=0}^{n}\sum_{j=0}^{m} a_{ij}(\varphi - \varphi_o)^i (S - S_o)^j + b_s + b_r = \mathrm{TEC}_s \tag{1.6}$$

Generally, this algorithm assumes the coefficients of polynomial remain unchanged in a period, and the biases do not vary in a day. Therefore, all observation equations in one day can be arranged into a set. Through least square method, polynomial coefficients and instrumental biases can be solved.

2.2 Correction of IF Combination

Clock error is the difference between clock time and standard time. The current GPS and BDS clock products are based on P_1–P_2 IF observation combinations and I_6 observations, respectively. Upon conducting SPP by the other observations, the instrumental biases cannot be regardless. Through the method above and the broadcast ephemeris, the biases can be eliminated.

For GPS, if SPP is conducted by C_1–P_2 IF observation combinations, the corrected IF combination can be listed as below [3]:

$$\mathrm{IF} = \frac{f_1^2}{f_1^2 - f_2^2}\cdot C_1 - \frac{f_2^2}{f_1^2 - f_2^2}\cdot P_2 + \delta - \frac{cf_1^2}{f_1^2 - f_2^2}\cdot (b_{c_1-p_2} - b_{p_1-p_2}) \tag{1.7}$$

where δ stands for the other corrections. c is the light speed.

For BDS, if SPP is conducted by I_2–I_7 IF observation combinations, the corrected IF combination can be listed as below [4]:

$$\mathrm{IF} = \frac{f_1^2}{f_1^2 - f_2^2}\cdot I_2 - \frac{f_2^2}{f_1^2 - f_2^2}\cdot I_7 + \delta - \frac{cf_2^2}{f_1^2 - f_2^2}\cdot b_{I_2-I_7} - c\cdot \mathrm{TGD}_1 \tag{1.8}$$

where TGD_1 exists in the ephemeris and stands for I_2–I_6 instrumental bias.

3 Assessments on SPP

3.1 Source and Processing of Data

In order to analyze the effect of estimation on SPP, we estimate the instrumental biases using GPS and BDS dual frequency data from a single station, respectively, and proceed to conduct SPP using instrumental biases corrected data and uncorrected data, respectively.

GPS dual frequency data from SHAO station (31.1°N, 121.2°E) and BDS dual frequency data from JFNG station (30.5°N, 114.5°E) in 29th April 2014 are downloaded from IGS (ftp://cddis.gsfc.nasa.gov/pub/gps/data/daily/) and are used to estimate C_1–P_1 and I_2–I_7 instrumental biases. Then we use GPS and BDS dual frequency data received in national astronomical observatories (40.0°N, 116.4°E) on the same day with 10° cut-off elevation angle and half minute epoch interval to conduct SPP.

For instrumental bias estimation, the coefficients change every 2 hours and instrumental biases do not vary in a day. Upon conducting SPP, broadcast ephemeris is used to locate the satellites. The troposphere delay is corrected by Hopfield model. Equal weight least square method is utilized.

3.2 Estimated Instrumental Biases

Estimated through the method above, C_1–P_1 and I_2–I_7 instrumental biases are shown in Fig. 2. Obviously C_1–P_1 biases indeed exist. As they can cause an error larger than 0.5 m for pseudorange, they cannot be ignored upon conducting SPP. The I_2–I_7 biases may be larger than 10 ns and are unable to get by some receivers. That may be a reason that the clock products of BDS are worse than GPS [16]. The estimated instrumental biases are compared with the biases offered by IGG (ftp://cddis.gsfc.nasa.gov/pub/gps/products/mgex/dcb), whose RMS are generally superior to 0.1 ns, as shown in Fig. 3. The differences indicate that the instrumental biases estimated by the method are superior to 1 ns for C_1–P_1 and 2 ns for I_2–I_7. The average accuracy is 0.30 ns for C_1–P_1 and 0.86 ns for I_2–I_7. Some differences are relatively larger because the elevation angles of satellites are smaller or the data are less. If an appropriate weighting method is chosen, the influences can be limited.

3.3 Results and Analyses

We conduct SPP using GPS and BDS uncorrected data, and again conduct SPP using the instrumental biases corrected data. The results are shown in Figs. 4 and 5.

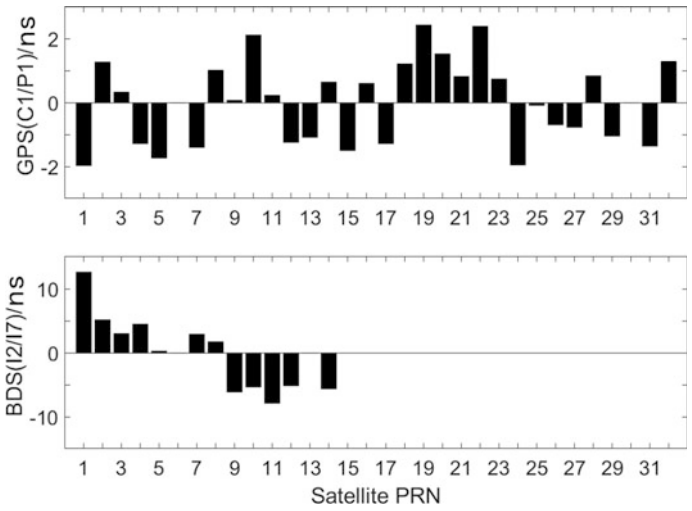

Fig. 2 Estimated instrumental biases

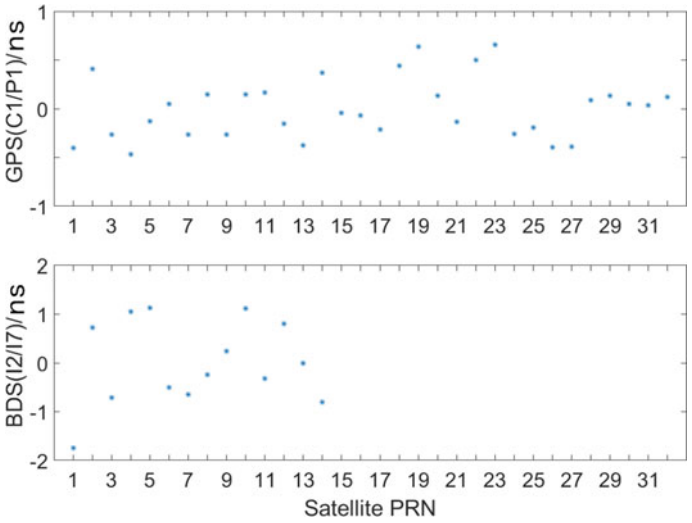

Fig. 3 Differences between estimated instrumental biases and IGG products

In Fig. 4, the GPS results through corrected data are stabler than those through uncorrected data, especially in height direction. Because the instrumental biases of satellites are not equal, the system error changes with different visible satellites in different epochs. Although the mean of the results in one day can eliminate the most of the system error, the system error may be larger than 10 m with several epochs.

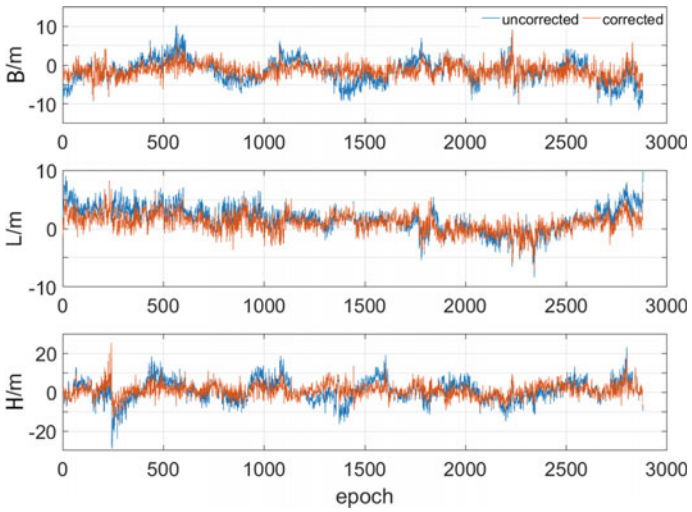

Fig. 4 Errors of GPS SPP

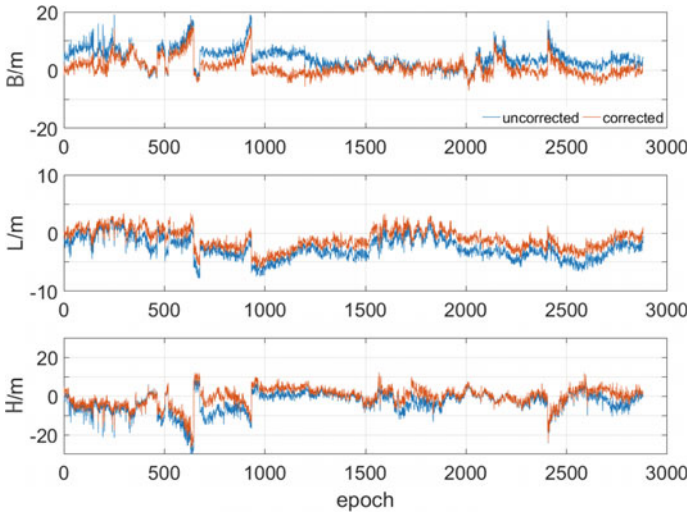

Fig. 5 Errors of BDS SPP

In Fig. 5, the stability of the results through corrected data is similar to that through uncorrected data, while the accuracy of the former is higher. Because there are GEO (geostationary earth orbit) satellites in BDS, the mean of the results in one day cannot eliminate the system error. But with the instrumental biases corrected, most of the system error can be eliminated.

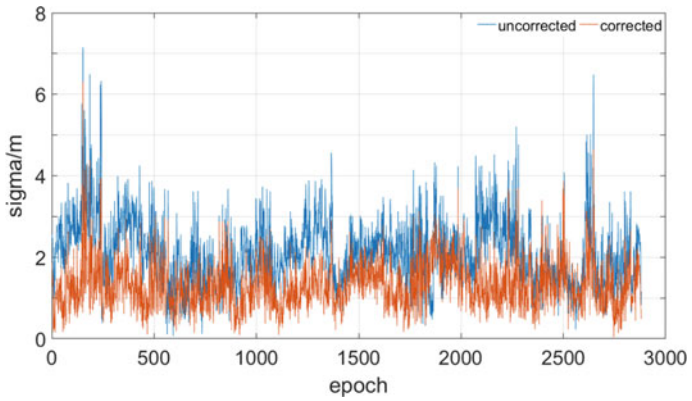

Fig. 6 Middle errors of unit weight of GPS SPP

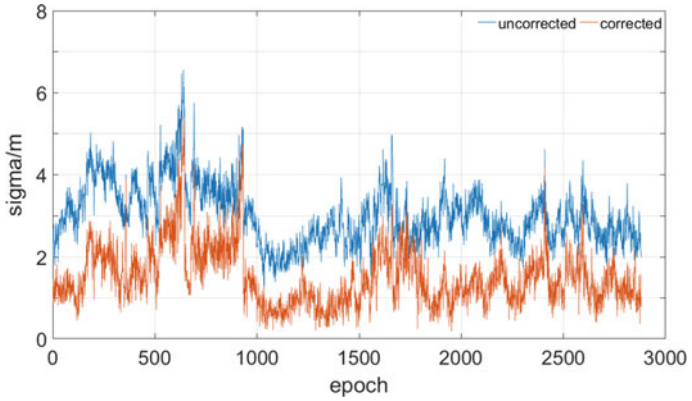

Fig. 7 Middle errors of unit weight of BDS SPP

Figures 6 and 7 are the middle errors of unit weight (sigma) which are related with the errors of pseudoranges. The middle errors of unit weight of corrected data are smaller than uncorrected data with a decrease by 37.56% for GPS SPP and 50.33% for BDS SPP. It indicates that the accuracy can improve if the instrumental biases are eliminated. Before elimination the middle error of unit weight of BDS is larger than that of GPS, but after elimination they are similar. With C_1–P_1 biases of GPS being smaller than I_2–I_7 biases of BDS, the effects of elimination for GPS are smaller. Especially for BDS, the instrumental biases ought to be eliminated.

Table 1 SPP results of GPS and BDS

		Mean of PDOP/m	Mean of sigma/m	B/m	Std L/m	H/m	Inside precision/m	Outside precision/m
	Uncorrected	2.12	2.13	3.05	2.19	5.63	5.91	6.24
GPS (C_1–P_1)	Corrected	2.12	1.33	1.90	1.62	3.58	3.76	4.10
	Uncorrected	2.46	3.02	3.46	1.88	5.38	5.62	7.64
BDS (I_2–I_7)	Corrected	2.46	1.50	3.08	1.74	4.91	4.95	5.09

3.4 Discussion

The precision of SPP is determined by geometric distribution of satellites and accuracy of ranging. The former can be expressed as PDOP (position dilution of precision) and the latter can be expressed as the middle error of unit weight. With the instrumental biases eliminated, the accuracy of ranging can improve, so the middle error of unit weight declines. In Table 1, after elimination the deviations in three directions decline, which accords with Figs. 4 and 5. According to the standard coordinate, the outside precision can be computed. After elimination, for GPS the inside precision and the outside precision improve by 36.38 and 36.41%, respectively. The improvements of BDS are 11.92 and 33.38%, respectively. It indicates that the instrumental bias elimination mainly improves stability for GPS and reduces the deviation with standard coordinate for BDS. That accords with the analyses in 1.3.3.

4 Summary

This paper introduces a single station based instrumental bias estimation method, and then analyzes the effect on SPP. First, we study the polynomial based estimation model. Second, the instrumental bias elimination of C_1–P_1 in GPS and I_2–I_7 in BDS is introduced. Finally, the comparison of SPP results through corrected and uncorrected data is given.

Comparing the estimated instrumental biases with IGG products, the average accuracy is 0.30 ns for C_1–P_1 and 0.86 ns for I_2–I_7. The differences with IGG products indicate that the instrumental biases estimated by the method are superior to 1 ns for C_1–P_1 and 2 ns for I_2–I_7. With the C_1–P_1 instrumental biases eliminated, the inside precision and the outside precision of GPS SPP improve by 36.38 and 36.41%, and the middle error of unit weight declines by 37.56%. With the I_2–I_7 instrumental biases eliminated, the inside precision and the outside precision of BDS SPP improve by 11.92 and 33.38%, and the middle error of unit weight declines by 50.33%. With the instrumental bias estimation method, the stability and accuracy improve a lot.

Acknowledgements This work is supported by the National Natural Science Foundation of China (Grant Nos.11473045, 11403045 and 11503040).

References

1. Ma G, Gao W, Li J, Chen Y, Shen H (2013) Estimation of GPS instrumental biases from small scale network. Adv Space Res 54(5):871–882. doi:10.1016/j.asr.2013.01.008
2. Li H, Xu T, Li B, Huang S, Wang J (2016) A new differential code bias (C_1–P_1) estimation method and its performance evaluation. GPS Solut 20(3):321–329. doi:10.1007/s10291-015-0438-4
3. ICDG (2013) Global positioning systems directorate system engineering and integration interface specification IS-GPS-200G, in Navstar GPS space segment/navigation user interfaces. DC, USA, Washington
4. CSNO (2013) BeiDou Navigation satellite system signal in space interface control document open service signal (Version 2.0). China Satellite Navigation Office
5. Lanyi GE, Roth T (1988) A comparison of mapped and measured total ionospheric electron content using global positioning system and beacon satellite observations. Radio Sci 23(4): 483–492. doi:10.1029/RS023i004p00483
6. Coco DS, Coker C, Dahlke SR, Clynch JR (1991) Variability of GPS satellite differential group delay biases. IEEE Trans Aerosp Electron Syst 27(6):931–938. doi:10.1109/7.104264
7. Wilson DB, Mannucci AJ, Edwards CD, Roth T(1992) Global ionospheric maps using a global network of GPS receivers. In: Presentation at the international Beacon satellite symposium, MIT, Cambridge, MA, 6–12 July 1992
8. Sardón E, Rius A, Zarraoa N (1994) Estimation of the transmitter and receiver differential biases and the ionospheric total electron content from global positioning system observations. Radio Sci 29(3):577–586. doi:10.1029/94RS00449
9. Ma G, Maruyama T (2003) Derivation of TEC and estimation of instrumental biases from GEONET in Japan. Ann Geophys 21(10):2083–2093. doi:10.5194/angeo-21-2083-2003
10. Arikan F, Nayir H, Sezen U, Arikan O (2008) Estimation of single station interfrequency receiver bias using GPS-TEC. Radio Sci 43(4):RS4004.doi:10.1029/2007RS003785
11. Gao Y, Lahaye F, Héroux P, Liao X, Beck N, Olynik M (2001) Modeling and estimation of C1–P1 bias in GPS receivers. J Geodesy 74(9):621–626. doi:10.1007/s001900000117
12. Zhang X, Li X, Guo F (2011) Satellite clock estimation at 1 Hz for realtime kinematic PPP applications. GPS Solut 15(4):315–324. doi:10.1007/s10291-010-0191-7
13. Fan L, Li M, Wang C, Shi C (2016) BeiDou satellite's differential code biases estimation based on uncombined precise point positioning with triple-frequency observable. Adv Space Res. doi:10.1016/j.asr.2016.07.014
14. Mannucci AJ, Wilson BD, Yuan DN, Ho CH, Lindqwister UJ, Runge TF (1998) A global mapping technique for GPS derived ionospheric electron content measurements. Radio Sci 33(3):565–582. doi:10.1029/97RS02707
15. Brunini C, Camilion E, Azpilicueta F (2011) Simulation study of the influence of the ionospheric layer height in the thin layer ionospheric model. J Geodesy 85(9):637–645. doi:10.1007/s00190-011-0470-2
16. Ji S, Xu Y, Chen W, Wang Z, Weng D, Huang B, Fan S, Sun G (2014) Comparison of standalone performance between COMPASS and GPS. J Navig 67(1):37–48. doi:10.1017/S0373463313000477

Characteristic Analysis of Offshore Zenith Tropospheric Delay Based on GPS/BDS/GLONASS PPP

Xue Wang, Lin Zhao, Liang Li, Peng Cui and Jie Zhang

Abstract In order to study the characteristics of zenith tropospheric delay (ZTD) at sea, the Precise Point Positioning (PPP) was used to process the data from 7 International GNSS Service (IGS) reference stations distributed in South China Sea. These stations can process GPS, BDS, and GLONASS data simultaneously. The offshore ZTD was estimated by random walk model. In order to evaluate the accuracy of the estimated ZTD, the ZTD data from three of the stations were used to compare with ZTD products of 300s sampling from IGS. The results show that the ZTD estimation results from GPS/BDS/GLONSS-based PPP is consistent with the trend of the ZTD products provided by IGS, and the position error in the convergence state is less than 10 mm. By calculating the ZTD time series of day of year (DOY) 14–154, 2016, the mean diurnal ZTD values at each of local time (LT = 1, 2, …, 24) were obtained. The results shows that the mean diurnal ZTD time series have two peak values, which are around noon and midnight local time, moreover, the maximum peak is around midnight. The ZTD estimation results of offshore and inland are compared and analyzed. The results show that ZTD of offshore stations is about 6–19 cm larger than that of inland stations. The maximum ZTD value can be observed at equatorial locations. Moreover, the change of ZTD from offshore stations is more intense, its peak-to-peak value of mean diurnal ZTD time series is larger than the inland by approximately 6 mm.

Keywords Precise point positioning · Zenith tropospheric delay · Characteristic analysis

X. Wang (✉) · L. Zhao · L. Li (✉) · P. Cui · J. Zhang
College of Automation, Harbin Engineering University, Harbin 150001, China
e-mail: wangxue_407@heu.edu.cn

L. Li
e-mail: liliang@hrbeu.edu.cn

J. Sun et al. (eds.), *China Satellite Navigation Conference (CSNC) 2017 Proceedings: Volume III*, Lecture Notes in Electrical Engineering 439,
DOI 10.1007/978-981-10-4594-3_25

1 Introduction

Since 1970s, with the rapid development of electronic information technology, many disciplines are related to radio waves. When through the earth outer atmosphere the radio signal is bound to be affected by atmosphere refraction from ionospheric delay and troposphere delay [1]. In the field of satellite navigation, the ionospheric delay influences are eliminated typically by dual-frequency combination, while the tropospheric delay error cannot be eliminated by dual-frequency combination for the reason that it is independent of frequency. The tropospheric delay, especially its wet component, varies greatly with the meteorological parameters such as humidity and temperature, and it is difficult to obtain accurate corrections though the model [2]. Scholars have done a lot of research work on the ZTD estimation and its mechanism. Jin analyzed ZTD data from 151 globally distributed IGS reference stations, significant diurnal and semidiurnal oscillations of ZTD can be found in the study [3]. Rzepecka analyzed tropospheric time series data from four years and two permanent stations located in Central Europe region, obtaining annual and semiannual signal [4]. Qu studied the ZTD of the region of China, the studies show that there is a very strong annual variation [1]. At present, relatively few researches focus on tropospheric delay characteristics at sea. The climate of sea is characterized by high humidity and the weather is more intense and complex than that of the land, this makes the law of tropospheric delay influence at sea different from that of the inland areas.

Most methods of estimating ZTD based on PPP is to use GPS dual-frequency observations [5]. With the development of GNSS modernization, the combination of multiple systems can provide more observational redundancy, which can further enhance the performance of tropospheric delay extraction. In this paper, the technology of GPS/BDS/GLONASS PPP was used to obtained information of oceanic tropospheric delay, and its characteristic is analyzed by ZTD time series data, providing a reference for research work of tropospheric delay correction.

Considering the large-scale change characteristics of tropospheric delay, based on the observation data of the IGS reference stations in the offshore (less than 10 km from coastline), the ZTD and its horizontal gradient were estimated on the basis of achieving the positioning accuracy of millimeter scale, to ensure accurate analysis of the oceanic ZTD.

2 The Method of Estimate ZTD Based on GPS/BDS/GLONASS PPP

In the technology of combined GPS/BDS/GLONSS PPP, precise ephemeris and clock products are introduced to correct satellite orbit and clock error, and dual-frequency combinations are used to eliminate the influence of the first-order

term of ionospheric delay. The combined observation equations can be expressed as follows:

$$P_{\mathrm{IF}}^{g} = \frac{f_{1g}^2 P_1^g - f_{2g}^2 P_2^g}{f_{1g}^2 - f_{2g}^2} = \rho^g - cdT^g + M^g d_{\mathrm{trop}} + \varepsilon_{P_{\mathrm{IF}}}^g \tag{1}$$

$$\phi_{\mathrm{IF}}^{g} = \frac{f_{1g}^2 \phi_1^g - f_{2g}^2 \phi_2^g}{f_{1g}^2 - f_{2g}^2} = \rho^g - cdT^g + M^g d_{\mathrm{trop}} + N_{\mathrm{IF}}^g + \varepsilon_{\phi_{\mathrm{IF}}}^g \tag{2}$$

$$P_{\mathrm{IF}}^{c} = \frac{f_{1c}^2 P_1^c - f_{2c}^2 P_2^c}{f_{1c}^2 - f_{2c}^2} = \rho^c - cdT^c + M^c d_{\mathrm{trop}} + \varepsilon_{P_{\mathrm{IF}}}^c \tag{3}$$

$$\phi_{\mathrm{IF}}^{c} = \frac{f_{1c}^2 \phi_1^c - f_{2c}^2 \phi_2^c}{f_{1c}^2 - f_{2c}^2} = \rho^c - cdT^c + M^c d_{\mathrm{trop}} + N_{\mathrm{IF}}^c + \varepsilon_{\phi_{\mathrm{IF}}}^c \tag{4}$$

$$P_{\mathrm{IF}}^{r} = \frac{f_{1r}^2 P_1^r - f_{2r}^2 P_2^r}{f_{1r}^2 - f_{2r}^2} = \rho^r - cdT^r + M^r d_{\mathrm{trop}} + \varepsilon_{P_{\mathrm{IF}}}^r \tag{5}$$

$$\phi_{\mathrm{IF}}^{r} = \frac{f_1^{r2} \phi_1^r - f_{2r}^2 \phi_2^r}{f_{1r}^2 - f_{2r}^2} = \rho^r - cdT^r + M^r d_{\mathrm{trop}} + N_{\mathrm{IF}}^r + \varepsilon_{\phi_{\mathrm{IF}}}^r, \tag{6}$$

where g, c and r represent GPS, BDS and GLONASS, respectively, ϕ_{IF} and P_{IF} are carrier-phase and pseudorange observation of ionosphere-free combination, f_i is frequency on L_i carrier-phase; ρ is geometric distance, c is the vacuum speed of light, dT is clock error of receiver, $\mathrm{d_{trop}}$ and M are ZTD and its mapping function, respectively, N_{IF} is ionosphere-free ambiguity, ε is the multipath effect and measurement noise.

The tropospheric delay on the propagation path is equal to the sum of zenith hydrostatic delay (ZHD) and zenith wet delay (ZWD) multiplying their corresponding mapping function [6]. The formula is as follows:

$$Z(e) = Z_h \times MF_h(e) + Z_w \times MF_w(e), \tag{7}$$

where Z_h and Z_w are ZHD and ZWD, $MF(\bullet)$ is mapping function, e is elevation angle.

Equation (7) is based on the hypothesis that the atmosphere is homogeneous in all directions, which is inconsistent with the fact. Therefore, the researchers proposed a new tropospheric delay model that adding horizontal gradients as [7, 8],

$$Z(e) = Z_h \times MF_h(e) + Z_w \times MF_{\mathrm{w}}(e) + MF(e)_{azi} \bullet (G_{\mathrm{N}} \cos\phi + G_{\mathrm{E}} \sin\phi), \tag{8}$$

where $MF(e)_{azi}$ denotes the gradient mapping function, G_{N} is gradient parameter of north-south direction, G_{E} is gradient parameter of east-west direction, ϕ is azimuth, other parameters are the same as those of Eq. (7).

Table 1 Parameters estimation strategy

Estimated parameters	Processing strategy
Receiver coordinates	Estimation, constant processing, the apriori constraint 100 m,
Receiver clock error	Estimation, as a white noise process, the apriori constraint is 1000 m
Zenith tropospheric delay	Estimation, correction model of ZHD is Saastamoinen, mapping function is GMF model
Horizontal gradients parameters	Gradient parameter of east-west direction and north-south direction were estimated
Carrier-phase ambiguity	Estimation, constant processing, the apriori constraint is 1000 m,

According to Eq. (1–8), the zenith tropospheric delay and tropospheric horizontal gradients parameters can be estimated by using PPP.

Estimating ZTD based on PPP, its data processing strategy is as follows, satellite orbit error and its clock error are corrected by using precise ephemeris and clock products, the pseudorange and carrier-phase of the dual-frequency ionosphere-free combination are taken as observations. Using empirical model for the correction of the zenith hydrostatic delay, earth rotation, relativistic effect, phase wind up, tide errors (contained earth tide, ocean tide and pole shift tide), antenna phase center of satellite and receiver, and the multipath error has been well suppressed during the smoothing process. Station coordinates, receiver clock error, tropospheric delay, horizontal gradients parameters and carrier-phase ambiguity are estimated as unknown parameters by using Kalman filtering (KF) [9]. Parameter estimation strategies are shown in Table 1.

3 Data Processing Result and Analysis

In this paper, the experimental data are from DOY 14–154, 2016 and 7 stations located in South China Sea, the ZTD of all stations are estimated using GPS/BDS/GLONASS PPP. The distribution of stations is shown in Fig. 1. 15 min precise ephemeris and 5 min clock products were provided by GNSS Research Center of Wuhan University.

3.1 The Accuracy Analysis of ZTD Estimation Based on GPS/BDS/GLONASS PPP

In order to evaluate the accuracy of the estimated ZTD, the ZTD data from three of the stations were used to compare with ZTD products of 300s sampling from IGS.

The estimated ZTD data from the three stations and ZTD products provided by IGS on DOY 132, 2016 are shown in Fig. 2. As can be seen from Fig. 2, whether

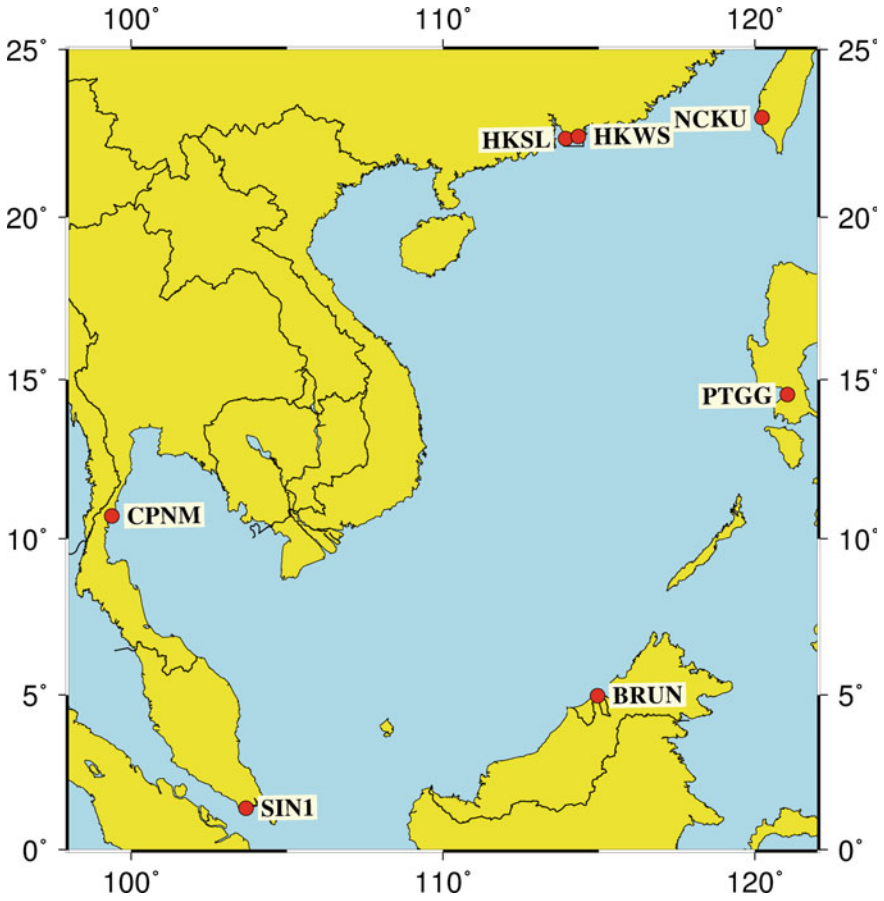

Fig. 1 Distribution of experimental stations

based on single system or multisystem, the ZTD estimated by PPP technology is consistent with the trend of the ZTD products provided by IGS, and the deviation after convergence of the filter is mostly less than 10 mm. In order to further analyze the accuracy of estimated ZTD, Table 2 shows the statistical results of the difference between the estimated result of each station and the ZTD products from IGS, the statistical data are from DOY 130–134, 2016. The mean values between the ZTD data estimated by the technology of GPS/BDS/GLONSS PPP and ZTD products provided by IGS is less than 10 mm and the RMS is less than 15 mm. Compared with single system, the accuracy of ZTD of multisystem is not significantly improved. However, the multisystem combination increases the number of visible satellites, which is beneficial to improve the reliability of solution.

From the analysis above, it can be shown that the ZTD estimated by using GPS/BDS/GLONASS PPP has strong reliability.

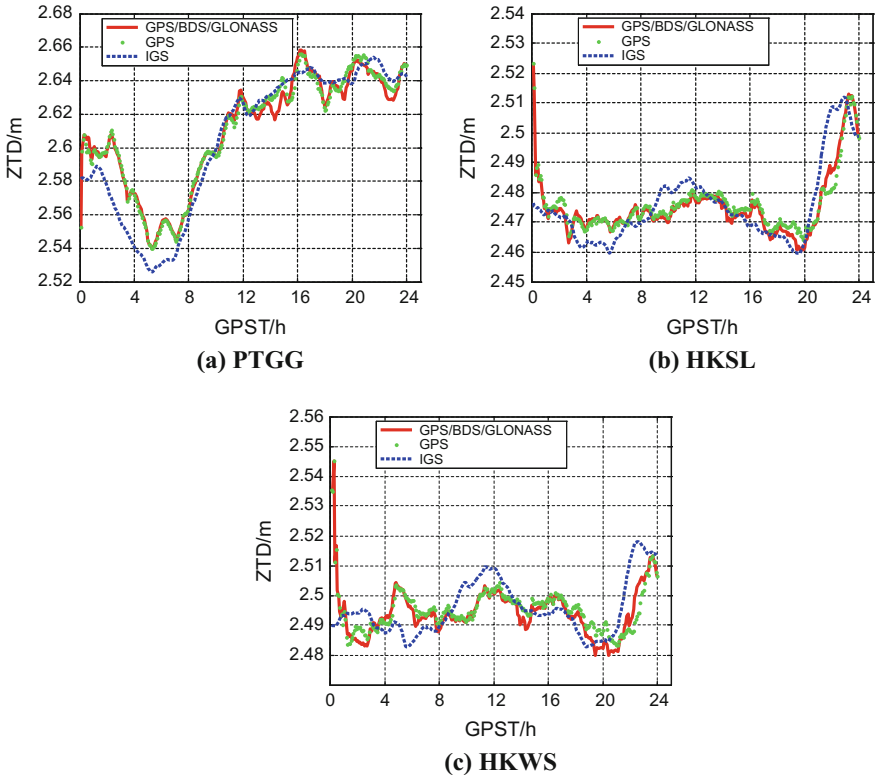

Fig. 2 Comparison between PPP-derived ZTD and IGS products

Table 2 Statistic of the differences between PPP-derived TD and IGS products

	GPS-IGS			GPS/BDS/GLO-IGS		
	Mean(m)	STD(m)	RMS(m)	Mean(m)	STD(m)	RMS(m)
PTGG	0.009	0.014	0.009	0.009	0.014	0.014
HKSL	0.007	0.009	0.012	0.007	0.007	0.012
HKWS	0.008	0.010	0.013	0.006	0.008	0.012

3.2 The Characteristic Analysis of Tropospheric Delay at Sea

In order to study the characteristics of tropospheric delay variation on the sea, the ZTD estimation results of 7 stations in Fig. 1 were analyzed. The mean and standard deviation of the ZTD time series within 30 min before and after the hour (LT = 1, 2,…, 24) of the day are calculated based on the local time. According to the statistic of ZTD average value of DOY 14–154, 2016, the mean diurnal ZTD values at each of local time (LT = 1, 2, …, 24) were obtained. The results are shown in Fig. 3. Two peaks appeared in Fig. 3, and the maximum peak appears at

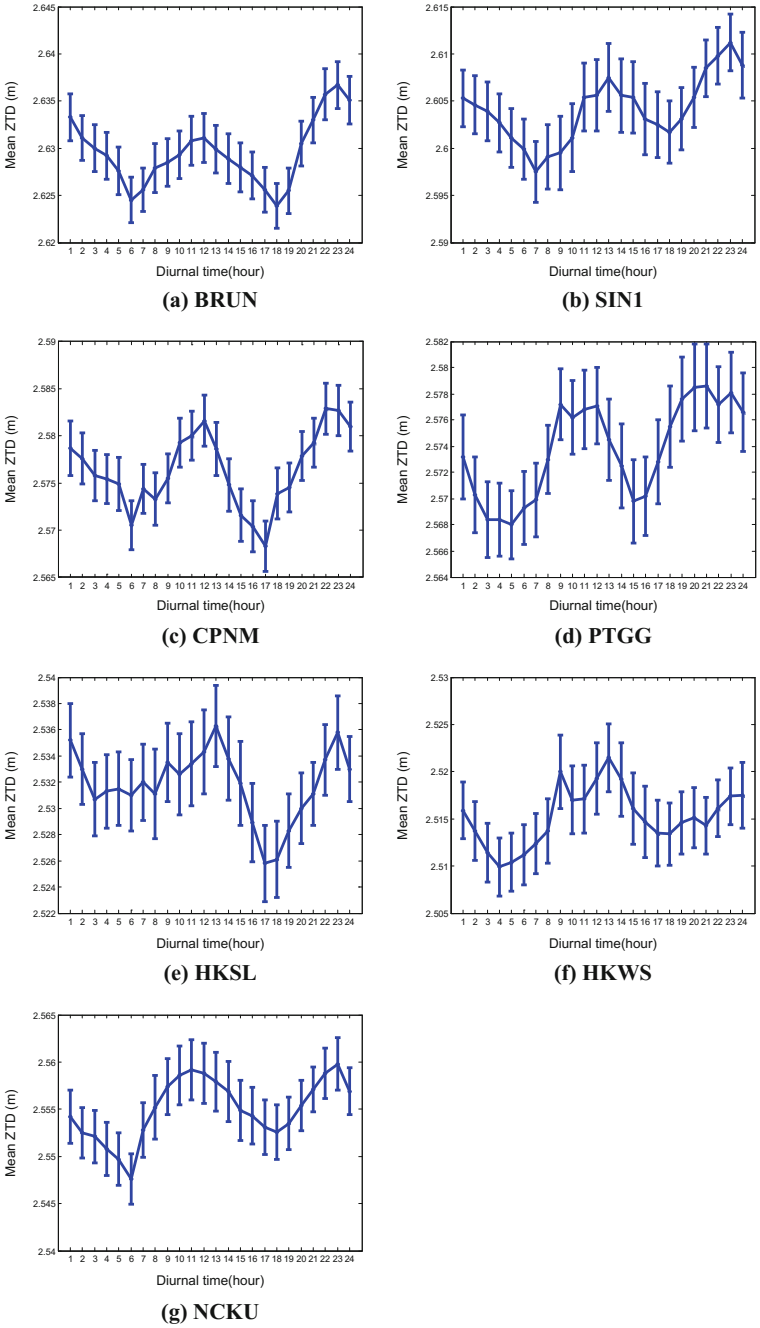

Fig. 3 Mean diurnal ZTD values at each location time with error bar of offshore stations

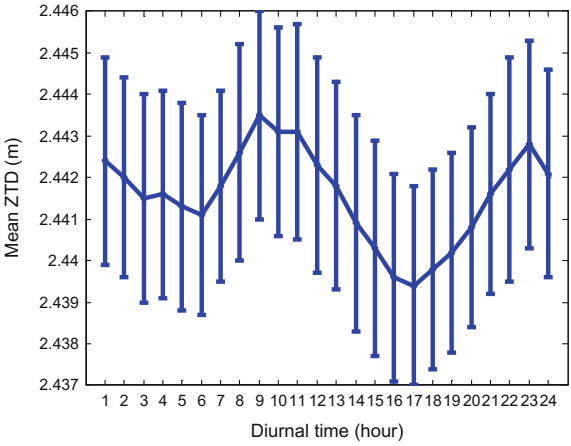

Fig. 4 Mean diurnal ZTD values at each location time with error bar of inland station

midnight of local time. Because the BDS observation data published by most of the test stations used in this paper are less than one year, it is difficult to form an effect research on the seasonal variation and annual variation of tropospheric delay in the South China Sea. Since the research focus of this paper is to analyze the characteristics of tropospheric delay at sea, In order to further analyze the ZTD estimation results of 7 offshore stations in Fig. 1, the same method was used to estimate the ZTD of the inland stations under the conditions of ensuring similar altitude and latitude, which aims to show the characteristics of tropospheric delay at sea by comparative analysis. Figure 4 shows the mean diurnal ZTD values at inland station, the station is more than 500 km far from the coastline. Comparing Figs. 3, 4, it is found that the ZTD of the offshore station is generally larger than that of the inland station. The ZTD estimation results of the offshore and inland in the same period are compared and analyzed, the results show that ZTD of offshore stations is about 6-19 cm larger than that of inland stations, and the ZTD of stations located at low latitudes near the equator is greatest. Moreover, the change of ZTD of offshore stations is more intense, its peak-to-peak value of mean diurnal ZTD time series is larger than that of inland.

4 Conclusion

The ZTD values of 7 IGS stations in the South China Sea were estimated based on GPS/BDS/GLONASS PPP. Tropospheric delay products provided by IGS are used as “the true value” to verify the reliability of the estimated ZTD. Taking the large-scale characteristic of the tropospheric delay into account, the variation characteristic of the tropospheric delay in the South China Sea was investigated through statistical analysis of the estimated ZTD time series of 140 days. The results show that two mean diurnal ZTD variation peaks appeared on the sea, which

are around noon and midnight local time, respectively, and the maximum peak appears around midnight. The ZTD estimation results of offshore and inland in the same period are compared and analyzed, the results show that ZTD of offshore stations is about 6–19 cm larger than that of inland stations, and the ZTD of stations located at low latitudes near the equator is greatest. Moreover, the change of ZTD of offshore stations is more intense, its peak-to-peak value of mean diurnal ZTD time series is larger than that of inland. Due to the BDS observation data of South China Sea are relatively few, seasonal variation and annual variation of the tropospheric delay cannot be studied. With the further increase of observation data, a more comprehensive analysis of the characteristic of offshore ZTD is the next step to carry out the work. The study shows that it is necessary to take account the characteristic of the tropospheric delay different from that of the land when the PPP was applied on the sea. To achieve positioning accuracy of cm or mm level, it is necessary to study the processing method of the tropospheric delay error in offshore application.

Acknowledgements We acknowledge the IGS for providing static GPS data. This research was jointly funded by the China Natural Science Foundation (No. 61304235, 61303008, 61273081, 61304234), the Fundamental Research Funds for Central Universities (No. HEUCF160416) and the Postdoctoral Scientific Research Foundation, Heilongjiang Province (No. LBH-Q15033).

References

1. Weijing Q (2007) The research and application of zenith troposphere delay in the region of China. Univesity of Chinese Academy of Sciences
2. Xingwang Z, Shengli W, chao L GNSS precise point positioning theories and methods. Press of University of Technology of China
3. Jin S, Luo OF, Gleason S (2009) Characterization of diurnal cycles in ZTD from a decade of global GPS observations. J Geod 83:537–545
4. Rzepecka Z 2015 Time series analysis of radio signal wet tropospheric delays for short-term forcast. Acta Geodynamica ET Geomater 1–10
5. Li Li, Sichun Long, Jun Shen et al (2014) Monitoring ZTD high frequency variation by using dynamic PPP. J Geodesy Geodyn 34(2):74–78
6. Kaifeng Li, Yongzhong Ouyang, Xiuping Lu, Taiqi Wu (2013) Research on tropospheric delay difference estimation technology in the hydrographic positioning. Geomatics Infomations Sci Wuhan Univ 38(8):930–934
7. Shirong Y, Shunagcheng Z Jingnan L (2008) Precision analysis of precise point positioning based tropospheric delay estimation. Geomatics Infomations Sci Wuhan Univ 33(8):788–791
8. Macmillan DS (1995) Atmospheric gradients form very baseline interferometry observations. Geophys Res Lett 22(9):1041–1044
9. Shirong Y (2002) Research on the theoretical methodology of precise point positioning using un-differenced GPS data Wuhan University

GPS/BDS Real-Time Precise Point Positioning for Kinematic Maritime Positioning

Fuxin Yang, Liang Li, Lin Zhao and Chun Cheng

Abstract Real-time precise point positioning (PPP) has been evolved as a powerful technique to achieve globally homogenous decimeter or even centimeter positioning accuracy, which is widely used for maritime precise positioning applications. Currently, the research of the real-time PPP for maritime applications mainly focuses on GPS and GLONASS. In addition, the real-time PPP for kinematic maritime positioning is at least limited by two issues, (i) The real-time availability of the correction products for satellite orbits and clocks; (ii) The error correction related to the marine environment, especially for the estimation of wet zenith troposphere delay (ZWD) is challenged by complex fluctuations of marine atmospheric weather and the severe multipath caused by the sea clutter reflection. In this contribution, using the State-Space Representation correction products based on Radio Commission for Maritime Services (RTCM-SSR), we develop a GPS/BDS real-time kinematic maritime PPP. On the one hand, a piece-wise method is adopted to estimate the ZWD and the horizontal gradient. On the other hand, a robust sequential least squares (RSLSQ) PPP estimator is adopted based on IGG-III model to restrain the unmolded gross error. Based on the 6 h maritime data, the results show that the up direction accuracy and the convergence time of GPS, BDS and GPS/BDS, respectively, are improved based on 0.5 window length for ZWD estimation and the RSLSQ estimator. In addition, the horizontal accuracy of real-time single BDS and GPS using RTCM-SSR can achieve the accuracy of sub-decimeter level when the positioning error is convergence. Compared with the single constellation, the positioning accuracy and the convergence time of the real-time GPS/BDS using RTCM-SSR improves, respectively, by 10 and 18%, and the kinematic positioning accuracy in horizontal is better than 30 cm.

Keywords GPS/BDS · PPP · RTCM-SSR · Troposphere estimation · RSLSQ

F. Yang (✉) · L. Li (✉) · L. Zhao · C. Cheng
College of Automation, Harbin Engineering University, Harbin 150001, China
e-mail: yangfuxin@hrbeu.edu.cn

L. Li
e-mail: liliang@hrbeu.edu.cn

J. Sun et al. (eds.), *China Satellite Navigation Conference (CSNC) 2017 Proceedings: Volume III*, Lecture Notes in Electrical Engineering 439,
DOI 10.1007/978-981-10-4594-3_26

1 Introduction

High-precision kinematic position information plays a vital role in marine applications, such as marine development, marine mapping, and marine search. The global positioning system (GPS) can provide a positioning accuracy of decimeter to centimeter level in a global reference frame, thus, it is recognized by International Maritime Organization (IMO) for a future maritime navigation [1]. Currently, real-time precise point positioning (PPP) has been evolved as a powerful technique, which is widely used for maritime precise positioning applications [2]. However, compared with the ground-based PPP, the real-time PPP kinematic maritime positioning is not only limited by the real-time availability of the correction products for satellite orbits and clocks, but also depend on the accurate error model correction under the complex fluctuations of atmospheric weather on the sea.

The performances of real-time PPP depend on the quality of real-time corrections, mainly including satellite orbits and clocks. Currently, on the one hand, with the available of the IGS real-time service (RTS), the horizontal positioning accuracy for kinematic ground-based is better than 50 cm [3]. On the other hand, Relevant researchers proposed SBAS-PPP method to achieve kinematic positioning based on the real-time correction products including satellite orbit, satellite clock and ionosphere corrections which are provided by EGNOS. However, the kinematic horizontal accuracy is about 90 cm, because of the resolution of long-term position corrections and fast corrections is 0.125 m, which limits the accuracy of SBAS-PPP [4]. However, the above researches focused mainly on the ground-based real-time kinematic PPP, the research on the maritime kinematic PPP is relatively rare. Furthermore, the real-time correction products can be provided by the commercial companies such as Fugro and Trimble for maritime applications, the accuracy of float solutions can be reach 10 cm with the long convergence time of 20 min, and the convergence time can significantly be reduced by fixing the carrier phase ambiguities [5]. However, the study of real-time PPP for kinematic maritime positioning focused on GPS and GLONASS.

Accurate error model correction is the key to real-time PPP to improve positioning accuracy and accelerate convergence time. Compared with ground-based PPP, the main difference between maritime PPP is reflected on the error correction models which are related to the signal propagation environment. For the GNSS maritime positioning, on the one hand, the humidity and water vapor change greatly, which make the wet part of zenith troposphere delay (ZWD) change complexly [6]. Meanwhile, there is a strong correlation between troposphere parameters and other estimated parameters, and the anomalous tropospheric estimation residuals will degrade the positioning accuracy [7]. However, the study of the troposphere error model correction mainly focuses on the ground-based PPP. On the other hand, the positioning accuracy will inevitably be affected by the multipath effect, which is mainly caused by the hull itself and the sea surface, especially for the low elevation angle satellites [8]. By suppressing or eliminating the multipath errors in code observations, the convergence time of PPP will be accelerated [9].

Considering the effects of the corrections of low-quality real-time precision satellite orbit and clock, inaccurate tropospheric delay correction and the anomalous multipath on real-time PPP maritime kinematic positioning performance, this paper contributes to modeling and assessment of dual-frequency ionosphere-free (IF) real-time float PPP based on GPS/BDS for kinematic maritime positioning using RTCM-SSR. Firstly, the piece-wise method of troposphere estimation with the accurate troposphere model for maritime positioning is introduced. Secondly, the adjustment model for GPS/BDS based on the RSLSQ using IGG-III model is introduced to estimate rover parameters, which will restrain the anomalous unmolded errors caused by multipath and troposphere corrections for low elevation satellites. Finally, the performances of kinematic maritime positioning are analyzed for BDS, GPS and GPS/BDS based on RSLSQ, and the conclusions and remarks will be summarized.

2 Observation Error Models Correction

The accurate correction model is the key for the real-time PPP to improve positioning accuracy and accelerate convergence time [10]. This section presents the mathematical models for dual-frequency IF PPP. After a short description of the dual-frequency IF model, in order to improve the positioning performance, the real-time satellite orbit and clock corrections using RTCM-SSR and the accurate troposphere estimation model are introduced in detail.

2.1 Ionosphere-Free (IF) PPP Model

The dual-frequency IF combination is widely used by PPP model, which can be simplified as [11]:

$$P_{\mathrm{IF}} = \frac{f_1^2}{f_1^2 - f_2^2} P_1 - \frac{f_2^2}{f_1^2 - f_2^2} P_2 = \rho + dt_{\mathrm{r}} + dt^s + d_{\mathrm{trop}} + \varepsilon_{P_{\mathrm{IF}}} \tag{1}$$

$$\Phi_{\mathrm{IF}} = \frac{f_1^2}{f_1^2 - f_2^2} \Phi_1 - \frac{f_2^2}{f_1^2 - f_2^2} \Phi_2 = \rho + dt_{\mathrm{r}} + dt^s + d_{\mathrm{trop}} + N_{\mathrm{IF}} + B_{\mathrm{IF}} + \varepsilon_{\Phi_{\mathrm{IF}}}, \tag{2}$$

where P_1, P_2, Φ_1 and Φ_2 denote the code and phase at carrier L1 and L2, respectively; P_{IF} and Φ_{IF} refer to the IF code and phase, respectively; f_1 and f_2 present the frequency at carrier L1 and L2, respectively; ρ denotes the geometric distance between satellite and receiver; dt_{r} and dt^s present the receiver and satellite clock error, respectively; d_{trop} is troposphere delay error; N_{IF} and B_{IF} denote the IF integer phase ambiguity and the initial phase delay; $\varepsilon_{P_{\mathrm{IF}}}$ and $\varepsilon_{\Phi_{\mathrm{IF}}}$ present the multipath and receiver noise for the IF code and phase, respectively.

Based on Eqs. 1 and 2, the relativity effects, phase wind-up, as well as earth tides have been corrected according to the existing models [12]. Therefore, in order to ensure the high accuracy and accelerate convergence time, it is necessary to deal with the remaining error sources in Eqs. (1) and (2) correctly, such as the satellites orbit, satellites clock and troposphere delay errors.

2.2 Real-Time Satellite Orbit and Clock Corrections

Unlike precise ephemeris from IGS, the precise satellites orbit and clock consist of the broadcast ephemerides and the real-time corrections in RTCM-SSR formats. Therefore, the precise satellite orbit and clock corrections at any epoch can be calculated by subtracting the real-time correction from the broadcast ephemerides at the same epoch as follows [13]:

$$\begin{bmatrix} \delta_{\mathrm{r}} \\ \delta_{\mathrm{a}} \\ \delta_{\mathrm{c}} \end{bmatrix}_t = \begin{bmatrix} \delta_{\mathrm{r}} \\ \delta_{\mathrm{a}} \\ \delta_{\mathrm{c}} \end{bmatrix}_{t_0} + \begin{bmatrix} \dot{\delta}_{\mathrm{r}} \\ \dot{\delta}_{\mathrm{a}} \\ \dot{\delta}_{\mathrm{c}} \end{bmatrix} \cdot (t - t_0) \tag{3}$$

$$\begin{bmatrix} \delta_x \\ \delta_y \\ \delta_z \end{bmatrix}_t = \boldsymbol{R} \cdot \begin{bmatrix} \delta_r \\ \delta_{\mathrm{a}} \\ \delta_{\mathrm{c}} \end{bmatrix}_t \tag{4}$$

$$\boldsymbol{R} = \left[\frac{\dot{r}}{|\dot{r}|} \times \frac{r \times \dot{r}}{|r \times \dot{r}|} \quad \frac{\dot{r}}{|\dot{r}|} \quad \frac{r \times \dot{r}}{|r \times \dot{r}|} \right]^T \tag{5}$$

$$t_{\mathrm{c}} = C_0 + C_1 \cdot (t - t_0) + C_2 \cdot (t - t_0)^2, \tag{6}$$

where δ_{r}, δ_{a} and δ_{c} are the radial, along-track, and cross-track corrections, t_0 and t are the issue of data (IOD) and the current epoch, and $\dot{\delta}_{\mathrm{r}}$, $\dot{\delta}_{\mathrm{a}}$ and $\dot{\delta}_{\mathrm{c}}$ are the rate of the radial, along-track, and cross-track corrections. δ_x,δ_y and δ_z are the orbital corrections in ECEF coordinate system, and $\boldsymbol{R}$ is the transformation matrix, where r and $\dot{r}$ are the satellite unit and velocity vectors, computed from broadcast ephemerides. t_{c} is the satellite clock correction to the broadcast clock correction, and C_0, C_1, and C_2 are the polynomial coefficients of real-time satellite clock corrections.

2.3 The Atmosphere Error Correction

The atmospheric error for PPP includes two parts, i.e., the ionospheric and the tropospheric errors. For the ionosphere error, the first order term is eliminated by the IF model, while the remaining ionosphere delay error is the higher order terms, which has several centimeters effect on positioning accuracy [14]. However, the troposphere delay as another major atmospheric source must be corrected [15].

In general, the tropospheric error can be separated into a dominate hydrostatic part and a smaller wet part, in which the hydrostatic part can be molded with accuracy up to a few millimeters, while the wet part should be estimated with other parameters [16]. Considering the wet part of troposphere delay error could change fast and the azimuthal inhomogeneity on the sea, a piece-wise method is adopted to estimate the ZWD and gradient based on a more precise troposphere delay model including a gradient member in several interval with other parameters, which is suitable for the complexly change of ZWD. The troposphere error can be written as [17],

$$d_{\text{trop}} = m(\text{el})_{\text{h}} \cdot \text{d}_{\text{h}} + m(\text{el})_{\text{w}} \cdot d_{\text{w}} + m(\text{el})_{\text{az}} \cdot (G_{\text{N}} \cos(\text{az}) + G_{\text{E}} \sin(\text{az})), \quad (7)$$

where $m(\text{el})_{\text{h}}$ and $m(\text{el})_{\text{w}}$ are the hydrostatic and wet mapping functions based on global mapping function, respectively; d_{h} and d_{w} denote the hydrostatic and wet delay, respectively; G_{N} and G_{E} present the north and east troposphere gradient for estimation. el and az denote elevation angle and azimuth angle, respectively. $m(\text{el})_{\text{az}}$ presents the gradient mapping function, which are used to convert the troposphere delay along the zenith direction to the line of slight direction, $m(\text{el})_{\text{az}} = 1/(\sin(\text{el})\ \cos(\text{el}) + 0.0032)$.

In addition, for the carrier phase, the initial phase delay cannot be canceled and will be mapped into ambiguities. This mapping will not be a problem since the ambiguities are estimated as a lumped term and treated as float values. The multipath and receiver noise are constrained by a sine elevation weighting stochastic model.

3 User Positioning Algorithm

With the accuracy corrected dual-frequency IF code and phase observations, the position coordinates can be precisely resolved. Let us assume that there are n satellites available, the measurement equation can be written as:

$$\begin{bmatrix} \tilde{P}_{\text{IF}} \\ \tilde{\Phi}_{\text{IF}} \end{bmatrix} = \begin{bmatrix} G & M_{\text{RC}} & M_T & 0 \\ G & M_{\text{RC}} & M_T & I \end{bmatrix} \begin{bmatrix} x \\ \text{clk} \\ \beta \\ n_{\text{IF}} \end{bmatrix} + R \rightarrow V = H\Delta + R \quad (8)$$

$$R = \begin{bmatrix} \sigma^2_{\text{UDRE}} + \sigma^2_{\text{trop}} + \sigma^2_{\tilde{P}_{\text{IF}}} & \sigma^2_{\text{UDRE}} + \sigma^2_{\text{trop}} \\ \sigma^2_{\text{UDRE}} + \sigma^2_{\text{trop}} & \sigma^2_{\text{UDRE}} + \sigma^2_{\text{trop}} + \sigma^2_{\tilde{\Phi}_{\text{IF}}} \end{bmatrix} \otimes I, \quad (9)$$

where $\tilde{P}_{\text{IF}}$, $\tilde{\Phi}_{\text{IF}}$ are the $n \times 1$ code and phase observation residual, Δ is the corrections to the a priori parameters: the corrections to the position coordinates $x = [\delta x\ \delta y\ \delta z]^T$ with the $n \times 3$ observation matrix $\boldsymbol{G}$, the corrections to the receiver clock bias $\text{clk} = [dt\ \text{ISB}]^T$ with $n \times 3$ matrix design M_{RC}, the corrections to the zenith wet

troposphere residual $\beta = [d_w\ G_N\ G_E]^T$ with the $n \times 3$ design matrix M_T from Eq. (7), n_{IF} is the $n \times 1$ corrections to the ambiguities, I is the identity matrix with the rank n. $\boldsymbol{R}$ is the variance-covariance for the observation residual, $\otimes$ is the Kronecker product operator, σ^2_{UDRE}, σ^2_{trop}, $\sigma^2_{\tilde{P}_{IF}}$ and $\sigma^2_{\tilde{\Phi}_{IF}}$ are the STD of residual range, troposphere, code and phase noise. Assuming that the STDs of code and phase are 0.3 and 0.003 m, respectively, and the observation of each frequency is independent.

With the proposed mathematical model (8) and stochastic model (9), we can use the RSLSQ based on IGG-III model to estimate the receiver position [18], which has a positive effect on resistance against outliers by adjusting the stochastic model by Eqs. (11) and (12). It can be written as follows:

$$\hat{\Delta} = (Q_\Delta + H^T \bar{R}^{-1} H)^{-1} H^T \bar{R}^{-1} V \tag{10}$$

$$\bar{R}_{i,j} = R_{i,j}/\alpha_i \tag{11}$$

$$\alpha_i = \begin{cases} 1 & \left|\tilde{V}_i\right| \le k_0 \\ \frac{k_0}{\left|\tilde{V}_i\right|}\left(\frac{k_1 - \left|\tilde{V}_i\right|}{k_1 - k_0}\right)^2 & k_0 < \left|\tilde{V}_i\right| \le k_1 \\ 10^{-8} & \left|\tilde{V}_i\right| > k_1 \end{cases} \tag{12}$$

where Q_Δ is the variance-covariance matrix for Δ, and $\hat{\Delta}$ is the corrections to the priori parameters. $\bar{R}_{i,j}$ is the equivalent measurement variance to R, a_i is the variance-covariance amplification factor, $\tilde{V}_i$ denotes the standardized residual, k_0 and $k_1$are the thresholds, the practical values are 1.5 and 3, respectively.

4 Data Testing and Analysis

The kinematic experiment is carried out based on 6 h marine data collected by the Novatel PP6 receiver and the Novatel 703 antenna on 13/3/2016, the sample time is 1s. RTCM-SSR comes from the GNSS center of Wuhan University via CLK01 (http://ntrip.gnsslab.cn). On the one hand, the performances of real-time kinematic maritime positioning are analyzed based on different window lengths of troposphere estimation. On the other hand, the performances of positioning are analyzed based on different systems between SLSQ and RSLSQ, respectively, the position performance is evaluated by the metrics of position accuracy and convergence time, it is noted that the convergence time is defined as the time when the horizontal accuracy reach 0.5 m. The cut-off elevation angle is set as 15°. In addition, the reference position coordinates are given by the network RTK. The red line in Fig. 1 shows the motion trajectory of the ship, which starts at 31°22′N, 121°38′E, ends at 30°41′N, 122°56′E. Figures 2 and 3 show the number of visible satellites and GDOP values for different systems.

Fig. 1 The ship motion trajectory

Fig. 2 The number of visible satellites

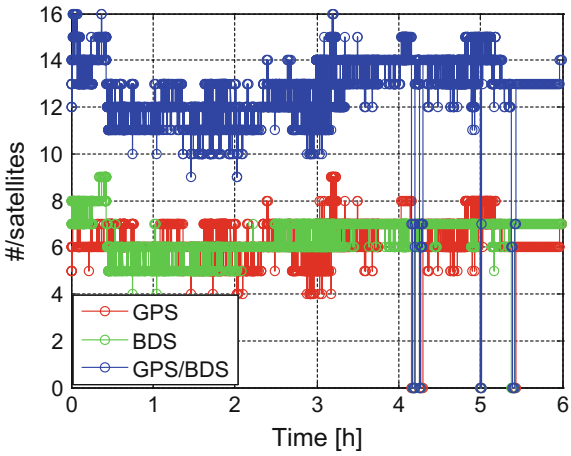

Fig. 3 The GDOP values for GPS, BDS and GPS/BDS

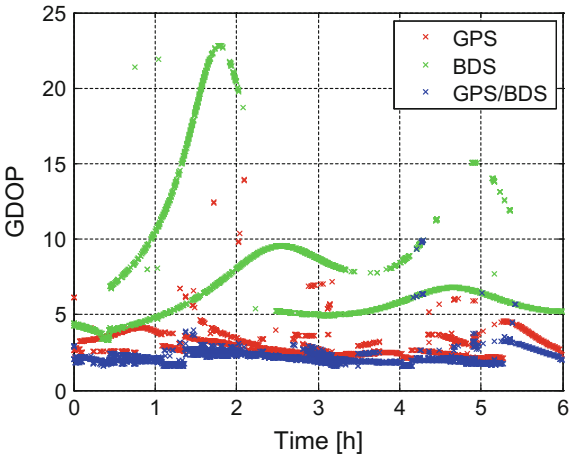

4.1 Troposphere Delay Estimation

The piece-wise method is firstly adopted based on 0.5, 1, 1.5, and 2 h to estimate the troposphere parameters, and the positioning accuracy is indirectly measured by the tropospheric delay correction accuracy. Based on the 2 h window length, which is usually selected for ground-based PPP [19], the difference between different window lengths for GPS/BDS ZWD and position coordinates estimation as shown from Figs. 4 and 5. Table 1 gives the RMS of real-time kinematic positioning errors comparison for the different window lengths.

The results show that the up direction has a strong correlation to the ZWD, as shown in Fig. 5. Combined with Table 1, it also shows that the up direction position accuracy of GMF with the 0.5 h window length improve 6.1, 14.3 and

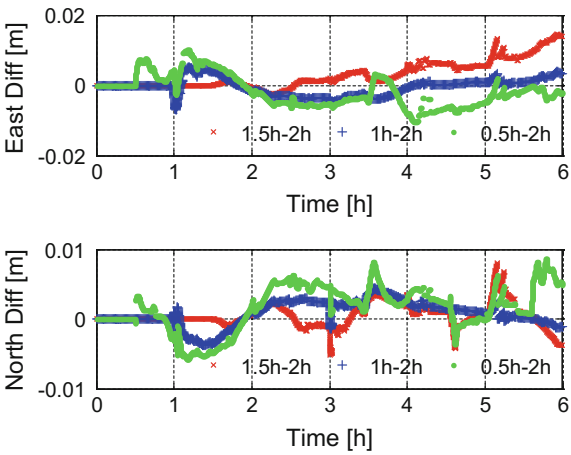

Fig. 4 The difference in the east and north

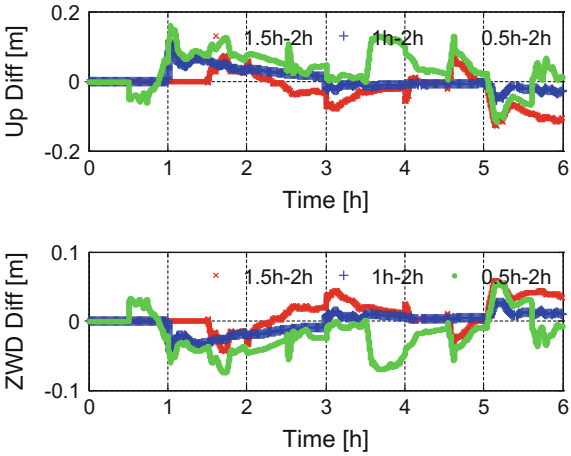

Fig. 5 The difference in the up and ZWD

Table 1 The RMS of real-time kinematic positioning errors comparison for the different window length

System	GMF-30	GMF-60	GMF-90	GMF-120
	ENU RMS(m)	ENU RMS(m)	ENU RMS(m)	ENU RMS(m)
GPS	0.123	0.134	0.130	0.137
	0.151	0.147	0.147	0.152
	0.460	0.485	0.496	0.492
BDS	0.189	0.190	0.190	0.193
	0.141	0.142	0.145	0.144
	0.234	0.278	0.300	0.293
GPS/BDS	0.091	0.098	0.095	0.102
	0.151	0.151	0.152	0.152
	0.225	0.258	0.277	0.291

22.1%, compared to the other window lengths. Meanwhile the east and north position accuracy is similar to the others, as shown in Fig. 4. Therefore, it reflects that the change of ZWD is fast on the sea indirectly. It is noted that the ENU in Table 1 means the east, the north and the up direction.

4.2 *Real-Time Kinematic Performances for Maritime Positioning*

Based on the 0.5 h window length, the real-time kinematic maritime positioning using RTCM-SSR is analyzed with different constellations. Figures 6, 7, 8 present the position errors of GPS/BDS in each positioning component between SLSQ and RSLSQ. Figures 9, 10 and 11 show the position errors in each positioning component for different constellations based on the RSLSQ.

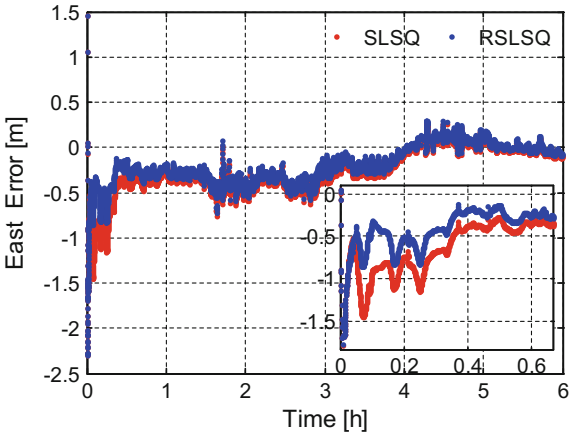

Fig. 6 The difference in the east direction

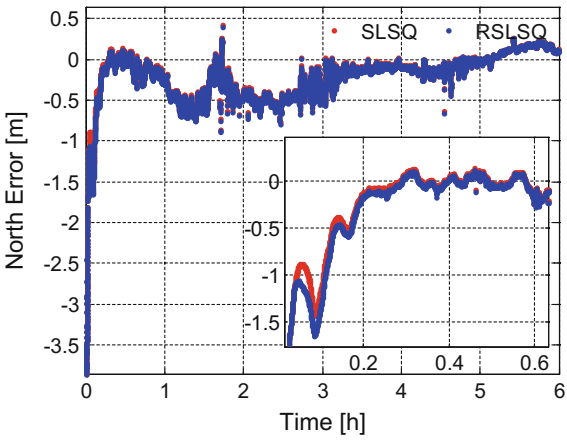

Fig. 7 The difference in the north direction

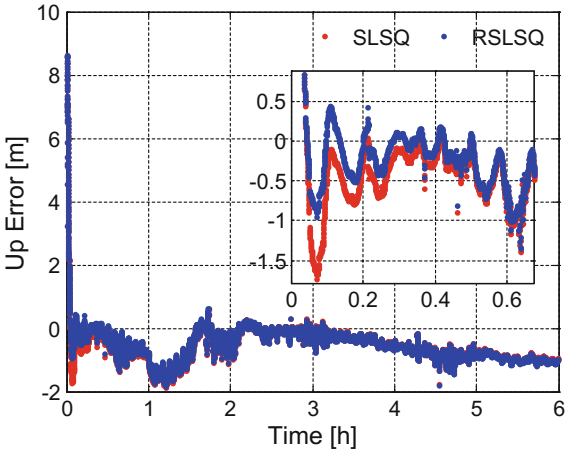

Fig. 8 The difference in the up direction

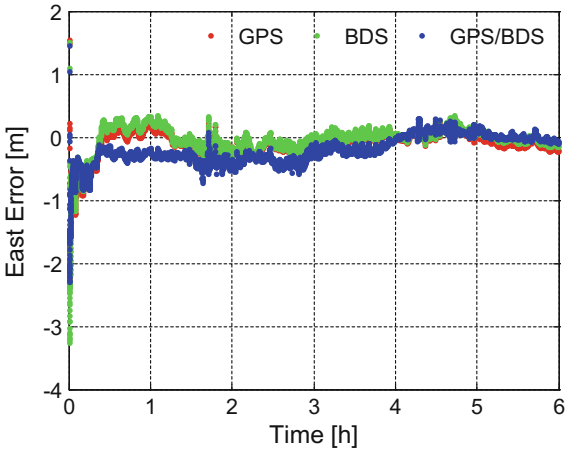

Fig. 9 The east errors for three constellations

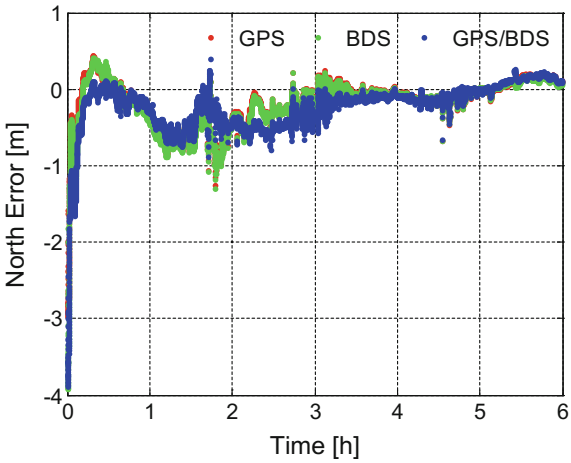

Fig. 10 The north errors for three constellations

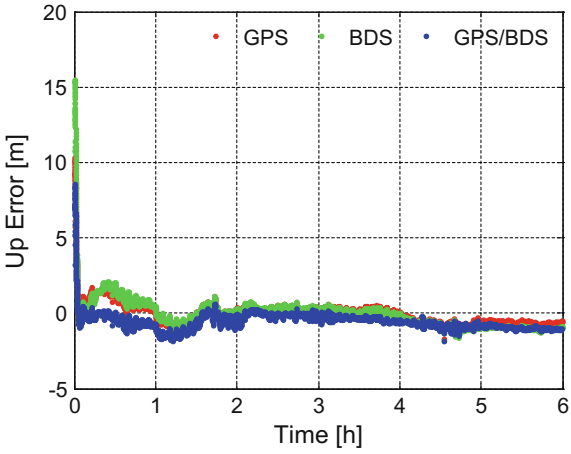

Fig. 11 The up errors for three constellations

Combining Figs. 6, 7 and 8 with Table 2, GPS, BDS, and GPS/BDS have a faster convergence time based on RSLSQ, which improve 12, 2.6 and 14.3%, respectively, because of the RSLSQ restrains the unmolded errors. It is noted that the CT means the convergence time.

When the positioning accuracy converges, the horizontal positioning accuracy of GPS, BDS and GPS/BDS are better than 30 cm, and the single BDS has a longer convergence time, because the initial GDOP values are larger. Compared with the single constellation, the positioning accuracy and the convergence time of the real-time GPS/BDS using RTCM-SSR improve, respectively by 10 and 18%. Through combining Figs. 2, 9, 10 and 11, it can be observed that the position errors of single constellation are dramatically increasing especially when the number of available satellites for positioning is few and the GDOP is large. Once the available

Table 2 Real-time kinematic positioning performance comparison of two method for GPS, BDS and GPS/BDS

System	SLSQ		RSLSQ	
	ENU RMS(m)	CT(min)	ENU RMS(m)	CT(min)
GPS	0.123	25	0.101	22
	0.151		0.152	
	0.460		0.472	
BDS	0.189	77	0.167	75
	0.141		0.151	
	0.234		0.213	
GPS/BDS	0.113	21	0.091	18
	0.152		0.151	
	0.225		0.235	

satellites of single constellation were less than five, the positioning will be re-initialized, which is seriously affect the continuity of maritime positioning. Meanwhile, some outliers in the single constellation solutions can be mitigated based on GPS/BDS, as shown in Fig. 2.

5 Conclusion

The results of the experiment show that the up direction has a strong correlation to the ZWD, and the up direction position accuracy of GMF with the 0.5 h window length improve 6.1, 14.3, and 22.1%, compared to the other window lengths, which reflects that the change of ZWD is fast on the sea indirectly. Therefore, in order to accuracy estimate the ZWD, it is necessary to consider the change characteristic of ZWD on the sea, especially we focus on the up positioning accuracy for kinematic maritime applications. Meanwhile, compared with the traditional SLSQ method, GPS, BDS, and GPS/BDS have a faster convergence time based on RSLSQ, which improve 12, 2.6 and 14.3%, respectively. When the positioning accuracy converges, the horizontal positioning accuracy of GPS, BDS and GPS/BDS can reach sub-decimeter level. Compared with the single constellation, the positioning accuracy and the convergence time of the real-time GPS/BDS using RTCM-SSR improves, respectively, by 10 and 18%, some outliers in the single constellation solutions can be mitigated based on GPS/BDS.

Acknowledgements This research was jointly funded by National Natural Science Foundation of China (Nos.61304235, 61273081, 61304234, 61633008), the Fundamental Research Funds for Central Universities (No. HEUCF160416, HEUCFP201617), the Post-Doctoral Scientific Research Foundation, Heilongjiang Province (No. LBH-Q15033).

References

1. Policy RM (2001) Requirements for a future global navigation satellite system (GNSS). IMO, Resolut A 915:22–29
2. Geng J, Teferle FN, Meng X, Dodson AH (2010) Kinematic precise point positioning at remote marine platforms. GPS Solutions 14(4):343–350
3. Chen J, Li H, Wu B, Zhang Y, Wang J, Hu C (2013) Performance of real-time precise point positioning. Mar Geodesy 36(1):98–108
4. Zhao Y, Zhao L, Li L, Yang F (2016) A novel SBAS-assisted single-frequency precise point positioning method. In: China satellite navigation conference (CSNC) 2016 proceedings, vol III. Springer, Singapore, pp 373–386
5. Liu X, Goode M, Tegedor J, Vigen E, Oerpen O, Strandli R (2015) Real-time multi-constellation precise point positioning with integer ambiguity resolution. In: Navigation world congress (IAIN), 2015 International association of institutes of. IEEE, pp 1–7
6. Kaifeng LI, LU (2013) A differential estimation technique of troposphere delay for precise positioning in hydrographic surveying. Geomatics & Information Science of Wuhan University
7. Kjørsvik NS, Gjevestad NJ GO, Øvstedal O (2006) Handling of the tropospheric delay in kinematic precise point positioning
8. Liu Y, Dang Y, Qingdao (2011) Research on multipath effect model of sea surface. J Geodesy Geodyn 31(2):121–124
9. Seepersad G, Bisnath S (2015) Reduction of ppp convergence period through pseudorange multipath and noise mitigation. GPS Solutions 19(3):369–379
10. Li L, Jia C, Zhao L, Cheng J, Liu J, Ding J (2016) Real-time single frequency precise point positioning using sbas corrections. Sensors 16(8)
11. Zumberge JF, Heflin MB, Jefferson DC, Watkins MM, Webb FH (1997) Precise point positioning for the efficient and robust analysis of gps data from large networks. J Geophys Res Solid Earth 102(B3):5005–5017
12. Kouba J (2003) A guide to using international gps service (igs) products. Maryland Biol Stream Surv Data Versar Inc, 4(3):106
13. Standard R 10403.2. Differential GNSS (Global navigation satellite systems) Services–Version, 3
14. Bassiri S, Hajj GA (1993) High-order ionospheric effects on the global positioning system observables and means of modeling them 18
15. Oliveira PS, D, Morel L, Fund F, Legros R, Monico JFG, Durand S, et al. (2016) Modeling tropospheric wet delays with dense and sparse network configurations for ppp-rtk. Gps Solutions 1–14
16. Bevis M, Businger S, Herring TA, Rocken C, Anthes RA, Ware RH (1992) Gps meteorology: remote sensing of atmospheric water vapor using the global positioning system. J Geophys Res Atmos 97(D14):15787–15801
17. Chen G, Herring TA (1997) Effects of atmospheric azimuthal asymmetry on the analysis of space geodetic data. J Geophys Res Atmos 102(B9):20489–20502
18. Yang Y (1996) Adaptive robust least squares estimation. Acta Geodaetica Cartogr Sin 25 (3):206–211
19. Pan L, Xing L, Lei W, Yuan C (2010) Effect of the troposphere zenith delay estimation method on precise point positioning. Geomatics Inf Sci Wuhan Univ 35(7):850–853

Applicability Analysis of Troposphere Mapping Functions in China

Zong-qiang Liu, Ya-min Dang, Qiang Yang and Hu Wang

Abstract The tropospheric mapping function has a direct influence on the tropospheric delay correction. This paper introduces three models: NMF, VMF1 and GMF. Based on the data of the CORS station located in China and some of the surrounding IGS station and combined with ground-based GPS meteorological technology, we can through GAMIT/GLOBK the wet and dry delay of troposphere, and the delay error is obtained. According to the data, the applicability of the three mapping functions in China is analyzed. Results showed that: When the baseline is calculated in China, it is shown that the three mapping functions have higher accuracy in the horizontal direction, and the accuracy is relatively poor in the vertical direction. With the increase of the cutoff angle, the errors of the three mapping functions in N, E and U are gradually increased, and the cutoff angle of 10° is recommended. The model of GMF and NMF showed a certain latitude correlation and VMF1 showed a strong randomness. The accuracy of NMF is obviously lower than GMF and VMF1, and the mean delay deviation of the VMF1 is less than GMF. The model of VMF1 is recommended in China and GMF is used as a backup function.

Keywords Mapping functions · China · Applicability

1 Introduction

In the data processing of high precision GPS, tropospheric delay is an important source of error. It can make the error of electromagnetic wave to reach 2.3 m in the zenith direction, when the satellite elevation angle of 10° can reach 15–20 m [1].

Z. Liu
Shandong University of Science and Technology, Qingdao 266590, Shandong, China

Z. Liu (✉) · Y. Dang · Q. Yang · H. Wang
Chinese Academy of Surveying and Mapping, No. 28, Lotus Pond West Road, Haidian District, Beijing 100830, China
e-mail: bestlzq@126.com

J. Sun et al. (eds.), *China Satellite Navigation Conference (CSNC) 2017 Proceedings: Volume III*, Lecture Notes in Electrical Engineering 439,
DOI 10.1007/978-981-10-4594-3_27

The influence of the troposphere on the electromagnetic wave signal is non dispersive refraction, and the refractive index has nothing to do with the wavelength or frequency of the electromagnetic wave, so the double frequency or multi-frequency signals can not be used to eliminate and solve the delay. At present, most of the atmospheric models are used to correct tropospheric refraction. Due to the complex geophysical parameters such as location, climate, and so on, the mapping function can be obtained with certain regional characteristics [2–4]. Therefore, the applicability of tropospheric mapping functions in different regions is worthy of study.

In recent years, many experts and scholars at home and abroad have studied the influence of mapping function in GPS data processing. J. Boehm and A. E. Niell use the global VLBI data from 1984 to 2005 to analyze the 3 mapping functions (GMF, NMF, VMF1). The results show that better results can be obtained by using VMF1, the horizontal direction can be improved by 3%, while in the U direction can reach up to 7% [5]; By processing the data of Hongkong CORS station, Jiang Guangwei thinks that the VMF1 mapping function can meet the need of real-time meteorological water vapor change, and the precision is the highest. GMF can replace the VMF1 mapping function after the data processing [6]; In 2009, Jiang Weiping thinks that the accuracy of GMF model is better than NMF model by processing a project data [7]. In this paper, by analyzing the data of the national CORS station, the applicability of the three mapping functions in China is analyzed from the aspect of the value of the height angle and the position of the station, and some useful conclusions are obtained.

2 The Tropospheric Mapping Functions

The tropospheric delay mapping function can be divided into two categories: one is the empirical model based on the observed data, and the other is the model of the actual meteorological data. The typical representative of the former model is the NMF model and the GMF model, and the other representatives of the model are the VMF1 models [8]. These three models are used continued-fraction expressed in the form of projection function [9]. As shown in formula (1):

$$m_i(E) = \frac{\dfrac{1}{1+\dfrac{a_i}{1+\dfrac{b_i}{1+c_i}}}}{\dfrac{1}{\sin E+\dfrac{a_i}{\sin E+\dfrac{b_i}{\sin E+c_i}}}} + v_i(i=h,w) \tag{1}$$

In the formula, E denotes altitude angle of satellite; a_i, b_i, c_i denotes the calculated coefficient of the corresponding mapping function of the dry and wet; v_h, v_w denotes the dry delay and wet delay correction, and $v_w = 0$,

Table 1 The main differences between the three mapping functions

Mapping function	Proposed person	Country	Build time	Data sources	Input parameter
NMF	Neill	U.S.A	1996	Radiosonde station	Station latitude, Elevation, DOY
VMF1	Boehm	Austria	2004	Global numerical weather model	VMF1 lattice
GMF	Boehm	Austria	2006	(ERA-40)	Station coordinate, DOY

$$v_h = \left[\frac{1}{\sin E} - \frac{1+\dfrac{\mathrm{a}}{1+\dfrac{\mathrm{b}}{1+\mathrm{c}}}}{\sin E + \dfrac{\mathrm{a}}{\sin E + \dfrac{\mathrm{b}}{\sin E + \mathrm{c}}}} \right] \cdot h_{\text{测站}} \tag{2}$$

The main difference between the three mapping functions lies in a_i, b_i, c_i [10, 11] (Table 1).

3 The Experimental Data

Select 20 national CORS stations (HLNJ, NMXW, LNQY, XJFH, XJYL, XJPS, QHGE, XZLZ, XNIN, HEHD, YNQJ, BJYQ, AHSX, ZJXC, JXPX, HNJH, FJZA, GDZJ, SXJX, CQPS) in 2016, as well as in China and the surrounding area of the 8 IGS stations (and Chinese BJFS, WUHN, SHAO, URUM, LHAZ, DAEJ, TCMS, POL2). In total, 28 sites were analyzed as shown in Fig. 1.

In order to compare the mapping function of baseline solution accuracy, 8 IGS stations were set as fixed station: geocentric latitude and longitude is set to 0.05 m, the slack is set to 0.10 m. The 20 national CORS station is set to non-fixed station: station coordinates restriction is 9.999, 9.999, 9.999 m. Using the SP3 precise ephemeris. Baseline processing type is relaxation solution (RELAX.). The selection type of the observations using the linear combination of the ionosphere free (LC_AUTCLN). The tropospheric refraction model using Saastamoinen, zenith delay model 13, radiation model is the BERNE model, using ITRF2008 reference frame.

4 The Analysis of the Influence of Altitude Angle Parameters on the Tropospheric Mapping Function

Based on the GAMIT software, the following three schemes are used to analyze the influence of the cutoff height angle on the baseline solution of the three kinds of tropospheric mapping functions:

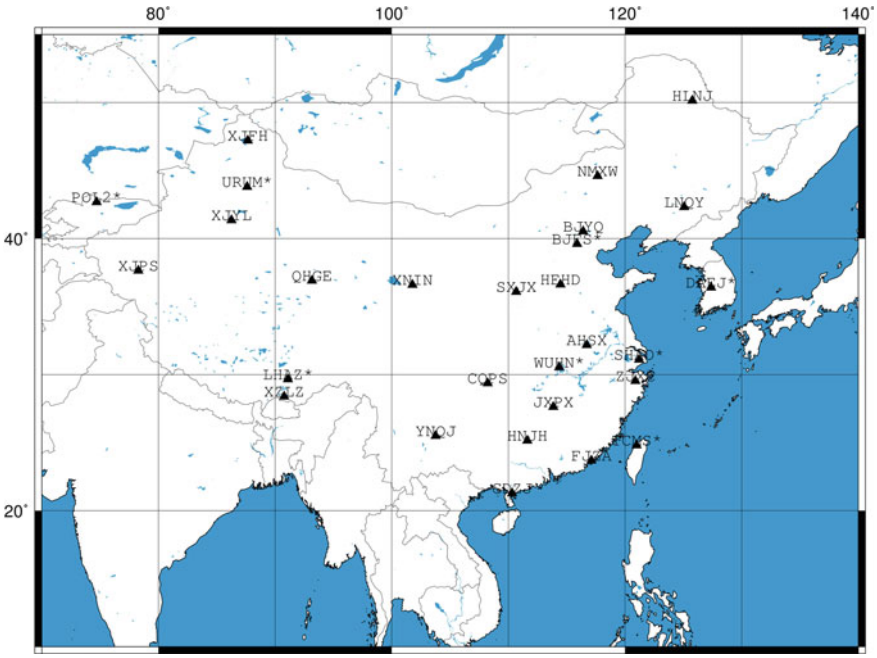

Fig. 1 GPS points bitmap in China

Scheme 1: the height angle is 5°, 10°, 15°, 20°, 25° and 30° GMF mapping function;
Scheme 2: the height angle is 5°, 10°, 15°, 20°, 25° and 30° NMF mapping function;
Scheme 3: the height angle is 5°, 10°, 15°, 20°, 25° and 30° VMF1 mapping function.

Nrms (Normalized Root Mean Square) is used to indicate the degree of deviation from the weighted average of the baseline paper calculated in a single period. It is residual error from the epoch ambiguity. Nrms is an important index to measure the GAMIT calculation results, the calculation formula is as follows:

$$\mathrm{NRMS} = \sqrt{\frac{1}{N}\sum_{i=1}^{n}\frac{(Y_i - Y)^2}{\delta_i^2}} \tag{3}$$

If the NRMS value is greater than 0.3, it indicates that the result is a problem. For example: jump without repair; coordinate measuring starting point station problem, etc. If the value of NRMS is less than 0.3, it is considered to be a successful solution. Generally, the smaller the NRMS, the higher the accuracy of the solution (Fig. 2).

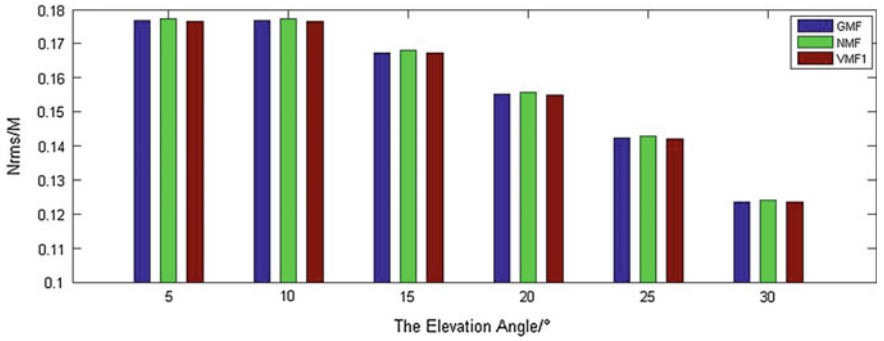

Fig. 2 Nrms values of different mapping functions at different cutoff height angle

Table 2 NRMS mean value of three mapping functions at different cutoff height angle

Mapping function	Cutoff height angle					
	5°	10°	15°	20°	25°	30°
GMF	0.1778	0.1778	0.1685	0.1562	0.1433	0.1246
NMF	0.1783	0.1783	0.1691	0.1567	0.1439	0.1251
VMF1	0.1777	0.1777	0.1683	0.1560	0.1431	0.1246

If the altitude angle is too small, it will lead to the increase of tropospheric delay and multipath effect will be more obvious. Furthermore, the accuracy of the baseline is affected. If the satellite altitude angle is too large, it will cause too much loss of observation data. Therefore, one of the important criteria to evaluate the mapping function is to obtain a better solution of the baseline quality at a relatively low height angle.

As seen from Table 2 and Fig. 3, the average Nrms values obtained by using VMF1, GMF, and NMF mapping functions are less than 0.2, which can meet the requirement of calculation. Among them, the Nrms value of the three mapping functions at each cutoff height angle is very small. Generally, the Nrms value of NMF is slightly larger, indicating that the use of VMF1 and GMF in processing precision of baseline is better than that of NMF. When the cutoff height angle of satellite is 5 and 10, the Nrms value of the baseline solution is the same as that of the three mapping functions. With the increase of the cutoff angle, the Nrms value of the three mapping functions is significantly reduced. It shows that the data quality is good.

Figure 3 shows that when the height angle of the satellite is between 5 and 10, there is no difference in the baseline error. The three mapping functions are better than 7 mm in the N direction, the accuracy of E is better than 8 mm, and the accuracy of U is better than 15 mm, which indicates that the three mapping functions have higher accuracy in the horizontal direction, and the accuracy is relatively poor in the vertical direction. With the increasing of the height of the cutoff angle, the errors of the three mapping functions in N, E and U are gradually

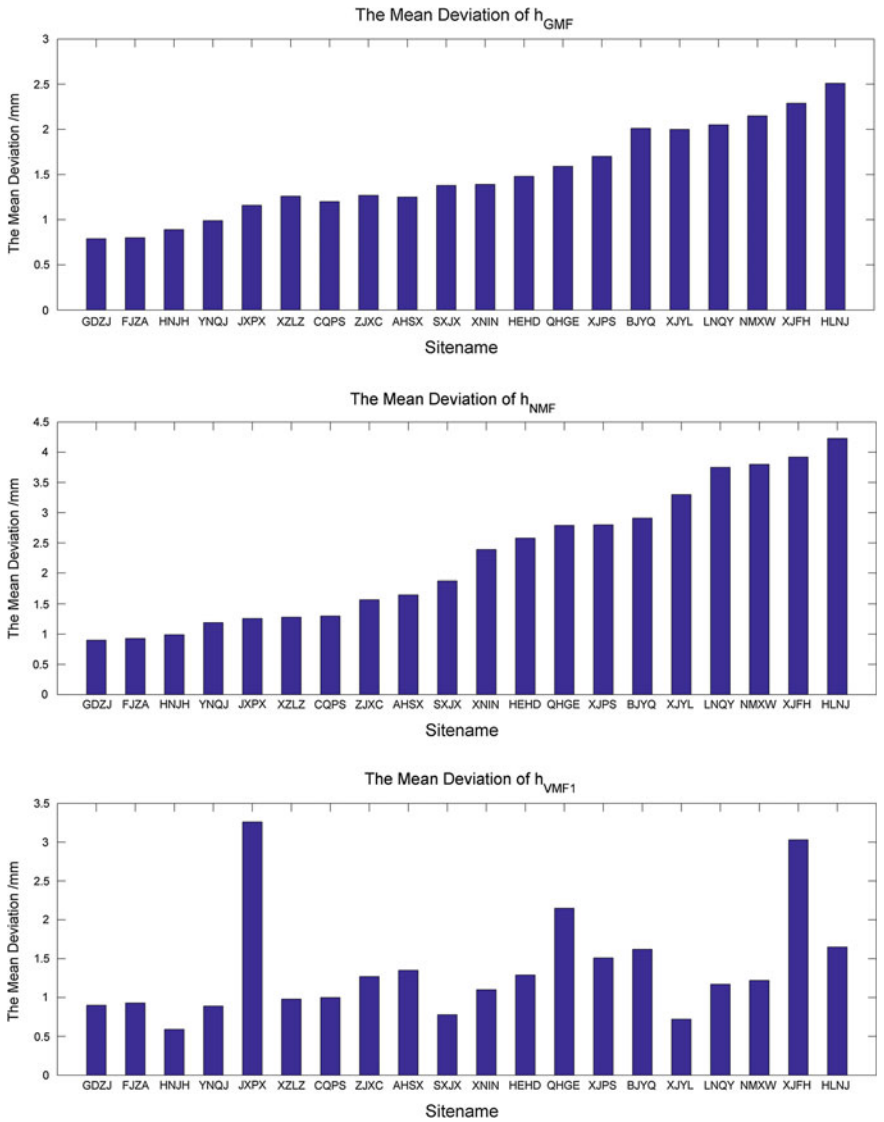

Fig. 3 Dry delay average values of the 3 mapping function

increased. Due to the altitude angle of 10°, the influence of the tropospheric delay is greater when the altitude angle is selected at 5°, while considering the influence of geometric distribution of satellites and multipath effect. Therefore, we recommend to choose the cutoff angle of 10° when the baseline is calculated in china (Table 3).

Table 3 Baseline error

Mapping function	Cutoff height angle/degree	ΔN/mm	ΔE/mm	ΔU/mm
GMF	5	7.7111	8.8876	15.2509
	10	7.7111	8.8876	15.2509
	15	8.3885	9.4967	18.1258
	20	9.2749	10.2692	22.5319
	25	10.4591	11.2012	29.5664
	30	12.5424	12.9463	44.2055
VMF1	5	7.7108	8.887	15.2422
	10	7.7108	8.887	15.2422
	15	8.3956	9.4989	18.1435
	20	9.2766	10.2712	22.5555
	25	10.4508	11.197	29.518
	30	12.5482	12.9515	44.2038
NMF	5	7.712	8.8879	15.2538
	10	7.712	8.8879	15.2538
	15	8.4037	9.506	18.1855
	20	9.282	10.2757	22.5696
	25	10.4759	11.2134	29.6584
	30	12.5627	12.9628	44.1874

5 The Influence of the Station Position on the Calculation Precision

5.1 Data Acquisition

The use of GLOBK will use the results of GAMIT solve can get the exact coordinates of the 28 stations. Then the exact coordinates of the 28 stations are used as a priori coordinates to input into the lfile., and the sittbl is used to constrain the coordinates of each site to the millimeter level. Because the research in this paper has found that the accuracy of the 10° elevation angle is the best when the baseline is calculated in China, so the cutoff angle of altitude of 10° is used to solve the problem by using GAMIT.

Use the sh_metutil command to invoke the metutil function and gets the zenith total delay L_t from the *O* file in the SOLVE file. Meanwhile, the tropospheric dry delay L_h can be modeled by the meteorological data [12–14]. The calculation method is as follows:

$$L_h = 0.0022768P/f(\varphi, h) \tag{4}$$

In the formula, P is representative measuring station ground pressure, $f(\varphi, h)$ is:

$$f(\varphi, h) = 1 - 0.00266\cos 2\varphi - 0.00028h \tag{5}$$

In the formula, φ is station latitude, h is altitude of station. The station ground meteorological parameters into the model to calculate delay L_h. Through the formula (6) can get wet delay L_w.

$$L_w = L_t - L_h \tag{6}$$

Thus, the dry delay and wet delay of the station can be obtained. According to the formula (7), the delay error of the three mapping functions at the cutoff angle of 10° can be obtained.

$$\xi_i^k = L_i \cdot f_i^k - L_i \tag{7}$$

In the formula, f is projection factor, L_i is the dry and wet zenith delay component, k is three kinds of tropospheric mapping functions [10].

5.2 Data Analysis

Figures 3 and 4 shows the dry and wet delay results of three mapping functions. According to the latitude of the station, the station name be expanded according to small to large in order in x axis, while y axis representing station dry (wet) delay. In consideration of clear expression, the three kinds of mapping function name preceded by h and w, respectively, represent the dry and wet delay.

As seen from Fig. 3, about h_{GMF}, the dry delay mean deviation of GDZJ, FJZA, HNJH, YNQI is less than 1 mm. The deviation value of LNQY, NMXW, XJFH, HLNJ is more than 2 mm, and the other stations are in the 1–2 mm. With the increase of latitude, the dry delay deviation mean as a whole is a rising trend the results show that when the GMF function is used to deal with the data in China, the precision of the time delay is related to the latitude: the higher the latitude, the worse the accuracy.

Compared to h_{GMF}, the mean delay deviation of h_{NMF} significantly higher and the station HLNJ reaches 4.23 mm The results show that the GMF function is more accurate than the NMF function to obtain the dry delay in the area of China. Meanwhile, h_{NMF} Shows the same latitude correlation with h_{GMF}.

For the h_{VMF1}, the mean deviation of the eight stations is less than 1 mm, and the average of the nine stations is about 1.5 mm. The overall accuracy is obviously better than that of the average h_{GMF}, h_{NMF}. However, it did not show a similar latitude correlation with GMF and NMF. But the deviation value of station JXPX, QHGE, XJFH was relatively large, which indicated that the relative applicability of VMF1 mapping function in these three stations was bad.

For the w_{GMF}, we can be seen from Fig. 4 that the mean deviation of the 20 stations is mostly about 0.18 mm, and there is no obvious correlation with the

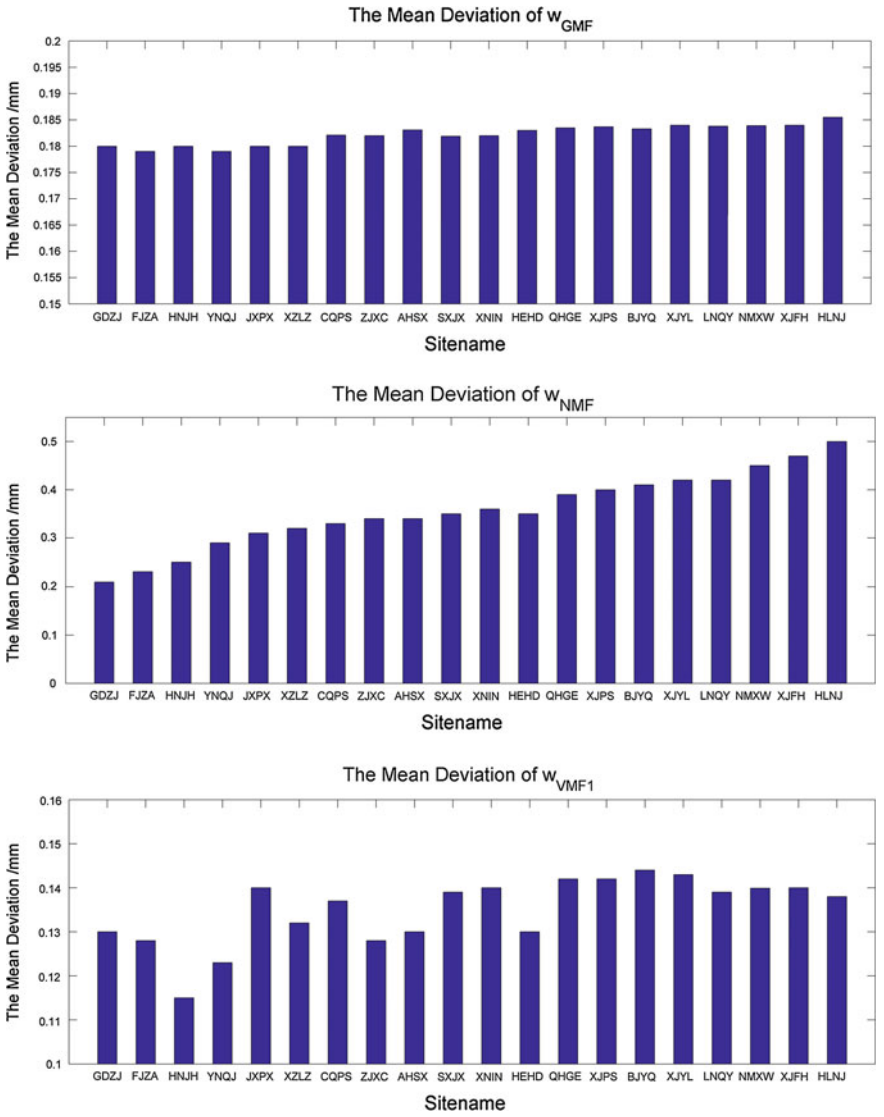

Fig. 4 Wet delay average values of the 3 mapping function

latitude of h_{GMF}. w_{VMF1} also showed the same randomness, but more uniform than the distribution of w_{GMF}, and the deviation mean accuracy is higher. However, w_{NMF} showed a more obvious correlation with latitude: the lower the latitude, the worse the accuracy, but the accuracy is relatively poor, the minimum deviation of the mean also reached 0.21 mm.

6 Conclusions

Based on the data of 20 CORS stations and 8 IGS stations, this paper analyzes the applicability of GMF, VMF1 and NMF mapping functions in China from the aspects of height angle parameters and station position. Results show:

(1) The accuracy of the three mapping functions in the horizontal direction is better than that in the vertical direction. When the satellite altitude angle is 5° and 10°, there is no difference in the accuracy of the baseline solution. With the increase of the height angle, the solution accuracy becomes worse. Taking into account the influence of tropospheric water vapor, satellite geometric distribution and multipath effects, it is recommended to select a cutoff angle of 10° in china.
(2) $h_{GMF}, h_{NMF}, w_{NMF}$ showed the same latitude correlation. In this case, h_{GMF}, h_{NMF} showed that: the higher the latitude, the lower the accuracy. But w_{NMF} showed that the lower the latitude, the lower the accuracy. However, h_{VMF1}, w_{VMF1}, w_{GMF} show a strong randomness.
(3) When the three mapping functions are used to deal with the data of China, the accuracy of NMF is significantly lower than that of GMF and VMF1, and the mean delay deviation of the VMF1 is less than GMF, so VMF1 is recommended in China, and GMF is used as the reserve function.

But in the three mapping functions, only the VMF1 coefficient a is obtained based on the measured meteorological data, other parameters are according to the observation data of a certain period of time is obtained, which will be the applicability of the mapping function in a region is limited, so according to the site to establish accurate troposphere mapping function of a region is worth further study.

References

1. Dodson AH, Chen W, Baker HC (2001) Assessment of EGNOS tropospheric correction model. J Navig 54(1):37–55
2. Yoaz B-S, Kroger E et al (1998) Estimating horizontal gradients of tropospheric path delay with a single GPS receiver. J Geophys Res Solid Earth, 103(B3):5019–5035
3. Janes HW, Langley, RB Newby et al (1991) Analysis of tropospheric delay prediction models: comparisons with ray-tracing and implications for GPS relative positioning. J Geodesy 65(3):151–161
4. Niell AE (2001) Preliminary evaluation of atmospheric mapping functions based on numerical weather models. Phys Chem Earth Part A 26(6–8):475–480
5. Boehm J, Niell A, Tregoning P et al (2006) Global Mapping Function (GMF): a new empirical mapping function based on numerical weather model data. Geophys Res Lett 25 (7):7304–7308
6. Jiang G, Tian X et al (2013) Analysis of the influence of tropospheric mapping function in high precision GNSS services. Mapp Eng 22(5):13–15
7. Jiang W, Li Z, Lei Q (2009) A new empirical projection function GMF analysis. Geodesy Geodyn 29(5):85–88

8. Kouba J (2008) Implementation and testing of the gridded Vienna Mapping Function 1 (VMF1). J Geodesy 82(4):193–205
9. Urquhart L, Nievinski FG et al (2014) Assessment of troposphere mapping functions using three-dimensional ray-tracing. GPS Solutions 18(3):345–354
10. Guo J, Zhang D, Shi J et al (2015) Accuracy of three typical tropospheric mapping functions in China using ray tracing method. J Wuhan Univ 40(2):182–187
11. Li F, Zhang Q et al (2015) The influence of tropospheric mapping function on GPS baseline calculation in Antarctic region. Bull Surveying Mapp 12:5–9
12. Cao Y, Liu J et al (2010) Study on atmospheric water vapor resource based on GPS tomography. J Nat Resour 25(10):1786–1796
13. Gorgeous C, Yinghua G, Zhaolin Z et al (2007) Application of ground GPS water vapor data in the study of "7. 10" rainstorm process in Beijing. Meteorology, 33(12):16–22
14. Liupeng W, Zhengdong B, Guo JJ et al (2007) Foundation GPS PWV sequence and RH sequence of relative humidity in rainstorm process. Sci Surveying Mapp 32(3):142–143

A Multi-Redundancies Network RTK Atmospheric Errors Interpolation Method Based on Delaunay Triangulated Network

Rui Shang, Chengfa Gao, Shuguo Pan, Denghui Wang and Longlei Qiao

Abstract Routine Network Real-time Kinematic (NRTK) techniques always use triangle as the interpolation unit to solve the users' ambiguity and atmospheric effects. Because of the limitation of the calculating unit, the correction information based on virtual reference station (VRS) technique cannot fully use the information from all the reference stations, so that the users' RTK initialization speed and positioning accuracy would be seriously affected. In order to avoid the loss of observation information, two interpolation methods, MLIM for ionosphere and RELIM for troposphere, were proposed in the paper. Relying on the existing Delaunay Triangulated Network (DTN) structure, the optimal and suboptimal units were selected to increase the interpolation baselines number. Using the data from the Earth Scope Plate Boundary, our methods obtained more accurate interpolation accuracy by 3 times and 6 to 30 times higher for ionosphere and troposphere, respectively, compared with the traditional models. Besides, these two models can get more stable performance regardless the change of satellites elevation and the altitude differences among reference stations. In addition, we developed an alternative integrity monitoring method for rover station, with the interpolating monitoring precision of centimeter level. The proposed method is feasible to evaluate the actual integrity index and monitor the actual accuracy in the users' position.

Keywords DTN · NRTK · Atmospheric delay · Interpolation model · Integrity monitoring

R. Shang · C. Gao (✉) · D. Wang · L. Qiao
School of Transportation, Southeast University, 2 Sipailou, Nanjing 210096, China
e-mail: gaochfa@seu.edu.cn

R. Shang
e-mail: shangrui1994@foxmail.com; 220152496@seu.edu.cn

S. Pan (✉)
School of Instrument Science and Engineering, Southeast University,
2 Sipailou, Nanjing 210096, China
e-mail: psg@seu.edu.cn

J. Sun et al. (eds.), *China Satellite Navigation Conference (CSNC) 2017 Proceedings: Volume III*, Lecture Notes in Electrical Engineering 439,
DOI 10.1007/978-981-10-4594-3_28

1 Introduction

The continuous improvement of the Global Navigation Satellite System (GNSS) as along with the integration of satellite navigation and Internet technology has greatly expanded depth and range of the application of high precision positioning technology. NRTK technique with a representative of the VRS technology can provide a centimeter level positioning and has effectively improved the application of satellite navigation system [1]. The existing VRS technology generally uses the DTN to build spatial errors model, this calculation unit can ensure optimal network construction as well as the independent solution of each baseline [2]. However, due to the limitation of the triangular structure, users can not make full use of the redundant information of surrounding reference stations. Because of this, interpolation accuracy is seriously affected when large elevation differences exists among reference stations. What is more, due to the lack of baselines, the interpolation results could not be effectively checked.

Among the existing errors models for NRTK, the linear interpolation model (LIM), the linear combination model (LCM), the distance-based linear Interpolation method (DIM) and the low-order surface model (LSM) are mostly used [2]. Based on these models and the conventional usage method of DTN, scholars home and abroad have taken a lot of measures to improve the RTK interpolation accuracy, especially for the reference stations with large elevation differences. Many researchers have raised star structure to increase reference stations [3, 4]. However, it is not able to program star structure for automatically running. Some researchers also enhanced elevation correct model upon LCM [5]. However, these methods have limited effect while the incensement problem of redundant information still exists. Focus on atmospheric interpolation accuracy monitoring, some researchers studied un-difference ionospheric residual integrity monitoring index [6] while some other put forward ionospheric and tropospheric residual integrity monitoring index [2]. However, these methods are not suitable for real-time monitoring.

In this paper, a solution based on DTN is proposed in order to solve problem mentioned above. With a process of selecting optimal and suboptimal triangular units to increase redundant information, MLIM and RELIM models are introduced based on the chosen units. Besides, a set of integrity monitoring index can be generated by baselines atmosphere delay correction.

2 Redundant Triangulation Algorithm

In order to ensure the continuous operation of the software, Gauss Plan Coordinates of the CORS reference stations must be used to make the polygon net in the initialization stage of the CORS system. The structure of the polygon net directly affect the ambiguity resolution efficiency of baselines and atmosphere interpolation accuracy of the virtual stations [2]. Since the DTN has taken advantages of unique,

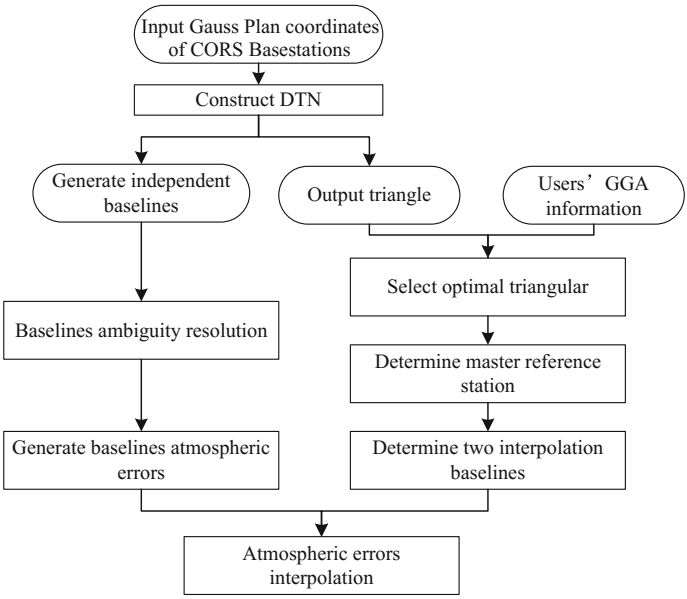

Fig. 1 The conventional usage of the DTN

Fig. 2 The example of conventional method

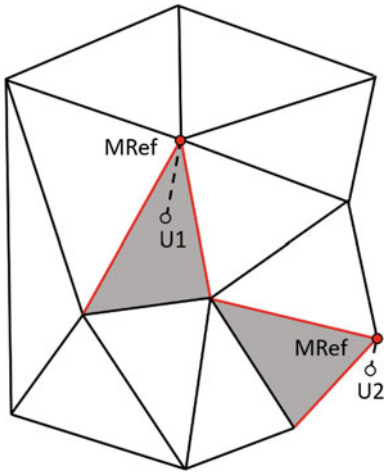

optimal and being prone to automatization, it has been employed in the conventional NRTK software [7]. The usual usage of the DTN is as shown in Fig. 1.

When the conventional method is used to choose interpolation baselines, in case of user U1 shows in Fig. 2, when the rover station is located in the DTN, the triangle which contains the rover station is determined as the optimal triangle. In this triangle, the nearest reference station is determined as the main reference station

(MRef), and the two baselines connected with the main reference station can be used as the interpolation baselines. In the other case of user U2 shows in Fig. 2, the rover station is outside of the scope of the DTN. The triangle, whose center of gravity is nearest to the rover station, is chosen as the optimal triangle. In this case, the method of main reference station and interpolation baselines selection is the same as U1 [2].

Although the conventional usage of DTN has many advantages, the available interpolation baselines are too few for each rover station, the optionality of interpolation model is restricted. Taking into account the positive and negative of conventional method, a kind of redundancy method based on DTN is proposed in this paper. The idea is shown in Fig. 3.

In traditional way, after determining the two main interpolation baselines (ML), the choosing criterion of suboptimal triangular elements should rely on the interpolation baselines sharing. As the user U1 shows in Fig. 4, when the rover station is located in the DTN, two suboptimal triangles and two redundant interpolation baselines (RL) can be obtained. As user U2 and U3 show in Fig. 4, when the main reference station is located on the boundary of the DTN and only one triangle shares the baseline with the optimal, one redundant interpolation baseline can be

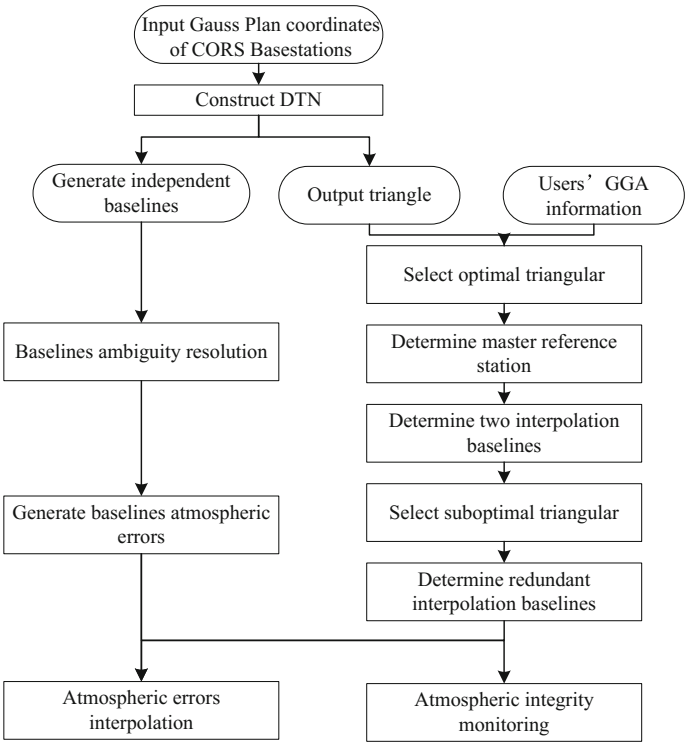

Fig. 3 The flowchart of the redundancy method

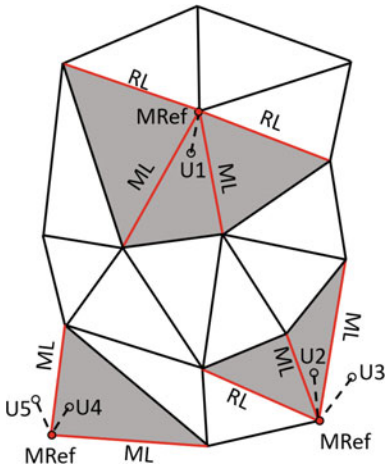

Fig. 4 The example of redundancy method

obtained. As the user U4 and U5 show in Fig. 4, when the main reference station is located on the boundary of the DTN and no triangle shares the baseline with the optimal, there is no redundant interpolation baseline left.

By adopting the redundancy method based on DTN, not only the optimal construction of DTN can be preserved, but also neighboring reference stations can be fully used. Furthermore, with this method can solve the problem of using redundant information in the current NRTK software, and it is easy to be realized by programming.

3 Atmospheric Errors Interpolation Models and the Integrity Monitoring of the Rover Station

The double-difference ambiguities between each reference station and the main reference station must be correctly determined before the atmospheric interpolation. For long baseline, the effects of ionosphere delay and tropospheric delay should be considered. Restricted by the troposphere model correction accuracy, the method of parameter estimation is used to calculate the tropospheric delay. And the ionosphere is treated by the three step solutions of the combination of wide lane and ionosphere-free model [8]. After obtaining the correct ionosphere and tropospheric delays of each baseline, the value of atmospheric delay correction on each baseline would be recalculated by unifying the pivot satellite of each baseline, and then can be used to realize the atmospheric interpolation.

Since the ionosphere errors has a strong spatial and temporal correlation and troposphere errors is closely related to the height parameter, it is needed to use different methods to calculate the interpolated value of troposphere and ionosphere delay according to correlation characteristics [9–13]. Constrained by the number of interpolation baselines, conventional RTK usually use the LIM for atmospheric

interpolation. Under the redundant method proposed by this paper, when the rover station is located in the DTN, the number of interpolation baselines is up to 4, when the rover station is outside the DTN, the number of interpolation baselines is 3. As the baselines increase, more interpolation models suitable for NRTK can be proposed.

3.1 Ionosphere Interpolation Model

According to carrier double-difference observation equations, reference stations' double differential ionosphere delay can be written as Eq. (1):

$$\Delta\nabla I = \frac{f_2^2}{f_1^2 - f_2^2}[(\lambda_1\Delta\nabla\varphi_1 - \lambda_2\Delta\nabla\varphi_2) + (\lambda_1\Delta\nabla N_1 - \lambda_2\Delta\nabla N_2)] - \frac{f_2^2}{f_1^2 - f_2^2}(\Delta\nabla\varepsilon_1 - \Delta\nabla\varepsilon_2) \tag{1}$$

where $\Delta\nabla$ is the double-difference operator, $\Delta\nabla I$ is double-difference ionosphere delay, $\lambda_i, f_i (i = 1, 2)$ are L1 and L2 carrier wavelength and frequency, $\varphi_i (i = 1, 2)$ are the carrier phase observations, N_i is the inter ambiguity, $\varepsilon_i (i = 1, 2)$ are the effects of the carrier phase observation's noise and not-modeled errors. For the baseline of 200 km or less, random noise errors is less than 3 mm, and therefore can be ignored, so the above models can be simplified as Eq. (2):

$$\Delta\nabla I = \frac{f_2^2}{f_1^2 - f_2^2}[(\lambda_1\Delta\nabla\varphi_1 - \lambda_2\Delta\nabla\varphi_2) + (\lambda_1\Delta\nabla N_1 - \lambda_2\Delta\nabla N_2)] \tag{2}$$

It has been proved that LIM can fit the ionosphere well in the conventional triangular calculation unit, so based on LIM, a new model for NRTK ionosphere interpolation named multiple-redundant linear interpolation model (MLIM) is established as Eq. (3):

$$\Delta\nabla I_{u,n} = a_1\Delta x_{u,n} + a_2\Delta y_{u,n} \tag{3}$$

$$a = (B^T B)^{-1} B^T L \tag{4}$$

$$B = \begin{bmatrix} \Delta x_{1,n} & \Delta y_{1,n} \\ \Delta x_{2,n} & \Delta y_{2,n} \\ \vdots & \vdots \\ \Delta x_{n-1,n} & \Delta y_{n-1,n} \end{bmatrix} \tag{5}$$

$$L = [\,\Delta\nabla I_{1,n} \quad \Delta\nabla I_{2,n} \quad \ldots \quad \Delta\nabla I_{n-1,n}\,]^T \tag{6}$$

where $\Delta\nabla I$ is double-difference ionosphere delay, $1,\ldots,n$ represent the number of reference stations, $1,2,\ldots,n-1$ represent the auxiliary reference stations, n represents the main reference station, u represents the rover station, a_1, a_2 are the linear interpolation coefficients, $\Delta x, \Delta y$ represent the difference of plane coordinate between the main reference station and the auxiliary reference stations [2].

3.2 Troposphere Interpolation Model

According to the double-difference carrier-phase observation equation, double-difference troposphere errors correction can be calculated as Eq. (7) [11].

$$\Delta\nabla T = \frac{cf_1(\Delta\nabla\varphi_1 - \Delta\nabla N_1)}{f_1^2 - f_2^2} - \frac{cf_2(\Delta\nabla\varphi_2 - \Delta\nabla N_2)}{f_1^2 - f_2^2} - \Delta\nabla\rho \tag{7}$$

where $\Delta\nabla$ is the double-difference operator, $\Delta\nabla T$ is double-difference troposphere errors correction, ρ is geometric distance between the satellite and the receiver, $\lambda_i, f_i (i = 1,2)$ are L1 and L2 carrier wavelength and frequency, $\phi_i (i = 1,2)$ are the carrier phase observations, N_i is the inter ambiguity.

Troposphere errors is affected by the horizontal direction and the station elevation. When the rover station in the horizontal direction is strongly constrained within a region constituted by the reference stations, it may stay away from the surface in the area interpolation model in elevation direction, so the corrections of tropospheric delay of the rover station must consider the impact of the elevation factor [11].

Considering the influence of the elevation, based on LIM, a model named revise elevation linear interpolation model (RELIM) is developed for NRTK troposphere interpolation as Eq. (8):

$$\Delta\nabla T_{u,n} = a_1\Delta x_{u,n} + a_2\Delta y_{u,n} + a_3\Delta h_{u,n} \tag{8}$$

$$a = (B^T B)^{-1} B^T L \tag{9}$$

$$B = \begin{bmatrix} \Delta x_{1,n} & \Delta y_{1,n} & \Delta h_{1,n} \\ \Delta x_{2,n} & \Delta y_{2,n} & \Delta h_{1,n} \\ \vdots & \vdots & \vdots \\ \Delta x_{n-1,n} & \Delta y_{n-1,n} & \Delta h_{1,n} \end{bmatrix} \tag{10}$$

$$L = \begin{bmatrix} \Delta\nabla T_{1,n} & \Delta\nabla T_{2,n} & \ldots & \Delta\nabla T_{n-1,n} \end{bmatrix}^T \tag{11}$$

where $\Delta\nabla T$ is double-difference troposphere errors correction, $1,\cdots,n$ represent the number of reference stations, $1,2,\cdots,n-1$ represent the auxiliary reference stations, n represents the main reference station, u represents the rover station,

a_1, a_2, a_3 are the linear interpolation coefficients, $\Delta x, \Delta y$ represent the difference of plane coordinate between the main reference station and the auxiliary reference stations, Δh represents the elevation difference.

3.3 Atmospheric Integrity Monitoring Index

Ionosphere and troposphere interpolation accuracy are the most important factors that affect the positioning precision of RTK users. In order to guarantee users location accuracy, it is necessary to monitor the ionosphere and troposphere interpolation accuracy of each user in real time. The ionosphere and troposphere integrity index can measure the residual errors of the ionosphere and troposphere well. On the basis of redundant method, this paper presents a kind of real-time integrity monitoring index. The calculation procedures are as following:

In the first stage, as shown in Fig. 5a, two redundant baselines (RL1, RL2) together with main baseline 1 (ML1) are used to calculate ionosphere interpolation of main baseline 2 (ML2) with MLIM, calculate troposphere interpolation with RELIM. After that, calculating the difference of ionosphere and troposphere between interpolation and estimate values of all satellites on the ML2. The difference is used to calculate weighted RMS of each epoch for ML2, which is marked as ARMS. As shown in Fig. 5b, the two redundant baselines (RL1, RL2) and the main baseline 2 (ML2) will serve as the interpolation baselines to interpolate the main baseline 1 (ML1), using the same method to calculate weighted RMS of each epoch for ML1, marked here as BRMS. Finally, according to ARMS and BRMS, LIM is used to calculate the users' ionosphere and troposphere integrity index, named after Real-Time Ionospheric Residual Integrity Monitoring (RTIRIM) and Real-Time Tropospheric Residual Integrity Monitoring (RTTRIM) as Eq. (12).

$$RIM = a_1 \Delta x_{u,n} + a_2 \Delta y_{u,n} \tag{12}$$

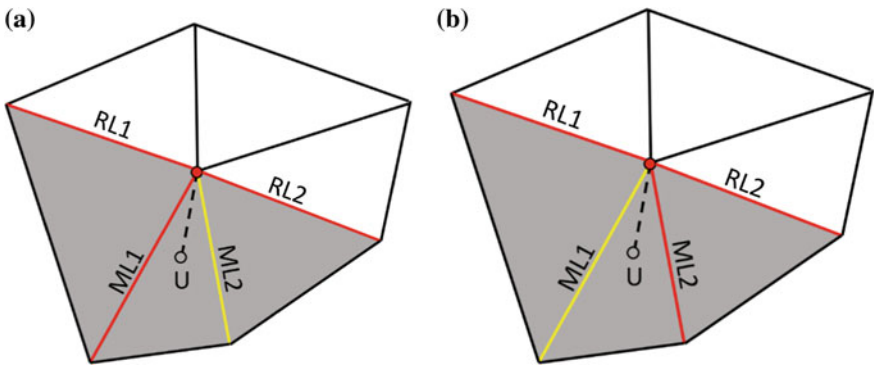

Fig. 5 Integrity monitoring example

$$a = (B^T B)^{-1} B^T L \tag{13}$$

$$B = \begin{bmatrix} \Delta x_{1,n} & \Delta y_{1,n} \\ \Delta x_{2,n} & \Delta y_{2,n} \end{bmatrix} \tag{14}$$

$$L = [\,\mathrm{ARMS} \quad \mathrm{BRMS}\,]^T \tag{15}$$

Satellite weighting method as following:

$$P(z) = \cos^2(z) \tag{16}$$

where RIM represent the RTIRIM and the RTTRIM, 1, 2 represent the number of reference stations, n represents the main reference station; u represents the rover station, Δx, Δy represent the difference of plane coordinate between the main reference station and the auxiliary reference stations, Z represents the Satellite altitude angle.

4 Experiments

The GPS data in 2013/08/08 from PBO (Plate Boundary Observatory) supplied by UNAVCO [14] is used to interpolate and do integrity monitoring experiments. The length of time for observed data is 24 h, the data sampling rate is 15 s. The names and distributions of the six selected reference stations are shown in Fig. 6, the difference of elevation among stations is as shown in Fig. 7. In the process of the experiment, the G19 satellite which has two times elevation angle fluctuation is analyzed, the change of elevation angle about G19 is shown in Fig. 8.

In order to verify ionosphere interpolation accuracy of MLIM proposed in this paper, LIM and LSM are selected for performance comparisons, in which LIM is based on conventional method while LSM based on redundant method. What's more, in order to verify the troposphere interpolation accuracy of RELIM presented

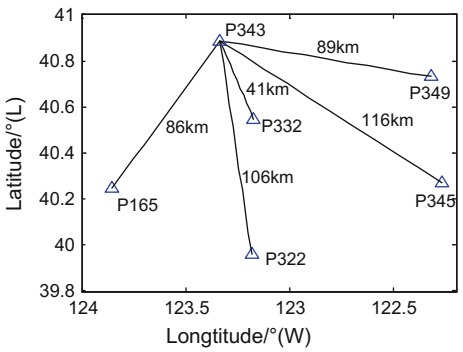

Fig. 6 Distribution of stations

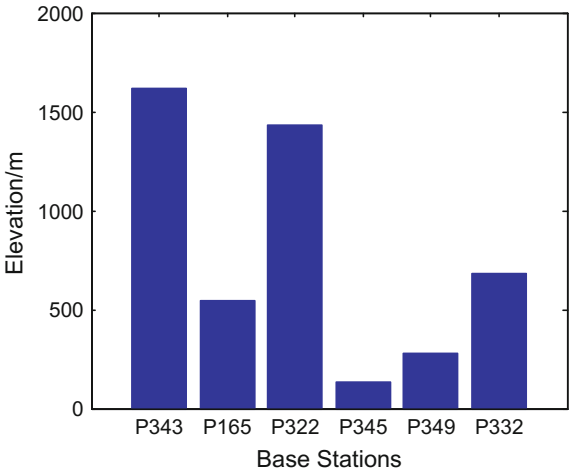

Fig. 7 Difference of elevation among stations

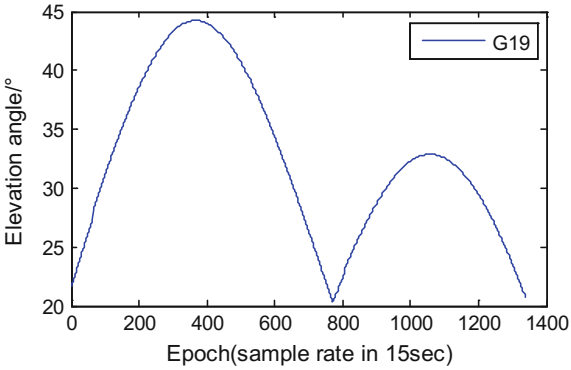

Fig. 8 The change of elevation angle of G19

in the article, HLCM and MHM, which are proposed in literature [4] and literature [6], are introduced for performance comparisons. Here HLCM is based on conventional method and MHM is based on redundant method. For each session, there are two network configurations for analysis interpolation results, one is the rover station within the network, and the other is the rover station outside the network. It should be noted that when the rover station is out of range, there are only 3 interpolation baselines. So MHM cannot be used for troposphere interpolation.

4.1 Rover Station Is Within the Network

As the rover station is located in the DTN, P343 serve as the main reference station and P332 serve as the rover station. For conventional method, P322, P345 serve as

the interpolation reference stations. For redundant method, P165, P322, P345, P349 serve as the interpolation reference stations. Figure 4 shows the variation of ionosphere biases for LIM, LSM and MLIM. Figure 5 shows the variation of troposphere for LIM, HLCM, MHM and RELIM.

4.2 Rover Station Is Outside the Network

As the rover station is located outside the DTN, P343 serve as the main reference station and P349 serve as the rover station. For conventional method, P322, P345 serve as the interpolation reference stations. For redundant method, P165, P322, P345 serve as the interpolation reference stations. Figure 11 shows the variation of ionosphere biases for LIM, LSM, and MLIM. Figure 12 shows the variation of troposphere for LIM, HLCM, and RELIM. The Root-Mean-Square (RMS) of the interpolation results for ionosphere and troposphere are shown in the Tables 1 and 2.

From Figs. 9 and 11, it is easy to see that for ionosphere interpolation, the MLIM put forward by this paper is superior to conventional model since the former are more close to zero. From Figs. 8, 10 and 12, it is obvious that for the troposphere delay correction, since without consider the difference of the reference

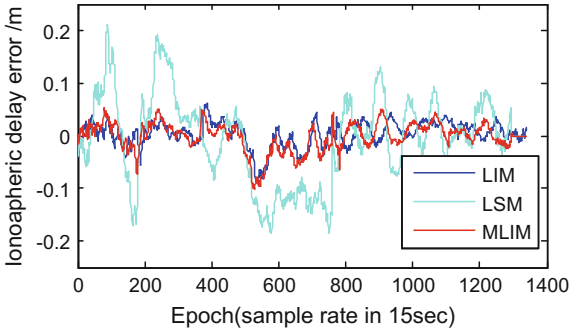

Fig. 9 The variation of ionosphere biases

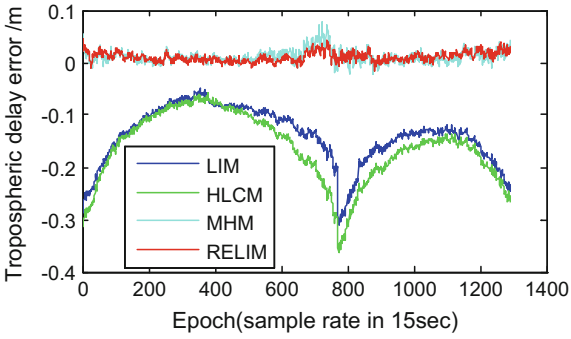

Fig. 10 The variation of troposphere biases

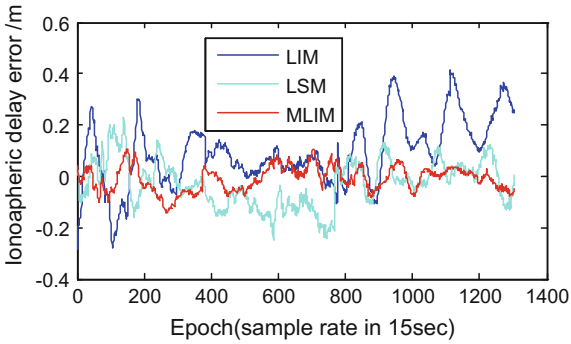

Fig. 11 The variation of ionosphere biases

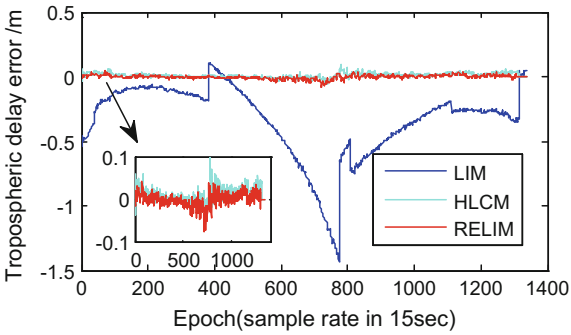

Fig. 12 The variation of troposphere biases

Table 1 The RMS of the interpolation results for ionosphere model (m)

	LIM	LSM	MLIM
Inside the DTN	0.0267	0.0840	0.0284
Outside the DTN	0.1471	0.1117	0.0497

Table 2 The RMS of the interpolation results for troposphere model (m)

	LIM	HLCM	LSM	RELIM
Inside the DTN	0.1549	0.1811	0.0170	0.0148
Outside the DTN	0.4536	0.0204	–	0.0151

stations, the accuracy of traditional interpolation model LIM changes with the elevation angle, the performance of HLCM is unstable in two cases, and the LSM cannot be used when the rover station is outside the DTN, only the RELIM put forward by this paper can keep the variation stable and its interpolation accuracy high whether in-or outside the DTN.

Analysis from Tables 1 and 2, first consider the case rover station inside DTN. As for ionosphere, the accuracy of MLIM nearly equal with LIM, and more than three times of LSM. As for troposphere, the accuracy of RELIM is about the same to the LSM and nearly six times as accurate as the LIM and HLCM. Then consider

the case rover station outside of DTN. As for ionosphere, the accuracy of MLIM is triple of LIM and LSM. As for troposphere, the accuracy of RELIM is a little better than that of HLCM and is 30 times higher than that of LIM.

To sum up, in either case, MLIM and RELIM can get high and stable ionosphere and troposphere interpolation accuracy, regardless change of the satellite's elevation.

4.3 Integrity Monitoring Experiment

In this experiment, we choose P343 station as the main reference station and P349 as the rover station. The baseline P343-P165, P343-P349 represent the RL1 and the RL2. The baseline P343-P322, P343-P345 represent the ML1 and the ML2. Figure 13 shows the ionosphere integrity monitoring information and Fig. 14 shows the troposphere integrity monitoring information. In order to investigate the performance of integrity monitoring method, the double-difference ionospheric and tropospheric delay of the baseline P343-P332 is obtained as the true value.

In Fig. 13, it should be noted that the irregular vibration is caused by the change of the satellite number. Compared with the ionospheric delay, the tropospheric delay perform a better conformity. The main reason is that the ionospheric delay

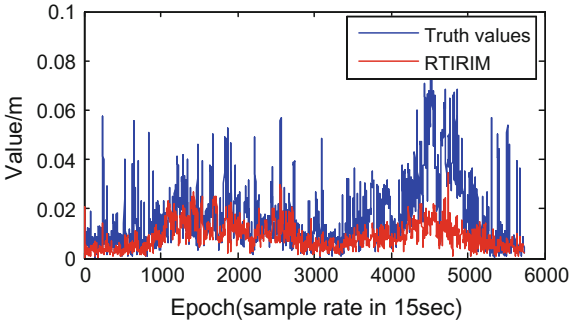

Fig. 13 Ionosphere integrity monitoring information

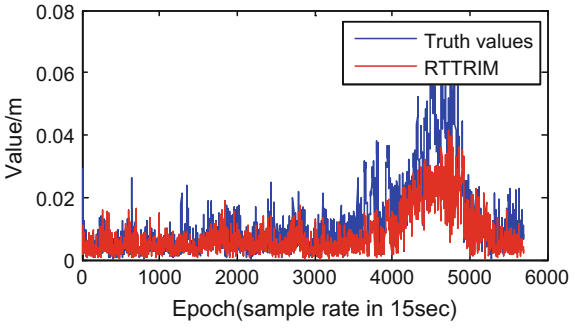

Fig. 14 Troposphere integrity monitoring information

Table 3 The RMS of integrity monitoring (m)

Ionosphere	Troposphere
0.0143	0.0098

shows a more serious instability in short-term spatiotemporal scales. The RMS of the integrity monitoring results are shown in the Table 3.

In Table 3, it clearly shows that the integrity monitoring results can reach centimeter level interpolating accuracy for ionospheric and tropospheric delay. In general, the monitoring method proposed in this paper can be used to evaluate the actual integrity index in the regional CORS and monitor the actual accuracy in the users' position.

5 Conclusion

A redundant method based on DTN for RTK is proposed to solve redundant problem in this paper. The real-life GPS data from PBO contributed to the analysis of interpolation methods in regional CORS. By realizing the redundant interpolation method, a pair of regional modeling methods (MLIM and RELIM) and a real-time monitoring scheme are also proposed. There some conclusions as following:

(1) By selecting sub optimal triangular units, the redundant method is able to achieve more available interpolation baselines for users. And the problem that users cannot make full use of the redundant information can be solved in the current NRTK software.
(2) For the regional modeling methods of ionosphere and troposphere delay, the method of MLIM can significantly improve the accuracy of ionosphere interpolation model by 3 times and the accuracy of RELIM is 6 to 30 times higher than traditional troposphere model. And these new methods can get more stable performance whether the rover station is in or outside the network. What is more, the two models can also avoid the influence for interpolation accuracy causing by the change of satellites elevation angles and the altitude differences among reference stations.
(3) The integrity monitoring results shows the monitoring method can reach centimeter level interpolating accuracy for ionospheric and tropospheric delay in the regional CORS. And it is feasible to evaluate the actual integrity index and monitor the actual accuracy in the users' position.

Last but not least, it should be noted that the atmospheric integrity monitoring method proposed in this research is based on the regional CORS. The influence of interpolation accuracy on the users' positioning results should be further researched.

Acknowledgements We would like to express our thanks to Ye Fei of the Instrument Science and Engineering, Southeast University for his kind help in the revision process of this paper. This work was supported by the National Key Research & Development Plan of China (2016YFB0502101), the National Natural Science Foundation of China (41574026) and the Primary Research & Development Plan of Jiangsu Province (BE2016176).

References

1. Landau H, Vollath U, Chen X (2002) Virtual reference station systems. Positioning 1(2):137–143
2. Dingfa H (2011) GPS Enhanced reference station network theory. The Science Publishing Company
3. Xuefeng S, Chengfa G, Shuguo P (2012) Algorithm for network RTK(VRS) based on star structure. Acta Geod Cartogr Sin 41(1):33–40
4. Wu B, Gao C, Pan S, et al (2015) Regional modeling of atmosphere delay in network rtk based on multiple reference station and precision analysis. In: China satellite navigation conference (CSNC) 2015 proceedings, Vol II. Springer Berlin Heidelberg, pp 439–448
5. Wang D, Gao C, Pan S (2012) Analysis and modeling of tropospheric delay of network RTK. In: China satellite navigation conference (CSNC)
6. Chen X, Landau H, Vollath U, et al (2003) New tools for network rtk integrity monitoring. In: Proceedings of international technical meeting of the satellite division of the institute of navigation
7. Rong Z, Hui L, Yichun Y, et al (2005) Application of delaunay triangulated network to continuous operational reference system. Wtusm Bull Sci Technol 6
8. Tang W (2007) Three steps method to determine double difference ambiguities resolution of network RTK reference station. Geomatics and Inf Sci Wuhan Univ 32(4):305–308
9. Chenggang Li (2007) Generation and Distribution Technique of Precise Differential Corrections for GPS/VRS Network. Southwest Jiaotong Univ, Chengdu
10. Cheng-Gang LI, Huang DF, Yuan LG, et al (2005) Ionospheric biases modeling technique for GPS multiple reference stations. J Southwest Jiaotong Univ 5
11. Chenggang L, Dingfa H, Letao Z Tropospheric modeling technology of GPS/VRS reference station network. Sci surveying Mapp 32(4 Jul)
12. Wu S, Zhang K, Silcock D (2009) Differences in accuracies and fitting surface planes of two error models for NRTK in GPSnet. J Global Positioning Syst 8(2):154–163
13. Ke F, Wang Q, Pan S (2012) Network RTK atmosphere error interpolation estimation model based on mapping function. Geomatics and Inf Sci Wuhan Univ 37(1):73–76
14. ftp://garner.ucsd.edu/rinex, Accessed 8 Aug 2013

An Accurate Height Reduction Model for Zenith Tropospheric Delay Correction Using ECMWF Data

Yufeng Hu and Yibin Yao

Abstract Tropospheric delay is a major error source in geodetic techniques. In recent years, the Numerical Weather Models (NWMs), such as the European Centre for Medium Range Weather Forecasts (ECMWF), have been increasingly used in the atmospheric delay processing of space geodetic observations. It is necessary for the GNSS users to make height reduction for the troposphere products from ECMWF to obtain the accurate Zenith Tropospheric Delay (ZTD). Based on the ECMWF data, a new height reduction model for ZTD called Gaussian function model is proposed, which is suitable for the ZTD correction from ECMWF data. The internal accuracy of the proposed model is 0.9 cm. The validation by the troposphere products of 162 globally distributed IGS stations at 2015 shows that the annual average bias and Root Mean Square error (RMS) of the Gaussian function model are 0.14 and 1.55 cm respectively, and the Gaussian function model is stable throughout the year. The testing results from the ZTD profiles derived from radiosonde data shows that, the Gaussian function model performs well above 5 km height.

Keywords Zenith tropospheric delay · NWMs · ECMWF · Height reduction · Gaussian function model

1 Introduction

When passing through the atmosphere, the radio signals are affected by the atmospheric refraction. Bending and delay occur in the propagation, which result in atmospheric delays. The ionospheric delay can be eliminated by dual frequency correction [1], while the tropospheric delay cannot be eliminated in this way due to

Y. Hu (✉) · Y. Yao
School of Geodesy and Geomatics, Wuhan University, Wuhan 430079, China
e-mail: yfhu@whu.edu.cn

J. Sun et al. (eds.), *China Satellite Navigation Conference (CSNC) 2017 Proceedings: Volume III*, Lecture Notes in Electrical Engineering 439,
DOI 10.1007/978-981-10-4594-3_29

its non-dispersion, so the tropospheric delay becomes a major source of error in space geodetic techniques. In spatial geodetic data processing, the tropospheric delay on the propagation path is generally expressed as the product of the Zenith Total Delay (ZTD) and the Mapping Function (MF). Furthermore, ZTD can be divided into Zenith Hydrostatic Delay (ZHD) and Zenith Wet Delay (ZWD) [2].

In data processing, ZTD are generally estimated using empirical tropospheric models. The traditional models such as Sasstamoinen model [3], Black model [4] and Hopfield model [5] are highly dependent on the meteorological measurements and their correction performances are not ideal. With the development of ZTD modeling, the blind tropospheric models such as UNB3m model [6], GPT2w model [7] and ITG model [8] were proposed. The blind tropospheric models do not need the real meteorological measurements as input, which can provide the users with tropospheric delay corrections just based on the station location information and the time, while the accuracy of blind tropospheric models is about 4 cm due to the limited temporal and spatial resolutions [9]. In recent years, with the improvement of the earth observation network and the increase of observation data, the troposphere delay correction has been transferred from a simple closed data model to a correction model which relies on a large amount of external data. Various Numerical Weather Models (NWMs) like National Centers for Environmental Predication (NCEP) and European Centre for Medium Range Weather Forecasts (ECMWF) have been developed to assimilate various meteorological data and publish reanalysis data of various types of meteorological elements on the website. The tropospheric delay can be calculated directly from these reanalysis meteorological data, which has become an effective solution to tropospheric delay correction [10] and has been increasingly adopted in the atmospheric delay processing of space geodetic observations to improve the accuracy of the analysis results. Based on the ECMWF data, Böhm and Schuh [11] developed a project called Global Geodetic Observing System (GGOS) Atmosphere to provide tropospheric products including tropospheric delay, mapping function coefficients, weighted mean temperature, etc. The accuracy of the GGOS tropospheric delay is lower than its data source ECMWF. Chen et al. [12] showed that the accuracy of ECMWF ZTD is higher than that of NCEP, and the ECMWF ZTD has higher stability and applicability.

Since the NWMs like ECMWF is in the form of grid, for the GNSS users, the ECMWF troposphere products cannot be directly used due to the height difference between the stations and the grid points, which need height reduction. Currently, the commonly used method of height reduction for ZTD is exponential function. In this paper, we aimed to establish a high precision model to realize the accurate height reduction for ECMWF ZTD. Firstly, ECMWF ZTD were used to analyze the characteristics of the change with height. On this basis, a new model of the ZTD height reduction- Gaussian function model was proposed. The accuracy of Gaussian function model was verified by IGS tropospheric products and radiosonde data, and comparisons with the exponential function model and corresponding analysis were carried out.

2 Processing of ECMWF Data

The pressure levels data of ECMWF mainly include the geopotential height, temperature, and specific humidity for the 37 specific pressure levels. The height of the top level is usually 50 km, and there is rather few water vapors above this height, so the wet delay can be ignored. According to the Sasstamoinen model, the ZHD above the top level is about 2.3 mm which should be taken into account in ZTD calculation.

The geopotential height provided by ECWMF is the ratio of geopotential to gravity acceleration. It is generally used in meteorology research, but the calculation of the tropospheric delay in geodetic surveys is based on orthometric height. If the difference between these two height systems is not dealt with, the calculated tropospheric delays will result in a deviation of about 5 mm. The common convention method between two kinds of height systems is [13]:

$$\begin{cases} h = \frac{R_e(\varphi)\cdot\Phi}{\frac{g(\varphi)}{g_0}R_e(\varphi)-\Phi} \\ g(\varphi) = \gamma_e \frac{1+k\ \sin^2\varphi}{\sqrt{1-e^2\sin^2\varphi}} \\ R_e(\varphi) = \frac{a}{1+f+m-2f\ \sin^2\varphi} \end{cases} \tag{1}$$

In Eq. (1), φ is the latitude; h and Φ are the orthometric height and geopotential height in km, respectively; $g(\varphi)$ is the gravity acceleration at latitude φ; g_0 is the gravity constant (9.80665 m/s^2); $R_e(\varphi)$ is the earth's curvature radius at latitude φ; a, f, m, k, e^2, γ_e are constants which can be seen in [13].

For each specific pressure level, the atmospheric reflective index can be calculated as [12]:

$$\begin{cases} N = k_1\frac{P-e}{T} + k_2\frac{e}{T} + k_3\frac{e}{T^2} \\ e = h \times P/0.622 \end{cases} \tag{2}$$

In Eq. (2), k_1 is 77.60 K/Pa; k_2 is 64.79 K/Pa; k_3 is 377,600.0 K^2/Pa; P is the atmospheric pressure of the level; e represents the water vapor pressure; T represents the temperature and h represents the specific humidity.

After the height h and the refractive index N of each level are obtained, firstly the ZHD above the top level is calculated through the Sasstamonien model:

$$\mathrm{ZHD} = \frac{0.0022767 \cdot P}{1 - \cos(2\varphi) - 0.00028 \cdot h} \tag{3}$$

Then the ZTD can be calculated by numerical integration, as follows:

$$\mathrm{ZTD}_i = 10^{-6}\int_S N \cdot ds = 10^{-6}\sum_i N_i \cdot \Delta s_i \tag{4}$$

In Eq. (4), N_i denotes the refractive index of level i; Δs_i is the thickness of level i. The integral value added with the ZHD above the top level is the final ZTD of the grid point.

We randomly selected 6 grid points distributed at different locations in the world to analyze the relationship between ZTD and height (at 0:00 UTC on Jan. 1, 2015), and plotted the change of ZTD with height in Fig. 1 using the pressure levels data of ECWMF. From Fig. 1, we can see that ZTD shows downward trend with height increasing. The ZTD of each grid point decreases gradually with height increasing, and the change pattern conforms to a very smooth curve. In particular, the change of ZTD is more intense in the height range of 0–10 km, and the total amount of ZTD decreases by about 2 m at 10 km height. After 10 km height, the decay speed of ZTD begins to slow down. When the height exceeds 20 km, the downward trend of ZTD become slighter, after 40 km height the trend is almost a straight line. According to the variation of ZTD with height, we usually use quadratic polynomial [14] or exponential function [15] to fit the change, in which the exponential

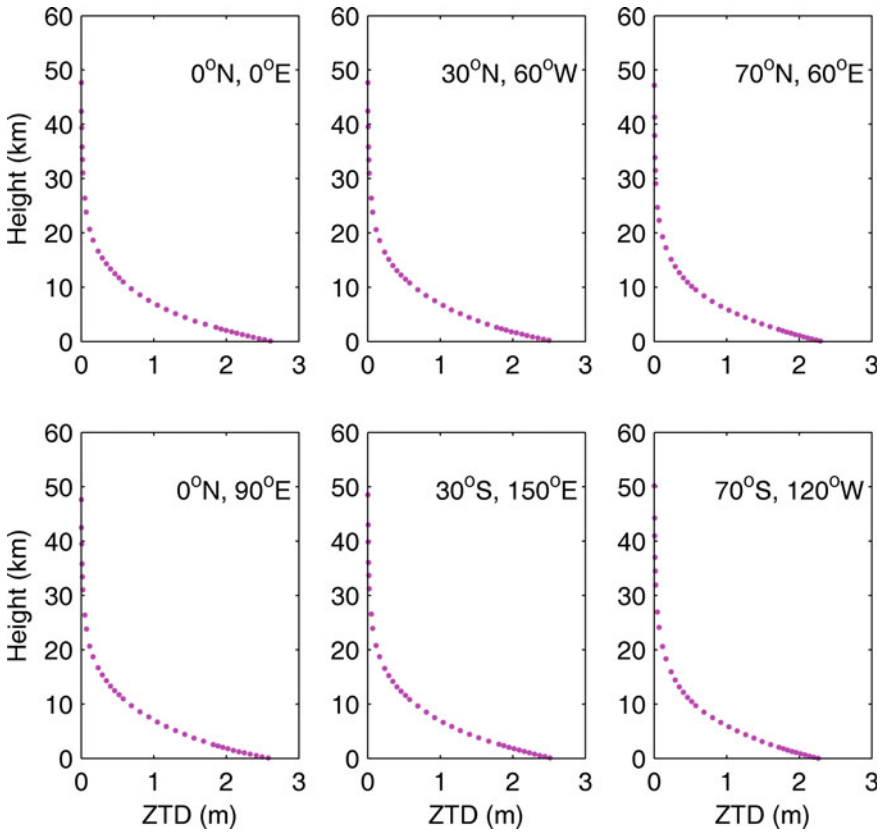

Fig. 1 Relationship between ZTD and height

function is better [16]. In other science fields, the Gaussian function is often used to fit the data points set, in this paper we attempted to apply this method to the ZTD fitting with height.

3 Gaussian Function Model for ZTD Height Reduction

The fitting formula of Gaussian function is as follows:

$$\mathrm{ZTD_H} = a \cdot \exp\left\{-\frac{(H-b)^2}{c^2}\right\} \tag{5}$$

In Eq. (5), $\mathrm{ZTD_H}$ is the ZTD value at target height H; a, b and c are the Gaussian function coefficients. We used the monthly mean pressure profiles of ECMWF with a horizontal resolution of 5°×5° from 2001 to 2010, and fitted the ZTD with height according to Eq. (5). In order to compare and analyze the fitting performances of different functions, we additionally used Eq. (6) to conduct the exponential function fitting.

$$\mathrm{ZTD_H} = \mathrm{ZTD_0} \cdot \exp\left\{-\frac{H-H_0}{H_S}\right\} \tag{6}$$

In Eq. (6), $\mathrm{ZTD_H}$ is the ZTD value at target height H; $\mathrm{ZTD_0}$ is the ZTD value at height H_0; H_S is the scale height.

After fitting Eqs. (5) and (6) to the ZTD of ECMWF grid points, we obtained the time series of two kinds of function model coefficients for each decade. It should be pointed out that after the experimental analysis, the time series of b, c, and H_s showed seasonal variation characteristics but the magnitude is small. The influence of the introduction of their periodic terms on the final ZTD estimation is ignorable. Therefore, we only used the annual mean values of these coefficients as the empirical model coefficients to calculate height reduction for ZTD. In addition, after fitting according to Eqs. (5) and (6), we obtain the RMS of the fitting residuals, which is the internal accuracy of the fitting model. The accuracy of the internal model reflects the model error which can be used to assess whether the application of the model is reasonable. The statistical results of the two function models are shown in Table 1. As can be seen from Table 1, the Gaussian function model has a global average internal accuracies of 0.9 cm, which is 0.7 mm less than that of the exponential function model (1.6 cm) and has a smaller range of residuals.

Table 1 Fitting accuracies of the two functional models (unit: cm)

Function model	Min RMS	Max RMS	Mean RMS
Gaussian	0.3	1.6	0.9
Exponential	1.1	2.6	1.6

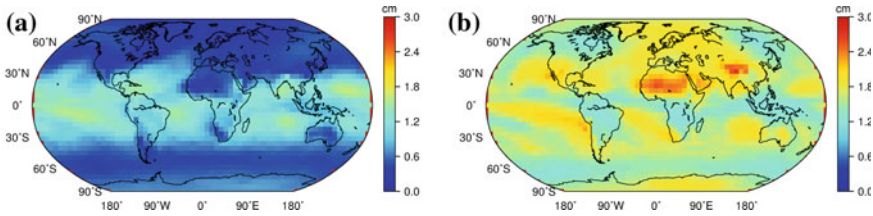

Fig. 2 Global distributions of internal accuracies of Gaussian function model (**a**) and exponential function model (**b**)

Figure 2 shows the global distribution of the internal accuracies (residual RMS) of the two function models. It can be seen that the Gaussian function model is superior to the exponential function model in almost all regions of the world, especially in the middle and high latitudes regions, the residual RMS of the Gaussian function model is only a few millimeters, which is one order of magnitude lower than that of the exponential function model. The error in the Central Asia and North Africa region is reduced by nearly 3 cm, which shows that the Gaussian function model can describe ZTD changes with height more accurately and is more stable on a global scale. At the same time, the errors of the two functions in the low latitude areas are larger than those in other areas, which may be related to the active convection of water vapor in these areas [17]. Figure 3 shows the fitting performances of two models at the grid point (10°N, 0°E) on January 2013. It can be seen from Fig. 3 that the Gaussian function model is stable, highly consistent with the ECMWF ZTD data, showing little deviation with height increasing. In contrast, the stability of the exponential function model is worse, with significant positive or negative bias at different heights, whose bias is close to even 5 cm in the range of 15–25 km.

The Gaussian function model for ZTD height reduction developed by us is in the form of grid with a horizontal resolution of 5°×5°, which can provide the Gaussian reduction coefficients at any position and realize the height reduction for ECMWF ZTD with high accuracy. When the ECMWF ZTD data are used to correct the tropospheric delay, the four ECMWF grid points surrounding the target point are selected, and the Gaussian function coefficients of the four ECMWF grid points are calculated by bilinear interpolation using the Gaussian function model. Then, the ZTD height reductions of the ECMWF ZTD of four grid points are calculated by Eq. (7) to get the ZTD at the height of target point for each grid point. Finally, the ZTD of target point is calculated by bilinear interpolation.

$$\begin{aligned} \mathrm{ZTD_t} &= \mathrm{ZTD_g} \cdot a \cdot \exp\left\{-\frac{(H_\mathrm{t}-b)^2}{c^2}\right\} / a \cdot \exp\left\{-\frac{(H_\mathrm{g}-b)^2}{c^2}\right\} \\ &= \mathrm{ZTD_g} \cdot \exp\left\{\frac{(H_\mathrm{g}-b)^2-(H_\mathrm{t}-b)^2}{c^2}\right\} \end{aligned} \tag{7}$$

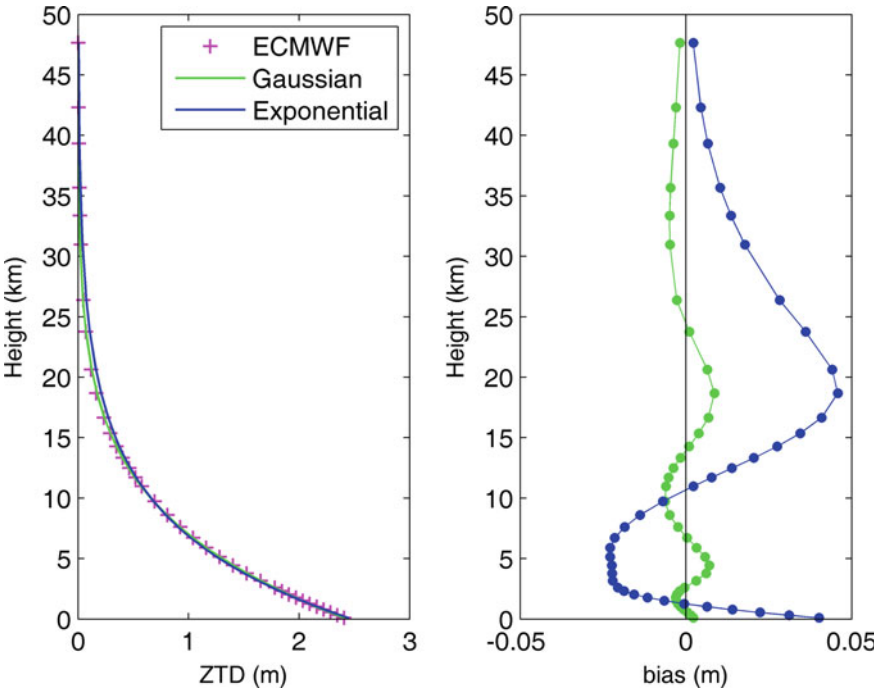

Fig. 3 Fitting results (*left*) and bias (*right*) of the two function models at grid point (10°N, 0°E)

In Eq. (7), ZTD_t is the ZTD at target point to be solved; ZTD_g is the ZTD at grid point; H_t is the height of the target point; H_g is the grid point height; a, b, and c are Gaussian function coefficients of the grid point. It should be noted that the application of the exponential function model is similar to the Gaussian function model, both of which use the bilinear interpolation method to solve the reduction coefficients and then perform the height reduction.

4 Model Validation

In order to test the precision and stability of ECMWF ZTD height reduction using Gaussian function model, IGS tropospheric products and radiosonde data were used as external data sources to conduct validation and the comparisons with exponential function model were carried out.

IGS provides tropospheric products from 1998 to the present, with a time resolution of 5 min. The accuracy of IGS tropospheric products are very high, which are often regarded as a true value in tropospheric models validations. We selected IGS tropospheric products of a total of 162 IGS stations in the world in 2015 as the reference values. Using the 2.5° × 2.5° grid ZTD from ECMWF data in 2015 combined with Gaussian function model and exponential model for height

reduction, we got the bias and RMS of the two models which are shown in Table 2. Table 2 shows that the annual average bias is 0.14 cm and the annual average RMS is 1.55 cm using the Gaussian function model. The annual mean bias is −0.16 cm and the annual mean RMS is 1.78 cm using the exponential function. Compared with the exponential function model, the bias of the Gaussian function model reduces slightly and the RMS decrease by 2.3 mm.

Figure 4 shows the global distributions of RMS in the two functional models. It can be seen from the Fig. 4 that the Gaussian function model improves the accuracy in the middle latitude areas such as North America and South Africa, and is stable in the high latitudes with reduction errors less than 1 cm. Figure 5 shows the

Table 2 Reduction error statistics of the two functional models compared with IGS data in 2015 (unit: cm)

	Bias			RMS		
	Mean	Min	Max	Mean	Min	Max
Gaussian function	0.14	−2.88	1.08	1.55	0.40	3.93
Exponential function	−0.16	−5.2	1.44	1.78	0.44	5.86

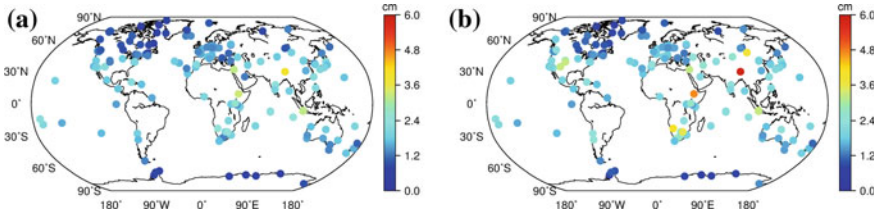

Fig. 4 Global distributions of RMS of the Gaussian function model (**a**) and exponential function model (**b**)

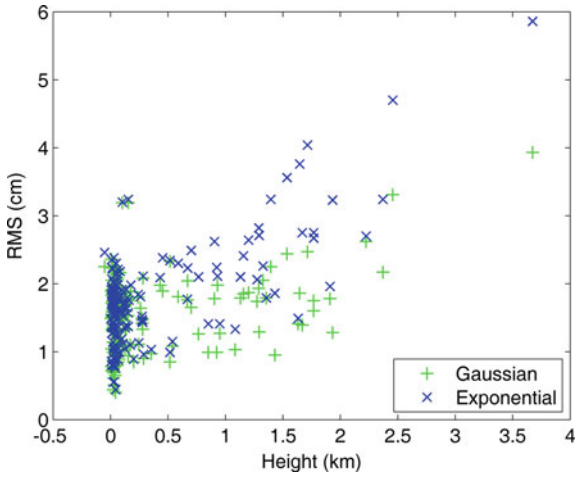

Fig. 5 RMSs of two function models with height

accuracies of the two functional models with respect to height. The height of most IGS stations are less than 500 m, and the Gaussian function model is better than the exponential function model at this low altitude. With the increase of the height, the result of the Gaussian function model begins to be significantly better than the exponential function model. Especially at the lhaz station with a height of 3673 m, the RMS of the Gaussian function is reduced by 1.93 cm compared with the exponential function model. In order to verify the stability of the height reduction model in time, Fig. 6 shows the reduction biases of the Gaussian function model and the exponential function model at the IGS station func in the whole year 2015. There is no significant seasonal difference in the reduction biases for the both two functional models, which further proves the reasonability of the simplification of periodic terms when we built the Gaussian function model for height reduction. For the whole year 2015, the Gaussian function model performs better than the exponential function model, which shows that the temporal stability of the Gaussian function model is higher.

In order to verify the accuracy of the Gaussian model at different heights, we use the radiosonde data which can provide the profile data to conduct validation analysis, since the maximum height of IGS stations is less than 5 km. The radiosonde is a sounding technique which uses radar sounding balloons to collect meteorological information at different heights in the vertical direction of the atmosphere. It can obtain high accuracy profiles of various meteorological elements. At present, the Integrated Global Radiosonde Archive (IGRA) website (ftp://ftp.Ncdc.noaa.gov/pub/data/igra/) provides free download of global radiosonde data. ZTD is calculated via the Eqs. (2) and (4) using the geopotential height, temperature and vapor pressure of each level provided by radiosonde, and the calculation results of ZTD are regarded as the ZTD reference in the following validation. We randomly selected two ZTD profiles of radiosonde stations 01028 (74.5°N, 19.0°E) at high latitude and 82599 (5.9°S, 35.2°W) at low latitude to

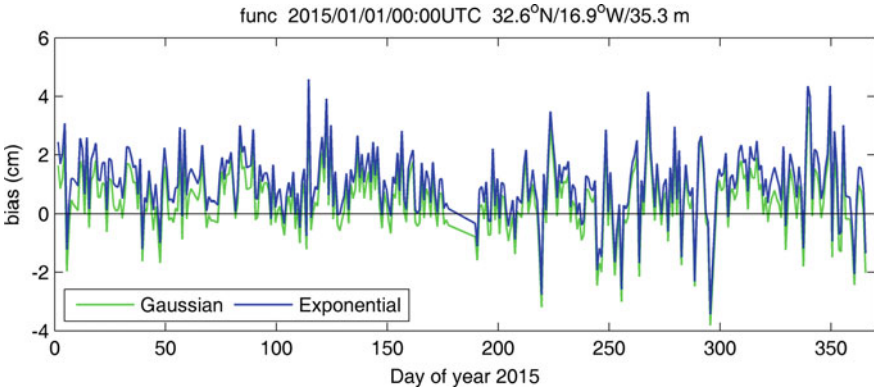

Fig. 6 Reduction biases of the Gaussian function model and the exponential function model at the IGS station func in the whole year 2015

validate the performances of ECMWF ZTD height reduction using Gaussian function model and exponential function model at 0:00 UTC on January 1, 2015. Figure 7 shows the reduction results of two functional models in the case of the two radiosonde stations. We can see after the reduction, ECMWF ZTD and radiosonde ZTD is very consistent, indicating ECMWF ZTD with high accuracy. In the two radiosonde stations, the Gaussian function model is better than the exponential function, and the reduction bias is small. In particular, for the 01028 radiosonde station at the higher heights, the biases of the two functional models are negative at height below 10 km, indicating that the reduction results of ECMWF ZTD are underestimated. Above 10 km the biases become positive, indicating the results are overestimated. For the 82599 radiosonde station at low latitude, the reduction biases of the two functional models are mainly negative, and the bias are larger compared to the results at high latitude. Combining Figs. 2 and 4, the accuracies of the two reduction models at low latitude regions are obviously worse than that of other regions.

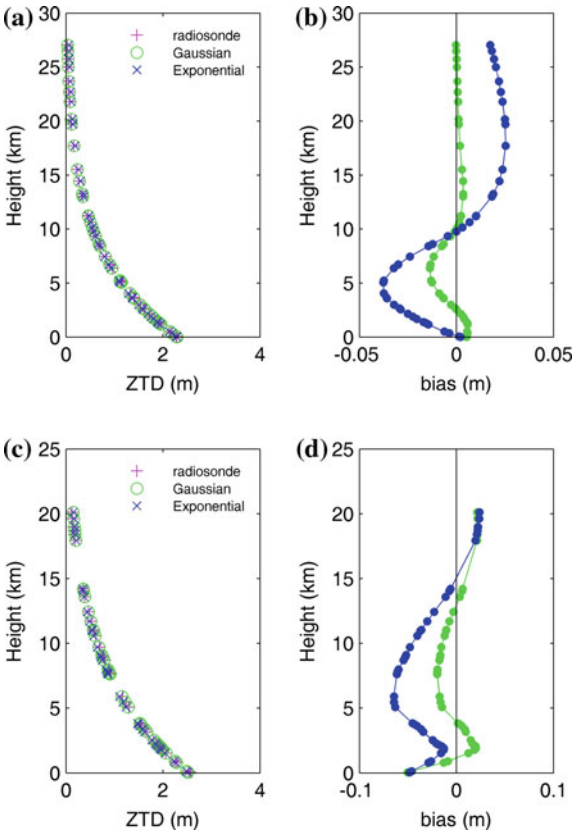

Fig. 7 Correction performances (**a**) and the corresponding biases (**b**) at radiosonde station 01028, as well as the correction performance (**c**) and the corresponding biases (**d**) at radiosonde station 82599, for the Gaussian function model and exponential function model

5 Conclusions

The height reduction needs to be carefully dealt with when applying ECMWF tropospheric delay. In this paper, taking into account the variation of ZTD with height, a Gaussian function reduction model is established with an internal accuracy of 0.9 cm, which is significantly better than that of the exponential function model (1.6 cm). Using the Gaussian function model for the height reduction of ECMWF ZTD, the results (bias: 0.14 cm, RMS: 1.55 cm) compared to the tropospheric products of 162 globally distributed IGS stations in 2015 are significantly better than the exponential function model (bias: −0.16 cm, RMS: 1.78 cm), and the temporal stability of Gaussian function model is better than that of the exponential function model. According to radiosonde's ZTD profile tests, the Gaussian model performs well over 5 km height, and the results are closer to the ZTD real profile.

The Gaussian function model proposed in this paper can be applied to ZTD reduction at different heights. However, it is worth noting that the model's bias in the low latitude and low altitude regions is apparently worse than that in other regions, and how to weaken the bias to build a more accurate model needs further studies.

Acknowledgements Thanks to ECMWF, IGS and IGRA for providing relevant data. This research was supported by the National Key Research and Development Program of China (2016YFB0501803) and the National Natural Science Foundation of China (41574028) and the Key Laboratory of Geospace Environment and Geodesy, Ministry of Education, Wuhan University (16–02–03).

References

1. Spilker JJ (1978) GPS signal structure and performance characteristics. Navigation 25(2):121–146
2. Davis JL, Herring TA, Shapiro II, Rogers AEE, Elgered G (1985) Geodesy by radio interferometry: Effects of atmospheric modeling errors on estimates of baseline length. Radio sci 20(6):1593–1607
3. Saastamoinen J (1972) Atmospheric correction for the troposphere and stratosphere in radio ranging satellites. The use of artificial satellites for geodesy 247–2511
4. Black HD (1978) An easily implemented algorithm for the tropospheric range correction. J Geophys Res Solid Earth 83(B4):1825–1828
5. Hopfield HS (1969) Two-quartic tropospheric refractivity profile for correcting satellite data. J Geophys Res 74(18):4487–4499
6. Leandro R, Santos MC, Langley RB (2006) UNB neutral atmosphere models: development and performance. Proc ION NTM 52(1):564–573
7. Böhm J, Möller G, Schindelegger M, Pain G, Weber R (2015) Development of an improved empirical model for slant delays in the troposphere (GPT2w). GPS Solutions 19(3):433–441
8. Yao Y, Xu C, Shi J, Cao N, Zhang B, Yang J. (2015) ITG: a new global gnss tropospheric correction model. Sci Rep, 5

9. Möller G, Weber R, Böhm J (2014) Improved troposphere blind models based on numerical weather data. Navigation 61(3):203–211
10. Nafisi V, Urquhart L, Santos MC, Nievinski FG, Bohm J, Wijaya DD, Zus F (2012) Comparison of ray-tracing packages for troposphere delays. IEEE Trans Geosci Remote Sens 50(2):469–481
11. Böhm J, Schuh H (eds) (2013) Atmospheric effects in space geodesy. Springer, Berlin, Germany, pp 73–129
12. Chen Q, Song S, Heise S, Liou YA, Zhu W, Zhao J (2011) Assessment of ZTD derived from ECMWF/NCEP data with GPS ZTD over China. GPS Solutions 15(4):415–425
13. Vedel H (2000) Conversion of WGS84 geometric heights to NWP model HIRLAM geopotential heights. Dan Meteorol Ins
14. Song S, Zhu W, Chen Q, Liou Y (2011) Establishment of a new tropospheric delay correction model over China area. Sci China Phys Mech Astron 54(12):2271–2283
15. Jin S, Park JU, Cho JH, Park PH (2007) Seasonal variability of GPS—derived zenith tropospheric delay (1994–2006) and climate implications. Journal of Geophysical Research: Atmospheres, 112(D9)
16. Yao YB, He CY, Zhang B, Xu CQ (2013) A new global zenith tropospheric delay model GZTD. Chinese J Geophys-Chinese Ed 56(7):2218–2227 doi:10.6038/cjg20130709
17. Trenberth KE, Fasullo J, Smith L (2005) Trends and variability in column-integrated atmospheric water vapor. Clim Dyn 24(7–8):741–758

Centimeter Level Precise Positioning with a Low-Cost GNSS Antenna

Xiang Zuo, Yuanjun Chen, Xiaoyu Shi and Chenggang Li

Abstract The demand for lower priced precise positioning is growing rapidly, as evident in the areas of intelligent transportation systems, precise agriculture, and unmanned aerial vehicle (UAV) guidance. High precise positioning can be achieved with Real-Time Kinematics (RTK) technology, which is a differential method that is generally applied to geodetic receivers and can typically provide centimeter level solutions within only a few seconds if corrections from a physical or virtual reference station are available. In recent years, low-cost GNSS receivers, such as U-blox, have been proven to be able to perform stable RTK comparable to geodetic-grade receivers. Instead of using a consumer-grade antenna, a geodetic one is usually chosen to perform reliable integer-ambiguity resolution in low-cost RTK. There are two disadvantages of using geodetic antenna. First, the size of a geodetic antenna is not small enough to be placed on platform such as agricultural UAVs. Second, the price of a geodetic-grade antenna is much more expensive than a consumer-grade one. In this paper, we proposed a combined BDS/GPS RTK algorithm to obtain centimeter level positioning using a low-cost single-frequency helix antenna. The results show that a positioning accuracy of 2–3 cm (>95%) is achievable in static mode, with an ambiguity fixing rate greater than 98%. For kinematic test, the ambiguity fixing rate is about 95% with a false fixing rate less than 0.015%, and a dynamic positioning accuracy of 5 cm in horizontal and 10 cm in vertical can also be obtained for more than 95% of the time.

Keywords Single-frequency · RTK · Helix antenna · Low-cost · UAV · Ambiguity resolution

X. Zuo (✉) · Y. Chen · X. Shi · C. Li
Hi-Target Surveying Instrument Co. Ltd., Guangzhou 511400, China
e-mail: zxwhuy@gmail.com

J. Sun et al. (eds.), *China Satellite Navigation Conference (CSNC) 2017 Proceedings: Volume III*, Lecture Notes in Electrical Engineering 439,
DOI 10.1007/978-981-10-4594-3_30

1 Introduction

Low-cost GNSS receivers, such as U-blox, have become mass-market devices used by millions of people every day. Current single point solutions routinely offer a positioning accuracy of 5–10 m, which have satisfied the requirements of various applications such as mobile phone location and car navigation. However, this is not adequate for some new applications, such as intelligent transportation systems, precise agriculture, and unmanned aerial vehicle (UAV) guidance, which require submeter or centimeter level positioning accuracy. High precise positioning can be achieved with Real-Time Kinematics (RTK) technology, which is a differential method that is generally applied to geodetic-grade receivers and can typically provide centimeter level solutions with only a few seconds of convergence time if a physical or virtual close reference station is available. With the advancement in GNSS receiver hardware technologies in recent years, more and more low-cost receivers could output raw code, Doppler and carrier phase measurements from multiple constellations. The potential possibility of applying RTK on low-cost receivers makes it an attractive research topic around the world [1–5].

According to the past researches, antenna is the key issue in low-cost RTK and a geodetic antenna is usually chosen to perform reliable integer-ambiguity resolution [6]. There are two disadvantages of using geodetic antenna. Firstly, the size of a geodetic antenna is not small enough to be placed on some platform such as agricultural UAVs. Secondly, the price of a geodetic antenna is much more expensive than a consumer-grade one. In this paper, we proposed an advanced multi-GNSS RTK algorithm to obtain centimeter level positioning by using strategies such as combined BDS/GPS observations, multipath mitigation, robust Kalman filter and partial ambiguity resolution (PAR). To validate the effect of our algorithm, both static and kinematic tests were conducted by using reference station of Hi-Target Continuously Operating Reference Stations Network (HT-CORS) within a short baseline (<10 km).

2 Precise Positioning Strategy for Low-Cost Antenna

2.1 Combined BDS/GPS Measurement Model

The $L1$ pseudorange and carrier phase measurements can be expressed in units of meters as:

$$\begin{aligned} P_1 &= \rho + c(dt - dT) + I_1 + T + b_{\mathrm{r},P1} - b^{\mathrm{s}}_{P1} + \varepsilon_{P1} \\ L_1 &= \rho + c(dt - dT) - I_1 + T + b_{\mathrm{r},L1} - b^{\mathrm{s}}_{L1} + \lambda_1 N_1 + \varepsilon_{L1}, \end{aligned} \tag{1}$$

where P_1 and L_1 are the pseudorange and carrier phase measurements on frequency $L1$, respectively; ρ is the geometric distance between a satellite and a receiver; c is

the speed of light; dt and dT are the clock biases of the receiver and satellite, respectively; I_1 and T are the ionospheric and tropospheric delay, respectively; λ_1 denotes the signal wavelength and N_1 is the carrier phase ambiguity; $b_{r,P1}$ and $b_{r,L1}$ are code and carrier phase hardware biases in receiver; b^s_{P1} and b^s_{L1} are code and carrier phase hardware biases on satellite, respectively; and finally, ε_{P1} and ε_{L1} contains all unmodeled error sources, such as measurement noise, multipath, antenna phase center variations, etc.

Now suppose that two stations exist spatially close to each other and differencing measurements between two receivers gives the double-difference (DD) equation:

$$\begin{aligned} \Delta\nabla P_1^{i,j} &= \Delta\nabla\rho + \varepsilon_{\Delta\nabla P1} \\ \Delta\nabla L_1^{i,j} &= \Delta\nabla\rho + \lambda_1 \cdot \Delta\nabla N_1^{i,j} + \varepsilon_{\Delta\nabla L1}, \end{aligned} \tag{2}$$

where $\Delta\nabla P_1^{i,j}$ and $\Delta\nabla L_1^{i,j}$ are the virtual DD pseudorange and carrier phase observations between satellite i and j, respectively; $\Delta\nabla\rho$ is the DD geometric distance; $\Delta\nabla N_1^{i,j}$ is the DD ambiguity; $\varepsilon_{\Delta\nabla P1}$ and $\varepsilon_{\Delta\nabla L1}$ are the DD observations noise.

Equation (2) is the unified formation for both BDS and GPS measurement model and is based on the assumption that atmosphere delays are canceled out in a short baseline. So the remaining unknowns are baseline vector and DD ambiguities. In this paper, an Extended Kalman Filter (EKF) is applied to estimate the unknown parameters.

One of the main challenges for low-cost RTK is that only limited satellites are available due to signal obstruction when using single GPS system. Thanks to the GEO and IGSO satellites of BDS, we are able to track more satellites (almost double number) with a higher elevation, which can greatly improve satellites visibility and geometry structure in urban areas as shown in Fig. 1.

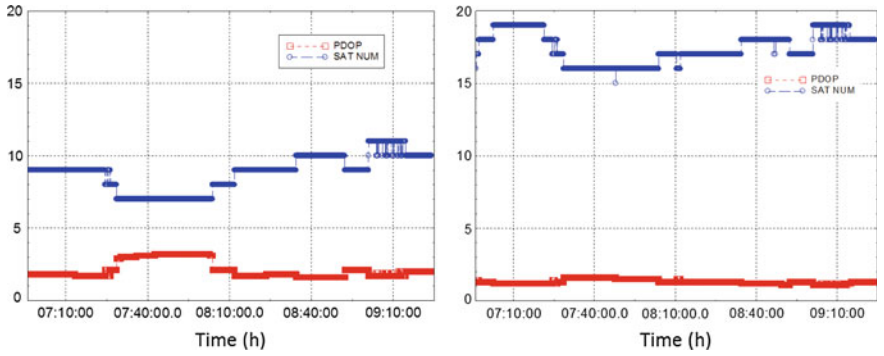

(a) GPS only model (b) BDS& GPS combined model

Fig. 1 The valid satellites number and PDOP value of **a** GPS only model and **b** BDS&GPS combined model (elevation angle >10°)

2.2 Multipath Mitigation Strategy

As we all know, customer-grade antenna is usually designed for mass-market applications, so constraints in power consumption and costs are very stringent and then result in lower quality measurements compared to high-precision antenna. In the case of a helix antenna, the code measurements of both BDS and GPS may suffer from serious multipath as shown in Fig. 2, which is the primary impediment to fast resolution of integer ambiguities.

Two steps are adopted in this article to mitigate multipath error. Firstly, all measurements including code, carrier phase and Doppler are strictly selected using both elevation and carrier-to-noise ratio (C/N0) masks, which aims to reject non-line-of-sight (NLOS) and multipath-contaminated measurements as much as possible. For elevation mask, we can choose 10 or 15 as threshold. But for C/N0 mask, it is much receiver and antenna-dependent and the empirical value can be obtained from data collection and analysis in advance. Then, we take special care to appropriately weight each measurement, especially the code measurement. A function of elevation is often used to model code and phase measurements noise and it differs little from a function of C/N0 when applied to geodetic receivers. However, result is not always the same for a low-cost antenna. As we can see in Fig. 3, the signal power of BDS GEOs and IGSOs can be very low even with a high elevation, which usually indicates a poor signal. So in this paper, an empirical weighting scheme proposed by Realini [2] is adopted, which is based on both

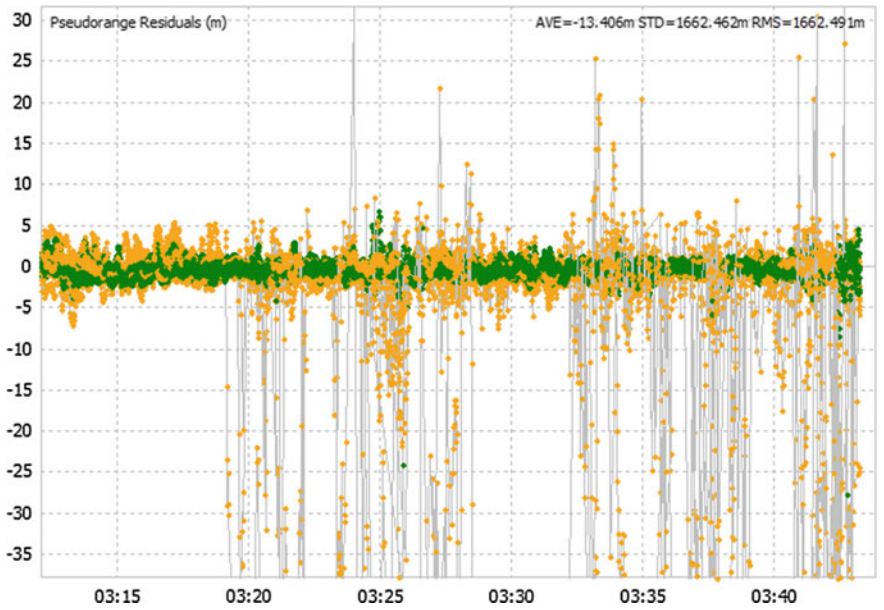

Fig. 2 Code measurement residuals of a Helix antenna (BDS&GPS)

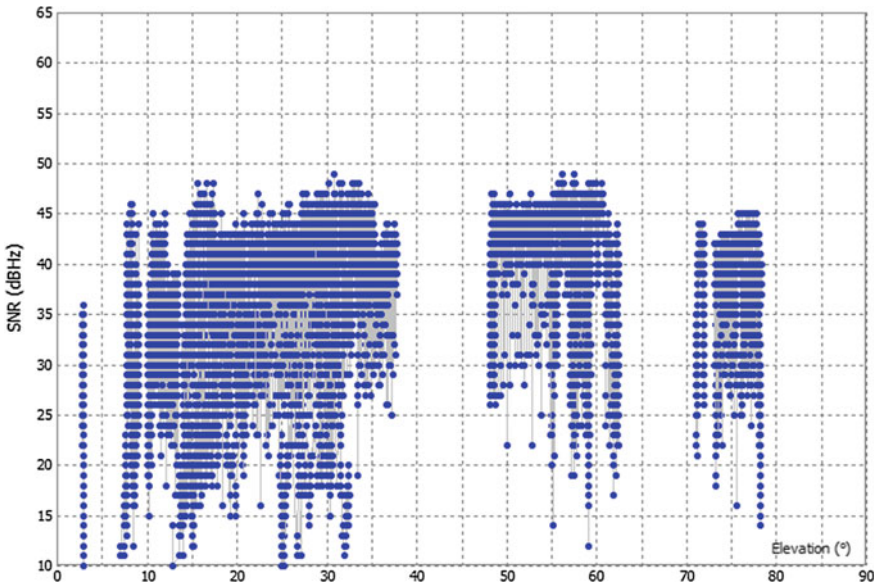

Fig. 3 Relationship of SNR and elevation of a Helix antenna (BDS)

elevation and C/N0 and can reflect the actual multipath error more precisely than using an elevation-based only weighting model.

2.3 *Robust Kalman Filtering*

Furthermore, a robust Kalman filter is used to take care of the biased measurements, in which small-undetected outliers and cycle slips may remain after data preprocessing. In the robust Kalman filter, we adjust the weight matrix of the observables accordingly by taking the posteriori residuals into account.

In the case of independent observations, the weight matrix P can be adjusted as [7, 8]:

$$\bar{p}_i = \begin{cases} p_i, & |\tilde{v}_i| \le k_0 \\ p_i \frac{k_0}{|\tilde{v}_i|} \left(\frac{k_1 - |\tilde{v}_i|}{k_1 - k_0} \right)^2, & k_0 < |\tilde{v}_i| \le k_1, \\ 0, & |\tilde{v}_i| > k_1 \end{cases} \tag{3}$$

where p_i is the diagonal element of weight matrix P, $\tilde{v}_i$ is the ith element of normalized residuals vector, k_0 and k_1 are constants, which is usually chosen as $k_0 =$ 1.5–2.0, $k_1 =$ 3.0–8.5, If observations are dependent, the non-diagonal element of weight matrix P should also be considered.

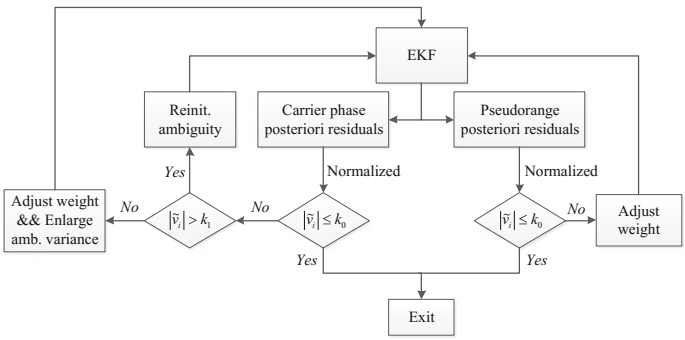

Fig. 4 The procedure of robust Kalman filter

Figure 4 shows the procedure of robust Kalman filter adopted in this paper. For pseudorange residuals, if the absolute value of $\tilde{v}_i$ is greater than k_0, then the according weight matrix is adjusted using Eq. (3). For carrier phase residuals, the state of ambiguity parameter will be reinitialized if $|\tilde{v}_i| > k_i$ which means a cycle slip is identified. Otherwise, the weight of phase measurement is adjusted and the variance of DD ambiguity is enlarged if $|\tilde{v}_i| > k_o$ and $|\tilde{v}_i| \le k_1$. The new procedure is performed in a iterative calculation at each discrete epoch and only the observation with a max $|\tilde{v}_i|$ is adjusted during each iteration.

2.4 *Partial Ambiguity Resolution*

RTK can achieve centimeter positioning accuracy only when the integer DD ambiguities are correctly fixed. However, low-cost single-frequency receiver can be less efficient in ambiguity resolution compared to the geodetic receiver, due to the large noise on pseudorange and frequent cycle slips on carrier phase. In order to perform reliable integer-ambiguity resolution, a PAR strategy is developed as shown in Fig. 5.

First, all float ambiguities estimated by EKF are selected based on elevation angle and continually tracking epochs, and satellites with a cycle slip on carrier phase are also rejected. Then full ambiguity resolution (FAR) with all the selected ambiguity candidates is performed using the LAMBDA method [9]. If FAR fails, that is, whether the success rate P_s [10] is smaller than the predefined value P_0 or the ratio test fails. Then the full set of the ambiguities is sorted according to the probability P_r (rounding to the nearest integer), which is calculated with the following formula [11]:

$$P_{\mathrm{r}} = 1 - \sum_{i=1}^{\infty} \left[\mathrm{erfc}\left(\frac{i - \left| \hat{X} - \breve{X} \right|}{\sqrt{2}\sigma} \right) - \mathrm{erfc}\left(\frac{i + \left| \hat{X} - \breve{X} \right|}{\sqrt{2}\sigma} \right) \right] \tag{4}$$

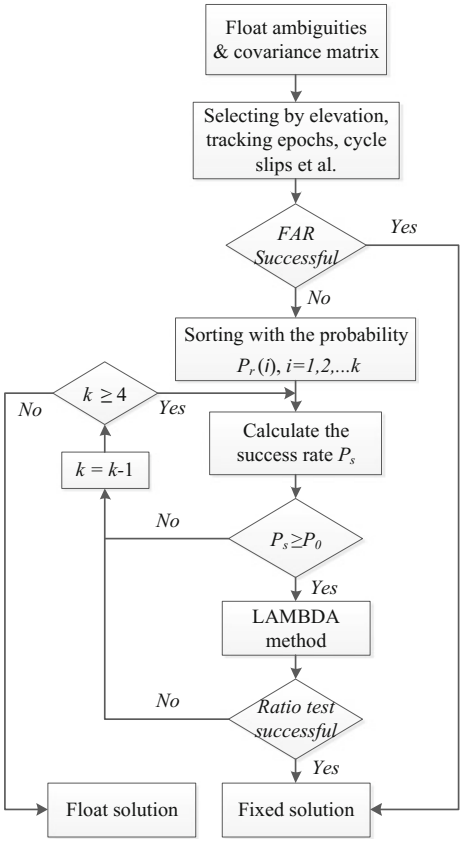

Fig. 5 The scheme of partial ambiguity resolution

with

$$\operatorname{erfc}(x) = \frac{2}{\sqrt{\pi}} \int_{x}^{\infty} e^{-t^2} \mathrm{d}t, \tag{5}$$

where $\hat{X}$ is the float estimation and σ its standard deviation (STD), and $\breve{X}$ the nearest integer of $\hat{X}$. This is aimed to select the subset of ambiguities which has the higher probability of successful fixing. And the ambiguity with the lowest probability of rounding fixing will not be fixed. If the success rate P_s fulfills the predefined criterion and the ratio test is accepted, then we get an ambiguity-fixed solution. Otherwise, the above steps will be repeated and the remaining subset of ambiguities is fixed using the LAMBDA method again until no more valid ambiguities can be fixed.

3 Results and Analysis

3.1 Test Equipment

To evaluate our RTK algorithm, a low-cost single-frequency module named Hi-wear and a geodetic receiver named iRTK2 are used in the tests, as shown in Fig. 6. Our RTK algorithm is programmed in Hi-wear, which can receive both BDS and GPS raw measurements and need to connect to a smart phone via Bluetooth communication to receive RTK corrections and display positioning results (see Fig. 7). Hi-wear is equipped with an AH-3128 helix antenna, of which the basic characteristics are detailed in Table 1.

The purpose of iRTK2 is to provide a reference position solution. The offset of antenna phase center between iRTK2 and Hi-wear was calibrated in advance for positioning accuracy comparison. All data were collected at a rate of 1 Hz and satellites with elevation below 12° were ignored in the RTK computations in each test.

(a) Hi-wear (b) iRTK2 (c) Test scenario

Fig. 6 GNSS devices used in the tests. **a** Hi-wear **b** iRTK2 **c** Test scenario

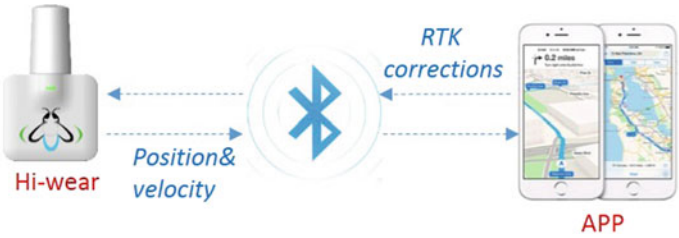

Fig. 7 The workflow of Hi-wear module

Table 1 Properties of AH-3128 Helix antenna

Parameter	Characteristic
Frequency	1561 MHz (BDS B1)
	1575 MHz (GPS L1)
	1602 MHz (GLONASS G1)
Gain	28 dB (typical)
Axial ratio	0.5 dB (typical)
Size	24.4 mm (Φ) × 47.4 mm (H)
Weight	14 g

3.2 Static Test

In the static test, Hi-wear was placed in a fixed point with open sky view, which was about 6.7 km away from the single-base station. The RTK corrections was received via GPRS/3G connections and data were collected for about 2 h in August 30, 2016. For comparison, the average of all the ambiguity-fixed solutions is chosen as the reference point.

Figure 8 shows the positioning bias in East, North, and Up (ENU) directions of static test. The rate of ambiguity fixing is about 98.8% with few epochs wrong-fixed. Most of horizontal positioning bias is within 2 cm and the 2D RMS is about 1.1 cm (see Table 2). Except for few wrong-fixed epochs, vertical error is almost within 3 cm with a RMS less than 1 cm.

It seems evident that once the ambiguities are fixed correctly for the first time, the solutions remain stable and un-interrupted. This is a notable advantage for

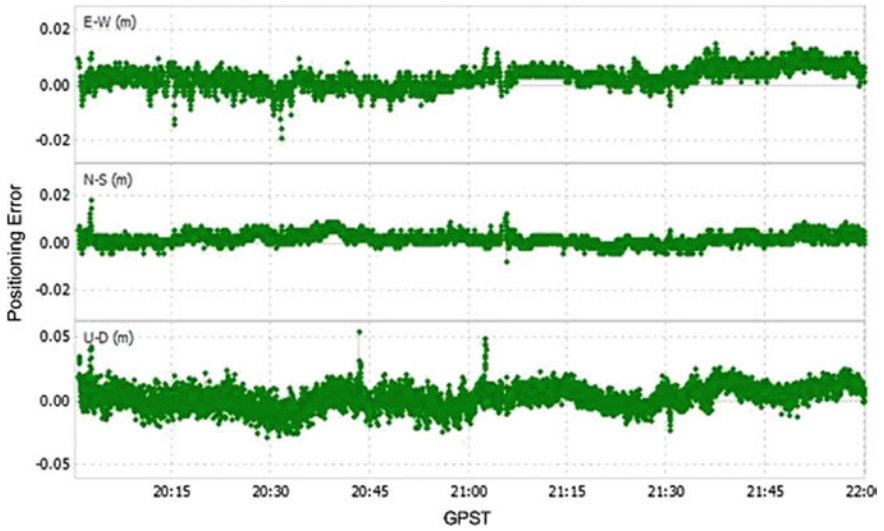

Fig. 8 Positioning error in East, North and Up direction of static test (only ambiguity-fixed solutions are plotted)

Table 2 Position accuracy of static test

Static test	Mean/cm	STD/cm	RMS/cm
E	0.3	0.4	0.5
N	0.2	0.3	0.3
U	0.3	0.9	0.9

application with stationary and continuous observation like crustal deformation monitoring. A low-cost receiver with a low-priced antenna will greatly benefit the cost of similar applications.

3.3 Kinematic Test

In the kinematic test, the helix antenna of Hi-wear was placed on top of iRTK2 (see Fig. 6c) and the offset between two antenna phase centers were calibrated in advance for accuracy analysis. Kinematic data were collected in driving mode (velocity less than 5 m/s) with time span of about 30 min in September 23, 2016. The test site was located about 6.7 km away from the single-base station. The positioning error is shown in Fig. 9.

For kinematic test, the ambiguity fixing rate is about 95%, with a false fixing rate less than 0.015%. Horizontal positioning error is almost within 5 cm with a 2D RMS about 3.6 cm (see Table 3). For vertical direction, positioning bias is almost

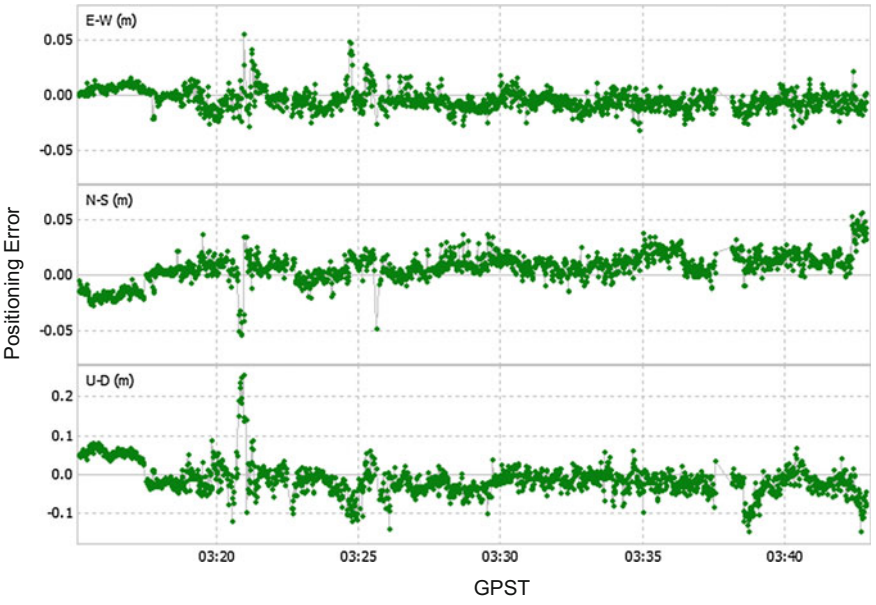

Fig. 9 Positioning error in East, North and Up direction of kinematic test (only ambiguity-fixed solutions are plotted)

Table 3 Position accuracy of kinematic test

Kinematic test	Mean/cm	STD/cm	RMS/cm
E	0.4	0.9	1.0
N	0.9	1.3	1.5
U	1.1	4.0	4.1

within 10 cm and RMS is less than 5 cm. Because of the inconsistency between two antenna phase centers, some calibration error may be included in the positioning bias due to the instability of helix antenna in dynamic mode, especially for vertical direction. When the ambiguities are fixed incorrectly, the vertical accuracy also degrades more severely than horizontal.

It's worth noting that fast ambiguity resolution fix is the key issue for kinematic applications. It is always hard to get a fixed solution when many cycle slips and severe multipath error occur in dynamic environment, which is the focuses of our future work. However, conclusion is still obvious and promising that centimeter level positioning accuracy can be achieved by using a consumer-grade antenna instead of using an expensive geodetic-grade one.

4 Summary and Discussion

Using a low-cost GNSS antenna instead of a geodetic-grade one will greatly benefit the collapse in prices of precise positioning. In this paper, a single-frequency BDS/GPS RTK algorithm for low-cost receiver with a low-cost antenna is proposed. The test results show that a positioning accuracy of 2–3 cm (>95%) is achievable in static mode and a dynamic positioning accuracy of 5 cm in horizontal and 10 cm in vertical is also achievable for more than 95% of the time. The work in this article indicates that using a consumer-grade antenna can also obtain comparable centimeter level accuracy instead of using a geodetic one in short baseline, making it a promising technique in high precise applications like crustal deformation monitoring and UAV guidance.

In the future, the performance of RTK test with long time and medium-long baseline RTK will be the focus of this research.

Acknowledgements This work was supported by the "Collaborative Precision Positioning Project" (No. 2016YFB0501900) of National key Research Program of China.

References

1. Takasu T, Yasuda A (2008) Evaluation of RTK-GPS performance with low-cost single-frequency GPS receivers. In: Proceedings of international symposium on GPS/GNSS, pp 852–861
2. Realini E (2009) GoGPS-free and constrained relative kinematic positioning with low cost receivers Politecnico di Milano

3. Carcanague S (2013) Low-cost GPS/GLONASS precise positioning algorithm in constrained environment. Institute National Polytechnique de Toulouse-INPT
4. Stempfhuber W, Buchholz M (2011) A precise, low-cost RTK GNSS system for UAV applications. Conference on unmanned aerial vehicle in geomatics, zürich, pp 289–293
5. Cai Y, Cheng P, Meng X et al (2011) Using network RTK corrections and low-cost GPS receiver for precise mass market positioning and navigation applications. IEEE 2011:345–349
6. Pesyna KM Jr, Heath RW Jr, Humphreys TE (2014) Centimeter positioning with a smartphone-quality GNSS antenna. Proceedings of the ION GNSS, Tampa, FL
7. Huber PJ (1964) Robust estimation of a location parameter. Ann Math Stat 35(1):73–101
8. Yang Y (1993) Robust estimation and its applications. Bayi, Beijing
9. Teunissen PJG (1993) Least-squares estimation of the integer GPS ambiguities
10. Teunissen PJG (1999) An optimality property of the integer least squares estimator. J Geod 73 (11):587–593
11. Dong D, Bock Y (1989) Global positioning system network analysis with phase ambiguity resolution applied to crustal deformation studies in California. J Geophys Res 94(B4):3949–3966

Triple-Frequency Carrier Ambiguity Resolution with Low Noise and Ionosphere-Free Impact for BDS

Jing Cao, Baowang Lian and Yulong Song

Abstract Ambiguity resolution is the key to achieve rapid and accurate positioning, which is always the focus of GNSS research. The BeiDou navigation system provides triple-frequency signals, which can be combined into different forms. Based on these combinations, we can realize precise positioning and fix the ambiguity. First, we analyze the noise characteristics of combined observations and current ionosphere-free three-carrier ambiguity resolution (TCAR) algorithms. Second, we propose a TCAR algorithm with low noise and ionosphere-free impact, which is processed by the least squares principle under geometry model. After that, we achieve static positioning. Finally, in order to verify noise effect of combination and the performance of TCAR algorithms, a series of tests are conducted on real observations in short baseline and medium baseline. What is more, comparisons are made between current algorithms and the proposed algorithm. The results indicate that the proposed TCAR algorithm can improve ambiguity resolution success rate effectively, and then achieve precise positioning reliably.

Keywords Precise positioning · TCAR · Low combined noise · Ionosphere-free · Success rate

1 Introduction

With the development of GNSS technology, high-precision positioning has received a lot of attention. Precise positioning technology relies on the successful AR (ambiguity resolution), besides traditional single or dual-frequency AR cannot afford the requirement of precise positioning. So more research efforts have been made towards multi-frequency signals, according to previous research, the AR

J. Cao (✉) · B. Lian · Y. Song
Department of Electronics Engineering, Northwestern Polytechnical University, Xi'an 710129, China
e-mail: caojing5121@sina.com; 979838093@qq.com

J. Sun et al. (eds.), *China Satellite Navigation Conference (CSNC) 2017 Proceedings: Volume III*, Lecture Notes in Electrical Engineering 439,
DOI 10.1007/978-981-10-4594-3_31

success rate and positioning accuracy can be significantly enhanced with combined multi-frequency signals.

Multi-frequency AR can avoid complex calculation of traditional ambiguity search methods, meanwhile combined signals will provide measurements with longer wavelength and less noise which are easy to fix ambiguities. The earliest studies are three-carrier ambiguity resolution methods (TCAR) and the cascading integer resolution (CIR) method described by Frossell and Hatch [1, 2], which were all bootstrapping ways based on geometry-free models. Ji et al. [3] defined a set of optimal combinations of Galileo signals and compared the performance of epochwise ambiguity resolution, respectively, using CIR and LAMBDA [4] method (least squares ambiguity decorrelation adjustment). In addition, Feng [5, 6] proposed a general geometry-based TCAR strategy, and analyzed the detailed errors of "virtual" signals. Tang et al. [7] estimated the ambiguities with models of B1-B2 and B1-B3 combination, which avoided the neglect of ionospheric delay when evaluated the NL (narrow lane) ambiguities within WL (wide lane) combination. Besides, Zhang [8] made the performance analysis of current TCAR algorithms, as a result, it indicated that different levels of improvement could be observed by these TCAR algorithms.

On the basis of current geometry-free TCAR [8] and ionosphere-free TCAR algorithms [7], this paper selects the optimal combinations with lower noise and longer wavelength. We propose a new TCAR method which is ionospheric free in WL and NL signals, taking the ionospheric parameters into consideration, and fix the float ambiguities with LAMBDA method in the end. The detailed algorithm process is represented. Considering the error level in different length of baselines varies, we use real BeiDou B1 (1561.098 MHz), B2 (1207.140 MHz), B3 (1268.520 MHz) observational data with baselines of 6.5 m and 26.3 km. In order to analyze the performance of new algorithm, the ratio test of fixed ambiguities, position error, and success rate of ambiguities have been made.

For convenience, we mark the traditional TCAR method to be Algorithm-A, the ionosphere-free TCAR algorithm to be Algorithm-B, and the proposed ionosphere-free method to be Algorithm-C.

2 BeiDou Combined Observational Models and Characteristics

2.1 Fundamental Mathematics Model

Given the original single-frequency double-differenced pseudorange and carrier phase measurements, the combined triple-frequency DD observations [5] can be expressed as

$$\Delta P_{(i,j,k)} = \frac{i \cdot f_1 \cdot \Delta P_1 + j \cdot f_2 \cdot \Delta P_2 + k \cdot f_3 \cdot \Delta P_3}{i \cdot f_1 + j \cdot f_2 + k \cdot f_3} \tag{1}$$

$$\Delta \phi_{(i,j,k)} = \frac{i \cdot f_1 \cdot \Delta \phi_1 + j \cdot f_2 \cdot \Delta \phi_2 + k \cdot f_3 \cdot \Delta \phi_3}{i \cdot f_1 + j \cdot f_2 + k \cdot f_3} \tag{2}$$

$$\Delta \phi_{(i,j,k)} = i \cdot \Delta \phi_1 + j \cdot \Delta \phi_2 + k \cdot \Delta \phi_3 \tag{3}$$

where the integers (*i, j, k*) denote the arbitrary combination coefficients, ΔP_i and $\Delta \phi_i$ are the DD code and phase measurements, respectively, f_i is the frequency of signal B_i. Model (2) is the measurement in meters, and model (3) is the measurement in cycles. The combined frequency, corresponding wavelength, and the integer ambiguity are defined as

$$f_{(i,j,k)} = i \cdot f_1 + j \cdot f_2 + k \cdot f_3 \tag{4}$$

$$\lambda_{(i,j,k)} = \frac{c}{i \cdot f_1 + j \cdot f_2 + k \cdot f_3} \tag{5}$$

$$\Delta N_{(i,j,k)} = i \cdot \Delta N_1 + j \cdot \Delta N_2 + k \cdot \Delta N_3 \tag{6}$$

The combined first-order ionospheric scale factor (ISF) $\beta_{(i,j,k)}$ and the phase noise factor (PNF) $\mu_{(i,j,k)}$ [5] are expressed as

$$\beta_{(i,j,k)} = \frac{f_1^2 \cdot (i/f_1 + j/f_2 + k/f_3)}{i \cdot f_1 + j \cdot f_2 + k \cdot f_3} \tag{7}$$

$$\mu^2_{(i,j,k)} = \frac{(i \cdot f_1)^2 + (j \cdot f_2)^2 + (k \cdot f_3)^2}{(i \cdot f_1 + j \cdot f_2 + k \cdot f_3)^2} \tag{8}$$

Assuming the code and carrier phase measurements of signal B_i have the same standard deviations, i.e., $\sigma_{\Delta P_1} = \sigma_{\Delta P_2} = \sigma_{\Delta P_3} \equiv \sigma_{\Delta P}$, $\sigma_{\Delta \phi_1} = \sigma_{\Delta \phi_2} = \sigma_{\Delta \phi_3} \equiv \sigma_{\Delta \phi}$, then the combined noise level can be defined as

$$\sigma^2_{\varepsilon_{\Delta P_{(i,j,k)}}} = \frac{(i \cdot f_1)^2 + (j \cdot f_2)^2 + (k \cdot f_3)^2}{(i \cdot f_1 + j \cdot f_2 + k \cdot f_3)^2} \sigma^2_{\Delta P} \tag{9}$$

$$\sigma^2_{\varepsilon_{\Delta \phi_{(i,j,k)}}} = \frac{(i \cdot f_1)^2 + (j \cdot f_2)^2 + (k \cdot f_3)^2}{(i \cdot f_1 + j \cdot f_2 + k \cdot f_3)^2} \sigma^2_{\Delta \phi} \tag{10}$$

In addition, the noises also include the DD satellite orbital error $\Delta \delta_{\text{orb}}$ and the DD tropospheric delay $\Delta \delta_{\text{tro}}$. Taking all these noise factors into account, the combined triple-frequency signal can be expressed as

$$\Delta P_{(i,j,k)} = \Delta\rho + \Delta\delta_{\text{orb}} + \Delta\delta_{\text{tro}} + \beta_{(i,j,k)}\Delta\delta I_1 + \varepsilon_{\Delta P_{(i,j,k)}} \tag{11}$$

$$\Delta\phi_{(i,j,k)} = \Delta\rho + \Delta\delta_{\text{orb}} + \Delta\delta_{\text{tro}} - \beta_{(i,j,k)}\Delta\delta I_1 - \lambda_{(i,j,k)}\Delta N_{(i,j,k)} + \varepsilon_{\Delta\phi_{(i,j,k)}} \tag{12}$$

where $\Delta\rho$ represents the DD geometric distance between satellite and receiver, and $\Delta\delta I_1$ is the DD first-order ionospheric delay on the B1 carrier.

According to the phase observation model, total noise level of carrier phase (in meters) is as follows:

$$\sigma_{\text{TN}} = \sqrt{\left(\beta_{(i,j,k)}\Delta\delta I_1\right)^2 + \Delta\delta_{\text{orb}}^2 + \Delta\delta_{\text{tro}}^2 + \mu_{(i,j,k)}^2\sigma_{\Delta\phi}^2}. \tag{13}$$

2.2 The BeiDou Observations and Characteristics

Table 1 gives the DD noise budgets for short baseline and medium baseline in this paper. On this basis, noises of common EWL and WL combinations have been concluded in Table 2.

Table 1 DD noise budgets for short and medium baseline

Error factor in DD measurement	Short baseline (0–20 km) (cm)	Medium baseline (20–100 km) (cm)
Phase noise of B1	≈1	≈1
1st-order iono delay	<10	<40
Trop delay	<1	≈2.5
Orbit error	<0.5	<1

Table 2 The noise characteristics of common combined signals

Coefficients			$\lambda_{(i,j,k)}/m$	$\beta_{(i,j,k)}$	$\mu_{(i,j,k)}$	σ_{TN}/m ($\sigma_{\Delta\phi}$ = 1 cm)	
i	j	k				$\Delta\delta I_1$ = 10 cm	$\Delta\delta I_1$ = 40 cm
						$\Delta\delta_{tro}$ = 1 cm	$\Delta\delta_{tro}$ = 2.5 cm
						$\Delta\delta_{orb}$ = 0.5 cm	$\Delta\delta_{orb}$ = 1 cm
0	−1	1	4.8842	−1.5915	28.5287	0.3269	0.6981
1	4	−5	6.3707	0.6521	172.6135	1.7274	1.7459
1	3	−4	2.7646	−0.6179	59.2629	0.5959	0.6427
1	2	−3	1.7654	−0.9698	28.0859	0.3020	0.4826
1	1	−2	1.2967	−1.1348	13.9022	0.1798	0.4755
1	0	−1	1.0247	−1.2306	6.8751	0.1414	0.4977
1	−1	0	0.847	−1.2932	5.5752	0.1413	0.5210

Table 3 Short baseline information

No.	Distance (m)	Date	Duration (n)	Interval (s)	Location
Day 287	6.5	2016.10.13	20	1	NWPU
Day 288	6.5	2016.10.14	20	1	NWPU
Day 289	6.5	2016.10.15	20	1	NWPU

The wavelengths of EWL (0, −1, 1) and (1, 4, −5) are so long which are beneficial for fixing ambiguity. By analyzing the first-order ionospheric delay and the total noise, we can see that contributions of ionospheric delay to the total noise can be centimeter. For the short baseline, the total noise of WL combinations (1, 0, −1) and (1, −1, 0) is smaller, but for the medium baseline, WL combinations (1, 2, −3) and (1, 1, −2) bring the smaller total noise in theory. In order to verify the effect of combined noise, we apply these different WL combinations in later TCAR algorithms. Choosing WL combinations from Table 3, we mark (1, 0, −1) and (1, −1, 0) to be Condition-1, moreover, (1, 2, −3) and (1, 1, −2) to be Condition-2.

3 Algorithm-A

The traditional TCAR model can be formed as the linear combinations between code and phase measurements. Choosing the combinations EWL (0, −1, 1), WL (1, 0, −1) and NL (1, 0, 0) for ambiguity resolution, the mathematical model can be expressed as

$$\Delta\breve{N}_{w1} = \left[\frac{\Delta P - \Delta\phi_{w1}}{\lambda_{w1}}\right]_{\text{round}} \tag{14a}$$

$$\Delta\breve{N}_{w2} = \left[\frac{\Delta\phi_{w1} + \lambda_{w1}\Delta\breve{N}_{w1} - \Delta\phi_{w2}}{\lambda_{w2}}\right]_{\text{round}} \tag{14b}$$

$$\Delta\breve{N}_{w3} = \left[\frac{\Delta\phi_{w2} + \lambda_{w2}\Delta\breve{N}_{w2} - \Delta\phi_{w3}}{\lambda_{w3}}\right]_{\text{round}} \tag{14c}$$

$$\begin{aligned} N_1 &= \breve{N}_{w3} \\ N_3 &= N_1 - \breve{N}_{w2} \\ N_2 &= N_3 - \breve{N}_{w1} \end{aligned} \tag{15}$$

where $w1$, $w2$, and $w3$ are the combinations of EWL, WL, and NL; ΔP in (14a) is selected as (0, 1, 1). $\Delta_{\breve{N}_i}$ and λ_{wi} are DD ambiguity and wavelength of the

corresponding combination. $[\cdot]_{\text{round}}$ means rounding for the float ambiguity, and ΔN_i is the original ambiguity (i = 1, 2, 3). Finally, the original ambiguity of triple-signals can be carried out by (15).

4 Algorithm-B

Tang et al. [7] applied the ionosphere-free TCAR with EWL (0, −1, 1) and (1, 4, −5), WL (1, 0, −1) and (1, −1, 0), NL (1, 0, 0) combinations, in this paper, we introduce the Algorithm-B by choosing WL combinations (1, 2, −3) and (1, 1, −2).

4.1 EWL Resolution

First we estimated two uncorrelated EWL ambiguities ($\Delta N_{(0,-1,1)}$ and $\Delta N_{(1,4,-5)}$) [9], whose wavelengths are 4.88 and 6.37 m. Assuming that $\sigma_{\Delta \mathrm{P}_{(0,1,1)}} = 0.5$ m and $\sigma_{\Delta\phi_{(0,-1,1)}} = 0.01$ m, the standard deviations of float ambiguities are estimated by (16). The results are $\sigma_{\Delta N_{(0,-1,1)}} \approx 00.0986$ and $\sigma_{\Delta N_{(1,4,-5)}} \approx 00.3610$ m, when we apply the traditional TCAR method (14a) to evaluate the EWL ambiguities. Therefore, $\Delta N_{(0,-1,1)}$ can be directly rounding by (17), and the success rate will reach to 100%. For the STD of $\Delta N_{(1,4,-5)}$ is bigger, as a result, we resolve the ambiguity according to the following Eq. (18) under the least square principle.

$$\sigma_{\Delta N_{(i,j,k)}} = \sqrt{\frac{f_2^2 + f_3^2}{f_{(0,1,1)}^2}\sigma_{\Delta \mathrm{P}_{(0,1,1)}}^2 + \frac{(if_1)^2 + (jf_2)^2 + (kf_3)^2}{f_{(i,j,k)}^2}\sigma_{\Delta\phi_{(i,j,k)}}^2 + \left(\beta_{(i,j,k)}\Delta\delta I_1\right)^2} \tag{16}$$

$$\Delta N_{(0,-1,1)} = \left[\frac{\Delta P_{(0,1,1)} - \Delta\phi_{(0,-1,1)}}{\lambda_{(0,-1,1)}}\right]_{\text{round}} \tag{17}$$

$$\begin{bmatrix} \Delta P_{(0,1,1)} \\ \Delta\phi_{(1,4,-5)} \end{bmatrix} = \begin{bmatrix} A & 0 \\ A & I \cdot \lambda_{(1,4,-5)} \end{bmatrix} \begin{bmatrix} X \\ \Delta N_{(1,4,-5)} \end{bmatrix} + \begin{bmatrix} \varepsilon_{\Delta P_{(0,1,1)}} \\ \varepsilon_{\Delta\phi_{(1,4,-5)}} \end{bmatrix} \tag{18}$$

where matrix A represents the linear coefficient matrix, I is the identity matrix, and X denotes the baseline parameters. The float $\Delta N_{(1,4,-5)}$ can be fixed by the LAMBDA method. Owing to the wavelengths of two EWL are all long enough, so the success probability can reach to 100%.

4.2 WL Resolution

On basis of two EWL ambiguities, the WL ambiguities can be directly derived according to the linear relationship (19) and (20). Meanwhile, the AR reliability will be inherited to 100%.

$$\Delta N_{(1,2,-3)} = \Delta N_{(1,4,-5)} + 2 \cdot \Delta N_{(0,-1,1)} \tag{19}$$

$$\Delta N_{(1,1,-2)} = \Delta N_{(1,4,-5)} + 3 \cdot \Delta N_{(0,-1,1)} \tag{20}$$

4.3 NL Resolution

After WL resolution, $\Delta N_{(1,2,-3)}$ and $\Delta N_{(1,1,-2)}$ are fixed. By combining B1-B2, and B1-B3 signals, the ionosphere-free combinations IF12 and IF13 can be expressed as follows:

$$\begin{aligned} \Delta N_{\mathrm{IF12}} &= \Delta N_1 - \frac{f_2}{f_1}\Delta N_2 \\ \Delta N_{\mathrm{IF13}} &= \Delta N_1 - \frac{f_3}{f_1}\Delta N_3 \end{aligned} \tag{21}$$

Utilizing the relationship (22) between NL, EWL, and WL combinations, the Eq. (21) can be adapted to (23), and for convenience, we mark $m = (f_1 - f_2)/f_1$ and $n = (f_1 - f_3)/f_1$.

$$\begin{aligned} \Delta N_2 &= \Delta N_1 - \left(\Delta N_{(1,2,-3)} + 3 \cdot \Delta N_{(0,-1,1)}\right) \\ \Delta N_3 &= \Delta N_1 - \left(\Delta N_{(1,1,-2)} + \Delta N_{(0,-1,1)}\right) \end{aligned} \tag{22}$$

$$\begin{aligned} \Delta N_{\mathrm{IF12}} &= \frac{f_1 - f_2}{f_1}\Delta N_1 + \frac{f_2}{f_1}\left(\Delta N_{(1,2,-3)} + 3 \cdot \Delta N_{(0,-1,1)}\right) \\ \Delta N_{\mathrm{IF13}} &= \frac{f_1 - f_3}{f_1}\Delta N_1 + \frac{f_3}{f_1}\left(\Delta N_{(1,1,-2)} + \Delta N_{(0,-1,1)}\right) \end{aligned} \tag{23}$$

The final step is to use the LS principle to resolve NL ambiguities by the following equation:

$$\begin{bmatrix} \Delta\phi_{\mathrm{IF12}} \\ \Delta\phi_{\mathrm{IF13}} \\ \Delta\phi_{(1,0,0)} \end{bmatrix} = \begin{bmatrix} A & \mathrm{m}\lambda_{\mathrm{IF12}} \cdot \mathrm{I} \\ \mathrm{A} & n\lambda_{\mathrm{IF13}} \cdot \mathrm{I} \\ \mathrm{A} & \lambda_{(1,0,0)} \cdot \mathrm{I} \end{bmatrix} \begin{bmatrix} X \\ \Delta N_{(1,0,0)} \end{bmatrix} + \begin{bmatrix} \varepsilon_{\Delta\phi_{\mathrm{IF12}}} \\ \varepsilon_{\Delta\phi_{\mathrm{IF13}}} \\ \varepsilon_{\Delta\phi_{(1,0,0)}} \end{bmatrix} \tag{24}$$

where λ_{IF12} and λ_{IF13} are the corresponding wavelengths of combinations IF12 and IF13.

Apparently, the float ambiguities and covariance of B1 signal can be solved from (24), so we apply the LAMBDA method to determine the integer ambiguities, and then evaluate the original ambiguities of B2 and B3 signals by (22).

5 Algorithm-C

As ionospheric delay is always the key limitation to the AR, which could not be mostly eliminated by the DD processing, especially for the longer baseline. In the above algorithms, the traditional TCAR methods did not take ionospheric delay into account, so we propose a modified ionospheric-free algorithm based on current Algorithm-B. In order to solve for the ambiguity, the least squares (LS) principle is applied under the geometry model. Since the ambiguities are fixed to integers, we can figure out the original ambiguities step by step with the precise observations.

The difference between Algorithm-C and Algorithm-B lies in the NL resolution. This proposed algorithm takes the ionospheric delay both in WL and NL into account, in addition, the ionosphere-free combinations of IF12 and IF13 are used to estimate the ambiguities.

In this proposed algorithm, the ionosphere effect, together with position and ambiguities are considered as unknown parameters in NL equation as follows.

$$\begin{bmatrix} \Delta\tilde{\phi}_{(1,2,-3)} \\ \Delta\phi_{\mathrm{IF12}} \\ \Delta\phi_{\mathrm{IF13}} \\ \Delta\phi_{(1,0,)} \end{bmatrix} = \begin{bmatrix} A & 0 & \mathrm{a}\cdot\mathrm{I} \\ A & \mathrm{m}\lambda_{\mathrm{IF12}}\cdot\mathrm{I} & 0 \\ \mathrm{A} & n\lambda_{\mathrm{IF13}}\cdot\mathrm{I} & 0 \\ \mathrm{A} & \lambda_{(1,0,0)}\cdot\mathrm{I} & \mathrm{I} \end{bmatrix} \begin{bmatrix} X \\ \Delta N_{(1,0,0)} \\ \Delta\delta I_1 \end{bmatrix} + \begin{bmatrix} \varepsilon_{\Delta\phi_{(1,2,-3)}} \\ \varepsilon_{\Delta\phi_{\mathrm{IF12}}} \\ \varepsilon_{\Delta\phi_{\mathrm{IF13}}} \\ \varepsilon_{\Delta\phi_{(1,0,0)}} \end{bmatrix} \tag{25}$$

where $\Delta\tilde{\phi}_{(1,2,-3)}$ is the precise observation without ambiguity, $\Delta\delta I_1$ is the ionospheric delay of NL (1, 0, 0), in addition, on account of the relationship of ionospheric delay and carrier frequencies, $a = \lambda^2_{(1,2,-3)} \Big/ \lambda^2_{(1,0,0)}$.

Likewise, applying the LAMBDA method to determine the inter ambiguities, the original ambiguities of B2 and B3 signals will be resolved.

6 Experiments Analysis

All the algorithms in this paper are processing epoch by epoch. The integer ambiguities can be achieved by LAMBDA method, and inspected by ratio-test. We set the threshold value to be 2, if ratio value is bigger than 2, then we accept the integer ambiguity.

The AR success rate, also known as the AR reliability, is used to evaluate the TCAR performance which is expected to be higher. It is defined as the percentage

of the correctly solved epoch number N_{success} to the total epoch number N_{total} in the following equation,

$$P = \frac{N_{\text{success}}}{N_{\text{total}}} \times 100\% \tag{26}$$

In order to demonstrate the performances of the above TCAR algorithms, this paper collects observation data of three stations which are XBGA1, XBGD2, and HTTH with Trimble NetR9 receivers. On basis of Condition-1 and Condition-2, a series of experiments are carried out in short baseline of 6.5 m and medium baseline of 26.3 km, by using BeiDou B1, B2, and B3 observations with same period time. The ephemeris is from BeiDou broadcast data and the elevation cutoff angle is set to 10°, simultaneously, the satellite with the largest elevation will be as the reference for all computation.

Table 3 gives the data information of short baseline 6.5 m, and the two stations are in NWPU, collecting BeiDou data from 2 o'clock to 22 o'clock. Table 4 gives the data information of medium baseline 26.3 km, and the two stations are located in NWPU and Xi'an, collecting BeiDou data from 0 o'clock to 20 o'clock.

Figure 1 shows the number of available satellites and the PDOP value during the experiment on Day 289 of short baseline and Day 180 of medium baseline. The lower the PDOP value, the better the geometric distribution. It can be seen that all the PDOP values are below 4.

Figures 2 and 3 show the DD ionospheric delay estimated by Algorithm-C, it can be seen from the RMS that the noise of ionospheric delay in short baseline is within 1 cm, and the noise of ionosphere in medium baseline is within 8 cm.

Figure 4 depicts the ratio value which is gained by LAMBDA method in (25). It is clear that all ratio values are beyond the threshold 2, so integers in Condition-1 and Condition-2 are accepted.

6.1 Short Baseline Result

For short baseline data on Day 289, Fig. 5 depicts the position accuracy in the east (E), north(N), and up(U) by Algorithm-A, Algorithm-B, and Algorithm-C.

Testing all data of short baseline, Table 5 makes statistics of the RMS of ENU errors in Condition-1 and Condition-2. The AR success rates are shown in Table 6.

Table 4 Medium baseline information

No	Distance (km)	Date	Duration (h)	Interval (s)	Location
Day 177	26.3	2016.06.25	20	1	NWPU-Xi'an
Day 179	26.3	2016.06.27	20	1	NWPU-Xi'an
Day 180	26.3	2016.06.28	20	1	NWPU-Xi'an

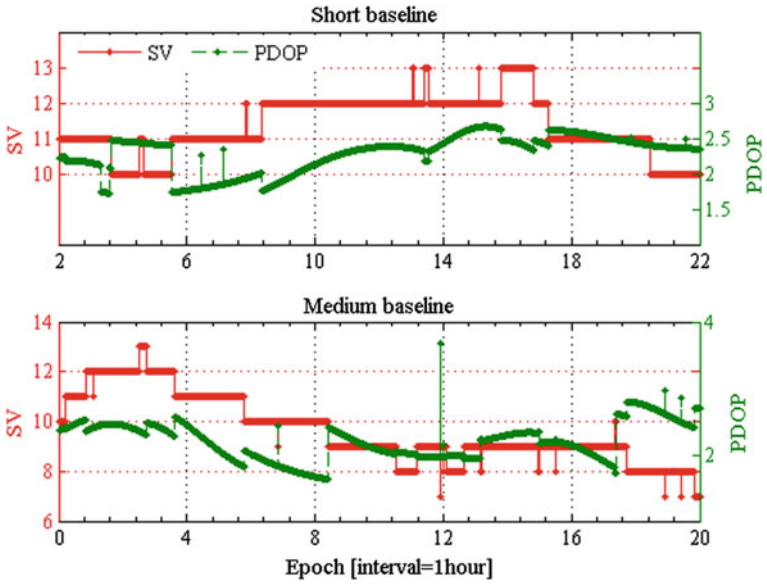

Fig. 1 The available satellites and PDOP value

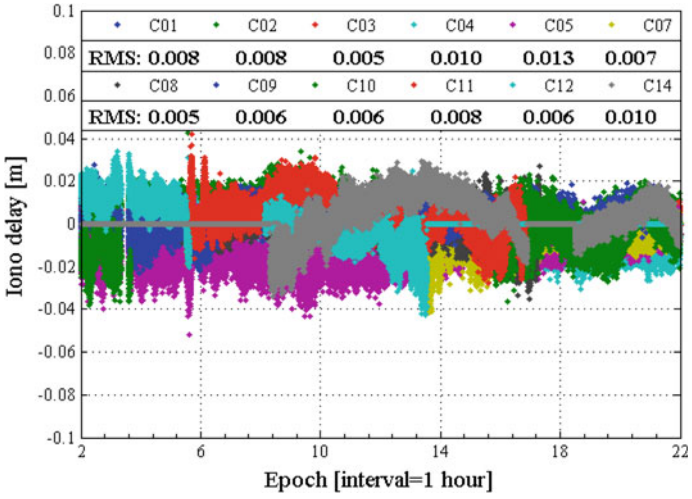

Fig. 2 The DD ionospheric delay of the short baseline

From Tables 5 and 6, a comparison of performance between Algorithm-A, Algorithm-B, and Algorithm-C are conducted over short baseline. The result indicates that the Algorithm-A receives worst serious impact with the combination noise in Condition-2. From all three TCAR algorithms, it turns out that the RMS of position accuracy and AR reliability are better in Condition-1. So the experiment

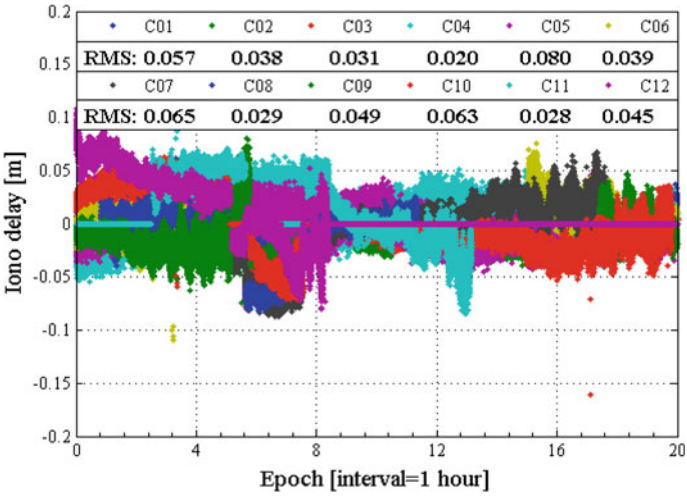

Fig. 3 The DD ionospheric delay of the medium baseline

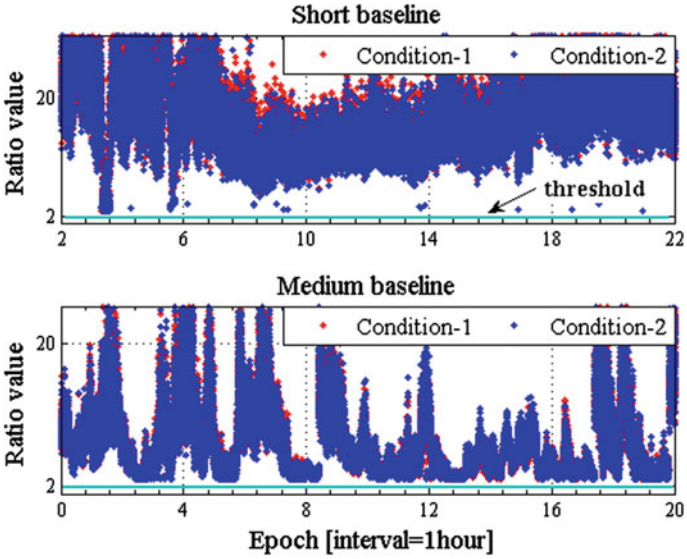

Fig. 4 The ratio value of LAMBDA method

confirms to the theoretical analysis, and the noise in combination is indeed the key limitation in AR.

Algorithm-B without ionospheric delay shows better accuracy than Algorithm-A, meanwhile, the proposed Algorithm-C in this paper evaluates the ionospheric delay parameters, which not only has the best position accuracy, but also reaches 96% success rate in short baseline.

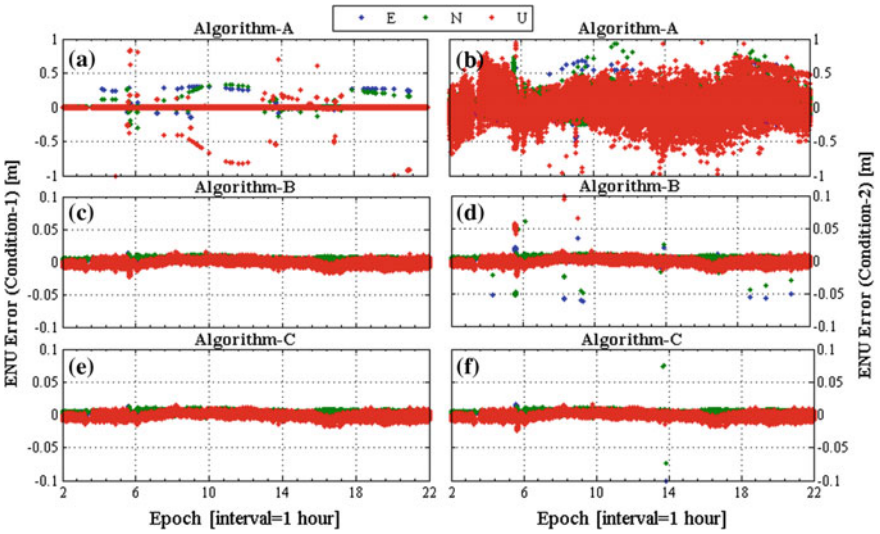

Fig. 5 The position accuracy in ENU of Algorithm-A, Algorithm-B, and Algorithm-C (Short baseline) **a**, **c**, **e** are based on Condition-1, **b**, **d**, **f** are based on Condition-2

Table 5 The RMS of position accuracy (short baseline, in meters)

Day	Condition	Algorithm-A			Algorithm-B			Algorithm-C		
		E	N	U	E	N	U	E	N	U
287	Condition-1	0.007	0.023	0.048	0.002	0.003	0.009	0.002	0.002	0.005
	Condition-2	0.069	0.198	0.279	0.003	0.008	0.034	0.005	0.064	0.027
288	Condition-1	0.005	0.008	0.024	0.003	0.003	0.004	0.002	0.002	0.004
	Condition-2	0.099	0.103	0.178	0.003	0.004	0.014	0.003	0.007	0.018
289	Condition-1	0.009	0.016	0.045	0.003	0.005	0.005	0.003	0.005	0.004
	Condition-2	0.075	0.114	0.210	0.004	0.007	0.015	0.006	0.016	0.022

Table 6 AR success rate (short baseline)

Day	Condition	Algorithm-A (%)	Algorithm-B (%)	Algorithm-C (%)
Day 287	Condition-1	74.99	89.71	96.79
	Condition-2	60.01	85.17	92.22
Day 288	Condition-1	76.01	94.49	98.89
	Condition-2	64.99	88.98	94.49
Day 289	Condition-1	79.48	93.94	98.73
	Condition-2	57.91	85.25	93.05

6.2 Medium Baseline Result

Similarly, with data on Day 180 of medium baseline, the position accuracy gained by three TCAR algorithms is showed in Fig. 6.

After making statistics for position accuracy of medium baseline, Table 7 concludes the RMS of ENU errors in Condition-1 and Condition-2. With processing data of medium baseline by Algorithm-A, Algorithm-B and Algorithm-C, the AR success rates of ambiguities are shown in Table 8.

Comparing the results of medium baseline, we can see that the position accuracy in Condition-2 is worse than that in Condition-1, especially by Algorithm-A. Two conditions make the minor effects on Algorithm-B, but the severe impact on Algorithm-A and Algorithm-C. From the noise of combined observations of medium baseline in Table 2, we can see the noise level of Condition-1 is similar to Condition-2. However, due to the linear combination, it makes the serious effect in practice by noises both in three frequency signals. The proposed Algorithm-C estimates the ionospheric delay in centimeter, and performs 90% success rate which performs best in all three algorithms.

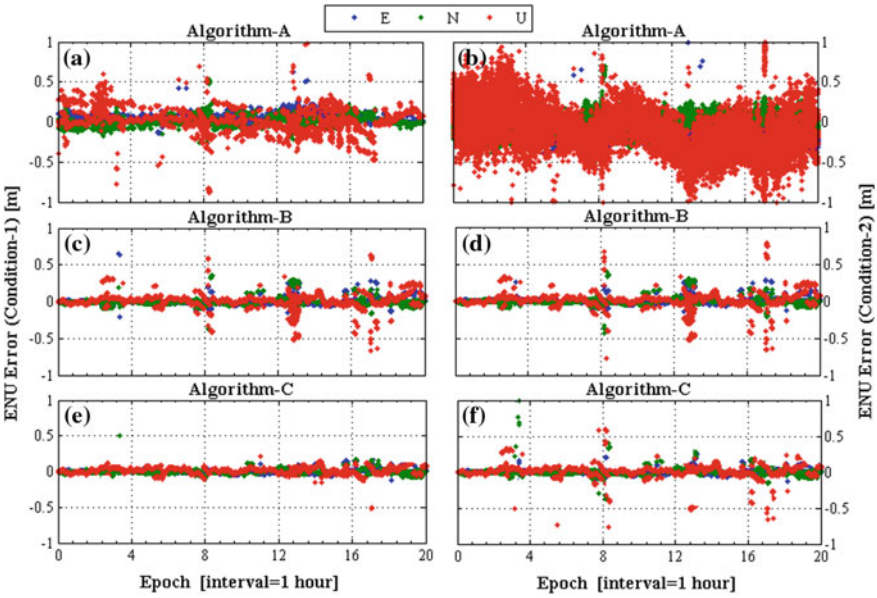

Fig. 6 The position accuracy in ENU of Algorithm-A, Algorithm-B, and Algorithm-C (Medium baseline) **a, c, e** are based on Condition-1, **b, d, f** are based on Condition-2

Table 7 The RMS of position accuracy (Medium baseline, in meters)

Day	Condition	Algorithm-A			Algorithm-B			Algorithm-C		
		E	N	U	E	N	U	E	N	U
177	Condition-1	0.032	0.052	0.133	0.022	0.022	0.051	0.020	0.020	0.046
	Condition-2	0.073	0.087	0.233	0.022	0.022	0.051	0.022	0.022	0.051
179	Condition-1	0.075	0.076	0.152	0.042	0.037	0.123	0.028	0.021	0.057
	Condition-2	0.101	0.099	0.416	0.043	0.038	0.126	0.028	0.022	0.058
180	Condition-1	0.029	0.023	0.045	0.043	0.047	0.080	0.019	0.021	0.040
	Condition-2	0.126	0.093	0.275	0.043	0.048	0.081	0.042	0.046	0.080

Table 8 AR success rate (Medium baseline)

Day	Condition	Algorithm-A (%)	Algorithm-B (%)	Algorithm-C (%)
Day177	Condition-1	60.78	85.99	93.28
	Condition-2	50.65	74.19	85.43
Day179	Condition-1	67.26	87.74	91.10
	Condition-2	52.68	75.64	82.21
Day180	Condition-1	68.27	87.09	92.57
	Condition-2	50.79	78.81	85.45

7 Conclusion

In this paper, we theoretically analyze the main noise of combined observations and select the optimal EWL combinations (0, −1, 1) and (1, 4, −5), in addition, compare the noise of WL in Condition-1 and Condition-2.

Based on the current TCAR algorithms, we propose the Algorithm-C which applies the IF combinations and WL combinations, meanwhile, including parameters of ionospheric delay. By making experiments over short baseline and medium baseline with these three TCAR algorithms, the following conclusions are drawn.

(1) As expected to the theoretical analysis, the combination noise of short baseline in Condition-1 is lower and it turns to be the optimal WL combinations. Owing to the noise in three signals are all brought in, Condition-1 still has the lower noise than Condition-2 in medium baseline.
(2) The traditional Algorithm-A is only adapted to short baseline which performs low reliable. Algorithm-B could perform acceptable results, and it reaches 85% success rate in medium baseline. In comparison, the proposed Algorithm-C achieves the best performance with the high success rate 96% of short baseline and 90% of medium baseline, in addition, realizes millimeter positioning accuracy in short baseline and centimeter accuracy in medium baseline. So Algorithm-C can be used for short and medium baseline with high reliability.

References

1. Forssell B, Martin-Neira M, Harris RA (1997) Carrier phase ambiguity resolution in GNSS. In: Proceeding ION GPS, Institute of Navigation, Kansas City, Missouri, Sept, pp 1727–1736
2. Hatch R, Jung J, Enge P, Pervan B (2000) Civilian GPS: the benefits if three frequencies. GPS Solut 3(4):1–9
3. Ji S, Chen W, Zhao C, Ding X, Chen Y (2007) Single epoch ambiguity resolution for Galileo with the CAR and LAMBDA methods. GPS Solut 11:259–268
4. Teunissen PJG (1995) The least-squares ambiguity decorrelation adjustment: a meth od for fast GPS integer ambiguity estimation. J Geod 70(1–2):65–82
5. Feng Y (2008) GNSS three carrier ambiguity resolution using ionosphere-reduced virtual signals. J Geodesy 82(12):847–862
6. Feng Y, Rizos C, Higgins (2007) Multiple carrier ambiguity resolution and performance benefits for RTK and PPP positioning services in regional areas. In: Proceedings of ION GNSS 20th international technical meeting of the satellite division, pp 668–678
7. Tang W, Deng C, Shi C, Liu J (2014) Triple-frequency carrier ambiguity resolution for Beidou navigation satellite system. GPS Solut 18:335–344
8. Zhang X, He X (2016) Performance analysis of triple-frequency ambiguity resolution with BeiDou observations. GPS Solut 20:269–281
9. Chen D, Ye S (2016) A geometry-free and ionosphere-free multipath mitigation method for BDS three-frequency ambiguity resolution. J Geod 90:703–714

Performance Analysis of Multi-GNSS Precise Point Positioning

Jiang Guo, Xiaotao Li, Xingyu Chen, Jianghui Geng, Qiang Wen and YuanXin Pan

Abstract Currently, there are mainly four global navigation satellite systems (GNSS): GPS, GLONASS, Galileo, and BeiDou. GPS and GLONASS are already mature while Galileo is developing rapidly, and now the number of Galileo In-Orbit Validation (IOV) satellites has reached 18. BeiDou has provided services for the Asia Pacific region since 2012. In addition, the Japanese regional navigation and positioning system QZSS is also developing quickly. It can be predicted that the number of satellites which can be observed in the Asia Pacific region will exceed 100 in the near future. In this study, 6 stations and IGS products such as precise orbit and clock are selected for the IF (ionospheric-free) PPP to analyze the performance of multi-GNSS PPP. It can be concluded that combination of multi-GNSS combination do make contributions to the improvement of positioning accuracy compared with single-system based PPP. In addition, the authors also do some research on elevation cut-off angles in multi-GNSS PPP.

Keywords Multi-GNSS · PPP · Accuracy analysis

1 Introduction

GPS was established by the United States Naval Observatory (USNO) in 1990s, and it contained 24 In-orbit satellites initially. GPS is being modernized now and the satellite number of GPS reaches 32. GLONASS was developed by Russia and now it has 24 In-Orbit validation satellites. Both GPS and GLONASS can provide services across the globe, but different from CDMA signals of GPS, GLONASS operate on FDMA. Now Russia is modernizing GLONASS system to change it to CDMA [1]. Besides these two complete Global Navigation Systems, BeiDou and Galileo are developing quickly. In the next two years, BeiDou and Galileo will mature while BeiDou is operating over Asia only now and Galileo have only 11 full

J. Guo (✉) · X. Li · X. Chen · J. Geng · Q. Wen · Y. Pan
GNSS Research Center, Wuhan University, Wuhan, China
e-mail: guojiang@whu.edu.cn

J. Sun et al. (eds.), *China Satellite Navigation Conference (CSNC) 2017 Proceedings: Volume III*, Lecture Notes in Electrical Engineering 439,
DOI 10.1007/978-981-10-4594-3_32

operational capability (FOC) satellites. It is pretty true that the emerging of BeiDou and Galileo will make a great difference to the GNSS positioning performance. The combinations of different GNSS do make significant contribution to the improvement of PNT accuracy [2]. Moreover, Quasi-Zenith Satellite System (QZSS), a local area argument system of GPS, can be also used for navigation and positioning.

In the new period of GNSS, Multi-GNSS Experiment (MGEX) was initiated by the International GNSS Service [3] in 2012. Coming with this experiment, precise orbits and clocks of satellites for BDS [4], Galileo [5], QZSS [6] have provided by some IGS Analysis Centers.

It has been proved that the combination of GPS/GLONASS can make improvement on the PPP convergence time and positioning accuracy compared with GPS-only PPP [1]. And for multi-GNSS combined Precise Point Positioning (PPP) [7] with raw observations, the convergence has been significantly improved too [8].

In this study, the performance of multi-GNSS has been evaluated with ionospheric-free (IF) dual-frequency observations. Precise orbit, satellite clocks products of MGEX provided by GFZ (Geo Forschungs Zentrum Potsdam) are used for data processing. Traditional IF model is used to eliminate the influence of ionospheric delays. Finally, the results are presented for 6 stations around Asia for 150–160 days of 2016.

2 Function Models of Multi-GNSS PPP

The observation equations of carrier phase and pseudorange can be expressed as follows:

$$\begin{aligned} P_i^s &= \rho^s + cdt - cdt^s + m^s T + \gamma_i I_1 + b_i - b_i^s \\ L_i^s &= \rho^s + cdt - cdt^s + m^s T - \gamma_i I_1 + \lambda_i N_i^s \end{aligned} \tag{2.1}$$

Where indicates s, i refer to the satellite, and receiver, respectively; ρ is the geometric distance between the phase center of the satellite and receiver antennas at the signal transmitting and receiving time; c denotes the speed of light; dt is receiver clock bias; dt^s is satellites clock; m^s and T is wet mapping function and frequency independent tropospheric delay, respectively; $\gamma_i = f_1^2/f_i^2$, I_1 is the ionosphere delay of the signal path at frequency i; b_i and b_i^s are the code bias of receiver and satellite; N_i^s is non-integer ambiguity, which include the receiver- and satellite-dependent uncalibrated phase delay [9]; λ_i is the wavelength.

IF observation equations of GNSS can be expanded as follows:

$$\begin{aligned} P_{\mathrm{if}}^s &= \rho^s + cdt_s + m^s T + b_{s,\mathrm{if}} - b_{\mathrm{if}}^s \\ L_{\mathrm{if}}^s &= \rho^s + cdt_s + m^s T + \lambda_{s,\mathrm{if}} N_{\mathrm{if}}^s \end{aligned} \tag{2.2}$$

Where $b_{s,if}$ and b_{if}^{s} are the code bias of receiver and satellite for IF observation. N_{if}^{s} is ambiguity of IF observation. dt_s is $dt - dt^s$.

For multi-GNSS PPP, the differences of time references and hardware delays are not negligible. There is only one hardware delay of receiver for GPS, BDS, Galileo, for each station since they emit CDMA signals. Different with GPS, GLONASS emit FDMA signals, as a result, different satellite signals are received by different path of receiver, causing the different hardware delays between GLONASS satellites. Normally, only one receiver clock error is estimated for each station in multi-GNSS PPP, so the difference of time reference and hardware delay of receiver must be modeled. If we take receiver clock error for GPS as reference, the equations of multi-PPP can be expressed as follows:

$$\begin{cases} P_{if}^{G} = \rho^{G} + (cdt_{G} + b_{G,if}) + m^{G}T \\ L_{if}^{G} = \rho^{G} + (cdt_{G} + b_{G,if}) + m^{G}T + (\lambda_{G,if}N_{if}^{G} - b_{G,if}) \end{cases} \tag{2.3}$$

$$\begin{cases} P_{if}^{R} = \rho^{R} + (cdt_{G} + b_{G,if}) + (cdt_{R} - cdt_{G} + b_{R,if}^{j} - b_{G,if}) + m^{R}T \\ L_{if}^{R} = \rho^{R} + (cdt_{G} + b_{G,if}) + (cdt_{R} - cdt_{G} + b_{R,if}^{j} - b_{G,if}) + m^{R}T + (\lambda_{R,if}N_{if}^{R} - b_{R,if}^{j}) \end{cases} \tag{2.4}$$

$$\begin{cases} P_{if}^{S} = \rho^{S} + (cdt_{G} + b_{G,if}) + (cdt_{S} - cdt_{G} + b_{S,if} - b_{G,if}) + m^{S}T \\ L_{if}^{S} = \rho^{S} + (cdt_{G} + b_{G,if}) + (cdt_{S} - cdt_{G} + b_{S,if} - b_{G,if}) + m^{S}T + (\lambda_{S,if}N_{if}^{S} - b_{S,if}) \end{cases} \tag{2.5}$$

Where G, R indicate GPS, GLONASS, respectively, and S indicates BDS, Galileo, QZSS, respectively. Considering the linear correlation of several parameters, parameter combination strategy [10–12] is used for removing rank defect. Let

$$\begin{cases} dt = cdt_{G} + b_{G,if}, \widetilde{N}_{if}^{G} = N_{if}^{G} - b_{G,if}/\lambda_{G,if} \\ \mathrm{ISB}_{R,G}^{j} = (cdt_{R} - cdt_{G}) + (b_{R,if}^{j} - b_{G,if}), \widetilde{N}_{if}^{R} = N_{if}^{R} - b_{R,if}^{j}/\lambda_{R,if} \\ \mathrm{ISB}_{S,G} = (cdt_{S} - cdt_{G}) + (b_{S,if} - b_{G,if}), \widetilde{N}_{if}^{S} = N_{if}^{S} - b_{S,if}/\lambda_{S,if} \end{cases} \tag{2.6}$$

ISB indicates inter-system bias, whose first term is difference of time reference and second term is difference of hardware delay for IF pseudorange observation. Moreover, each GLONASS satellite has its own $\mathrm{ISB}_{R,G}^{j}$. After emerging parameters, the equations are simplified as follows:

$$\begin{cases} P_{if}^{G} = \rho^{G} + \widetilde{dt} + m^{G}T \\ L_{if}^{G} = \rho^{G} + \widetilde{dt} + m^{G}T + \widetilde{N}_{if}^{G} \end{cases} \tag{2.7}$$

$$\begin{cases} P_{\mathrm{if}}^{\mathrm{R}} = \rho^{\mathrm{R}} + \tilde{dt} + \mathrm{ISB}_{\mathrm{R,G}}^{i} + m^{\mathrm{R}}T \\ L_{\mathrm{if}}^{\mathrm{R}} = \rho^{\mathrm{R}} + \tilde{dt} + \mathrm{ISB}_{\mathrm{R,G}}^{i} + m^{\mathrm{R}}T + \tilde{N}_{\mathrm{if}}^{\mathrm{R}} \end{cases} \tag{2.8}$$

$$\begin{cases} P_{\mathrm{if}}^{\mathrm{S}} = \rho^{\mathrm{S}} + \tilde{dt} + \mathrm{ISB}_{\mathrm{S,G}} + m^{\mathrm{S}}T \\ L_{\mathrm{if}}^{\mathrm{S}} = \rho^{\mathrm{S}} + \tilde{dt} + \mathrm{ISB}_{\mathrm{R,G}} + m^{\mathrm{S}}T + \tilde{N}_{\mathrm{if}}^{\mathrm{S}} \end{cases} \tag{2.9}$$

3 Data Processing Strategy

Precise multi-GNSS orbit and satellite clock products from GFZ are chosen for analyzing 6 stations data from 150 to 160 of 2016. Raw observations were replaced by IF observations to eliminate the ionosphere delays. Least square estimator (LSQ) is used to estimates parameters such as receiver clock. Troposphere delay is regarded as random-walk process. Furthermore, time-dependent parameters are filtered and smoothed by Kalman filter, and thus convergence performance of Multi-system PPP cannot be assessed in the time series analysis of kinematic positioning. Table 1 summarized the details of data processing strategy.

Table 1 Multi-GNSS data processing strategy

Item	Models
Systems	GPS + GLONASS + BeiDou + Galileo
Frequency	GPS: L1_L2; GLS: G1_G2; BDS: B1_B2; Gal: E1_E5a
Estimate strategy	Least square + Kalman filter
Observation	Ionosphere-free phase and pseudorange, cutoff elevation 10°, frequency of sampling 30 s
Orbit clock product	MGEX product provided by GFZ, orbit frequency 15 min, Clock frequency 5 min
Power chosen strategy	$p = 1$, $e > 30°$, $p = 1/2\sin e$, $e \leq 30°$
Accuracy of observation	BeiDou GEO, pseudorange: 4.0 m, phase: 4.0 cm; Other satellites, pseudorange: 2.0 m, phase: 2.0 cm
Satellite PCO PCV correction	igs08_1911.atx
Receiver PCO PCV correction	GPS, GLONASS: igs08_1911.atx; BeiDou, Galileo: the same as GPS
Tropospheric delay	Initial model + Random-walk process
Ionospheric delay	Eliminated by ionosphere-free combination
Receiver clock	Estimated, white noise
ISB	Estimated as constant
Ambiguity	Estimated, constant for each arc

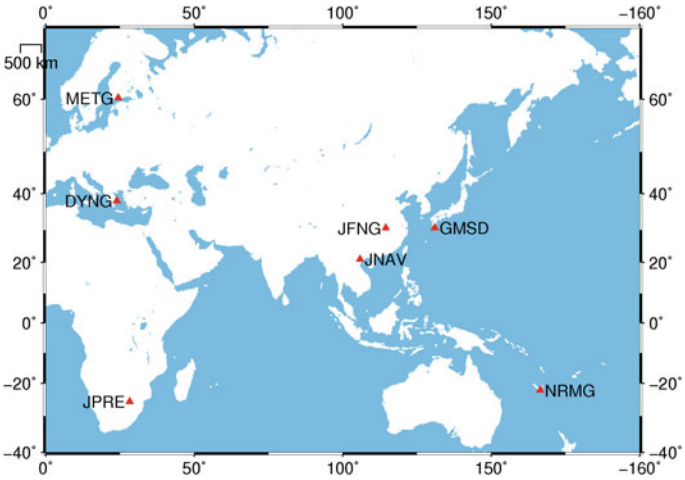

Fig. 1 Distribution of stations

In this study we choose 6 stations of MGEX from Asia, Europe, Africa and Australia which can receive GPS, GLONASS, BeiDou, Galileo and QZSS signals to test the positioning performance of multi-GNSS PPP. Observation data span 11 days from May 29, 2016 to June 8, 2016. Figure 1 shows the distribution of stations. Kinematic positioning is carried out to assess the performance of multi-GNSS PPP by analyzing the residuals, accuracy of positioning and different results for several cut-off elevations.

Figure 2 shows the sky plot of four GNSS and period of tracking time, different systems is represented by different colors. It is easy to find that 5 GEO satellites are visible all day long and distribute on the south of JFNG station, whose elevation angle range from 30° to 60°. For IGSO satellites, their ground trajectory looks like a "∞", and their average visible time one day is about 20 h; sky plots for BeiDou MEO satellites are similar to other systems.

4 Results and Analysis

4.1 Kinematic Positioning

In this test, five models: G, G/R, G/R/C, G/R/C/E, G/R/C(+GEO)/E/J are used for kinematic PPP. It is worth mentioning that GEO satellites are not used in data processing unless they are pointed specially. Take day June 8 as an instance for kinematic positioning. Figure 3 displays the kinematic positioning error of multi-GNSS PPP of JNAV. From Fig. 3, combinations of GRCE/GRC share the similar accuracy of positioning because of the few numbers of Galileo satellites. Compared with GPS-only PPP, multi-GNSS PPP make a significant contribution to

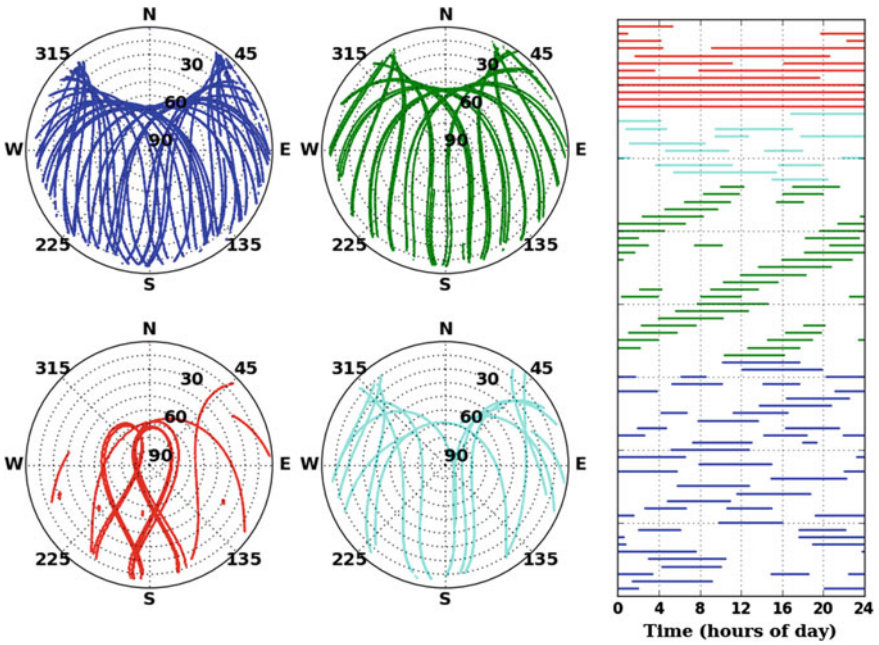

Fig. 2 Sky plot and arc of tracking data of JFNG on DOY 159 in 2016 (*blue*: GPS; *green*: GLONASS; *red*: BeiDou; *cyan*: Galileo)

the improvement of positioning accuracy. When coming to the multi-system PPP with GEO satellites, the results got even worse because of the limit orbit of GEO. So a weight reducing for GEO is needed when combined with GEO satellites.

Figure 4 shows the performance comparison of PPP for three GNSS systems: GPS, GLONASS, and BeiDou at JFNG on DOY 154 of 2016. Among three systems, GPS has highest accuracy, while BeiDou has a 10 cm level error in vertical direction. One reason maybe BeiDou has fewer visible satellites than GPS. In some cases the number of visible satellites of BeiDou is only 4.

4.2 Availability and Reliability

The availability and reliability of GPS-only PPP may have a sharp decrease at some cases such as in the gorge or on the street. Positioning results get worse at these places because there are few visible satellites there and multipath influence is increased too. To analysis the performance of GPS-only PPP and multi-GNSS PPP in these situations, three kinds of cut-off elevations and two models: GPS, GPS + GLONASS + Galileo + BeiDou are chosen for data processing. And Fig. 5 reveals the result. With the increasing of cut-off elevation, visible satellites are decreasing too. When the cut-off elevation is set as 30°, the number of visible GPS

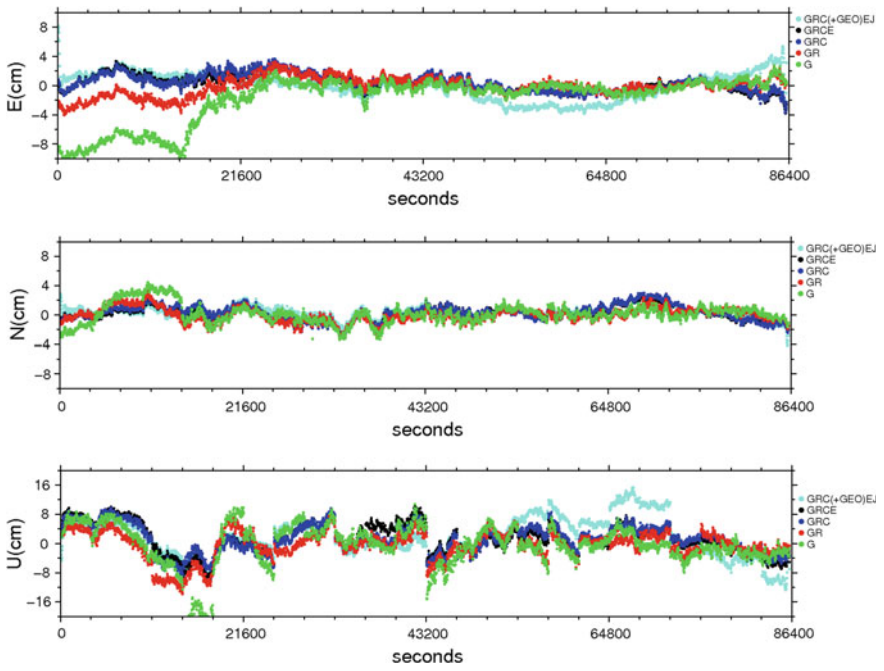

Fig. 3 Positioning results of multi-GNSS PPP

satellites down to about 5 and number of visible satellites of four systems can still remain 15. The positioning accuracy of multi-GNSS still has a good performance when changing cut-off elevation from 10° to 30°. When the cut-off elevation is set as 40°, the number of visible satellites of GPS is less than 5 and positioning results fluctuated significantly at three directions; As for quad-GNSS PPP, the number of visible satellites can still remain 10, positioning results maintain good stability at horizontal direction when slight shakes show on vertical direction. So multi-system combination makes the number of visible satellites for the station increase and can contribute to the availability and reliability of the positioning results.

4.3 Accuracy Analysis

The RMSs of positioning error of kinematic PPP for GPS-only and multi-GNSS (GRCE) of 6 stations chosen in this study over DOY (day of year) 150–160 in 2016 are displayed in Fig. 6. Static PPP positioning results are regarded as the true value of the station coordinates. Empty area represents there are no observations. It is obvious that for stations like JNAV, METG, NRMG, and JFNG, multi-GNSS (GRCE) do contribute a lot to the improvement of positioning accuracy compared with GPS-only PPP. But for JPRE, performance of multi-GNSS gets slightly worse

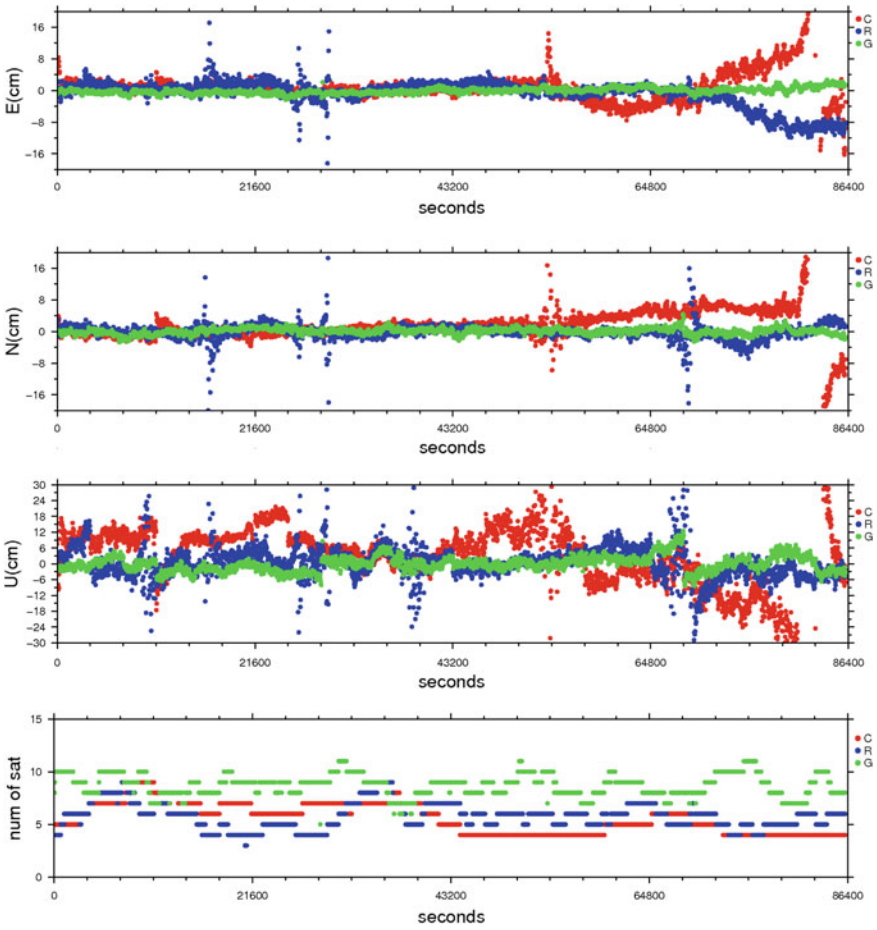

Fig. 4 Results of single-system PPP

than GPS-only PPP. This is because the positioning error of GPS-only PPP reach to 5 mm and positioning accuracy of multi-GNSS combined PPP is limited by the accuracy of orbit and satellite clock product of the other GNSS like BeiDou, GLONASS, and Galileo and the average RMS of positioning error for GPS-only PPP at E, N, and U directions are 1.19, 0.86, and 3.27 cm, respectively. For multi-GNSS (GRCE) PPP, the average RMS of positioning error at these three directions are 0.80, 0.74, 2.56 cm.

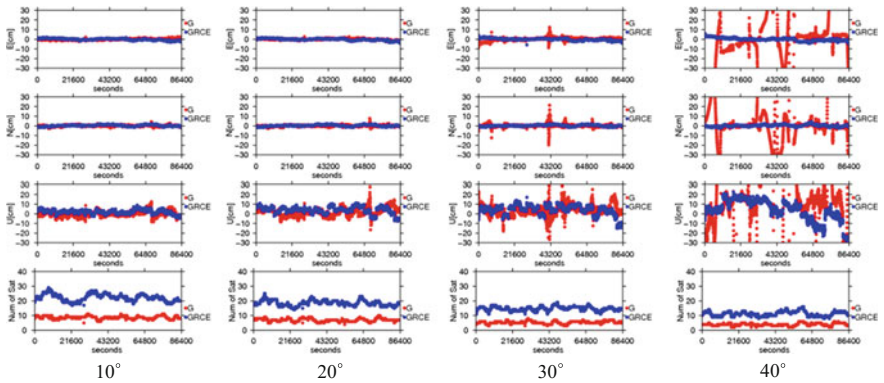

Fig. 5 Comparison of kinematic PPP solution in single- and quad-system mode under different elevation cut-offs, satellite number at JFNG on DOY 159 in 2016

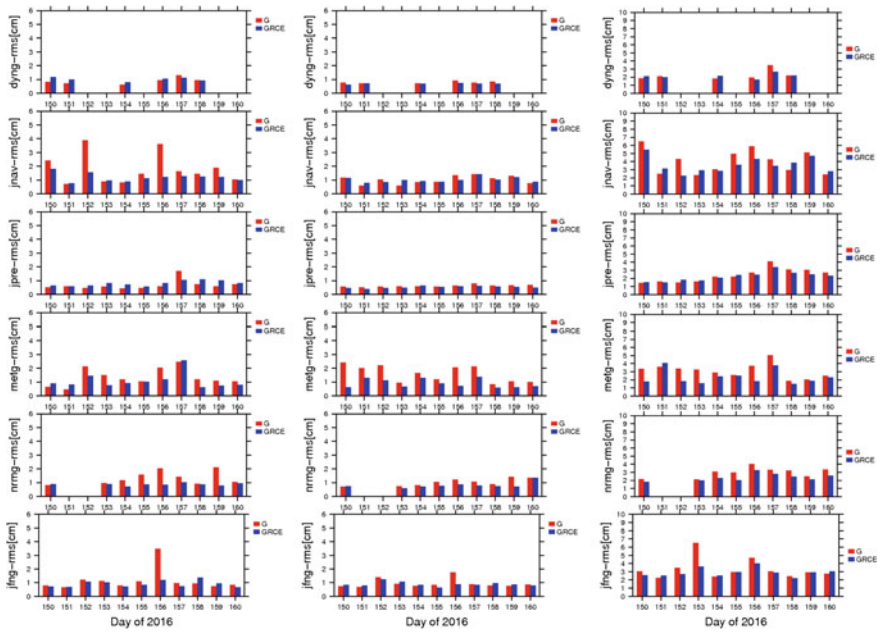

Fig. 6 The RMS statistics of positioning error for kinematic PPP solution in single- and quad-system mode

5 Conclusion

This study has presented five systems' combined PPP model based on a least-squares estimator and ionosphere-free observations. Detailed analysis has been made with ten days of data collected from 6 MGEX stations. And conclusions about the performance of multi-GNSS combined dual-frequency PPP are as follows:

(1) For the single-system PPP, GPS has the best reliability and stability than GLONASS and BeiDou; the poorest accuracy of BeiDou is caused by the lack of visible satellites at station and bad carrier-phase and pseudorange accuracy of GEO satellites.
(2) Multi-GNSS combined dual-frequency PPP can improve the performance of GPS-only PPP in positioning accuracy. Accuracy of east, north, and up directions improved from 1.2, 0.9, 3.3 cm to 0.8, 0.7, 2.6 cm, respectively. But when the positioning errors for GPS-only PPP reach a very low level (about 5 mm),the contribution of multi-GNSS to improving the positioning performance is quite limited.
(3) Compared with single-system PPP, multi-GNSS combined PPP make the number of satellites of stations increased obviously, thus the availability and reliability of positioning results improve at the same time; In gorge, street and other places with complex environment, the improvement would be more remarkable.

References

1. Cai C, Gao Y (2013) Modeling and assessment of combined GPS/GLONASS precise point positioning. GPS Solut 17(2):233–236
2. Ge M, Zhang HP, Jia XL, Song SL, Wickert J (2012) What is achievable with the current COMPASS constellation? GPS World p 29–34
3. Dow JM, Neilan RE, Rizos C (2009) The international GNSS service in a changing landscape of global navigation satellite systems. J Geod 83(3–4):191–198
4. Zhao Q, Guo J, Li M, Qu L, Hu Z, Shi C, Liu J (2013) Initial results of precise orbit and clock determination for COMPASS navigation satellite system. J Geod 87(5):475–486
5. Hackel S, Steigenberger P, Hugentobler U, Uhlemann M, Montenbruck O (2013) Galileo orbit determination using combined GNSS and SLR observations. GPS Solut 19(1):15–25
6. Steigenberger P, Hauschild A, Montenbruck O, Rodriguez-Solano C, Hugentobler U (2013) Orbit and clock determination of QZS-1 based on the CONGO network. Navig 60(1):31–40
7. Zumberge JF, Heflin MB, Jefferson DC, Watkins MM, Webb FH (1997) Precise point for the efficient and robust analysis of GPS data from large networks. J Geophys Res 102(B3):5005–5017. doi:10.1029/96JB03860
8. Lou YD, Zheng F, Gu SF, Charles Wang, Guo HL, Feng YM (2015) Multi-GNSS precise point positioning with raw single-frequency and dual-frequency measurement models. GPS Solut. doi:10.1007/s10291-015-0495-8

9. Ge M, Gendt G, Rothacher M, Shi C, Liu J (2008) Resolution of GPS carrier-phase ambiguities in precise point positioning (PPP) with daily observations. J Geod 82(7):389–399. doi:10.1007/s00190-008-0300-2
10. Geng J, Meng X, Dodson A et al (2010) Rapid re-convergences to ambiguity-fixed solutions in precise point positioning. J Geodesy 84(12):705–714
11. Geng J, Meng X, Dodson A et al (2010) Integer ambiguity resolution in precise point positioning: method comparison. J Geodesy 84(9):569–581
12. Geng J, Shi C, Ge M et al (2012) Improving the estimation of fractional-cycle biases for ambiguity resolution in precise point positioning. J Geodesy 86(8):579–589

The Positioning Performance Analysis of BDS/GPS Single Frequency-Single Epoch of Asia Pacific Region for Short Baseline

Xin Liu, Qiuzhao Zhang and Wei Yang

Abstract Not only is single frequency receiver structure simple and cheap, but also cycle slip is not detected and repaired for single epoch, but the ambiguity success rate is not high, so ambiguity resolution of single frequency-single epoch is the hotspot of research for the high-precision positioning of Global Navigation Satellite System (GNSS). The performance of single frequency-single epoch ambiguity resolution for Global Positioning System (GPS) only having Medium Earth Orbit (MEO) satellites is limited. However, performance of single frequency-single epoch ambiguity resolution for BeiDou Navigation Satellite System (BDS), having Geosynchronous Orbit (GEO), Inclined Geosynchronous Satellite Orbit (IGSO) and MEO satellites, is different to GPS, because of the particularity of its satellite constellation design. With the constant development and improvement of BDS, the single frequency-single epoch positioning applications of BDS will also be more and more wide, so the analysis of current BDS and BDS/GPS single frequency-single epoch ambiguity resolution performance is of great significance. The paper analyzed BDS single frequency-single epoch ambiguity resolution performance from the perspectives of Position Dilution of Precision (PDOP), Ambiguity Dilution of Precision (ADOP), the number of satellite, ambiguity success rate and the precision of baseline vector etc., for the BDS data which had different baseline lengths (0.05, 5, and 10, 15 km) and different periods of time (day and night, the ionosphere effect is different) from the Hong Kong station and Xuzhou region, at the same time compared with GPS and BDS/GPS. The conclusions of single frequency-single epoch ambiguity resolution of short baseline are as follows: Regardless of day and night, the BDS single frequency-single epoch ambiguity resolution performance is better than that of GPS, and during the day the baseline length which can be calculated (referring to a baseline with a success rate greater than 96%) is about 5–7 km; BDS single frequency-single epoch ambiguity resolution performance at night is better than the day, and the baseline length calculated at night can reach 10 km; GPS and BDS combined system can make up

X. Liu · Q. Zhang (✉) · W. Yang
School of Environment Science and Spatial Informatics,
China University of Mining and Technology, Xuzhou 221116, China
e-mail: qiuzhaocumt@cumt.edu.cn; cumt2015lx@163.com

J. Sun et al. (eds.), *China Satellite Navigation Conference (CSNC) 2017 Proceedings: Volume III*, Lecture Notes in Electrical Engineering 439,
DOI 10.1007/978-981-10-4594-3_33

the deficiency of single system and greatly improves single frequency-single epoch ambiguity resolution performance, and when the baseline length is 15 km, single frequency-single epoch ambiguity can also be fixed.

Keywords GPS · BDS · GPS/BDS · Single frequency-single epoch · Ambiguity resolution · Position performance

1 Introduction

Single frequency-single epoch ambiguity resolution has been a hot research topic because of its low success rate. Now the research mainly focuses on the ambiguity rapid determination of GPS's single frequency-single epoch, for its mature development. At present, the main method of ambiguity rapid determination for single frequency-single epoch is adding constraints: Tang weiming put forward two-step search algorithm with baseline length [10, 5] mentioned the constraint ambiguity resolution model for single epoch; based on the characteristics of building deformation monitoring, a single epoch algorithm with deformation characteristics and maximum deformation constraint conditions was proposed [2, 12]. Odolinski proposed single frequency single-baseline real-time kinematic combining four satellite systems calibrating the inter-system biases [9, 8]. However the study has the following problems: (1) the studies of single frequency-single epoch ambiguity resolution performance under short baseline for BDS are less; (2) the studies of the contrastive analysis of single frequency-single epoch ambiguity resolution performance under short baseline between BDS and GPS are less; (3) the studies of improving single frequency-single epoch ambiguity resolution performance for combination of satellite systems are less. It is in December 27, 2012 that BDS first provided services to the Asia Pacific region, which marks the birth of a new navigation system. BDS's constellation includes GEO, IGSO, MEO [13], and the difference between BDS and GPS shows that BDS's single frequency-single epoch ambiguity resolution performance is different from GPS. At the same time, BDS is constantly developing and improving, BDS single epoch ambiguity resolution performance is also changing and its application will also be more and more extensive, so the study of BDS's single frequency-single epoch ambiguity resolution performance is necessary. The emergence of the BDS greatly increases the number of satellites and improves satellite distribution, and it will be helpful to improve the single frequency-single epoch ambiguity resolution performance for multi-satellite systems. In summary, the research of BDS's single frequency-single epoch ambiguity resolution performance is significant. The paper analyzes BDS single frequency-single epoch ambiguity resolution performance from PDOP, ADOP, the number of satellite, ambiguity success rate, the precision of baseline vector etc., for the BDS data which are different baselines and different periods of time (day and night, the ionosphere effect is different), and at the same time compared with GPS and BDS/GPS.

2 Mathematical Model

2.1 Function Model

The unification of coordinate system and the unification of time system will be faced, when the GPS/BDS dual system is used. At the aspect of coordinate system, the change of the same point for World Geodetic System 1984 (WGS84) coordinate system of GPS and China Geodetic Coordinate System CGCS2000 coordinate system of BDS caused by the difference of ellipticity of spheroid can be neglected, so in this paper, coordinate system will be based on WGS84 coordinate system. At the aspect of time system, the time system is unified to GPS Time (GPST). The relationship between GPST and BDS Time (BDT): GPST = BDT + (1356 week, 14 s) [3].

Because the double difference virtual observations can eliminate or greatly reduce most influences of errors, so this paper adopts double difference observations: a satellite of the largest elevation angle in the field of view is used as the reference satellite, and then respectively make subtraction between single difference observation equation of the reference satellite and the single difference observation equation of the rest of the satellite to make up the double difference observation equation [14].

Double difference observation equation of dual system of GPS/BDS: choose reference satellite from GPS and BDS respectively, the double difference observation equations are formed in each system, and then the double difference observation equation of the dual system is formed by the superposition of the two systems of double difference observation equation, namely

$$\begin{aligned} \boldsymbol{c}^{\mathrm{g}} &= \boldsymbol{\rho}^{\mathrm{g}} + \begin{bmatrix} \boldsymbol{l}^{\mathrm{g}} & \boldsymbol{m}^{\mathrm{g}} & \boldsymbol{n}^{\mathrm{g}} \end{bmatrix} \cdot \begin{bmatrix} \delta x & \delta y & \delta z \end{bmatrix}^{\mathrm{T}} + \boldsymbol{\varepsilon}_{\mathrm{r}}^{\mathrm{g}}, \\ \boldsymbol{c}^{\mathrm{b}} &= \boldsymbol{\rho}^{\mathrm{b}} + \begin{bmatrix} \boldsymbol{l}^{\mathrm{b}} & \boldsymbol{m}^{\mathrm{b}} & \boldsymbol{n}^{\mathrm{b}} \end{bmatrix} \cdot \begin{bmatrix} \delta x & \delta y & \delta z \end{bmatrix}^{\mathrm{T}} + \boldsymbol{\varepsilon}_{\mathrm{r}}^{\mathrm{b}}, \end{aligned} \tag{2.1}$$

$$\begin{aligned} \lambda^{\mathrm{g}}\boldsymbol{\varphi}^{\mathrm{g}} &= \boldsymbol{\rho}^{\mathrm{g}} + \begin{bmatrix} \boldsymbol{l}^{\mathrm{g}} & \boldsymbol{m}^{\mathrm{g}} & \boldsymbol{n}^{\mathrm{g}} \end{bmatrix} \cdot \begin{bmatrix} \delta x & \delta y & \delta z \end{bmatrix}^{\mathrm{T}} - \lambda^{\mathrm{g}}\boldsymbol{N}^{\mathrm{g}} + \boldsymbol{\varepsilon}_{\mathrm{h}}^{\mathrm{g}}, \\ \lambda^{b}\boldsymbol{\varphi}^{\mathrm{b}} &= \boldsymbol{\rho}^{\mathrm{b}} + \begin{bmatrix} \boldsymbol{l}^{\mathrm{b}} & \boldsymbol{m}^{\mathrm{b}} & \boldsymbol{n}^{\mathrm{b}} \end{bmatrix} \cdot \begin{bmatrix} \delta x & \delta y & \delta z \end{bmatrix}^{\mathrm{T}} - \lambda^{\mathrm{b}}\boldsymbol{N}^{\mathrm{b}} + \boldsymbol{\varepsilon}_{\mathrm{h}}^{\mathrm{b}}, \end{aligned} \tag{2.2}$$

In the formula, the S in $\boldsymbol{c}^{\mathbf{s}}$, $\boldsymbol{\varphi}^{\mathbf{s}}$, $\boldsymbol{\rho}^{\mathbf{s}}$, $\boldsymbol{l}^{\mathbf{s}}$, $\boldsymbol{m}^{\mathbf{s}}$, $\boldsymbol{n}^{\mathbf{s}}$, $\boldsymbol{N}^{\mathbf{s}}$, $\boldsymbol{\varepsilon}_{\mathrm{r}}^{\mathrm{s}}$, $\boldsymbol{\varepsilon}_{\mathrm{h}}^{\mathrm{s}}$ represents g (GPS) or B (BDS), the double difference pseudorange observation vectors $\boldsymbol{c}$, double difference carrier phase observation vectors $\boldsymbol{\varphi}$, double difference geometric distance vectors $\boldsymbol{\rho}$, the corrections (residuals) of the baseline vector in the X, Y, and Z directions δX, δY, δZ, respectively, double difference cosine vector from the station to the satellite in X, Y and Z directions $\boldsymbol{l}$, $\boldsymbol{m}$, $\boldsymbol{n}$, respectively, double difference carrier integer ambiguity vectors $\boldsymbol{N}$, carrier phase wavelength λ, observed noise vector for double difference observations of pseudorange and double difference observations of carrier $\boldsymbol{\varepsilon}_{\mathrm{r}}$, $\boldsymbol{\varepsilon}_{\mathrm{h}}$ respectively.

Equations (2.1) and (2.2) are rewritten in the form of matrix as follows:

$$\begin{bmatrix} \boldsymbol{A}^{\mathrm{g}} & 0 & 0 \\ \boldsymbol{A}^{\mathrm{b}} & 0 & 0 \\ \boldsymbol{A}^{\mathrm{g}} & \boldsymbol{\lambda}^{\mathrm{g}} & 0 \\ \boldsymbol{A}^{\mathrm{b}} & 0 & \boldsymbol{\lambda}^{\mathrm{b}} \end{bmatrix} \begin{bmatrix} \mathrm{d}\boldsymbol{a} \\ \boldsymbol{N}^{\mathrm{g}} \\ \boldsymbol{N}^{\mathrm{b}} \end{bmatrix} = \begin{bmatrix} \boldsymbol{v}_{\mathrm{r}}^{\mathrm{g}} \\ \boldsymbol{v}_{\mathrm{r}}^{\mathrm{b}} \\ \boldsymbol{v}_{\mathrm{h}}^{\mathrm{g}} \\ \boldsymbol{v}_{\mathrm{h}}^{\mathrm{b}} \end{bmatrix} \tag{2.3}$$

where: $\boldsymbol{A}^{\mathrm{s}} = [\boldsymbol{l}^{\mathrm{s}} \quad \boldsymbol{m}^{\mathrm{s}} \quad \boldsymbol{n}^{\mathrm{s}}]$; $\mathrm{d}\boldsymbol{a} = [\delta x \quad \delta y \quad \delta z]$.

In the formula, $\boldsymbol{v}_{\mathrm{r}}^{\mathrm{s}}$, $\boldsymbol{v}_{\mathrm{h}}^{\mathrm{s}}$ are correction (residual) vectors of double difference observations of pseudorange and double difference observations of carrier respectively, s = g or b.

2.2 Stochastic Model

In this paper, the classic weight of elevation was used, which means that the larger the elevation angle is, the greater the weight is. The weight of rules are as follows: (1) carrier phase observations are not correlated with pseudorange observations, and different satellite observations are independent of each other [4]; (2) Since the carrier phase accuracy is several orders of magnitude higher than the pseudorange accuracy, the relationship between the carrier phase observations and the pseudorange observation weights is $\mathrm{P_h} = 10^4 \mathrm{P_r}$, where $\mathrm{P_h}$ and $\mathrm{P_r}$ are the weights of the carrier phase and the pseudorange observations, respectively [14]; (3) the observations of GPS and BDS in the two systems are independent of each other [1].

The covariance of each non-difference observation:

$$q^2 = 1/\sin^2\theta \tag{2.4}$$

where q^2 is covariance of non-difference observations, the θ is the elevation angle.

The cofactor matrix for the double differential observations of the BDS system can be expressed as

$$\bar{\boldsymbol{Q}} = \begin{bmatrix} q_{dd1}^2 & R^2 & \cdots & R^2 \\ R^2 & q_{dd2}^2 & \cdots & R^2 \\ \vdots & \vdots & \vdots & \vdots \\ R^2 & R^2 & \cdots & q_{ddn}^2 \end{bmatrix} \tag{2.5}$$

$$\begin{aligned} q_{ddi}^2 &= (q_f^r)^2 + (q_u^r)^2 + (q_f^i)^2 + (q_u^i)^2 \\ R^2 &= (q_f^r)^2 + (q_u^r)^2 \end{aligned} \tag{2.6}$$

where q_{ddi}^2 is covariance of the ith double difference observation, R^2 is the relevant weight reciprocal of single difference observation between station and rover for reference satellite, $\left(q_f^r\right)^2$ is covariance of non-difference observations for reference

satellite in station, $\left(q_u^r\right)^2$ is covariance of non-difference observations for reference satellite in rover, $\left(q_f^i\right)^2$ is covariance of non-difference observations for ith satellite in station, $\left(q_u^i\right)^2$ is covariance of non-difference observations for ith satellite in rover.

Based on the above conditions, the two-system non-difference stochastic model is abbreviated as

$$\boldsymbol{Q} = \begin{bmatrix} \text{cod}*\bar{\boldsymbol{Q}}_{\mathbf{GPS}} & 0 & 0 & 0 \\ 0 & \text{cod}*\bar{\boldsymbol{Q}}_{\mathbf{BDS}} & 0 & 0 \\ 0 & 0 & \text{ph}*\bar{\boldsymbol{Q}}_{\mathbf{GPS}} & 0 \\ 0 & 0 & 0 & \text{ph}*\bar{\boldsymbol{Q}}_{\mathbf{BDS}} \end{bmatrix} \tag{2.7}$$

where cod = 0.3^2, ph = 0.003^2.

Least-squares method can be applied to Eqs. (2.3) and (2.7) to obtain the floating ambiguity solution and its cofactor matrix $\boldsymbol{Q}_{\hat{a}\hat{a}}$, and then the fixed ambiguity solution can be obtained by Lambda [11].

3 ADOP Theory [6, 7]

$$ADOP = \left|\boldsymbol{Q}_{\hat{a}\hat{a}}\right|^{1/2n} \tag{3.1}$$

where n is the number of double difference ambiguity.

ADOP can also be approximated as

$$\text{ADOP} = \frac{\sqrt{2}|C_h|^{\frac{1}{2j}}}{\breve{\lambda}} \left[\frac{1}{e_k^T R_k^{-1} e_k}\right]^{\frac{1}{2}} \left[\frac{\sum_{s=1}^{m} w_s}{\prod_{s=1}^{m} w_s}\right]^{\frac{1}{2(m-1)}} \left[1+\frac{1}{\eta}\right]^{\frac{1}{2j}} \left[1+\frac{1}{\delta}\right]^{\frac{v}{2j(m-1)}} \tag{3.2}$$

where, j is number of frequencies, $\breve{\lambda} = \prod_{i=1}^{j} \lambda_i^{1/j}$, λ is the wavelength, C_h is the variance factor of phase observables, $e_k = [1, \ldots\ldots, 1]$, R_k is the temporal correlation matrix, k is the number of epoch, when $k = 1$, $R_k = 1$, w is the satellite-dependent weight, m is the number of satellite, when ionosphere parameter is fixed, $\eta = \infty$, when ionosphere parameter is floating, $\eta = \left[\mu^T C_r^{-1} \mu\right] / \left[\mu^T C_h^{-1} \mu\right]$, where, μ is coefficient matrix of ionospheric parameters, C_r is the variance factor of pseud-orange observables, v is the number of parameters except of double difference ambiguities, when ionosphere parameter is fixed, $\delta = \left[e_j^T C_r^{-1} e_j\right] / \left[e_j^T C_h^{-1} e_j\right]$, e_j is similar to e_k.

$\breve{\lambda} = \lambda_i$, $i = 1$ or 2, and $k = 1$, namely $e_k = 1$, $R_k = 1$ in the single frequency-single epoch mathematical model, at the same time, supposing that the double difference model can eliminate the ionosphere in a short baseline, namely ionosphere parameter is fixed, so $\eta = \infty$, $\delta = \left[e_j^T C_r^{-1} e_j\right] \Big/ \left[e_j^T C_h^{-1} e_j\right]$.

Then Eq. (3.2) can be written as:

$$\mathrm{ADOP} = \frac{\sqrt{2}|C_h|^{\frac{1}{2}}}{\lambda_i} \left[\frac{\sum_{s=1}^{m} w_s}{\prod_{s=1}^{m} w_s}\right]^{\frac{1}{2(m-1)}} \left[1 + \frac{C_h}{C_r}\right]^{\frac{3}{2(m-1)}} \tag{3.3}$$

Let $f_1 = \frac{\sqrt{2}|C_h|^{\frac{1}{2}}}{\lambda_i}$, $f_2 = \left[\frac{\sum_{s=1}^{m} w_s}{\prod_{s=1}^{m} w_s}\right]^{\frac{1}{2(m-1)}}$, $f_3 = \left[1 + \frac{C_h}{C_r}\right]^{\frac{3}{2(m-1)}}$, then Eq. (3.3) can be abbreviated as:

$$\mathrm{ADOP} = f_1 * f_2 * f_3 \tag{3.4}$$

As can be seen from Tables 1 and 2, there is no much difference of f_1 and f_3 between BDS and GPS. From Table 2, the number of BDS high-elevation satellite is much more than the number of GPS high-elevation satellite. In the weight part, the weight was carried out according to the elevation, so for w, the majority w of BDS is greater than that of GPS, which will lead to $\left[\frac{\sum_{s=1}^{m} w_s}{\prod_{s=1}^{m} w_s}\right]_{\mathrm{BDS}} < \left[\frac{\sum_{s=1}^{m} w_s}{\prod_{s=1}^{m} w_s}\right]_{\mathrm{GPS}}$. From Table 2, we could also know that BDS average number of satellites were more than GPS, so $f_2^{\mathrm{BDS}} < f_2^{\mathrm{GPS}}$. To sum up, we got the result:

$$\mathrm{ADOP}_{\mathrm{BDS}} < \mathrm{ADOP}_{\mathrm{GPS}}.$$

Table 1 Carrier wavelength and the standard deviations of carrier and Pseudorange

System	Frequency band	Pseudorange (cm)	Carrier phase (mm)	Wavelength of carrier (cm)
GPS	L1	37	2.5	19.03
	L2	27	2.6	24.42
BDS	B1	31	2.5	19.2
	B2	30	3.3	24.83

Table 2 Average number of satellites at different cutoff heights

	10°	30°	40°
GPS	9	5.35	2.67
BDS	10.57	8.57	7.1
BDS/GPS	19.57	13.92	10.86

4 Experimental Design and Analysis

In this paper, the experiments of single frequency-single epoch ambiguity resolution of GPS, BDS, and GPS/BDS were performed on the data of 0.05, 5, 10, and 15 km respectively whose sampling intervals were 1 s. Single frequency-single epoch ambiguity resolution performance of BDS was analyzed from the perspectives of number of observed satellites, PDOP, ADOP, ambiguity fixed success rate and baseline vector precision, and at the same time compared with GPS and BDS/GPS. Data of 0.05 km was from the Trimble R10 receiver, other data from the Hong Kong Base Station. The period of all data was from July 2016 to November 2016. The cut-off elevation angle was set to 10° and the SNR threshold was set to 30 when experimental data were processed. In order to analyze the effects of ionospheric residuals on the ambiguity resolution of single frequency-single epoch for short baseline, the data were divided into two groups: daytime (group A: 9:00–19:00) and evening (group B: 20:00–8:00 the next day). The success rate was calculated as: Success rate = Number of Successful Epochs/Total Epochs and results of baseline vector precision, ADOP and PDOP were all successful epochs in experiments. In terms of baseline vector accuracy, the baseline vector obtained from the known precise Hong Kong base station coordinates was took as the true value and the baseline vector error maps were obtained by comparing the baseline vector and the true value calculated in this paper.

4.1 0.05 km Baseline

1. Group A
2. Group B

Comparing the groups A and B, at the aspect of success rate, the success rate of BDS/GPS was stable, groups A and B all higher than 99%, and BDS and GPS were similar, whose success rates were all higher than 97%, but worse than BDS/GPS, so at the aspect of success rate, BDS/GPS was most stable, and BDS and GPS were similar, worse than BDS/GPS. As can be seen from Table 3, under the same conditions, the ADOP of daytime and night of 0.05 km baseline was $ADOP_{BDS/GPS} < ADOP_{BDS} < ADOP_{GPS}$, which was consistent with the success rate, namely the smaller the ADOP, the higher the ambiguity success rate. In terms of PDOP, as can be known from Figs. 4 and 8, $PDOP_{BDS/GPS} < PDOP_{GPS} < PDOP_{BDS}$. As can be seen from Figs. 2 and 6, in terms of baseline vector accuracy, accuracy from high to low order was BDS/GPS, GPS, BDS, which was consistent with the PDOP, namely the smaller the PDOP, the higher the baseline vector accuracy. Only when the baseline vector accuracy of BDS of group B higher than the corresponding baseline vector accuracy in group A and other

Table 3 The ambiguity success rate and mean ADOP of 0.05, 5, 10, 15 km baseline

	System	0.05 km			5 km			10 km			15 km		
		Total epoch	Mean ADOP	Success rate (%)	Total epoch	Mean ADOP	Success rate (%)	Total epoch	Mean ADOP	Success rate (%)	Total epoch	Mean ADOP	Success rate
A	GPS	11,721	0.285	98.56	10,800	0.284	54.52	10,800	0.284	16.23	10,800	0.274	19.43
	BDS	11,721	0.28	98.71	10,800	0.206	96.41	10,800	0.162	85.12	10,800	0.204	35.44
	BDS/GPS	11,721	0.115	100.00	10,800	0.088	99.96	10,800	0.081	99.93	10,800	0.076	82.84
B	GPS	11,955	0.302	98.98	10,800	0.238	84.73	10,800	0.297	63.44	10,800	0.234	68.45
	BDS	11,955	0.243	99.96	10,800	0.158	99.97	10,800	0.224	99.08	10,800	0.196	83.94
	BDS/GPS	11,955	0.102	100.00	10,800	0.076	99.97	10,800	0.078	99.97	10,800	0.081	99.97

combinations were similar. From Figs. 4 and 8, the reason was that BDS satellites in group B were more evenly distributed than BDS satellites in group A. The maximum error of baseline vector in EN direction was about 2 cm, U direction about 5 cm for three systems. In summary, the ambiguity resolution performance of the single frequency-single epoch at night was similar to that of daytime, and the ambiguity resolution performance single frequency-single epoch from high to low was BDS/GPS, BDS, GPS, for 0.05 km baseline (Figs. 1, 3, 5, 6 and 7).

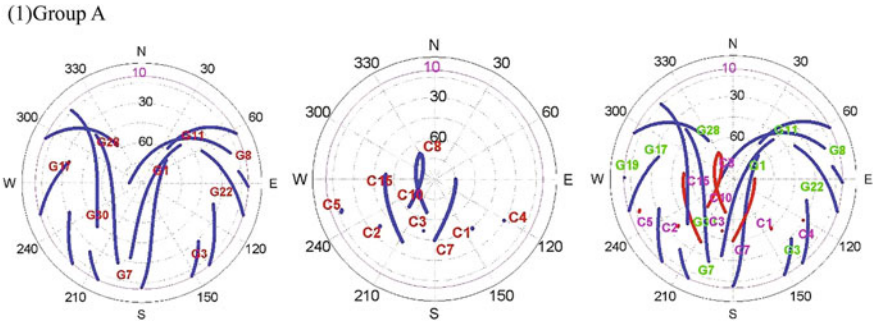

Fig. 1 The satellite skyplot of GPS, BDS, BDS/GPS

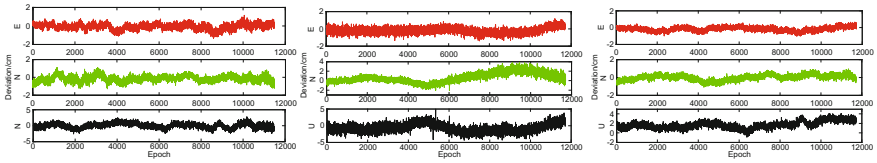

Fig. 2 Error graph of baseline of GPS, BDS, BDS/GPS

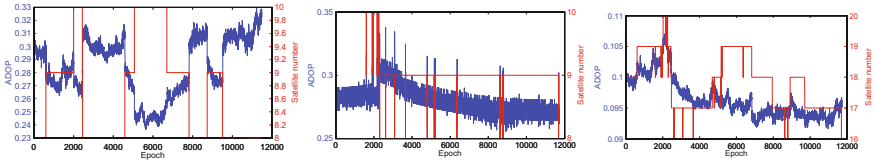

Fig. 3 The ADOP of GPS, BDS, BDS/GPS

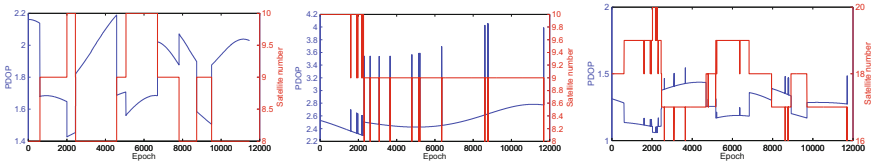

Fig. 4 The PDOP of GPS, BDS, BDS/GPS

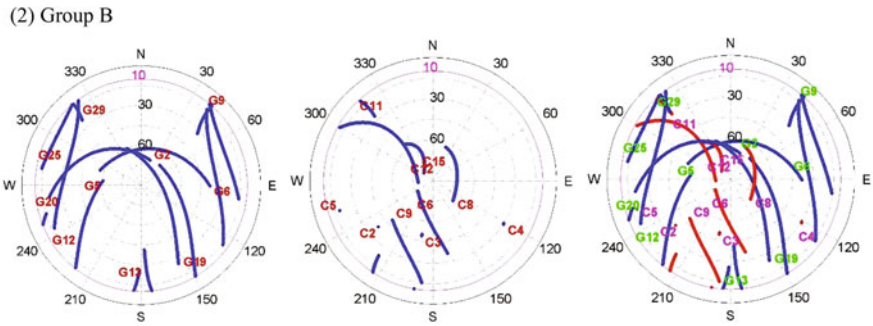

Fig. 5 The satellite skyplot of GPS, BDS, BDS/GPS

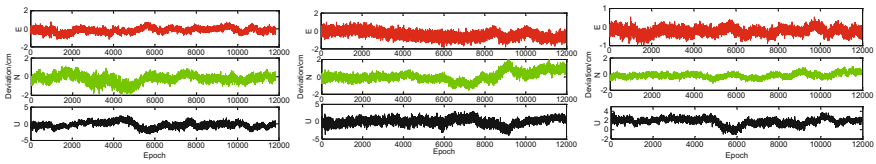

Fig. 6 Error graph of baseline of GPS, BDS, BDS/GPS

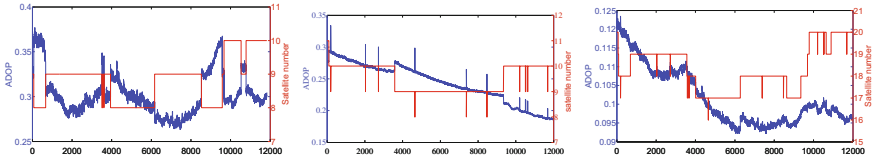

Fig. 7 The ADOP of GPS, BDS, BDS/GPS

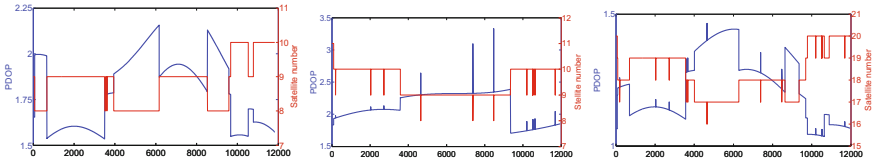

Fig. 8 The PDOP of GPS, BDS, BDS/GPS

4.2 5 km Baseline

1. Group A
2. Group B

As can be seen from Fig. 10, there was a large anomaly for BDS after the 7000 epoch. The reason is that this part of the data was in the time period 11:00 ~ 12:00, and this time period was greatly affected by the ionosphere which led to the large

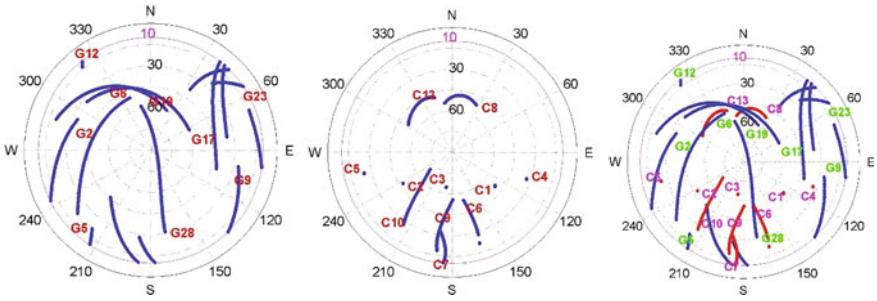

Fig. 9 The satellite skyplot of GPS, BDS, BDS/GPS

anomaly of baseline vector. As can be seen from Fig. 11, the number of BDS satellite changed more frequently, the reason was the signal-to-noise ratio was set to 30 in the experiment and signal-to-noise ratio of GEO5 fluctuated greatly which led to the BDS satellites frequently change (Fig. 9).

Comparing the groups A and B, at the aspect of success rate, the success rate of BDS/GPS was most stable, groups A and B all higher than 99%, BDS was more stable, success rate of group B higher than that of group A, groups A and B all higher than 96%, and the success rates of groups A and B in GPS were lower, whose success rates were less than 85%. So in terms of success rate, BDS/GPS was the most stable, BDS more, GPS the worst. From Table 3, under the same conditions, the ADOP of daytime and night of 5 km baseline was $ADOP_{BDS/GPS} < ADOP_{BDS} < ADOP_{GPS}$, which was consistent with the success rate, namely the smaller the ADOP, the higher the ambiguity success rate. In terms of PDOP, as can be known from Figs. 12 and 16, $PDOP_{BDS/GPS} < PDOP_{GPS} \leq PDOP_{BDS}$. Theoretically, the accuracy of baseline vector from high to low was BDS/GPS, GPS and BDS, but the experimental results were not so. From Fig. 10, accuracy of BDS/GPD and BDS was similar and GPS was better than BDS in the daytime. The maximum error in EN direction was about 3 cm, U direction about 10 cm. At night, the accuracy of BDS/GPS was highest and BDS and GPS were similar. The maximum error in EN direction was about 3 cm, U direction about 4 cm. Overall, the baseline vector accuracy of group B was higher than that of group A for all three systems. The reason of the PDOP of the three systems in the daytime is not consistent with the baseline vector accuracy was that for the epoch affected largely by ionosphere, the ambiguities were fixed, however the accuracy of baseline vectors were worse because of ionosphere. In summary, the ambiguity resolution performance of the single frequency-single epoch at night was better than that of daytime, and the ambiguity resolution performance single frequency-single epoch from high to low was BDS/GPS, BDS, GPS, for 5 km baseline (Figs. 13, 14 and 15).

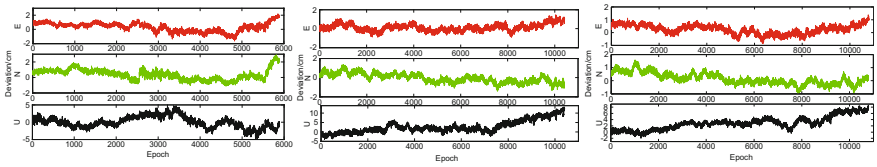

Fig. 10 Error graph of baseline of GPS, BDS, BDS/GPS

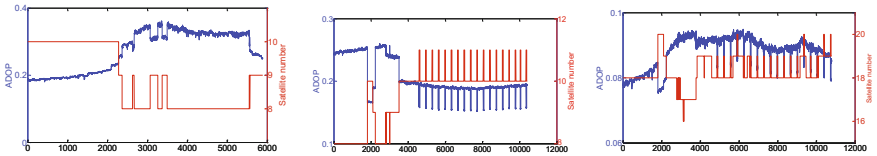

Fig. 11 The ADOP of GPS, BDS, BDS/GPS

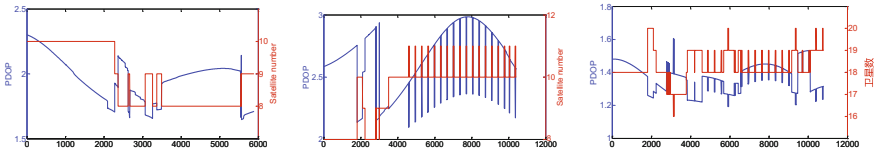

Fig. 12 The PDOP of GPS, BDS, BDS/GPS

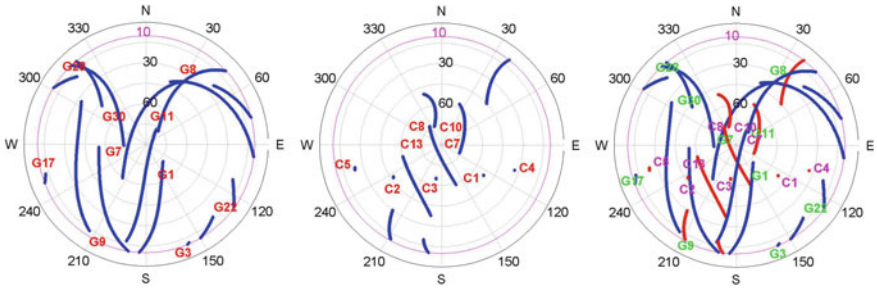

Fig. 13 The satellite skyplot of GPS, BDS, BDS/GPS

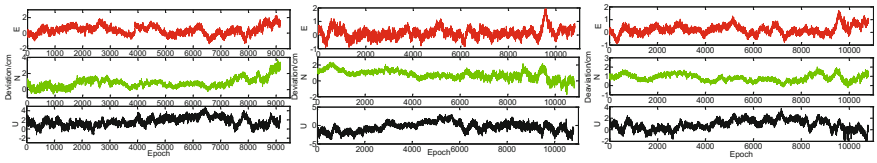

Fig. 14 Error graph of baseline of GPS, BDS, BDS/GPS

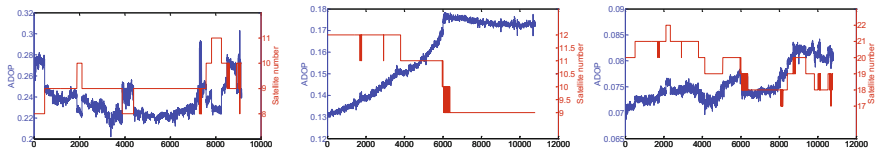

Fig. 15 The ADOP of GPS, BDS, BDS/GPS

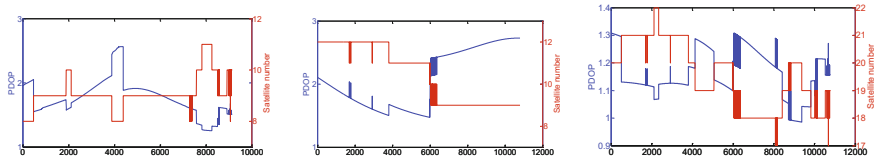

Fig. 16 The PDOP of GPS, BDS, BDS/GPS

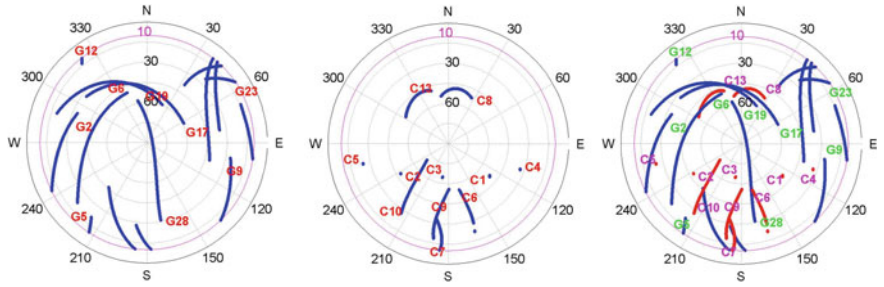

Fig. 17 The satellite skyplot of GPS, BDS, BDS/GPS

4.3 10 km Baseline

1. Group A
2. Group B

As can be seen from Fig. 18, three systems were abnormal and the reason for the existence of anomalies was the same as the 5 km baseline experiment (Figs. 17 and 19).

Comparing the groups A and B, at the aspect of success rate, the success rate of BDS/GPS was most stable, success rates of groups A and B are all higher than 99%, BDS was more stable, group B success rate higher than 97%, success rate of group B much higher than that of group A, and the success rate of group B in GPS was much higher than that of group A, but success rates of two group of GPS were less than 65%. From Table 3, under the same conditions, the ADOP of daytime and night of 10 km baseline was $ADOP_{BDS/GPS} < ADOP_{BDS} < ADOP_{GPS}$, which was consistent with the success rate, namely the smaller the ADOP, the higher the ambiguity success rate. In terms of PDOP, as can be known from Figs. 20 and 24, $PDOP_{BDS/GPS} < PDOP_{GPS} \leq PDOP_{BDS}$. From Fig. 18, the accuracy of GPS and

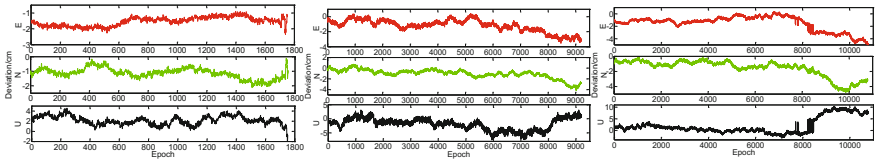

Fig. 18 Error graph of baseline of GPS, BDS, BDS/GPS

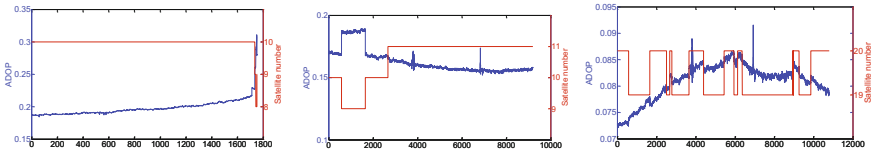

Fig. 19 The ADOP of GPS, BDS, BDS/GPS

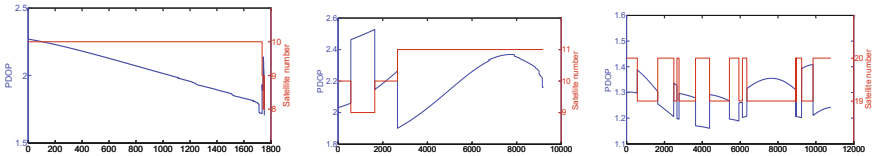

Fig. 20 The PDOP of GPS, BDS, BDS/GPS

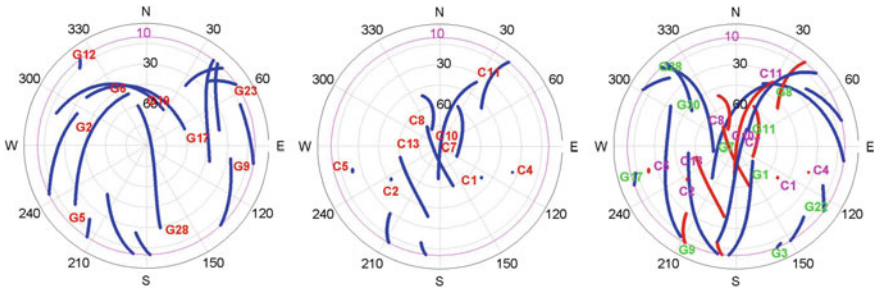

Fig. 21 The satellite skyplot of GPS, BDS, BDS/GPS

BDS was similar in the daytime, and BDS/GPS was worse relatively. The maximum error in EN direction was about 5 cm, U direction about 10 cm. At night, BDS/GPS accuracy was slightly higher than BDS and GPS. The maximum error in EN direction was about 3 cm, U direction about 6 cm. Overall, the baseline vector accuracy of group B was higher than that of group A for all three systems. The reason of the PDOP of the three systems in the daytime is not consistent with the baseline vector accuracy and was same as the 5 km baseline experiment. In summary, the ambiguity resolution performance of the single frequency-single epoch at night was better than that of daytime, and the ambiguity resolution performance single frequency-single epoch from high to low was BDS/GPS, BDS, GPS, for 10 km baseline (Figs. 21, 22 and 23).

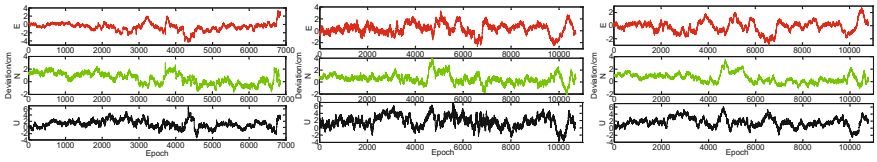

Fig. 22 Error graph of baseline of GPS, BDS, BDS/GPS

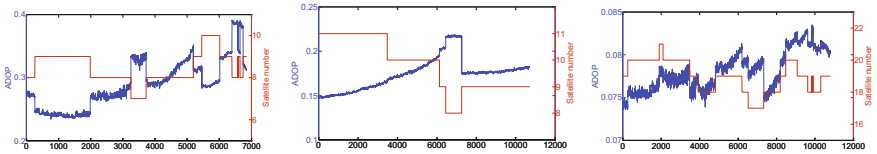

Fig. 23 The ADOP of GPS, BDS, BDS/GPS

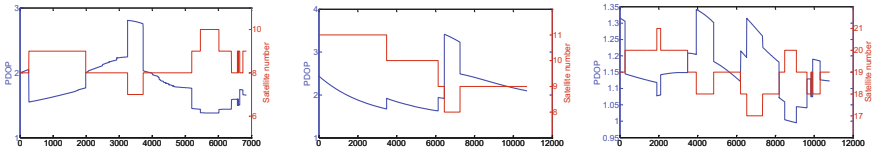

Fig. 24 The PDOP of GPS, BDS, BDS/GPS

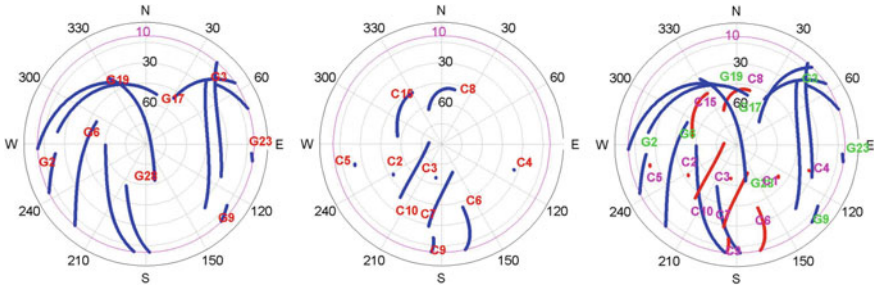

Fig. 25 The satellite skyplot of GPS, BDS, BDS/GPS

4.4 15 km Baseline

1. Group A
2. Group B

As can be seen from Fig. 26, three systems were abnormal and the reason for the existence of anomalies was that though the 15 km baseline was short baseline, the double difference ionospheric error was still large after making double difference, which led to the worse accuracy of baseline vector (Figs. 25, 27 and 28).

Comparing the groups A and B, at the aspect of success rate, for three systems the success rates of group A were all very low and the success rates of group B were very low except BDS/GPS whose success rate was higher than 97%, however group B were much higher than the corresponding values of group A. The order of success rates of the two groups from high to low was followed by BDS/GPS, BDS, GPS. From Table 3, under the same conditions, the ADOP of daytime and night of 15 km baseline was $ADOP_{BDS/GPS} < ADOP_{BDS} < ADOP_{GPS}$, which was consistent with the success rate, namely the smaller the ADOP, the higher the ambiguity success rate. In terms of PDOP, as can be known from Figs. 20 and 24, $PDOP_{BDS/GPS} < PDOP_{GPS} \leq PDOP_{BDS}$. From Fig. 26, the accuracy of three system was similar in the daytime. The maximum error in EN direction was about 5 cm, U direction about 8 cm. At night, BDS/GPS accuracy was slightly higher than BDS and GPS. The maximum error in EN direction was about 3 cm, U direction about 6 cm. Overall, the baseline vector accuracy of group B was higher than that of group A for all three systems. The reason of the PDOP of the three systems in the daytime is not consistent with the baseline vector accuracy was same as the 5 km baseline experiment. In summary, the ambiguity resolution performance of the single frequency-single epoch at night was better than that of daytime, and the ambiguity resolution performance single frequency-single epoch from high to low was BDS/GPS, BDS, GPS, for 15 km baseline (Figs. 29, 30, 31 and 32).

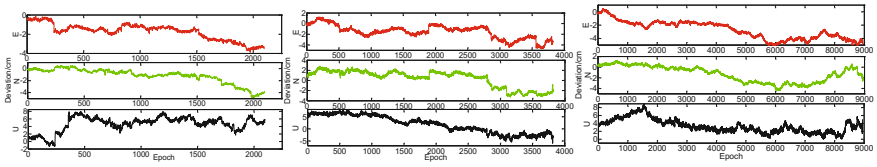

Fig. 26 Error graph of baseline of GPS, BDS, BDS/GPS

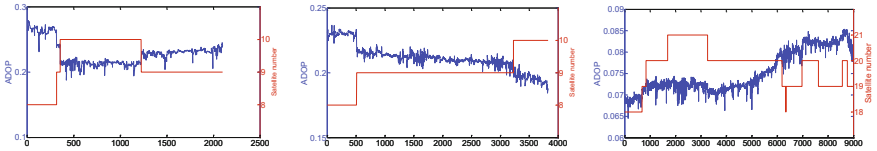

Fig. 27 The ADOP of GPS, BDS, BDS/GPS

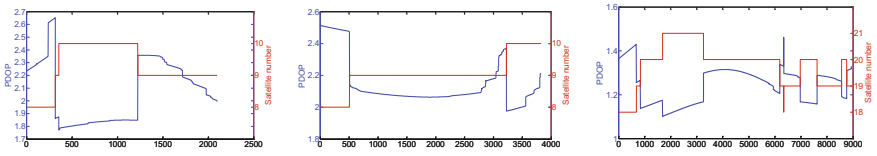

Fig. 28 The PDOP of GPS, BDS, BDS/GPS

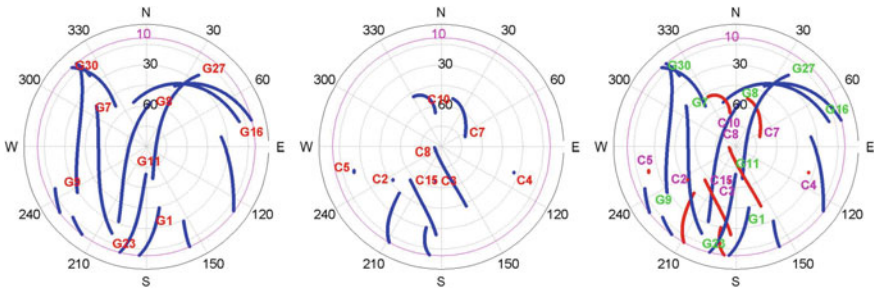

Fig. 29 The satellite skyplot of GPS, BDS, BDS/GPS

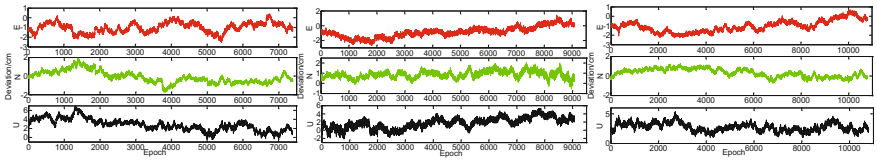

Fig. 30 Error graph of baseline of GPS, BDS, BDS/GPS

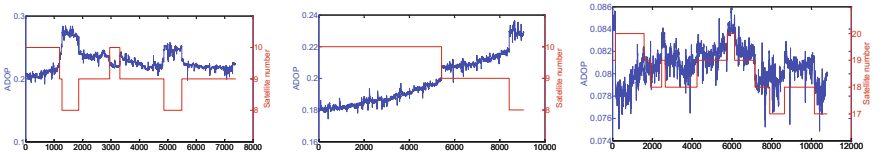

Fig. 31 The ADOP of GPS, BDS, BDS/GPS

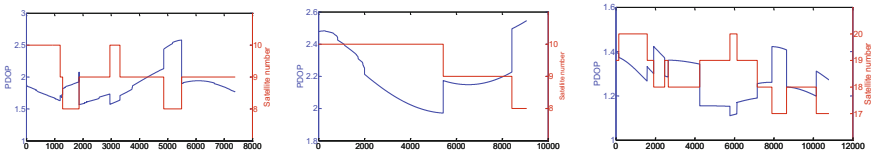

Fig. 32 The PDOP of GPS, BDS, BDS/GPS

Conclusions are obtained as follows by comparisons of the experiments results of 0.05, 5, 10, 15 km:

1. For the 0.05 km short baseline, the experimental results of GPS, BDS, and GPS/BDS were the same in both A and B experiments, the double difference could eliminate the ionospheric residuals as far as possible: In terms of baseline vector precision, the maximum error of E and N direction was about 3 cm and U direction error was poor, about 5 cm; The success rate were all above 97.

2. Comparing the mean ADOP of daytime and night of Table 3, ① Most of the night ADOP value was less than the corresponding system day ADOP value, but it was not much difference. ② The ADOP values of different baseline lengths of the same system had no obvious regularity. ③ ADOP values of the combined systems at daytime and at night were more stable than those of a single system.
3. Comparing the 5, 10, 15 km results of daytime, at the aspect of success rate, the longer the baseline length was, the lower the ambiguity fixed success rate was and the order of success rates from large to small was BDS/GPS, BDS, GPS. In terms of baseline vector precision, the longer the baseline was, the lower the baseline vector precision was and the highest precision of the baseline vector was BDS/GPS, the GPS and BDS similar, but all reach the centimeter-level precision.
4. Comparing the 5, 10, 15 km results of the night, at the aspect of success rate, the longer the baseline length was, the lower the ambiguity fixed success rate was, the order of success rates from large to small was BDS/GPS, BDS, GPS, and among them the success rate of BDS/GPS was more stable, whose success rate were all higher than 99%. In terms of baseline vector precision, the longer the baseline was, the lower the baseline vector precision was and the highest precision of the baseline vector was BDS/GPS, the GPS and BDS similar, but all reach the centimeter-level precision.
5. Comparing the 5, 10, 15 km results of the day and night, at the aspect of success rate, the success rate of the night was much higher than the day on the whole. In terms of baseline vector precision, the baseline vector precisions of the night were much higher than those of the day, due to the small impact of the ionosphere at night.
6. From the experimental results of the daytime, in the daytime, the length of baseline was not more than 15 km that the single frequency-single epoch ambiguity resolution could be carried out for BDS/GPS. In the daytime, the length of baseline was not more than 10 km that the single frequency-single epoch ambiguity resolution could be carried out for BDS. In the daytime, the length of baseline was not more than 5 km that the single frequency-single epoch ambiguity resolution could be carried out for GPS.
7. From the experimental results of the night, at night, the length of baseline was more than 15 km that the single frequency-single epoch ambiguity resolution could be carried out for BDS/GPS. At night, the length of baseline was more than 10 km that the single frequency-single epoch ambiguity resolution could be carried out for BDS. At night, the length of baseline was not more than 5 km that the single frequency- single epoch ambiguity resolution could be carried out for GPS.

In summary, to evaluate the performance of single frequency-single epoch ambiguity resolution from the perspectives of ambiguity fixed success rate and baseline vector precision, for Asia Pacific Region, we can get the conclusion: (1) BDS single frequency-single ambiguity resolution performance is far better than GPS and GPS/BDS is much better than single system. (2) The ambiguity resolution

performance of single frequency-single epoch at night is much better than that of daytime, due to the small impact of the ionosphere at night.

So, BDS constellation is better at aspect of ambiguity resolution performance of single frequency-single epoch, and we believe, with the development of BDS, the ambiguity resolution performance of single frequency-single epoch will be further improved, which will promote the popularity of single frequency single epoch navigation and positioning applications.

Acknowledgements The authors are grateful for the support of the National Natural Science Foundation of China (NO. 41504032), the Natural Science Foundation of Jiangsu Province (NO. BK20150175) and the Priority Academic Program Development of Jiangsu Higher Education Institutions (PAPD).

References

1. Deng C, Tang W, Liu J et al (2014) Reliable single-epoch ambiguity resolution for short baselines using combined GPS/BeiDou system. GPS Solutions 18(3):375–386
2. Dai Wujiao ZJ, Xiaoli D et al (2007) Single epoch ambiguity resolution in structure monitoring using GPS. Geomatics Inf Sci Wuhan Univ 32(3):234–238
3. Gao X, Guo J, Cheng P (2012) Fusion positioning of BeiDou/GPS based on spatio temporal system unification. Acta Geodaet Cartographica Sin 41(5):743–748
4. Huang S, Xie T (2009) A GPS dynamic single epoch orientation algorithm with single-frequency receivers and its data analysis. GNSS World China 34(4):52–55
5. Li Bofeng, Shen Yunzhong (2009) Fast GPS ambiguity resolution constraint to available conditions. Geomatics Inf Sci Wuhan Univ 34(1):117–121
6. Odijk D, Teunissen PJG (2007) Sensitivity of adop to changes in the single-baseline GNSS model. Artif Satellites 42(2):71–96
7. Odijk D, Teunissen PJG (2008) ADOP in closed form for a hierarchy of multi-frequency single-baseline GNSS models. J Geodesy 82(8):473–492
8. Odolinski R, Teunissen PJG (2016) Single-frequency, dual-GNSS versus dual-frequency, single-GNSS: a low-cost and high-grade receivers GPS-BDS RTK analysis. J Geodesy, 1–24
9. Odolinski R, Teunissen PJ, Odijk D (2015) Combined BDS, Galileo, QZSS and GPS single-frequency RTK. GPS Solutions 19(1):151–163
10. Tang W, Li Di CF (2013) Research on single epoch orientation algorithm of BeiDou navigation satellite system. Geomatics Inf Sci Wuhan Univ 38(9):1014–1017
11. Teunissen PJG (1994) The least-squares ambiguity decorrelation adjustment: a method for fast GPS integer ambiguity estimation. J Geodesy 70:65–82
12. Xiong Y, Huang D, Zhang Xianzhou (2001) A reliable GPS single epoch processing algorithm with known deformation interval constraints. Geomatics Inf Sci Wuhan Univ 26(1):51–57
13. Yang Y, Li J, Wang A et al (2014) Preliminary assessment of the navigation and positioning performance of BeiDou regional navigation satellite system. Sci China Earth Sci 44(1):72–81
14. Zhu H, Gao X, Mi Jinzhong et al (2011) An algorithm of GPS ambiguity resolution on single-epoch. Sci Surveying Mapp 36(4):9–11

The Wide- and Local-Area Combined GNSS Real-Time Precise Positioning Service System and Products

ZhiQiang Dai, Qile Zhao, Yifei Lv, Jia Song, Jinning Zhou, Sheng Yang and Mingze Gu

Abstract With the development of Global Navigation Satellite System (GNSS), Multi-GNSS combined real-time precision positioning has become the current trend of GNSS application. Though every navigation system can provide the Standard Point Positioning (SPP) service, it is limited to the low precise navigation because of the low accuracy. The external precise orbit and clock correction is necessary to improve the positioning accuracy. Based on the super-fast precise orbit product of Wuhan University, we estimate the precise orbit and clock correction for GPS, GLONASS, BDS and Galileo system, which can support the wide-area precise positioning. For the local-area users, the real-time service system can provide the FCB and tropospheric and ionospheric delay correction model. All these products are encoded and broadcasted to the precise positioning users via Internet. Users can use these real-time products to correct the orbit and clock error of broadcast ephemeris to improve the SPP precision effectively, or carry out the regular real-time PPP positioning. Meanwhile, given the FCB and atmospheric delay correction products, users can also carry out the PPP-RTK positioning.

Keywords GNSS · BDS · Real-time precise positioning · Augmentation system · Wide area · Local area

1 Introduction

GNSS navigation and positioning technology and theory have experienced a comprehensive and rapid development. On the one hand, the navigation satellite system has evolved from the early GPS and GLONASS to the current GPS, GLONASS, Galileo and BDS four systems, from the traditional double-frequency

Z. Dai (✉)
School of Geodesy and Geomatics, Wuhan University, Wuhan 430079, China
e-mail: dzq@whu.edu.cn

Q. Zhao · Y. Lv · J. Song · J. Zhou · S. Yang · M. Gu
GNSS Research Center, Wuhan University, Wuhan 430079, China

J. Sun et al. (eds.), *China Satellite Navigation Conference (CSNC) 2017 Proceedings: Volume III*, Lecture Notes in Electrical Engineering 439,
DOI 10.1007/978-981-10-4594-3_34

signal to the present three-frequency and multi-frequency signals, from a single MEO constellation to the present GEO, IGSO and MEO hybrid constellations; on the other hand, navigation and positioning algorithms and data processing theory have evolved from the original post-processing to real-time processing, differential processing to single-station processing, low precision to high precision, single-system processing to multi-system combination processing development. Multi-navigation system, multi-frequency navigation signal, multi-observation type and real-time high-precision application are the development trends of modern GNSS technology and theory.

All of various applications and data processing mode using GNSS to navigation guiding and positioning except Standard Point Positioning (SPP), need provide supplementary information besides observation and broadcast ephemeris. For example, Precise Point Positioning (PPP) requires precise orbit and clock error products, real-time GPS (Real-Time DGPS, RTD; Real-time Kinematic, RTK) needs observation of differential reference station, NRTK (net-RTK) asks for observation error from net references or virtual reference station, and QADGPS (wide-area differential) requires differential correction provided by reference stations. In other words, GNSS real-time precise positioning all need support from extern supplementary system or information, from observations of one reference station to precise positioning product provided by net reference, and the more precise the application is, the more precise extern information will be required.

Real-time precision positioning of GNSS requires the support of many real-time products generated by ground reference station networks, including a series of real-time precision data processing such as GNSS navigation satellite orbit determination, satellite hardware delay estimation and atmospheric error modelling. The theory of navigation satellites precise orbit determination has already become mature, and research institutions can provide multi-system ultra-fast orbit product. Real-time clock error estimation has developed a variety of methods, but IGS has not yet provided Beidou, Galileo and other emerging systems real-time clock products, multi-system real-time clock error estimates need to solve the problem of computing efficiency. The research of FCB estimation and PPP ambiguity fix starts late, but it has become more and more mature, forming UPD/FCB and integer clock/decoupling two methods, and they are theoretically equivalent. The wide-area ionosphere is generally modelled using grid or polynomial fitting methods, and IGS and other research institutions have been able to provide global or regional grid models. At present, the traditional RTK or CORS model is still adopted in regional precision atmospheric delay modelling, and a few scholars have studied the modelling research based on PPP mode. Although there are lots of research of real-time precise positioning of data processing theory and methods, only a few real-time precise positioning service systems achieve and integrate these algorithms, such as Trimble's RTX and Fugro's StarFix.

To satisfy demands of multi-system GNSS real-time precise positioning application, this paper proposes a set of real-time precision positioning service system which is compatible with wide area and local area, and realizes the core algorithm of data processing. Based on the multi-scale ground tracking system, the system can generate real-time precise positioning service products such as orbit corrections, satellite FCB, wide-area ionospheric grid model, regional precision troposphere/ionosphere model. The real-time service performance of the system and the product is verified by the analysis of product precision and multiple models of PPP positioning test, which is based on the real measured data.

2 Real-Time Precise Positioning Service System Design

GNSS observing would be affected by several measurement errors, so real-time precise positioning users should consider those errors adequately to resolve precise position. Post-users, who do not make high demand of real-time, can download post-precise products from FTP of IGS or other analytic centres to resolve positions. Meantime, real-time users use Internet or other communication links to get real-time precise orbit/clock product, or acquire real-time satellites DCB to improve real-time positioning quality further. Therefore, real-time precise positioning needs support from various real-time precise products, the product generation involves a series of theories and algorithms, and relative data processing system needs many functional modules to combine and co-process.

Accomplishing wide-/local-area real-time precise system needs a set of real-time precise positioning data processing systems, which includes plenty of estimate modules and functions such as orbit/clock corrections, satellite DCB, atmospheric delay correction and so on. Figure 1 shows the design of wide-/local-area real-time precise system framework. The system consists of real-time data stream, cores processing, real-time products and real-time service, whose function is described in the picture. Among them, core processing part includes three modules: real-time orbit correction and wide-area ionosphere modelling modules estimates real-time precise clock correction of satellites, products orbit/clock correction and wide-area ionosphere model based on global net real-time data stream; real-time FCB estimate module evaluates satellites' phase hardware delay based on wide-area net real-time stream and orbit/clock products; local area atmosphere delay module estimates zenith tropospheric delay and slant ionosphere delay, establish corresponding model based on local-area real-time stream and clock, FCB products. All the core processing products are written into corresponding real-time data system, then system service part select, combine and re-define the real-time products according to users' positioning demand and reference net scale, generate products of corresponding mode, and broadcast for users to real-time positioning in various mode.

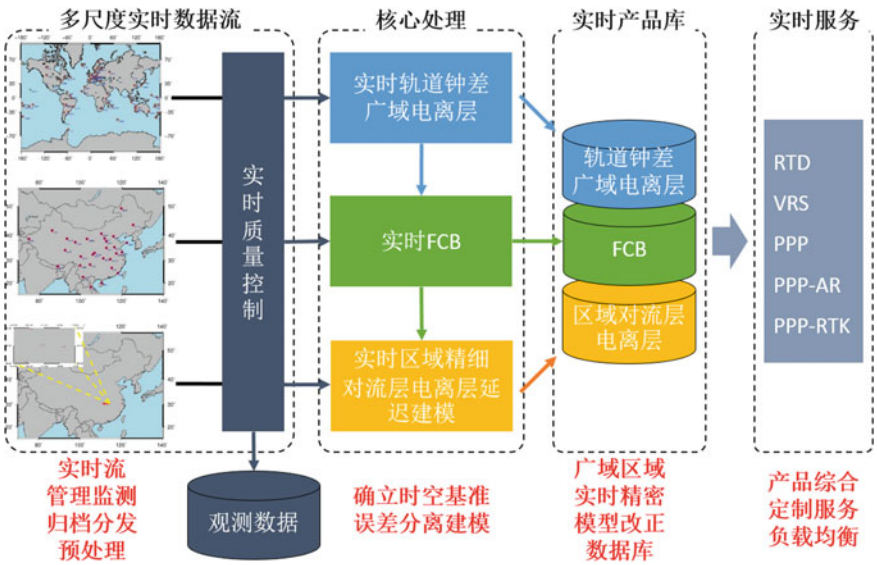

Fig. 1 Wide-area, local real-time precision positioning service architecture

3 Real-Time Precise Positioning Service Products

3.1 Real-Time Precise Clock Correction

Precise orbit and clock product, vital initial data for GNSS data processing, is the spatial and temporal basis for real-time precise positioning and the pre-conditions for precise positioning. So far, the precision of IGS super-fast precast orbit is 5 cm, which is equal to post-product and satisfies real-time demand, but precision of precast clock correction is only 1.5 ns, slightly better than broadcast navigation, which is not up to real-time precise positioning demand, and acquire real-time observations based on ground conference net for real-time estimate. The real-time obit/clock processing module in system is based on multi-system super-fast orbit of Wuhan University, and adopts non-differential dual-thread algorithm to estimate real-time clock product for GPS, GLONASS, BDS and Galileo system. Figure 2 shows the accuracy statistics of real-time clock product, and also shows the clock correction of epoch difference method to compare. According to the picture, the real-time clock correction precisions of GPS, GLONASS, BDS and Galileo system which uses method in this paper, are all better than epoch difference method.

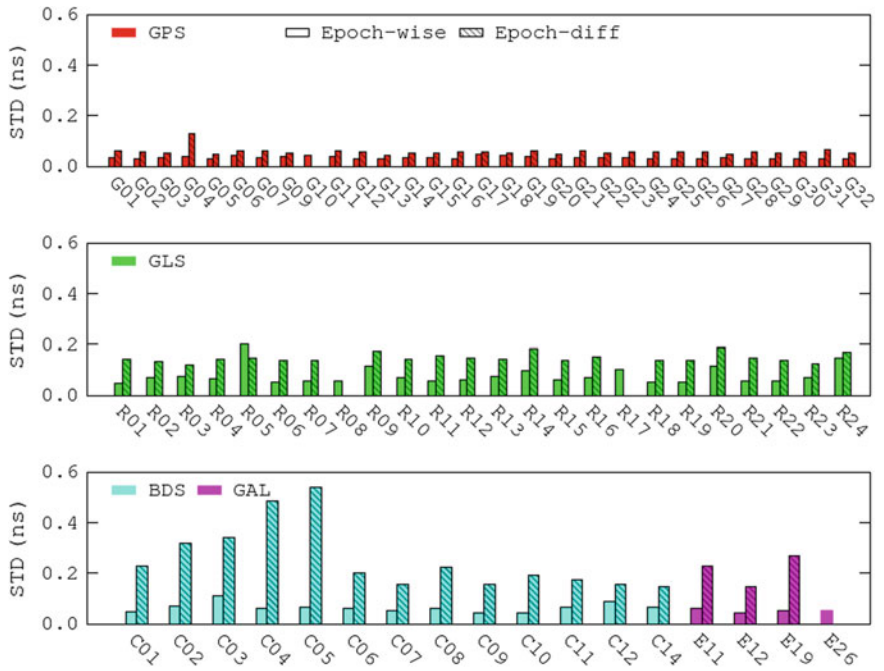

Fig. 2 STD of multi-system real-time clock differential products compared to WUM after-event precision products

3.2 GPS/BDS Satellite Hardware Delay Estimation

Traditional GNSS non-differential data processing does not consider FCB (Fractional Cycle Bias) of phase observations, so the ambiguity parameter is real number and cannot use integer constraint condition to improve position precision. With further development of GNSS data processing theory, new PPP-AR technic is able to achieve non-differential ambiguity fixed based on satellite hardware delay product, thus to improve the positioning result. Satellite hardware delay product is vital to non-differential ambiguity fixed. According to types of final products, FCB estimate methods are divided into two kinds. One is UPD/FCB method which generates UPD/FCB production; the other is decoupled clock/integer clock method, which combines FCB and satellite clock correction and generates phrase clock productions with FCB information to support non-differential ambiguity fixed in user side. Geng et al. have analysed those methods and proved that they are

equivalent [6, 10]. For the observation methods applied, satellite hardware delay estimate can adopt non-differential model, inter-satellite single-difference model and double-difference model. Inter-satellite single-difference model eliminates the effect of receiver hardware delays and needs single station only, so it is most widely used. Non-difference model is similar to inter-satellite single-difference model, but still requires to solve receiver hardware delay; double-difference model select special benchmark for transforming fixed double-difference ambiguity to non-difference/single-difference ambiguity, thus to estimate hardware delay. This paper has achieved non-difference FCB estimate, supports ambiguity observations from various sources and provides real-time FCB products of GPS and BDS satellites. Figure 3 shows FCB time series of GPS and BeiDou IGSO, MEO satellites, which are based on MGEX net.

3.3 Wide-Area Ionosphere Model

In order to improve precision of ionosphere model, usually ionosphere measured models such as CODE global ionosphere grid model are established, which are based on GNSS observations from ground conference net. There are two usual methods to establish measured model, functional basis model and grid model method, both use ionosphere delay observations from ground conference station to fitting. Functional basis model method applies optimal estimation method to fitting a series mathematical function expression which uses time and space as variables, to describe zenith TEC value of arbitrary time and space. Grid model method divided global/local-area ionosphere into equal-interval grid and uses ionosphere delay of grid point as parameters to be estimated. It describes ionosphere delay of any interpolate point as linear combination or nonlinear combination of grid point ionosphere delays, which estimates ionosphere delays of grid points based on plenty of ionosphere delay observations. Wide-area positioning service establishes ionosphere grid model based on real-area net, so that users can interpolate grid to correct ionosphere delay. Figure 4 shows differences between satellites STEC using Chinese area ionosphere grid model and satellites STEC using phrase observations. According to it, we can include that correction precision of local-area ionosphere grid model changes over a wide range. Usually its change is less than ± 5 TECU, sometimes would be large. This ionosphere product can be applied for SPP users to correct and achieve RTD positioning service (Table 1).

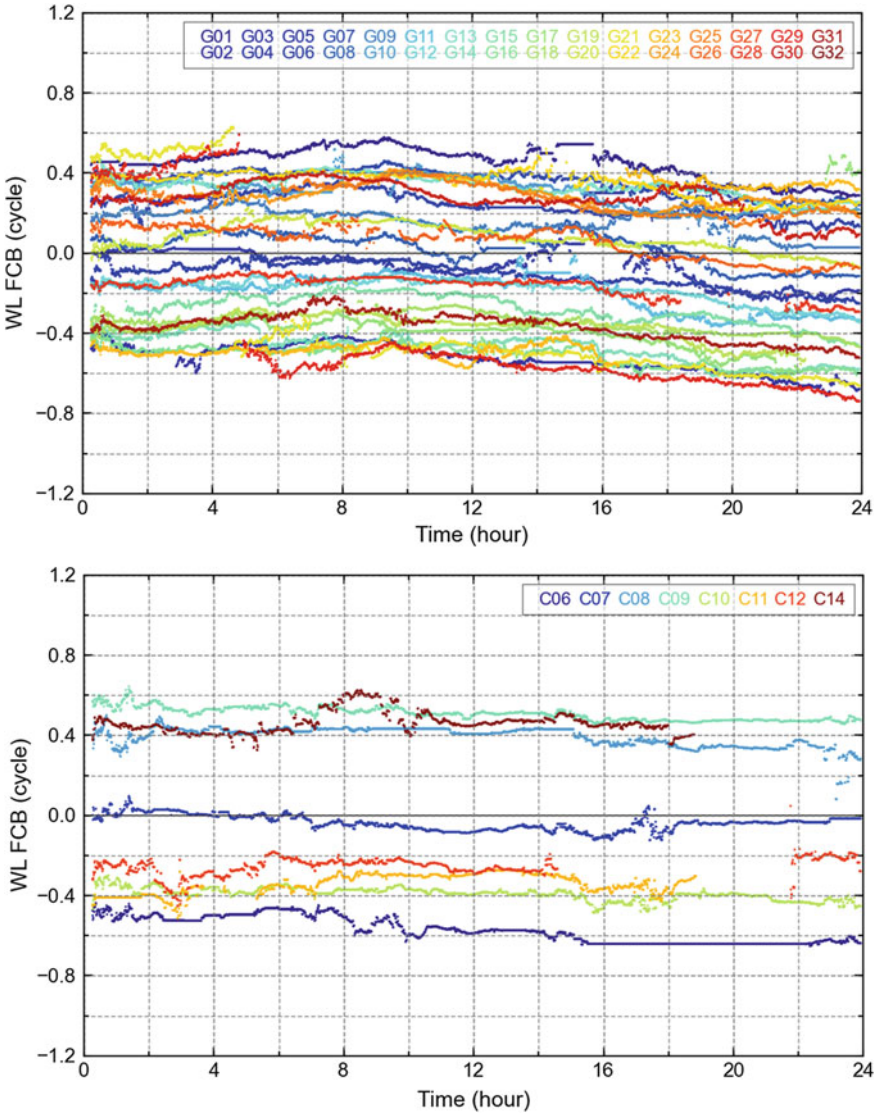

Fig. 3 FCB sequence of wide lane and narrow lane of GPS, IGSO and MEO

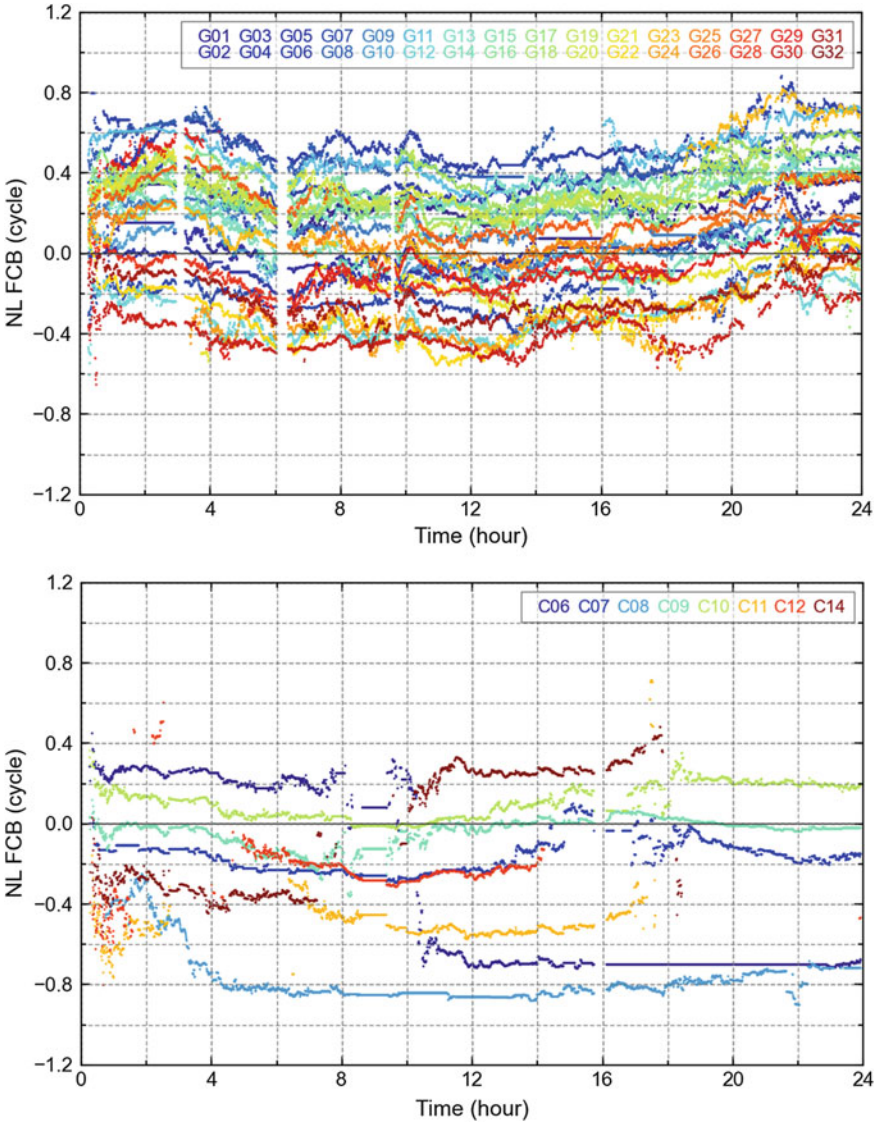

Fig. 3 (continued)

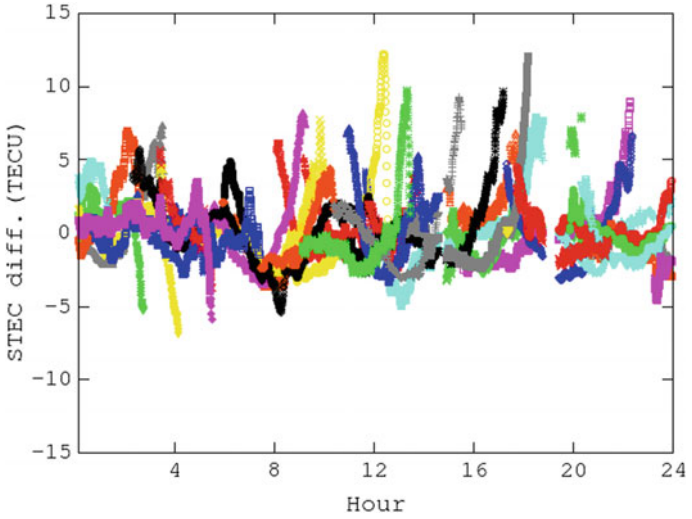

Fig. 4 STEC difference between regional grid ionospheric model and phase observation

Table 1 Accuracy of ionospheric grid based on ground station evaluation (TECU)

HBZG	HLAR	JSYC	NMBT	SDRC	XIAM	XJKE	XZYD
2.50	5.03	2.59	2.46	2.72	5.08	4.45	4.57

3.4 Local-Area Precise Troposphere and Ionosphere Model

During the process of real-time positioning service, in order to get precise troposphere correction of user station, we can use ZTD of PPP real-time estimate conference stations to set troposphere model, then evaluate ZTD correction of user stations by interpolating or fitting. Up to now, troposphere delays estimated in real-time PPP mode have achieved great precision. The station ZTD precision solved in real-time PPP mode is better than 1 cm, is 0.5 cm or so, and its system bias compared to IGS troposphere product is small too, mostly it is between −0.5 and 0.5 cm. Besides, ZTD solved by measured observations can acquire high precisions, has little bias compares to IGS products, and single-day precisions of each stations stay stable. Figure 5 shows distribution of stations which are used for ZTD interpolation in 40 km range local-area CORS network, red for conference station, green for imitating user stations. For accuracy analysis, we differ ZTD interpolation result of each station with PPP estimate result, evaluate RMS of difference, and count accuracy of model results. According to accuracy analysis,

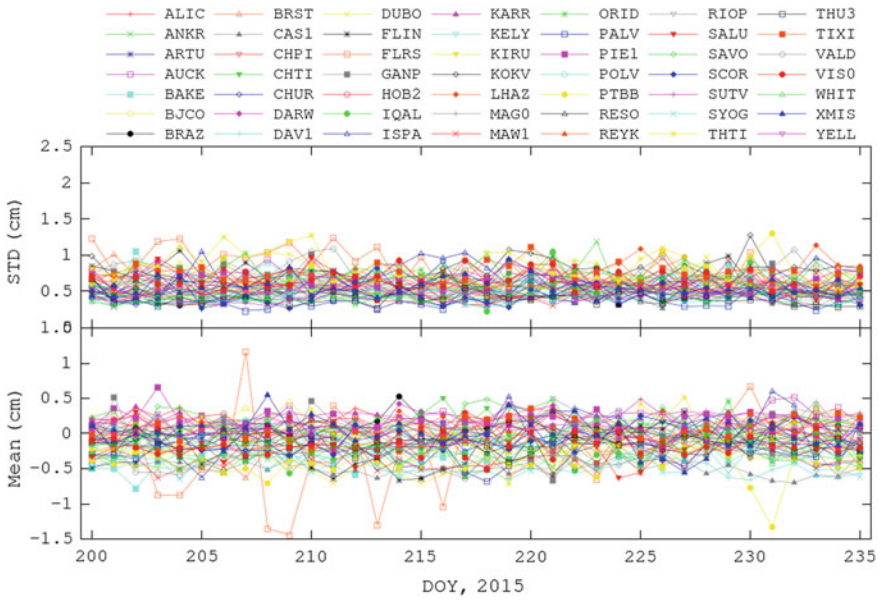

Fig. 5 Differences of IGS stations between IGS tropospheric products and ZTD calculated by PPP filter solution

Table 2 Accuracy statistics of ionospheric interpolation at regional CORS stations

OHAL	OHDT	SIDN
0.042	0.289	0.171

interpolation precision of local-area ZTD is able to reach above 1 cm, which is equal to result that PPP estimates directly, and significantly better than result of troposphere models (Table 2).

Precise positioning users only care for ionosphere delay on the propagation path, and do not care for ionosphere information in other position. In order to avoid projection error of zenith ionosphere delay during the process of model establishing and correcting, and make full use of spatial correlation of neighbouring stations' ionosphere delays, we can use conference stations around user stations to establish slant ionosphere model on propagation path, then count user slant ionosphere delay. Figure 6 shows differences between measured value and interpolation value estimated by slant ionosphere delay of conference station and satellites. The left part is the result of local-area CORS network, the right part is the result of wide area.

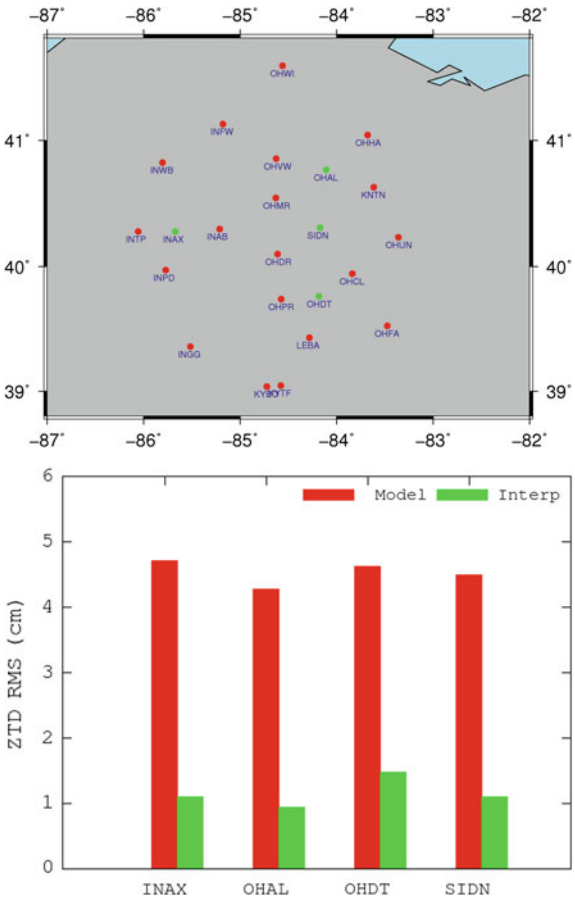

Fig. 6 Distribution of reference stations and Rover stations in regional CORS network and the corresponding ZTD interpolation statistics

According to the picture, user slant ionosphere based on neighbouring conference interpolation matches well to real observations. The difference of local-area network is about 0.2 TECU and the difference of wide-area network is about 0.5 TECU. In conclusion, this method has good adaptability and can be applied to providing precise ionosphere delay correction during real-time data processing (Fig. 7).

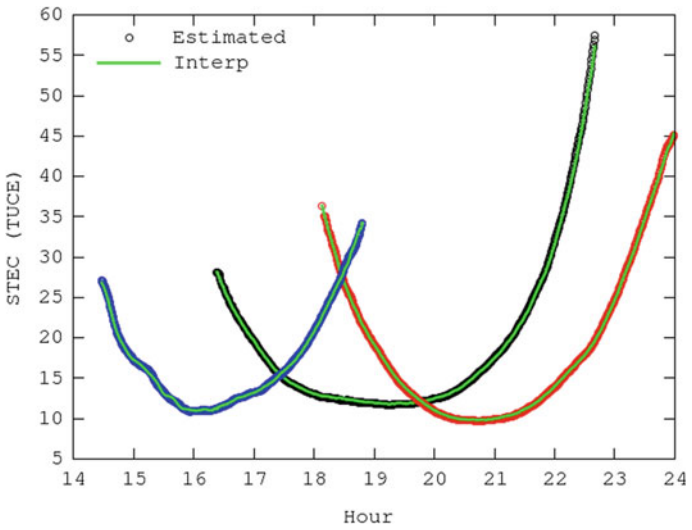

Fig. 7 Comparison of inclined diameter ionosphere and measured values interpolated by regional

4 System Implementation and Verification

As can be seen from Fig. 1, the wide- and local-area real-time precise positioning system introduced in this text is capable of generating several kinds of real-time positioning products, and by making different combinations of these products, we will be able to provide positioning services of multiple patterns. By now, we have preliminarily implemented part of the functionalities of the system and tested them with real experimented products.

4.1 Single-Frequency Pseudo-Range Positioning

The real-time clock correction and atmospheric delay products generated in the text can provide RTD service for users who are doing navigation based on pseudo-range observations. In order to check the service performance of different products, we selected four CMONOC stations of different latitudes and longitudes in China to do positioning experiments. The testing program was developed based on RTKLIB 2.4.3, and Table 3 presents the specific testing schemes.

Table 3 Schemes of performance test of pseudo-range positioning with real-time products

No.	Type	Instruction
A	SPP	Standard point positioning with only pseudo-range observations and broadcast ephemeris
B	SPP + SSR	Precise orbit and clock correction parameters added on the basis of mode A
C	SPP + SSR + ZTD	Tropospheric delay products added on the basis of mode B
D	SPP + SSR + ZTD + ION_GRID	Grid ionospheric products of China area added on the basis of mode C
E	SPP + SSR + ZTD + ION_SLANT	Slant ionospheric delay introduced in the text added on the basis of No. C

Figure 8 is the result of differentiated E/N/U time series between the positioning results of different testing schemes and the real coordinate of station XIAM (left) and the result of the whole stations' mean values of positioning accuracy of multiple days in different testing schemes. By analysing the figure, we reached the following conclusions:

(1) The ionospheric delay is the overriding error source in navigation and positioning based on pseudo-range observations, particularly remarkable in areas of low longitude. If the issue of ionospheric delay is not correctly solved, hardly possible it will be to reach the real-time accuracy of sub-metre in RTD positioning.
(2) Orbit and clock correction parameters given by broadcast ephemeris are the major error sources, too. By adjusting broadcast ephemeris using real-time precise orbit and clock correction products, we improve the accuracy of pseudo-range positioning apparently and improvement remains stable.
(3) The tropospheric delay products do not play an important role in pseudo-range positioning, so we may estimate the tropospheric delay with mathematical model directly in real application.
(4) Area grid ionospheric delay products decrease the positioning error caused by ionospheric delay effectively. However, when the ionosphere reacts actively, the effectiveness is reduced greatly.
(5) The slant-path ionospheric interpolation model proposed in this text further improves the positioning accuracy and the improvement keeps stable relatively. While we provide users with real-time RTD service, it's feasible that we build the grid model of every satellite available in the service area.

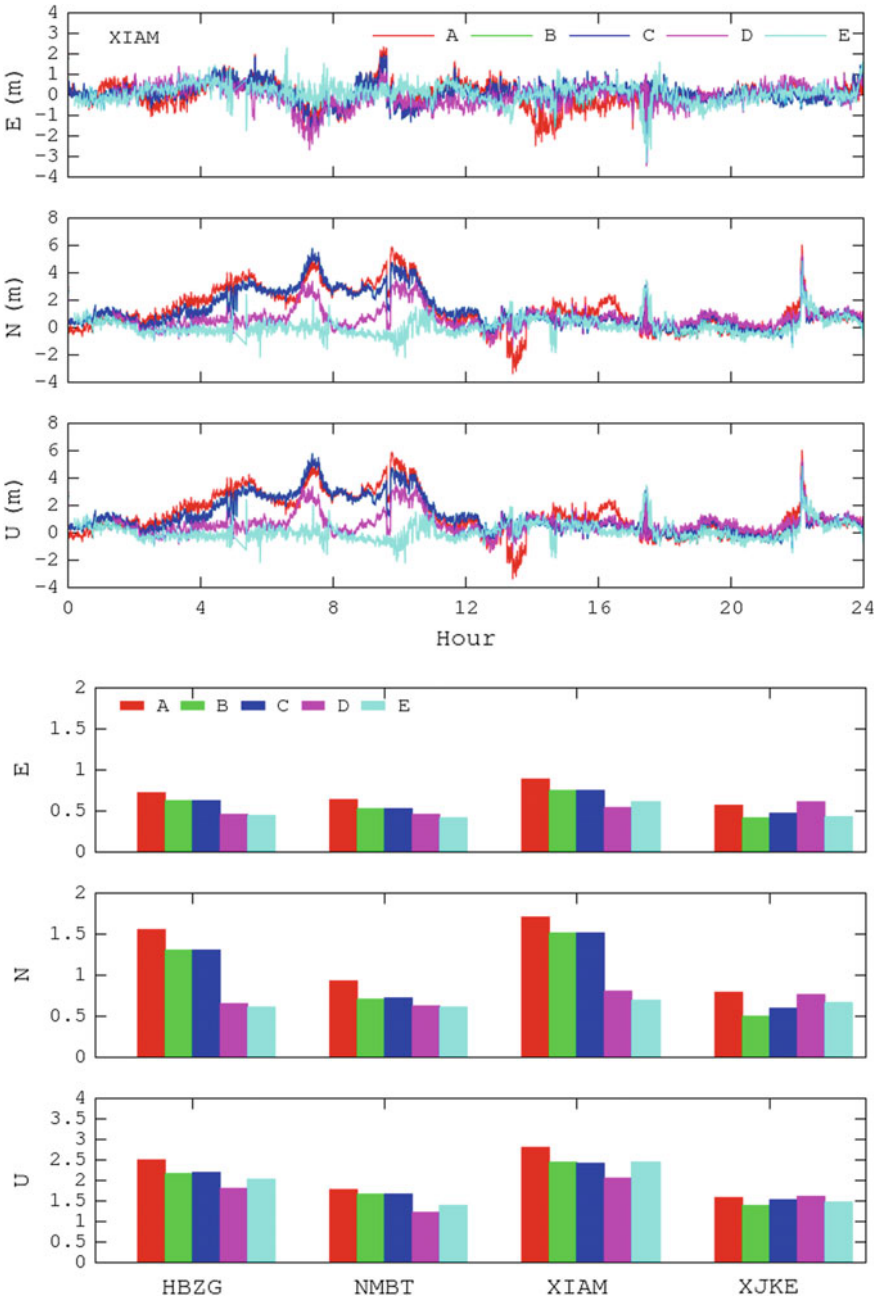

Fig. 8 Mean accuracy of differentiated E/N/U time series between positioning results of different SPP testing schemes and real station coordinate

4.2 Single-Frequency PPP

We estimated zenith tropospheric delay and slant-path ionospheric delay and established the model of regional atmospheric delay correction based on the PPP ambiguity fixing of the reference station. Single-frequency users can do real-time precise positioning with precise regional tropospheric and ionospheric model in order to eliminate atmospheric error as much as possible.

Figure 9 shows the differentiated E/N/U time series between the result of GPS single-frequency real-time PPP and the real coordinates of two CORS stations before and after the atmospheric delay correction was added. As the result shows, after we included the atmospheric delay correction from regional reference stations, there was a remarkable accuracy improvement of single-frequency PPP against traditional U of C method, which can be proved by facts that the noise of E/N/U time series was evidently reduced and that the system converged a lot faster. Statistic results show that the three-dimensional accuracy of the two stations were improved by 57.04 and 47.19%, respectively, clearly verifying that the regional tropospheric and ionospheric products do improve the quality of real-time precise positioning.

4.3 PPP-AR Positioning

Real-time FCB products help users fix the PPP ambiguity, which will improve the positioning accuracy one step further. With the FCB products and the real-time clock correction products generated in this text, we did a user-end PPP ambiguity fixing test. In the test, we calculated the E/N/U time series of static-simulated dynamic positioning with PPP traditional floating point ambiguity solution and PPP ambiguity fixing algorithm, respectively, and Fig. 10 shows the result of the test. By analysing the result, we find out that FCB products can perfectly help fix the ambiguity of GPS and BeiDou dynamic PPP. Compared with the float PPP solution, ambiguity fixing PPP has a more stable and precise E/N/U time series. Ambiguity fixing improves the accuracy of PPP effectively and the result is also a verification of the performance of GPS and BeiDou FCB products in PPP ambiguity fixing.

When the PPP ambiguity fixing is done with the combination of GPS and BeiDou system, the accuracy is promoted more obviously. Figure 11 shows the 30-day average of the accuracy of the float solution of GPS-only dynamic PPP and the fixed solution of the combined GPS/BeiDou dynamic PPP in E, N and U

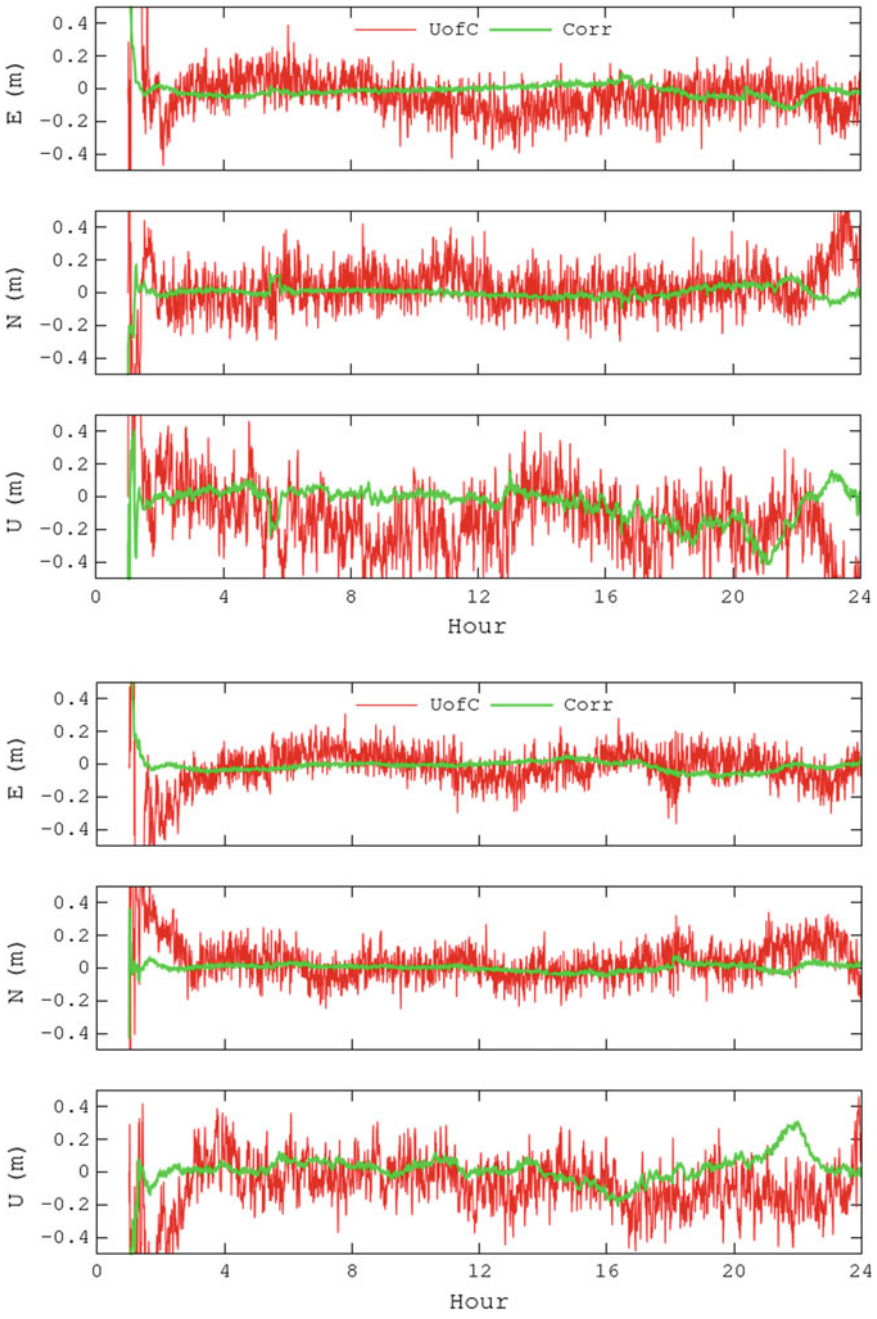

Fig. 9 Differentiated E/N/U time series between the real coordinate and the result of U of C method and between the real coordinate and the result of single-frequency PPP with regional atmospheric delay correction

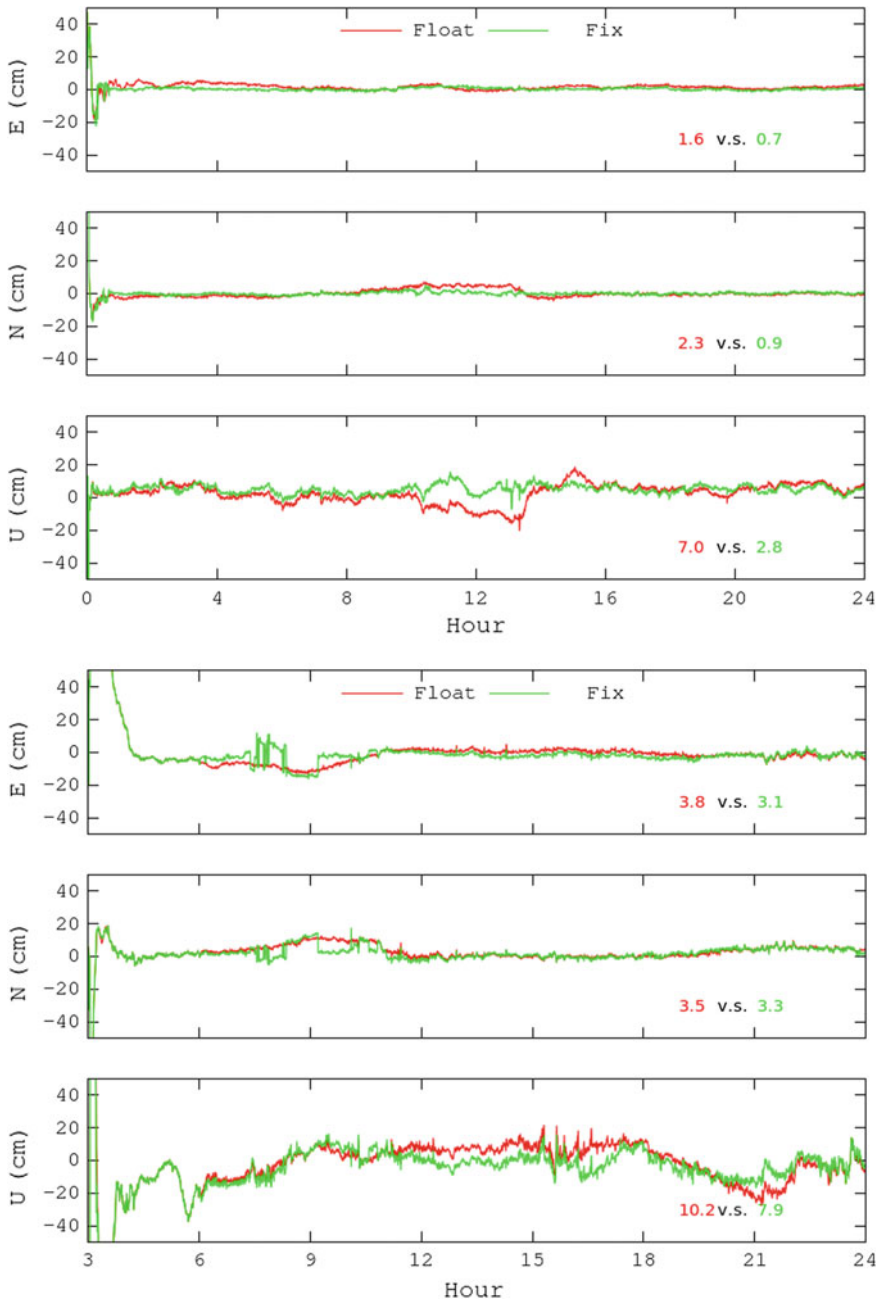

Fig. 10 The E/N/U time series of floating point solution (*red*) and fixed solution (*green*) of GPS and BeiDou dynamic PPP calculation based on FCB products

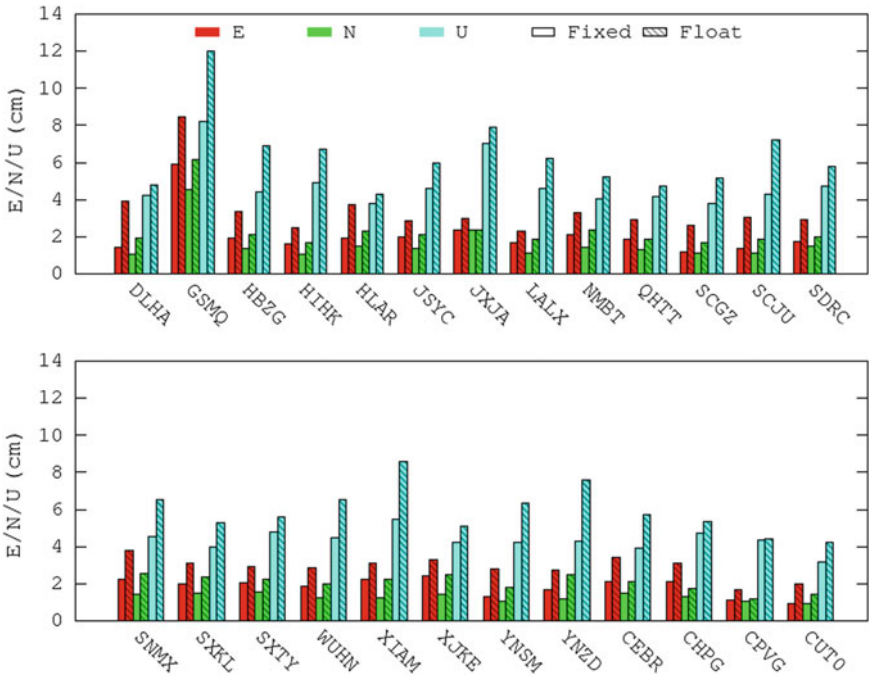

Fig. 11 The accuracy of combined GPS/BeiDou dynamic PPP floating point solution and ambiguity fixed solution in E, N and U directions

directions in some test stations. It can be seen from the figure that the ambiguity fixation in the process of combined GPS/BeiDou dynamic PPP can remarkably improve the accuracy of the PPP floating point solution of single GPS system, and statistics show that the three-dimensional accuracy promotion percentage is 5.21–43.53%, most better than 20%.

5 Conclusion

In this paper, a real-time precise positioning service system with wide area and local area is designed. Based on the real-time observation data of the ground reference network, we did some work including estimation of the real-time orbit and clock correction as well as FCB products, wide-area ionospheric modelling and regional precise modelling of troposphere and ionosphere. The corresponding products include orbit and clock correction, GPS/BeiDou FCB, wide-area grid ionospheric

model and regional precise tropospheric and ionospheric models, and based on these products, we generated different types of real-time positioning service products in reference to the users' designated positioning patterns accuracy demands and finally, a real-time positioning service system compatible with wide and local area was achieved. At present, we have made a preliminary implementation of the above system, and are able to generate the corresponding real-time service products on the basis of ground observation networks of different scales. In this paper, the accuracy of real-time service products is analysed. The accuracy of real-time clock correction of GPS, GLONASS, BDS and Galileo is about 0.1 ns, and the interpolation accuracy of wide-area ionospheric grid model is $\sim$5 TECU. The regional tropospheric and ionospheric interpolation accuracy is 1 cm and $\sim$0.2 TECU, respectively. To test the service performance of different type of products, we did tests of single-frequency pseudo-range positioning, single-frequency PPP, double-frequency PPP and PPP-AR. The results verified the positioning performance of these products in positioning service, proving that the system designed and the products generated in this paper can provide users with precise positioning service effectively.

References

1. Chen X, Allison T, Cao W et al (2011) Trimble RTX, an innovative new approach for network RTK. In: Proceedings of ION GNSS-2011. Portland, OR, pp 2214–2219
2. Collins P (2008) Isolating and estimating undifferenced GPS integer ambiguities. Proceedings of the 2008 national technical meeting of the institute of navigation. San Diego, CA, pp 720–732
3. Dai X, Ge M, Lou Y et al (2015) Estimating the yaw-attitude of BDS IGSO and MEO satellites. J Geod 89:1005–1018. doi:10.1007/s00190-015-0829-x
4. Ge M, Chen J, Douša J et al (2011) Development of the GFZ real-time precise point positioning service. In: EGU2011. Vienna, Austria
5. Ge M, Gendt G, Rothacher M et al (2008) Resolution of GPS carrier-phase ambiguities in precise point positioning (PPP) with daily observations. J Geod 82:389–399. doi:10.1007/s00190-007-0187-4
6. Geng J, Meng X, Dodson AH, Teferle FN (2010) Integer ambiguity resolution in precise point positioning: method comparison. J Geod 84:569–581. doi:10.1007/s00190-010-0399-x
7. Guo J, Xu X, Zhao Q, Liu J (2015) Precise orbit determination for quad-constellation satellites at Wuhan University: strategy, result validation, and comparison. J Geod 90:143–159. doi:10.1007/s00190-015-0862-9
8. Laurichesse D, Mercier F (2007) Integer ambiguity resolution on undifferenced GPS phase measurements and its application to PPP. Proceedings of the 20th international technical meeting of the satellite division of the institute of navigation. Fort Worth, TX, pp 839–848
9. Liu X, Goode M, Tegedor J et al (2015) Real-time multi-constellation precise point positioning with integer ambiguity resolution. In: 2015 International association of institutes of navigation world congress (IAIN), pp 1–7
10. Teunissen PJG, Khodabandeh A (2014) Review and principles of PPP-RTK methods. J Geod 1–24. doi:10.1007/s00190-014-0771-3

11. Zumberge JF, Heflin MB, Jefferson DC et al (1997) Precise point positioning for the efficient and robust analysis of GPS data from large networks. J Geophys Res Solid Earth 102:5005–5017. doi:10.1029/96JB03860
12. Shirong Ye (2002) Theory and its realization of GPS precise point positioning using un-differenced phase observation. Wuhan University, Wuhan
13. Weiwei S (2011) Research on real-time clock offset determination and real-time precise point positioning. Wuhan University, Wuhan
14. Zhenghang L, Jinsong H (2005) GPS surveying and data processing. Wuhan University Press, Wuhan
15. Shengfeng G (2013) Research on the zero-difference un-combined data processing model for multi-frequency GNSS and its application. Wuhan University, Wuhan
16. Xingxing L (2013) Rapid ambiguity resolution in GNSS precise point positioning. Wuhan University, Wuhan

Real-Time Detection and Repair of Cycle Slips in Triple-Frequency BDS Measurements

Huabo Wei, Xiaoqing Zhang, Zhanyu Zhang, Yu Li and Ruifan Pang

Abstract To improve the effectiveness and reliability of cycle slips detection and repair, a real-time algorithm to detect, determine, and validate the cycle slips for triple-frequency BDS is proposed in this study, in which the geometry-free (GF) combination noise residual method and the GF code and phase combination method are utilized. At first, the optimal BDS triple-frequency GF phase combinations are selected. Then the GF code and phase combination method are used to detect all the cycle slips. After the cycle slips are detected, an effective simple round method using the optimal triple-frequency GF code and phase combinations is applied to calculate the cycle slips. The workflow of entire algorithm for cycle slips detection and repair is also designed. Finally, a BDS triple-frequency test is performed to test the proposed algorithm. Results show that the successive mixed small and big cycle slips can be detected and repaired effectively in real time. The 5-min signal unlock time and 1 small cycle slips can be also detected and corrected.

Keywords BDS · Triple frequency · Geometry-free · Cycle slips detection and repair

1 Introduction

The obstructions of the satellite signal with trees, buildings, and low SNR with bad ionospheric conditions, multipath, high receiver dynamics, low satellite elevation and the receiver software can cause cycle slips [1]. Considering the requirement of high accuracy navigation services, a method that can effectively detect and repair single or double receiver jumps in real time is desired. Modern GNSS (i.e., BeiDou Navigation Satellite System (BDS) and GPS) techniques introduce triple-frequency signals that are beneficial for cycle slip detection and repair. Some researchers have been study many methods to detect and repair cycle slips in traditional applications

H. Wei (✉) · X. Zhang · Z. Zhang · Y. Li · R. Pang
China Aeronautical Radio Electronics Research Institute, Shanghai, China
e-mail: wei_huabo@126.com

J. Sun et al. (eds.), *China Satellite Navigation Conference (CSNC) 2017 Proceedings: Volume III*, Lecture Notes in Electrical Engineering 439,
DOI 10.1007/978-981-10-4594-3_35

of double-differenced (DD) navigation and positioning, such as phase differencing over time, Doppler integration, phase-phase ionospheric residuals, phase-code comparisons and triple-difference phase combinations [2–5]. The performance of cycle slips detection and repair using BDS triple-frequency measurement is also presented [6, 7].

However, the triple-frequency GF phase combination and GF code and phase combinations using BDS for cycle slips detect and repair did not provide a detail analysis. The effectiveness and capability of the optimal BDS triple-frequency combinations are also not validated in BDS real data. In this paper, the optimal BDS triple-frequency GF phase combinations are selected. The triple-frequency GF code and phase optimal integer combinations are also given for cycle slips detection and repair. The workflow of the proposed algorithm using the GF combination noise residual method and the GF code and phase combination method is designed. Finally, the BDS experiment is carried out to test some kinds of cycle slips case with the proposed algorithm.

2 BDS Triple-Frequency GF Combination Noise Residual Method

The code and phase observations of BDS can be expressed as:

$$P_i = \rho + c(\mathrm{d}t_r - \mathrm{d}t^s) + T + I_i + \varepsilon_{Pi} \tag{1}$$

$$\Phi_i = \rho + c(\mathrm{d}t_r - \mathrm{d}t^s) + T - I_i + \lambda_i N_i + \varepsilon_{\Phi i} \tag{2}$$

where P_i and Φ_i represent code and phase observation on frequency B_i $(i = 1, 2, 3)$, and ρ is the geometry distance from satellite antenna to receiver antenna, respectively. λ_i and N_i denote the wavelength and ambiguity of the signal on frequency B_i, $\mathrm{d}t_s$, $\mathrm{d}t_r$, I_i, T denote satellite clock error, receiver clock error, ionospheric delay, and tropospheric delay error, respectively,c is light velocity, and ε_{Pi},$\varepsilon_{\Phi i}$ denote code and phase noise, respectively.

Based on the theory of phase combination [8], the triple-frequency phase combination can be expressed as:

$$\begin{aligned}\Phi_{(i,j,k)} &= i\Phi_1 + j\Phi_2 + k\Phi_3 \\ &= (i+j+k)(\rho + c(\mathrm{d}t_r - \mathrm{d}t_s) + T) - \kappa_{(i,j,k)} I_1 \\ &\quad + (i\lambda_1 N_1 + j\lambda_2 N_2 + k\lambda_3 N_3) + \varepsilon_{\Phi_{(i,j,k)}},\end{aligned} \tag{3}$$

where i, j, k is combination scalar, $\varepsilon_{\Phi_{(i,j,k)}} = i\varepsilon_{\Phi 1} + j\varepsilon_{\Phi 2} + k\varepsilon_{\Phi 3}$ is the phase combination noise. $\kappa_{(i,j,k)} = i\lambda_1 + j\lambda_2 f_1/f_2 + k\lambda_3 f_1/f_3$ is ionospheric delay amplification factor. The condition $i + j + k = 0$ cancels the denotes amplification factor of the combination term and the other nondispersive terms, such as the troposphere delay,

satellite orbit bias and clock bias, as well as receiver clock bias. The combination observation is only affected by the ionospheric delay residuals and noise.

The time differenced of (3) can be written as:

$$\Delta\Phi_{(i,j,k)} = -\kappa_{(i,j,k)}\Delta I_1 + (i\lambda_1\Delta N_1 + j\lambda_2\Delta N_2 + k\lambda_3\Delta N_3) + \varepsilon_{\Delta\Phi_{(i,j,k)}}, \tag{4}$$

where Δ denote single-differenced (SD) operator.

For the purpose of simplicity, we assume that the same standard deviations for the phase observations in cycles on any frequency B_i. The standard deviation (STD) of phase combination $\sigma_{(i,j,k)}$ is expressed as:

$$\sigma_{(i,j,k)} = \sqrt{2}\sqrt{(i\lambda_1)^2 + (j\lambda_2)^2 + (k\lambda_3)^2}\sigma_\varphi. \tag{5}$$

An excellent phase combination should reduce the ionospheric error and noise as much as possible [9]. Since it is generally supposed to be a normally distributed error, the following inequality can be used to judge whether cycle slip occurs at the current epoch:

$$|i\lambda_1\Delta N_1 + j\lambda_2\Delta N_2 + k\lambda_3\Delta N_3| > l\sigma_{(i,j,k)}, \tag{6}$$

where l is a coefficient. Usually, we can take 3 (99.7% confidence level) or 4 (99.9% confidence level) as the threshold coefficient of cycle slip. If the condition (6) is satisfied, we conclude that a cycle slip group has occurred. If the condition of (6) is not satisfied, there is no cycle slips, or some special cycle slip groups may cannot be detected by (6) [7, 10, 11].

The ideal GF phase combination for cycle slips detection should satisfy the following equation:

$$\begin{cases} i+j+k=0 \\ i\lambda_1 + j\lambda_2 f_1/f_2 + k\lambda_3 f_1/f_3 = \min \\ \sqrt{(i\lambda_1)^2 + (j\lambda_2)^2 + (k\lambda_3)^2} = \min. \end{cases} \tag{7}$$

The insensitivity GF phase combinations satisfy the following equation:

$$\Delta N_{(i,j,k)} = |i\lambda_1\Delta N_1 + j\lambda_2\Delta N_2 + k\lambda_3\Delta N_3| < l\sigma_{(i,j,k)}. \tag{8}$$

The combination integer coefficient (i, j, k), which should be meet gcd (i, j, k) = 1, can be choose in integer field. So, the cycle slips $\Delta N_{(i,j,k)}$ may be any integer. The between-epoch ionospheric error on a single carrier signal is usually at millimeter level between two close epochs with high data rate, and furthermore, the selected phase combination can guarantee that the combined ionospheric error is ignorable. The number of insensitive cycle slips relies on phase combination noise in cycles and confidence level.

We assume that the noise STD is $\sigma_\varphi = 0.01$ and the confidence level is $l = 4$. To guarantee small ionospheric delay and combination noise, we define $\kappa_{(i,j,k)} < 0.2$ and $\sigma_{(i,j,k)} < 0.02$.The optimal BDS GF phase combinations selected are presented in Table 1. Total 9 combinations satisfy the requirement and number of the insensitive cycle slip groups of those combinations is counted within the range of 0–10 cycles are shown in Table 1.

The smallest cycle slip of size 1 can be detected from the Table 1. Each combination has lots of insensitive cycle slip groups. The dual frequency ionospheric residual combinations are also contained in Table 1. The ionospheric scale factor of the combination (1, 3, −4), (1, 2, −3), (0, 1, −1) is less than 0.01, which can detect small cycle slips with large variation ionosphric delay. The combination noise of the (0, 1, −1), (1, 0, −1), (1, 1, −2) is much small than the other combinations.

Because of lots of insensitivity cycle slips groups, the single GF phase combination cannot detect all cycle slips. Due to $i + j + k = 0$, only two different combinations can utilize to offset insensitivity cycle slips each other.

Any two combinations in Table 1 are selected to yield 36 unite combinations, which are given in Table 2. The numbers of the most insensitive cycle slip groups ranging from [0, 0, 1] to [10, 10, 10] and from [0, 0, 1] to [100, 100, 100] of the combinations are also counted and analyzed, respectively. Table 2 shows that the smaller cycle slips ranging [0, 0, 1] to [10, 10, 10] cycles can be detected by most of the unite combinations. But every unite combination has several insensitive cycle slip groups within the range cycles. Therefore, it is crucial to choose optimal unite combination to detect cycle slips. Any combination is united with (1, −1, 0), (1, −2, 1) and (1, −3, 2) has better capability for cycle slips detection. It also could be found that the BDS GF combination noise residual method just applies to small cycle slip.

To analyze of the 36 unity combinations, all insensitive cycle slip groups ranging from [0, 0, 0] to [100, 100, 100] cycles are summarized in Table 3, expect for the unity combinations with more than 4 insensitive groups.

Table 1 BDS optimal triple-frequency GF phase combinations and characteristic

No.	(i, j, k)	$\kappa_{(i,j,k)}$	$\sigma_{(i,j,k)}$	Insensitivity No.
1	(0, 1,−1)	0.030329	0.004848	21
2	(1, −3, 2)	−0.18979	0.01277	16
3	(1, −2, 1)	−0.15946	0.008239	13
4	(1, −1, 0)	−0.12913	0.00444	21
5	(1, 0, −1)	−0.0988	0.004307	21
6	(1, 1, −2)	−0.06847	0.008025	16
7	(1, 2, −3)	−0.03814	0.01254	15
8	(1, 3, −4)	−0.00781	0.017237	17
9	(2, 1, −3)	−0.16727	0.011932	15

Table 2 BDS optimal triple-frequency GF phase unity combinations and characteristic

Combination	<10	<100	Combination	<10	<100	Combination	<10	<100
(0, 1,−1) (1, −3, 2)	0	4	(1, −3, 2) (1, 3, −4)	0	2	(1, −1, 0) (1, 3, −4)	0	1
(0, 1, −1) (1, −2, 1)	0	3	(1, −3, 2) (2, 1, −3)	0	1	(1, −1, 0) (2, 1, −3)	0	1
(0, 1, −1) (1, −1, 0)	0	1	(1, −2, 1) (1, −1, 0)	0	2	(1, 0, −1) (1, 1, −2)	0	4
(0, 1, −1) (1, 0, −1)	0	2	(1, −2, 1) (1, 0, −1)	0	1	(1, 0, −1) (1, 2, −3)	0	2
(0, 1, −1) (1, 1, −2)	0	2	(1, −2, 1) (1, 1, −2)	0	1	(1, 0, −1) (1, 3, −4)	0	2
(0, 1, −1) (1, 2, −3)	1	4	(1, −3, 2) (1, 2, −3)	0	2	(1, 0, −1) (2, 1, −3)	0	6
(0, 1, −1) (1, 3, −4)	1	7	(1, −2, 1) (1, 2, −3)	0	2	(1, 1, −2) (1, 2, −3)	0	8
(0, 1, −1) (2, 1, −3)	0	2	(1, −2, 1) (1, 3, −4)	0	2	(1, 1, −2) (1, 3, −4)	0	6
(1, −3, 2) (1, −2, 1)	1	11	(1, −2, 1) (2, 1, −3)	0	1	(1, 1, −2) (2, 1, −3)	1	10
(1, −3, 2) (1, −1, 0)	0	2	(1, −1, 0) (1, 0, 1)	0	2	(1, 2, −3) (1, 3, −4)	2	26
(1, −3, 2) (1, 0, −1)	0	2	(1, −1, 0) (1, 1, −2)	0	1	(1, 2, −3) (2, 1, −3)	0	4
(1, −3, 2) (1, 1, −2)	0	1	(1, −1, 0) (1, 2, −3)	0	1	(1, 3, −4) (2, 1, −3)	0	4

Table 3 The insensitive cycle slip groups of BDS triple-frequency GF phase unity combinations

Combination	Insensitive cycle slips	Combination	Insensitive cycle slips
(0, 1, −1) (1, −3, 2)	[26, 20, 21] [49, 38, 40] [52, 40, 42] [75, 58, 61]	(0, 1, −1) (1, 2, −3)	[1, 1, 1] [26, 20 21] [27, 21, 22] [75, 58, 61]
(1, 3, −4) (2, 1, −3)	[27, 21, 22] [54, 42, 44] [74, 57, 60] [75, 58, 61]	(1, 2, −3) (2, 1, −3)	[27, 21, 22] [54, 42, 44] [74, 57, 60] [75, 58, 61]
(0, 1, −1) (1, −2, 1)	[26, 20, 21] [49, 38, 40] [75, 58, 61]	(1, 0, −1) (1, 1, −2)	[21, 16, 17] [27, 21, 22] [48, 37, 39] [75, 58, 61]
(0, 1, −1) (1, 0, −1)	[27, 21, 22] [75, 58, 61]	(1, −1, 0) (1, 0, −1)	[53, 41, 43] [75, 58, 61]
(0, 1, −1) (1, 1, −2)	[27, 21, 22] [75, 58, 61]	(1, 0, −1) (1, 3, −4)	[27, 21, 22] [75, 58, 61]
(0, 1, −1) (2, 1, −3)	[27, 21, 22] [75, 58, 61]	(1, −2, 1) (1, 3, −4)	[26, 20, 21] [75, 58, 61]
(1, −3, 2) (1, 0, −1)	[53, 41, 43] [75, 58, 61]	(1, 0, −1) (1, 2, −3)	[27, 21, 22] [75, 58, 61]
(1, −3, 2) (1, 3, −4)	[26, 20, 21] [75, 58, 61]	(1, −3, 2) (1, −1, 0)	[53, 41, 43] [75, 58, 61]
(1, −2, 1) (1, −1, 0)	[53, 41, 43] [75, 58, 61]	(1, −2, 1) (1, 2, −3)	[26, 20, 21] [75, 58, 61]
(1, −2, 1) (1, 0, −1)	[53, 41, 43] [75, 58, 61]	(1, −3, 2) (1, 2, −3)	[26, 20, 21] [75, 58, 61]
(1, −3, 2) (1, 1, −2)	[75, 58, 61]	(1, −1, 0) (2, 1, −3)	[75, 58, 61]
(1, −3, 2) (2, 1, −3)	[75, 58, 61]	(1, −1, 0) (1, 3, −4)	[75, 58, 61]
(0, 1, −1) (1, −1, 0)	[75, 58, 61]	(1, −2, 1) (2, 1, −3)	[75, 58, 61]
(1, −2, 1) (1, 1, −2)	[75, 58, 61]	(1, −1, 0) (1, 2, −3)	[75, 58, 61]
(1, −1, 0) (1, 1, −2)	[75, 58, 61]	–	–

Table 3 shows that the [75, 58, 61] exists in all unity combinations. Within 20 cycle slips groups can be detected by this BDS GF phase combination method.

3 BDS Triple-Frequency GF Code and Phase Combination Method

The triple-frequency phase observation can be expressed in cycle as [12]:

$$\varphi_{(i,j,k)} = i\varphi_1 + j\varphi_2 + k\varphi_3, \tag{9}$$

where i, j, k are the phase combination scalars $(i, j, k \in N)$. Similarly, the triple-frequency code and phase observation can be written in meters as [13]:

$$\Phi_{(i,j,k)} = \varphi_{(i,j,k)}\lambda_{(i,j,k)} = \rho + c(\mathrm{d}t_r - \mathrm{d}t_s) + \lambda_{(i,j,k)}N_{(i,j,k)} + T - \kappa_{(i,j,k)}I_1 + \varepsilon_{\Phi_{(i,j,k)}} \tag{10}$$

$$P_{(i,j,k)} = \rho + c(\mathrm{d}t_r - \mathrm{d}t_s) + T + \beta_{(i,j,k)}I_1 + \varepsilon_{P_{(i,j,k)}}, \tag{11}$$

where $N_{(i,j,k)} = iN_1 + jN_2 + kN_3$ is combination integer ambiguity, $f_{(i,j,k)} = if_1 + jf_2 + kf_3$ is combination frequency, $\lambda_{(i,j,k)} = c/f_{(i,j,k)}$ is wave length.

The ionospheric amplification $\kappa_{(i,j,k)}$ of the combination can be expressed as:

$$\kappa_{(i,j,k)} = \left(\frac{i}{f_1} + \frac{j}{f_2} + \frac{k}{f_3}\right)\frac{f_1^2}{f_{(i,j,k)}}. \tag{12}$$

We assume that the same STD for the phase observables on all three frequencies expressed in cycles and the same STD σ_P of the code observables on all three frequencies. Then, combination code and phase observation noise can be expressed in meter as:

$$\sigma_{\Phi_{(i,j,k)}}[m] = \sqrt{i^2 + j^2 + k^2}\lambda_{(i,j,k)}\sigma_\varphi \tag{13}$$

$$\sigma_{P_{(i,j,k)}}[m] = \sqrt{(if_1)^2 + (jf_2)^2 + (kf_3)^2}\sigma_P/(if_1 + jf_2 + kf_3). \tag{14}$$

By subtracting SD Eq. (11) with SD Eq. (10), one obtains an explicit solution for any code combination (a, b, c):*e goes here*

$$\Delta\hat{N}_{(i,j,k)} = \frac{\Delta\Phi_{(i,j,k)} - \Delta P_{(a,b,c)}}{\lambda_{(i,j,k)}} - \frac{\kappa_{(i,j,k)} + \kappa_{(a,b,c)}}{\lambda_{(i,j,k)}}\Delta I_1 + \frac{\Delta\varepsilon_{\Phi_{(i,j,k)}} - \Delta\varepsilon_{P_{(a,b,c)}}}{\lambda_{(i,j,k)}}. \tag{15}$$

The STD of $\Delta\hat{N}_{(i,j,k)}$ can be expressed as:

$$\sigma_{\Delta\hat{N}_{(i,j,k)}} = \sqrt{2}\sqrt{(i^2 + j^2 + k^2)\cdot\sigma_{e_\varphi}^2 + \sigma_{P_{(a,b,c)}}^2/\lambda_{(i,j,k)}^2}. \tag{16}$$

Since the environment delays usually vary slowly in interval time. If the wavelength is long enough, Eq. (16) can be used to detect the cycle slip. If the $\left|\Delta\hat{N}_{(i,j,k)}\right|$ satisfy the following equation, we can conclude that a cycle slips group arises on this satellite.

$$\left|\Delta\hat{N}_{(i,j,k)}\right| = \left|\Delta\Phi_{(i,j,k)} - \Delta P_{(a,b,c)}/\lambda_{(i,j,k)}\right| > l\sigma_{\Delta\hat{N}_{(i,j,k)}}, \tag{17}$$

where l is a coefficient. Usually, we can take 3 (99.7% confidence level) or 4 (99.9% confidence level) as the threshold coefficient of cycle slip.

Assuming that the $\Delta\hat{N}_{(i,j,k)} \in N\left(\Delta N_{(i,j,k)}, \sigma^2_{\Delta\hat{N}_{(i,j,k)}}\right)$ fits normally distributed. The integer cycle slip can be given as [14]:

$$\Delta\breve{N}_{(i,j,k)} = \text{round}\left[\Delta\hat{N}_{(i,j,k)}\right]. \tag{18}$$

The smaller STD of $\Delta\hat{N}_{(i,j,k)}$, the higher success rate to repair cycle slip is obtained. When $\sigma_{\Delta\hat{N}_{(i,j,k)}}$ less than 0.25 cycles, the success rate is greater than 95.5%. When $\sigma_{\Delta\hat{N}_{(i,j,k)}}$ less than 0.2 cycles, the success rate is greater than 98.8%. When $\sigma_{\Delta\hat{N}_{(i,j,k)}}$ less than 0.1 cycles, the success rate is greater than 99.9%.

To reduce the combination ionospheric error, code and phase noise error, the optimal code combinations (a, b, c) and phase combinations (i, j, k) should be searched, see [15, 16], and the code combinations need to satisfy the following principle :

$$\begin{cases} \left|\frac{\kappa_{(i,j,k)} + \kappa_{(a,b,c)}}{\lambda_{(i,j,k)}}\right| = \tilde{\kappa}_{(i,j,k)} = \min \\ a^2 + b^2 + c^2 = \min \end{cases}. \tag{19}$$

We assume that the phase noise of BDS is $\sigma_\varphi = 0.01$ cycles and the code noise of BDS is $\sigma_P = 0.3\,m$. Some optimal combinations are listed in Table 4.

Table 4 shows that the phase combination has big effect on ionospheric scale factor. The phase combinations with $i + j + k = 0$ has best capability for cycle slip detection and repair, which not only has small combination noise but tolerates larger change ionospheric delay in interval time. When the phase combinations are $i + j + k = 1$, the combination noise less than 0.2, which can detect and correct cycle slips with high success rate. But the ionospheric scale factor of those combinations nears to 12. Because three independent combinations are required, two combinations can be chose in $i + j + k = 0$ and the other one is selected in $i + j + k = 1$ set.

Although the combinations with $i + j + k = 0$ have same performance, we suggest selecting long wavelength combinations to control the effect by code noise and multipath error, such as [(0, −1, 1), (0, 1, 1)], [(−1, −5, 6), (1, 1, 1)]. Due to the

Table 4 BDS optimal triple-frequency GF code and phase combinations and characteristic

$i+j+k$	Phase			Code			$\tilde{\kappa}_{(i,j,k)}$	Combination noise	Wave length
	i	j	k	a	b	c			
0	−1	−5	6	1	1	1	−0.3631	0.079	20.932
				−8	7	4	0.0022	0.2339	
	−1	−6	7	7	10	9	−0.3964	0.1025	3.96
	0	−1	1	0	1	1	0	0.0457	4.884
				3	4	4	−0.0389	0.0382	
	1	4	−5	1	1	1	0.3163	0.0703	6.371
				10	−10	1	0.0156	0.2042	
	1	3	−4	9	−6	2	2.1707e-04	0.1928	2.765
				4	5	5	0.2804	0.0808	
	1	2	−3	5	6	6	0.2368	0.105	1.765
				7	−2	2	8.0512e-4	0.1804	
	1	0	−1	6	2	3	−8.5242e-04	0.1958	1.0247
	1	−1	0	10	7	5	0.0014	0.2177	0.8470
1	−4	1	4	5	6	5	11.7078	0.0613	8.1403
	−3	6	−2	1	1	1	12.069	0.071	13.321
	−5	−4	10	9	10	9	11.3443	0.1224	5.861
	−2	10	−7	1	1	1	12.385	0.13	4.31
	−3	5	−1	1	1	1	12.022	0.077	3.574
	−4	0	5	3	4	4	11.6715	0.0856	3.053
	−3	4	0	3	4	4	11.9939	0.0977	2.064
	−4	−1	6	4	5	5	11.6284	0.1175	1.879
	−3	3	1	4	5	5	11.9424	0.1271	1.451

same ionospheric scale factor for the combinations with $i + j + k = 1$, we chose the combination [(−3, 6, 2), (1, 1, 1)], which has largest wavelength and small STD.

For the combination [(0, −1, 1), (0, 1, 1)], the ionospheric scale factor and the STD are $\tilde{\kappa}_{(i,j,k)} = 0$ and $\sigma_{\hat{N}_{(i,j,k)}} = 0.046$, respectively. The success rate is more than 99.9%, and this combination is insensitive to the ionospheric error. The ionospheric scale factor and the STD of [(−1, −5, 6), (1, 1, 1)] are $\tilde{\kappa}_{(i,j,k)} = -0.363$ and $\sigma_{\hat{N}_{(i,j,k)}} = 0.079$, respectively. If the between-epoch ionospheric error is less than 0.3 m on frequency B1, The success rate is more than 98.8%. For the combination [(−3, 6, 2), (1, 1, 1)], the ionospheric scale factor and the STD are $\tilde{\kappa}_{(i,j,k)} = 12.069$ and $\sigma_{\hat{N}_{(i,j,k)}} = 0.071$, respectively. When the between-epoch ionospheric error less than 0.01 m on frequency B1, the success rate is more than 98.8%. Therefore, only the between-epoch ionospheric error less than 0.01 m on frequency B1, the BDS GF code and phase combination can be used to detect and repair cycle slips effectively.

4 The Workflow of the Algorithm for Cycle Sips Detection and Repair

The workflow of the proposed algorithm for cycle slips detection and repair using the selection BDS GF phase combinations and BDS GF code and phase combinations is presented as follows.

Step 1: The BDS GF phase combinations [(0, 1, −1), (1, 0, −1)] and Eq. (4)–(6) are used to detect small cycle slips groups.

Step 2: The BDS phase and code combinations [(0, −1, 1), (0, 1, 1)] with $i + j + k = 0$ are utilized to construct the following model to detect and correct cycle slips in phase combination (0, −1, 1):

$$\Delta N_{(0,-1,1)} = \text{round}\left[\frac{\Delta\Phi_{(0,-1,1)} - \Delta P_{(0,1,1)}}{\lambda_{(0,-1,1)}}\right] \tag{20}$$

Step 3: The BDS phase and code combinations [(−1, −5, 6), (1, 1, 1)] with $i + j + k = 0$ are exploited to construct the following model to detect and correct cycle slips in phase combination [−1, −5, 6]:

$$\Delta N_{(-1,-5,6)} = \text{round}\left[\frac{\Delta\Phi_{(-1,-5,6)} - \Delta P_{(1,1,1)}}{\lambda_{-1,-5,6}}\right] \tag{21}$$

Step 4: The BDS code and phase combination [(−3, 6, 2), (1, 1, 1)] with $i + j + k = 1$ is exploited to construct the following model to detect and correct cycle slips in phase combination(−3, 6, 2):

$$\Delta\hat{N}_{(-3,6,-2)} = \text{round}\left[\frac{\Delta\Phi_{(-3,6,-2)} - \Delta P_{(1,1,1)}}{\lambda_{(-3,6,-2)}}\right] \tag{22}$$

Due to larger ionospheric scale factor, this combination just applied to short lock time and less time differenced ionospheric error.

Step 5: When cycle slips on $\Delta\breve{N}_{(0,-1,1)}, \Delta\breve{N}_{(-1,-5,6)}, \Delta\breve{N}_{(-3,6,-2)}$ have been determined, cycle slips $\left[\Delta\breve{N}_1,\ \Delta\breve{N}_2,\ \Delta\breve{N}_3\right]$ on the original phase observations can be uniquely identified and corrected [13].

Step 6: The BDS GF combination noise residual method with [(0, 1, −1), (1, 0, −1)] is used to verify the resolve cycle slips $\left[\Delta\breve{N}_1, \Delta\breve{N}_2, \Delta\breve{N}_3\right]$.

$$\Delta\tilde{\Phi}_{(i,j,k)} = \Delta\Phi_{(i,j,k)} - \left(i\lambda_1\Delta\breve{N}_1 + j\lambda_2\Delta\breve{N}_2 + k\lambda_3\Delta\breve{N}_3\right) < 4\sigma_{\tilde{N}_{(i,j,k)}} \quad (23)$$

If the resolve cycle slips $\left[\Delta\breve{N}_1, \Delta\breve{N}_2, \Delta\breve{N}_3\right]$ satisfy Eq. (23) expect for insensitivity combination, it is indicated that the cycle slips has been corrected, or it need to resolve the ambiguities.

5 Data Analysis

The capability of the proposed algorithm to detect and repair cycle slips has been tested by real triple-frequency BDS data collected at Shanghai. A 1975s dataset referring to December 05, 2016 starting from 2:05:26.000 UTC to 2:38:20.000 UTC has been provided. 6 BDS satellites are tracked in our experiment, including PRN 1, 4, 5, 6, 8 and 9. The data sampling interval is 1 s. The sky plot of the tracked BDS satellites is shown in Fig 1a.

Some artificial jumps were added to be sure that the program detects the correct epoch and estimates the correct amplitude. And different cycle slip cases, such as small cycle slips, big cycle slips, successive cycle slips and particular case are studied comprehensively. As of this research, the elevation of the GEO satellites varies over a small range, whereas those of IGSO satellites change significantly. The triple-frequency observations of BDS C01 (in GEO) and C08 (in IGSO) are used to assess the performance of the proposed algorithm.

To test performance of all GF phase combinations in Table 2, the small successive jumps ranging from [1, 0, 0] to [3, 3, 3] and big successive insensitive jumps are added to detect and correct those jumps in epoch 101–104 and 201–204 of BDS C8 and C1. Moreover, the added jumps are also detected and repaired by the proposed method. The statistical results are summarized in Table 5.

If the flag equals to 1, it is indicated that the cycle slip have been detected or corrected successfully. If the flag equals to 0, it is indicated that the cycle slip could not been detected or corrected. Table 5 shows that the selection combinations can detect small successive jumps, but for in insensitivity jumps. The small successive jumps and the big successive insensitivity jumps for each combination can be detected and corrected accurately by the proposed algorithm. The estimated jumps have also been verified correctly by GF phase combinations.

Table 5 The statistical result for jumps detection and repair

Satellite	Epoch	Jumps	Flag of jump detection	Flag of jump repair	Flag of jumps test
C1(GEO)	101–104	[1, 0, 0]–[3, 3 ,3]	1	1	1
	201–204	Insensitive jumps	0	1	1
C8(IGSO)	101–104	[1, 0, 0]–[3, 3, 3]	1	1	1
	201–204	Insensitive jumps	0	1	1

Then the small continuous jumps [0, 1, 1] are added in epoch 100, 104 and 106, respectively. The larger continuous insensitive jumps [75, 58, 61] are added in epoch 102, 108 and 110, respectively. The test result is shown in Fig. 1b. The results of detection and repair cycle slips using BDS GF code and phase combinations are showed in the three right side figures of the Fig. 1b. The three left side figures of Fig. 1b represent the detection result by BDS GF phase combinations. Figure 1b demonstrates that the BDS GF phase combination can detect three small jumps but for three big jumps and the proposed algorithm can detect and correct mixed small and big continuous jumps in real time.

Moreover, the small successive cycle slips [0, 1, 1] with 5 min unlock time are added at the epoch 100 and 400. The proposed method is applied to detect and correct those jumps and the result is shown in Fig. 2.

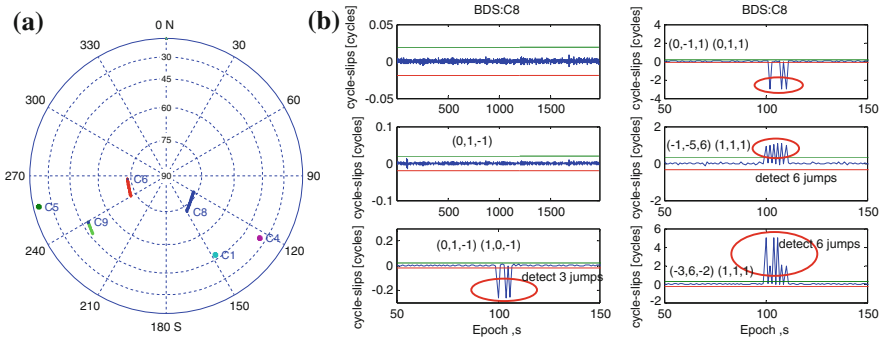

Fig. 1 The sky plot of the tracked BDS satellites (**a**), The mixed small and larger continuous jumps test with the proposed algorithm (**b**)

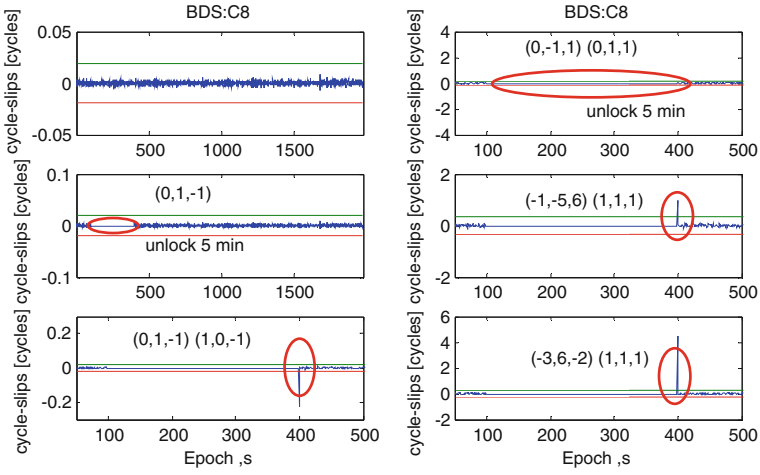

Fig. 2 The small successive cycle slips test with 5 min unlock time

From Fig. 2, it could be seen that the proposed algorithm and selection optimal combinations can detect and correct 5 min unlock time small continuous jumps.

6 Conclusions

A real-time cycle slip detection and repair method is proposed for triple-frequency BDS data. The optimal BDS triple-frequency GF phase combinations and the optimal BDS triple-frequency GF code and phase combinations for cycle slips detection and repair are selected on the basis of the optimization function. The BDS triple-frequency test is carried out to verify the proposed method. Various types of cycle slips have been simulated in the test. Within 20 cycle slips groups can be detected by this BDS GF phase combination method. The triple-frequency GF code and phase combinations [(0, −1, 1), (0, 1, 1)], [(−1, −5, 6), (1, 1, 1)] and [(−3, 6, 2), (1, 1, 1)] present better performance than the others combinations for cycle slips detection and repair in real time. All artificial jumps added to real data have been correctly detected and estimated in real time. The 5 min signal unlock time and 1 small cycle slip can be also detected and repaired.

References

1. Hofmann-Wellenhof B, Lichteneggr H, Collins (2001) Global positioning system-theory and practice fifth, revised edition
2. Xu G (2007) GPS-Theory, algorithms and application, 2nd edn. Springer, Berlin
3. Xu D, Kou Y (2011) Instantaneous cycle slip detection and repair for a standalone triple-frequency GPS receiver. In: Proceeding ION-ITM-2011, Institute of Navigation, San Diego, CA, pp 3916–3922
4. Wu Y, Jin S, Wang Z (2010) Cycle slips detection using multi-frequency GPS carrier phase observation a simulation study. Adv Space Res 46(2):144–149
5. Liu Z (2011) A new automated cycle slip detection and repair method for a single dual-frequency GPS receiver. J Geod 85:171–183. doi:10.1007/s00190-010-0426
6. Zhao Q (2015) Real-time detection and repair of cycle slips in triple-frequency GNSS measurements. GPS Solut 19:381–391. doi:10.1007/s10291-014-0396-2
7. Huang L (2015) A new triple-frequency cycle slip detecting algorithm validated with BDS data GPS Solut. 15:487–495. doi:10.1007/s10291-015-0487-8
8. Cai C, Liu Z, Xia P et al (2013) Cycle slip detection and repair for undifferenced GPS observations under high ionospheric activity. GPS Solut 17(2):247–260
9. Banville S, Langley RB (2010) Instantaneous cycle slips correction for real time PPP applications. Navigation 57(4):325–334
10. Dai Z, Knedlik S, Loffeld O (2008) Real-time cycle-slip detection and determination for multiple frequency GNSS. In: Proceedings of the 5th workshop on positioning, navigation and communication 2008, Hannover, Germany, pp 37–43
11. Dai Z, Knedlik S, Loffeld O (2009) Instantaneous triple-frequency GPS cycle slip detection and repair. Int J Navig Obs 23(1):28–43. doi:10.1155/2009/407231
12. Feng Y (2008) GNSS three carrier ambiguity resolution using ionosphere-reduced virtual signals. J Geod 82(12):847–862

13. Cocard M, Bourgon S, Kamali O, Collins P (2008) A systematic investigation of optimal carrier-phase combinations for modernized triple-frequency GPS. J Geod 82(9):555–564
14. Verhagen S, Li B (2012) LAMBDA software package: Matlab implementation, version 3.0. Delft University of Technology and Curtin University, Perth Australia
15. Zhang X, He X (2015) BDS triple-frequency carrier-phase linear combination models and their characteristics. China Earth 58:896–905. doi:10.1007/s11430-014-5027-9
16. Li J, Yang Y, He H (2016) An analytical study on the carrier-phase linear combinations for trilp-frequency GNSS. J Geod. doi: 10.1007/s00190-016-0945-2
17. Maria Clara de Lacy (2012) Real-time cycle slip detection in triple-frequency GNSS. GPS Solut 16:353–362. doi:10.1007/s10291-011-0237-5
18. Melbourne WG (1985) The case for ranging in GPS-based geodetic systems. In: Proceeding positioning with GPS-1985, NGS, Rockville, MD, pp 373–386

Preliminary Study on Changes in Temperature and Its Implication on Vertical Displacements of Antarctic GPS Stations

Wenhao Li, Shengkai Zhang, Jintao Lei, Qingchuan Zhang and Chaohui Zhu

Abstract GPS is a highly precise tool in horizontal and vertical crustal motion studies. GPS coordinate time series are influenced by orbit error, clock error, and the effects of geophysical signals. Temperature variation is one of the reasons that cause GPS coordinate vertical displacements. Thermal expansion of GPS monument and nearby bedrock could result in vertical displacements in the coordinate time series. The effect of thermal expansion is especially prominent in Antarctica, where the difference of temperature is large. By analyzing 9 GPS stations in Antarctica, we show the effect of thermal expansion of GPS monument and nearby bedrock in vertical direction. The maximum amplitude can reach to 0.24 mm (CAS1) and the mean amplitude is 0.21 mm; the vertical displacements caused by thermal expansion show clear patterns of annul and semi-annul periods, and the amplitudes of the annual period are much larger than that of the semi-annual period.

Keywords Thermal expansion · Antarctic · Vertical displacement · GPS · Time series

1 Introduction

GPS is one of the most important tools in space geodesy, GPS time series contain copious information for geodynamics. To achieve higher accuracy in the horizontal and vertical directions, we need to take various errors into account when calculating GPS coordinate time series [1]. Sun et al. [2] find many periodical variations by analyzing ITRF2008 coordinate residual series, the precision of ITRF coordinates will be improved further if we remove the effects of periodical variations after investigating its mechanisms. GPS technical system error, surface mass loading and thermal expansion induced by temperature variations are contributors to displacements of GPS stations in vertical direction [3–5] present a theoretical model to

W. Li · S. Zhang (✉) · J. Lei · Q. Zhang · C. Zhu
Chinese Antarctic Center of Surveying and Mapping, Wuhan 430079, China
e-mail: zskai@whu.edu.cn; lwhmly@whu.edu.cn

J. Sun et al. (eds.), *China Satellite Navigation Conference (CSNC) 2017 Proceedings: Volume III*, Lecture Notes in Electrical Engineering 439,
DOI 10.1007/978-981-10-4594-3_36

estimate the effects of thermal expansion on GPS vertical displacements, and from their theoretical computation, the amplitude variations caused by thermal expansion were less than 0.5 mm. Yan et al. [6] present a more generalized model, it not only included the annual variation of temperature but also the effects of GPS monuments, and they calculate thermal effect on a global scale based on the global surface air temperature time series from the National Centers for Environmental Prediction/National Center for Atmospheric Research (NCEP/NCAR) reanalysis. The results show that the maximum amplitude of annual displacement induced by bedrock thermal expansion can reach about 1.3 mm, which is 2.6 times larger than that presented by Dong et al. [5]. Yan et al. [7] calculate the annual variations of GPS vertical displacements induced by the temperature variations in both above- and underground parts of GPS monument, using 23 GPS stations of the Crustal Movement Observation Network of China (CMONOC), the largest annual amplitude is 2.8 mm, and the annual amplitudes of 13 GPS stations exceed 1 mm. Jiang et al. [8] choose 3 GPS stations from low latitude, mid-latitude and high latitude areas, and find that the maximum displacements of GPS monument and nearby bedrock induced by thermal expansion could reach 0.57 and 1.85 mm, respectively, both annual and semi-annual variations could explain 11.2 and 3.3% of the total annual and semi-annual variations in the vertical direction. Xie et al. [9] calculate the GPS coordinate displacements induced by thermal expansion in Siberia and its adjacent areas, the results show that the mean annual amplitude of monument and bedrock are 1.08 and 0.75 mm, respectively, the maximum displacements are 3.74 and 1.19 mm, respectively. In Antarctica, the effects of thermal expansion are significant because of the large temperature variations and the extremely harsh environment, in this paper, we choose 9 GPS stations to further investigate the effects of thermal expansion in Antarctica.

2 Monument and Bedrock Thermal Expansion Models

The thermal-induced displacements of GPS stations fall in two parts: one is the underground foundation physically attaching the monument to the bedrock, the other is the supporting structures above the ground where GPS antenna is fixed.

2.1 Monument Thermal Expansion Model

The monuments of GPS are usually made of reinforced concrete, and the heights of monuments can reach dozens of meters, the monument height variation caused by thermal expansion is computed by Eq. (1) [7];

$$\Delta L(\Delta T) = L_0 \cdot \alpha \cdot \Delta T, \tag{1}$$

where ΔL is the height variation in meters, L_0 is the length of supporting structures in meters, α is the linear thermal expansion coefficient, and $\alpha = 12 \times 10^{-6}$ $(1/^{\circ}\mathrm{C})$, ΔT denotes the temperature variation.

2.2 Bedrock Thermal Expansion Model

The bedrock temperature variation is caused by the temperature variation of Earth surface, by means of thermal conduction, and it will finally result in the GPS coordinate variation in the vertical direction. The displacement of GPS station induced by the thermal expansion can be estimated by using Eq. (2) [5, 7];

$$\Delta h = \frac{1+r}{1-r}\alpha \sum_{1}^{n} A_i \sqrt{\frac{k}{\omega_i}} \cos(\omega_i \, \mathrm{t} - \frac{\pi}{4} - \varphi_i) \tag{2}$$

Here Δh is the displacement of GPS station, r is the Poisson's ratio, α has the same meaning as in Eq. (1). k is the thermal diffusivity, and $k = 1\,\mathrm{mm}^2/\mathrm{s}$, A_i ω_i φ_i are amplitude, angular frequency, and initial phase of the ith harmonic of land surface air temperature, respectively. n is the harmonic number, $\frac{1+r}{1-r}$ is used to take the thermal stress into account, and the phase of vertical displacements has a 45° delay following the surface temperature variations.

The combined results of Eq. (1). plus Eq. (2). are the GPS station displacements induced by monument and bedrock thermal expansion.

3 Data Sources

We select 9 GPS stations in Antarctica (63.32–77.84° S) to study the effects of thermal expansion (Fig.1), the time span is 2009–2013. The monument heights are collected from the station log files (downloaded from ftp://garner.ucsd.edu/docs); the coordinate time series are downloaded from Nevada Geodetic Laboratory (http://geodesy.unr.edu/NGLStationPages/GlobalStationList).

The temperature variations are derived from a daily land surface air temperature dataset, resolution is 0.5 × 0.5° latitude–longitude (http://apps.ecmwf.int/datasets/data/interim-full-daily), and time span coincided with that of coordinate time series. We compute the 9 GPS station temperatures by using linear interpolation, and then calculate the displacements induced by temperature variations in the vertical direction. Figure 1 is the distribution of 9 GPS stations in Antarctica, Table 1 lists the site locations, time spans, monument heights, and temperature variations. The maximum of temperature variations is DAV1, which can reach to 30 °C.

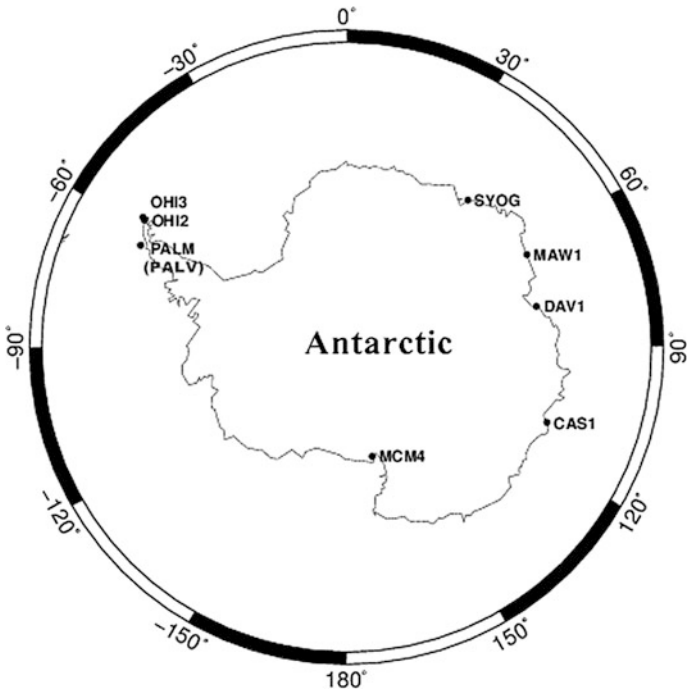

Fig. 1 The distribution of 9 GPS stations in Antarctica

Table 1 Statistics of detail information about GPS station

Station	Lat. (°)	Lon. (°)	Time span	Max tem variation (°C)	Height (m)	Max height variations (mm)
CAS1	−66.28	110.52	2009–2013	19.81	1.50	0.53
DAV1	−68.58	77.97	2009–2013	30.89	0.30	0.48
MAW1	−67.60	62.87	2009–2013	14.79	1.50	0.36
MCM4	−77.84	166.67	2009–2013	25.43	0.10	0.38
OHI2	−63.32	−57.90	2009–2013	20.33	1.40	0.72
OHI3	−63.32	−57.90	2009–2013	20.33	1.40	0.72
PALM	−64.78	−64.05	2009–2013	20.85	2.03	1.03
PALV	−64.78	−64.05	2009–2013	20.85	2.03	1.03
SYOG	−69.01	39.58	2009–2013	26.53	1.50	0.43

Table 2 The height variations of monument induced by thermal expansion (mm)

Station	Max	Min	Max variation	rms
CAS1	0.18	−0.24	0.43	0.008
DAV1	0.07	−0.13	0.20	0.002
MAW1	0.16	−0.16	0.32	0.006
MCM4	0.02	−0.02	0.05	0.000
OHI2	0.10	−0.52	0.61	0.011
OHI3	0.10	−0.52	0.61	0.011
PALM	0.17	−0.75	0.91	0.013
PALV	0.17	−0.75	0.91	0.013
SYOG	0.06	−0.11	0.17	0.001

4 Data Processing

4.1 Temperature Data Processing

We use temperature variations computed by means of linear interpolation to calculate the corresponding displacements in the vertical direction. Table 2 lists the height variations of monuments induced by thermal expansion [the results of Eq. (1)], Table 3 lists the displacement variations of bedrock induced by thermal expansion [the results of Eq. (2)], Table 2 indicates that the height variations of PALM and PALV are most remarkable, can be up to 0.91 mm, Table 3 indicates that the largest height variations of bedrock is DAV1, can be up to 0.40 mm.

4.2 Frequency Spectrum Analysis

We analyze the periodical variations of 9 GPS coordinate time series by means of Fourier transform and spectrum analysis, Figs. 2 and 3 illustrate the periods and corresponding amplitudes of vertical displacements induced by thermal expansion of CAS1 and DAV1, respectively. The results show that all the coordinate time

Table 3 The heights variations of bedrock induced by thermal expansion (mm)

Station	Max	Min	Max variation	rms
CAS1	0.10	−0.11	0.21	0.005
DAV1	0.18	−0.22	0.40	0.019
MAW1	0.09	−0.11	0.20	0.004
MCM4	0.2	−0.16	0.36	0.016
OHI2	0.09	−0.07	0.16	0.003
OHI3	0.09	−0.07	0.16	0.003
PALM	0.07	−0.06	0.13	0.002
PALV	0.07	−0.06	0.13	0.002
SYOG	0.17	−0.16	0.33	0.013

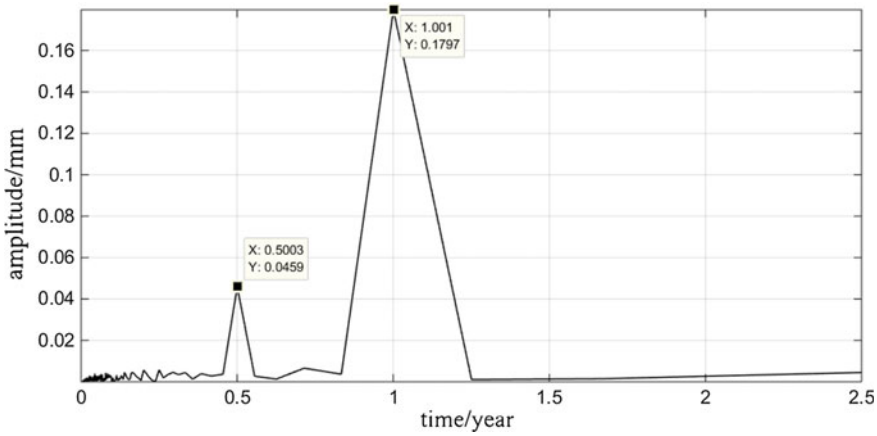

Fig. 2 Frequency spectrum of vertical variations (CAS1)

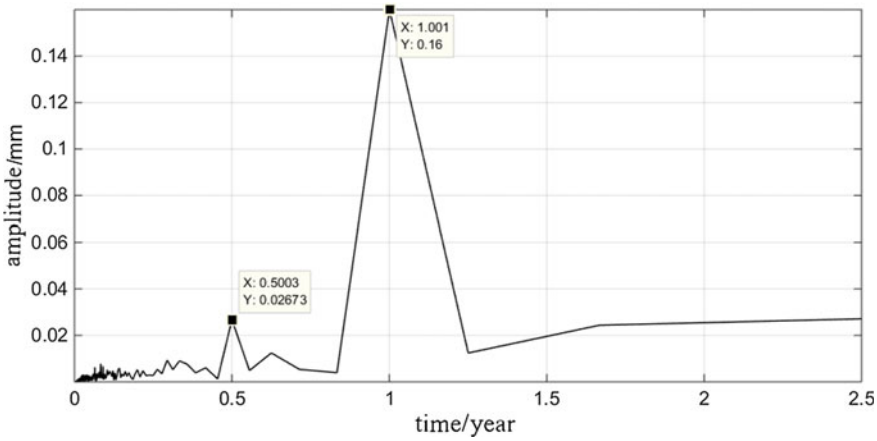

Fig. 3 Frequency spectrum of vertical variations (DAV1)

series exhibit both annual and semi-annual characteristics, but the effects of semi-annual characteristics are very small. Table 4 lists the calculated amplitudes of all GPS stations induced by monument and bedrock thermal expansion. The largest influence station is found at CAS1, the maximum of displacement can reach to 0.24 mm, the mean annual and semi-annual amplitude are 0.15 and 0.03 mm, respectively.

Table 4 Amplitudes of all GPS stations induced by monument and bedrock thermal expansion

Station	Maximum	Annual amplitude	Semi-annual amplitude	Percentage (%)
CAS1	0.238	0.160	0.027	16.88
DAV1	0.211	0.180	0.046	25.56
MAW1	0.203	0.085	0.031	36.47
MCM4	0.211	0.181	0.033	18.23
OHI2	0.182	0.121	0.048	39.67
OHI3	0.182	0.121	0.048	39.67
PALM	0.229	0.178	0.014	7.87
PALV	0.229	0.178	0.014	7.87
SYOG	0.212	0.169	0.026	15.38

4.3 Fitting Model

To further validate the existence of annual and semi-annual amplitudes, we fit the displacement variations using the method of least squares fit.

$$y_t = at + b + A_1 \sin(\omega_1 t - \varphi_1) + A_2 \sin(\omega_2 t - \varphi_2)\varepsilon_t. \quad (3)$$

Here y_t is the displacement induced by monument and bedrock thermal expansion, A_1, ω_1, φ_1 and A_2, ω_2, φ_2 are the annual and semi-annual amplitude, angular frequency and initial phase, respectively. a, b and ε t are the slope, intercept and random noise, respectively.

Since annual and semi-annual periods are evident from the above analysis, we assume angular frequency as an unknown parameter as well as other parameters using the method of least squares fit. Then we compare the result of considering both annual and semi-annual effects to the result of considering only annual effect. The results are listed in Tables 5 and 6, respectively. Figures 4 and 5 are the original time series of vertical variations caused by thermal expansion and the fitting curves of different fitting methods, the black lines are the original displacements induced by monument and bedrock thermal expansion, red lines are the results of considering both annual and semi-annual effects, blue lines are the results of considering only annual effects. Table 7 lists the annual and semi-annual amplitudes before and after removing the effect of monument and bedrock thermal expansion in the vertical direction.

The results show that ω_1 and ω_2 are quite close to 365 and 183 d, respectively, which denotes that the GPS vertical displacements caused by thermal expansion have the characteristics of annul and semi-annul variations. Table 7 lists the annual amplitudes (A_1) and semi-annual amplitudes (A_2) of 9 GPS stations computed from spectrum analysis, the "reduction" in the last column is the depressed percentage of annual amplitude after eliminating the effects of thermal expansion. We can conclude that the maximum degradation of annual amplitude is 5.49%, the mean degradation is 3.40%.

Table 5 Statistic results of least square fit considering both annual and semi-annual effects

Station	a/(mm/a)	b/mm	A_1/mm	$\omega_{1/d}$	φ_1/°	A_2/mm	$\omega_{2/d}$	φ_2/°
CAS1	−0.0352	0.0873	0.15	367.81	0.21	0.02	182.72	0.48
DAV1	−0.0028	0.0069	0.18	364.14	−0.25	0.05	182.72	−0.03
MAW1	−0.0042	0.0101	0.09	371.05	0.00	0.03	182.72	0.60
MCM4	−0.0013	0.0032	0.18	364.83	−0.07	0.03	182.72	−0.99
OHI2	0.0002	−0.0006	0.12	365.88	0.45	−0.05	182.72	0.49
OHI3	0.0002	−0.0006	0.12	365.88	0.45	−0.05	182.72	0.49
PALM	−0.0096	0.0238	0.18	366.11	0.38	−0.01	182.72	−0.99
PALV	−0.0096	0.0238	0.18	366.11	0.38	−0.01	182.72	−0.99
SYOG	0.0002	−0.0004	0.17	364.45	−0.03	0.03	182.72	−0.44

Table 6 Statistic results of least square fit considering only annual effects

Station	a/(mm/a)	b/mm	A_1/mm	$\omega_{1/d}$	φ_1/°
CAS1	−0.0352	0.0873	0.15	367.82	0.21
DAV1	−0.0028	0.0069	0.18	364.14	−0.25
MAW1	−0.0042	0.0101	0.09	371.06	0.00
MCM4	−0.0013	0.0032	0.18	364.83	−0.07
OHI2	0.0002	−0.0006	0.12	365.88	0.45
OHI3	0.0002	−0.0006	0.12	365.88	0.45
PALM	−0.0096	0.0238	0.18	366.11	0.38
PALV	−0.0096	0.0238	0.18	366.11	0.38
SYOG	0.0002	−0.0004	0.17	364.45	−0.03

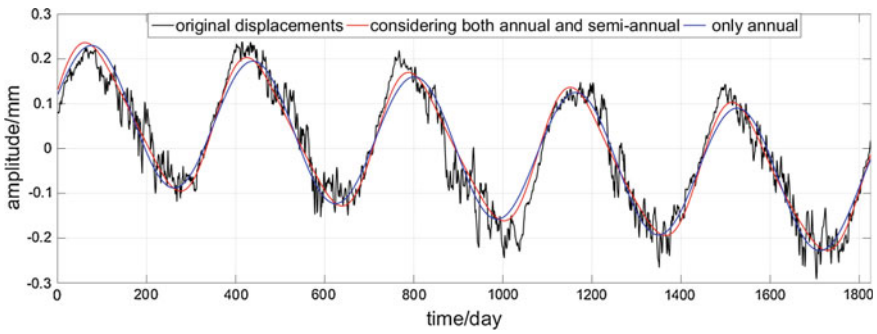

Fig. 4 Original time series of vertical variations caused by thermal expansion and the fitting curves of different fitting methods of CAS1

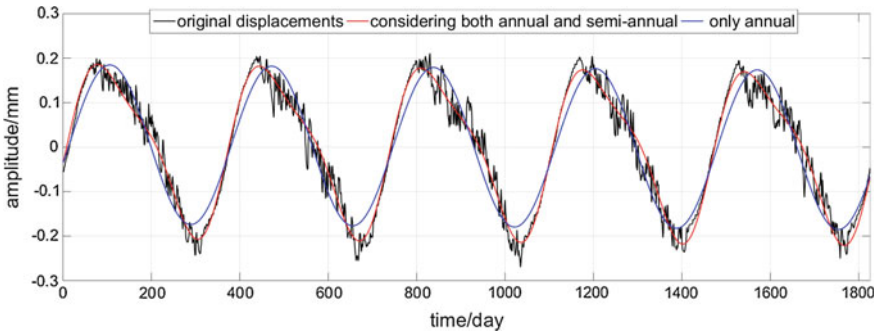

Fig. 5 Original time series of vertical variations caused by thermal expansion and the fitting curves of different fitting methods of DAV1

Table 7 Statistic results of annual and semi-annual amplitudes before and after removing the effect of monument and bedrock thermal expansion

Station	A_1 before	A_2 before	A_1 after	A_2 after	Reduction (%)
CAS1	2.18	1.12	2.06	1.12	5.49
DAV1	3.20	1.39	3.03	1.42	5.17
MAW1	2.07	1.15	2.00	1.16	3.43
MCM4	2.97	0.85	2.83	0.85	4.77
OHI2	3.98	0.92	3.94	0.88	0.99
OHI3	4.43	1.23	4.37	1.22	1.28
PALM	3.08	1.15	3.00	1.14	2.48
PALV	3.97	1.67	3.84	1.68	3.20
SYOG	2.80	0.39	2.70	0.41	3.79

5 Conclusion

Since the large temperature variations in Antarctica, the effects of thermal expansion are so significant that cannot be neglected. Through the analysis of the thermal expansion effects on the vertical displacements, we conclude that

1. The thermal expansion will contribute to the vertical displacements, the maximum value of annual amplitude can reach to 0.24 mm (CAS1), and the mean value is 0.15 mm.
2. The GPS vertical displacements caused by thermal expansions show clear periods of annual and semi-annul variations, and the amplitudes of annual variations are much larger than that of the semi-annual variations.
3. Thermal expansion is one of the reasons that cause vertical displacements, after eliminating it, the maximum annual amplitude will reduce 5.49% and the mean reduction value is 3.4%.
4. We compare the results of least square fit between considering both annual and semi-annual effects and only annual effects, the difference of annual amplitude is

very small, the maximum of semi-annual amplitude is approximately 0.05 mm. The effects of semi-annual variations caused by thermal expansion can be neglected at the present precision level, but the semi-annual variations cannot be neglected in some areas.

Acknowledgements This work is supported by the State Key Program of National Science of China (41531069), the State Program of National Science of China (41176173), and Chinese Polar Environment Comprehensive Investigation and Assessment Programs (CHINARE2017).

References

1. Beavan J (2005) Noise properties of continuous GPS data from concrete pillar geodetic monuments in New Zealand and comparison with data from U. S. deep drilled braced monuments. J Geophys Res 110: B08410, doi:10.1029/2005JB003642
2. Zhang S, Zhang M, Tang S (2006) Vertical crustal displacements due to atmospheric loading effects at GPS fiducial station in china. Geomatics Inf Sci Wuhan Univ 31(2):1090–1093
3. Wang M, Shen Z, Dong D (2005) Effects of non-tectonic crustal deformation on continuous GPS position time series and correction to them. Chin J Geophys 48(5):1045–1052
4. Zhou J, Sun H (2007) Loading effects on high precision GPS observations. Adv Earth Sci 22 (10):1036–1040
5. Dong D, Fang P, Bock Y, Cheng MK, Miyazaki S (2002) Anatomy of apparent seasonal variations from GPS-derived site position time series. J Geophys Res 107(B4): ETG9-1-ETG9-16
6. Yan H, Chen W, Zhu Y et al (2010) Thermal effects on vertical displacement of GPS stations in China. Chinese J Geophys 53(4):825–832 (in Chinese)
7. Yan H, Chen W, Zhu Y, et al (2009) Contributions of thermal expansion of monuments and nearby bedrock to observed GPS height changes. Geophys Res Lett 36 (13:L13301) doi:10.1029/2009GL038152
8. Jiang W, Wang K, Deng L et al (2015) Impact on nonlinear vertical variation of GNSS reference stations caused by thermal expansion. Acta Geodaetica Cartogr Sin 44(5):473–480
9. Xie S, Li F, Zhang J (2013) Bedrock and monument thermal expansions and their implications on vertical displacement of GPS stations: a case study in Siberia and its adjacent area 4th International workshop on multi-observations and interpretations of Tibet, Xinjiang and Siberia (TibXS), Yining, China, 29–31

An Improved Constraint Result Zone Search Algorithm for Measuring Attitude Based on Dual Frequency

Yuan Quan, Xiubin Zhao, Chunlei Pang, Yong Wang and Chao Gao

Abstract To mitigate the problem of larger search zone, low initializing efficiency and limited attitude accuracy existing in result zone searching algorithm bounded by ambiguity, an improved algorithm based on dual-frequency combination is proposed. The long wavelength of wide-lane combination is first applied to compress the searching zone. The integer ambiguity of wide lane can be fixed with the assistance of two-dimension result zone searching model. Then the initial integer ambiguity of narrow lane can be obtained based on the related constrained relationship between dual-frequency carriers. The final integer ambiguity of narrow lane can be obtained by the OVT window sliding test method. Taking the final integer ambiguity into narrow-lane carrier observation equation, we can get accurate baseline coordinates and angle information. Comparable experiments demonstrate that the initializing time is reduced by 13 s (from 53 s to 40 s). The baseline accuracy and attitude accuracy are enhanced by 15 and 18%, respectively. These indicate that the proposed method can be widely applied in static orientation and attitude measuring.

Keywords Integer ambiguity · Double-frequency combination · OVT test method · Attitude measurement

1 Introduction

As one of the main means of determining the attitude information, GPS carrier phase measurement has been widely used in precision positioning system with high positioning accuracy [1], because of its millimeter-sized high accuracy. However, the GPS carrier phase measurements contain unknown quantity, i.e., integer

Y. Quan (✉) · X. Zhao · C. Pang (✉) · Y. Wang · C. Gao
Information and Navigation College, Air Force Engineering University, Xi'an 710077, China
e-mail: yquan@stu.xidian.edu.cn

C. Pang
e-mail: chunleipcl@163.com

J. Sun et al. (eds.), *China Satellite Navigation Conference (CSNC) 2017 Proceedings: Volume III*, Lecture Notes in Electrical Engineering 439,
DOI 10.1007/978-981-10-4594-3_37

ambiguity, the determination of integer ambiguity is the key problem of positioning and attitude measurement technology [2, 3].

The least-squares search algorithm is an effective way [4, 5] for solving integer ambiguities. Its basic idea can be described as follows. There are only three independent parameters [6] in the integer ambiguity parameters. If there ambiguity parameters are known, these parameters can be substituted into the carrier observation equation to obtain baseline relative coordinates and get the remaining unknown ambiguity. Thus, the initialization efficiency can be improved. In recent years, many researchers have modified the least-squares optimization search algorithm. In [7], three-frequency combination was used to achieve a least-squares ambiguity real-time search based on BDS system. In [8], the search scope was reduced through the baseline constraint iterative least-squares algorithm. The search space was reduced by using planar search attitude angle method in [9]. In Li et al. [10], an constraint result zone search algorithm was proposed based on result zone search algorithm. Angle was used as the intermediate variables to derive the relationship between the main ambiguity and the attitude angle for the purpose of compressing the search space.

The above references show that compressing the search space is an effective way for rapid and accurate solution of ambiguity. In this paper, we use the wide-lane combination to further reduce the search range of the main ambiguity in anti-ambiguity range bound domain. Two-dimension result zone searching model is used to obtain all wide-lane integer ambiguity. Then the correct wide-lane ambiguity is fixed by ratio test of sum of baseline residual. Then narrow-lane ambiguity can be obtained by utilizing constraint relation of dual-frequency carrier. The correct solution is fixed by using the window sliding test method of OVT [11]. Finally, the baseline coordinates and attitude angle information can be achieved by substituting them into the carrier observation equation to obtain.

2 Constraint Result Zone Searching Algorithm

2.1 Two-Dimension Result Zone Searching Model

To simplify, the impact of noise is not taken into consideration. Assume the receiver A and the receiver B simultaneously observe the satellite i,j, the baseline vector of A to B is denoted as $\boldsymbol{d}$, the length denoted as $|\boldsymbol{d}|$. Then, the double-difference carrier phase equation of satellite i,j is

$$\lambda(\phi^{ij} + N^{ij}) = \left(\boldsymbol{S}_i - \boldsymbol{S}_j\right) \cdot \boldsymbol{d}, \tag{1}$$

where λ is carrier wave length, ϕ^{ij} is carrier phase observation, $\boldsymbol{S}_i$, and $\boldsymbol{S}_j$ are satellite vectors, N^{ij} is double-difference integer ambiguity.

In the coordinates of ENU, the baseline endpoint B is taken as the origin of coordinates. The heading angle and pitch angle of baseline AB are θ_B and ψ_B, respectively, The heading angle and pitch angle of satellite i and satellite j are (φ_i, θ_i) and (φ_j, θ_j). Taking satellite i as a benchmark, then we can rewrite Eq. (1) as [9]:

$$\begin{aligned}\phi^{ij} + N^{ij} = \left(\frac{d}{\lambda}\right) * [&\cos\theta_i - \cos\theta_{\mathrm{B}}\cos(\varphi_i - \theta_{\mathrm{B}}) + \sin\theta_B(\sin\theta_i - \sin\theta_j) \\ &- \cos(\theta_j)\cos\theta_B\cos(\varphi_j - \theta_B)]\end{aligned} \tag{2}$$

Equation (2) provides a new way to solve the integer ambiguity. We can use Eq. (2) to take two-dimensional ergodic search attitude angle on the attitude angle by a certain step. Step sizes $\Delta\theta_B$ and $\Delta\varphi_B$ can be determined by Eq. (3) as:

$$\begin{cases} \Delta\theta_B < \lambda/d(\sin\theta_{si} - \sin\theta_{sj}) \\ \Delta\varphi_B < \lambda/(1.5d) \end{cases} \tag{3}$$

We can get the float value of corresponding ambiguity by taking each group of attitude angle into Eq. (2). Then the set of all integer ambiguity can be obtained after the integer operation of ambiguity floating point solution.

2.2 Constraint Searching Domain Space

Apparently, the ergodic search efficiency is not high enough. If we can find out the attitude angle space by non-ergodic search, the search efficiency will be further improved.

Constraint domain search algorithm is a non-ergodic search algorithm which takes the double-difference ambiguity between the reference star and the two principal stars as the main ambiguity. In this algorithm, the two-dimension search range of the main ambiguity obtained for planar searching range is used to constrain the attitude angle space. Meanwhile, all candidate ambiguities are solved by the result zone search model, which replaces the original traversal method.

First, Eq. (1) can be rewritten as:

$$\lambda(\varphi^{ij} + N^{ij}) = \boldsymbol{d}\cdot(\boldsymbol{S}_i - \boldsymbol{S}_j) = |\boldsymbol{d}| \cdot |\boldsymbol{S}_i - \boldsymbol{S}_j| \cdot \boldsymbol{e}_d \cdot \boldsymbol{e}_{ij}, \tag{4}$$

where $\boldsymbol{e}_d = \boldsymbol{d}/|\boldsymbol{d}|$, $\boldsymbol{e}_{ij} = \boldsymbol{S}_i - \boldsymbol{S}_j/|\boldsymbol{S}_i - \boldsymbol{S}_j|$, by Eq. (4), we can get:

$$|\lambda(\varphi^{ij} + N^{ij})|/d \cdot |\boldsymbol{S}_i - \boldsymbol{S}_j| = |\boldsymbol{e}_d \cdot \boldsymbol{e}_{ij}| \le 1 \tag{5}$$

$$-d\cdot|\boldsymbol{S}_i - \boldsymbol{S}_j|/\lambda - \varphi^{ij} \le N_{ij} \le d \cdot |\boldsymbol{S}_i - \boldsymbol{S}_j|/\lambda - \varphi^{ij} \tag{6}$$

Accordingly, the main ambiguity search range can be obtained. Following the relationship between ambiguity and attitude angle [10], we have:

$$\begin{cases} \dfrac{\lambda(\varphi^{ik}+N^{ik})}{(d|S_i-S_k|)} = \cos\theta_B\cos\theta_{ik}\cos(\varphi_B-\varphi_{ik})+\sin\theta_B\sin\theta_{ik} \\ \dfrac{\lambda(\varphi^{ij}+N^{ij})}{(d|S_i-S_j|)} = \cos\theta_B\cos\theta_{ij}\cos(\varphi_B-\varphi_{ij})+\sin\theta_B\sin\theta_{ij} \end{cases} \tag{7}$$

For each (N^{ij}, N^{ik}), we can solve the corresponding elevation θ_B and heading angle φ_B using analytic method [9] based on the Eq. (7).

But each group of main ambiguity corresponds to 12 groups of pitch angle and heading angle [10]. According to the fact that actual ranges of pitch and heading angle are [−90°, 90°] and [0°, 360°], respectively, we can eliminate the error solution and the candidate attitude angle combinations are reduced to 1–2 groups. Substituting the candidate attitude angle combinations into Eq. (8), we can get the candidate ambiguity floating point solutions.

$$\begin{aligned} \hat{N}^{1x} = &-\phi^{1x}+\left(\frac{|\boldsymbol{d}|}{\lambda}\right) * [\cos\theta_1\cos\theta_B\cos(\varphi_1-\theta_B) \\ &+\sin\theta_B(\sin\theta_1 - \sin\theta_x)-\cos(\theta_x)\cos\theta_B\cos(\varphi_x-\theta_B)] \end{aligned} \tag{8}$$

2.3 Fixing Integer Ambiguity

The integer ambiguity $\bar{N}^{1x}$ can be obtained after the integer operation of above results. In order to get the correct solution, we need to fix all candidate ambiguity. All candidate integer ambiguity can be fixed through the following steps.

- Step. 1: Assuming that the current moment can be observed n satellites, we can obtain n double-difference carrier observation equations to construct a matrix. Then we take all candidate ambiguities into Eq. (9) to obtain the baseline vector.

$$\lambda\begin{bmatrix}\phi^{12}\\ \phi^{13}\\ \vdots\\ \phi^{l,n}\end{bmatrix} = \begin{bmatrix}\boldsymbol{S}_1-\boldsymbol{S}_2\\ \boldsymbol{S}_1-\boldsymbol{S}_3\\ \vdots\\ \boldsymbol{S}_1-\boldsymbol{S}_n\end{bmatrix}\boldsymbol{d}-\lambda\begin{bmatrix}N^{12}\\ N^{13}\\ \vdots\\ N^{l,n}\end{bmatrix} \tag{9}$$

- Step. 2: Fix the correct integer ambiguity solution based on the solution of baseline vector information obtained by multiple epochs and residual error sum ratio test.

$$\sum_{t=1}^{m}\left|x_j(t)^T x_j(t)-d^2\right|_{\text{次小}} / \left(\sum_{t=1}^{m}\left|x_i(t)^T x_i(t)-d^2\right|_{\text{最小}}\right) \geq 2 \tag{10}$$

This will get a set of correct integer ambiguity, Substituting it into Eq. (9) to solve the high-precision baseline vector $\boldsymbol{d}$. Assuming its coordinate is (d_e, d_n, d_u) in the EDU coordinate system, we can get the heading and pitch angle information.

$$\begin{cases} \varphi = \arctan(d_n/d_e) \\ \theta = \arctan\left(d_u/\sqrt{d_n^2+d_e^2}\right) \end{cases} \tag{11}$$

3 Ambiguity Inverse Resolution Algorithm Based on Dual-Frequency Correlation Relation

3.1 Linear Combination of Dual-Frequency Measurements

Double-difference carrier observation general formula of frequency $L1$ and $L2$ can be rewritten from Eq. (1) as:

$$\lambda_{Lx}(\phi_{Lx}^{ij}+N_{Lx}^{ij}) = \cdot\boldsymbol{S}_i - \boldsymbol{S}_j \cdot \boldsymbol{d} + \varepsilon_{Lx}^{ij}, \tag{12}$$

where x represent different frequencies, ε^{ij} is a set of error. The linear combination observation equation of dual-frequency dual-difference carrier phase measurement is:

$$\lambda_{k_1,k_2}\phi_{k_1,k_2}^{ij} = \left(\boldsymbol{S}_i - \boldsymbol{S}_j\right)\cdot\boldsymbol{d} + N_{k_1,k_2}^{ij} + \varepsilon_{k_1,k_2}^{ij} \tag{13}$$

k_1 and k_2 represents different linear combination coefficients, where

$$N_{k_1,k_2} = k_1 N_{L1}^{ij} + k_2 N_{L2}^{ij}, \quad \phi_{k_1,k_2}^{ij} = k_1\phi_{:L1}^{ij} + k_2\phi_{L2}^{ij},$$
$$\lambda_{k_1,k_2} = \frac{1}{k_1/\lambda_{L1} + k_2/\lambda_{L2}}, \quad \varepsilon_{k_1,k_2}^{ij} = k_1\varepsilon_{L1}^{ij} + k_2\varepsilon_{L2}^{ij}$$

Assume that the carrier phase measurement error of $L1$ and $L2$ frequency is independent of each other, i.e., $\sigma_{\phi_1} = \sigma_{\phi_2} = \sigma$. Then the error variance [12] of the measured value of ϕ_{k_1,k_2}^{ij} is $\sigma_{\phi_{k_1,k_2}} = \sqrt{k_1^2+k_2^2}\sigma$. The wavelength and the error variance of different coefficients are different, as shown in Table 1, where $\sigma = 0.05$ (circle).

From Table 1, we know the combination of different coefficients can be used to construct the wavelength of combined measurement with different length λ_{k_1,k_2}. Considering Eq. (6), we can note that with the increase of wavelength, the search range of the main ambiguity, the combination of the corresponding attitude angles,

Table 1 Wavelength and error mean square error of different coefficients

	$L1$	$L2$	(1,1)	(1, −1)	(−2, 3)	(4, −5)
λ_{k_1,k_2} (cm)	19	24.4	10.7	86.2	56.54	178.3
$\sigma_{\phi_{k_1,k_2}}$ (circuit)	0.05	0.05	0.07	0.07	0.18	0.32
$\sigma_{\phi_{k_1,k_2}}$ (cm)	0.95	1.22	0.092	6.034	10.177	57.060

and initialization time all decrease, but the measurement noise is enlarged, which may lead to the loss of correct ambiguity solution. It can be also seen that the error mean squared error of (1, 1) combination is smaller than the error of the original $L1$ or $L2$, which brings the higher accuracy of the solution of the baseline vector and attitude angle. In this paper, the combination of long wavelengths is used to compress the search space and reduce the initialization time. Simultaneously, the constraint relationship between the two frequencies is used to obtain the narrow-line ambiguity, for the purpose of getting higher accuracy of attitude angle information.

3.2 *Using Double-Frequency to Inverse Solve Narrow-Lane Ambiguity*

From the aforementioned statement, we can infer that dual combination of ambiguity is:

$$N_{k_1,k_2} = k_1 N_{L1}^{ij} + k_2 N_{L2}^{ij} \tag{14}$$

The $L1$ frequency and $L2$ frequency in Eq. (12) can be subtracted:

$$\lambda_{L1}\phi_{L1} - \lambda_{L2}\phi_{L2} = \lambda_{L1}N_{L1} - \lambda_{L2}N_{L2} + \lambda_{L1}\varepsilon_{L1} - \lambda_{L2}\varepsilon_{L2} \tag{15}$$

The float solution of ambiguity can be derived from Eqs. (14) and (15):

$$\begin{aligned}\hat{N}_{L1+L2} = \varepsilon_{N_{L1+L2}} + \widehat{N}_{L1+L2} = (k_2 - k_1)\frac{\lambda_{L1}\varepsilon_{L1} - \lambda_{L2}\varepsilon_{L2}}{k_2\lambda_{L1} + k_1\lambda_{L2}} \\ + \frac{(\lambda_{L2} + \lambda_{L1})N_{k_1,k_2} + (k_2 - k_1)(\lambda_{L1}\phi_{L1} - \lambda_{L2}\phi_{L2})}{k_2\lambda_{L1} + k_1\lambda_{L2}},\end{aligned} \tag{16}$$

where

$$\widehat{N}_{L1+L2} = \text{round}\left(\frac{(\lambda_{L2} + \lambda_{L1})N_{k_1,k_2} + (k_2 - k_1)(\lambda_{L1}\phi_{L1} - \lambda_{L2}\phi_{L2})}{k_2\lambda_{L1} + k_1\lambda_{L2}}\right)$$

From Eq (16), we can note that the narrow-lane ambiguity $\widehat{N}_{L1+L2}$ accuracy derived from the ambiguity of dual-frequency combination is related to the error term $\varepsilon_{N_{L1+L2}}$.

Table 2 The mean square error of narrow-lane ambiguity float solution using dual-frequency measurements of different linear combinations

Mean square error/(circuit)	(1, −1)	(−2, 3)	(4, −5)
$\sigma_{\varepsilon_{\widetilde{N}_{L1+L2}}}$	0.612	0.850	13.778

Assume that the carrier phase measurement errors at different frequencies are independent with each other. Then according to the error propagation law [13], the mean square error can be inferred as:

$$\sigma_{\varepsilon_{\widetilde{N}_{L1+L2}}} = \left|\frac{k_2 - k_1}{k_2\lambda_{L1} + k_1\lambda_{L2}}\right| \sqrt{\lambda_{L1}^2 + \lambda_{L2}^2}\sigma \tag{17}$$

Let $\sigma_{\varepsilon_1} = \sigma_{\varepsilon_2} = 0.05$ (circuit) [14]. According to the above equation, we can get the mean square error of narrow-lane ambiguity float solution obtained by dual-frequency measurements of different linear combinations (shown in Table 2).

It can be seen from Table 2 that the mean square errors of narrow-lane ambiguity derived from (1, −1) and (−2, 3) combinations are less than 1 circuit, and the mean square error based on (4, −5) combination is too large. Hence, it is not appropriate to use the combination (4, −5) to obtain narrow-lane ambiguity.

3.3 *Fix Integer Ambiguity by the Improved OVT Test Method*

3.3.1 OVT Test Method

Assume that each narrow-lane ambiguity group is composed of m ambiguities. After fixing a set of correct wide-lane ambiguity, we get the continuous n-unit narrow-lane ambiguity according to Eq. (15). The consistency can be checked as follows: if the same ambiguity is obtained for n consecutive units, it is regarded as the correct ambiguity; otherwise, we will repeat the above work to find the ambiguity solution satisfying the testing conditions.

In this testing method, the length of the detection window is n units. A new test will start from the next testing window if there exists ambiguity solution that does not meet the requirements in a test window. So it is desirable to improve the efficiency.

3.3.2 An Improved OVT Test Method

Based on above analysis, we propose an improved OVT test method. It is implemented according to the following steps. And the operation flow chart is shown in Fig. 1.

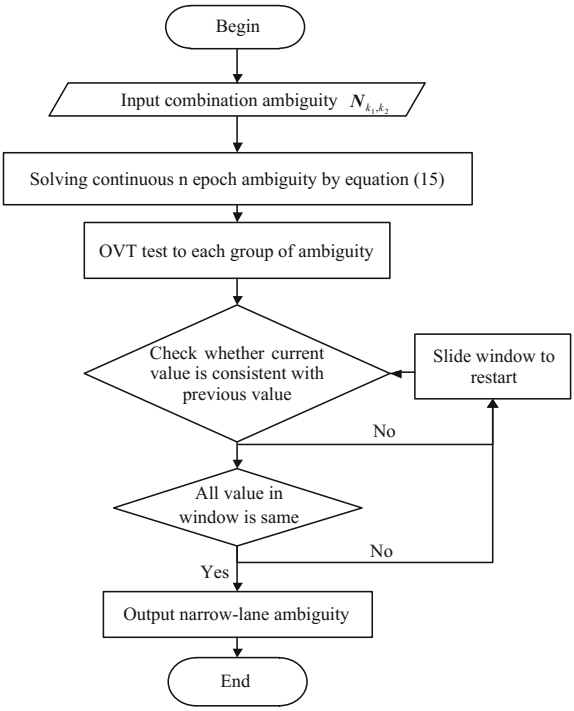

Fig. 1 The Improved OVT method flowchart

(1) The OVT test is carried out in parallel based on m ambiguity. The length of testing window is n.
(2) If the ambiguity is the same in the window length, the ambiguity solution is proved to be reliable.
(3) If a certain degree of ambiguity is inconsistent with the previous solution, restart to check from this moment, until we find the ambiguity solution that meets the test conditions.
(4) After all ambiguities have passed inspection, it determined that the narrow-lane ambiguity group is correct credible.

4 Experiment Analyses

4.1 Experimental Environment

Connecting two dual-frequency receivers and antennas at ends of the baseline, respectively, the baseline length was measured as 1.907 m, pitch angle and heading angle are 0.10° and 229.15° before the experiment, the sampling frequency is set to

1Hz, the visible satellites number is 8. In order of elevation angle, the PRN should be 31#, 32#, 14#, 25#, 3#, 16#, 29#, 20#, and seven groups of double-difference observation data are gained by seeking difference between other satellites and 31# which has the biggest elevation angle.

4.2 The Experimental Process and Analysis

The scheme 1 is used as the original algorithm, the scheme 2 is an improved algorithm which only uses wide-lane combination, and the scheme 3 is the algorithm in this paper. Before the experiment, using the traditional algorithm to solve the integer ambiguity of $L1/L2$ frequency and combined frequency, which is used as the real ambiguity value, to compare with the experimental group, as shown in Table 3.

Comparing the search space and the number of combinations of attitude angles of scheme 1 and scheme 3, we know that the dual-frequency combination of the longer wavelengths can effectively compress the search space, the experimental results from Table 4 show that the dual-frequency combination of longer wavelengths can improve the search efficiency. The search times decreased from 338 times to 171 times compared with the original algorithm. On the one hand, the algorithm reduces the amount of computation; on the other hand, it eliminates the partial error solution, which is helpful to improve the solution success rate.

Table 3 Integer ambiguity of $L1$, $L2$ frequency and combined frequency

	N_1	N_2	N_3	N_4	N_5	N_6	N_7
L1	8,388,613	8,388,608	6,626,635	8,388,609	6,626,631	6,626,617	6,626,615
L2	0	6	450,753	5	450,759	450,739	450,723
$N_{1,-1}$	8,388,613	8,388,602	6,175,882	8,388,604	6,175,872	6,175,878	6,175,892
$N_{-2,3}$	−16,777,226	−16,777,198	−11,901,011	−16,777,203	−11,900,985	−11,901,017	−11,901,061

Table 4 The searching range/times/corresponding attitude angles combination numbers of main ambiguity

Scheme	Main ambiguity search range	Main ambiguity search times	Attitude angle combination search times
Scheme1	[8,388,602,8,388,619][8,388,607,8,388,621]	270	338
Scheme3	[8,388,602,8,388,614][8,388,601,8,388,610]	130	171

However, Table 1 shows that the cost of improving the search efficiency is to enlarge the measurement noise, we analyzed the measured data and found that the success rate of integer ambiguity resolution using (1, −1) combination is about 91%, (−2, 3) combination is about 84%.

After successfully fixing a set of wide-lane ambiguity resolution, in order to verify that using the dual-frequency constraints can solve narrow-lane ambiguity, using Eq. (16) can obtain the corresponding narrow-lane ambiguity, as shown in Table 5, the success rate of (1, −1) combination is higher than (−2, 3) combination, consider the success rate of fixing correct integer ambiguity of (−2, 3) combination. In the end, we choose the (1, −1) combination to compress the search space.

Because solving ambiguity exists narrow certain probability of failure, we use the improved OVT method to fix it, fixed results as shown in Table 6, the test results show that the proposed method can effectively improve the success rate of solving single-frequency integer ambiguity, and making the final solution is correct and reliable.

Compared with scheme 1, scheme 2 from the initialization time, baseline length, pitch angle, the root mean square error (RMSE) to evaluate the performance of the scheme 3, from Table 7 and Figs. 2, 3, and 4, the baseline error, attitude angle error, and initialization time of scheme 3 are better than scheme 1; scheme 2 only reduces the search range by using the wide-lane combination, and directly uses the wide-lane carrier observation equation to solve the baseline vector and attitude angle information, the experimental results show that the wide-lane combination

Table 5 The success rate of the ambiguity resolution of the narrow-lane ambiguity without using OVT improved test method

	Ambiguity	N^{21} (%)	N^{31} (%)	N^{41} (%)	N^{51} (%)	N^{61} (%)	N^{71} (%)	Success rate (%)
(1, −1)	$\widehat{N}_{L1+L2}$	99	100	98	100	97	100	94.1
(−2, 3)		95	97	93	98	89	94	70.3

Table 6 The success rate of the ambiguity resolution of the narrow-lane ambiguity using OVT improved test method

	Ambiguity	N^{21}	N^{31}	N^{41}	N^{51}	N^{61}	N^{71}
1, −1	$\widehat{N}_{L1+L2}$	8,388,613	8,388,602	6,175,882	8,388,604	6,175,872	6,175,878
−2, 3		−16,777,226	−16,777,198	−11,901,011	−16,777,203	−11,900,985	−11,901,017

Table 7 Comparison of algorithm performance evaluation

Scheme	Baseline length RMSE	Heading angle RMSE	Pitch angle RMSE	Initialization time (s)
Scheme 1	0.0020	0.0561	0.0859	53
Scheme 2	0.0146	0.3879	0.8003	29
Scheme 3	0.0017	0.0436	0.0794	39

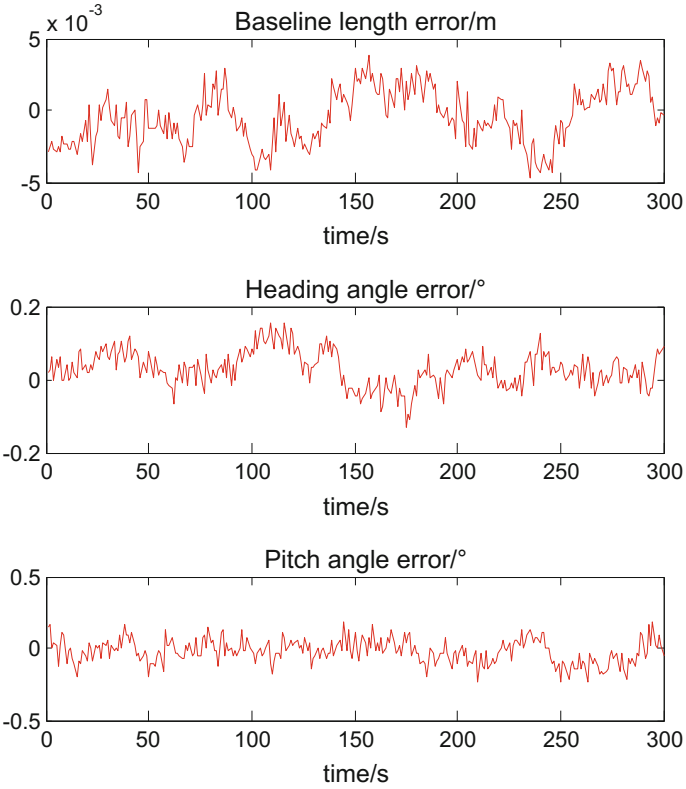

Fig. 2 Error of Scheme 1

makes the integer ambiguity easier to fix, the initialization time is greatly reduced, but the measurement error becomes larger and the solution accuracy becomes lower.

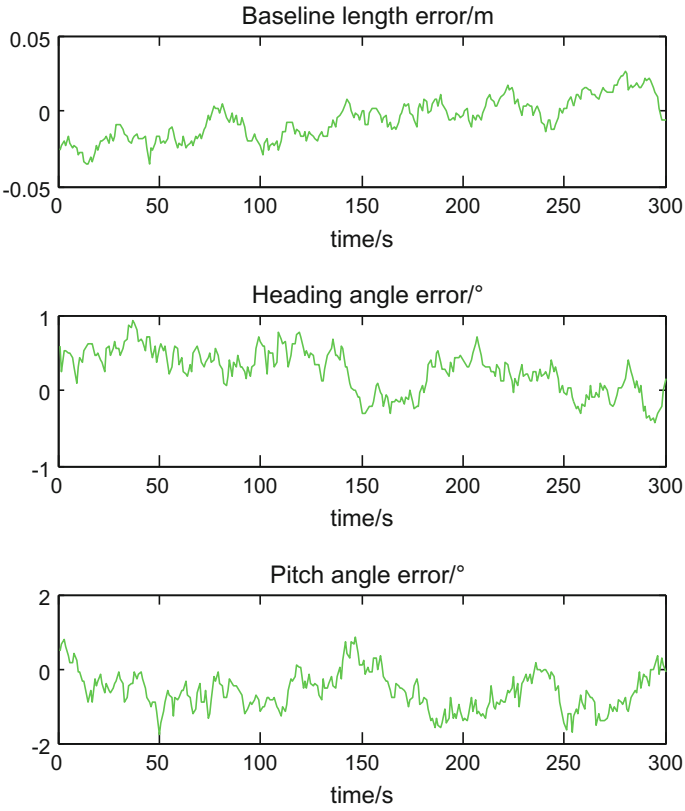

Fig. 3 Error of Scheme 2

5 Conclusion

In this paper, in order to improve the initialization efficiency and attitude angle accuracy of the constraint result zone search algorithm, an improved algorithm based on dual-frequency combination is proposed. Through the analysis of the measured data, we can get the following conclusions:

(1) The wide-lane combination can effectively improve the initialization efficiency of the constraint result zone search algorithm by compressing the search space and making full use of the observed information.
(2) It is feasible to solve the narrow-lane ambiguity by using the correlation relation of the dual-frequency carrier. The experiment shows that the success rate is high, and can be higher if combined with OVT test method.
(3) The algorithm can balance well between the efficiency and accuracy. It not only reduces the initialization time but also improves the precision of the attitude angle.

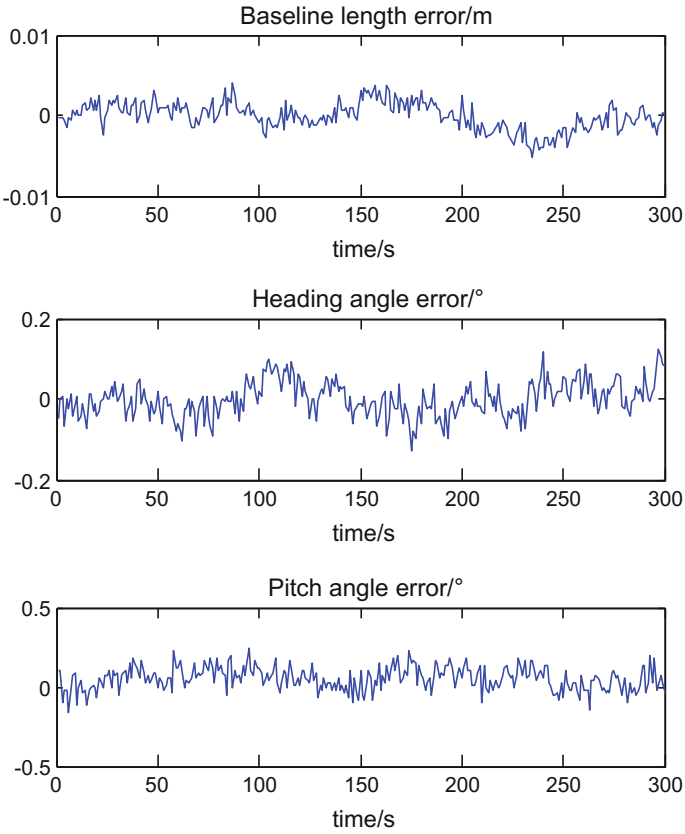

Fig. 4 Error of Scheme 3

References

1. Liu S, Zhang L, Li J, Luo Y (2016) Dual frequency long-short baseline ambiguity resolution for GNSS attitude determination. In: 2016 IEEE/ION position, location and navigation symposium (PLANS), pp 631–637
2. Xia K, Zhang X, Gao J (2008) Study on GPS attitude determination technology based on QPSO algorithm. In: Proceedings of the 7th world congress on intelligent control and automation, pp 1869–1873
3. Li B, Cao K, XU J (2013) Application of carrier phase differential relative navigation for shipboard landing of aircraft. In: China satellite navigation conference (CSNC) 2013 proceedings, pp 189–196
4. Liu JN, Deng CL, Tang WM (2014) Review of GNSS ambiguity validation theory. Geomatics Inf Sci Wuhan Uni 39(9):1009–1016
5. Teunissen PJG (2010) Integer least-squares theory for the GNSS compass. J Geodesy 84 (7):433–447
6. Purivigraipong S, Hodgart S et al (2010) Resolving integer ambiguity of GPS carrier phase difference. In: IEEE transactions on aerospace and electronic systems, pp 832–847

7. Liu M, Chai H, Dong B et al (2016) An algorithm of single-epoch integer ambiguity resolution for reference stations of BDS triple-frequency network RTK. In: China satellite navigation conference (CSNC) 2016 proceedings, vol. III. pp 337–345
8. Wang Y, Zhao XB, Pang CL et al (2016) Research on integer ambiguity resolution method with BDS and GPS single epoch dual-frequency data. In: China satellite navigation conference (CSNC) 2016 proceedings, vol III. pp 271–283
9. Pang CL, Zhao XB, Yu YL et al (2013) Method of fast attitude measurement based on two antennas assisted by accelerometer. Journal of Chinese Inertial Technology 21(6):749–752
10. Li SJ, Li ZA, Pang CL et al (2016) Improved algorithm based on result zone for GNSS attitude measurement. Journal on Communications 37(1):191–197
11. Wu SS, Zhao XB, Yu YL et al (2016) Direct calculation of BDS single-frequency integer ambiguity resolution in kinematic to kinematic based on dual-frequency correlation constraints. Electron Optics Control 23(11):43–46
12. Cocard M, Bourgon S, Kamali O et al (2008) A systematic investigation of optimal carrier-phase combinations for modernized triple-frequency GPS. J Geodesy 82(9):555–564
13. Wang Y, Zhao XB, Pang CL et al (2014) Antenna configuration and accuracy analysis of GNSS attitude determination system. Comput Meas Control 22(9):3024–3027
14. Li JL, Yang LY, Xu JY et al (2015) GNSS multi-carrier fast partial ambiguity resolution strategy tested with real BDS/GPS dual-and triple-frequency observations. GPS Solutions 19 (1):5–13

The Detection and Repair of Cycle-Slip Based on the Combination of BeiDou Triple-Frequency Observations

Xu Feng, Changjian Liu, Chen Liu, Lingfeng Xu and Ying Du

Abstract The theory of detection and repair of cycle-slip by combination of BeiDou triple-frequency observations has been described. The optimization principles of triple-frequency observations, and the threshold of cycle-slip, and the relationship between the STD and success rate of cycle-slip fixed have been discussed. In consideration of ionospheric delay, selecting the phase/pseudorange combination that is suitable for BeiDou triple-frequency and utilizing measured data to calculate the estimation of combined cycle-slip. Results show that the amount of STD of cycle-slip calculated by three-stage method is smaller than pseudorange/phase combination, ensuring the accuracy of cycle-slip detection and repair; and the workload of detection and repair of cycle-slip by three-stage method has been decreased compared with geometry-free phase combination.

Keywords BeiDou triple-frequency observations · The detection and repair of cycle-slip · Combination observations · Real time · Ionosphere delay

1 Introduction

Precise point positioning data quality control is an important premise to ensure the results of positioning [1], in which the detection and repair of cycle-slip are an important link. Triple-frequency observations, improving the success rate and accuracy of cycle-slip detection and repair, can obtain more combination with longer wavelength, less noise, and keep the cycle-slip as an integer than dual-frequency. Many scholars have conducted a lot of work in research to cycle-slip detection and repair, which provides a lot of reference to the development of BeiDou navigation system.

X. Feng (✉) · C. Liu · C. Liu (✉) · L. Xu · Y. Du
Institute of Geospatial Information, Information Engineering University, Zhengzhou, China
e-mail: 18666469529@163.com

C. Liu
e-mail: Liu_chen_vip@163.com

J. Sun et al. (eds.), *China Satellite Navigation Conference (CSNC) 2017 Proceedings: Volume III*, Lecture Notes in Electrical Engineering 439,
DOI 10.1007/978-981-10-4594-3_38

Literature [2] can realize real-time detection and repair of BeiDou triple-frequency cycle-slip by using a pseudorange-phase combination (0, 1, 1) and two geometry-free phase combinations (1, 4, 5), (1, 0, 1). After ignoring the ionospheric delay variation between epoch, literature [3] can realize real-time detection and repair of BeiDou triple-frequency cycle-slip by using a pseudorange-phase combination (1, 3, −4) and two geometry-free phase combinations (1, 1, −2), (1, −2, 1), and search algorithm is used to solve the unstable of equations. Pseudorange-phase combination has been analyzed in literature [4], with the results that the detection and repair success rate will be higher when the STD of combination is smaller. The variety of pseudorange and phase combinations of BDS has been analyzed and three linearly independent combinations have been selected based on the principle of multiple-frequency combination. Literature [5] utilizing the triple-frequency geometry-free phase combinations to detecting cycle-slip and utilizing a method like LAMBDA to determine the cycle-slip. The accuracy of geometry-free phase combination and phase-pseudorange combination has been compared under different sampling intervals in Literature [6]. It is recommended to utilize two geometry-free phase combinations to detect cycle-slip and utilize LAMBDA algorithm to repair when cycle-slip is confirmed. In literature [7], optimal BeiDou triple-frequency integer linear combination models with different character have been selected based on the roadway number, the ionosphere delay factor, and noise factor. In literature [8], the pseudorange-phase and geometry-free phase combination have been compared in detection and repair of cycle-slip. The phase-pseudorange will be chosen at first when integrating the computation of algorithm, complexity, and rounding error.

To ensure the matrix is reversible, a combination that satisfied the sum of coefficient is not equal to zero must be chosen, which will result in the ionospheric delay is remarkable. Ionospheric delay will result in the STD of cycle-slip detection larger, further causing the success rate of detection and repair of cycle-slip lower. In this paper, the method of detection and repair of cycle-slip has been analyzed in theoretical and experimental in consideration to the detection amount of cycle-slip.

2 Combination of Triple-Frequency Un-Differenced Observations

The original observation equation for pseudorange and carrier are as follows [5]:

$$P = \rho + c(\boldsymbol{\delta t}_R - \delta t^S) + T_{R_i} + I_{R_i} + \varepsilon_{R_i} + m_{R_i} \tag{1}$$

$$\begin{aligned} \phi = \lambda_i \phi_i = \rho + c(\delta t_R - \delta t^S) \\ + \lambda_i N + T_{\phi_i} - \beta_{\phi_i} \cdot I_{\phi_i} + \varepsilon_{\phi_i} + m_{\boldsymbol{\phi}_i}, \end{aligned} \tag{2}$$

where ϕ is the carrier phase measurement in meters; P is the pseudorange measurement in meters; ϕ_i is the carrier phase observation in cycles; λ_i is the corresponding wavelength; N_i is the integer ambiguity; ρ is the geometric distance

between the satellite and receiver; T is troposphere delay; I is ionospheric delay; $\beta_{\phi_i} = f_1^2/f_i^2$ is the ratio coefficient of the ionospheric delay of corresponding frequency; ε is the measurement noise; m is multipath error.

The combined pseudorange and phase observations can be defined as follows [6]:

$$P_{(a,b,c)} = \frac{af_1P_1 + bf_2P_2 + cf_3P_3}{af_1 + bf_2 + cf_3} \tag{3}$$

$$\phi_{(i,j,k)} = \frac{if_1\phi_1 + jf_2\phi_2 + kf_3\phi_3}{if_1 + jf_2 + kf_3} \tag{4}$$

The linearly combined frequency, wavelength, integer ambiguity, ratio coefficient of the ionospheric delay, and ratio coefficient of the observation noise can be defined as follows:

$$\begin{cases} f_{(i,j,k)} = i \cdot f_1 + j \cdot f_2 + k \cdot f_3 \\ \lambda_{(i,j,k)} = c/f_{(i,j,k)} = c/(i \cdot f_1 + j \cdot f_2 + k \cdot f_3) \\ N_{(i,j,k)} = i \cdot N_1 + j \cdot N_2 + k \cdot N_3 \\ \beta_{(i,j,k)} = \frac{f_1^2(i/f_1 + j/f_2 + k/f_3)}{i \cdot f_1 + j \cdot f_2 + k \cdot f_3} \\ \mu^2_{(i,j,k)} = \frac{(i \cdot f_1)^2 + (j \cdot f_2)^2 + (k \cdot f_3)^2}{(i \cdot f_1 + j \cdot f_2 + k \cdot f_3)^2} \end{cases} \tag{5}$$

where the phase combined coefficients i, j, and k are integers; pseudorange combined coefficients a, b, c are real number; $P_1, P_2, P_3, \phi_1, \phi_2, \phi_3$ respectively pseudorange and carrier phase observations corresponding to $B1$, $B2$, $B3$ frequency.

2.1 Detection and Repair of Cycle-Slip in Triple-Frequency Phase/Pseudorange Combination

For the subtracting of (1), (2) we can obtain:

$$N = \frac{\lambda\varphi - P + (I_\phi + I_R) - (\varepsilon_\phi - \varepsilon_R) - (m_\phi - m_R)}{\lambda} \tag{6}$$

From (6) we can obtain the integer ambiguity of combination $N_{(i,j,k)}$:

$$N_{(i,j,k)} = \left[\begin{matrix} \lambda_{(i,j,k)}\phi_{(i,j,k)} - P_{(a,b,c)} - \left(\beta_{\phi_{(i,j,k)}} + \beta_{P_{(a,b,c)}}\right)I - \\ (\varepsilon_{\phi_{(i,j,k)}} - \varepsilon_{R_{(a,b,c)}}) - (m_{\phi_{(i,j,k)}} - m_{R_{(a,b,c)}}) \end{matrix} \right] \Big/ \lambda_{(i,j,k)} \tag{7}$$

Then subtract it between the epochs, since the multipath effect varies slowly with time and the elevation angle is limited, the multipath can be eliminated between the epochs:

$$\begin{aligned}\Delta N_{(i,j,k)} &= N_{(i,j,k)}(t_1) - N_{(i,j,k)}(t_0) \\ &= \frac{\lambda_{(i,j,k)}\Delta\varphi_{(i,j,k)} - \Delta P_{(a,b,c)} - \left(\beta_{\varphi_{(i,j,k)}} + \beta_{P_{(a,b,c)}}\right)\Delta I - \left(\Delta\varepsilon_{\phi_{(i,j,k)}} - \Delta\varepsilon_{R_{(a,b,c)}}\right)}{\lambda_{(i,j,k)}} \\ &= \frac{\Delta\phi_{(i,j,k)} - \Delta P_{(a,b,c)} - \left(\beta_{\varphi_{(i,j,k)}} + \beta_{P_{(a,b,c)}}\right)\Delta I - \left(\Delta\varepsilon_{\phi_{(i,j,k)}} - \Delta\varepsilon_{R_{(a,b,c)}}\right)}{\lambda_{(i,j,k)}}\end{aligned} \tag{8}$$

The STD of the combined cycle-slip detection amount can be obtained:

$$\sigma_{\Delta N_{(i,j,k)}} = \sqrt{\sigma^2_{\Delta\phi_{(i,j,k)}} + \sigma^2_{\Delta P_{(a,b,c)}} + \left(\beta_{\varphi_{(i,j,k)}} + \beta_{P_{(a,b,c)}}\right)^2\sigma^2_{\Delta I}}/\lambda_{(i,j,k)} \tag{9}$$

When the ratio coefficient ionospheric delay is small, the ionospheric delay error can be neglected, the STD of the combined cycle-slip estimate is as follows:

$$\sigma_{\Delta N_{(i,j,k)}} = \sqrt{\sigma^2_{\Delta\phi_{(i,j,k)}} + \sigma^2_{\Delta P_{(a,b,c)}}}/\lambda_{(i,j,k)} \tag{10}$$

From the literature [9], take the pseudorange noise $\sigma_P = 0.3$ m, phase noise $\sigma_\phi = 0.002$ m.

The condition of cycle-slip detection can be express as follows:

$$\left|\Delta N_{(i,j,k)}\right| \geq n\sigma_{\Delta N_{(i,j,k)}} \tag{11}$$

n equals to 3 or 4 corresponding to the confidence level at 99.7 and 99.9% respectively. The cycle-slip estimation $\Delta\hat{N}_{(i,j,k)}$ is the rounding of $\Delta N_{(i,j,k)}$, the success rate of the detection of combined cycle-slip can be expressed as:

$$P_{\Delta\hat{N}_{(i,j,k)}} = P\left(\left|\Delta N_{(i,j,k)} - \Delta\hat{N}_{(i,j,k)}\right| < 0.5\right) = 2\phi\left(\frac{1}{2\sigma_{\Delta N(i,j,k)}}\right) - 1 \tag{12}$$

It can be seen that the smaller the STD of the cycle-slip detection amount, higher the success rate of the cycle-slip, the relationship is shown in Table 1.

When the STD is less than 0.15, it can be considered that the success rate of cycle-slip fixed is 100% [10].

Table 1 The relationship between STD and fixed success rate of combination cycle-slip detection amount

$\sigma_{\Delta N_{(i,j,k)}}$	$\frac{1}{\sigma_{\Delta N_{(i,j,k)}}}$	$P_{\Delta\hat{N}_{(i,j,k)}}$
0.1	1	1
0.15	0.9996	99.9%
0.2	0.9938	98.8%
0.25	0.97725	95.5%

Assuming that $\Delta N_1, \Delta N_2, \Delta N_3$ are cycle-slips of original frequency, then:

$$\begin{pmatrix} i_1 & j_1 & k_1 \\ i_2 & j_2 & k_2 \\ i_3 & j_3 & k_3 \end{pmatrix} \begin{pmatrix} \Delta N_1 \\ \Delta N_2 \\ \Delta N_3 \end{pmatrix} = \begin{pmatrix} \Delta N_{(i_1,j_1,k_1)} \\ \Delta N_{(i_2,j_2,k_2)} \\ \Delta N_{(i_3,j_3,k_3)} \end{pmatrix} \tag{13}$$

In order to maintain the cycle-slip as an integer, the set of coefficient matrix should be 1, then the cycle-slip of original frequency can be obtained:

$$\begin{pmatrix} \Delta N_1 \\ \Delta N_2 \\ \Delta N_3 \end{pmatrix} = \begin{pmatrix} i_1 & j_1 & k_1 \\ i_2 & j_2 & k_2 \\ i_3 & j_3 & k_3 \end{pmatrix}^{-1} \begin{pmatrix} \Delta N_{(i_1,j_1,k_1)} \\ \Delta N_{(i_2,j_2,k_2)} \\ \Delta N_{(i_3,j_3,k_3)} \end{pmatrix} \tag{14}$$

2.2 Selection of Triple-Frequency Combination Observation

The selection principle of triple-frequency combination observation [11, 12]:

1. Combined observation should have longer wavelength to reduce the influence of multipath effect, ionospheric delay, hardware delay, and pseudorange measurement noise on the sensitivity of cycle-slip detection between epochs.
2. Ratio coefficient of the ionospheric delay should be smaller. On the one hand, ionospheric delay will affect the cycle-slip detection amount; on the other hand, the ionospheric delay will affect the STD of cycle-slip detection amount, which further affect the success rate of cycle-slip detection.
3. Ratio coefficient of the observation noise should be smaller, due to excessive observation noise can interfere with cycle-slip detection.
4. The STD of cycle-slip detection amount should be smaller. On the one hand, smaller cycle-slip can be detected; on the other hand, the success rate of the cycle-slip detection can be guaranteed.

In order to make the STD of the combined cycle-slip detection amount minimum, it should satisfy $\sigma_{\Delta P_{(a,b,c)}} = \min$, then we can get $af_1 = bf_2 = cf_3$, so we take (4, 5, 5) as the combination of pseudorange. Based on the principles above, we choose the combination in the conditions that wavelength to be longer than 3 m, the STD of combined cycle-slip detection amount to be less than 0.15 weeks, the coefficient i, j, k change from -10 to 10. The optimal combinations are shown in Table 2 (no ionospheric delay).

As can be seen from table, when the sum of the combined coefficients is zero, the ratio coefficients of ionospheric delay are small. However, the coefficients matrix must be reversible, so at least one combination that the sum of combined coefficients is nonzero, in which ionospheric delay is too large to neglect and should be repaired.

Table 2 Optimal combination coefficients

(i,j,k)	λ/m	β	μ	$\sigma_{\Delta N_{(i,j,k)}}$
(−4,1,4)	8.140	12.234	0.081	0.087
(−3,6,−2)	13.321	12.612	0.099	0.101
(−1,−5,6)	20.932	−0.378	0.111	0.112
(0,−1,1)	4.884	−0.042	0.02	0.053
(1,4,−5)	6.371	0.336	0.092	0.086
(3,−7,3)	7.712	−12.653	0.116	0.120
(4,−2,−3)	12.211	−12.276	0.076	0.079

2.3 The Detection and Repair of Cycle-Slip by Three Steps

Step 1: Utilizing EWL to estimate cycle-slip. EWL processes long wavelength, small ratio coefficients of observation noise, and can eliminate the effect of ionospheric delay, it can be expressed as follows:

$$\Delta N_{(0,-1,1)} = \left(\frac{-f_2 \cdot \Delta\phi_2 + f_2 \cdot \Delta\phi_3}{-f_2 + f_3} - \frac{f_2 \cdot \Delta P_2 + f_3 \cdot \Delta P_3}{f_2 + f_3} \right) / \lambda_{(0,-1,1)} \tag{15}$$

The STD of combined cycle-slip detection amount of EWL:

$$\sigma_{\Delta N_{(0,-1,1)}} = \sqrt{\left(\frac{\left(f_2^2 + f_3^2\right) \cdot \sigma_{\Delta\phi}^2}{\left(-f_2 + f_3\right)^2} + \frac{\left(f_2^2 + f_3^2\right) \cdot \sigma_{\Delta P}^2}{\left(f_2 + f_3\right)^2} \right) / \lambda_{(0,-1,1)}^2} \tag{16}$$

In accordance with the accuracy of pseudorange and carrier phase, we can obtain that $\sigma_{\Delta N_{(0,-1,1)}} = 0.0636$. The cycle-slip estimation can be obtained as:

$$\Delta \hat{N}_{(0,-1,1)} = \mathrm{ROUND}\left(\Delta N_{(0,-1,1)}\right), \tag{17}$$

where ROUND is rounding function.

Step 2: Choosing (1, 4, −5) as the second combination due to its superior character. Ignoring the ionospheric delay, then:

$$\Delta N_{(1,4,-5)} = \left(\Delta\phi_{(1,4,-5)} - \Delta\phi_{(0,-1,1)} + \Delta \hat{N}_{(0,-1,1)} \right) / \lambda_{(1,4,-5)} \tag{18}$$

The STD of combined cycle-slip detection amount:

$$\sigma_{\Delta N_{(1,4,-5)}} = \sqrt{\left(\sigma_{\Delta\phi_{(1,4,-5)}}^2 + \sigma_{\Delta\phi_{(0,-1,1)}}^2 \right) / \lambda_{(1,4,-5)}^2} = 0.0776 \tag{19}$$

It can be seen that the STD is reduced compared with the pseudorange/phase combination. The cycle-slip estimation can be obtained as:

$$\Delta\hat{N}_{(1,4,-5)} = \mathrm{ROUND}\left(\Delta N_{(1,4,-5)}\right) \tag{20}$$

Step 3: According to coefficients matrix must be reversible, the combination that the sum of combined coefficients is nonzero should be chosen in this step, in which ionospheric delay is too large to neglect and should be repaired. The ionospheric delay between the epochs can be calculated as:

$$\Delta I = (\Delta\phi_1 - \Delta\phi_2)/\left(f_1^2/f_2^2 - 1\right), \tag{21}$$

where ΔI is the ionospheric delay between the epochs, ϕ_1, ϕ_2 are the originally un-differenced observation, f_1, f_2 are the corresponding frequencies. The STD of ΔI can be calculated as:

$$\sigma_{\Delta I} = \sqrt{2\sigma_{\Delta\phi}^2}/\left(f_1^2/f_2^2 - 1\right)^2 = 0.014\,\mathrm{m} \tag{22}$$

The cycle-slip detection amount:

$$\Delta N_{(i,j,k)} = \left(\Delta\phi_{(i,j,k)} - \Delta\phi_{(0,-1,1)} + \Delta\hat{N}_{(0,-1,1)} - \left(\beta_{(i,j,k)} - \beta_{(0,-1,1)}\right)\cdot\Delta I\right)/\lambda_{(i,j,k)} \tag{23}$$

The STD of cycle-slip detection amount:

$$\sigma_{\Delta N_{(i,j,k)}} = \sqrt{\left(\sigma_{\Delta\phi_{(0,-1,1)}}^2 + \sigma_{\Delta\phi_{(i,j,k)}}^2 + \left(\beta_{(i,j,k)} - \beta_{(0,-1,1)}\right)^2\cdot\sigma_{\Delta I}^2\right)/\lambda_{(i,j,k)}^2} \tag{24}$$

Based on the consideration of the ionospheric delay, the STD of he combination that the sum of combined coefficients is non-zero are shown as Table 3.

It can be seen that ionospheric delay results in the STD of phase/pseudorange combination larger than 0.15, further causing cycle-slip detection to appear as false positives or false negatives. When using three-step method, without introducing the pseudorange observation error, the STD of cycle-slip detection amount can still be controlled within 0.15, so as to ensure the success rate of the cycle-slip detection. In this paper, (−3, 6, −2) was chosen due to the minimum STD, then the cycle-slip estimation can be obtained:

$$\Delta\hat{N}_{(-3,6,-2)} = \mathrm{ROUND}\left(\Delta N_{(-3,6,-2)}\right) \tag{25}$$

Table 3 The STD of combined cycle-slip detection amount

Combination coefficients	STD of three-step	STD of phase/pseudorange combination
(−4,1,4)	0.2003	0.2223
(−3,6,−2)	0.1392	0.1672
(3,−7,3)	0.2177	0.2298
(4,−3,−3)	0.1409	0.1605

3 Experiment and Analysis

In this paper, October 31, 2016 may station BeiDou triple-frequency observation data was utilized to carry out experimental analysis (data source: ftp://cddis.gsfc.nasa.gov/pub/gps/data/campaign/mgex).

3.1 The Estimation of Ionospheric Delay

The ionospheric delays for the C02 and C05 satellites are calculated. The C02 satellite has 2490 epochs and the C05 satellite has 2458 epochs. The results are shown in Fig. 1.

It can be seen that ionospheric delay changes from −0.02 to 0.02 m, but the ratio coefficient of ionospheric delay of the third combination is too large to neglect the repair of ionospheric delay.

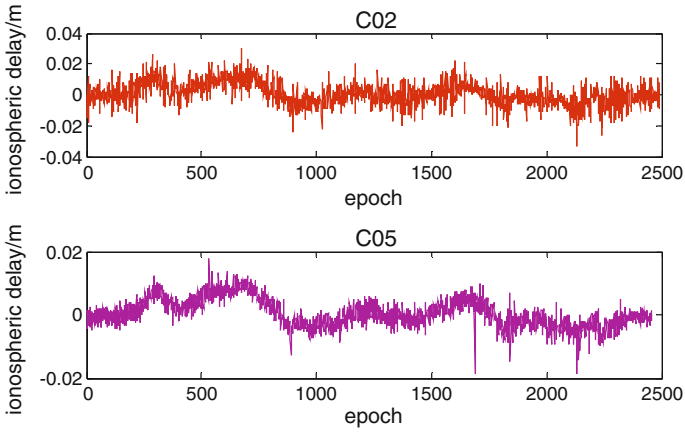

Fig. 1 The ionospheric delay of C02 and C05

3.2 The Detection of Cycle-Slip

Utilizing the three-step method to detect and repair the cycle-slip, the results are shown in Fig. 2.

From Figs. 2 and 3, it can be seen that the cycle-slip detection amount of C02 is the most within 0.2 week. The cycle-slip appeared at 2354th epoch of C05 satellites. In order to observe the situation of other epochs of C05, the 2354th epoch data was removed and the results are shown in Fig. 4.

The cycle-slip detection amount of C05 is the most within 0.2 week.

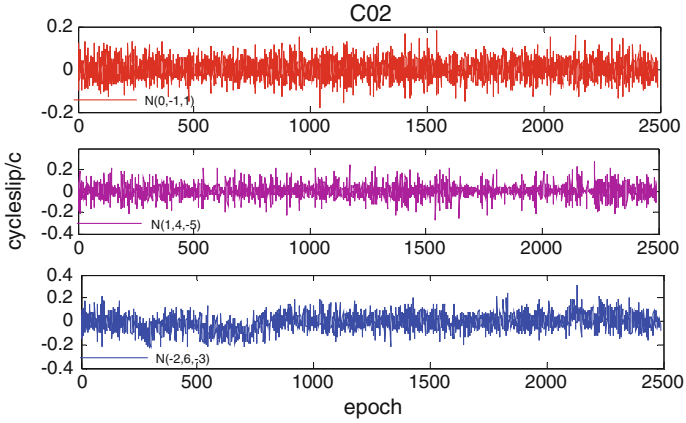

Fig. 2 The cycle-slip detection amount of C02

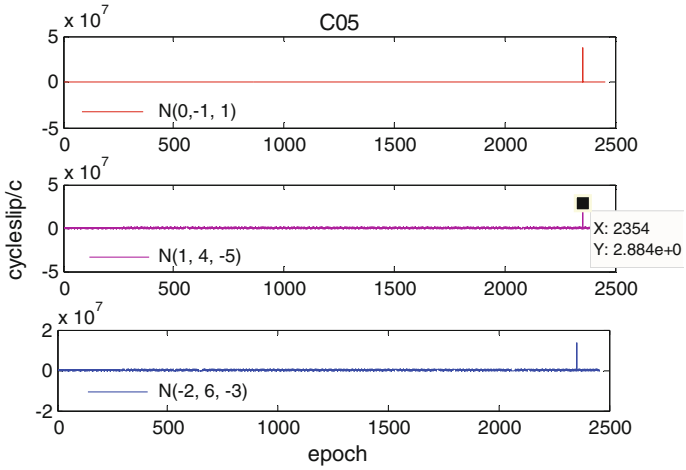

Fig. 3 The cycle-slip detection amount of C05

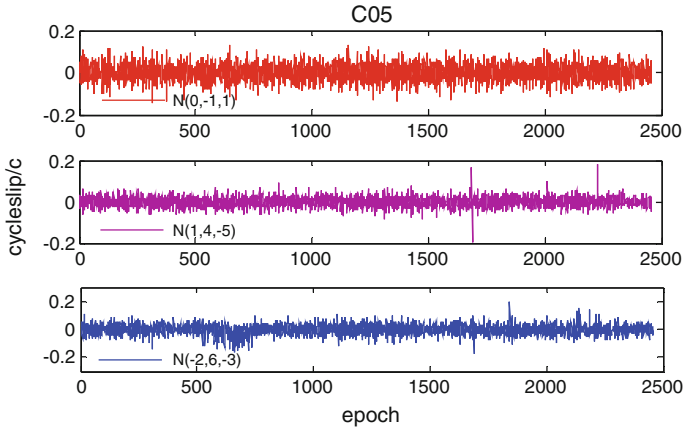

Fig. 4 The cycle-slip detection amount of C05 (2354th epoch removed)

Table 4 Simulated cycle-slip added

Epoch	500	1000	1500
Cycle-slip	(1,0,0)	(1,1,1)	(3,2,2)

Table 5 cycle-slip estimation

Epoch	500	1000	1500
(0,−1,1)	0	0	0
(1,4,−5)	1	0	1
(−3,6,−2)	−3	1	−1

3.3 Simulate Cycle-Slip

We add the simulated cycle-slip to the original observation data, and the cycle-slip should be located in the front, middle, and rear parts of the whole observation period. So we added the simulation cycle-slip at 500, 1000, and 1500 epochs as shown in Table 4.

The responding cycle-slip estimation should be as Table 5.

The experimental results of C02 were shown in Fig. 5.

The experimental results of C05 were shown in Fig. 6.

Figures 5 and 6 show that the actual calculation results are in good agreement with the theoretical prediction results. Cycle-slip (1, 0, 0), (1,1,1) can be respectively regarded as the sensitive cycle-slip of first two combinations, but all of them can be detected and repaired accurately, which verified the effectiveness of the method proposed in this paper.

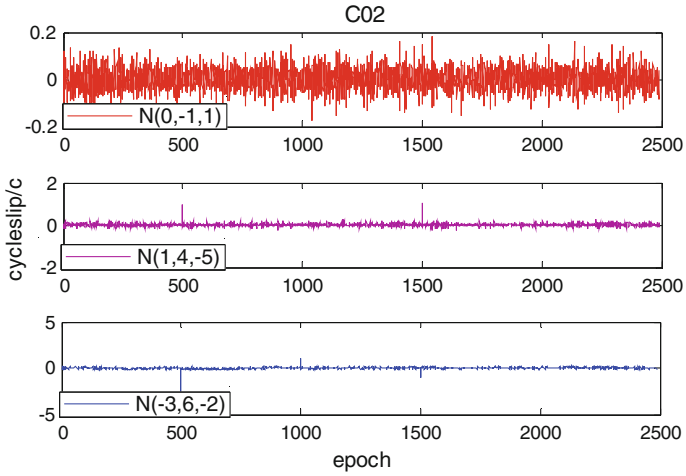

Fig. 5 The cycle-slip detection result of C02

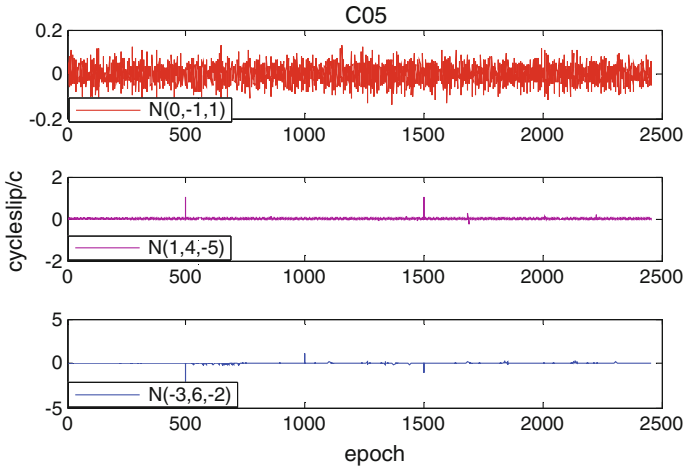

Fig. 6 The cycle-slip detection result of C05

4 Conclusion

Based on the theory of detection and repair of cycle-slip by combination of BeiDou triple-frequency observations, the relationship between the success rate of cycle-slip detection and the STD of cycle-slip detection amount has been discussed. The analysis shows that if the accuracy of cycle-slip detection and repair is guaranteed, the STD of cycle-slip detection should be less than 0.15 (cycle). In pseudorange/phase combination, when the sum of the combination coefficients is nonzero,

the oversize ionospheric delay error and the low accuracy of the pseudorange observation will result in the STD of cycle-slip detection amount much larger than 0.15, which will further result in the cycle-slip detection that will appear as false positives or false negatives. The STD of the cycle-slip detection amount can be controlled within 0.15 because of the pseudorange observations were not utilized in the third step by the three-step method proposed in this paper, which ensured the accuracy of cycle-slip detection and repair.

The measured data was utilized in the experimental analysis shown:

1. The triple-frequency combination utilized in this paper can detect and repair all cycle-slips and there is no insensitive cycle-slip.
2. The STD of cycle-slip calculated by three-step method is smaller than pseudorange/phase combination, ensuring the accuracy of cycle-slip detection and repair; and the workload of detection and repair of cycle-slip by three-step method decreased compared with geometry-free phase combination.
3. The method put forward in this paper is reliable to detect and repair the cycle-slip in real time.

Acknowledgements We greatly thank the four reviewers whose detailed suggestions improved the quality of the paper. This research was supported by National Natural Science Foundation of China (060229).

References

1. Li Z, Huang J (2005) The measurement and data processing of GPS. WuHan University Press, Wuhan
2. Yifei Y, Jinxiang G, Jian W et al (2014) Real-time cycle-slip detection and repair for compass triple-frequency carrier phase observations. China Uni Mining Techol 43(6):1140–1148
3. Lingyong H, Lijie S, Yan W (2012) BeiDou triple-frequency geometry-free phase combination for cycle-slip detection and correction. Acta Geodaetica et Cartographica Sinica 41(5):763–768
4. Li J, Yang J, Xu J (2014) Real-time cycle-slip detection and repair based on code-phase combinations for GNSS triple-frequency undifferenced observations. Acta Geodaetica Cartogr Sin 05:467–472
5. Dai Z, Knedlik S, Loffeld O (2008) Real-time cycle-slip detection and determination for multiple frequency GNSS. In: Positioning, navigation and communication, 2008. WPNC 2008. 5th workshop on IEEE, pp 37–43
6. Xiao G, Sui L, Gan YU et al (2014) Comparative study of three kinds of BeiDou real-time cycle-slip detection and repair methods. Acta Geodaetica et Cartographica Sinica 05:467–472
7. Zhao L (2012) The application of triple-frequency data combination in cycle-slip detection and repairing. Technical University, LiaoNing
8. Zhang X, He Y (2015) The model and characteristic of BeiDou triple-frequency data linear combination. Sci China Earth Sci 06:601–610
9. Yang Y, Li J, Wang A (2014) Preliminary assessment of the navigation and positioning performance of BeiDou regional navigation satellite system. Sci China Earth Sci 57(1):144

10. Li L, Lv Z, Yang C (2015) The comparison of Pseudo-range/Phase and geometric-free phase combination detection and repair for multi-frequency cycle-slip. J Geodesy Geodynamics 03:396–400
11. Zhao Q, Sun B, Dai Z et al (2014) Real-time detection and repair of cycle slips in triple-frequency GNSS measurements. GPS Solutions 19(3):381–391
12. Baoqi S, Jikun O, Chuanzhen S et al (2010) A triple-frequency data optimized combination for compass cycle-slip detection. Geomatics Info Sci Wuhan Uni 10:1157–1160
13. Feng Y (2008) GNSS Three carrier ambiguity resolution using ionosphere-reduced virtual signals. J Geodesy 82(12):847–862

Research on Fast RTK GNSS Algorithm Based on Partial Ambiguity Resolution

Nannan Hu, Hongping Zhang, Yongzhong Shi, Ronghao Wei and Tuan Li

Abstract The key of GNSS RTK algorithm is the fast and reliable double difference integer ambiguity resolution. Currently widely used algorithm is the LAMBDA method based on the ambiguity search algorithm. But the search efficiency of LAMBDA method is gradually reduced with the increase of the degree of ambiguity. While multi-system compatible positioning is the trend of the GNSS development, the double difference ambiguity dimension is bound to increase significantly, thus reducing the search efficiency of the LAMBDA method. This paper puts forward a resolution in which dividing the ambiguity into different groups which is sorted by the elevation. First fix higher elevation ambiguity, and then to part of the ambiguity. Thus speeding up the ambiguity search efficiency. Based on the data of GPS and BeiDou system, this paper proves that this algorithm can improve the efficiency of the ambiguity resolution.

Keywords GNSS RTK · LAMBDA · Ambiguity grouping · Partial ambiguity resolution

1 Introduction

RTK (Real-Time Kinematic) is a high precision positioning technology for real-time dynamic positioning using GNSS carrier phase observations, and the key problem is to solve the integer ambiguity resolution [1]. LAMBDA algorithm is a widely used method to get the fix solution of ambiguity, but the search space increases as the number of ambiguity parameter increases, the search efficiency is

N. Hu (✉) · H. Zhang · T. Li
GNSS Research Center, Wuhan University, Wuhan, China
e-mail: nnhu163@163.com

Y. Shi
Zhejiang Surveying Institute of Estuary and Coast, Hangzhou, China

R. Wei
Zhejiang Provincial Key Laboratory of Estuary and Coast, Hangzhou, China

J. Sun et al. (eds.), *China Satellite Navigation Conference (CSNC) 2017 Proceedings: Volume III*, Lecture Notes in Electrical Engineering 439,
DOI 10.1007/978-981-10-4594-3_39

gradually reduced and fixed success rate will decrease [2]. Multi-system compatible positioning is the trend of development in GNSS positioning, the number of available satellites is greatly increased, and the search efficiency of LAMBDA method is reduced, thus reducing the efficiency of high precision positioning and reliability of RTK algorithm.

In view of this situation, on the one hand, many scholars improved the algorithm on LAMBDA [2, 3]; on the other hand, due to a large number of satellites available, fixed all the ambiguity of GNSS positioning is not necessary, it is useful to reduce the risk of fixing failure by only to fix part of the ambiguity [4]. A lot of achievements have been made in the study of partial ambiguity resolution. Yang et al. constructed an equation which only contains ambiguity parameters, suggested a parts ambiguities search method and showed that applying the parts search method can facilitate the efficiency and success rate of resolving GPS phase ambiguity by test data [5]; Brack used simulation data to improve that partial ambiguity resolution can increase the availability of an ambiguity fixed solution, but the precision is generally lower [6]; Odijk et al. demonstrated that partial ambiguity resolution can clearly shorten the time to reach centimeter-level accuracy for long baselines [7]. In this paper, an ambiguity grouping scheme is proposed to speed up the searching efficiency and improve the reliability.

The difference between the partial ambiguity fixing algorithm in this paper with the conventional RTK algorithm is that the conventional RTK algorithm in general can be divided into two steps, the first step is to solve ambiguity float solution, the second step is to search for fixed integer ambiguity based on float ambiguity and its variance matrix and solve precision coordinate with fixed ambiguities. In the partial ambiguity resolution, after obtaining the ambiguity float solution, sort the packet to all ambiguity parameters, and then fix partial ambiguities with higher elevation angle, use fixed ambiguities aids in fixing the other integer ambiguities, finally put fixed ambiguities back into the observation equations to get the fixed solution of coordinate parameters and other parameters.

2 Float Solution of Ambiguity

In RTK algorithm, the error sources of the observations are mainly double differential ionospheric delay and tropospheric delay. The double differential tropospheric delay can be divided into dry delay and wet delay, and the accuracy of dry delay model can reach mm [8]. However, it is difficult to establish an accurate model for the wet delay, so the double differential tropospheric wet delay is used as the parameter to be estimated. On the other hand, the double difference ionospheric delay can be eliminated by dual frequency ionosphere free combination observation. The double difference observation equation can be described as follows:

$$\begin{aligned}\lambda\Delta\nabla\varphi_{br}^{ij} &= \Delta\nabla\rho_{br}^{ij0} + \nabla l^{ij}dX + \nabla m^{ij}dY \\ &\quad + \nabla n^{ij}dZ - \lambda\Delta\nabla N_{br}^{ij} + \Delta\nabla T_{br}^{ij}\end{aligned} \tag{1}$$

where λ denotes the wavelength of the ionosphere-free combination observation, and $\Delta\nabla$ denotes the double difference operator, and subscript denotes the receiver id, b indicates base station, r indicates rover station, and superscript denotes satellite id, i indicates refer satellite and j indicates others, and φ denotes the carry phase observation of ionosphere-free combination, and ρ^0 denotes approximate geometric distance between receiver and satellite, and l, m, n denote the direction cosine between receiver and satellite, and dX, dY, dZ denote the coordinates correction of rover station, and N denotes the integer ambiguity of double difference, and T denotes double difference troposphere wet delay.

The tropospheric wet delay can be stated as follows for the tropospheric zenith wet delay and projection function

$$\begin{aligned}\Delta\nabla T_{br}^{ij} &= [f(E_r^j)T_{z,r} - f(E_b^j)T_{b,r}] \\ &\quad - [f(E_r^i)T_{z,r} - f(E_b^i)T_{z,b}]\end{aligned} \tag{2}$$

where f denotes mapping function, in this paper, we use the NMF model in which f is function of elevation angle, and E denotes the elevation angle, and T_z denotes tropospheric zenith wet delay.

Due to $E_b^i \cong E_r^i, E_b^j \cong E_r^j$, the average height angle can be used instead, as a result

$$\Delta\nabla T_{br}^{ij} = [f(\theta^j) - f(\theta^i)][T_{z,r} - T_{z,b}] \tag{3}$$

Set $\Delta T_{z,br} = T_{z,r} - T_{z,b}$ denotes the relative tropospheric zenith wet delay, treat it as the parameter to be estimated as well as coordinate parameters and ambiguities parameters simultaneously.

The stochastic model is based on the weighting scheme of elevation angle. According to the experience, the relative weight ratio of GPS and BeiDou is 1.5:1.

Use of Extended Kalman Filtering (EKF) algorithm [9] to estimate the parameters, in which set the state vector as follows:

$$\mathrm{X}_k = (dX, dY, dZ, \Delta T_{z,br}, \Delta\nabla\mathrm{N}) \tag{4}$$

In status updation, ambiguity parameters equal to the previous epoch state, coordinate parameters in static mode equals to the previous epoch state as well, in dynamic mode update by the DGNSS results in current epoch. Relative tropospheric zenith wet delay using the first-order Gauss Markov process estimation [10].

By using Kalman filter method we can estimate the state vector every epoch and get the float solution as well as its variance matrix as follows:

$$\begin{bmatrix} \widehat{\mathbf{b}} \\ \widehat{\mathbf{a}} \end{bmatrix}, \mathbf{D} = \begin{bmatrix} \mathbf{D}_{\widehat{\mathbf{b}}} & \mathbf{D}_{\widehat{\mathbf{a}}\widehat{\mathbf{b}}} \\ \mathbf{D}_{\widehat{\mathbf{b}}\widehat{\mathbf{a}}} & \mathbf{D}_{\widehat{\mathbf{a}}} \end{bmatrix} \tag{5}$$

where $\widehat{\mathrm{b}}$ denotes coordinate parameters and relative tropospheric zenith wet delay parameter, and $\widehat{a}$ denotes the ambiguity parameters, and D denotes the variance matrix.

3 Ambiguity Parameters Grouping

The conventional RTK algorithm uses LAMDA method [11, 12] to search for the fixed solution with the float ambiguity results and its variance directly. However, because of the increase of ambiguity parameter dimension in GNSS RTK multi-system joint positioning, ambiguity search range increased, thereby reducing the search efficiency of LAMBDA method, using the ambiguity grouping scheme to get partial ambiguity resolution is conducive to improve the search efficiency.

First of all, all visible satellites of the rover station are sorted from high to low, then generally choose the highest elevation angle of satellites as the reference satellite, the rest to set a fixed threshold (usually 25°–45°) were divided into two groups: higher elevation angle group and lower elevation angle group, state parameters are as follows:

$$\begin{bmatrix} \widehat{\mathbf{b}} & \widehat{\mathbf{a}}_{\mathbf{low}} & \widehat{\mathbf{a}}_{\mathbf{high}} \end{bmatrix}^{\mathrm{T}} \tag{6}$$

4 Fix Ambiguity Parameters

4.1 Ambiguity Fixing Method

Based on the formula (5), the way to get the solution of fixed ambiguity is to solve the integer vector that satisfies the minimum objective function as follows

$$\min \left\| \breve{\mathbf{a}} - \widehat{\mathbf{a}} \right\|^2_{\mathbf{D}^{-1}_{\widehat{\mathbf{a}}}} \tag{7}$$

In this paper, using LAMBDA algorithm to solve the integer ambiguity solution, its basic principle is through ambiguity integer transform of decorrelation reduces the ambiguity search range, and then through the sequential conditional least squares estimation integer search for integer ambiguity solution.

4.2 Fix the Ambiguities of Higher Elevation Satellites

Firstly, the ambiguity of a group of satellites with higher elevation angle should be fixed. The state parameter and its variance matrix are transformed as follows

$$\begin{bmatrix} \widehat{\beta} \\ \widehat{\mathbf{a}}_{\mathbf{high}} \end{bmatrix}, \mathbf{D} = \begin{bmatrix} \mathbf{D}_{\widehat{\beta}} & \mathbf{D}_{\widehat{\mathbf{a}}_{\mathbf{high}}\widehat{\beta}} \\ \mathbf{D}_{\widehat{\beta}\widehat{\mathbf{a}}} & \mathbf{D}_{\widehat{\mathbf{a}}_{\mathbf{high}}} \end{bmatrix}, \widehat{\beta} = \begin{bmatrix} \widehat{\mathbf{b}} \\ \widehat{\mathbf{a}}_{\mathbf{low}} \end{bmatrix} \tag{8}$$

Because the satellite elevation angle is higher, the influence of atmospheric delay and fewer ambiguity parameters are needed to search for, the fixed integer ambiguity solution can quickly obtain in the higher elevation group.

Although only use higher elevation angle satellites, the number of satellites is usually enough (more than 4) to estimate the parameters in multi-system GNSS positioning. In other words, we can just fix the higher elevation satellite and put them directly back to solve three-dimensional coordinate parameters. Nevertheless, if only using high elevation satellite, the satellite distribution of geometric structure is poor, the value of PDOP is relatively large [13], which may have a great impact on the accuracy of coordinate parameter estimation; on the other hand, considering the reliability of the positioning results and the utilization ratio of the observed data, after the higher elevation angle satellites are fixed, the partial ambiguity which have already been fixed can be treated as a constraint to assist the search and fixation of the ambiguity of the lower elevation angle satellites.

4.3 Ambiguity Partial Fixed Constraint

In order to make full use of the fixed ambiguity, the fixed ambiguity parameters and integer value can be used to construct the virtual observation equation, which are given a great weight; Then, add the virtual observation equation in the original Kalman filter observation equation, Kalman filter updates once again, access the new floating point solution and variance matrix; in the end, separate the low elevation angle satellites ambiguity from the float solution and its variance matrix, use LAMBDA method to search the integer solution. Ratio test is used to judge the validity of ambiguity. When the Ratio value is greater than 2, it is considered that the ambiguity is correct.

4.3.1 Constructing the Virtual Observation Equations of Fixed Ambiguities

After the partial ambiguities is fixed, the virtual observation equations can be constructed as follows:

$$\widehat{\mathbf{a}}_{\mathbf{high}} = \breve{\mathbf{a}}_{\mathbf{high}}, \mathbf{D}_{\widehat{\mathbf{a}}_{\mathbf{high}}} = \sigma^2 \mathrm{I} \tag{9}$$

Where $\breve{a}_{high}$ denotes the integer values of the fixed ambiguities, σ denotes the standard deviation of the virtual observation equations which should be less than one in a thousand of the wavelength of carry phase because the integer values fixed by LAMBDA method are supposed to be correct. I denotes a unit matrix in which the dimension equals the number of fixed ambiguities.

4.3.2 Recapitalize the Filter Observation Equations and Update

The combination of the virtual observation equation and the observation equation in the Kalman filter model is used, and the variance matrix is reconstructed. Furthermore, the new observation equation is used to update the Kalman filter, and a new ambiguity float solution is obtained.

$$\left[\widehat{\mathbf{b}}' \quad \widehat{\mathbf{a}}'_{\mathbf{low}} \quad \widehat{\mathbf{a}}'_{\mathbf{high}}\right]^{\mathrm{T}} \tag{10}$$

4.3.3 Fix the Ambiguity of Lower Elevation Satellites

$$\begin{bmatrix} \widehat{\alpha} \\ \widehat{\mathbf{a}}'_{\mathbf{low}} \end{bmatrix}, \quad \mathrm{D}' = \begin{bmatrix} \mathbf{D}'_{\widehat{\alpha}} & \mathbf{D}'_{\widehat{\mathbf{a}}_{\mathbf{low}}\widehat{\alpha}} \\ \mathbf{D}'_{\widehat{\alpha}\widehat{\mathbf{a}}} & \mathbf{D}'_{\widehat{\mathbf{a}}_{\mathbf{low}}} \end{bmatrix}, \quad \widehat{\alpha} = \begin{bmatrix} \widehat{\mathbf{b}}' \\ \widehat{\mathbf{a}}'_{\mathbf{high}} \end{bmatrix} \tag{11}$$

The LAMBDA method is used to search the integer ambiguity of the lower elevation satellites.

4.3.4 The Parameters Fixed Solution

After the completion of ambiguity fixing, putting the integer value back into the observation equations can obtain coordinate parameters with high precision.

5 Experimental Verification and Result Analysis

In order to verify the correctness of the algorithm, we use a set of static observation data of GPS/BeiDou dual system observation, the length of observation time is 4 h, the sampling interval is 1 s, the baseline length is 31.47 km. The solution uses ionosphere-free combination observations to eliminate double differential ionospheric delay, and estimates relative tropospheric zenith wet delay real time.

This experiment mainly analyzes the following contents: first, to validate whether the number of available satellites is sufficient to support the partial ambiguity resolution algorithm under the condition of the GPS/BeiDou system; second, according to the actual situation, choosing the appropriate grouping angle threshold, and take the PDOP (position precision attenuation factor) as the basis for the comparison of the intensity of satellite observation geometry; third, comparing the convergence time and success rate between the partial ambiguity fixing algorithm and conventional RTK algorithm; fourth, contrast the precision of coordinates between those two algorithms. Setting the satellite cut-off angle as 15°, the satellite number and PDOP value condition is shown in Fig. 1.

According to the situation of satellite observation, the angle threshold for higher elevation is set to 40°. After grouping, the satellite number and PDOP value of satellites whose elevation angle is larger than the threshold is shown in Fig. 2. There are enough satellites to support part of the ambiguity fixed algorithm, the height of 40° above the satellite is at least 7.

As we can see from Figs. 3 and 4, in this test, the partial ambiguity fixing scheme can obtain fixed ambiguity solution in the 269 epochs, much smaller than the conventional RTK ambiguity fixing time required for 6796 epochs, greatly improving the ambiguity fixing efficiency.

Figures 5, 6 and Table 1 show the coordinate parameter error, which denotes the difference between the true value of station coordinate and the results of the two schemes calculation results, we can see the two kinds of fixed position accuracy at the same level. The error of the conventional solution is around 2–3 cm in plane,

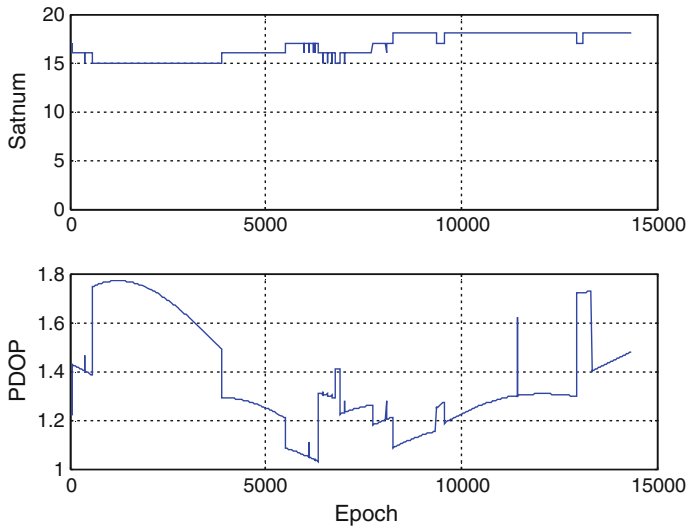

Fig. 1 GPS/BDS satellite number and PDOP value

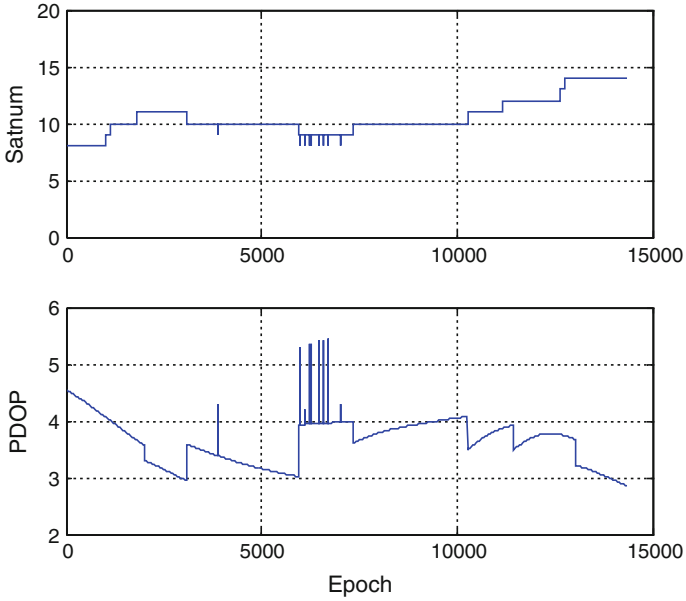

Fig. 2 GPS/BDS satellites with high elevation angle (>40°)

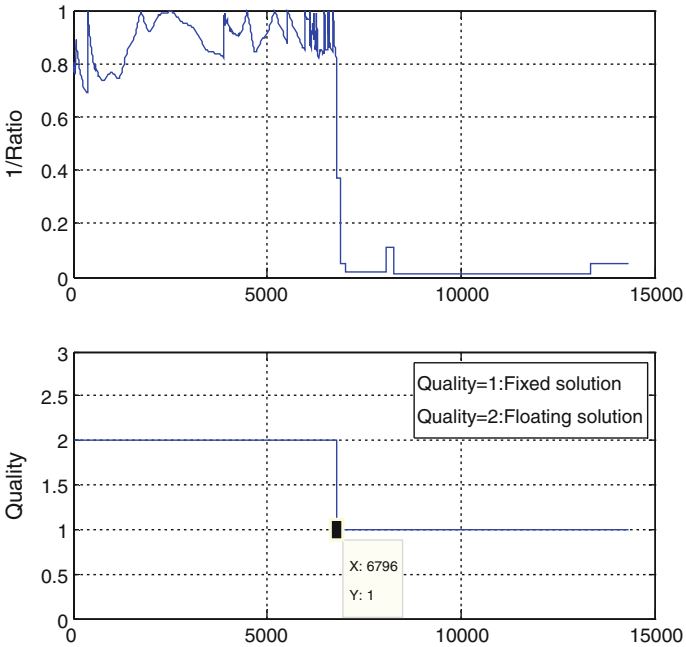

Fig. 3 Ambiguity solution quality in conventional RTK algorithm

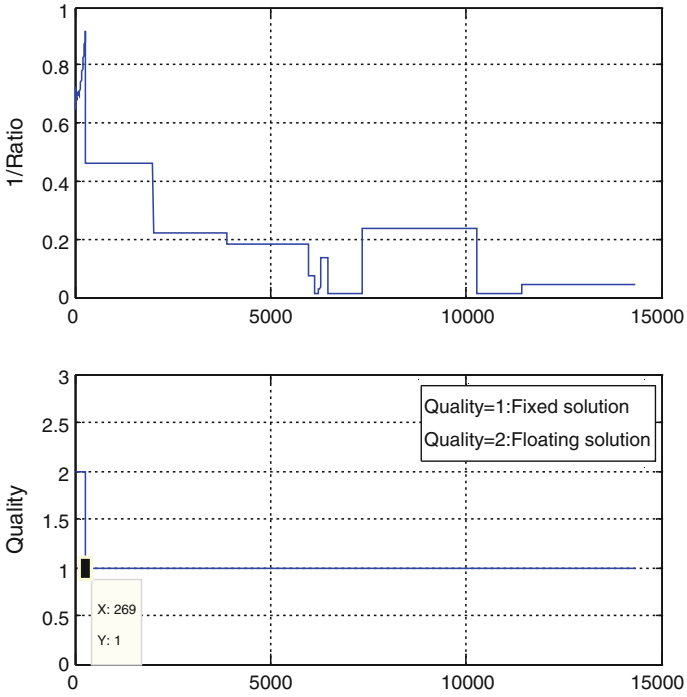

Fig. 4 Ambiguity solution quality in partial ambiguity fixing algorithm

1 dm in elevation; while the error of the scheme of partial fixing is slightly larger than the conventional scheme, which is because when only using the high altitude fixed satellite, satellite observation geometry is poor caused by a larger PDOP value, but the error is relatively small.

6 Experimental Verification and Result Analysis

The following conclusions can be obtained through the test: GPS/BeiDou dual system satellites is numerous, a large number of high elevation satellite can be used in the partial ambiguity fixing algorithm; when only using high elevation satellite, the geometry is poor, the PDOP value is relatively large; partial ambiguity fixing algorithm can significantly improve the efficiency and success rate of ambiguity fixing and reduce the convergence time. Meanwhile the accuracy of partial ambiguity fixing solution is roughly equivalent to the conventional RTK. It is verified that partial ambiguity fixing algorithm can improve the convergence speed and reliability of RTK.

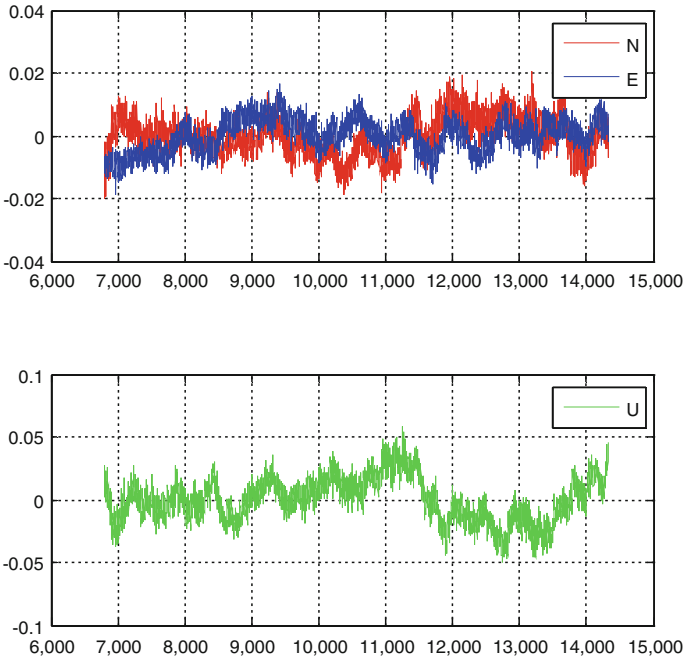

Fig. 5 Coordinate precision of ambiguity fixed solution in conventional RTK algorithm

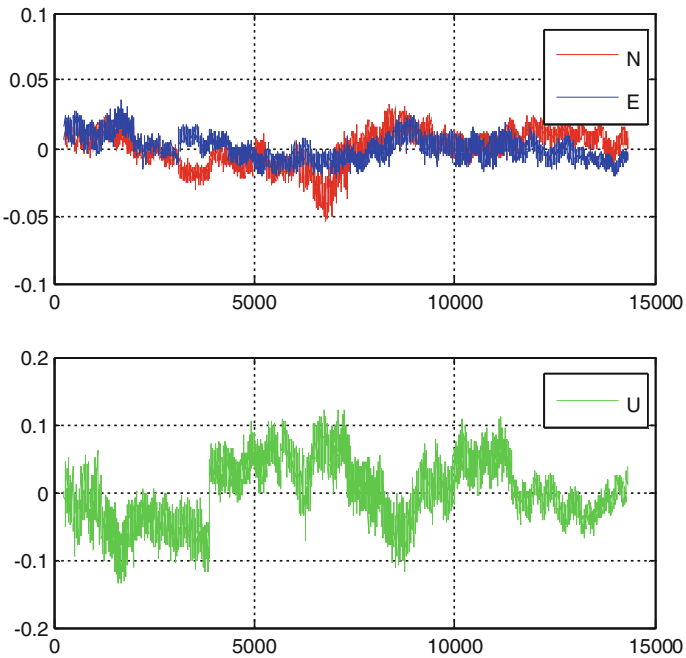

Fig. 6 Coordinate precision of ambiguity fixed solution in partial ambiguity fixing algorithm

Table 1 Positioning result errors comparison

		Error in N/m	Error in E/m	Error in U/m
The conventional solution	MAX	0.0229	0.0243	0.1489
	MEAN	0.0011	0.0041	0.0475
	RMS	0.0046	0.0068	0.0667
Partial ambiguity solution	MAX	0.0311	0.0509	0.2184
	MEAN	0.0022	0.0155	0.0957
	RMS	0.0128	0.0180	0.1063

Acknowledgements This work is supported by Zhejiang Science and Technology program (Cultivate Innovation Carrier) (No. 2017F10008).

References

1. Hofmann-Wellenhof B, Herbert L, Elmar W (2008) GNSS-Global Navigation Satellite Systems GPS, GLONASS, Galileo More, Surveying and Mapping Press, Beijing, pp 146–178
2. Xingwang Z, Qing W, Shuguo P, Jian D (2010) Partial ambiguity fixing algorithm based on LAMBDA and its performance analysis. J Chin Inerl Technol 18(6):665–669 (Ch)
3. Chengfa G, Yi Z, Dejun W (2006) Restricting GPS integer ambiguity by improved LAMBDA algorithm. Geomatics Inf Sci Wuhan Univ 32(8):744–747 (Ch)
4. Xingwang Z, Cuiying Z (2013) Partial ambiguity fixing method and analysis for precise point positioning. Chin Sp Sci Technol 2(1):37–43 (Ch)
5. Rengui Y, Jikun O, Yunbin Y (2007) Facilitating efficiency and success rate of resolving GPS phase ambiguity with parts search method. Geomatics Inf Sci Wuhan Univ 32(2): 160–163 (Ch)
6. Andreas B (2015) On reliable data-driven partial GNSS ambiguity resolution. GPS Solutions 19(3):411–422
7. Odijk D, Arora BS, Teunissen PJG (2014) Predicting the success rate of long-baseline GPS +Galileo (partial) ambiguity resolution. J Navig 67(3):385–401
8. Lei X, Guangxi Z, Yuqi W et al. (2005) Real time vehicles tracking based on Kalman filter in a video-based ITS[C]. In: Proceedings of IEEE conference on communications, circuits and system: IEEE, vol 2. HongKong, pp 883–886
9. Hu W, Jiexian W, Guixia B, Haojun L (2010) Research and accuracy analysis on real time kinematic positioning model. J Geodesy Geodyn 30(4):113–116 (Ch)
10. Yantian X, Pengfei C, Yanhui C (2013) Kalman filter algorithm for medium-range real-time kinematic positioning with one reference station. J Southwest Jiaotong Univ 48(2):317–322(Ch)
11. Teunissen P, Verhagen S (2009) GNSS carrier phase ambiguity resolution: challenges and open problems. In: International association of geodesy symposia: observing our changing earth. Springer, Berlin, pp 785–792
12. Xiaohua Y, Xiaowen C, Tianyang Z (2005) LAMBDA: a modified LAMBDA method for integer least squares estimation. J Geodesy 79(9):552–565
13. Yijun T, Dongqing Z, Hao (2015) BDS/GPS positioning analysis in various of cut-off elevations. J Geomatics Sci Technol 32(4):361–367 (Ch)

Part III
Atomic Clock and Time-Frequency Technology

Development of 15 kg Space Mini Passive Hydrogen Maser

Yonghui Xie, Tao Shuai, Pengfei Chen, Yuxian Pei, Xiaoyan Pan and Chuanfu Lin

Abstract Space mini passive hydrogen maser is one of the key technologies for satellite navigation system. Engineering model of 15 kg space mini passive hydrogen maser has been developed in Shanghai Astronomical Observatory. Key technologies such as miniatured cavity-bulb assembly, absorption pump, magnetic state selection system have been grasped. Weight of physical package is controlled within 10 kg and atomic signal is up to 2 dB. Miniature of electronic package is carried out while keeping its main system framework, and weight of 5 kg is achieved. Physics package and electrics package are integrated and system parameters are optimized, frequency stability of $1.5 \times 10^{-12}t^{-1/2}$(1 s $\leq t$ 10,000 s) and temperature coefficient of 8×10^{-14}/°C are measured. Engineering modification and environmental test are currently carried out.

Keywords Shanghai astronomical observatory · Mini · Passive hydrogen maser

1 Introduction

Passive hydrogen maser (PHM) has outstanding performance in long-term frequency stability and frequency drift of the order of E-15, which is very helpful for autonomous navigation of the Global Navigation System (GNSS). It's suitable to be the high performance atomic clock on-board, associating with rubidium clock, to improve system performance and reliability of the GNSS.

At the same time of accomplishing 23 kg space Passive Hydrogen Maser (PHM) and engineering application, Shanghai Astronomical Observatory has started research of key technologies of mini PHM since 2010 [1]. Emphasis have been laid within miniature of cavity-bulb assemble, vacuum system, and state selection system. With development of corresponding magnetic shield, dissociator and hydrogen source, weight of physics package has been controlled within 10 kg,

Y. Xie (✉) · T. Shuai · P. Chen · Y. Pei · X. Pan · C. Lin
Shanghai Astronomical Observatory, 80 Nandan Road, Shanghai, China
e-mail: xyh@shao.ac.cn

J. Sun et al. (eds.), *China Satellite Navigation Conference (CSNC) 2017 Proceedings: Volume III*, Lecture Notes in Electrical Engineering 439,
DOI 10.1007/978-981-10-4594-3_40

with atomic gain maintained up to 2 dB and line width of 4 Hz. Electronics package still remain Scheme of time-separated control method but modules are miniature and rearranged. Weight less than 5 kg is realized. After optimization of system parameters, frequency stability of $1.5 \times E^{-12}/t^{-1/2}$ is achieved. Magnetic sensitivity and temperature sensitivity are improved by the optimization of physics package. Power consumption is also an emphasis of research, temperature control layers of microwave cavity are reduced and voltage of dissociator is decreased. 20% of power consumption reduction is realized.

2 Physics Package

In PHM transition of hydrogen atom takes place in storage bulb and energy collected by microwave cavity. So parameters of cavity-bulb assembly, such as cavity Q factor, filling factor, storage time and relaxation rate, directly determines system performance [2].

Novel electrode microwave cavity has advantage in Q factor and weight compared to magnetron cavity, and has been applied successfully in our 23 kg space PHM. Its mechanical property and reliability have been proven to satisfy space application. So it is still adapted in mini space PHM (Fig. 1).

Redesign of the cavity-bulb assembly is necessary after cavity diameter and length compression. Structure parameters including bulb size, diameter and gaps of electrode are optimized to ensure cavity resonance frequency and filling factor.

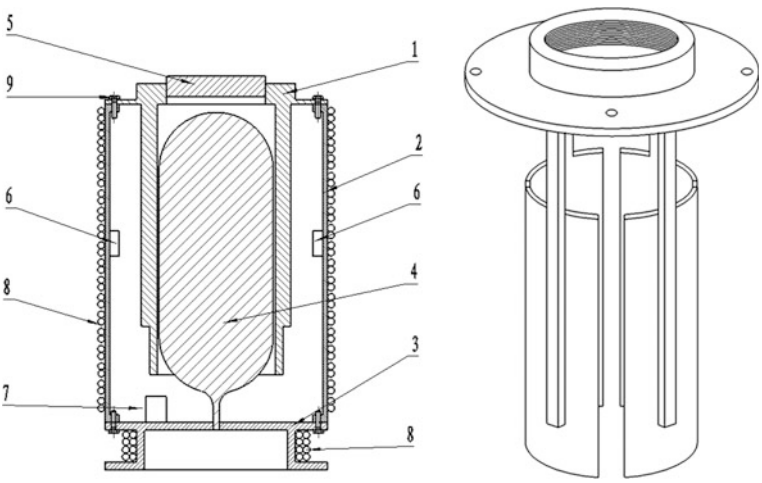

Fig. 1 Structure of novel kind of electrode cavity (*left*) and electrode tube (*right*). *1* electrode tube; *2* cylinder cavity; *3* base plate; *4* storage bulb; *5* frequency adjust knob; *6* coupling loop; *7* varactor diode loop; *8* thermal control coil

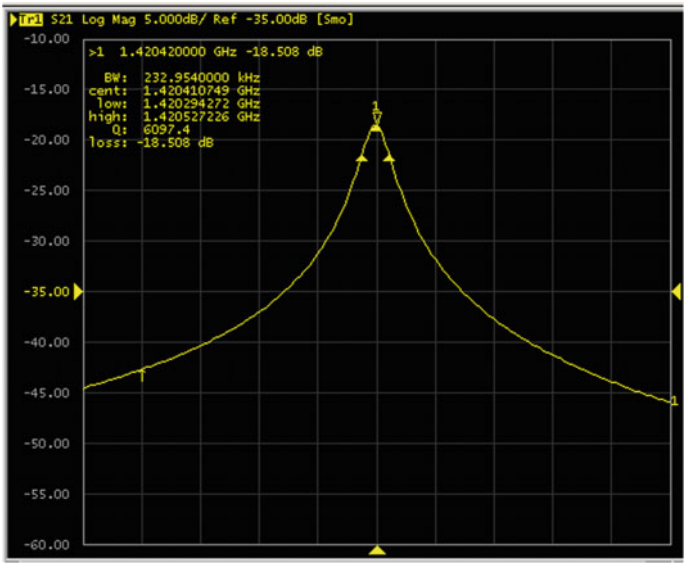

Fig. 2 Cavity resonance characteristics

Antennas of varactor and microwave coupling are properly reduced to maintain cavity Q factor at about 6000 (Fig. 2).

New getter material is adopted compared to traditional titanium getter in previous PHM. Activation temperature is limited within 500 °C which lightens thermal burden of the physics package in period of getter activation. Getter package is transformed from thin plate to small piece of 25 mm in diameter, which is grouped in series and 13 groups are installed in pump. This design provides more absorption area and coinciding higher pumping speed. Totally 400 g of getter is filled in the pump and absorption ability of 40 bar*L H2 is ensured.

A small ion pump is equipped in the vacuum system to eliminate residual gases. Operating current of the small ion pump is greatly reduced to less than 0.5 μA under new pump structure design, and application of a 1 L pump is sufficient for 10 years operation.

Outer vacuum chamber is designed to provide sealed situation for microwave cavity to prevent turbulence from environmental temperature and pressure fluctuation. Considering that after launch of satellite outer vacuum of PHM could be provided directly by orbit environment, outer vacuum chamber is only necessary in ground test period, so it is convenient to replace pump of outer vacuum by a temporary valve to simplify system structure and reduce weight.

Magnetic shielding consists of 4 layers of 1J85 cylinders. Diameter of the shielding are reduced following the cavity miniature. Thickness and gap of the layers are optimized, especially the axial thickness, to maintain overall shielding factor up to 50,000. Supporting structures are designed between gaps of each

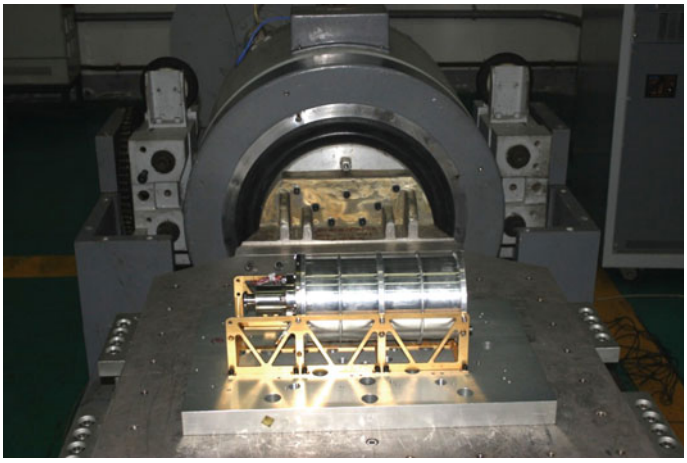

Fig. 3 Vibration test of key components of physics package

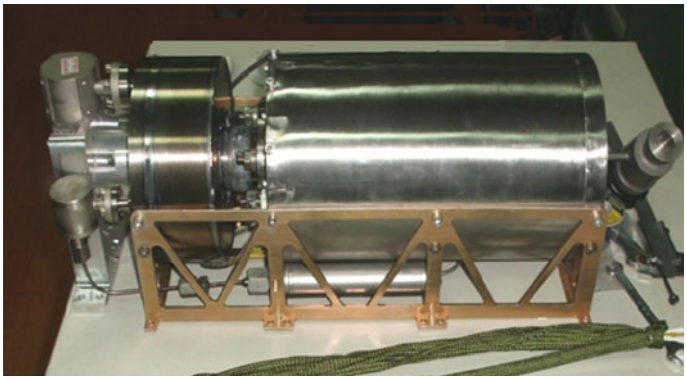

Fig. 4 Physics package of mini PHM

shielding to confirm tightly fixing of the magnetic shielding system in condition of vibration and shock.

We have carried out vibration test for key components of the physics package, including cavity-bulb assembly, magnetic shielding system and the getter. Parameters and performance of these components are stable after the test (Fig. 3).

Physics package is developed based on key components above and atomic signal is up to 3 dBm at −80 dBm input and 4 Hz in width. Theoretical frequency stability is better than $7 \times 10^{-13}/t^{-1/2}$ [3] (Figs. 4 and 5).

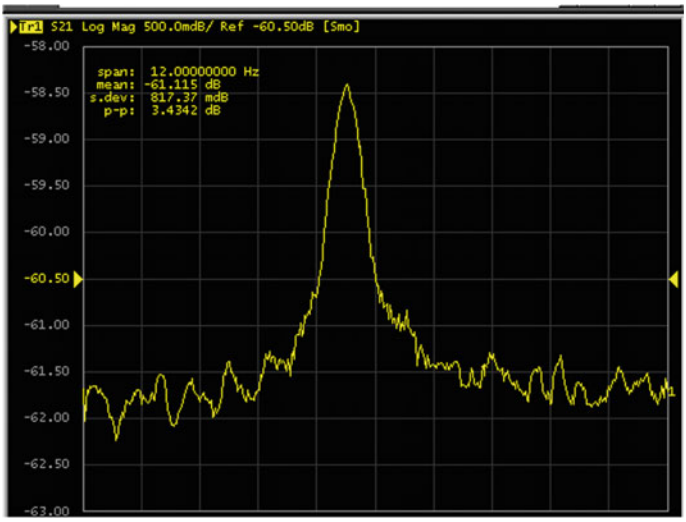

Fig. 5 Atomic signal of physics package of mini PHM, microwave input is −80 dBm, span is 50 Hz

3 Electronics Package

Scheme of time-separated control method has also been applied in 23 kg space PHM and its performance and reliability are sufficient for engineering application. This scheme is proved to have advantage in long-term frequency stability and drift. So it is still adopted in electronics package of mini PHM. In this control method there are two frequency control loops, VCXO control loop and cavity control loop, the former for lock of VCXO frequency and the latter for lock of cavity frequency, they are time separated to avoid mutual interference (Fig. 6).

Size and weight of electronics package of mini PHM are restricted according to that of physics package, so modules of electronics package are rearranged and modules with similar function are integrated. Single operational amplifiers are replaced by dual operational amplifiers. In the end 30% of volume reduction and 25% of weight reduction are achieved in electronics package.

To further diminish additional noise from electronics package and improve system stability, a 16-bit DA converter is applied in servo unit and its drive circuit and filter circuit are optimized. Loop parameters of servo unit are modified according to atomic signal of physics package of mini PHM.

Interface of telemetry, telecontrol and power supply are designed according to aerospace condition. Units sensitive to vibration, especially VCXO, are fastened. Thickness of outside shell of electronics package is set to fulfill anti-irradiation demand for more than 10 years (Fig. 7).

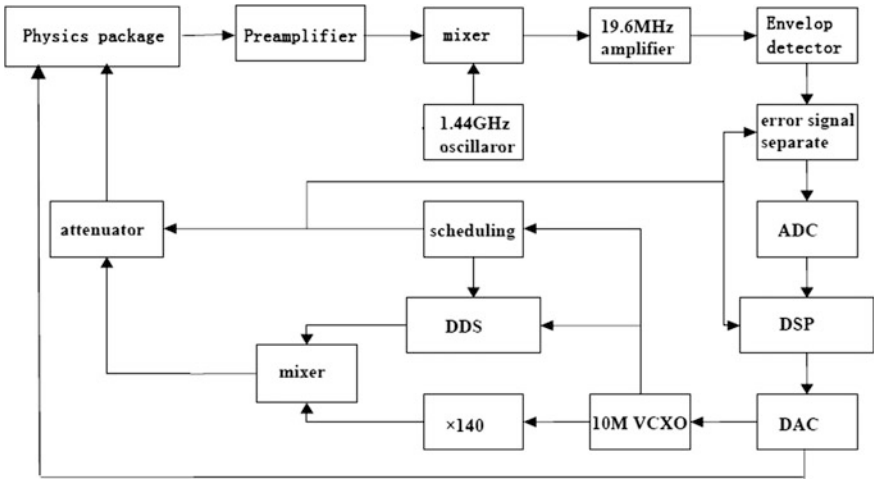

Fig. 6 Block diagram of electronics package

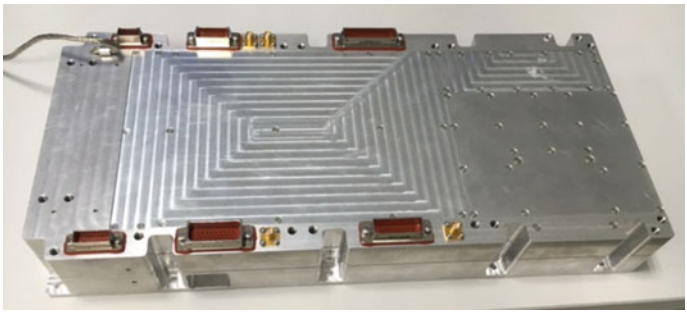

Fig. 7 Structure of electronics package

4 System Status and Performance

Physics package and electronics package are integrated and mini PHM is developed (Fig. 8).

Optimization and test of performance is emphasis in current stage. Main task includes temperature coefficient, magnetic coefficient, frequency drift, and frequency stability.

Test of temperature coefficient is currently carried out in atmosphere environment. Temperature raises from 20 to 36 °C and then drop back to 20 °C, in the process frequency shift is 1.2×10^{-13}, so temperature coefficient is 7.5×10^{-14}/°C. Considering physics package has better thermal control efficiency in vacuum environment, we could get a less temperature coefficient in that condition; corresponding test is just in progress (Fig. 9).

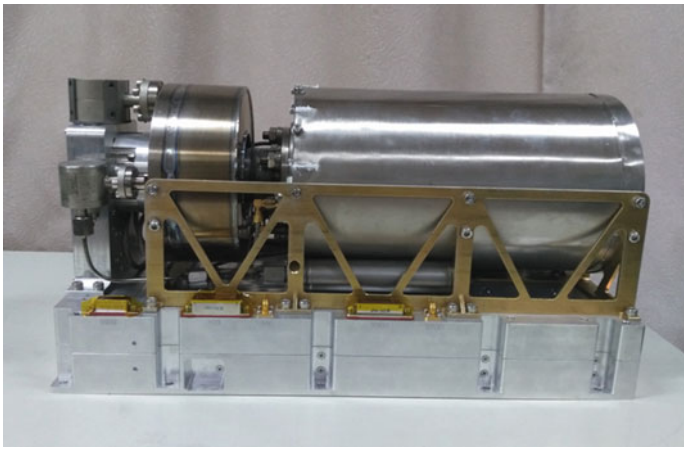

Fig. 8 Structure of mini PHM

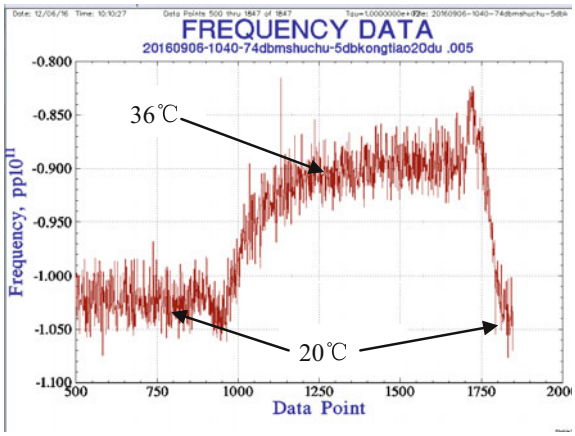

Fig. 9 Result of temperature coefficient test, averaged by 100 s

Magnitude of C field is appropriately decreased from previous 1 mG to improve system sensitivity to environmental magnetic field while atomic transition is not affected. Magnetic field for magnetic coefficient test is generated by Helmholtz coils. With 2 Gauss of environment magnetic change, frequency shift less than 6×10^{-13} is measured, which means magnetic coefficient less than 3×10^{-13}/Gauss (Fig. 10).

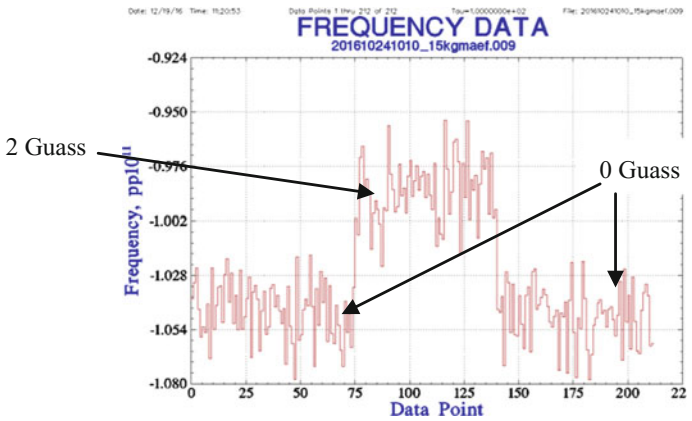

Fig. 10 Result of magnetic coefficient test, averaged by 100 s

Continuous performance test is carried out in atmosphere environment for 20 days. Frequency drift is measured to be 1.4×10^{-14}/day and frequency stability is $1.5 \times 10^{-12}/t^{-1/2}$(1−10,000 S), 9.8×10^{-15}/100,000 S. Performance test under vacuum environment with less temperature fluctuation could result in better frequency stability (Fig. 11).

5 Result

Prototype of mini PHM is developed in Shanghai Astronomical Observatory. Compared to previous PHM, Mini PHM has 35% of weight reduction and corresponding size and power consumption compression, while its performance, such as frequency stability and drift, is maintained, which contribute to wider application of PHM. Development of engineering models is also in progress.

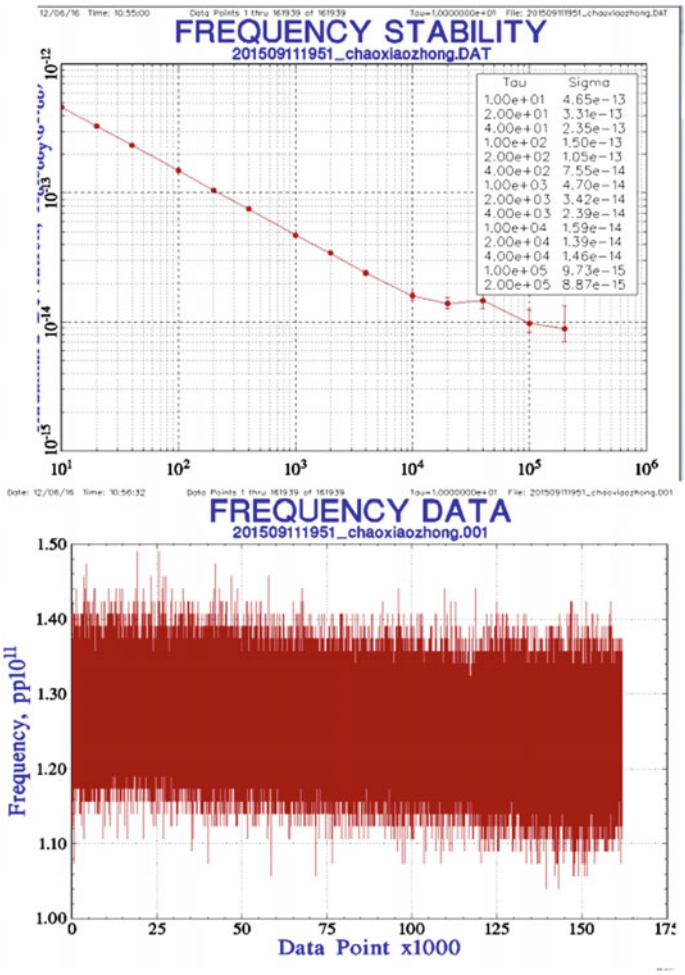

Fig. 11 Result of 20 days of continuous performance test

References

1. Xie Y, Chen P et al (2015) Development of space mini passive hydrogen maser, China Satellite Navigation Conference (CSNC). In: Proceedings vol 342 of the series lecture notes in electrical engineering, pp 343–349
2. Vanier J, Audoin C (1989) The quantum physics of atomic frequency standards (Chap. 6). Adam Hilger, Bristol
3. Wang Q, Mosset P, Droz F (1989) Verification and optimization of the physics parameters of the onboard galileo passive hydrogen maser. In: Vanier J, Audoin C (eds) The quantum physics of atomic frequency standards (Chap. 6), 38th PTTI meeting, Washington, 20062. Adam Hilger, Bristol

Verification and Analyzing of the Reliability and Lifetime of Space Passive Hydrogen Maser

Pengfei Chen, Yonghui Xie, Tao Shuai, Yang Zhao, Yuxian Pei, Chao Shen and Xiaoyan Pan

Abstract Space passive hydrogen maser has been applied on China's BeiDou Navigation Satellite System. Its long-term reliability and lifetime in orbit are significant topics needed to be verified. The repair methods are limited if space passive hydrogen maser breaks down in orbit. So it is necessary to simulate the onboard situation on ground for verification on the reliability and lifetime of space passive hydrogen maser. The major distinction between space environment and ground environment is their gaseous pressure. It is vacuum in orbit when it is atmospheric pressure on ground. Creating vacuum condition with vacuum container for space passive hydrogen maser, Shanghai Astronomical Observatory is verifying the long-term reliability and lifetime of space passive hydrogen maser. The performance and status data are acquired and analyzed after a period of testing. It indicates that the space passive hydrogen maser maintains excellent frequency performance during the testing period.

Keywords Hydrogen maser · Long-term · Reliability · Lifetime · Vacuum

1 Introduction

Space atomic clocks are vitally significant in the satellite navigation system. Their output signal's frequency stability and frequency drift directly affect the navigation and positioning accuracy. Passive hydrogen maser has good frequency stability, good frequency drift, small volume, and light weight. So it is widely used in the satellite navigation system, such as the European Space Agency's Galileo Navigation Satellite System and Russia's Global Navigation Satellite System (GLONASS) [1]. In order to improve the performance of BeiDou Navigation Satellite System, Shanghai Astronomical Observatory began to study space engineering application of passive hydrogen maser from 2010 supported by China

P. Chen (✉) · Y. Xie · T. Shuai · Y. Zhao · Y. Pei · C. Shen · X. Pan
Shanghai Astronomical Observatory, 80 Nandan Road, Shanghai 200030, China
e-mail: chenpengfei@shao.ac.cn

J. Sun et al. (eds.), *China Satellite Navigation Conference (CSNC) 2017 Proceedings: Volume III*, Lecture Notes in Electrical Engineering 439,
DOI 10.1007/978-981-10-4594-3_41

government. After years of development, performance indicators were improved and environmental adaptability problems were solved. The reliability and lifetime of space passive hydrogen maser in orbit are still not verified because of its long research cycle and huge resources cost. Recently a passive hydrogen maser is used to the verification experiment of its reliability and lifetime under vacuum after 18 months of various tests and environmental experiments.

2 Analyzing of the Reliability and Lifetime of Passive Hydrogen Maser

Passive hydrogen maser has been applied to all trades and professions on ground because of its excellent frequency stability and frequency drift. There are two challenges for space applications of passive hydrogen maser. The first is the effect of space environment on passive hydrogen maser. The other is long-term operational reliability and life expectancy. Space environment can be simulated on ground to examine the environment adaptability, which is called environmental acceptance test. The second challenge can be examined by long-time continuous running. Running in space is the most direct way which costs too much. In addition, if passive hydrogen maser breaks down in space, the remotely repair methods are limited. Exclusive of the unstable factors, the most significant difference between in orbit and on ground is vacuum. So the passive hydrogen maser can run in vacuum tank to examine its reliability and lifetime.

2.1 The Principle of Passive Hydrogen Maser

Passive hydrogen clock is composed of the physical system and electrical system, illustrated in Fig. 1. Physical system provides the needed hydrogen atoms and their 0–0 transition environment. Industrial hydrogen is stored in a steel tank in solid state. It is purified by refiner, and then ionized into atoms by ionization source. Hydrogen atoms in the (F = 1, mF = 0) and (F = 1, mF = 1) states pass through state selector, while hydrogen atoms in other states are deflected off. The hydrogen atoms in the (F = 1, mF = 0) state fulfill quantum transition induced by microwave. Energy containing frequency difference information was released. The vacuum environment is maintained by vacuum system, including a titanium getter pump and a titanium ion pump. Shielding system is composed of magnetic shield and solenoid, providing uniform magnetic field environment for quantum transition.

The electrical system supply microwave for inducing quantum transition [2] and translates the transition signal to direct-current voltages, which correct crystal output frequency and resonant frequency of microwave cavity. The Voltage Control X-tal Oscillator (VCXO) output frequency signal at 10 MHz. The signal is

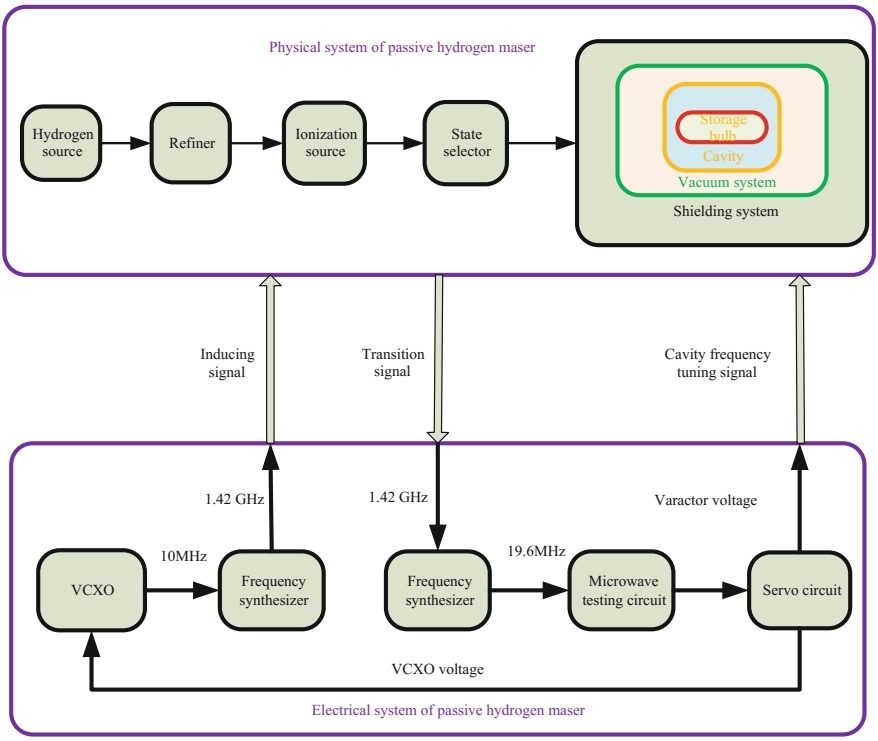

Fig. 1 Block diagram of space passive hydrogen maser

synthesized to microwave signal at 1.42 GHz. The microwave signal is imported into microwave cavity and interacts with hydrogen atoms releasing microwave signal at 1.42 GHz. The microwave signal is exported, mixed to 19.6 MHz. Then it is transformed to voltage signal by microwave testing circuit. The servo circuit can process the voltage signal and generate voltages of VCXO and varactor. The voltage of VCXO corrects the output frequency of VCXO, while the voltage of varactor corrects the resonance frequency of microwave cavity. Finally, the output frequency of VCXO is locked to hydrogen 0–0 quantum transition.

2.2 Analyzing of the Reliability and Lifetime of Passive Hydrogen Maser

The main performance indexes of passive hydrogen clock are frequency stability and frequency drift. So the most direct way to evaluate the reliability of the passive hydrogen maser is measuring the changes of frequency stability and frequency drift over time. If the frequency stability and frequency drift remain stable or have

decreasing trend, it proves that the passive hydrogen maser runs reliably. Otherwise the passive hydrogen maser is not reliable.

The evaluating of lifetime is by monitoring the state parameters and their change rates. Main state parameters are voltage of VCXO, voltage of varactor, Pk–Pk of second harmonic, light intensity of ionization source, and current of high-voltage power supply. The passive hydrogen clock has two frequency control loops individually for VCXO and the microwave cavity. The unlocking of any loop can cause serious degradation in performance of passive hydrogen maser. The output frequency of VCXO is adjusted by the controlling voltage [3]. The controlling voltage reflects the offset of its output frequency. If frequency drift of VCXO is too fast, soon VCXO is beyond the control scope of voltage. It will cause unlocking of VCXO frequency control loop. The voltage of varactor is similar to the voltage of VCXO. It can modify the resonance frequency of microwave cavity. If the frequency change of microwave cavity is out of varactor's adjusting range, the cavity is unlocked.

The energy releases when hydrogen atoms transit. The energy intensity affects frequency performance of passive hydrogen maser. It can be represented by Pk–Pk of second harmonic and light intensity of ionization source. Second harmonic is the signal which is produced by microwave test circuit. If second harmonic is too small, the servo circuit cannot be able to discern, which will lead to unlocking of passive hydrogen maser.

It gives out light when molecular hydrogen is ionized to atoms. The light intensity represents the flow rate of hydrogen which affects the quantum transition. The hydrogen is consumed when passive hydrogen maser works. When the hydrogen is exhausted, the passive hydrogen maser ends life. The light intensity is also affected by the cleanliness of ionization bulb. The decrease of the light intensity may not due to the decrease of the hydrogen flow rate. It needs to make a comprehensive judgment.

A combination of titanium getter pump and titanium ion pump maintains the vacuum pressure in the passive hydrogen maser. Titanium getter pump absorbs reactive gas, while titanium ion pump absorbs inert gas. Titanium ion pump requires high-voltage power supply with voltage of 3 kV, while titanium getter pump is a passive component. The current indicates the degree of vacuum in passive hydrogen maser. The lower the current is, the better the vacuum is. If the current keeps high for a long time, the vacuum is bad enough to decrease the lifetime of passive hydrogen maser.

2.3 Test System for Space Passive Hydrogen Maser

The test system for space passive hydrogen maser includes a vacuum tank, a vacuity monitoring subsystem, a temperature monitoring subsystem, a power supply subsystem, a performance monitoring subsystem, and a state monitoring subsystem. The system block diagram is shown in Fig. 2.

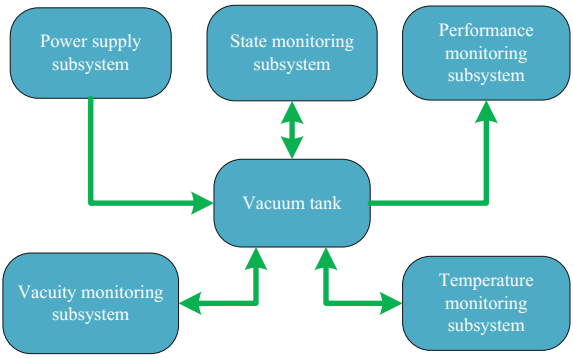

Fig. 2 Block diagram of test system for space hydrogen maser

The vacuum tank has a platform for the placement of space passive hydrogen maser. Gas pressure in the vacuum tank and temperature of the platform can be monitored. The vacuum monitoring subsystem is composed of a dry pump, a molecular pump, a resistance manometer and an ion gauge. Vacuum pressure in the vacuum tank is below 1×10^{-4} pa. The temperature fluctuations of platform in load are under 0.1 °C/h. Performance monitoring subsystem contains a frequency reference, a frequency comparator and a computer. The microwave connector on the vacuum tank connects frequency output of space passive hydrogen maser to frequency comparator. Power supply subsystem consists of several sets of dc-regulated power supply. State monitoring subsystem is composed of a data acquisition instrument and a computer, storing and displaying state parameters of space passive hydrogen maser. Power supply subsystem and state monitoring subsystem are connected to space passive hydrogen maser by low-frequency connector on the vacuum tank.

3 Verification of Reliability of Space Passive Hydrogen Maser

Space passive hydrogen maser runs under vacuum continuously. The degree of vacuum is maintained below 1×10^{-4} Pa. Temperature of the platform is maintained at 0 °C. The frequency output of the passive hydrogen maser is compared with VCH1003A by VCH314. At present, frequency comparison data of 187 days are obtained. Figure 3 shows the frequency curve of the space passive hydrogen maser averaged by 100 s. The frequency is continuous and without discontinuity in Fig. 3. Table 1 lists the data of its frequency stability and frequency drift. Figures 4 and 5 show the variation trend of the frequency stability and the frequency drift. It can be seen that, the frequency stability of passive hydrogen maser is stable and the frequency drift has decreased.

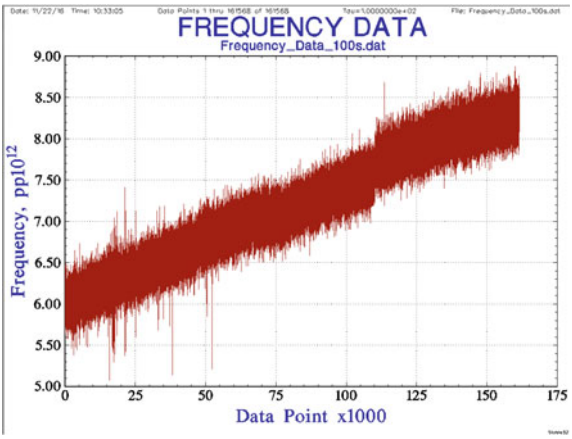

Fig. 3 100 s frequency curve

Table 1 Frequency stability and frequency drift data

Stage	Frequency stability						Frequency drift
	1 s	10 s	100 s	1000 s	10000 s	1 day	
First month	1.23e−12	5.27e−13	1.48e−13	4.57e−14	1.60e−14	1.07e−14	1.17e−14
Second month	1.14e−12	5.16e−13	1.47e−13	4.47e−14	1.46e−14	9.92e−15	1.23e−14
Third month	1.21e−12	5.16e−13	1.47e−13	4.57e−14	1.34e−14	1.17e−14	1.15e−14
Fourth month	1.11e−12	5.26e−13	1.48e−13	4.60e−14	1.64e−14	1.50e−14	1.30e−14
Fifth month	1.11e−12	5.23e−13	1.51e−13	4.56e−14	1.57e−14	9.14e−15	1.06e−14
Sixth month	1.11e−12	5.35e−13	1.55e−13	4.69e−14	1.46e−14	8.29e−15	1.01e−14
Seventh month	1.21e−12	5.40e−13	1.55e−13	4.87e−14	1.46e−14	8.88e−15	8.50e−15

4 Verification of Lifetime of Passive Hydrogen Maser

Five state parameters of passive hydrogen maser which affect its lifetime are tested along with the frequency signal. Figure 6 is the testing curve of VCXO voltage. It can be seen from the figure, the rate of change of the voltage decreases and the voltage tends to be a constant at 7.2 V which is within the voltage range, from 0.1 to 10 V. It reflects the VCXO output frequency tends to stable.

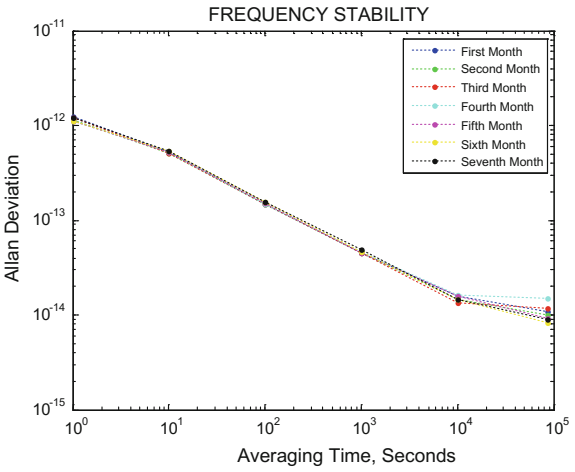

Fig. 4 Frequency stability curve

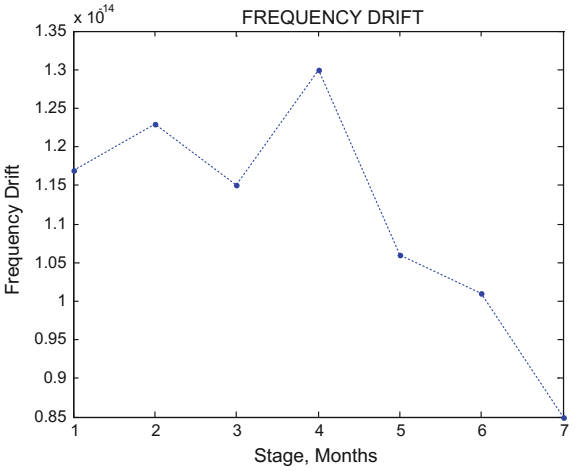

Fig. 5 Curve: change of frequency drift

The resonant frequency of the microwave cavity can be adjusted by varactor. Figure 7 is the testing curve of the voltage of varactor. As shown, varactor voltage, which reflects the drift of resonance frequency, is within the voltage range, from 0.1 to 12 V. So the change of microwave cavity's frequency is in the control range of varactor. What's more, the change of varactor voltage is linear.

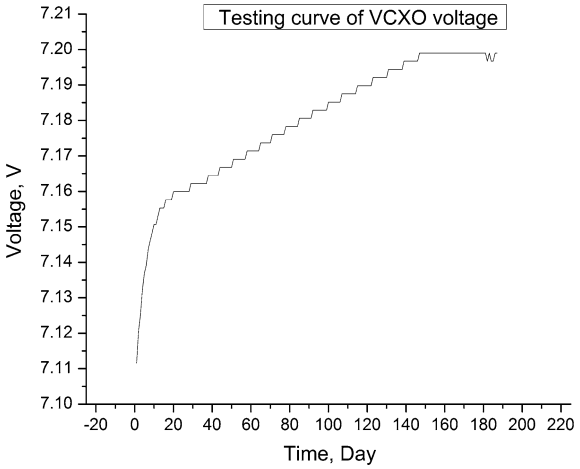

Fig. 6 Testing curve of VCXO voltage

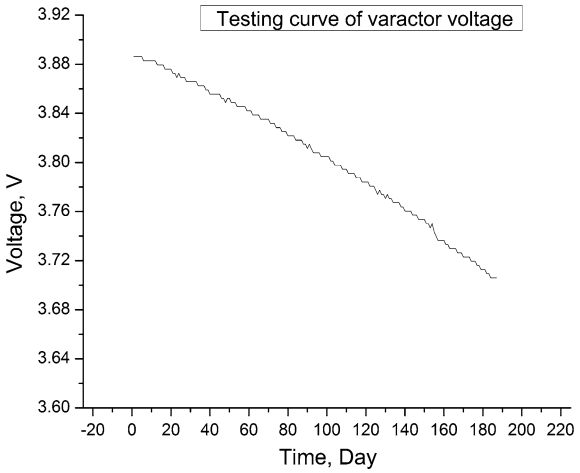

Fig. 7 Testing curve of the varactor voltage

The atomic signal level is a key element to the lifetime of passive hydrogen maser, which can be reacted by second harmonic Pk–Pk and light intensity of ionization source indirectly. Figures 8 and 9 are testing curves of second harmonic Pk–Pk and light intensity of ionization source respectively. The voltages of second harmonic Pk–Pk and light intensity are both within the voltage rang, from 0.1 to 5 V. The variation trend of the second harmonic Pk–Pk approximates to linear.

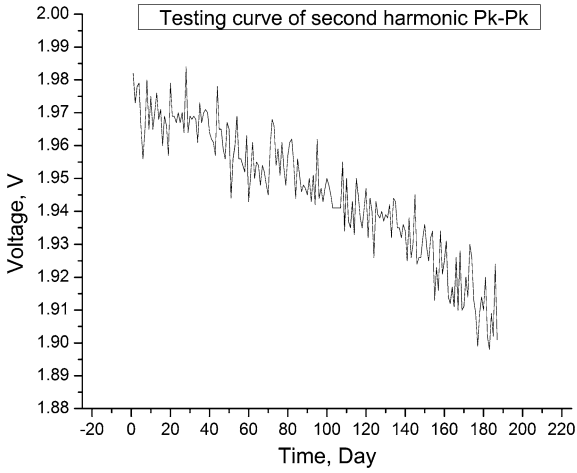

Fig. 8 Testing Curve of the second harmonic Pk–Pk

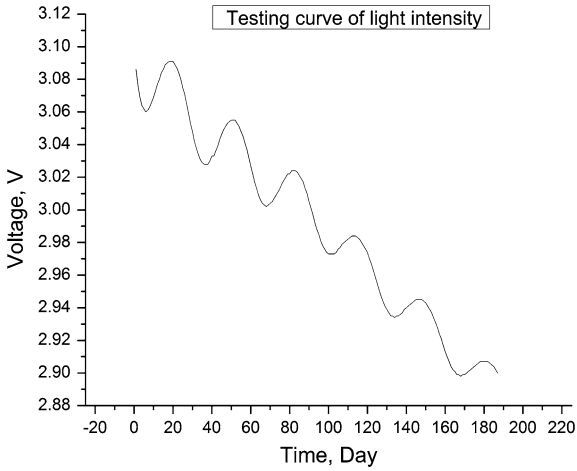

Fig. 9 Testing curve of the light intensity

The light intensity decreases in screw type. The atomic signal level satisfies the requirements of running for a long time according to the second harmonic Pk–Pk and light intensity.

The testing curve of current of the high-voltage power supply during examining time is weeny, far below the voltage range, 5 V and stable, as shown in Fig. 10. It presents that the internal vacuum pressure of the passive hydrogen maser is still high after a long-time work.

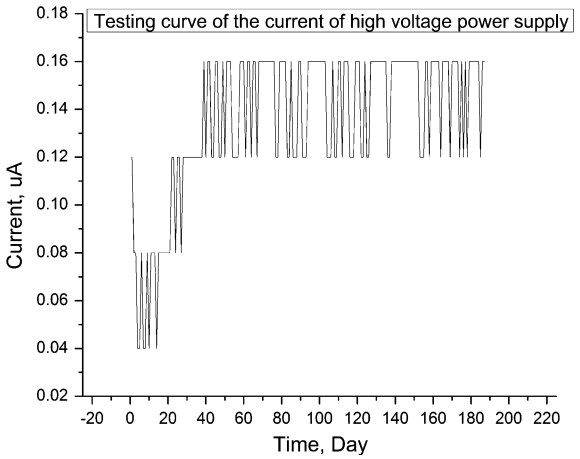

Fig. 10 Testing curve of the current of high voltage power supply

5 Conclusions

The passive hydrogen maser has run continuously under vacuum for 187 days. It is presented that the status and performance of space passive hydrogen maser are stable during the test period according to the experimental data. The monitoring of the passive hydrogen maser is continued. More data will be acquired to analyze the Reliability and Lifetime of Space Passive Hydrogen Maser.

References

1. Belloni M, Gioia M, Beretta S, et al, (2011) Space mini passive hydrogen maser—a compact passive hydrogen maser for space applications. In: 2011 Joint conference of the IEEE international on frequency control and the European frequency and time forum (FCS). IEEE, pp 1–5
2. Walls FL (1987) Characteristics and performance of miniature NBS passive hydrogen maser. IEEE Trans Instrum Meas IM-30(2):596–603
3. Shousong W (2000) Voltage controlled crystal oscillator and frequency modulation variable capacitance diode. Semicond Inform 4:14–17

Studying on the Leap Second Calculational Methods in BeiDou System

Mengfei Cheng, Fengfeng Shi, Jinfeng Xu, Yang Wang and Shengli Zhang

Abstract Time is one of the basic reference systems in satellite navigation systems. The time scale of Universal Time Coordinated (UTC) is an atomic uniform time scale, at the same time a leap second is adopted to approach Universal Time (UT). BeiDou Time (BDT) belongs to atomic time systems, and keeps in contact with UTC by leap seconds. User receivers in BeiDou Satellite Navigation System (BDS) calculate a leap second, according to the leap second algorithms in the Interface Control Document (ICD) and navigation messages. User receivers have different interpretations of how to calculate a leap second in BDS, in a result some user terminals did not successfully complete BDT to UTC on 30 June 2015 and 31 December 2016 in time. This paper takes the leap second on 31 December 2016 as an example, introduces how to calculate a leap second in BDS in detail, explains the meanings of time synchronization parameters of BDT to UTC, and shows the leap second calculational methods in each period before and after a leap second, helping user terminals in BDS to correct their leap second calculational methods. It is of an active guiding significance and great reference value for user receivers in BDS.

Keywords BDS · Receivers · A leap second · Time synchronization parameters · Calculational examples

1 Introduction

Time is one of the basic reference systems in satellite navigation systems, currently there are three time systems used widely: Atomic Time (AT), Universal Time (UT), and Universal Time Coordinated (UTC) [1]. When matter's internal atomic jumps, it will radiate an electromagnetic wave, and AT is the frequency of the wave, which has a high level of stability and reproducibility, so the atomic second is used as the System International second. International Time Bureau compares with atomic

M. Cheng (✉) · F. Shi · J. Xu · Y. Wang · S. Zhang
Beijing Satellite Navigation Center, Beijing 100094, China
e-mail: cmf100@163.com; 945910248@qq.com

J. Sun et al. (eds.), *China Satellite Navigation Conference (CSNC) 2017 Proceedings: Volume III*, Lecture Notes in Electrical Engineering 439,
DOI 10.1007/978-981-10-4594-3_42

clocks carefully chosen around the world, then calculates a unified atomic time system as International Atomic Time. UT is defined based on the earth's rotation, it is Greenwich Mean Time whose zero hour is the mean night, but the earth's rotation is not even. AT is more accurate and stable than UT, but UT is widely used in many fields, so AT cannot completely substitute for UT. Because the earth's rotation getting slower and slower, UT is getting slower and slower, then the difference between AT and UT is bigger and bigger. UTC is used since 1972 to avoid the harmful influence of the growing difference. The time scale of UTC is an atomic uniform time scale, at the same time a leap second is adopted for UTC to approach UT, so the value of UT-UTC is kept below 0.9 s [1–3]. The International Earth Rotation and Reference Systems Service (IERS) in Paris France is responsible for leap seconds, deciding when and how to add a positive or negative leap second to UTC, in general it is added at the end of 30 June or 31 December.

BeiDou Time (BDT) is the time reference of BeiDou Navigation Satellite System (BDS), which is called BeiDou System for short. It belongs to the atomic time system, so its time scale is an atomic uniform time scale, in addition it has continuity and no leap second. It starts from 0 h 0 m 0 s on 1 January 2016 UTC, described by week numbers and second numbers in week. BDT keeps in contact with UTC by UTC (NTSC), and the value of BDT-UTC is kept below 100 ns (modulo 1 s). The leap second information of BDT to UTC is broadcast in satellite navigation messages.

China Administration of Satellite Navigation System Office announced BeiDou Satellite Navigation System Interface Control Document of Space Signal for Public Service Signal 2.0 (BDS-SIS-ICD-2.0) on 1 December 2013, which introduces the relationship between BDT and UTC in detail. Since December 2012, BDS begins to provide service, and there is a positive leap second on 30 June 2015 and 31 December 2016, respectively. However, user receivers in BDS have different interpretations of how to calculate a leap second, in a result some user terminals did not successfully complete BDT to UTC on 30 June 2015 and 31 December 2016 in time.

This paper takes the leap second on 31 December 2016 as an example, introduces how to calculate a leap second in BDS in detail, explains the meanings of time synchronization parameters of BDT to UTC, and shows the leap second calculational methods in each period before and after a leap second, helping user terminals in BDS to correct their leap second calculational methods. It is of an active guiding significance and great reference value for user receivers in BDS.

2 The Leap Second Calculational Methods in BDS

2.1 Time Synchronization Parameters

BDS broadcasts navigation messages including the time synchronization parameters of BDT to UTC, $A_{0\mathrm{UTC}}, A_{1\mathrm{UTC}}, \Delta t_{\mathrm{LS}}, WN_{\mathrm{LSF}}, DN, \Delta t_{\mathrm{LSF}}$, their meanings are as follows [4].

A_{0UTC}, the clock difference of BDT to UTC, the number of bits is 32*, the scale factor is 2^{-30}, the unit is *second.*

A_{1UTC}, the clock velocity of BDT to UTC, the number of bits is 24*, the scale factor is 2^{-50}, the unit is *sec/sec.*

Δt_{LS}, delta time due to leap seconds, the accumulated value of BDT to UTC before the new leap second, the number of bits is 8*, the scale factor is 1, the unit is *second*.

WN_{LSF}, the week number of leap seconds, WN_{LSF} = (week number) [modulo 256], the number of bits is 8, the scale factor is 1, the unit is *week*.

DN, the day number of leap second, values span is 0–6 (from Sunday to Saturday), the number of bits is 8, the scale factor is 1, the unit is *day*.

Δt_{LSF}, delta time due to leap seconds, the accumulated value of BDT to UTC after the new leap second, the number of bits is 8*, the scale factor is 1, the unit is *second*.

In addition, * means that parameters so indicated shall be two's complement with the sigh bit (+ or −) occupying the most significant bit (MSB).

2.2 The Leap Second Algorithms of BDT to UTC

BDS broadcasts navigation messages including the time synchronization parameters, so receivers can get UTC by BDT, and the value of BDT-UTC is kept below 1 us. There are three UTC/BDT-time relationships, according to the leap second time and the user's present time [2, 4].

(1) Whenever the effectivity time indicated by the WN_{LSF} and the *DN* values is not in the past (relative to the user's present time), and the user's present time does not fall in the time span which starts at 8 h prior to the effectivity time and ends at 6 h after the effectivity time, the UTC/BDT-time relationship is given by

$$t_{UTC} = (t_E - \Delta t_{UTC})[\text{modulo } 86{,}400], \text{s} \tag{1}$$

and

$$\Delta t_{UTC} = \Delta t_{LS} + A_{0UTC} + A_{1UTC} \times t_E, \text{s} \tag{2}$$

(2) Whenever the user's present time falls within the time span of 8 h prior to the effectivity time to 6 h after the effectivity time, proper accommodation of the leap second event with a possible week number transition is provided by the following expression for UTC:

$$t_{UTC} = W[\text{modulo } (86{,}400 + \Delta t_{LSF} - \Delta t_{LS})], \text{s} \tag{3}$$

and

$$W = (t_{\mathrm{E}} - \Delta t_{\mathrm{UTC}} - 43{,}200)[\mathrm{modulo}\ 86{,}400] + 43{,}200, \mathrm{s} \tag{4}$$

$$\Delta t_{\mathrm{UTC}} = \Delta t_{\mathrm{LS}} + A_{0\mathrm{UTC}} + A_{1\mathrm{UTC}} \times t_{\mathrm{E}}, \mathrm{s} \tag{5}$$

(3) Whenever the effectivity time indicated by the WN_{LSF} and the DN values is in the "past" (relative to the user's present time), and the user's present time fall in the time span which starts at "6 h after the effectivity time", the UTC/BDT-time relationship is given by

$$t_{\mathrm{UTC}} = (t_{\mathrm{E}} - \Delta t_{\mathrm{UTC}})[\mathrm{modulo}\ 86,400], \mathrm{s} \tag{6}$$

and

$$\Delta t_{\mathrm{UTC}} = \Delta t_{\mathrm{LSF}} + A_{0\mathrm{UTC}} + A_{1\mathrm{UTC}} \times t_{\mathrm{E}}, \mathrm{s} \tag{7}$$

2.3 Additional Explanations

In BDS, the value span of DN is 0–6 (from Sunday to Saturday), but the Interface Control Document (ICD) of the Global Positioning System (GPS) in USA regulates that the value span of DN is 1–7 (from Sunday to Saturday), as a result there is a problem of mixed parameters for Global Navigation Satellite System (GNSS) receivers [4, 5].

WN_{LSF} is the week number of leap seconds, the number of bits is 8, the scale factor is 1, the unit is *week*, WN_{LSF} = (week number) [modulo 256]. For example, the week number of 31 December 2016 is 573, WN_{LSF} = (week number) [modulo 256] = 573 [modulo 256] = 61.

Modular operation is that the divisor and the dividend both round to the nearest integers, and get the remainder. Integers' modular operation A mod B is that:

(1) When the divisor A and the dividend B have the same symbol, the symbol of the result is same as the dividend B, and the absolute value of the result is $|A|$ mod $|B|$. For example, (3 + 0.1) [module 86,400] = 3 [module 86,400] = |3| module |86,400| = 3.

(2) When the divisor A and the dividend B have different symbols, the symbol of the result is same as the dividend B, and the absolute value of the result is $|B|$–($|A|$ mod $|B|$). For example, (−3 + 0.1) [module 86,400] = (−3) [module 86,400] = |86,400| − (|−3| mod| 86,400|) = 86,400 – 3 = 86,397.

3 The Leap Second Programmes in BDS

BDS contains two different services and work models, as Radio Determination Satellite Service (RDSS) and Radio Navigation Satellite Service (RNSS), their leap second programmes are also different.

3.1 The Leap Second Programme of RDSS

The leap second parameters in RDSS are the number of leap seconds and the state of a leap second. The number of leap seconds means the number of BDT-UTC at the user's present time. When a new leap second is not coming, the state of a leap second is 0; When the user's present time falls within the time span of 10 weeks prior to the leap second time to 1 day prior to the leap second time, the state of a leap second turns 1; When the leap second time passed, it turns 0. The ground control system broadcasts RDSS messages to the satellite system 1 times per minute.

Take the leap second on 31 December 2016 as an example, before the operation, the number of leap seconds is 3 and the state of a leap second is 0. After 10 weeks prior to the leap second time, the ground control system broadcasts pre adjustment leap second messages of RDSS to the satellite system, the number of leap seconds is 3 and the state of a leap second is 1. At the leap second time, 23 h 59 m 60 s on 31 December 2016 UTC, the number of leap seconds is 4 and the state of a leap second is 0.

3.2 The Leap Second Programme of RNSS

The synchronization parameters in RNSS are $\Delta t_{\mathrm{LS}}, WN_{\mathrm{LSF}}, DN, \Delta t_{\mathrm{LSF}}, A_{0\mathrm{UTC}}$, A_{1UTC}. The first four parameters should be focused, and they will update throughout the process.

Take the leap second on 31 December 2016 as an example, before the operation, the four parameters above are 3\239\2\3. After 10 weeks prior to the leap second time, the ground control system broadcasts leap second adjustment messages of RNSS to the satellite system, the four parameters above are 3\61\6\4. Five hours after the leap second time, the ground control system broadcasts the four parameters above to the satellite system which are 4\61\6\4, some satellites such as geo-synchronous orbit satellites in the antenna coverage will update the leap second parameters immediately, other satellites which are not in the antenna coverage will update the leap second parameters once they enter the antenna coverage, the ground control system broadcasts RNSS messages to the satellite system 1 times per hour, in generally the total satellites update the leap second parameters in 24 h. Six hours after the leap second time, the user system gets the updated leap second parameters broadcast by the satellite system.

4 Examples of the Leap Second Calculational Methods of RNSS User Receivers in BDS

Take the leap second on 31 December 2016 as an example, this section chooses some moments of BDT before and after the leap second time, and changes BDT to UTC according to formulas in Sect. 2.2 and parameters received by the user system.

4.1 Before the Leap Second Parameters Updated

Choosing a moment before the leap second parameters updated, BDT 560 week 518,403 s (0 h 0 m 3 s 1 October 2016 BDT), the time synchronization parameters in navigation messages are $A_{0\mathrm{UTC}} = -4 \times 10^{-9}$, $A_{1\mathrm{UTC}} = -2 \times 10^{-14}$, $\Delta t_{\mathrm{LS}} = 3$, $WN_{\mathrm{LSF}} = 239$, $DN = 2$, $\Delta t_{\mathrm{LSF}} = 3$. The last leap second is past, and the next leap second is not coming. Choose the formula 6.

$$\begin{aligned} t_{\mathrm{UTC}} &= (t_{\mathrm{E}} - \Delta t_{\mathrm{UTC}})[\mathrm{modulo}\ 86{,}400], \mathrm{s} \\ &= [t_{\mathrm{E}} - (\Delta t_{\mathrm{LSF}} + A_{0\mathrm{UTC}} + A_{1\mathrm{UTC}} \times t_{\mathrm{E}})][\mathrm{modulo}\ 86{,}400] \\ &= [518{,}403 - (3 + (-4 \times 10^{-9}) + (-2 \times 10^{-14}) \times 518{,}403)][\mathrm{modulo}\ 86{,}400] \\ &= [518{,}403 - 3 + 1.436806 \times 10^{-8})][\mathrm{modulo}\ 86{,}400] \\ &= 0 \end{aligned}$$

So we get 0 h 0 m 0 s 1 October 2016 UTC, then the difference value of BDT to UTC is 3.

4.2 After Some Leap Second Parameters Updated

4.2.1 Before 8 h Prior to the Leap Second Time

Choosing a moment after the leap second parameters updated and before 8 h prior to the leap second time, BDT 569 week 345,603 s (0 h 0 m 3 s 1 December 2016 BDT), the time synchronization parameters in navigation messages are $A_{0\mathrm{UTC}} = -8 \times 10^{-9}$, $A_{1\mathrm{UTC}} = 5 \times 10^{-12}$, $\Delta t_{\mathrm{LS}} = 3$, $WN_{\mathrm{LSF}} = 573\ [\mathrm{modulo}\ 256] = 61$, $DN = 6$, $\Delta t_{\mathrm{LSF}} = 4$. The last leap second is past, and the next leap second is not coming. Choose the formula 1.

$$
\begin{aligned}
t_{\mathrm{UTC}} &= (t_{\mathrm{E}} - \Delta t_{\mathrm{UTC}})[\text{modulo } 86{,}400], \text{s} \\
&= [t_{\mathrm{E}} - (\Delta t_{\mathrm{LS}} + A_{0\mathrm{UTC}} + A_{1\mathrm{UTC}} \times t_{\mathrm{E}})][\text{modulo } 86{,}400] \\
&= [345{,}603 - (3 + (-8 \times 10^{-9}) + 5 \times 10^{-12} \times 345{,}603)][\text{modulo } 86{,}400] \\
&= [345{,}603 - 3 + 1.728015 \times 10^{-6}][\text{modulo } 86{,}400] \\
&= 0
\end{aligned}
$$

So we get 0 h 0 m 0 s 1 December 2016 UTC, then the difference value of BDT to UTC is 3.

4.2.2 Within the Time Span of 8 h Prior to the Leap Second Time to 6 h After the Leap Second Time

Whenever the user's present time falls within the time span of 8 h prior to the leap second time to 6 h after the leap second time, Choose the formula 3.

Choosing a moment BDT 573 week 604,799 s (23 h 59 m 59 s 31 December 2016 BDT), the time synchronization parameters in navigation messages are $A_{0\mathrm{UTC}} = 1 \times 10^{-9}$, $A_{1\mathrm{UTC}} = 0$, $\Delta t_{\mathrm{LS}} = 3$, $WN_{\mathrm{LSF}} = 61$, $DN = 6$, $\Delta t_{\mathrm{LSF}} = 4$.

$$
\begin{aligned}
t_{\mathrm{UTC}} &= W[\text{modulo}(86{,}400 + \Delta t_{\mathrm{LSF}} - \Delta t_{\mathrm{LS}})], \text{s} \\
&= \{(t_{\mathrm{E}} - \Delta t_{\mathrm{UTC}} - 43{,}200)[\text{modulo } 86{,}400] + 43{,}200]\} \\
&\quad [\text{modulo}(86{,}400 + \Delta t_{\mathrm{LSF}} - \Delta t_{\mathrm{LS}})] \\
&= \{(t_{\mathrm{E}} - (\Delta t_{\mathrm{LS}} + A_{0\mathrm{UTC}} + A_{1\mathrm{UTC}} \times t_{\mathrm{E}}) - 43{,}200)[\text{modulo } 86{,}400] + 43{,}200\} \\
&\quad [\text{modulo}(86{,}400 + \Delta t_{\mathrm{LSF}} - \Delta t_{\mathrm{LS}})] \\
&= \big\{[604{,}799 - (3 + 1 \times 10^{-9} + 0 \times 237{,}543) - 43{,}200] \\
&\quad [\text{modulo } 86{,}400] + 43{,}200\}[\text{modulo } 86{,}401] \\
&= \big\{[561{,}596 - 1 \times 10^{-9}][\text{modulo } 86{,}400] + 43{,}200\}[\text{modulo } 86{,}401] \\
&= [43{,}196 + 43{,}200][\text{modulo } 86{,}401] \\
&= 86{,}396
\end{aligned}
$$

So we get 23 h 59 m 56 s 31 December 2016 UTC, then the difference value of BDT to UTC is 3.

Choosing a moment BDT 574 week 3 s (0 h 0 m 3 s 1 January 2017 BDT), the time synchronization parameters in navigation messages are $A_{0\mathrm{UTC}} = 1 \times 10^{-9}$, $A_{1\mathrm{UTC}} = 0$, $\Delta t_{\mathrm{LS}} = 3$, $WN_{\mathrm{LSF}} = 61$, $DN = 6$, $\Delta t_{\mathrm{LSF}} = 4$.

$$
\begin{aligned}
t_{\mathrm{UTC}} &= W[\mathrm{modulo}(86{,}400 + \Delta t_{\mathrm{LSF}} - \Delta t_{\mathrm{LS}})], \mathrm{s} \\
&= \{(t_{\mathrm{E}} - \Delta t_{\mathrm{UTC}} - 43{,}200)[\mathrm{modulo}\, 86{,}400] + 43{,}200]\} \\
&\quad [\mathrm{modulo}(86{,}400 + \Delta t_{\mathrm{LSF}} - \Delta t_{\mathrm{LS}})] \\
&= \{(t_{\mathrm{E}} - (\Delta t_{\mathrm{LS}} + A_{0\mathrm{UTC}} + A_{1\mathrm{UTC}} \times t_{\mathrm{E}}) - 43{,}200)[\mathrm{modulo}\, 86{,}400] + 43{,}200\} \\
&\quad [\mathrm{modulo}(86{,}400 + \Delta t_{\mathrm{LSF}} - \Delta t_{\mathrm{LS}})] \\
&= \left\{[3 - (3 + 1 \times 10^{-9} + 0 \times 3) - 43{,}200][\mathrm{modulo}\, 86{,}400] + 43{,}200\right\} \\
&\quad [\mathrm{modulo}\, 86{,}401] \\
&= \{(-1 \times 10^{-9} - 43{,}200)[\mathrm{modulo}\, 86{,}400] + 43{,}200\}[\mathrm{modulo}\, 86{,}401] \\
&= (43{,}200 + 43{,}200)[\mathrm{modulo}\, 86{,}401] \\
&= 86{,}400
\end{aligned}
$$

So we get 23 h 59 m 60 s 31 December 2016 UTC, then the difference value of BDT to UTC is 4.

Choosing a moment BDT 574 week 4 s (0 h 0 m 4 s 1 January 2017 BDT), the time synchronization parameters in navigation messages are $A_{0\mathrm{UTC}} = 1 \times 10^{-9}$, $A_{1\mathrm{UTC}} = 0$, $\Delta t_{\mathrm{LS}} = 3$, $WN_{\mathrm{LSF}} = 61$, $DN = 6$, $\Delta t_{\mathrm{LSF}} = 4$.

$$
\begin{aligned}
t_{\mathrm{UTC}} &= W[\mathrm{modulo}(86{,}400 + \Delta t_{\mathrm{LSF}} - \Delta t_{\mathrm{LS}})], \mathrm{s} \\
&= \{(t_{\mathrm{E}} - \Delta t_{\mathrm{UTC}} - 43{,}200)[\mathrm{modulo}\, 86{,}400] + 43{,}200]\} \\
&\quad [\mathrm{modulo}(86{,}400 + \Delta t_{\mathrm{LSF}} - \Delta t_{\mathrm{LS}})] \\
&= \{(t_{\mathrm{E}} - (\Delta t_{\mathrm{LS}} + A_{0\mathrm{UTC}} + A_{1\mathrm{UTC}} \times t_{\mathrm{E}}) - 43{,}200)[\mathrm{modulo}\, 86{,}400] + 43{,}200\} \\
&\quad [\mathrm{modulo}(86{,}400 + \Delta t_{\mathrm{LSF}} - \Delta t_{\mathrm{LS}})] \\
&= \left\{[4 - (3 + 1 \times 10^{-9} + 0 \times 3) - 43{,}200][\mathrm{modulo}\, 86{,}400] + 43{,}200\right\} \\
&\quad [\mathrm{modulo}\, 86{,}401] \\
&= \{(1 - 1 \times 10^{-9} - 43{,}200)[\mathrm{modulo}\, 86{,}400] + 43{,}200\}[\mathrm{modulo}\, 86{,}401] \\
&= (43{,}201 + 43{,}200)[\mathrm{modulo}\, 86{,}401] \\
&= 0
\end{aligned}
$$

So we get 0 h 0 m 0 s 1 January 2017 UTC, then the difference value of BDT to UTC is 4.

4.2.3 After 6 h After the Leap Second Time and Δt_{LS} Is not Totally Updated

Choosing a moment after 6 h after the leap second time and Δt_{LS} is not completely updated, BDT 574 week 21,604 s (6 h 0 m 4 s 1 January 2017 BDT), the time synchronization parameters in navigation messages are $A_{0\mathrm{UTC}} = 1 \times 10^{-9}$,

$A_{1UTC} = 0$, $WN_{LSF} = 61$, $DN = 6$, $\Delta t_{LSF} = 4$, some satellite broadcast $\Delta t_{LS} = 4$, but some satellite broadcast $\Delta t_{LS} = 3$. Whenever the effectivity time indicated by the WN_{LSF} and the DN values is in the "past" (relative to the user's present time), and the user's present time fall in the time span which starts at "6 h after the effectivity time". Choose the formula 6.

$$\begin{aligned} t_{UTC} &= (t_E - \Delta t_{UTC})[\text{modulo } 86{,}400], \text{s} \\ &= [t_E - (\Delta t_{LSF} + A_{0UTC} + A_{1UTC} \times t_E)][\text{modulo } 86{,}400] \\ &= [21{,}604 - (4 + 1 \times 10^{-9} + 0 \times 21{,}604)][\text{modulo } 86{,}400] \\ &= [21{,}600 - 1 \times 10^{-9}][\text{modulo } 86{,}400] \\ &= 21{,}600 \end{aligned}$$

So we get 6 h 0 m 0 s 1 January 2017 UTC, then the difference value of BDT to UTC is 4.

4.3 After All Leap Second Parameters Updated

Choosing a moment after 6 h after the leap second time and Δt_{LS} is updated, BDT 574 week 108,004 s (6 h 0 m 4 s 2 January 2017 BDT), the time synchronization parameters in navigation message are $A_{0UTC} = 2 \times 10^{-9}$, $A_{1UTC} = 0$, $\Delta t_{LS} = 4$, $WN_{LSF} = 61$, $DN = 6$, $\Delta t_{LSF} = 4$. Whenever the effectivity time indicated by the WN_{LSF} and the DN values is in the "past" (relative to the user's present time), and the user's present time fall in the time span which starts at "6 h after the effectivity time". Choose the formula 6.

$$\begin{aligned} t_{UTC} &= (t_E - \Delta t_{UTC})[\text{modulo } 86{,}400], \text{s} \\ &= [t_E - (\Delta t_{LSF} + A_{0UTC} + A_{1UTC} \times t_E)][\text{modulo } 86{,}400] \\ &= [108{,}004 - (4 + 2 \times 10^{-9} + 0 \times 21{,}604)][\text{modulo } 86{,}400] \\ &= [108{,}000 - 2 \times 10^{-9}][\text{modulo } 86{,}400] \\ &= 21{,}600 \end{aligned}$$

So we get 6 h 0 m 0 s 2 January 2017 UTC, then the difference value of BDT to UTC is 4.

5 Summary

The leap second operation of UTC is an important event that affects the time synchronization in many fields around the world, such as communications, electricity, finance, and so on. If user receivers in BDS can successfully change BDT to

UTC, it signifies the user service capability's improvement and perfection in BDS, and means there is a big step into the advanced navigation service system ranks. Based on the leap second on 30 June 2015, this paper publishes the calculational methods of the leap second on 31 December 2016 in detail, helping user terminals in BDS successfully change BDT to UTC in time. It is of an active guiding significance and great reference value for user receivers in BDS.

References

1. Haiying L, Huinan W, Zhiming C (2013) Principles and applications of satellite navigation. National Defense Industry Press, Beijing, pp 1–36
2. Xiaozhen Zhang (2014) GNSS interoperability parameters and signal analysis. National Time Service Center Chinese Academy of Science, Lintong Shanxi, pp 15–18
3. Zhengsheng C, Zhiping L, Lingyong H, Hao L (2013) Unified model and precision analysis of multi-GNSS time system. J Navig Pos 1(4):70–73
4. China administration of satellite navigation system office, BeiDou satellite navigation system interface control document of space signal for public service signal 2.0 (BDS-SIS-ICD-2.0), Beijing: China administration of satellite navigation system office, 2013.12, pp 35–38
5. Dunn MJ, Disl D (2011) Navstar GPS space segment/navigation user segment interfaces (IS-GPS-200F). Glob Position Syst Directorate, pp 118–126

The Identification of Satellite Clock Noise Based on LAG1 Autocorrelation of Overlapping Samples

Qingsong Ai, Tianhe Xu, Dawei Sun, Hongwei Xiong and Shengchao Wang

Abstract Atomic clock is composed of various components of electronic devices, and its comprehensive effect of the internal and external environment makes it get easily affected by many kinds of noise. The random part of the clock bias is mainly influenced by the noise. The noise identification of atomic clock plays an important role in establishing an accurate random model and the weighting strategy of multi-GNSS. The most common methods for power-law noise identification are slope method, B1 partial factor method, LAG1 autocorrelation function method, and so on. However, these methods have their own defects or shortcomings. In this paper, we propose an improved method of LAG1 autocorrelation function based on overlapping samples to accurately identify the type of noise. By this method, we analyzed the main noise types affecting GPS and BDS satellite clocks. The results showed that the BDS satellite clock is mainly affected by White FM, Flicker FM and Random Walk FM. GPS BLOCK IIA Cs, BLOCK IIA Rb, BLOCK IIR Rb, BLOCK IIR M and BLOCK IIF Cs are mainly affected by the White FM and Flicker PM, and BLOCK IIF Rb is mainly influenced by the White PM, Flicker PM and White FM. The proposed new method based on overlapping sampling of LAG1 autocorrelation function can accurately identify GPS satellite clock noise, because the frequency bias and drift is more stable.

Q. Ai · S. Wang
School of Geology Engineering and Surveying, Chang'an University,
No. 126, Yanta Road, Xi'an, Shanxi, China
e-mail: 1305583364@qq.com

T. Xu (✉)
Shandong University, Weihai, Shandong, China
e-mail: thxugfz@163.com

T. Xu
Weihai Key Laboratory of Satellite Navigation and Remote Sensing,
Weihai, Shandong, China

D. Sun
Qingdao Agricultural University, Qingdao, Shandong, China

H. Xiong
School of Information Engineering, China University of Geoscience, Wuhan, China

J. Sun et al. (eds.), *China Satellite Navigation Conference (CSNC) 2017 Proceedings: Volume III*, Lecture Notes in Electrical Engineering 439,
DOI 10.1007/978-981-10-4594-3_43

Keywords Power-law noise · Autocorrelation · Overlapping sample · Noise identification

1 Introduction

As a time and frequency standard, atomic clock's stability is influenced by many factors. The noise identification of the atomic clock has important practical significance in the processing and application of atomic clock signal. In order to take advantages of the atomic clock which has excellent performance in the calculation of atomic time, it is necessary to analyze its noise features in details [1]. As a special oscillator, the phase noise of atomic clock is in line with features of power-law spectral process [2, 3]. In 1971, Barnes et al. systematically developed a power-law spectrum model of frequency data, that is, the noise of atomic clock can be regarded as a linear combination of five kinds of noise components. The expression of the noise power-law spectral model is as follows.

$$S_y(f) = h_2 f^2 + h_1 f^1 + h_0 f^0 + h_{-1} f^{-1} + h_{-2} f^{-2} = \sum_{\alpha=-2}^{2} h_\alpha f^\alpha$$

where $S_y(f)$ is the power-law spectral density of single frequency data, the unit is 1/Hz, f the Fourier frequency with unit of Hz, α the integral coefficient of noise type, and h_α the coefficients of noise intensity.

According to the different values of α, the noise can be divided into five types: WPM $(\alpha = 2)$, FPM $(\alpha = 1)$, WFM $(a = 0)$, FFM $(\alpha = -1)$, and RWFM $(\alpha = -2)$ [4, 5].

Many scholars have carried out a lot of studies in the aspect of phase noise identification [6]. In that paper, the authors calculated the values of Allan variance and modified Allan variance in time domain base on a large number of phase or frequency data, and then plotted the curve of $\log \sigma_y(\tau) \sim \log(\tau)$. Based on the curve, the slope can be obtained by the least squares fitting. Comparing the slope with the Allan standard deviation noise discriminator, the type of noise could be roughly identified in a certain averaging time [6]. Howe Dave introduced the B1 partial factor method which used the correlation of the ratio (standard deviation and Allan variance) and the power spectral time domain exponent μ to identify the phase noise [7]. However, the method requires at least the stability of two points. If the amount of time series is small, it will lead to a large deviation in the noise recognition. In fact, the B1 partial factor method is also based on the Allan variance and the modified Allen variance, so the results are similar to the slope method. Before using the B1 partial factor method to identify the phase noise, we should remove the frequency drift of the phase sequence. When the sampling interval is equal to the averaging time (smoothing factor is one), the WPM and FPM cannot be identified on the basis of $R(n)$ function [8]. According to the deficiency of the above

two conventional methods, the LAG1 autocorrelation function method is used to analyze phase noise of GPS and BDS. Then, we proposed an improved LAG1 autocorrelation function method based on overlapping sampling.

2 The Principle and Experiment of LAG1 Autocorrelation Function Method

2.1 The Principle of LAG1 Autocorrelation Function Method

The autocorrelation function is used to reflect the similarity extent between the random error of the time series and its expectation. According to this function, the noise type of each averaging time can be calculated in details. So, it could be more accurate to analyze the noise of satellite clock bias than the conventional methods.

The formula of lag k autocorrelation function can be expressed as:

$$\rho_k = \frac{E[(z_t - \mu)(z_{t+k} - \mu)]}{\sigma_z^2},$$

where μ, δ_t^2 and E are the mean, variance, and expectation of z_t, respectively.

Thus, the estimate of the function can be expressed as:

$$r_k = \frac{\frac{1}{N}\sum_{t=1}^{N-k}(z_t - \bar{z})(z_{t+k} - \bar{z})}{\frac{1}{N}\sum_{t=1}^{N}(z_t - \bar{z})^2},$$

where the individual time series variables is formulated as $z_t = \frac{1}{m}\sum_{j=1}^{m} z_{(t-1)*m+j} \quad (t = 1, 2, \ldots, N)$.

The coefficients of LAG1 autocorrelation can be obtained by taking the step LAG parameter as $k = 1$. An effective method for identifying power-law noise using the LAG1 autocorrelation function is based on the characteristic of discrete time fractal noise, which has spectral densities of the form $(2\sin\pi f)^{-2\delta}$. While $\delta < 1/2$, the discrete noise sequence is stationary and the LAG1 autocorrelation parameter could be expressed as $\rho_1 = \delta/(1+\delta)$ [9, 10]. Then, we can get the noise by the equation $\delta = r_1/(1+r_1)$. When the sequence does not meet the stationary condition, the first difference should be performed in order to convert the noise sequence into a stationary process ($\delta < 0.25$). The noise identification criterion is $p = -\text{round}(2\delta) - 2d$, where the function round() is rounded to the nearest integer and d the order of the difference. If z_t is a τ-average of frequency data $y(t)$, then $\alpha = p$. If z_t is a τ-average of phase data $x(t)$, then $\alpha = p + 2$, where α is the usual

power-law exponent. In this way, we can get the noise type at any averaging time [11–13].

2.2 The Noise Analysis of on-Borne Atomic Clock

Here, we conduct a scheme to verify the validity of LAG1 algorithm. The test data is provided by IGS and Wuhan University, with a sampling interval of 5 min. The time span of the data for GPS is from March 24, 2014 to April 7, 2014, and for BDS from July 19, 2015 to August 11, 2015. For the gap of data, linear interpolation is used to fill. The results of GPS (G07, G08, G09, G23, G24, G26) and BDS (C01, C06, C14) are listed (Note: Alpha represents the result of LAG1 autocorrelation function method).

From the statistical results in Table 1, it can be seen that the BDS satellite clock bias is mainly affected by White FM, Flicker FM and Random Walk FM. GPS BLOCK IIA Cs, BLOCK IIA Rb, BLOCK IIR Rb, BLOCK IIR M and BLOCK IIF Cs are mainly affected by the White FM and Flicker PM, and BLOCK IIF Rb is mainly influenced by the White PM, Flicker PM and White FM. From Figs. 1, 2, 3, 4, 5 and 6, it is shown that the LAG1 autocorrelation algorithm can efficiently identify the phase noise of GPS and BDS satellite clocks with the relatively short of averaging time. With the prolongation of the τ-average, the results reveal severe fluctuation, which will interfere with the accurate identification of phase noise. This character is consistent with the autocorrelation function method under the limit of the sampling size of 30.

3 The Principle and Experiment of Overlapping LAG1 Autocorrelation Function Method

3.1 The Principle of Overlapping LAG1 Autocorrelation Function Method

From the above analysis, we know that LAG1 autocorrelation function method can identify the noise when the τ-average is in a relatively short period of time. With the enlargement of the averaging time, the curve of power-law exponent fluctuates greatly which could bring large errors in noise identification. However, in practical applications, it is usually necessary to analyze the existence of noise types in the case of longer τ-average time. Therefore, this paper proposes a LAG1 autocorrelation function based on overlapping sampling to improve the performance of noise identification. The principle of the new method is to sample by sliding window overlay to form all possible averaging time series, and make full use of available data. At the same time, the conventional LAG1 autocorrelation function is used to

Table 1 The identified phase noise based on LAG1 autocorrelation method

Type of satellite	PRN	τ/s	α	Type of noise
BLOCK IIA Rb	G26	$3 \times 10^2 \sim 2 \times 10^4$	0, 1	WFM, FPM
		$> 2 \times 10^4$	1	FPM
BLOCK IIA Cs	G08	$3 \times 10^2 \sim 1.5 \times 10^4$	0	WFM
		$1.5 \times 10^4 \sim 3 \times 10^4$	1	FPM
		$> 10^4$	0	WFM
BLOCK IIR Rb	G23	$3 \times 10^2 \sim 3 \times 10^4$	1	FPM
		$> 3 \times 10^4$	0	WFM
BLOCK IIR M	G07	$3 \times 10^2 \sim 1.5 \times 10^3$	1	FPM
		$> 1.5 \times 10^3$	0	WFM
BLOCK IIF Rb	G09	$3 \times 10^2 \sim 1 \times 10^4$	0	WFM
		$1 \times 10^4 \sim 3 \times 10^4$	1, 2	FPM, WPM
		$> 3 \times 10^4$	1, 0	FPM, WFM
BLOCK IIF Cs	G24	$3 \times 10^2 \sim 3 \times 10^4$	0	WFM
		$> 3 \times 10^4$	1	FPM
GEO	C01	$3 \times 10^2 \sim 2 \times 10^3$	0	WFM
		$2 \times 10^3 \sim 1 \times 10^4$	−1	FFM
		$> 1 \times 10^4$	−2, −1	RWFM, FFM
IGSO	C06	$3 \times 10^2 \sim 6 \times 10^2$	0	WFM
		$6 \times 10^2 \sim 3 \times 10^4$	−1, −2	FFM, RWFM
		$> 3 \times 10^4$	0, −1	WFM, FFM
MEO	C14	$3 \times 10^2 \sim 2 \times 10^3$	0	WFM
		$2 \times 10^3 \sim 2 \times 10^4$	−1	FFM
		$> 2 \times 10^4$	−1, −2	FFM, RWFM

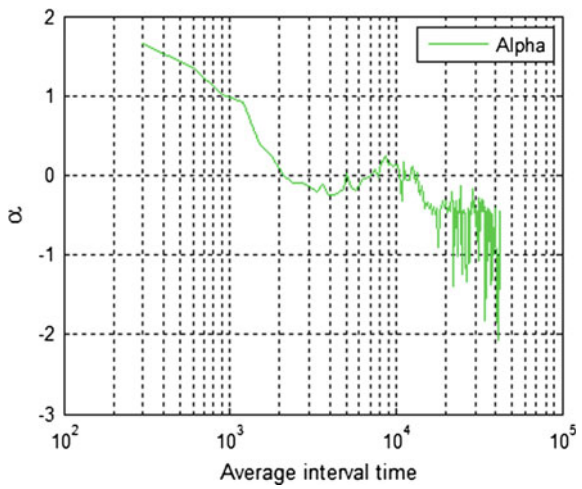

Fig. 1 The phase noise of G07

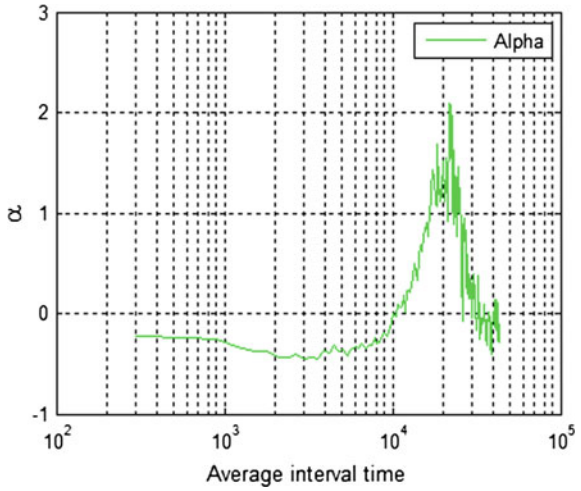

Fig. 2 The phase noise of G08

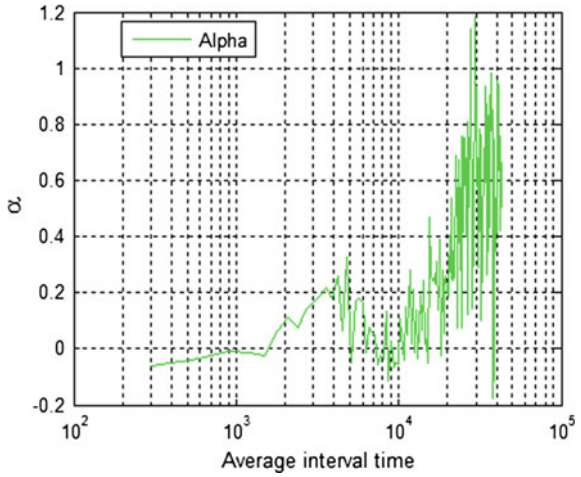

Fig. 3 The phase noise of G24

improve the reliability of noise identification. The principle of the two autocorrelation function methods is almost the same except for the difference of sampling method.

The variable z_t based on overlapping samples can be written as

$$z_i = \frac{1}{M} \sum_{k=i}^{i+M-1} z_k \quad (i = 1, 2, \ldots, N)$$

The difference of z_i is changed as

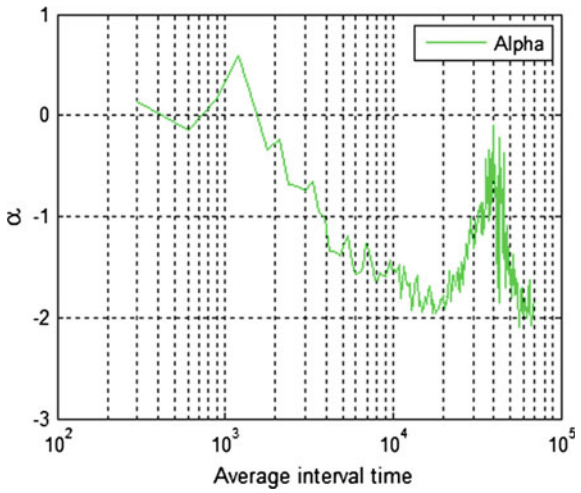

Fig. 4 The phase noise of C01

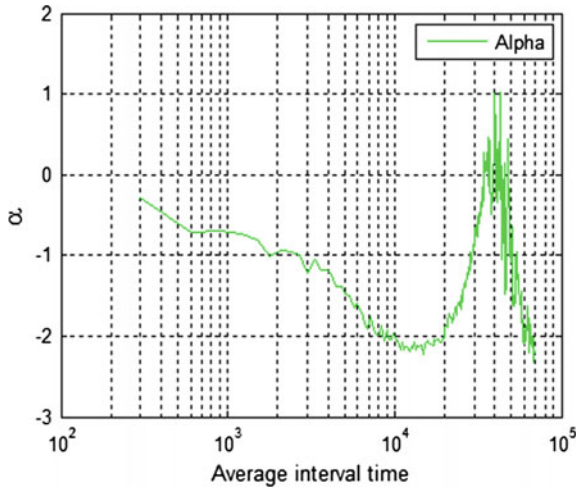

Fig. 5 The phase noise of C06

$$z_1 = z_{1+M} - z_1, \ldots, z_{N-M} = z_N - z_{N-M}$$

The noise identification flowchart of LAG1 autocorrelation function method based on overlapping sampling is as follows.

Done=False , d=0

While Not Done

$$\bar{z} = \frac{1}{N}\sum_{i=1}^{N} z_i \qquad r_1 = \frac{\sum_{t=1}^{N-M}(z_t - \bar{z})(z_{t+M} - \bar{z})}{\sum_{t=1}^{N}(z_t - \bar{z})^2}$$

$$\delta = r_1/(1+r_1)$$

If $d \geq d\min$ & ($\delta < 0.25 \mid d \geq d\max$)

$$p = -2(\delta + d)$$

Done=True

Else

$$z_1 = z_{1+M} - z_1, \cdots, z_{N-M} = z_N - z_{N-M}$$

$$N = N - M$$

$$d = d + 1$$

End if

End While

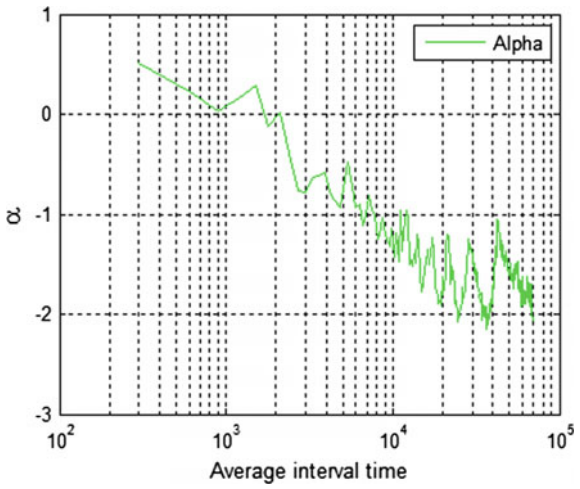

Fig. 6 The phase noise of C14

3.2 *The Noise Identification of on-Borne Atomic Clock Base on Overlapping Sample*

The second scheme used the same data to verify the validation of the proposed new method. Figures 7, 8, 9, 10, 11, and 12 show the results of noise analysis (Note: Alpha represents the result of classical LAG1 autocorrelation method, and Alpha-lap represents that of the overlapping LAG1 autocorrelation method).

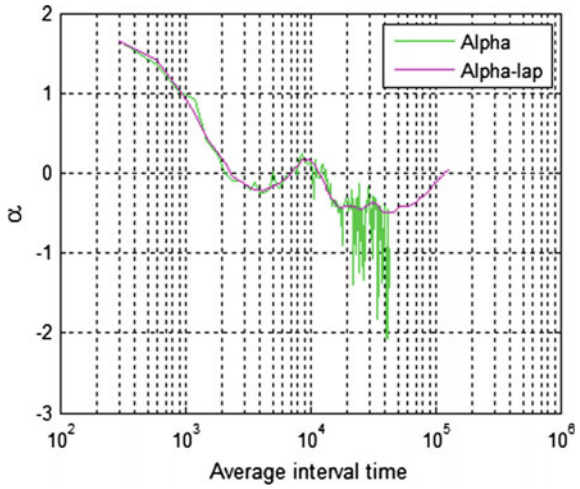

Fig. 7 The phase noise of G07

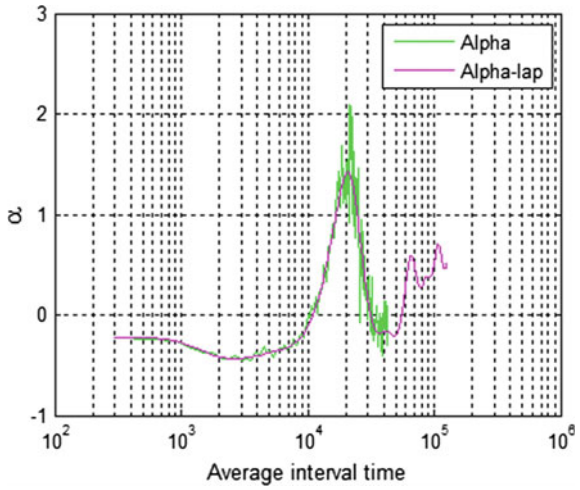

Fig. 8 The phase noise of G08

According to the results of the two schemes, it can be seen that the τ-average is expanded from 7×10^4 to $1 \sim 2 \times 10^5$ by using the overlapping sampling. The proposed method can identify the noise type when the sampling size is less than 30, which can eliminate the limitation of the sample size. In the case of long τ-average time, the corresponding value of the noise exponent is relatively smooth and does not fluctuate frequently. For GPS, the identified noise types based on the overlapping sampling are consistent with the non-overlapping algorithm from Figs. 7, 8 and 9. From the comparisons of Figs. 4, 5, 6, 10, 11 and 12, we can find

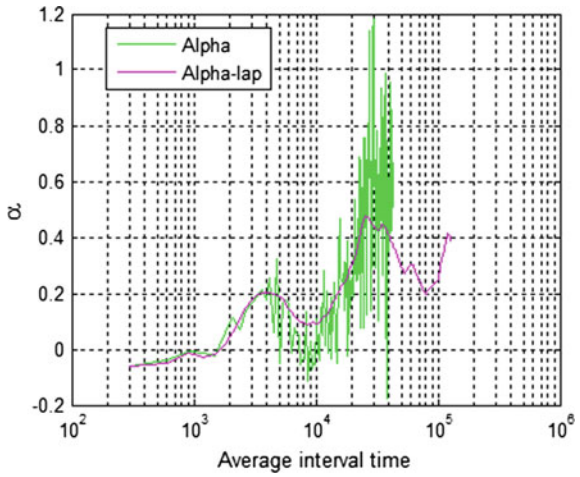

Fig. 9 The phase noise of G24

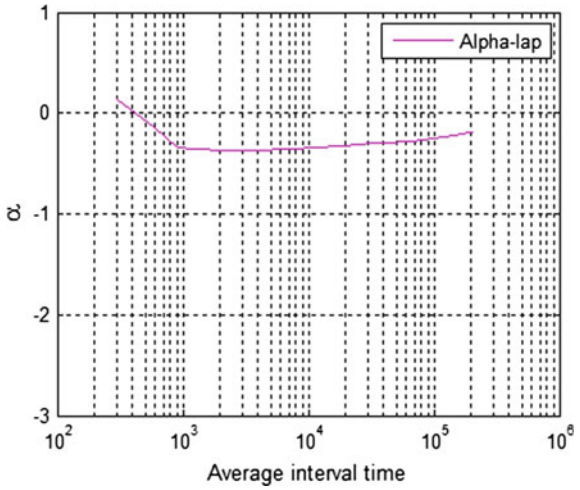

Fig. 10 The phase noise of C01

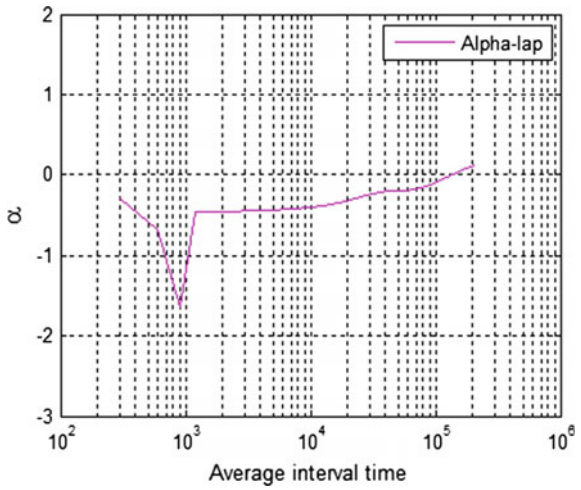

Fig. 11 The phase noise of C06

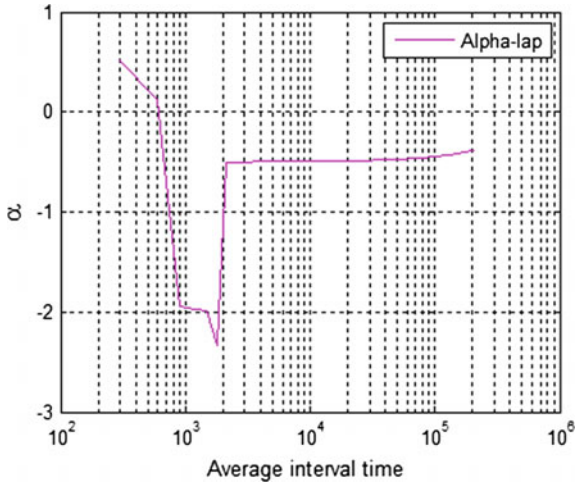

Fig. 12 The phase noise of C14

that there is a certain deviation for BDS between the identifying results of the two methods. This discrepancy may be related to the frequency stability of BDS satellite clock bias.

The frequency and the frequency difference sequences of C01 are displayed in Figs. 13 and 14. Form Fig. 13, we can find that obvious frequency deviation (the mean of all the frequency sequences is not equal to zero) and frequency drift (frequency series fluctuate significantly) phenomenon occurs in BDS satellite clock bias. However, the frequency of the first-order difference sequence tends to be stable from Fig. 14.

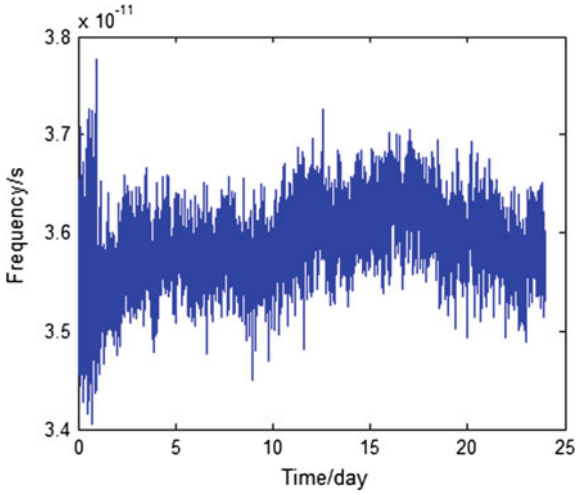

Fig. 13 The frequency of C01

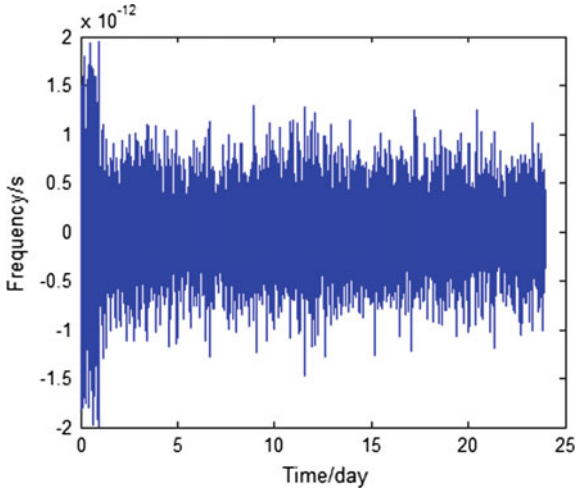

Fig. 14 The difference sequence frequency of C01

The noise analysis of the difference sequence is listed from Figs. 15, 16 and 17. The noise exponent of BDS is consistent based on the overlapping and nonoverlapping algorithms. It is confirmed from the previous opinion that the discrepancy of the two methods is mainly due to the frequency deviation and frequency drift. Therefore, the autocorrelation function method based on overlapping is more suitable for the time series which is relatively stable. So, the new method of noise identification is more suitable for GPS satellite clock bias at the present stage.

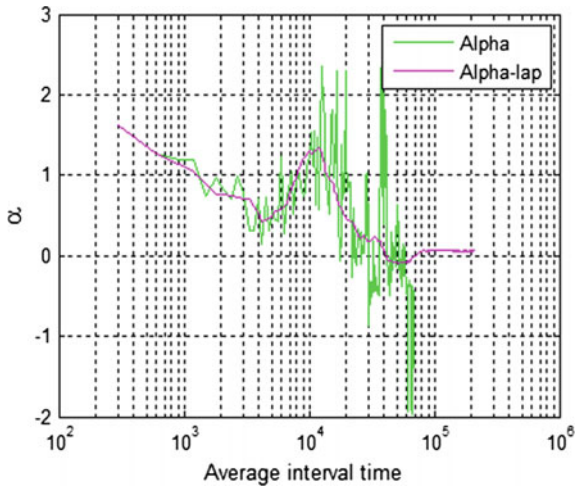

Fig. 15 The difference sequence noise of C01

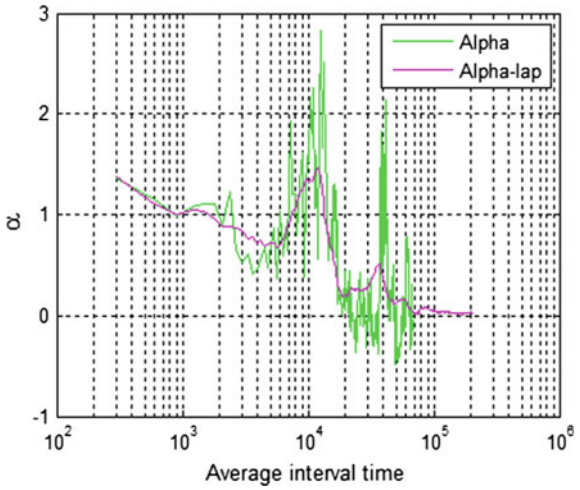

Fig. 16 The difference sequence noise of C06

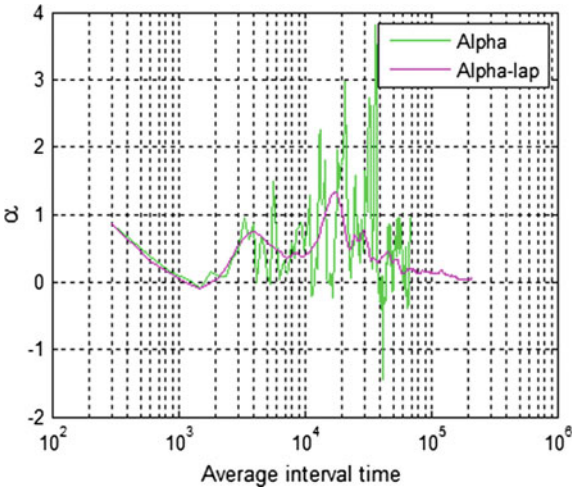

Fig. 17 The difference sequence noise of C14

4 Conclusions

In this paper, we first analyze the shortcomings of the conventional slope method, the B1 deviation factor method, and the classical LAG1 autocorrelation function method in noise identification. Then, according to the limitation and fluctuation of the classical LAG1 method in the long τ-average time of noise identification, we proposed the overlapping LAG1 autocorrelation function method. The testing results show that the BDS satellite clocks are mainly affected by White FM, Flicker FM, and Random Walk FM. GPS BLOCK IIA Cs, BLOCK IIA Rb, BLOCK IIR Rb, BLOCK IIR M and BLOCK IIF Cs are mainly affected by the White FM and Flicker PM, and BLOCK IIF Rb is mainly influenced by the White PM, Flicker PM and White FM. For GPS, the proposed new method can effectively solve the problem that the fluctuation and the limitation of sampling size. However, for BDS, the two noise identification methods are inconsistent based on phase sequence. The reason of the phenomenon is that there are serious frequency offset and frequency drift in the BDS satellite clock bias. Based on the characteristics of the proposed new method and satellite clock bias, it is suggested that the new method is better to identify the noise in GPS satellite clock bias. For BDS, it is recommended to still use the conventional non-overlapping LAG1 autocorrelation function method until the global BDS and more stability of the on-borne atomic clock are available.

Acknowledgements Thanks to the analysis center of Wuhan University for providing BDS satellite clock bias products. This study is supported by the foundation of natural science of china (Grant No. 41574013) and National key research and development program (Grant No. 2016YFB0501701).

References

1. Haibo Y, Shaowu D (2008) Main noise analysis and determination of an atomic clock. In: Instrumentation, automation and advanced integration technology conference
2. Barnes JA, Chi AR, Cutler LS et al (1971) Characterization of frequency stability IEEE Trans Instrum Meas IM-20(2):105–120
3. User manual—stable 32 frequency stability analysis. Hamilton Technical Service (2005)
4. Jie T (2015) Study on the GPS/BDS atomic clock performance and clock offset prediction model. Chang'an University, Xi'an
5. Yuting L, Chunhao H, Xiaofang W (2007) Research on noise processing of atomic clock based on wavelet analysis. In: National time frequency conference
6. Shenghong X, Zhiwu C, Maolei W, Jingfei Z (2014) The atomic clock offset simulation in the power law spectrum model and the noise type identification. Geomat Sci Eng 6:67–73
7. Howe D, Beard R, Greenhall C et al (2012) A total estimator of the Hadamard function used for GPS operations. IEEE Trans Ultrason Ferroelect Freq Control
8. Wenke Y (2008) The study of phase noise analysis and identification. Information and Communication Engineering Graduate School of National University of Defense Technology, Changsha
9. Fan L, Jianwen L, Hai H, Shizhong W, Ying Z (2014) Frequency stability analysis and noise identification of BD satellite clock. J Geomat Sci Technol 1:34–37
10. Hairong G (2006) Study on the analysis theories and algorithms of the time and frequency characterization for atomic clock of navigation satellites. Information Engineering University, Zhengzhou
11. Brockwell PJ, Davis RA (2005) Time series: theory and methods (2nd edn). Higher education press, 2005
12. Riley WJ (2007). Handbook of frequency stability analysis. NIST SP 1065:1–123
13. Riley WJ, Greenhal CA (2004) Power law noise identification using the lag 1 autocorrelation 2:576–580
14. Zhou C, Zhang Q, Yan S (2011) Power law noise identification using the LAG1 autocorrelation by overlapping samples. In: 10th International conference on electronic measurement and instruments (ICEMI), IEEE, pp 110–113

A Simple and Effective Method for Abnormal Data Processing of Atomic Clock Time Difference

Dongmei Yue, Yangqi Liu, Qiang Li and Zhen Qiu

Abstract Atomic clock time differences are most important original measurements for atomic time calculations of time-keeping system, whose qualities affect the continuities and stabilities of time scales directly. In actual measurement, the original data often appear to have gross errors such as phase jumps, frequency mutations influenced by measurement equipments and environment. How to find out and eliminate the abnormal data is essential. A simple and effective abnormal data processing method is proposed in this paper. The original data is one or two rank fitting according to its characteristics, then the fitting residual error can be obtained after deducting one or two ranks. The residual data show normal distribution, which is mainly composed of white noise. The 3σ method cannot effectively eliminate gross error when the distribution is very scattered. So this paper proposes an iteration method for gross error elimination using residual data. The phase jump and frequency mutation can be detected by the standard deviation of clean residual data and statistic value, it can be verified by atomic clock time difference predicting data. The method has stronger specific aim and practicability comparing with some theory of error processing method, and has been achieved good results in standard time-keeping and on-board atomic clock data processing.

Keywords Abnormal data · Gross error · The phase jump · Frequency mutation

D. Yue (✉) · Q. Li · Z. Qiu
Beijing Satellite Navigation Centre, Beijing, China
e-mail: dsps@sina.com

Y. Liu (✉)
Xinghan Time and Space Technology (Beijing) Inc., Beijing, China
e-mail: yangqi.liu@xhtime.cn

J. Sun et al. (eds.), *China Satellite Navigation Conference (CSNC) 2017 Proceedings: Volume III*, Lecture Notes in Electrical Engineering 439,
DOI 10.1007/978-981-10-4594-3_44

1 Introduction

Atomic clock difference measurements are the most important raw data in the time-keeping system, and the bases for calculating an ensemble time scale. Usually atomic clock differences are measured by time interval counters. Due to the measurement equipment, the impact of the environment and the atomic clock itself, the measurement data may have gross errors such as jump phase, frequency, and other abnormal circumstances, which directly affect the stabilities. Therefore, the effective data processing of atomic clock time difference is very important.

There are many methods to deal with the abnormal data, such as the Least-Squares Method, the Gross Errors Quasi-Verification Method, and the 3σ Criterion. These methods have advantages and shortcomings for different kinds of gross errors. Based on the actual characteristics of the measurements, we first use the least-squares method to obtain the first- or second-order terms of the measurements. After subtracting the first-order or second-order terms, we can get the residuals. The residual error is normal distribution and the gross error is eliminated. At the same time, judging such as jump phase and frequency conversion. The method is more pertinent, simple, and effective.

2 Atomic Clock Time Difference and Residual

At present, a clock ensemble is mainly composed of high-performance cesium clocks and hydrogen masers. The linear modeling below fits well for cesium clocks.

$$X(t) = A + Bt + N(t) \tag{1}$$

Due to the frequency drifts, hydrogen masers commonly use quadratic model.

$$X(t) = A + Bt + \frac{1}{2}Ct^2 + N(t) \tag{2}$$

A, *B,* and *C* in Eqs. (1) and (2) respectively reflect the phase, frequency, and frequency drift of the clock, and is the stochastic term, mainly composed of the measurement noise. Since the measurement noise is mainly white noise, the residual behaves like normal distribution or approximate normal distribution. As shown in Fig. 1.

According to the characteristics of the residuals, when the atomic clock time difference appears gross error and other abnormal data, the residual might also behaves anomalies, as is shown in Fig. 2.

Since the residuals approximate the normal distribution, the gross error can be detected by using the 3σ criterion, and the data corresponding to the original error can be eliminated. Therefore, the gross error data can be removed.

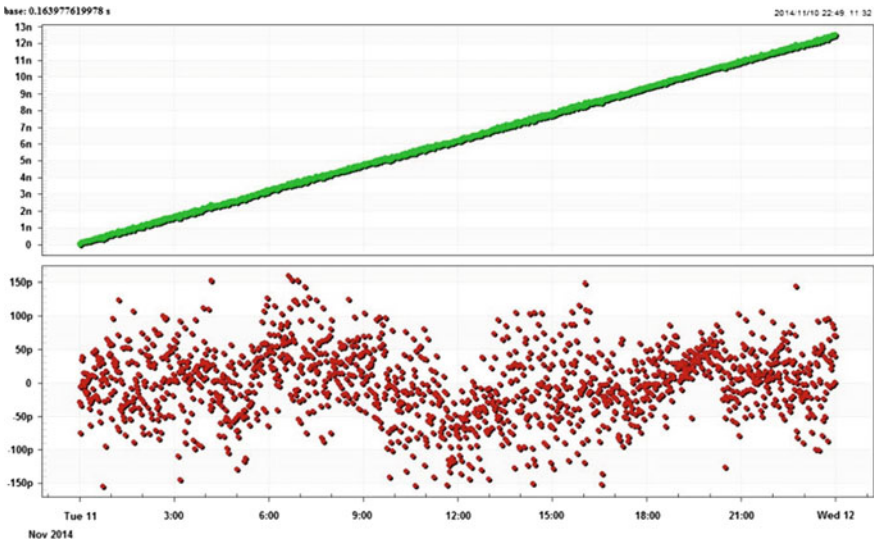

Fig. 1 Clock time difference and residual curve of atomic clock

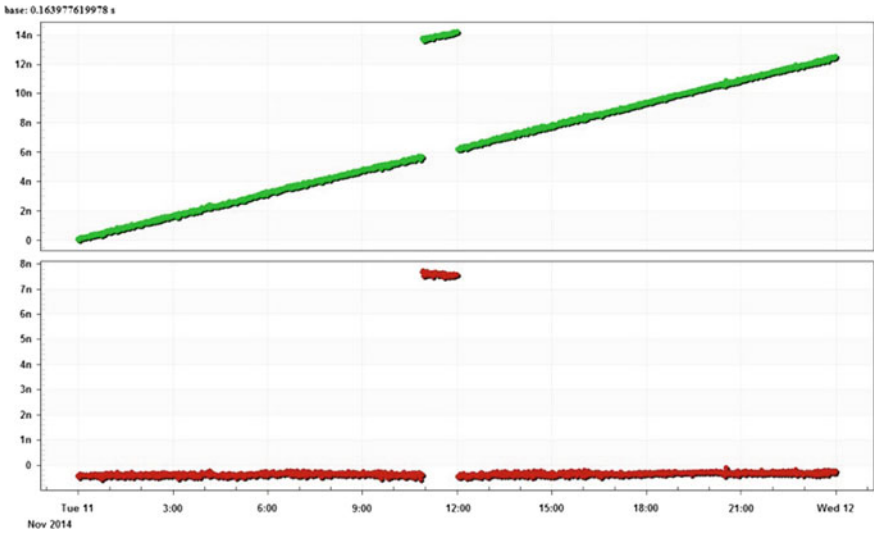

Fig. 2 Clock time difference and residual curve of atomic clock with gross error

Because of the influence of the frequency drift, the quadratic model is useful to obtain the residuals. However, the linear model cannot effectively eliminate some small gross errors, as is shown in Fig. 3.

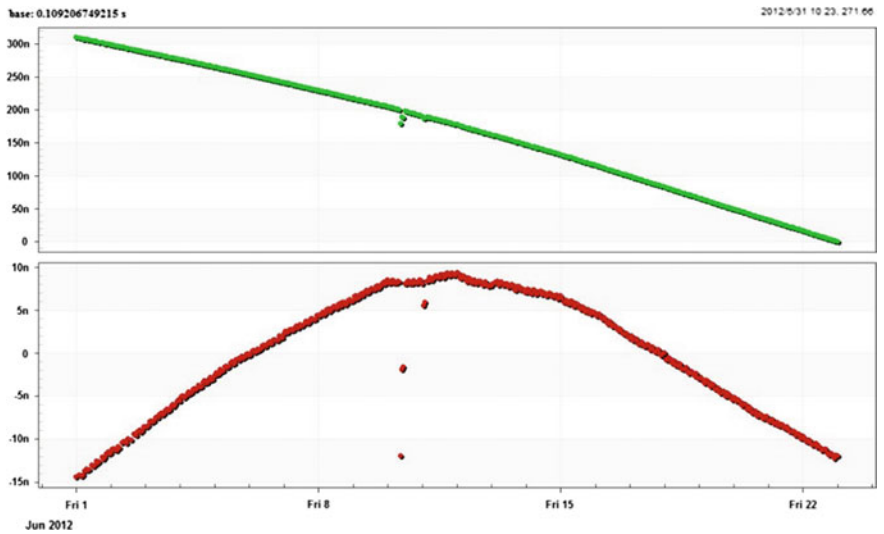

Fig. 3 The curve of the hydrogen maser time difference with gross error and the first-order residual after modeling

3 Gross Error Data Processing Flow

When a large number of gross errors occur, and the size and the distribution of the gross errors are uneven, the residual method cannot effectively remove all gross error. As shown in Fig. 4, a single elimination can only eliminate the largest number of gross errors.

In order to eliminate all the gross errors, the cyclic elimination method can be adopted. That is, after a gross error elimination, the processed data is re-modeled, and the second gross error is eliminated by residual method, until all the gross errors are removed. The effect of removing the gross error is shown in Fig. 5.

Since the standard deviation σ of the residual is calculated after every eliminations, the standard deviation of the residual will not change after all the residuals are removed. The operational process implementation is shown in Fig. 6.

Since the standard deviation σ of the residuals reflects the noise of the measuring equipment and the short-term stability of the atomic clock, the empirical value of the standard deviation σ of the residuals of the measured data can be statistically obtained from the empirical values of the measuring equipment and the atomic clock's own characteristics. When the gross error is removed and σ value is significantly larger than the statistical value, it is possible to judge the frequency change of the atomic clock time difference, that is one of the atomic clocks has a frequency mutation phenomenon. By comparing the standard variance of the residuals with at least three atomic clocks, it is possible to determine which atomic clock frequency is abruptly changed.

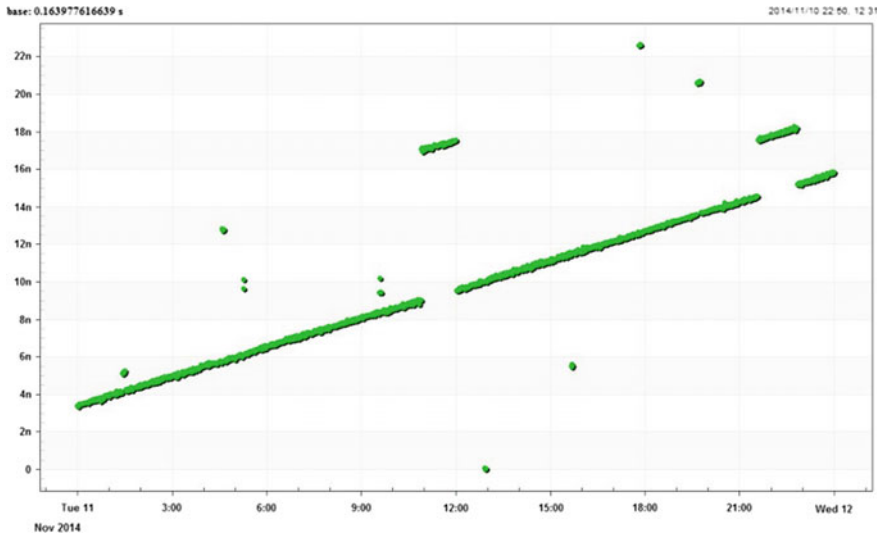

Fig. 4 The curve of the atomic clock time difference with a number of gross error

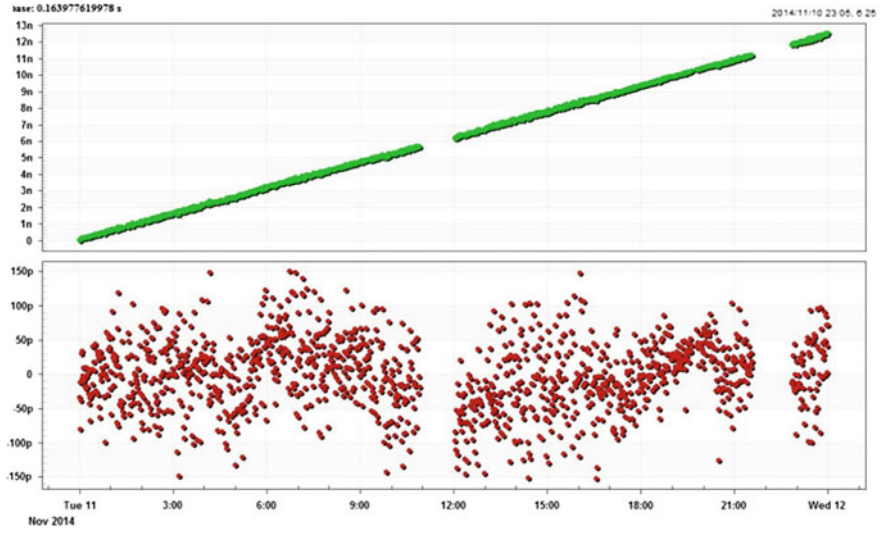

Fig. 5 Difference and residual of atomic clock after multi-gross errors removed

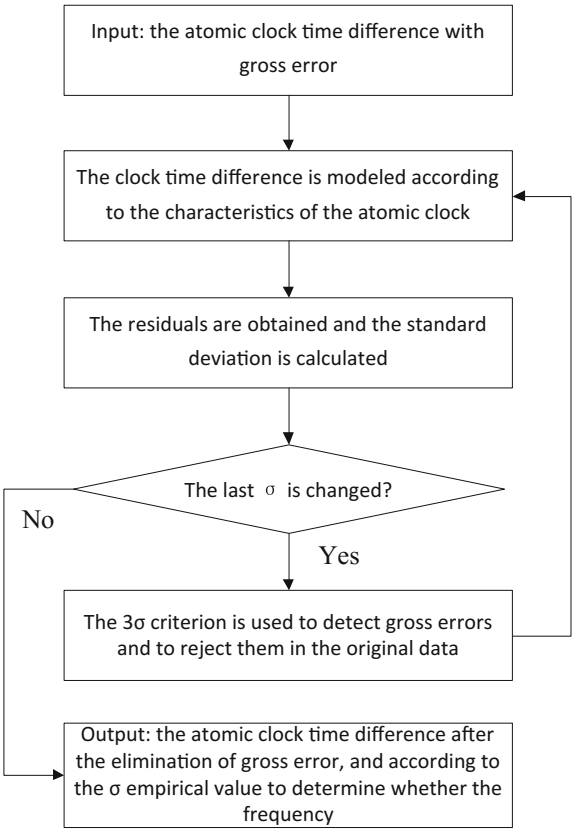

Fig. 6 Gross error data operation flow

4 Conclusion

In this paper, a simple and effective data processing method for atomic clock time difference is proposed. According to the characteristics of random noise of measurement equipment and the characteristics of high-performance punctual atomic clock, the atomic clock is modeled accordingly. Then, the original gross errors are detected and removed, and the standard variance of the residuals is used to stabilize. The loop detection method is used to eliminate all gross errors effectively. Based on the empirical value of the standard deviation σ of the residuals, the abrupt change of the atomic clock frequency can be detected, which provides an accurate reference for the atomic clock.

The exception of data processing method are only for the distinctive characteristics of high-performance atomic clock, cannot effectively model the high-performance crystal or rubidium clock, the effect of the gross difference in the removal of relatively poor, or even error out of gross errors, so when used, must be combined with the characteristics of their own measurement equipment and frequency source characteristics, accurate modeling, and rational use.

Performance Test and Power-Law Spectrum Analysis of Domestic Cesium Clocks

Xianglei Wang, Yan Du and Jun Zhang

Abstract The medium- and short-term stability of hydrogen clocks and the medium- and long-term stability of cesium clocks combine into a time-keeping clock set. This is a common practice in major time-keeping laboratories across the world. Domestic hydrogen clocks have been commercialized, while cesium clocks are subject to key technical bottlenecks. After years of technical research, domestic cesium clocks have achieved a rapid growth and commercialized cesium clocks have become available. In this paper, we observe cesium clocks over a long term, using a hydrogen clock as the reference signal and conduct a power-law spectrum analysis of domestic cesium clocks based on the test data. Results show that cesium clocks have flicker frequency modulation noise within 10 s and white frequency modulation noise from 10 s to 5 days. By using 1pps and frequency measurements, we analyze the consistency between 1pps and frequency signals output by domestic cesium clocks. Results show that the output of 1pps contains 100 ps jitter. The long-term performance is in full accord with that of frequency signals. This paper gives a preliminary assessment on the performance of domestic cesium clocks according to our test data. Cesium Clock A has a second stability of 2.8E−12 and a day stability of 3.4E−14, which is up to the level of 5071A high-performance tube. Cesium Clocks B and C have a second stability of 6.0E−12 and a day stability of 6.0E−14, which is up to the level of 5071A standard performance tube. Also some problems are found in the testing process. To make a comprehensive and accurate assessment of cesium clocks, we need test data over a longer term. In the future, domestic cesium clocks will continue to be tested. With the abundance of test data, domestic cesium clocks will be assessed more accurately, to provide accurate data support for the use of domestic cesium clocks in time-keeping laboratories.

Keywords BeiDou navigation system atomic clock stability power-law spectrum · Flicker frequency modulation noise

X. Wang (✉) · Y. Du · J. Zhang
Beijing Satellite Navigation Center, Beiqing Road No 22, Haidian District, Beijing 100094, China
e-mail: chxywxl@163.com; m13021977097@163.com

J. Sun et al. (eds.), *China Satellite Navigation Conference (CSNC) 2017 Proceedings: Volume III*, Lecture Notes in Electrical Engineering 439,
DOI 10.1007/978-981-10-4594-3_45

1 Introduction

Along with the building of a new generation of navigation system in China, to make the new generation of navigation system ascend to a world-leading level effectively, we in an increasingly urgent need of domestic high-performance cesium clocks. The medium- and short-term stability of hydrogen clocks and the medium and long-term stability of cesium clocks combine into a time-keeping clock set. This is a common practice in major time-keeping laboratories across the world. At present, domestic hydrogen clocks have been commercialized and widely applied in domestic time-keeping agencies and played an increasingly important role in BeiDou navigation satellite system, while cesium clocks are subject to key technical bottlenecks. After years of technical research, domestic cesium clocks have achieved a rapid growth and commercialized cesium clocks have become available. To put demands for a world-leading level and equipment nationalization into reality, Beijing Satellite Navigation Center has conducted a long-term performance test on multiple domestic cesium clocks, with hydrogen clocks as the reference. Based on these test data, a qualitative and quantitative analysis has been made of the power-law spectrum of cesium clock noise. With an international standard cesium clock, Agilent 5071A, as the benchmarking product, a detailed comparative analysis has been carried out.

2 Description of Testing Environment

The tested cesium clocks included four cesium clocks: Agilent 5071 and Cesium Clocks A, B, and C. The control was a long-term hydrogen clock in use in engineering. The performance of this hydrogen clock was known and superior to the performance index required by this measurement. In this test, the frequency output signals 5/10 MHz and 1pps output signals of cesium clocks were measured simultaneously. The test lasted 6 months. The physical environment was a room with constant temperature and humidity. A block diagram of the test is shown in Fig. 1.

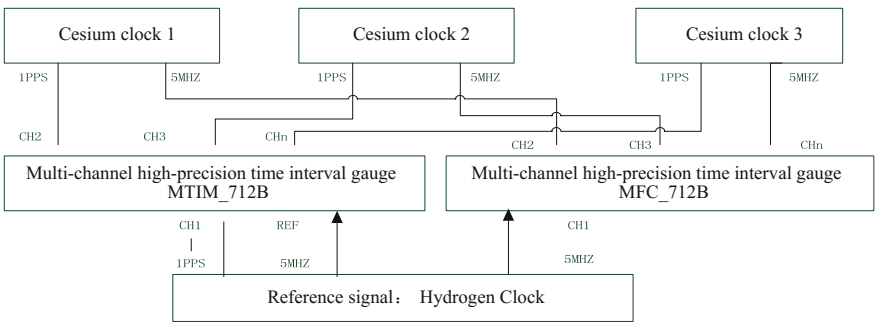

Fig. 1 Test the connection diagram

In this measurement, the multi-channel high-precision time interval gauge used to test 1pps signals was MTIM_712 manufactured by Beijing Yipu Time-frequency Technology Co., Ltd. The measured noise was 30 ps (RMS). The uncertainty of measurement was 100 ps (MAX). The multi-channel high-precision frequency standard comparator used to measure frequency signals was MFC_712 manufactured by Beijing Yipu Time-frequency Technology Co., Ltd. The background noises of measured frequency stability were 2.0E−12(1 s), 3.0E−3(10 S), 4.0E−14 (100 S) and 5.0E−15(1000 S). The measurement error was better than the performance index given in this measurement.

3 Analysis of Frequency Stability

3.1 An Analysis of Consistency Between 1pps Signals and Frequency Signals

To eliminate test system (including wiring and joint reliability) factors beyond atomic clocks effectively, according to zero correlation and independent measurement between two sets of measuring systems, the measured consistency between 1pps signals and frequency signals 5/10 MHz was a sufficient proof for the normal work and measurement accuracy of test system. When the difference between 1 pps signal and frequency signal measurements was greater than 1 ns, then the data shall be considered as outliers and removed. The performance analysis in this paper was a performance analysis with outliers removed.

The long-term phase difference between atomic clock 1 PPS output signals and frequency output signals was in full accord. A typical curve of their phase difference is shown in Fig. 2.

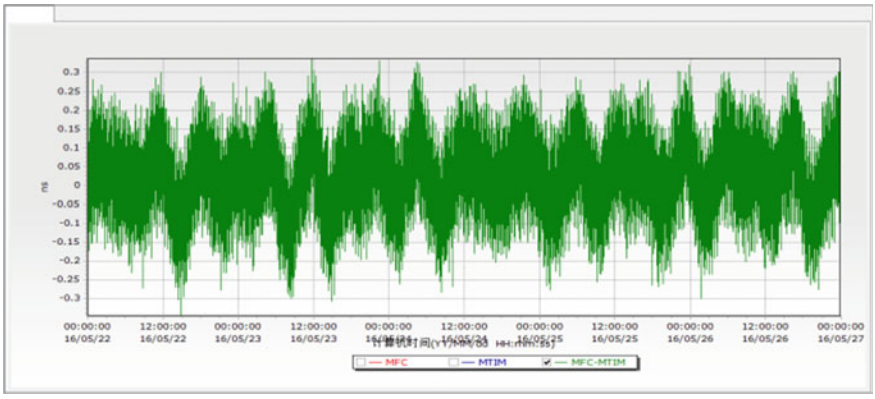

Fig. 2 The consistency curve between 1 pps and frequency signals

3.2 A Qualitative and Quantitative Analysis of Noise Types

3.2.1 The Noise Types and Power-Law Spectrum of Atomic Clocks

The noise types of atomic clocks included white phase modulation noise, flicker phase modulation noise, white frequency modulation noise, flicker frequency modulation noise, and random walk frequency noise. The power-law spectrum form of Allan variance for different noises is shown in Fig. 3.

3.2.2 A Power-Law Spectrum Analysis of Cesium Clock Noise

According to the measured Allan variance curves shown in Fig. 4, cesium clocks had flicker frequency modulation noise between 1 and 10 s. The noise level was between 2E−12 and 8E−12. The specific numerical values are shown in Table 1.

As shown in Table 1, compared with the "high performance tube" of Agilent 5071A cesium clock, domestic cesium clock fell into the white phase modulation noise interval between 1 and 10 s. Domestic Cesium Clock A reached the level of the "high performance tube" of Agilent 5071A. Domestic Cesium Clocks B and C reached the level of the "standard performance tube" of Agilent 5071A.

According to the measured Allan variance curves shown in Fig. 4, cesium clocks had white frequency modulation noise between 10 s and 5 days. The specific numerical values are shown in Table 2.

As shown in Table 2, compared with the "high performance tube" of Agilent 5071A cesium clock, domestic cesium clock fell into the white frequency

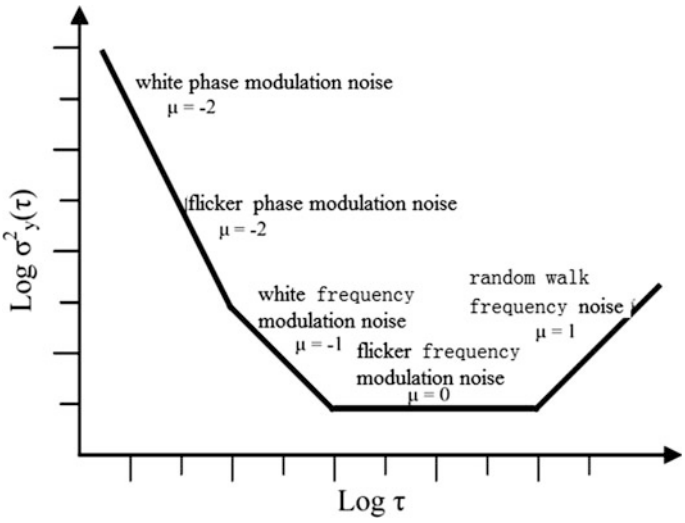

Fig. 3 A schematic of the power-law spectrum form of Allan variance

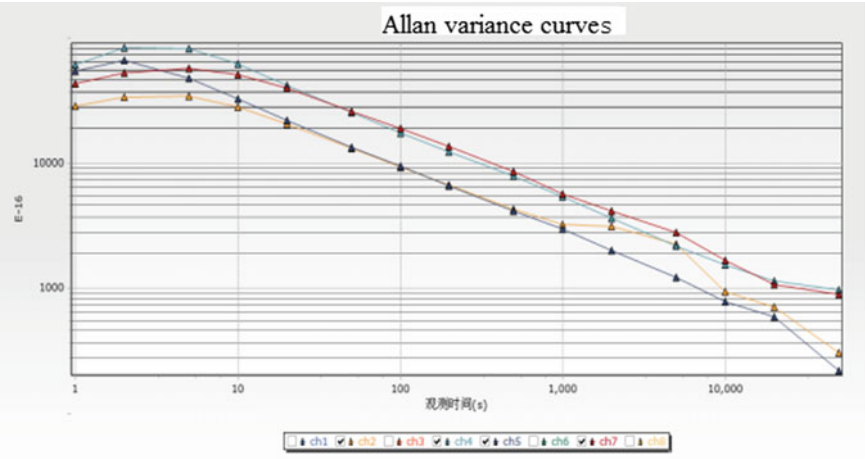

Fig. 4 A master curve of frequency stability (including ch7_ cesium clock c)

Table 1 An analysis of the flicker frequency modulation noise of cesium clocks (Allan variance: E−12)

时间窗口 (s)	铯钟A	铯钟B	铯钟C	5071A
1	2.844	6.105	4.304	5.405
2	3.374	8.330	5.265	6.596
5	3.424	8.220	5.731	4.741
10	2.810	6.172	5.089	3.263

Table 2 An analysis of the white frequency modulation noise of cesium clocks (Allan variance: E−12)

窗口 (s)	铯钟A	铯钟B	铯钟C	5071A
20	2.0619	4.1875	3.9458	2.2104
50	1.3237	2.5626	2.6058	1.331
100	0.9347	1.7514	1.88	0.9385
200	0.6706	1.2293	1.3525	0.6572
500	0.4283	0.7881	0.8563	0.4131
1000	0.3246	0.5395	0.5682	0.299
2000	0.3136	0.3648	0.4177	0.2008
5000	0.2256	0.2192	0.2816	0.1217
10,000	0.0948	0.1531	0.1668	0.0791
20,000	0.0708	0.1154	0.107	0.0598
50,000	0.0306	0.0972	0.089	0.0221
1 day	0.034	0.058		0.032
2 day	0.019	0.053		0.017
4 day	0.013	0.020		0.014
5 day	0.014	0.012		0.015

modulation noise interval between 10 s and 5 days. Domestic Cesium Clock A reached the level of the "high performance tube" of Agilent 5071A. Domestic Cesium Clocks B and C reached the level of the "standard performance tube" of Agilent 5071A.

4 Conclusion

In this paper, we observe cesium clocks over a long term, using a hydrogen clock with known performance as the reference signal and conduct a power-law spectrum analysis of domestic cesium clocks based on long-term observations. Test results show that cesium clocks had flicker frequency modulation noise within 10 s and white frequency modulation noise from 10 s to 5 days. Using 1pps and frequency measurements, the consistency between 1pps and frequency signals output by a domestic atomic clock is analyzed. Results show that 1 pps output contains 100 ps jitter. The performance is highly consistent over a long term. The paper analyzes the performance of domestic cesium clocks, using 6-month observations. Test results show that cesium Clock A has a second stability of 2.8E−12 and a day stability of 3.4E−14, which is up to the level of 5071A high performance tube. Cesium Clocks B and C have a second stability of 6.0E−12 and a day stability of 6.0E−14, which is up to the level of 5071A standard performance tube.

References

1. Yiwei WU (2011) Study and application of time scale in satellite navigation system. Master's thesis, National University of Defense Technology
2. Huijie S, Shaowu D (2015) Analysis of NTSC's timekeeping hydrogen masers. ACTA ASTRONOMICA SINTICA, pp 123–127
3. Huang G (2012) Research on algorithms of precise clock offset and quality evaluation of GNSS satellite clock. Doctor's dissertation, Chang'an University, pp 43–47
4. Jie Z (2013) Satellite clock performance analysis offset forecast. Master's thesis, Xidian University, 2013
5. Guo W (1992) A Stability analysis of the time scale of atomic clocks. Sci China: Mathematics 1:76–82
6. Ziyang Z, Tavella P (2007) Analysis of frequency stability and noise type of atomic clocks in Galileo EPTS. J Electron Meas Instrum 65–74
7. Hairong G (2006) A study on the theory and method of the atomic clock time-frequency characteristics of navigation satellites. Doctor's dissertation, The PLA Information Engineering University
8. Shaowu D (2007) Study on several important technical issues in time-keeping. Doctor's dissertation, Graduate School of Chinese Academy of Sciences (National Time Service Center)
9. Jinlun H, Dongrong J (1981) A practical modeling method by determining the noise intensity of atomic clocks, Shanghai astronomical observatory. Chinese Acad Sci 00:98–103
10. Wenke Y (2008) The phase noise analysis and identification of time-frequency signals. Master's thesis, National University of Defense Technology

High Precise Time Delay Measurement in Optical Fiber

Jingwen Dong, Bo Wang, Hongwei Si and Lijun Wang

Abstract Due to its properties of low attenuation, high capacity and reliability, the widespread optical fiber network has become an attractive option for long-distance transmission. The signal transmission delay in fiber, as an essential characteristic, becomes a significant parameter that has broad effects on the performance of optical communications, fiber timing distribution systems, phased array antennas, and some other large-scale scientific or engineering facilities. We report a novel method for signal transmission delay measurement in optical fibers. Based on phase discrimination, dual-frequency locking and measurement, it achieves a very high measurement precision of 0.2 ps with a 0.1 ps resolution, and dynamic range over 50 km. Using a phase shift and frequency locking technique, the measurement ambiguity can be resolved within only a few seconds. It greatly simplifies the measurement procedure and requires much simpler equipment. A good agreement in measurement results with the conventional pulsed method is obtained as well.

Keywords Optical fiber · Transmission · Time delay

1 Introduction

Optical fiber is one of signal transmission medium. With low loss, high capacity, high reliability, and many other advantages, it is increasingly widely used in various fields. The fiber transmission delay (FTD) is an important parameter of the transmission characteristics for signal transmission in optical fiber. For digital fiber-optic communications [1–3], the FTD measurement is used to estimate the transmission

J. Dong · B. Wang (✉) · H. Si · L. Wang
Department of Precision Instrument, State Key Laboratory of Precision Measurement Technology and Instruments, Tsinghua University, Beijing 100084, China
e-mail: bo.wang@tsinghua.edu.cn

L. Wang
Department of Physics, Tsinghua University, Beijing 100084, China

J. Sun et al. (eds.), *China Satellite Navigation Conference (CSNC) 2017 Proceedings: Volume III*, Lecture Notes in Electrical Engineering 439,
DOI 10.1007/978-981-10-4594-3_46

distance, the signal distortion caused by chromatic dispersion, etc. In wavelength-division multiplexing system, the FTD is closely related to the communication bandwidth, error rate, and many other important characteristic parameters. For fiber-based time and frequency distribution and synchronization [4–7], the accuracy of FTD measurement directly determines the time synchronization accuracy. In optically controlled phased array antenna [8–10], the FTD measurement is used to control the time delay of the transmitted signal in order for specified transmit direction angle. In distributed array system [11–13], FTD measurement plays a key role in beamforming.

Up to now, many techniques for FTD measurement in time domain [14–17] or frequency domain [18–20] have been developed and successfully employed. The traditional time-domain measurement methods called pulse methods, include laser pulse method and microwave pulse method. In these methods, the time interval of the before and after transmitted pulse signals is directly measured. Pulse methods using optical time-domain reflectometer (OTDR) or time interval counter (TIC) are conventional methods still in use due to its efficiency and flexibility. However, due to the pulse width and the limited bandwidth of the receiver, they have drawbacks of low accuracy and existing dead zones. Recently, efforts have been made to meet requirements of high accuracy based on propagation delay measurement in frequency domain. In these methods, the FTD measurement is usually converted into the longitudinal mode spacing measurement of a fiber laser or the beating frequency measurement of a ring cavity. Compared with the traditional method, they have higher precision reaching the order of picosecond. But it is inevitable to introduce ambiguity, which need to be solved during the FTD measurement, making complex equipment, cumbersome and time-consuming measurement process.

We reported a novel method for FTD measurement [21, 22]. Based on phase discrimination, dual-frequency locking and measurement, it achieves a very high measurement accuracy of 0.2 ps with a 0.1 ps resolution, and a large dynamic range over 50 km. Using a phase shift and frequency locking technique, the measurement ambiguity can be resolved within only a few seconds. It greatly simplifies the measurement procedure and requires much simpler equipment. A good agreement in measurement results with the conventional pulsed method is obtained as well.

2 Methods

2.1 Transmission Delay Measurement Based on Frequency Locking

Figure 1 shows the schematic of the frequency locking based FTD measurement system. The main idea is transferring a laser light modulated by a microwave signal through the fiber under test (FUT) to make the frequency of the signal (f) locked onto the FTD (t). Thus, the FTD measurement is converted into the frequency measurement. A 1 GHz microwave signal generated by a voltage controlled signal

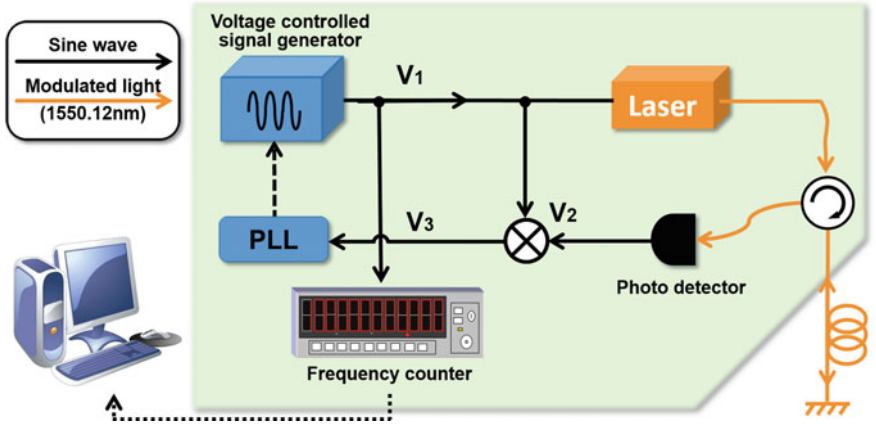

Fig. 1 Schematics of the frequency locking-based fiber transfer delay measurement system

generator modulates a 1550 nm laser light. After single passing the internal fiber and double passing the FUT, the laser light is detected by a photo detector. Via frequency mixing and filtering operations, an error signal $V_3 \propto \cos(\phi_p)$ is obtained to control the frequency of the microwave signal, yielding $V_3 \propto \cos(\phi_p) = 0$. Here, ϕ_p denotes the transmission induced phase delay, thus $\phi_p = 2\pi f \cdot t$. The following equation is valid:

$$\phi_p = (N + \frac{1}{2})\pi = 2\pi f \cdot t. \tag{1}$$

Here, N is an integer and can be considered as an ambiguity of the FTD measurement. Equation (1) can be further modified as

$$t = \left(\frac{N}{2} + \frac{1}{4}\right)\frac{1}{f} \tag{2}$$

In this way, the frequency of the microwave signal f locked onto the FTD (t). The frequency f is precisely measured by a frequency counter. The ambiguity N need to be further resolved.

2.2 *Ambiguity Resolving Methods and Optimization*

Equation 2 can be modified as

$$N = \frac{4t \cdot f - 1}{2}. \tag{3}$$

To get N, the square wave signals before and after transmission are used to measure the coarse FTD (t_{coarse}) by a time interval counter (TIC) (Fig. 2a) [21].

In order to simplifiers the measurement procedure and the equipment, a novel method for ambiguity resolving based on phase discrimination, dual-frequency locking, and measurement has been employed (Fig. 2b) [22]. The square wave generator, microwave switch, and TIC are replaced by a frequency synthesizer. Through changing the frequency of the microwave signal in a wide range, we get two locked frequencies (f_1, f_2) and corresponding ambiguities (N_1, N_2). The following equation is valid:

$$t = \frac{N_2 - N_1}{2(f_2 - f_1)} \tag{4}$$

$(N_2 - N_1)$ is obtained from frequency scanning and zero-crossing detection of the error signal V_3.

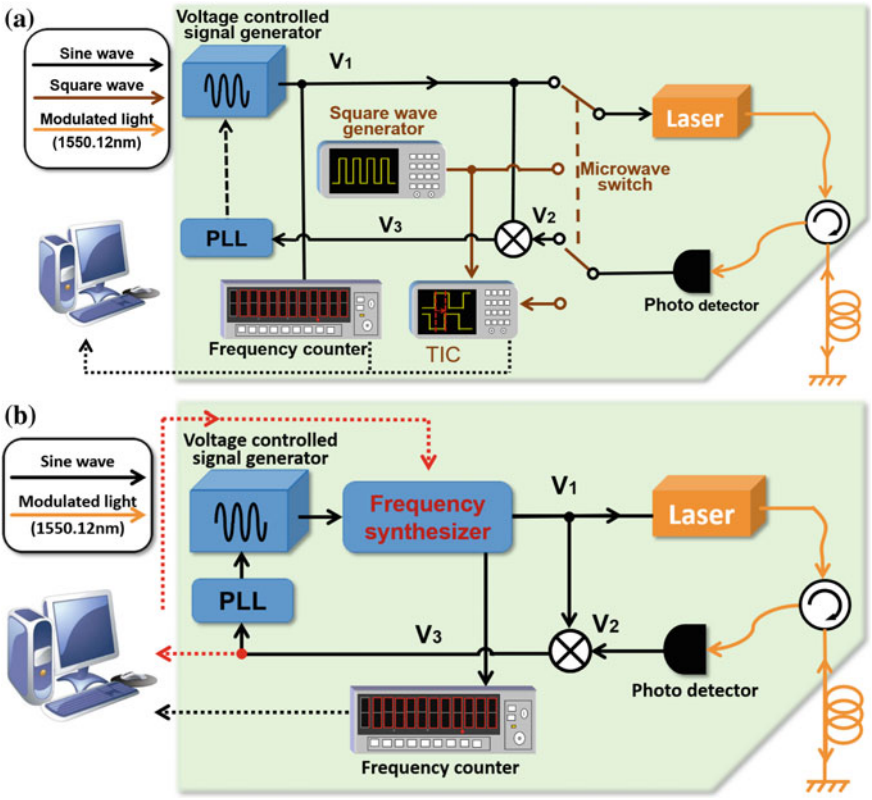

Fig. 2 Schematics of the ambiguity resolving methods. **a** Square wave transmission method. **b** Double-frequency locking method

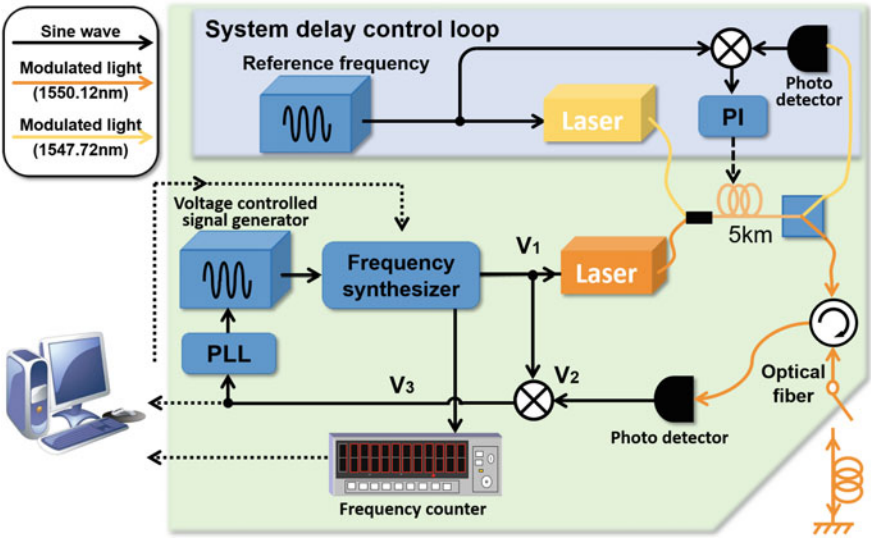

Fig. 3 Schematics of the fiber transfer delay measurement system based on zero calibration

In this way, coarse FTD (t_{coarse}) is obtained. According to Eq. (3), both N_1 and N_2 can be determined. In this way, the optimized FTD measurement method will no longer depend on the conventional pulse method, and becomes much more convenient and faster.

2.3 System Delay Calibration

Without FUT connected, the laser light is reflected by the end face of the optical switch (FC/PC connector). System delay is calibrated via the same method to get one-way FUT delay. For long-term, continuous measurement, a system delay control (SDC) loop is added to compensate the system delay fluctuation caused by temperature variations (shown in Fig. 3). Another 1547 nm laser light modulated by an H-Maser referenced 1 GHz signal is coupled into the internal fiber together with the 1550 nm laser light. Then, the 1547 nm laser light is detected by another photo detector. After frequency mixing and filtering operations, an error signal proportional to the system phase delay is obtained. A PI controller uses the error signal to change the temperature of the internal fiber, making the system delay stabilized.

3 Results

To verify the accuracy and the measurement range of the FTD measurement system, we used it to measure the FTD of a 2 m long fiber and a 50 km long fiber. As a comparison, we also used TIC to measure the same fibers by transferring a pulse signal.

3.1 *Transmission Delay Measurement Results of 2 m Long Fiber*

We repeat tests at different times of the day, and the system delay calibration has been done before each test. The results are shown in Fig. 4. It can be seen that the mean values of all measured FTDs using both methods agree very well. In the measurement using commercial TIC, the statistical error reaches approximately 13 ps and the mean value fluctuation is around ±5 ps. In contrast, the statistical error of the proposed method is only 0.1 ps, which reflects the resolution of the measurement system. And the mean value fluctuation decreases to ±0.2 ps, reflecting the accuracy of the measurement system.

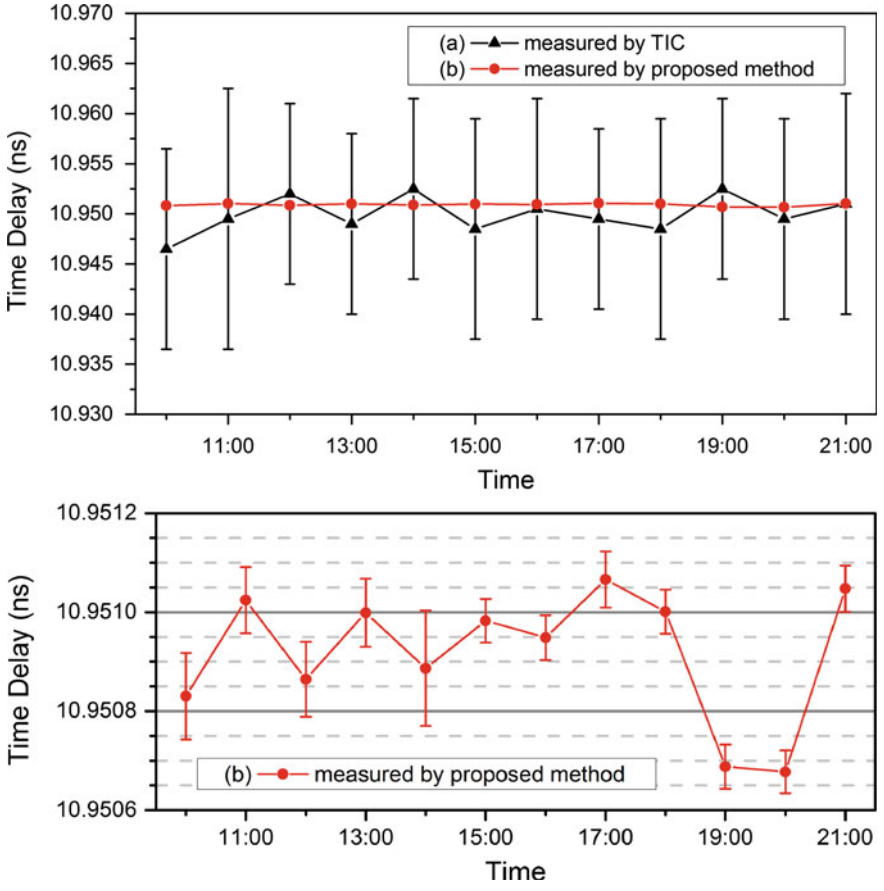

Fig. 4 Results of the measured transfer delay of 2 m long fiber

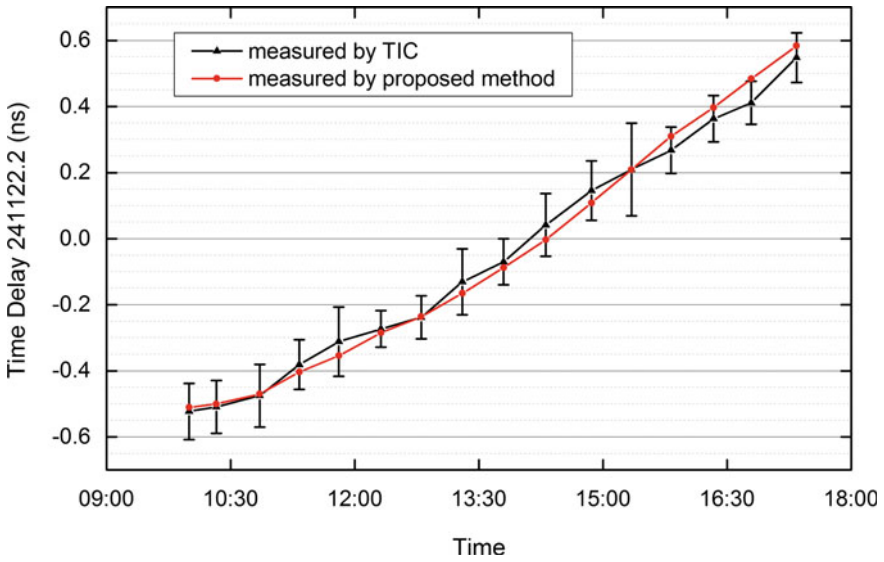

Fig. 5 Results of the measured transfer delay of 50 km long fiber

3.2 Transmission Delay Measurement Results of 50 Km Long Fiber

To demonstrate the measurement range of the proposed FTD measurement method, we also measure the FTD of a 50 km fiber spool. Comparison tests using two methods have also been carried out at different times of the day. The results are shown in Fig. 5. It can be seen that the mean values using two methods are well overlapped. The long-term variation of 1100 ps is caused by temperature variation during the measurement time. When using a commercial TIC, the statistical error increases to 100 ps because of the pulse broadening and nonlinear optical distortion. On the other hand, by using the proposed method, the statistical error is below 0.4 ps. It indicates that this method also has a large dynamic range of at least up to 50 km, while at the mean time preserving an extremely high resolution.

4 Conclusion

We report a novel method for signal transmission delay measurement in optical fibers. Based on phase discrimination, dual-frequency locking and measurement, it achieves a very high measurement accuracy of 0.2 ps with a 0.1 ps resolution, and dynamic range over 50 km. Using a phase shift and frequency locking technique,

the measurement ambiguity can be resolved within only a few seconds. It greatly simplifies the measurement procedure and requires much simpler equipment. A good agreement in measurement results with the conventional pulsed method is obtained as well.

Using this new method, time delay measurements in optical fibers no longer need to rely on the conventional pulsed method and it can become much more convenient, faster and more precise. At present, for long-term measurement, the system delay fluctuation is the main error source which restricts the measurement precision. In later research, we should further promote the control precision and simplify the system structure. In addition, the number of measurement channels can be further extended. In this way, the measurement method will be better applied in both military and civil fields.

Acknowledgements We acknowledge the financial support from the Program of International S&T Cooperation (No. 2016YFE0100200).

References

1. Essiambre RJ, Kramer G, Winzer PJ et al (2010) Capacity limits of optical fiber networks. J Lightwave Technol 28(4):662–701
2. Okawachi Y, Bigelow MS, Sharping JE et al (2005) Tunable all-optical delays via Brillouin slow light in an optical fiber. Phys Rev Lett 94(15):511–513
3. Lenz G, Eggleton BJ, Madsen CK et al (2001) Optical delay lines based on optical filters. IEEE J Quantum Electron 37(4):525–532
4. Jefferts SR, Weiss MA, Levine J et al (1997) Two-way time and frequency transfer using optical fibers. IEEE Trans Instrum Meas 46(2):209–211
5. Rost M, Fujieda M, Piester D (2010) Time transfer through optical fibers (TTTOF): progress on calibrated clock comparisons. Noordwijk
6. Wang B, Gao C, Chen WL et al (2012) Precise and continuous time and frequency synchronisation at the 5 × 10–19 accuracy level. Sci Rep 2(2):556
7. Piester D, Rost M, Fujieda M et al (2011) Remote atomic clock synchronization via satellites and optical fibers. Adv Radio Sci 9:1–7
8. Frigyes I, Seeds AJ (1995) Optically generated true-time delay in phased-array antennas. IEEE Trans Microw Theory Tech 43(9):2378–2386
9. Ng W, Walston AA, Tangonan GL et al (1991) The first demonstration of an optically steered microwave phased array antenna using true-time delay. J Lightwave Technol 9(9):1124–1131
10. Jeon HB, Jeong JW, Lee H (2012) Optical true time-delay for phased-array antenna system using dispersion compensating module and a multi-wavelength fiber laser. Opto-electronics and communications conference. IEEE, pp 387–388
11. Shillue W (2008) Fiber distribution of local oscillator for atacama large millimeter array. Conference on optical fiber communication/national fiber optic engineers conference, 2008. OFC/NFOEC 2008. 24–28 Feb. 2008, San Diego, CA, USA, pp 1–3
12. https://www.ptb.de/emrp/neatft_publications.html. Accessed 17 Jan 2017
13. Wang B, Zhu X, Gao C et al (2015) Square kilometre array telescope—precision reference frequency synchronisation via 1f-2f dissemination. Sci Rep: 5
14. Rost M, Piester D, Yang W et al (2012) Time transfer through optical fibers over a distance of 73 km with an uncertainty below 100 ps. Metrologia 49(6):772–778

15. Personick SD (1977) Photon probe—an optical-fiber time-domain reflectometer. Bell Labs Tech J 56(3):355–366
16. Lacaita AL, Francese PA, Cova SD et al (1993) Single-photon optical-time-domain reflectometer at 1.3 Mum with 5-cm resolution and high sensitivity. Opt Lett 18(13):1110–1112
17. Kalisz J (2004) Review of methods for time interval measurements with picosecond resolution. Metrologia Int J Sci Metrol 41(1):17–32
18. Hu YL, Zhan L, Zhang ZX et al (2007) High-resolution measurement of fiber length by using a mode-locked fiber laser configuration. Opt Lett 32(12):1605–1607
19. Yun K, Li J, Zhang G et al (2008) Simple and highly accurate technique for time delay measurement in optical fibers by free-running laser configuration. Opt Lett 33(15):1732–1734
20. Set SY, Jablonski MK, Hsu K et al (2004) Rapid amplitude and group-delay measurement system based on intra-cavity-modulated swept-lasers. IEEE Trans Instrum Meas 53(1):192–196
21. Dong JW, Wang B, Gao C et al (2015) Highly accurate fiber transfer delay measurement with large dynamic range. Opt Express 24(2)
22. Dong JW, Wang B, Gao C et al (2016) Accurate and fast fiber transfer delay measurement based on phase discrimination and frequency measurement. Rev Sci Instrum 87(9):662–701

Design of a Miniaturized High-Performance Rubidium Atomic Frequency Standard

Chen Wang, Pengfei Wang, Shidong Yan, Shengguo He, Fang Wang, Feng Zhao and Ganghua Mei

Abstract A miniaturized high-performance rubidium atomic frequency standard (RAFS) is introduced in this paper. Physics package is composed of a newly developed slotted tube microwave cavity and a ^{87}Rb spectral lamp with Xe as starter gas. Optical and hyperfine filter techniques are used in the design of the physics package. A PLL frequency multiplier is designed with a digital synthesizer chip with ultra-low-noise floor. The produced microwave interrogating signal is of low phase noise. To meet the needs of possible space applications, the RAFS has rigid mechanical structure and reliable thermal structure. The volume of the RAFS is 300 mL, and the short-term frequency stability is measured to be $1.5 \times 10^{-12}/\sqrt{\tau}$.

Keywords Rubidium atomic frequency standard · High performance · Miniaturization · Frequency stability

1 Introduction

Owing to its small volume, lightweight and low power consumption, rubidium atomic frequency standard (RAFS) has been widely used in satellite navigation, telecommunication, and many other fields. High performance and miniaturization are always main direction for development of the RAFS, while it is difficult to make the RAFS of high performance and small size simultaneously. For example, the RAFS applied in navigation satellites reached $1 \times 10^{-12}/\sqrt{\tau}$ in frequency stability, but its volume can be as large as 4–5 L [1]; a commercial RAFS can be as small as 300 mL,

C. Wang (✉) · P. Wang · S. Yan · S. He · F. Wang · F. Zhao · G. Mei
Key Laboratory of Atomic Frequency Standards of Chinese Academy of Sciences, Wuhan Institute of Physics and Mathematics, Wuhan 430071, China
e-mail: wwwchen120@163.com

G. Mei
e-mail: mei@wipm.ac.cn

C. Wang
University of Chinese Academy of Sciences, Beijing 100049, China

J. Sun et al. (eds.), *China Satellite Navigation Conference (CSNC) 2017 Proceedings: Volume III*, Lecture Notes in Electrical Engineering 439,
DOI 10.1007/978-981-10-4594-3_47

while its best stability is about $5 \times 10^{-12}/\sqrt{\tau}$ [2]. In this paper, a miniaturized high-performance RAFS is introduced. The RAFS is of a size comparable to typical commercial ones and of much better stability.

The RAFS is actually a frequency-locked loop composed of physics package, electronic system, and crystal oscillator. In the loop the physics package acts as a frequency discriminator. The frequency stability of RAFS consequently depends on the signal-to-noise ratio (S/N) of the physics package. The stability can be expressed as [3]:

$$\sigma(\tau) = \frac{1}{v_0 k_D} \sqrt{\frac{S_N}{2\tau}}, \tag{1}$$

where v_0 is the clock transition frequency of ^{87}Rb atoms, k_D is the discrimination slope depending on the intensity of the clock transition signal, and S_N is the power spectral density of the noise of the signal. S_N includes the shot noise S_{shot} and the intermodulation noise S_{int}, which come from the physics package and the electronic system respectively.

In this work, both physics package and electronic system were miniaturized. Meanwhile, much attention was paid to reduce the shot noise and the intermodulation noise of discrimination signal for realizing good frequency stability of the RAFS.

2 Physics Package

2.1 Structure

The physics package consists of a rubidium spectral lamp and a cavity-cell assembly, as shown in Fig. 1.

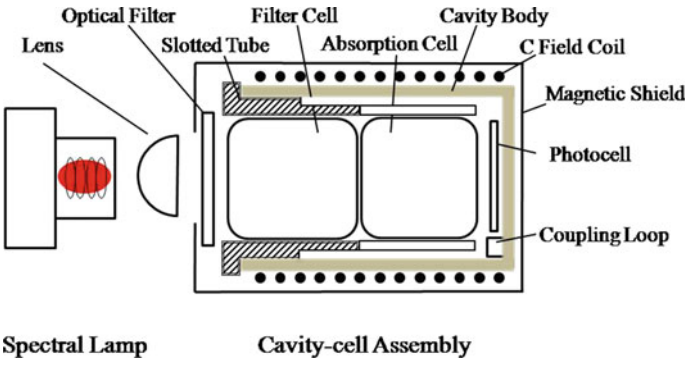

Fig. 1 Structure of physics package

Optical filter and hyperfine filter techniques are employed in the design of the physics package. After being collimated by the lens, the light emitted from the ^{87}Rb spectral lamp passes through the band-pass optical filter and the ^{85}Rb filter cell. The optical filter is used to remove the spectral lines of starter gas, and the filter cell, to remove the *a* hyperfine component of ^{87}Rb, letting only the *b* component of ^{87}Rb to pass through. The light then enters the absorption cell, where ^{87}Rb atoms are optically pumped. Meanwhile, the interrogating microwave signal, originated from a crystal oscillator, is fed into the cavity by a coupling loop to excite the clock transition of ^{87}Rb atoms. A photocell behind the absorption cell is used to detect the intensity variation of transmitted light, which contains message of frequency deviation of the interrogating signal from the clock transition signal. The light detection signal is used to generate an error signal to control the output frequency of the crystal oscillator. A Helmholtz coil provides a weak static magnetic field, defining the quantization axis for clock transition. Two layers of magnetic shield, made of high permeability material, are employed to eliminate the influence of external magnetic fields on the clock transition.

2.2 Spectral Lamp

The spectral lamp is an electrodeless discharge lamp. The lamp consists of a drive circuit and a glass bulb containing ^{87}Rb vapor and starter gas. To reduce the volume of the lamp, Clapp oscillating circuit with simple structure and stable oscillating signal is employed as the drive circuit. The bulb, with 6 mm in diameter, and the drive circuit are assembled in a metal box. To avoid overheating effect, the bulb was mounted in a metal sink. To reduce RF power consumption, the bulb was made of thin-wall glass, thus improving coupling efficiency of the RF signal into the bulb.

The frequency stability of a RAFS is related to spectral property of the pumping light, which remarkably depends on species of starter gas [4]. Xe is chosen as the starter gas in our design. According to previous researches [5], this kind of lamp is of small profile distortion and narrow line width in rubidium spectra, helpful to increase light pumping efficiency and improve the frequency stability of RAFS. Besides, the lamp works at low temperature and thus has low thermal power consumption, therefore the use of this kind of lamp helps to avoid overheating effect of the lamp itself and the whole RAFS unit. The light components of Xe gas, which has nothing to do with clock signal but acts as shot noise only, can be filtered out completely by the band-pass optical filter.

The lamp has a volume of 10 mL, a power supply of 13 V, and work temperature of 100 °C.

2.3 Cavity-Cell Assembly

The clock transition of the RAFS is a microwave-induced magnetic resonance transition, which can be driven only by the magnetic component of microwave paralleling to quantization axis. Consequently, in order to enhance the intensity of the atomic signal, magnetic lines of microwave in microwave cavity should be parallel to cavity axis and distribute uniformly and densely as much as possible. According to electromagnetic field theory, the orientation and distribution of the microwave field is determined by the structure of the microwave cavity. Therefore, microwave cavity plays important role in realization of high performance of RAFS.

In our physics package, the microwave cavity is designed in the scheme of slotted tube cavity, developed firstly in our laboratory [6]. The cavity is mainly composed of a metal cylinder and a slotted tube. The resonance frequency and field distribution of the cavity are determined by the slotted tube. The slotted tube used in this work is shown in Fig. 2.

The slotted tube is a metal cylinder with inner diameter of 12 mm, and there are two uniformly distributed electrodes and slots on the top of the tube. The working principle of the cavity is similar to that of the magnetron cavity. The electrodes and slots act as inductor and capacitor respectively, therefore the slotted tube is in fact an inductive–capacitive structure. When a microwave signal with the same frequency as the intrinsic frequency of the inductive–capacitive structure is fed into the cavity, standing microwave field will be stimulated inside the cavity. The microwave field exists in the upper part, and does not exist in the lower part. Based on this feature, a highly integrated cavity-cell assembly can be realized by placing the absorption cell in the upper part and the filter in the lower part.

Magnetic lines distribution of the microwave field in the cavity was simulated by high-frequency simulation software, and the result is shown in Fig. 3. It could be found that, in the upper part of the cavity, the magnetic lines are highly parallel to

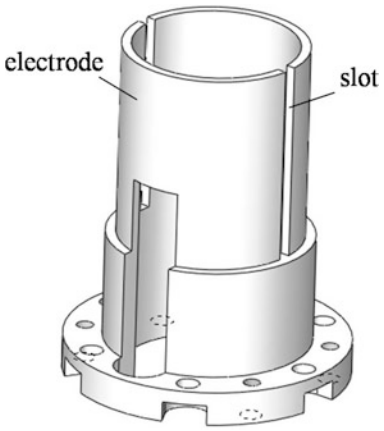

Fig. 2 Structure of slotted tube

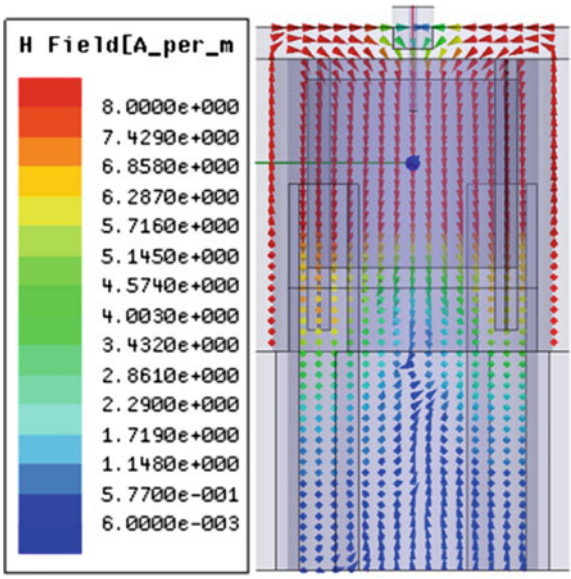

Fig. 3 Simulated magnetic lines distribution in the microwave cavity

the cavity axis, and the resonance mode is quite similar to TE_{011} mode. This kind of resonance helps to obtain strong atomic transition signal.

To decrease volume of the cavity-cell assembly, resistance wire wound around the cavity cylinder was used for heating the cavity-cell assembly. To improve the heating efficiency and reduce the power consumption, low thermal conductivity material was used to thermally isolate the cavity-cell assembly. The volume of cavity-cell assembly is 22 mL.

2.4 Frequency Discrimination Characteristic

In order to estimate the performance of the physical package, the frequency discrimination curve was measured. As shown in Fig. 4, the discrimination slope of the curve was 0.24 nA/Hz.

Power spectral density of shot noise generated by photo detector is expressed as $S_{\text{shot}} = 2eI_0$, where e is the electronic charge, I_0 is background current. The measured I_0 was 20 μA. According to Eq. (1), the contribution of physics package to frequency stability, i.e. the shot noise limit, could be expressed as [3]:

$$\sigma(\tau) = \frac{\sqrt{2eI_0}}{k_d v_0 \sqrt{2\tau}}. \tag{2}$$

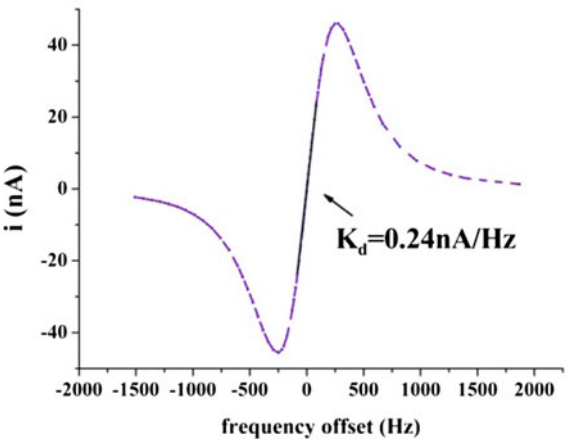

Fig. 4 Measured *S* curve of physics package

Substituting the measured discrimination slope and background current into Eq. (2), the shot noise limit was evaluated to be $1.1 \times 10^{-12}/\sqrt{\tau}$.

3 Electronics System

3.1 Design Scheme

Electronic design of the RAFS is shown in Fig. 5. Main part of the electronics is a 455.645XXXMHz (shortly 455 MHz) frequency multiplier, containing an oven-control and voltage-control crystal oscillator (OCVCXO), a phase-locked loop (PLL), a loop filter and a voltage control oscillator (VCO). The OCVCXO produces 10 MHz reference signal, and the VCO produces the 455 MHz signal. The 455 MHz signal is converted to a 10 MHz signal by the divider. The two 10 MHz signals from the divider and the OCVCXO respectively are phase compared in the phase frequency detector (PFD), and the phase error is converted to a correction current through the charge pump (CP). The loop filter transforms the correction current to a voltage signal. The voltage signal is used to control the output frequency of the VCO, making the 455 MHz signal as stable as the 10 MHz reference signal. The digital chip HMC703, containing divider, PFD and CP, is chosen to realize functions of the PLL. Frequency modulation of the 455 MHz signal was realized by setting two dividing coefficients of the divider with very small difference through CPU control of registers of the chip. The modulation frequency is 136 Hz. The microwave interrogating signal with frequency of 6834 MHz is finally produced by a follow-up $\times 15$ SRD multiplier, which is then fed into the physics package to stimulate the atomic discrimination signal. After being amplified, the signal goes to the servo circuit where it is demodulated synchronously with the demodulation signal generated by the CPU, yielding the

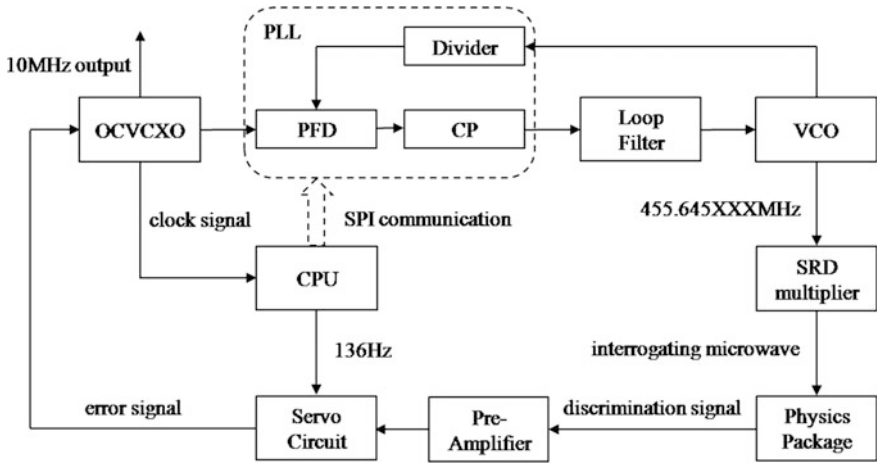

Fig. 5 Frequency-locked loop of the RAFS

error signal to control the frequency of the OCVCXO. Finally, the frequency of the OCVCXO is locked to the atomic clock transition frequency, producing standard 10 MHz signal.

3.2 Design of PCB Boards

To miniaturize the RAFS unit, all electronic modules are integrated in two PCB boards. One is supporting circuit, in which power supply, temperature control, and C-field circuits are integrated. The other one is frequency control loop circuit, in which crystal oscillator, frequency synthesizer, preamplifier, and servo circuits are integrated.

The loop circuit containing almost all the functional modules for frequency locking determines the performance of the electronic system to a great degree. In board level design, emphasis is given to suppressing ambient radiation and cross talk of signals, thus ensuring integrity of signals. For this purpose, first, the multilayer PCB board is adopted, and lamination structure of PCB board is optimized; secondly, an independent plane layer is used for power supply; third, electronic components are laid out according to their functional partition, and routings are optimized to avoid mutual interference between high- and low-speed signals.

3.3 Intermodulation Noise

The response of the physics package to the interrogating microwave signal is of nonlinear property, therefore the frequency noise of the interrogating signal at

Fourier frequencies close to $2nf_m$, can be converted into frequency noise at f_m, i.e., the intermodulation noise [7]. The intermodulation noise cannot be filtered out by either the physics package or the servo circuit, and acts as the white frequency noise that affects the frequency stability of RAFS. The intermodulation noise mainly comes from the phase noise of interrogating microwave at secondary modulation frequency $2f_m$, i.e., $L_\varphi(2f_m)$. Contribution of $L_\varphi(2f_m)$ to RAFS stability can be expressed as:

$$\sigma(\tau) = \frac{f_m}{f_0} \cdot \frac{2\sqrt{2}}{3} \cdot 10^{L_\varphi(2f_m)/20} \tau^{-1/2}. \tag{3}$$

As shown in Fig. 5, the 6834 MHz microwave signal is generated from the 455 MHz signal by a ×15 SRD multiplier. The SRD multiplication process does not introduce additional noise, therefore only the phase noise of 455 MHz signal at $2f_m$ (272 Hz) needs to be considered in design of the microwave chain. The phase noise of 455 MHz signal was theoretically simulated [8]. As shown in Fig. 6, almost all the parts of frequency synthesizer, including the VCO, the loop filter, the reference oscillator (Ref), the chip and the phase-locked loop (SDM), contribute to the noise, while the largest contributions come from the chip and the reference oscillator. Figure 6 shows also that the ideal phase noise of the 455 MHz signal at 272 Hz is −112 dBc/Hz, the frequency stability limited by electronic circuits was then calculated to be $7.4 \times 10^{-13}/\sqrt{\tau}$ according to Eq. (3).

The noise of the 455 MHz signal was practically measured with a PN9000 noise spectrum analyzer. Results are listed in Table 1. From Table 1 we see that the measured value of the phase noise at 272 Hz is −106.2 dBc/Hz. The limitation of the noise to the RAFS stability was calculated to be $1.4 \times 10^{-12}/\sqrt{\tau}$ by using

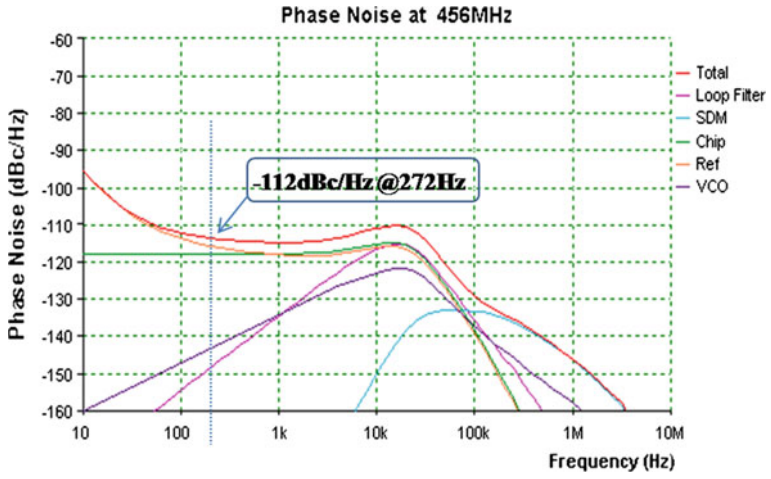

Fig. 6 Simulated phase noise curve of PLL output signal

Table 1 Measured phase noise of the 455 MHz signal

$L_{\varphi}(f)$ of 455.645XXXMHz (dBc/Hz)				
@10 Hz	@100 Hz	@272 Hz	@1 kHz	@10 kHz
−85.0	−100.0	−106.2	−110.0	−110.1

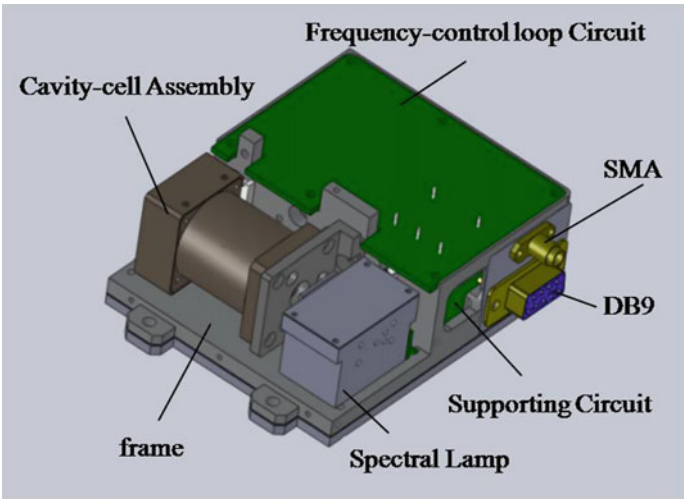

Fig. 7 Structure of the RAFS

Eq. (3), larger than the simulated result. The result is still acceptable, since the operation parameters of the electronic parts assumed in modeling simulation could not be exactly accurate.

4 Structure and Performance of the RAFS

The RAFS is composed of 4 main parts, i.e. cavity-cell assembly, spectral lamp, frequency control loop circuit and supporting circuit, as shown in Fig. 7.

The four parts and their large power devices were mounted on the metal frame. The frame has a platform and an electric shielding box. The spectral lamp and the cavity-cell assembly are installed on the platform, and the two circuit boards, installed in the shielding box. This design is of advantage as follows. Firstly, the RAFS will be of rigid structure; second, mutual electromagnetic interference between the electronic system and physical package is reduced; third, the over-heating effect of the RAFS can be avoid. All these features are important for possible space application of the RAFS. The SMA provides output of 10 MHz standard signal. The DB9 serial port is used for power input and monitoring of the operation parameters of the RAFS.

The frequency stability of the RAFS was measured with a Picotime frequency stability analyzer produced by SpectraTime. The reference source was an active

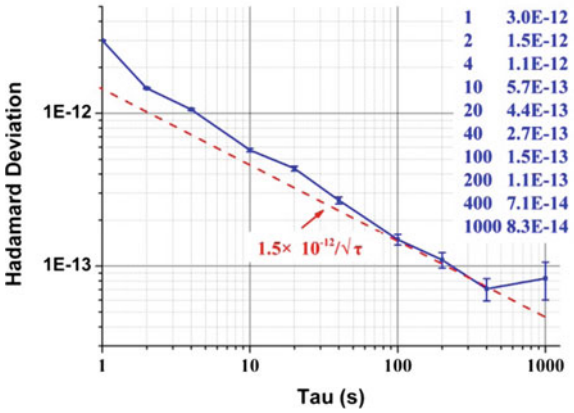

Fig. 8 Measured stability of the RAFS

Table 2 Specifications of the RAFS

Feature		Unit	Characteristics
Weight		kg	0.57
Size		mm^3	91 × 71 × 40
Warm-up power consumption		W	<20
Stable power consumption		W	≤12
Output power		dBm	7–8
SSB	1 Hz	dBc/Hz	−92
	10 Hz	dBc/Hz	−120
	100 Hz	dBc/Hz	−140
	1 kHz	dBc/Hz	−145
	10 kHz	dBc/Hz	−152
	100 kHz	dBc/Hz	−152
Harmonic distortion		dBc	<−30
Nonharmonically		dBc	<−70

hydrogen maser. Results are shown in Fig. 8. The frequency stabilities with average time of 1, 10, and 100 s are 3.0×10^{-12}, 5.7×10^{-13}, and 1.5×10^{-13} respectively. According to the manual of Picotime [9], it limits the test frequency stability by $3.0 \times 10^{-12}/\tau$. We believe that the 1 and 10 s stabilities have been limited by measurement capability of the Picotime, and the result of 100 s stability is more credible. For this reason, the short-term frequency stability of the RAFS should be about $1.5 \times 10^{-12}/\sqrt{\tau}$.

As mentioned in 2.4 and 3.3, frequency stabilities limited by shot noise and intermodulation noise are 1.1×10^{-12} and 1.4×10^{-12} respectively. Thus the frequency stability of the RAFS is counted to be 1.7×10^{-12} theoretically, which is very close to the test result. So the test frequency stability is credible.

Other specifications of the RAFS are listed in Table 2. The volume of the RAFS is about 300 mL. Compared with RAFS products with this kind of size,

the main performances of the RAFS, including frequency stability and phase noise, are prominent.

5 Summary

In this paper, a miniaturized high-performance RAFS is designed and realized. A miniaturized spectral lamp with Xe as starter gas and a highly integrated cavity-cell assembly are used in design of physics package. The frequency synthesizer is realized by a digital phase-locked loop chip with ultra-low-noise floor. The interrogating microwave signal has low phase noise. To meet the needs of possible space application, the whole unit is of rigid mechanical structure and reliable thermal structure. The volume of the RAFS is 300 mL, the short-term frequency stability reaches $1.5 \times 10^{-12}/\sqrt{\tau}$. As we know, the RAFS is of best stability performance compared with other RAFS products with the same size.

References

1. Dupuis RT, Lynch TJ, Vaccaro JR Rubidium frequency standard for the GPS-IIF program and modifications for the RAFSMOD program. PerkinElmer Optoelectronics, Salem, MA 01970 USA. pp 655–660
2. Cao Y, Yang L, Li Q, Zhao H, Lin Q (2011) Runchang Du An ultra-miniature Rb atomic clock compatible with OCXO. Proceedings of the IEEE international frequency control symposium and exposition
3. Vanier J (1981) On the signal-to-noise ratio and short-term stability of passive rubidium frequency standards. IEEE Trans Instrum Meas 30(4):277–282
4. He S, Hao Q, Xu F, Wang F, Zhao F, Da Z, Mei G (2016) A study on self-absorption of spectral lines of rubidium spectral lamp. Chin J Magn Reson 33(2):288–294
5. Hao Q, He S, Xu F, Zhao F, Mei G (2015) Influence of the lamp spectral profile on short-term stability and light shift of a rubidium atomic clock. China satellite navigation conference (CSNC) 2015 proceedings, vol III, pp 387–397
6. Mei G (2001) Miniaturized microwave cavity for atomic frequency standard. US Patent: 6225870B1
7. Walls FL (1989) Stability of frequency locked loops. Frequency standards and metrology. Springer, New York, pp 145–149
8. HMC703LP4E.datasheet. http://www.hittite.com
9. iTest+R PicoTimeTM Manual. http://www.SpectraTime.com

High Gain, Low Noise, and Long Lifetime MCP Electron Multiplier for Cesium Clock

Yifei Wang, Xi Zhu, Lianshan Gao and Haibo Chen

Abstract In this article, the Micro-Channel Plate Electron Multiplier is studied to carry out the microcurrent multiplication process in order to solve the short lifetime problem of the Electron Multiplier of the present Cesium Clock. Based on the current parameters of the Micro Channel Plate Electron Multiplier, the gain is enhanced by selecting the structure parameters and the application of the cascade structure, the noise is reduced by the improvement of the structure and handing procedure, the lifetime is enhanced by optimization of the working parameters, thus a high gain, low noise, and long lifetime Micro-Channel Plate Electron Multiplier is obtained, which could improve the performance of the Cesium Clock for the navigation system.

Keywords Cesium clock · Electron multiplier · Gain · Decay rate · Noise

1 Introduction

Cesium Clocks with high long-term stability, high frequency repeatability and "zero shift" characteristic, play an important effect in the navigation systems. For example, the newest GPSIIF system satellite carries Rubidium clock and Cesium Clocks for time and frequency standard [1]. High-performance Cesium Clocks are highly required for the "Beidou" system (BDS). However, the present Cesium Clocks suffer from short lifetime problem, which is induced by the disadvantage of the Electron Multiplier. In the cesium beam tube (CBT), the cesium atoms are ionized to form the microcurrent input single, then the multiplication process is carried out by the Electron Multiplier to form the output single of the CBT. As the present Electron Multipliers are still not ready for application, we propose the application of the Micro-Channel Plate (MCP) Electron Multiplier in the cesium beam tube to carry out the multiplication process. For each MCP Electron Multiplier is constituted by thousands of microchannels, and each microchannel

Y. Wang (✉) · X. Zhu · L. Gao · H. Chen
No. 203 Institute of CASIC, Yongding Road 50, Beijing 100854, China
e-mail: su.fei@163.com

J. Sun et al. (eds.), *China Satellite Navigation Conference (CSNC) 2017 Proceedings: Volume III*, Lecture Notes in Electrical Engineering 439,
DOI 10.1007/978-981-10-4594-3_48

could carry out the multiplication process separately, thus the reliability of the MCP Electron Multiplier is much greater than the present Electron Multiplier.

To carry out the multiplication process for the CBT, the MCP Electron Multiplier should attain the following parameters: gain $G \geq 10^5$, noise current $I_A \leq 1 \times 10^{-11}$ A, daily decay rate $\sigma < 0.0005$. These parameters could ensure the noise–signal ratio and lifetime of 3 years for the CBT. However, the present MCP Electron Multipliers used in night vision devices with the parameters of: $G \geq 10^3$, $I_A \leq 5 \times 10^{-12}$ A, and $\sigma < 0.005$ could not satisfy the requirement of the CBT [2]. In this case, we introduce the cascade structure MCP (CSMCP) with two MCP Electron Multipliers connection in series. The CSMCP could attain high gain with $G \geq 10^5$, but induces higher noise current and decay rate. In the present work, the gain of the MCP is enhanced by the improvement of the structure parameter and the application of the cascade structure, the noise of the MCP is reduced by the improvement of the structure and handing procedure, the lifetime of the MCP is enhanced by optimizing of the working parameters thus a high gain, low noise, and long lifetime MCP Electron Multiplier is obtained, which could improve the performance of the Cesium Clock for the navigation system.

2 Experimental

MCP Electron Multipliers with outdiameter of 25 mm, diameter to length ratio $\alpha = 40$, and slant angle $\theta = 7°$ are selected. The cascade MCP Electron Multipliers with operational area ratios (OAR) of 50% (LOAR) and 65% (HOAR) are assembled in special designed fixtures, which are isolated by ceramic rings. The measurements are carried out at about 5E-6 Pa after a vacuum bake of 200 °C, 24 h in the special designed dynamic measurement device. The measurement system is shown in Fig. 1. The electron beam generated by the electron gun, adjusted by the shield, gained by the single MCP or CSMCP, obtained by the anode and then measured by the Keythley 6430. The working voltages are provided by the series resistors, which are also shown in Fig. 1. MCP1 and MCP2 could be put on working voltage of 600–1000 V as required.

3 Results and Discussions

3.1 Gain

The gain of a single channel of the MCP could be expressed as [3]:

$$G = \delta^n, \tag{1}$$

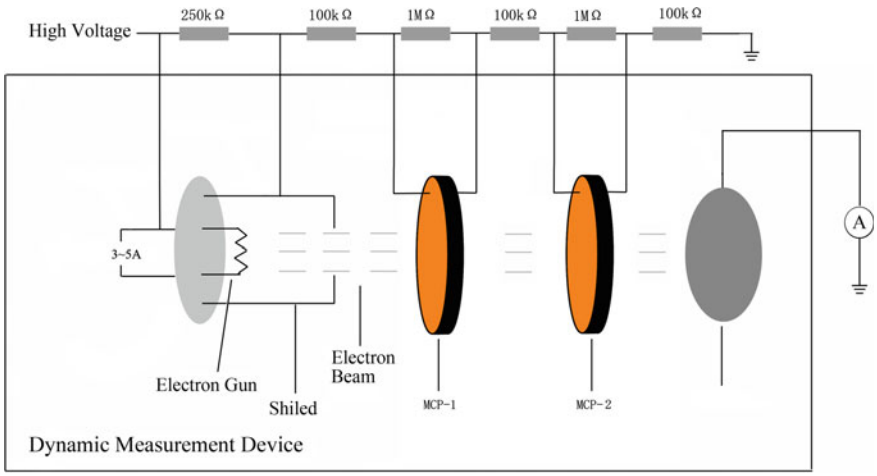

Fig. 1 The diagram of measurement system

where δ is the secondary emission coefficient, n is the secondary emission times. Furthermore, we have:

$$G = \left[\frac{KU^2}{4v_0\alpha^2 \sin\theta}\right]^{\frac{4v_0\alpha^2 \sin\theta}{U}}, \tag{2}$$

where K is a parameter represents the secondary emission property of the secondary emission material, U is the working voltage, v_0 is the electron emission potential, θ is the slant angle, and α is the diameter to length ratio. We can infer that the gain of single channel of the MCP is affected by the K, U, θ and α. To achieve an optimum effect, the above parameters must be systemically considered. Genially speaking, larger U, θ and α could lead to higher gain, but also leads to short lifetime and higher noise problem. As the gain of single MCP is not enough for the CBT, we choose the relatively lower θ and α to have a systemically result, and U is decided by the testing results. Meanwhile, the gain is also related on the OAR of the MCP. The present MCP has the OAR of 50–65%, while the MCP with OAR >70% is generally difficult to achieve, and suffers from uncertainty of technological process. In the present work, we have the LOAR and HOAR MCPs with OAR of 50 and 65% for contrast, respectively.

The Voltage dependences of gain for the MCP are shown in Fig. 2. The gain of single LOAR MCP rises with rising U, and reaches the highest value of $G = 6350$ at the highest U of 1000 V, which is still not enough for the CBT. The gain of the LOAR CSMCP experiences a strong improvement at low working voltages of $U < 700$ V, but start to saturate at $U \geq 750$ V, and reaches $G = 1.16 \times 10^5$ at $U = 850$ V, which is determined by the Self-saturating Feature of the MCP [4]. To ensure that the gain is still sufficient after decaying and electron beam striking, we consider that the gain of CSMCP needs further improvement, and the

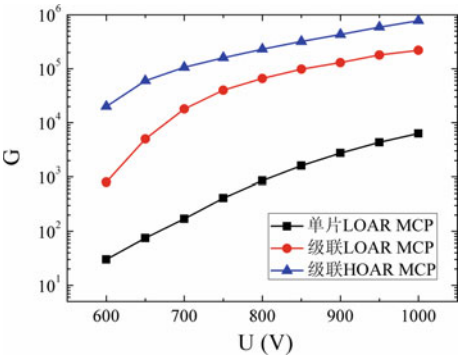

Fig. 2 Voltage dependence of gain for the MCP

LOAR CSMCP is not enough for application. The gain of the HOAR CSMCP is also shown in Fig. 2, the curve current is resemble with the LOAR CSMCP, but with much higher gain of $G = 2.3 \times 10^5$ at $U = 800$ V, which is sufficient for CBT applications. Higher OAR Do have a better effect on gain.

3.2 Noise

The noise of the MCP is expressed by the noise current, which is defined as the output current of the MCP with working voltage but zero input electron beam current exerted [3]. The noise current of single MCP is about 10^{-12} A. However, the noise current of the first MCP is gained by the second MCP and forms a very high noise current in the CSMCP. Supposing two MCP of the CSPCM with gains of 500, and the noise current of the first MCP is 1 pA, after gained by the second by the second MCP, the total noise current of the CSMCP could reach 0.5 nA, which is far from our expectation. The noise current of the MCP mainly comes from the gas molecule adsorbed on the inside surface of the micro channel, which are ionized, accelerated and gained by the working voltage. To reduce the noise current, the preparation techniques of the MCP must be optimized firstly with less defects thus less gas molecule adsorbed on the inside surface of the micro channel. The handling processes of vacuum baking and electron beam striking should also be introduced. During storing, transporting and assembling processes, the MCP should be kept away from exposing in air as much as possible.

To reduce the noise current, inspections of the MCP for defects with microscope and electron imagery are first executed; vacuum baking at 200 °C for 24 h and electron beam striking are also carried out before measurements. The electron beam striking quantity is shown in Fig. 3, the working voltage of four sections are 500, 550, 600 and 650 V, respectively. The theoretical quantity is 13 μA h, while the actual quantity is 11.5 μA h because of the decay. The Voltage dependence of noise current for the LOAR CSMCP is shown in Fig. 4, the noise current rises with rising working voltage. At $U = 850$ V where the gain could reach 10^5, the noise

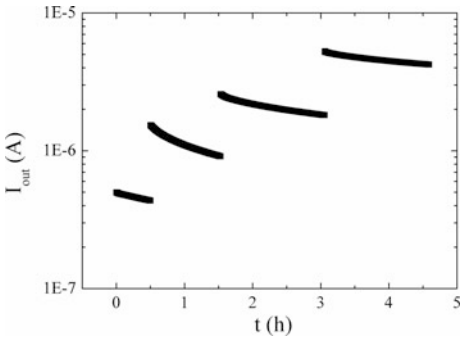

Fig. 3 Electron beam striking quantity for the single LOAR MCP

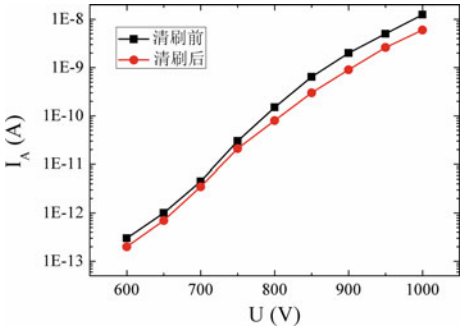

Fig. 4 Voltage dependence of noise current for the LOAR CSMCP

current of the LOAR CSMCP before electron beam striking reaches I_A = 2 nA, which is too high for CBT application. After electron beam striking, the noise current drops to about 50%, which is also not low enough. Meanwhile, the gain of the LOAR CSMCP after electron beam striking also drops to 65%. The noise–signal ratio enhancing brought by electron beam striking is limited. We consider this result for two reasons: 1. The LOAR MCP exposes in air for too much time during assembly process; 2. electron beam striking quantity is still not sufficient.

To solve the two problems above, we made optimization during the assembly process to reduce the exposure time in air, and enhanced the electron beam striking quantity, which is shown in Fig. 5. The working voltage of four sections are 500, 550, 600 and 650 V, while the theoretical and actual quantities are 39.5 and 35.8 μA h, respectively.

The Voltage dependence of noise current for the HOAR CSMCP is shown in Fig. 6. Before electron beam striking, the HOAR CSMCP has a higher noise current at low voltage because of more micro channel thus the inner surface area and defects. However, after electron beam striking, the noise current reduced evidently to I_A = 8 pA at U = 800 V while the HOAR CSMCP achieves $G > 10^5$ at the same time. The noise current reduces to 1.6% while the gain reduces to 45%. Thus we can infer that larger electron beam striking quantity do enhances the noise–signal ratio evidently. The HOAR CSMCP with high noise–signal ratio $>10^4$ could make Cesium Clocks to be with practical applications.

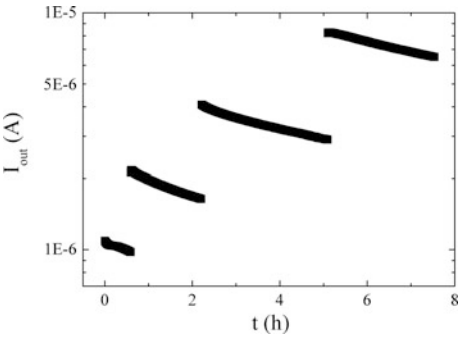

Fig. 5 Electron beam striking quantity for the single HOAR MCP

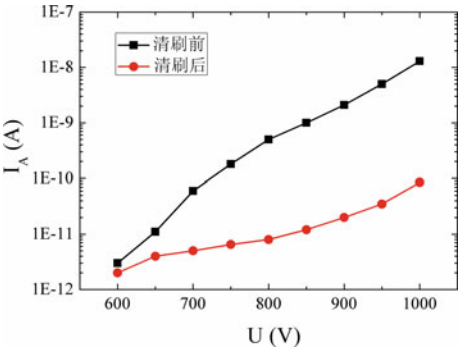

Fig. 6 Voltage dependence of noise current for the HOAR CSMCP

3.3 *Lifetime*

The lifetime of the MCP is expressed by the decay rate. A daily decay rate of $\sigma = 0.0005$ equals a lifetime of 3 years, which could make the Cesium Clock to be with practical applications. The lifetime of a MCP determines from its structure, handling procedure as well as the working parameters. MCP for night vision has a best working voltage of about 22 times its diameter to length ratio [5]. As for MCP used in CBT, the working voltage should be determined at a minimum value that contents the gain and noise, which could reduce the impaction from the electrons to the second emission material on the inner surface of the micro channel, thus extends the lifetime. According to the gain and noise results and the above discussions, we consider the best working voltage for the HOAR CSMCP is at $U = 835$ V, and a long term of gain test is carried out with the input current of 50 pA to achieve the decay rate, the results are shown in Fig. 7. In the beginning of the test, the gain rises with time, and reaches the maximum at day 15 with $G = 1.82 \times 10^5$, then drops slowly to $G = 1.81 \times 10^5$ at day 20. This behavior is similar to the ones in long lifetime Cesium Clocks [6], thus a long lifetime of the HOAR CSMCP could be expected. The total decay from day 15 to day 20 is 0.0054 while the equivalent daily decay rate is $\sigma = 2.2 \times 10^{-5,}$ which is much better than the expecting daily

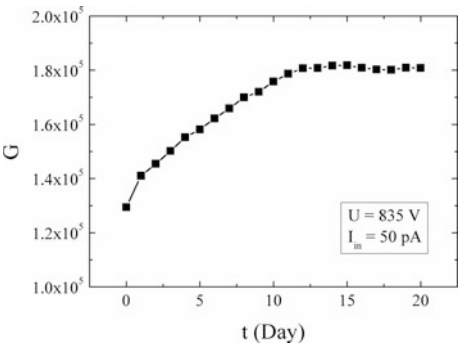

Fig. 7 The gain time curve for the HOAR MCP

decay rate of $\sigma = 0.0005$. Furthermore, for the high-performance Cesium Clocks with input current of 10 pA, the equivalent daily decay rate could also reach $0.0002 < \sigma < 0.0005$. This result could make Cesium Clocks to be with practical applications.

3.4 Conclusions

The Micro-Channel Plate Electron Multiplier is studied to carry out the microcurrent multiplication process in order to solve the short lifetime problem of the Electron Multiplier of the Cesium Clock. By selecting the structure parameter and the application of the cascade structure, the improvement of the structure and handing procedure and the optimizing of the working parameters, a High Gain, Low Noise, and Long lifetime Micro-Channel Plate Electron Multiplier with $G > 10^5$, $I_A < 10$ pA and $\sigma = 2.2 \times 10^{-5}$ is obtained, which could improve the performance of the Cesium Clock for the navigation system.

References

1. Gu Y, Chen Z, huai P (2008) The developments of atom clocks in navigation systems. Space International, vol 10
2. Pan J (2004) Microchannel plates and its main characteristics. J Appl Opt 25(5):25–29
3. Wu K. Research on the measurement system for the characteristic parameters of microchannel plate, Master thesis
4. Pan J. The developments of low noise high resolution microchannel plate, Master thesis
5. Guest AJ (1971) A computer model of channel multiplier plate performances, Aeta Electron 14 (1): 79
6. Liu C, Wang, Qi Y (2004) Monitoring and analyses of the internal operating parameters of cesium clock HP5071A, Publications of the Shaanxi astronomical observatory, vol 06

Joint Time and Frequency Transfer and Multipoint Time Synchronization via Urban Fiber and Its Application in CEI

Youzhen Gui, Jialiang Wang, Haitao Li, Shaowu Chen, Nan Cheng, Qin Liu, Zitong Feng, Fei Yang, Wei Chen and Haiwen Cai

Abstract High-precision time and frequency signals play an important role in many areas such as modern communication, navigation, and baseline interferometry. Joint time and frequency transfer of one central station to two client stations via urban fiber was demonstrated. Time synchronization among the stations can be realized by feedforward compensating the calibrated delays. Frequency deviation at the level of 1. 2E-14 @1 s, 1.5E-19 @1 day for the shorter link 14 km. And that of 4.6E-14@1 s, 2.6E-19 @1 day for the longer link of 110 km. Time synchronization for the two client stations are achieved after delay calibration, which are 25.4 ps (14 km) and 20.9 ps (110 km) respectively. This method of synchronization was used in the system of short-base Connected Elements Interferometry (CEI), realizing better accuracy of orbit measurement.

Keywords Laser technique · Time and frequency transfer · Optic fiber · Atomic clock · CEI

1 Introduction

With the progress of the atomic clocks, the stability of commercial hydrogen clocks has reached to 10–13@1 s. Moreover, the stability of the optical clocks has come to 10–16@1 s. As the fast development of high stability of clocks, the traditional GPS

Z. Feng · F. Yang · W. Chen · H. Cai (✉)
Key Laboratory of All Solid-State Laser and Applied Techniques,
Shanghai Institute of Optics and Fine Mechanics, CAS, Shanghai 201800, China
e-mail: hwcai@siom.ac.cn

Y. Gui · J. Wang · N. Cheng · Q. Liu
Key Laboratory for Quantum Optics, Shanghai Institute of Optics and Fine Mechanics, CAS, Shanghai, China
e-mail: yzgui@siom.ac.cn

H. Li · S. Chen
Beijing Institute of Tracking and Telecommunication Technology, Beijing, China

J. Sun et al. (eds.), *China Satellite Navigation Conference (CSNC) 2017 Proceedings: Volume III*, Lecture Notes in Electrical Engineering 439,
DOI 10.1007/978-981-10-4594-3_49

based time and frequency transfer is not able to provide good short-term stability. As a matter of fact it leads to the rise of the fiber based frequency transfer which can be as an alternative choice of the GPS methods. With characteristic of low transmission loss, anti-electromagnetic interference and high stability, fiber-based frequency transfer can fulfill the needs of the transmission of high-precision clock. In recent years, great processes have been made on the time and frequency transfer via fiber, such as: simultaneous transfer of radio frequency and time and also time synchronization in Poland [1]; radio frequency transfer along internet data traffic over public fiber in France [2]; optical frequency transfer over a single span 1840 km fiber with ultrastable performance in PTB [3]. Our team has realized frequency transfer and time synchronization simultaneously over the cascaded link of 430 km [4]. The group [5] from Tsinghua University demonstrated accurate frequency transfer and time synchronization based on WDM technology, realizing 50 ps precision.

Fiber-based time and frequency transfer has great application on radio astronomy observation, deep space network, phased-array radar, and so on. Based on the active optical compensation of link delay, frequency stability of 2E-14/1 s, 5E-18/1 day was realized in the deep space network of NASA [6]. Square kilometer array (SKA) composed of thousands of detection arrays will benefit from fiber time and frequency synchronization network for the uniform time standard. It will lead to better accuracy [7].

In this paper, time and frequency synchronization comes into realization among three points with urban fiber network. 10 MHz frequency signal from the central station and the generated 1 pps time signal are transferred to two remote sites, which are far from the center station 14 and 110 km respectively. The distance between two remote sites is about 50 km. Time synchronization between two sites through fibers can reduce the error from delay measurement of independent clocks. Connected Element Interferometry (CEI) between the two sites was demonstrated for geostationary satellites. The accuracy of the differential time delay is superior to 0.2 ns, the accuracy of relative position of two GEO satellite is superior to 50 m.

2 Fiber Time and Frequency Synchronization Scheme

2.1 Principal and Set-up

The schematic diagram of the fiber-based frequency dissemination is shown in Fig. 1. 10 MHz frequency signal and 1 pps (one pulse per second) time signal from the central station (H-maser) are combined through WDM and sent to the two remote sites along two links. Here, we mark the nearer site 14 km from the central one as SH, and the further one 110 km, and the following is the same. As in Fig. 1, the first section 7 km of 110 km is aerial optical cable, with loss 15 dB. So there are two bidirectional Erbium-doped Fiber Amplifier (EDFA) are inserted into this link. One 10 MHz frequency signal and two 1 pps time signals modulate the optical

carrier from distributed feedback laser (DFB) at different wavelength (C36, C33 and C35 channel). Here, 10 MHz frequency is boosted to 1 GHz for better signal-to-noise ratio and the two 1 pps signals are delayed by two time delay generators (Time Delay 1 and Time Delay 2) to feedforward compensate the propagation delay of 1 pps and to synchronize 1 pps of the central site with the remote site [8]. One DWDM is used to combine three modulated lasers. Two optical delay lines are applied to compensate the fluctuation of propagation delay of the two links. In each remote site, one DWDM is used to separate the light modulated by frequency and 1 pps time signal. The demodulated 1 GHz frequency signal and 1 pps signal are split up into more channels. 1 GHz and 1 pps signal modulate the intensity of two lasers at different wavelength (C37, C34 channel) and they are sent back via the same link to the center site and detected by two photodiodes. For choosing the different wavelength channel, it will lead to noise from dispersion. Therefore, when we design bidirectional dual-wavelength time and frequency transfer system, it is necessary to reduce wavelength difference of time and frequency signal and the wavelength difference between the forward and backward signal. In our system, we choose the forward signal as frequency signal wavelength C36 channel and time signal wavelength C33/C35 channel. For the backward signal, frequency is on C37 channel and time is on C34 channel.

For the above system, we take one of the two remote sites for example, the returned signals to the center site are detected by PDs then one 1 pps time signal and one frequency signal are in hand. The round-trip 1 pps with together the original 1 pps from H-maser are inputted into Time Interval Count (TIC)to acquire the total delay of round-trip. While, the round-trip frequency signal with together the original frequency from H-maser are inputted into phase detector to acquire the round-trip link noise. The output of phase detector is sent to proportion-integral-derivative (PID) module to drive the controllable fiber delay line (CFDL). In Fig. 1, CFDL1 is used for noise compensation of 14 km link and CFDL2 is used for noise compensation of 110 km. Two CFDLs both include two parts of the fast one and the slow one, the dynamical range of the fast one is 15 ps with response width over 1 kHz, while the slow one is temperature-controlled fiber loop. Length of fiber loop for the shorter link noise compensation is 1 km, and that of the longer link is 10 km. When the link is stabilized, whatever signals transferred on this link are stable. The propagation delay will keep constant when the link is stabilized, so we

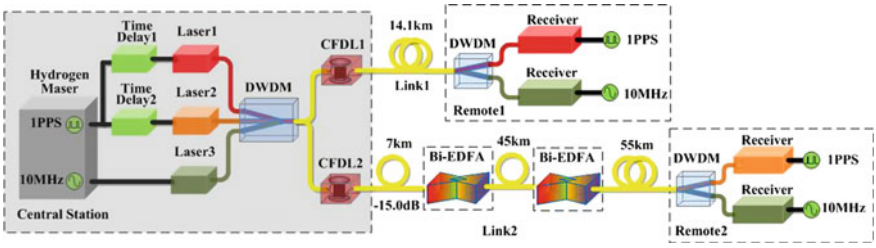

Fig. 1 Principle of frequency transfer and time synchronization via field fiber network

only need to compensate the absolute delay difference to realize 1 pps time synchronization between the center site and remote site.

2.2 Fast and Large Dynamic Range of CFDL

In the above longer link 110 km, the first section 7 km is old and aerial cable, with total loss 15 dB. So there are two bidirectional Erbium-doped Fiber Amplifier (EDFA) are inserted into the link. Meanwhile, the temperature range of aerial cable is much bigger than that of buried cable. It is challenge for the feedback ability of compensation system. In our system, we have improved a lot both in installation of Thermoelectric Cooler (TEC) and its drive circuit of CFDL. This enhances the dynamic range of CFDL and rate of temperature rising/falling. In Fig. 2, the performance of 10 km CFDL is given. It can be seen that fast temperature rising can be achieved when in low temperature, while the heating rate decreases when it reaches 45 °C. Correspondingly, fast temperature falling can be achieved when in high temperature, while the cooling rate will decrease when working-point reaches 35 °C. The right curve of Fig. 2 shows the dynamic range and its cooling rate of 10 km CFDL. After the improvement, the cooling rate is enhanced from 1.42 to 8.02 mV/s (@22 °C). This makes it is enough for the temperature fluctuation of aerial cable.

2.3 Frequency Division Clock Time Synchronization

Because the 1 pps is low frequency and wideband signal, the distortion of 1 pps signal will happen when Electro-Optic Modulator (EOM) is added, which will degrade the short-term stability of 1 pps. Meanwhile, it is easily affected by aging and temperature drift, which will degrade the long-term stability of 1 pps. To provide both stable and accurate time signal in the remote station, we also have demonstrated the flexibility of frequency division clock time synchronization and

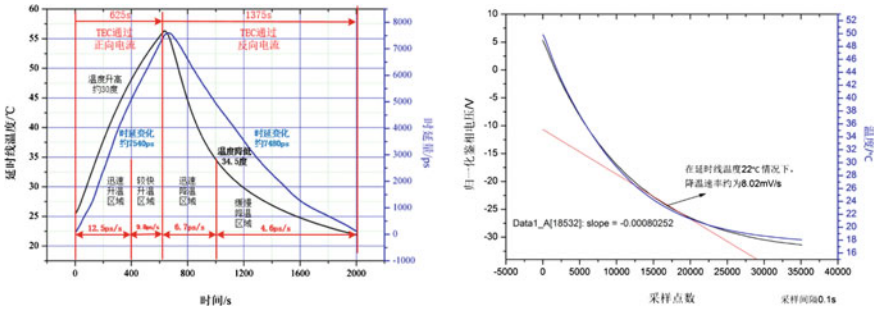

Fig. 2 Rate of heating/cooling of fiber delay line

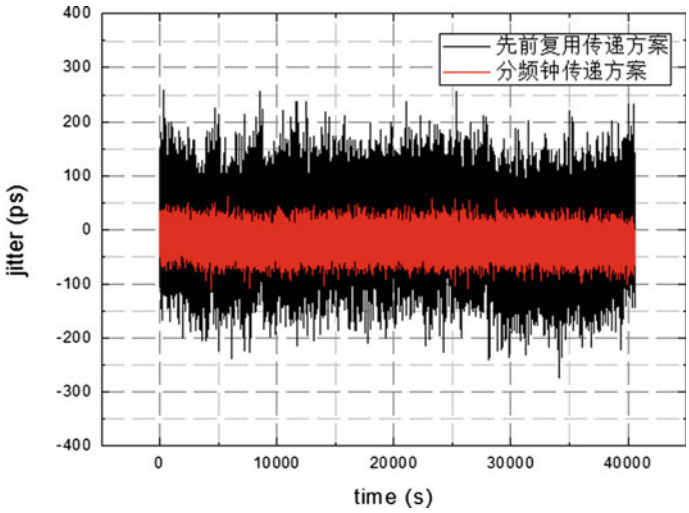

Fig. 3 Time transfer by frequency division clock

compared it with direct modulation of 1 pps time synchronization as shown in Fig. 1. Frequency division clock time synchronization is the method that 1 pps signal can be generated from the transferred frequency signal in the remote site. This can prevent the noises in the process of EOM in the direct modulation method. Also, it avoids the drift of bias point of EOM.

In the 110 km urban fiber link, we compared the results of direct modulation time synchronization and frequency division clock time synchronization, shown as in Fig. 3. The peak-to-peak jitter of 1 pps in the former scheme is 520 ps, while in the latter scheme is only 160 ps. The improvement is threefold, that is to say, frequency division clock time synchronization can upgrade the stability of 1 pps.

3 Experimental Results

In the field test, for the reason that the central station and remote station are not in the same place, we make the test of round-trip link in the central station to evaluate the performance of single-trip at the remote station. The returned 1 GHz frequency signal is filtered and amplified and partly mixed with the original 1 GHz (10 MHz is boosted to 1 GHz) to acquire phase fluctuation. The phase error signal is used to drive CFDL to stabilize the link. While the other part of the returned 1 GHz and the original 1 GHz are inputted to phase discriminator to get the fractional frequency stability. The fractional frequency stability of 14 and 110 km is shown in Fig. 4.

The fractional frequency stability for the shorter link 14 km is 1.2E-14/1 s, and the long-term stability is 1.5E-19/1 day. For the longer link 110 km, stability is

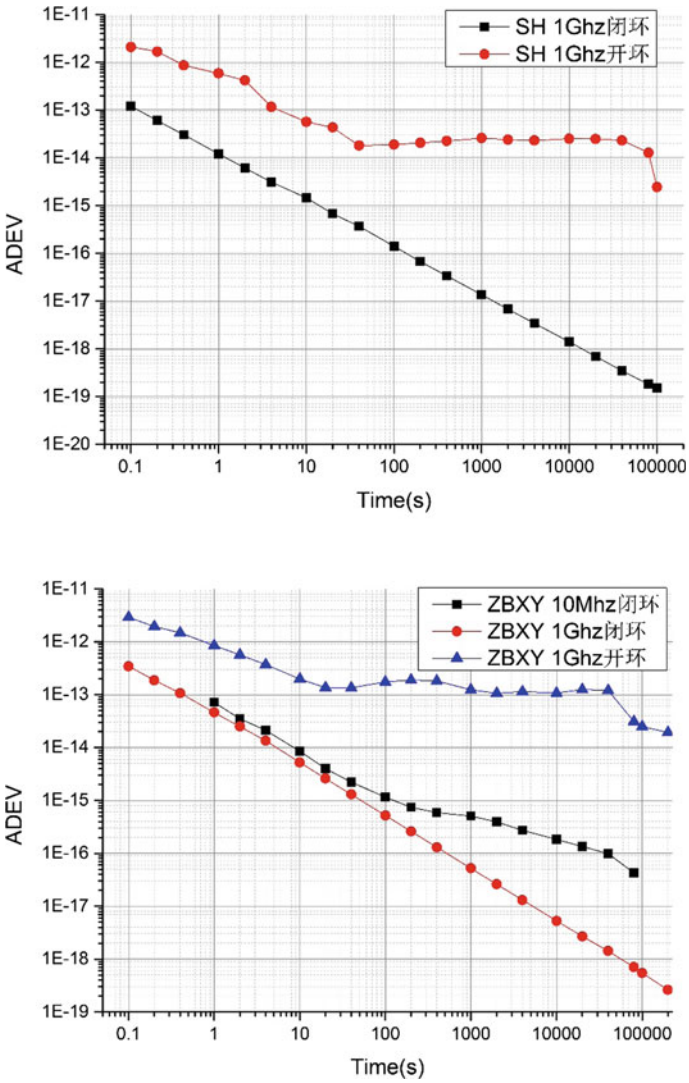

Fig. 4 ADEV of two fiber links (*top* 14 km, *bottom* 110 km)

4.6E-14/1 s, 2.6E-19/1 day. For the longer link, we also give the result that 10 MHz phase detection by phase noise test TSC5125A. Compared the stability of 10 MHz by TSC5125A with the stability of 1 GHz by home-made phase detector in Fig. 4, it can be seen that the short-term stability of 10 MHz and 1 GHz is almost the same, while long-term stability of 1 GHz is better than that of 10 MHz. The explanation is that the up-converter and downconverter of frequency is out of loop, which are susceptible to environmental temperature.

Similarly, the returned 1 pps signal is inputted to Pulse Distribution Amplifier (PDA). Then it enters into the TIC with the original 1 pps from H-maser to get the fluctuation of propagation delay, shown in Fig. 5. After the delay calibration of system devices and other asymmetric delays, we can achieve the accurate time synchronization, see Ref. [8].

After the real time compensation of delay, the peak-to-peak time jitter of 14 km link is 250 ps, with the value of RMS 25.4 ps. The peak-to-peak time jitter of 110 km link is 174 ps, with the value of RMS 20.9 ps.

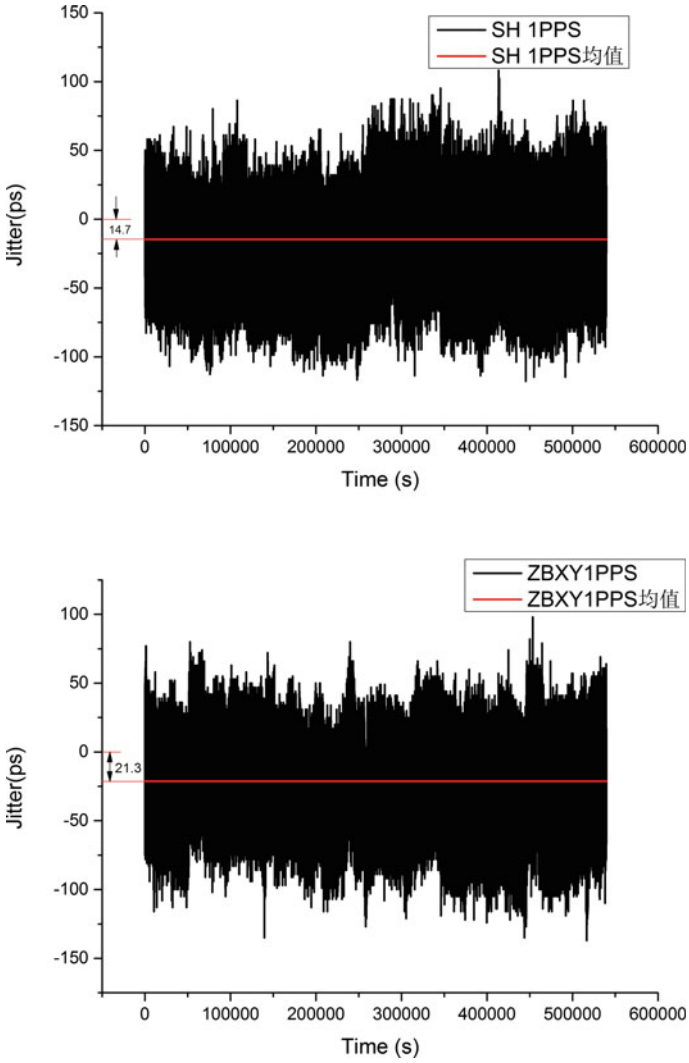

Fig. 5 Time jitter of two fiber links (*top* 14 km, *bottom* 110 km)

4 CEI Demonstration Based on Fiber Time and Frequency Synchronization

A Connected Element Interferometry system for demonstration is established by using two ground stations, the distance between them is about 50 km. Two ground stations are connected by optical fiber, frequency transferring and time synchronization is realized between the central station and the two ground stations via optical fiber. The law interferometry data are recorded. After the correlation processing, the time delay from the satellite to two ground stations is calculated. The observation is successfully taken on two Geosynchronous Earth Orbit (GEO) satellites. As they are in the same beam, the differential time delay between two satellites is obtained. The accuracy of the differential time delay is superior to 0.2 ns, the accuracy of relative position of two GEO satellites is superior to 50 m. The results show that this technology would be used in the high accuracy orbit determination for GEO and HEO.

5 Conclusion

According to the actual application demand, it utilizes the urban fiber network to realize time and frequency synchronization among one central station and two remote stations. The fractional frequency stability for 14 km link is 1.2E-14/1 s, 1.9E-19/1 day, and for the 110 km link is 4.6E-14/1 s, 2.6E-19/1 day. The uncertainty of synchronization between the central station and the remote station is below 25 ps. This kind of fiber time and frequency system is applicable to the demand on high stability of H-maser and precise measurement of delay. Results show that this technology would be used in the high accuracy orbit determination for GEO and HEO.

References

1. Krehlik P, Śliwczyński Ł, Łukaszbuczek, Lipiński M (2012) Fiber-optic joint time and frequency transfer with active stabilization of the propagation delay. IEEE Trans Instrum Meas 61(10):2844–2851
2. Lopez O, Haboucha A, Chanteau B, Chardonnet C, Amy-Klein A, Santarelli G (2012) Ultra-stable long distance optical frequency distribution using the Internet fiber network. Opt Express 20:23518–23526
3. Droste S, Ozimek F, Udem TH, Predehl, Hansch TW, Schnatz H, Grosche G, Holzwarth R (2013) Optical-frequency transfer over a single-span 1840 km fiber link, PRL, 111, p 110801
4. Liu Q, Han SL, Wang JL, Feng ZT, Chen W, Cheng N, Gui YZ, Cai HW, Han SS (2016) Simultaneous frequency transfer and time synchronization over a 430 km fiber backbone network using a cascaded system, Chin Opt Lett 14:070602

5. Wang B, Gao C, Chen WL, Miao J, Zhu X, Bai Y, Zhang JW, Feng YY, Li TC, Wang LJ (2012) Precise and continuous time and frequency synchronization at the 5E-19 accuracy level. Sci Rep 2:556–560
6. Calhoun M, Sydnor R, Diener W, Stabilized A (2002) 100-megahertz and 1-gigahertz reference frequency distribution for Cassini radio science. IPN Progress Report February, 15:42
7. http://www.skatelescope.org
8. Cheng N, Chen W, Liu Q, Xu D, Yang F, Gui YZ, Cai HW (2015) Time synchronization technique for joint time and frequency transfer via optical fiber. Chin J Lasers 42:0705002

Research on Microwave Oscillator Based on Cryogenically Cooled Sapphire Cavity

Xi Zhu, Yifei Wang, Haibo Chen, Kai Huang and Lianshan Gao

Abstract Microwave oscillator based on cryogenically cooled sapphire cavity has advantages of extremely high-Q factor and low noise, and thus it has a wide application prospect. On the basis of theoretical calculation by HFSS software, a sapphire dielectric resonator working at whispery gallery (WG) mode is developed. Cooperating with servo loop, an oscillator is constructed. In order to ensure high-Q factor, low-temperature device based on digital PID control program is used to stabilize temperature of the resonator within a range of 4.2–15 K, with fluctuation below 1 mK. To further reduce phase noise, Pound circuitry is used to control phase of the oscillating frequency signal. When oscillating frequency is 9.2 GHz, single sideband (SSB) phase noise is measured.

Keywords Microwave oscillator · Sapphire cavity · Phase noise · Q factor

1 Introduction

With advantages of highly stable frequency and low-phase noise, high-performance microwave frequency sources are widely applied in radar, communication systems, and metrology [1–3], and this becomes a powerful drive of their development in China nowadays. While limited by Q factor of resonators, there are still disadvantages in short-term frequency stability of present microwave frequency sources. Therefore, many application requirements cannot be satisfied. It is noteworthy that sapphire crystal has extremely low loss tangent at low temperature, and this property makes it an optimal option for the development of high-performance dielectric resonance oscillators. At room temperature, Q factor of X band sapphire dielectric resonator oscillators is about 10^5. While at liquid helium temperature the Q factor is above 10^9 [4–8], high-Q factor can prominently optimize frequency stability of oscillators. As early as 1970s, the research group from Moscow State

X. Zhu (✉) · Y. Wang · H. Chen · K. Huang · L. Gao
Beijing Institute of Radio Measurement and Metrology, Beijing 100854, China
e-mail: 1989zhuxi@163.com

J. Sun et al. (eds.), *China Satellite Navigation Conference (CSNC) 2017 Proceedings: Volume III*, Lecture Notes in Electrical Engineering 439,
DOI 10.1007/978-981-10-4594-3_50

University conducted pioneering research on cryogenically cooled sapphire dielectric resonator oscillators consisting of a sapphire coated with niobium or lead films, and Q factor was about 10^9 [9, 10]. In the mid-1980s, the research group from Jet Propulsion Laboratory (JPL) developed superconducting cavity maser oscillator with sapphire coated with superconducting lead, and ruby Maser was used as the source of excitation. Frequency stability demonstrated was better than 10^{-14} at 100 s [11]. At the same time, the cryogenic sapphire oscillator project at the University of Western Australia (UWA) which loaded sapphire into a superconducting niobium cavity exhibited frequency stability better than one part in 10^{-14} [6, 12]. After so many years development and tireless efforts made by several teams all over the world, the frequency stability of cryogenic sapphire oscillator is at the 10^{-16} level [13]. Driven by great demands, the development of cryogenic sapphire oscillator is heading in two directions: high-frequency stability and high practicality. In pursuit of providing technological approaches for resolving national requirements, we designed and constructed a cryogenic sapphire oscillator based on a sapphire whispering-gallery mode resonator cooled near 7 K. This work lays the foundation of making the cryogenic sapphire oscillators more practical and miniaturization.

In this paper we outline the design of sapphire dielectric resonator via HFSS software. In order to obtain a high-quality resonator, digital PID control program is used to stabilize its temperature within a permissible range from 4.2 to 15 K, while the temperature fluctuation is less than 1 mK. On this basis, Pound circuit is utilized to stabilize phase of the oscillator frequency signal, and hence, its phase noise can be further decreased. With output frequency 9.2 GHz, single side band (SSB) phase noise of free running oscillator and oscillator with loop closed are measured respectively.

2 Sapphire Dielectric Resonator

At the end of nineteenth century, during the study of acoustic wave, Lord Rayleigh found that high-frequency acoustic wave can propagate along confocal plane, namely echo effect [14]. As to microwave, whispering-gallery mode was realized when isotropic or weak anisotropic material (i.e., sapphire) was adopted. Specifically, when the refractive index of medium in resonator is much larger than that of cavity wall, signal transferred can be total internal reflected by cavity wall. So the signal would transfer in the resonator with decreased radiation loss and high-Q factor. The parameters of resonator working at a whispering-gallery mode can be analytic calculated by combining Maxwell equations with boundary conditions or numerical calculated by finite element simulation. In this paper, HFSS software is adopted to simulate sapphire dielectric resonator whose structure is shown in Fig. 1. The resonator could work at whispering-gallery mode when its geometry (namely parameter D_1, D_2, H_1, H_2) is appropriate, and the working frequency can also be calculated. After simulating calculation, $D_1 = 51$ mm,

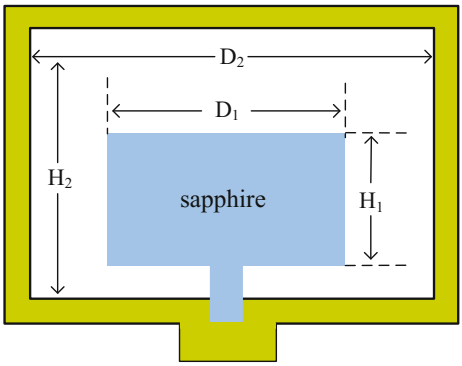

Fig. 1 Schematic of sapphire dielectric resonator

D_2 = 90 mm, H_1 = 30 mm,and H_2 = 53 mm are currently adopted in our resonator. At room temperature (300 K), the dielectric coefficients perpendicular and parallel to c-axis of sapphire crystal are $\varepsilon_t = 9.39$, $\varepsilon_z = 11.52$, respectively. The frequency of the resonator is 9.1 GHz, and the electromagnetic mode of sapphire is $WGH_{12,0,0}$ which are calculated by redial, azimuthal, and z-direction of the sapphire crystal. More clearly, the mode distribution is shown in Fig. 2.

After the electromagnetic mode is selected, the way to couple power into and out of the cavity can also be chosen according to the distribution of electromagnetic field. There are two ways of coupling: straight and loop antenna probe. In our system, two loop antenna probes are adopted and they are inserted into the cavity through a small hole in the wall, respectively. These positions also have the strongest magnetic field strength and are symmetry around the axis of sapphire, while the loop plane is parallel to the axis. If the coupling coefficient is appropriate, the resonator will perform well.

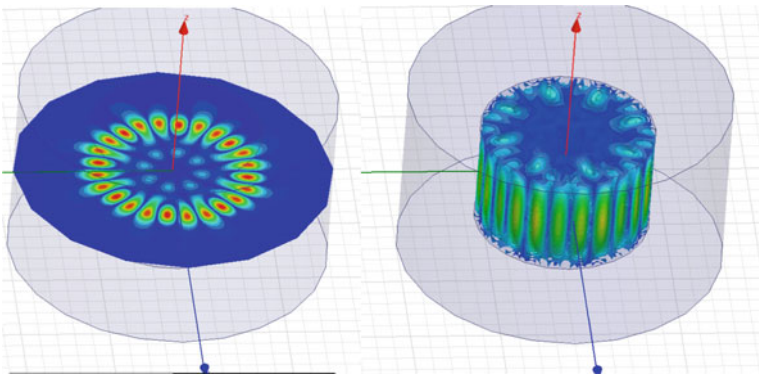

Fig. 2 $WGE_{7,1,2}$ mode

Fig. 3 Photo of sapphire dielectric resonator

To stabilize the temperature of sapphire, pure copper with good thermal performance is used as resonator cavity. The photo of sapphire dielectric resonator is shown in Fig. 3.

3 High Stable Low-Temperature Controller System

The Q factor increase with the resonator is cooled. Furthermore, as the frequency of resonator is highly dependent on temperature fluctuation and vibration, the temperature controller system should keep temperature ultra highly stable and keep vibration of the system ultra small. In our system, closed cycle cryocooler which do not need regular refills of liquid helium is utilized to housing the resonator. Figure 4 shows a schematic diagram of the insert and closed cycle cryocooler. Liquid helium is constantly reliquified by a cold head, and then flows into liquid helium can through infusion tube. While heat exchange between liquid helium and resonator through three shores uninterruptedly, the sapphire will be cooled. When absorbing heat, liquid helium would evaporate. Then the gas helium will backflow to the cold head with heat exchange between gas helium and baffles to reduce convection and maintain temperature within the cryocooler, and the gas helium will be liquified by the cold head again. Temperature of the cryocooler is controlled by digital PID control program and vibration-damping equipment is also adopted. Therefore, the temperature of resonator is stabilized at a set point within a range of 4.2–15 K, while temperature fluctuation is less than 1 mK. Mechanical vibration is less than 0.001 μm. In our experiment, when the temperature of resonator kept steady near 7 K, loaded Q factor is 3×10^8 with frequency 9.2 GHz, as shown in Fig. 5.

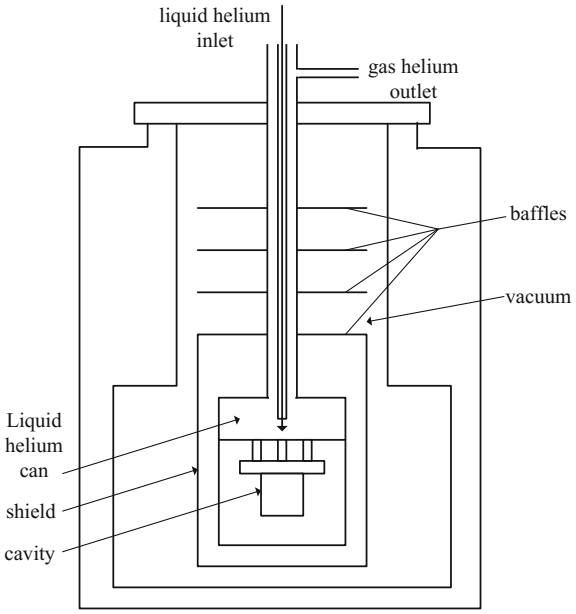

Fig. 4 Schematic diagram of the insert and closed cycle cryocooler

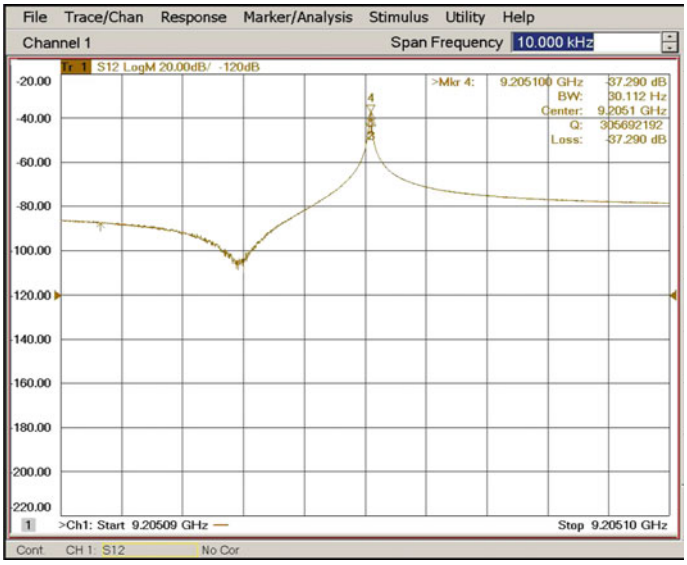

Fig. 5 The frequency and Q factor of sapphire dielectric resonator at 7 K

4 Oscillator

The oscillator circuit using a Pound frequency locking technique is described in Fig. 6 [15, 16]. It is split into two parts: main control loop, mainly including sapphire dielectric resonator, low noise amplifier, phase shifter, and circulator, which is used to sustain oscillating with desired frequency. Phase control loop, based on the Pound frequency discriminator principle, mainly including lock-in amplifier, power detector, voltage-controlled phase shifter, and integrator, which is used to stabilize phase of the circulating signal. Afterward, amplitude control loop which is used to stabilize amplitude of the circulating signal and AM control loop which is used to modify additional amplitude modulation effect caused by voltage-controlled phase shifter. This can decrease the conversion of amplitude noise to phase noise and further improve the performance of the oscillator. According to Leeson's formula, the phase noise of the oscillator can be expressed as

$$L_{\text{osc}} = 10 \cdot \log\left[1 + \frac{f_0^2}{4Q_L^2 f_m^2}\right] + 10 \cdot \log\left[\frac{\alpha}{f_m} + \frac{GFkT}{P}\right],$$

where f_{m} is the difference between output frequency signal and resonant frequency f_0, Q_L is loaded Q factor of resonant, G is the gain of amplifier, is the noise index of amplifier, is the Boltzmann's constant, is the temperature, and is the effective output power of amplifier. From this equation we can see that phase noise of oscillator

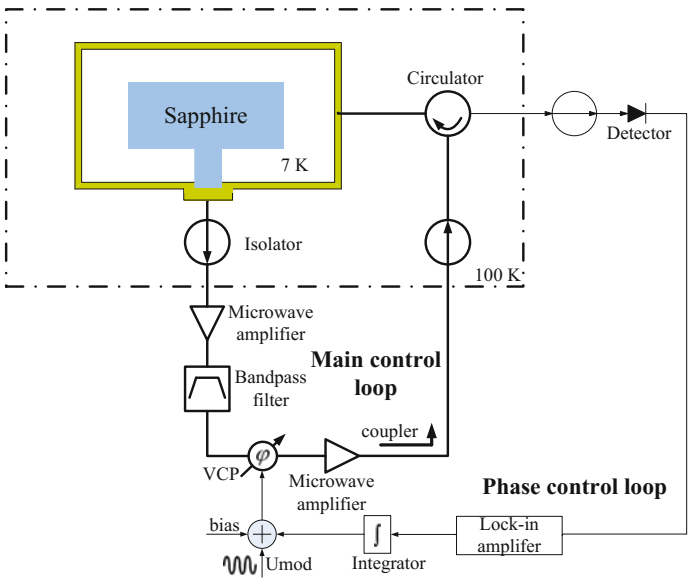

Fig. 6 Oscillator circuit design

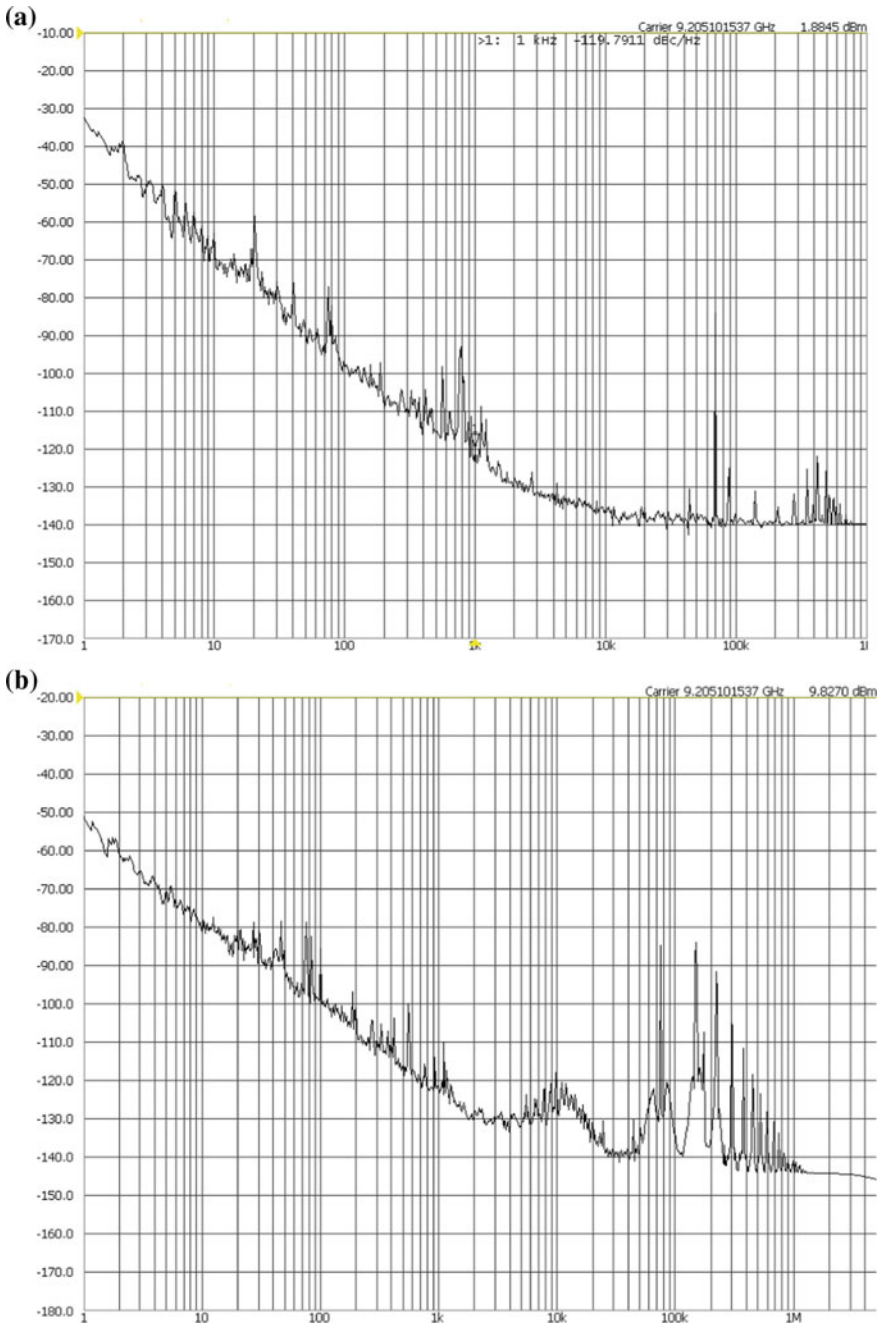

Fig. 7 **a** Single sideband phase noise of free running oscillator. **b** Single sideband phase noise of oscillator with loop closed

consists of that of resonant and control system especially amplifier. So the noise index of devices used in circuit should keep low.

5 Results

Single side band (SSB) phase noise of free running oscillator and oscillator with loop closed are measured by signal analyzer (Agilent 5052), respectively, as shown in Fig. 7. When the loop is closed, the phase noise is optimized. At present, there are only two control systems adopted to sustain oscillating with desired frequency and stabilize phase of the signal. Later, the two other control loops, amplitude control loop and AM control loop, can also be adopted to further improve the performance of the oscillator. For the output, signal of cryogenic sapphire oscillator is ultra stable, and we plan to construct two oscillators which lightly differ from each other, and obtain a low-frequency signal by mixing the two output signals. This is what we will do in the future.

6 Conclusion

This article outlines the development of cryogenic sapphire oscillator and summarizes the latest results of frequency stability. Temperature of resonator could be stabilized at 7 K with the fluctuation below 1 mK. Loaded Q factor 3×10^8 was measured at 9.2 GHz. SSB phase noise free running oscillator and oscillator with loop closed are also obtained. When the loop is closed, the phase noise is optimized. We will improve the oscillator circuit next step, so the frequency stability will be optimized furthermore to some extent.

References

1. Hartnett JG, Nand NR (2010) Ultra-low vibration pluse-tube cryocooler stabilized cryogenic sapphire oscillator with 10^{-16} fractional frequency stability. IEEE Trans Microwave Theory Tech 10:1–8
2. Tobar ME, Hartnett JG, Ivanov EN et al (2000) Cryogenically cooled sapphire-rutile dielectric resonators for ultrahigh-frequency stable oscillators for terrestrial and space applications. IEEE Trans Microwave Theory Tech 48:1265–1269
3. Vitusevich SA, Schieber K, Ghosh IS et al (2003) Design and characterization of an all-cryogenic low phase-noise sapphire K-band oscillator for satellite communication. IEEE Trans Microwave Theory Tech 51:163–169
4. Dick GJ, Saunders J (1990) Measurement and analysis of a microwave oscillator stabilized by a sapphire dielectric ring resonator for ultra-low noise. IEEE Trans Ultrason Ferroelectr Freq Control 37:339–346

5. Tobar ME, Mann AG (1991) Resonant frequencies of higher order modes in cylindrical anisotropic dielectric resonators. IEEE Trans Microwave Theory Tech 39:2077–2082
6. Ivanov EN, Blair DG, Kalinichev VI (1993) Approximate approach to the design of shielded dielectric disk resonators with whispering-gallery modes. IEEE Trans Microwave Theory Tech 41:632–638
7. Taber RC, Flory CA (1995) Microwave oscillators incorporating cryogenic sapphire dielectric resonators. IEEE Trans Ultrason Ferroelectr Freq Control 42:111–119
8. Kobayashi Y, Senju T (1993) Resonant modes in shielded uniaxial-anisotropic dielectric rod resonators. IEEE Trans Microwave Theory Tech 41:2198–2205
9. Braginsky V, Panov V (1979) Superconducting resonators on sapphire. IEEE Trans Magn 15 (1):30–32
10. Braginsky V, Panov V, Vasiliev S (1981) The properties of superconducting resonators on sapphire. IEEE Trans Magn 17(1):30–32
11. Dick GJ, Strayer DM (1987) Measurements and analysis of cryogenic sapphire dielectric resonators and DROs. In: Proceedings of 41st annual symposium on frequency control, p 487
12. Fisk PTH, Sellars MJ, Lawn MA et al (1995) Very high Q microwave spectroscopy on trapped $^{171}Yb^{+}$ ions: application as a frequency standard. IEEE Trans Instrum Meas 44(2): 113–116
13. Fluhr C, Grop S, Dubois B et al (2016) Characterization of the individual short-term frequency stability of cryogenic sapphire oscillators at the 10^{-16} level. IEEE Trans Ultrason Ferroelectr Freq Control 63:915–921
14. Rayleigh L (1910) The problem of the whispering gallery. Phil Mag 20:1001–1004
15. Grop S, Bourgeois PY, Bazin N et al (2010) A crycooled 10 GHz oscillator with 10^{-15} frequency stability. Rev Sci Instrum (81):pp 025102-1–7
16. Grop S, Bourgeois PY, Boudot R et al (2010) 10 GHz cryocooled sapphire oscillator with extremely low phase noise. Electron Lett 46: 420–422

Part IV
Policies and Regulations, Standards and Intellectual Properties

Analysis of GNSS User/Industry Interoperability Viewpoint Survey Results

Tao Han, Xiaochun Lu, Juan Du, Xiaozhen Zhang and Yongqiang Ji

Abstract One of the main purposes of UNOOSA establishing the International Committee on Global Navigation Satellite System (ICG) is to promote compatibility and interoperability between Global Navigation Satellite Systems (GNSS). The ICG also established the Working Group S to be in charge of the research and coordination of GNSS compatibility and interoperability. In November 2013, WG-S established the Interoperability Task Force, to collect and research on the worldwide user/industry viewpoint on GNSS interoperability, in order to form the user/industry interoperability requirements. First, the survey results of user/industry viewpoint on interoperability from China were analysed by grey sequence analysis. The analysis results show that users are mainly concerning about "interoperable parameters". After that, the common questions in the questionnaire from GPS, GLONASS, QZSS and BDS are analysed. A quantitative analysis model for the differences in the interoperability viewpoint is established; and the viewpoints are divided into three categories according to the different degrees. At last, some suggestions for interoperability from the above modelling are proposed.

Keywords User interoperability viewpoint · Questionnaire · Grey relational grade · Proposal

T. Han (✉)
College of Geology Engineering and Geomatics, Chang'an University,
126 Yanta Road, Xi'an 710054, People's Republic of China
e-mail: hantao@ntsc.ac.cn

T. Han · Y. Ji
Foundation Education Department, Xi'an Siyuan University,
Xi'an, People's Republic of China

X. Lu · J. Du · X. Zhang
National Time Service Center, Chinese Academy of Sciences,
Xi'an, People's Republic of China

J. Sun et al. (eds.), *China Satellite Navigation Conference (CSNC) 2017 Proceedings: Volume III*, Lecture Notes in Electrical Engineering 439,
DOI 10.1007/978-981-10-4594-3_51

1 Background

GNSS compatibility and interoperability is not only the hot topic in the field of worldwide GNSS, but also one the prerequisites of realizing multi-GNSS navigation [1]. Now, it is more than a decade since the conception of GNSS interoperability was brown. Scholars around the world have very active research on GNSS interoperability during the decade. A series of international coordination are carried out among system providers.

Till now, interoperability between different GNSSs is unsettled [2]. There are three main reasons: inconformity of system construction progress, undefined user requirements and disunited assessment method [3, 4]. The two built GNSSs are GPS and GLONASS. The interoperability between the two systems is not able to realize at present, since they are adopting different modulations, CDMA in GPS and FDMA in GLONASS. Other systems, Beidou and Galileo, are not interoperable at their present stage. The UN established the ICG (International Committee on Global Navigation Satellite Systems) to be an official platform for GNSS compatibility and interoperability international coordination. The WG-S (used to be WG-A) of ICG builds a subgroup to promote interoperability among systems. One of its main purposes is to investigate, straighten up, and research the user requirements of GNSS interoperability [2]. Interoperability evaluation must be considered from two aspects. On the one hand, according to the concept of interoperability, the most fundamental beneficiary of interoperability is GNSS users. Thus, GNSS interoperability should be evaluated by the user. On the other hand, the application of satellite navigation is very extensive, involving different fields. Then, user requirements are also different. Therefore, the evaluation of interoperability should not only stand in the user's viewpoint, but also consider the needs of different types of users [3, 5].

This paper focuses on the needs of users for interoperability research, and based on the ICG advocated investigation questionnaire in user interoperability viewpoint. The Chinese interoperability point of view survey results are further analysed by establishing mathematical model. The modelling results revealed some of the conclusions behind the data.

2 User Interoperability Perspective Research Activities

2.1 Questionnaire Recovery Situation

In April 2013, the ICG S Group held an Interoperability Workshop, which presented the User/Industry Interoperability Perspective Questionnaire [6]. GNSS users and equipment manufacturers are invited to seek technical advice and advice on interoperability through technical research. At the beginning of 2014,

Table 1 Questionnaire statistics (Classified by user type)

User type	Sent	Valid	Recovery rate (%)	Percentage (%)
Transportation and life safety	52	50	96.2	41.7
Medium/high precision applications	34	32	94.1	26.7
Mass application	34	30	88.2	25
Total	120	112	–	93.4

Table 2 Questionnaire statistics (Classified by user type)

User type	Sent	Valid	Recovery rate (%)	Percentage (%)
Research institute	40	38	95	31.7
Enterprise	65	62	95.4	51.7
Colleges and universities	15	12	80	10
Total	120	112	–	93.4

Beidou system based on this questionnaire in our country conducted a wide range of interoperability research [7]. In the same year, GLONASS system also carried out the research activities.

The survey is mainly for the satellite navigation of China's research institutes, enterprises and universities, and some experts and professors to issue questionnaires; a total of 120, 112 valid questionnaires were recovered, accounting for 93.4% of the total. Tables 1 and 2, respectively, show the data according to the user and the unit divided by the questionnaire collection situation.

Compared to the entire satellite navigation industry, the total number of questionnaires is slightly less, and it is recommended in the future with the assistance of government departments to expand the scope of research.

2.2 Data Validity Analysis

The reliability of the questionnaire was employed to test the reliability of the collected data. The purpose is to analyse whether the indicators of the questionnaire are used to measure the same concept or goal. The reliability also reflects the rationality of questionnaire design. Cronbach α coefficient is the most common index to depict reliability of the questionnaire. There is a positive proportion between the system value and Cronbach α coefficient. The greater the Cronbach α coefficient is, the higher the credibility of questionnaire is. The correspondence between questionnaire reliability and coefficient is shown in Table 3 [8]. The Cronbach α of Beidou's user interoperability questionnaire recovery is 0.647. From the reliability provided in Table 3, the reliability level of Cronbach α value of this investigation is "credible".

Table 3 Judgment rule of Cronbach α

Cronbach's alpha	Internal consistency
$0.9 \leq \alpha$	Excellent
$0.7 \leq \alpha < 0.9$	Good
$0.5 \leq \alpha < 0.7$	Acceptable
$0.4 \leq \alpha < 0.5$	Questionable
$0.3 \leq \alpha < 0.4$	Poor
$\alpha < 0.3$	Unacceptable

Table 4 Classification of questionnaire

Question type	Specific question
Interoperability parameter	–Interoperability parameters content –Third—party interoperability parameters broadcast mode –System time bias between each other or an unified time scale –How to get system time offset –Space time coordinate parameter using method –Coordinate deviation compensation method –Should a reference frame be fixed as a coordinate conversion standard
Central frequency	–Importance of common central frequency –Center frequency of new CDMA signal in L1 band –Necessity of new signals do not in L1 band –Interoperability in a third central frequency
Modulation	–Signal facing patent litigation solution –Whether to use all constellation signals from a market perspective –Use CDMA signal or FDMA signal –Interest in continually using L1 C/A signal –Interest in E5b signals
Signal bandwidth	–Minimum bandwidth for future GNSS signals –Whether increasing signal bandwidth is helpful to reduce multipath error –Acceptable maximum code and carrier offset in single frequency interoperability –Acceptable maximum code and carrier offset in double/triple frequency interoperability
Signal quality	–Whether to limit the number of signals according to some certain criteria –Providers ensures signal to achieve a minimum performance standards –Method for processing the signals who do not meet the performance criteria –Upper limitation of center frequency hopping

2.3 Question Type Classification

Through the repeated discussions of interoperability task group in ICG WG-S, the questionnaire of the factors affecting user/industry interoperability requirements is made by a list of 25 interoperability-related questions. According to the problem attribute, it can be classified into five categories: interoperability parameter, central frequency, modulation, signal bandwidth, and signal quality. They are jointly responsible for "user/industry interoperability requirements" (as shown in Table 4).

In order to express concisely, the description of each question has simplified in this paper. The actual description of the questionnaire can be found in the reports of group ICG WG-S [6, 7]. In addition, answers to these questions can be found in the research report of Lu Xiaochun [7].

3 Analysis of Questionnaire Survey in Beidou

The goal of this chapter is to select the most concerned part of the user from 25 questions. According to the degree of correlation between users and problems, data mining is carried out by grey correlation degree method.

3.1 Grey Relational Degree Calculation

3.1.1 The Method

Grey relational grade method is a common data mining method. The purpose is to use the data relationship between the factors to reflect the degree of similarity or difference between them [8, 9].

Suppose there are m questions in the GNSS interoperability questionnaire. Each question has n responses (User feedback):

$$\begin{aligned} &X_1 = (x_1(1), x_2(2), \cdots, x_1(n));\\ &X_2 = (x_2(1), x_2(2), \cdots, x_2(n));\\ &\cdots\\ &X_m = (x_m(1), x_m(2), \cdots, x_m(n)). \end{aligned} \tag{1}$$

For $\xi \in (0, 1)$, let

$$\begin{aligned} &\gamma(x_0(k), x_i(k))\\ &= \frac{\min_i(\min_k|x_0(k) - x_i(k)|) + \xi \max_i(\max_k|x_0(k) - x_i(k)|)}{\xi \max_i(\max_k|x_0(k) - x_i(k)|) + |x_0(k) - x_i(k)|}. \end{aligned} \tag{2}$$

Then we have

$$\gamma(X_0, X_i) = \frac{1}{n}\sum_{k=1}^{n}\gamma(x_0(k), x_i(k)). \tag{3}$$

Thus, $\gamma(X_0, X_i)$ is called the grey relational degree between X_0 and X_i. ξ is the resolution coefficient.

If the degree $\gamma(X_0, X_i)$ is the maximum, then the index X_i and index X_0 are closest. That is to say, the correlation degree between the i-th question and the surveying purpose is better than other questions. Accordingly, the order of importance of each questionnaire question can be discharged.

3.1.2 Computational Step

There are 112 group survey data for the 25 questions. Suppose "User type" is the standard sequence X_0. The grey relational degree computation flow between X_0 and the left 24 questions is shown as follows.

Step 1: Calculate the initial value of each sequence:

$$X_i' = \frac{X_i}{x_i(1)} = \left(x_i'(1), x_i'(2), \cdots, x_i'(n)\right), \quad (i = 0, 1, \cdots, 24, \quad n = 112.). \tag{4}$$

Step 2: Calculate the difference sequence:

$$\begin{aligned} &\Delta_i(k) = |x_0(k) - x_i(k)|, \quad \Delta_i = (\Delta_i(1), \Delta_i(2), \cdots, \Delta_i(n)), \\ &\quad i = 1, 2, \cdots, 12, \quad n = 112. \end{aligned} \tag{5}$$

Step 3: Calculate the maximum/minimum difference:

$$M = \max_i \left(\max_k (\Delta_i(k)) \right), \quad m = \min_i \left(\min_k (\Delta_i(k)) \right). \tag{6}$$

Step 4: Calculate the correlation coefficient:

$$\begin{aligned} &\gamma_{0i}(k) = \frac{m + \xi M}{\Delta_i(k) + \xi M}, \\ &\xi \in (0, 1), \quad k = 1, 2, \cdots, n; \quad i = 1, 2, \cdots, m. \end{aligned} \tag{7}$$

Step 5: Calculate the grey relational degree:

$$\gamma_{0i} = \frac{1}{n} \sum_{k=1}^{n} \gamma_{0i}(k); \quad i = 1, 2, \cdots, m. \tag{8}$$

3.1.3 Calculation Result

Compute the grey relational degree of user interoperability survey data collected in Beidou. The following results are obtained under the resolution coefficient ξ = 0.4, 0.5, 0.6 and 0.8, respectively (Fig. 1).

Take the grey relational degree curve when ξ = 0.5 as an example. Twelve questions have the grey relational degree bigger than 0.85 (see Table 5).

The "Degree" in Table 5 refers to the grey relational degree. According to the results of the above questionnaire screening results, we can get the most concerned about the user interoperability elements after further research.

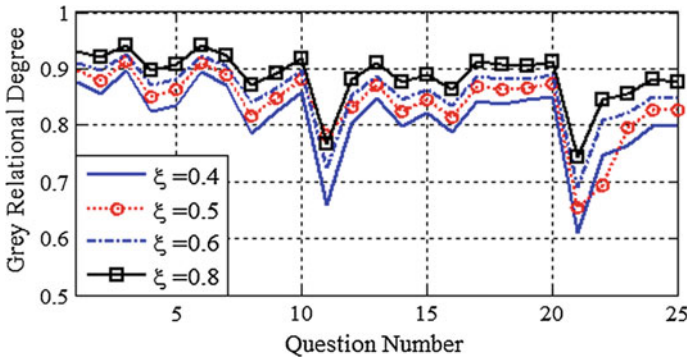

Fig. 1 Curves of *grey* relational degree in the questionnaire

Table 5 Grey relational degree (>0.85) order of questionnaire

Question	Degree
Importance of common central frequency	0.913
System time bias between each other or an unified time scale	0.910
Space time coordinate parameter using method	0.895
Coordinate deviation compensation method	0.889
Interoperability parameters content	0.881
Center frequency of new CDMA signal in L1 band	0.879
How to get system time offset	0.873
Should a reference frame be fixed as a coordinate conversion standard	0.869
Increasing signal bandwidth is helpful to reduce multipath error	0.869
Interoperability in a third central frequency	0.863
Acceptable maximum code and carrier offset in single frequency interoperability	0.862
Providers ensures signal to achieve a minimum performance standards	0.851

3.2 User Requirement Relevance Analysis

According to the screening results, we can calculate the proportion of selected questions in different categories (see Table 6).

Obviously, "interoperability parameters" and "central frequency" have the higher proportion. "Interoperability parameters" has the highest proportion. This shows that users are primarily concerned with interoperability parameters, followed by signal frequency.

The signal modulation of each system has been determined (or going to be determined). There is hardly chance to change their mind. Thus, the "modulation" obtained a low attention. Table 7 is obtained after a subdivision of the "interoperability parameters"-related questions.

From Table 7, we obtain the following results. GNSS users are main concern about the system time interoperability and system coordinate interoperability. The users pay more concerning on "how to use", and pay more attention on "information differences".

Table 6 Chosen ratio of selected questions in different categories

Statistic value	Total	Chosen	Ratio (%)
Interoperability parameters	7	6	85.7
Central frequency	4	3	75.0
Modulation	5	0	0.0
Signal bandwidth	4	2	50.0
Signal quality	4	1	25.0

Table 7 Detailed classification of interoperability-related questions

Questions	Detailed category	Chosen
Interoperability parameters content	Algorithm	Yes
Third-party interoperability parameters broadcast mode	System time	Yes
System time bias between each other or an unified time scale	System time	Yes
How to get system time offset	System time	Yes
Space time coordinate parameter using method	System coordinate	Yes
Coordinate deviation compensation method	System coordinate	Yes
Should a reference frame be fixed as a coordinate conversion standard	Parameter acquisition	No

4 The Difference Between Users from Different GNSSs

4.1 Common Questions

The questionnaires of each GNSSs are the revised one of the same original questionnaires [6]. There are 10 common questions in the questionnaire of Beidou, GPS, GLONASS and QZSS (see Table 8).

The statistical results from these questions of these systems are different. Research on the difference of the answers from each GNSS is helpful to understand the differences and similarities of the viewpoint between the users from different GNSSs.

The differences of user views on interoperability between systems can be seen in Table 9. It is necessary to quantify the difference measurement.

Table 8 Common questions

No.	Questions
1	What types of applications do receivers from your company (or receiver designs) support?
2	Do you prefer new CDMA signals at "L1" to be centred at 1575.42 MHz or have some of them elsewhere, e.g., at 1602 MHz?
3	Once there are a large number of good CDMA signals, do see any commercial interest in FDMA signals? Why or Why Not?
4	Given that L5/E5a/B2a will be transmitted by most GNSS providers, do you intend to use the E5b signal? –If so, for what purpose?
5	Assuming signal quality is acceptable from every provider, would you limit the number of signals used by provider or by other criteria? What criteria?
6	For best interoperability, how important is a common center frequency? How important is a common signal spectrum (PSD)?
7	Will you provide "tri-lane" capability in the future? If so, do you prefer: B3 (1268.52 MHz)? E6 (1278.75 MHz)? L2 (1227.6 MHz)? L2 + B3 + E6? S Band? C Band?
8	Does a wider satellite transmitter bandwidth help with multipath mitigation?
9	Would you recommend GNSS or SBAS services provide interoperability parameters: system clock offsets; geodesy offsets; ARAIM parameters; Others? –Should they be provided by other means so as not to compromise TTFF or other navigation capabilities?
10	Should the international community strive to protect all GNSS signal bands from terrestrial signal interference?

Table 9 Chosen ratio of common questions

NO.	Options	Answers			
		Beidou (%)	QZSS (%)	GLONASS (%)	GPS (%)
1	Transportation and safety life	44.7	50.0	48.0	18.2
	Medium/high precision	28.3	17.0	24.0	45.5
	Consumer application	27.0	33.0	28.0	36.4
2	1575.42 MHz	50.0	83.0	0.0	50.0
	Other	14.3	0.0	100.0	50.0
	Do not care	35.7	17.0	0.0	0.0
3	Yes	21.4	0.0	57.0	18.0
	No	57.1	100.0	43.0	82.0
	Not sure	21.5	0.0	0.0	0.0
4	Yes	42.9	33.0	60.0	40.0
	No	35.7	67.0	40.0	40.0
	Not sure	21.4	0.0	0.0	20.0
5	Yes	57.1	33.0	43.0	78.0
	No	14.3	33.0	57.0	22.0
	Not sure	28.6	34.0	0.0	0.0
6	Yes	75.0	83.0	20.0	67.0
	No	25.0	0.0	80.0	33.0
	Not sure	0.0	17.0	0.0	0.0
7	Yes	92.9	34.0	100.0	46.0
	No	0.0	33.0	0.0	36.0
	Not sure	7.1	33.0	0.0	18.0
8	Yes	50.0	67.0	80.0	80.0
	No	0.0	0.0	20.0	10.0
	Not sure	50.0	33.0	0.0	10.0
9	Yes	71.5	83.0	100.0	100.0
	No	7.0	0.0	0.0	0.0
	Not sure	21.5	17.0	0.0	0.0
10	Yes	100.0	100.0	100.0	100.0
	No	0.0	0.0	0.0	0.0
	Not sure	0.0	0.0	0.0	0.0

4.2 Analytical Method Modelling

The purpose of this paper is to find out the common understanding and differentiated understanding of interoperability between providers and users of each system.

For question i, suppose the statistical results of the j-th system denotes as vector $\overrightarrow{A}_{i,j} = (x, y, z)$, and satisfying

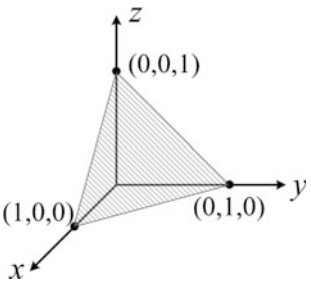

Fig. 2 Vector plane of the *i*-th question

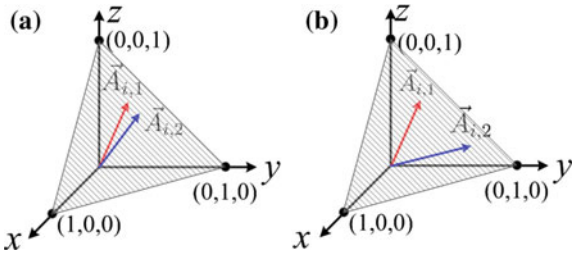

Fig. 3 Projection of viewpoint difference in vector plane (**a** Similar, **b** Large)

$$x + y + z = 1; \quad x, y, z \in [0, 1]. \tag{9}$$

Then, the statistical results of each system on *i*-th question can be written as a vector (three-dimensional). The vector space coordinate system in the trajectory is shown in Fig. 2.

If system 1 and system 2 have the same view on question *i*, the distance between $\overrightarrow{A}_{i,1}$ and $\overrightarrow{A}_{i,2}$ is closer (see Fig. 3a). On the contrary, the distance is far (see Fig. 3b).

In this way, the distance between the vector $\overrightarrow{A}_{i,1}$ and $\overrightarrow{A}_{i,2}$ can be defined to measure the difference of view between system 1 and system 2 on the *i*-th question. However, if the Euclidean distance between two points on the plane is directly used to represent the difference, it is not accurate. For example, let $\overrightarrow{A}_{i,1} = (0.3, 0.3, 0.4)$ and $\overrightarrow{A}_{i,2} = (0.3, 0.4, 0.3)$, the distance is $\sqrt{0.02}$. While let $\overrightarrow{A}'_{i,1} = (0.3, 0.3, 0.4)$ and $\overrightarrow{A}'_{i,2} = (0.3, 0.39, 0.41)$, the new distance is $\sqrt{0.0202}$. Obviously, vector $\overrightarrow{A}_{i,1}$ and $\overrightarrow{A}_{i,2}$ is further and $\overrightarrow{A}'_{i,1}$ and $\overrightarrow{A}'_{i,2}$ is closer. But their Euclidean distance value shows an opposite result. Thus, we have the following analysis.

For the distance $\left|\overrightarrow{A}_{i,j} - \overrightarrow{A}_{i,k}\right| (j \neq k)$, we have

$$\left|\overrightarrow{A}_{i,j} - \overrightarrow{A}_{i,k}\right|^2 = \left|\overrightarrow{A}_{i,j}\right|^2 + \left|\overrightarrow{A}_{i,k}\right|^2 - 2\left|\overrightarrow{A}_{i,j}\right| \cdot \left|\overrightarrow{A}_{i,k}\right| \cos\left\langle \overrightarrow{A}_{i,j}, \overrightarrow{A}_{i,k} \right\rangle, \tag{10}$$

where $\left\langle \overrightarrow{A}_{i,j}, \overrightarrow{A}_{i,k} \right\rangle$ denotes the angle from $\overrightarrow{A}_{i,j}$ to $\overrightarrow{A}_{i,k}$. This angle can reflect the difference between n $\overrightarrow{A}_{i,j}$ and $\overrightarrow{A}_{i,k}$. From expression (10), the Euclidean distance does not only contain the angle between vector $\overrightarrow{A}_{i,j}$ and $\overrightarrow{A}_{i,k}$, but also the length of $\overrightarrow{A}_{i,j}$ and $\overrightarrow{A}_{i,k}$. Then modular length influences the distance. In order to eliminate the impact of the module length, the vector $\overrightarrow{A}_{i,j}$ can project to the sphere $x^2 + y^2 + z^2 = 1$ (the first hexagram) that is unitized, as shown in Fig. 4.

For common Question 1, we have

$$\begin{cases} \overrightarrow{A}_{1,1} = (0.447, 0.283, 0.270), \\ \overrightarrow{A}_{1,2} = (0.500, 0.170, 0.330), \\ \overrightarrow{A}_{1,3} = (0.480, 0.240, 0.280), \\ \overrightarrow{A}_{1,4} = (0.182, 0.455, 0.364). \end{cases}$$

where $j = 1$ denotes Beidou, $j = 2$ denotes QZSS, $j = 3$ denotes GLONASS and $j = 4$ denotes GPS. The above vector is projected on the spherical surface as shown in Fig. 4, and we obtain

$$\begin{cases} \vec{a}_{1,1} = (0.752566, 0.476457, 0.45457), \\ \vec{a}_{1,2} = (0.802909, 0.272989, 0.52992), \\ \vec{a}_{1,3} = (0.792982, 0.396491, 0.46257), \\ \vec{a}_{1,4} = (0.298142, 0.745356, 0.59629). \end{cases}$$

Find the distance between the two vectors of the four vectors, and get

$$\begin{aligned} \left|\vec{a}_{1,1} - \vec{a}_{1,2}\right| &= 0.222736, \quad \left|\vec{a}_{1,1} - \vec{a}_{1,3}\right| = 0.089956, \\ \left|\vec{a}_{1,1} - \vec{a}_{1,4}\right| &= 0.546709, \quad \left|\vec{a}_{1,2} - \vec{a}_{1,3}\right| = 0.141021, \\ \left|\vec{a}_{1,2} - \vec{a}_{1,4}\right| &= 0.694496, \quad \left|\vec{a}_{1,3} - \vec{a}_{1,4}\right| = 0.620042. \end{aligned}$$

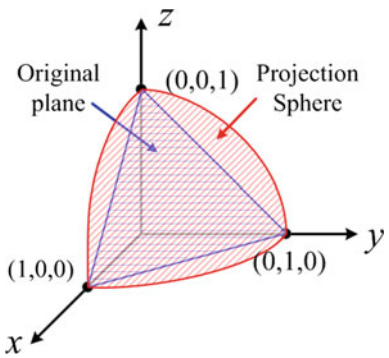

Fig. 4 Sphere projection of vector plane in the *i*-th question

The mean of the above six "distances" is $\text{mean}(V_1) = 0.385827$. This value represents the difference between the views of the four system providers on the interoperability questionnaires. Thus it can be used as a measure of this difference. If $\text{mean}(V_i)$ is smaller, it indicates that the four system vendors shared the same opinion on the interoperability questionnaire common question i. On the other hand, the opinions of the various systems on the same question are quite different.

4.3 Difference Analysis

In accordance with the above method, there can be 10 common questions in the statistical situation of the unit (the result to retain two decimal places). Figure 5 shows the measure of variability for each question. It also clearly reflects the viewpoint differences between common questions.

Question 1 (in which application is supported by your receiver or receiver signal) is of little variability, indicating that the user representatives of each system participating in the questionnaire are closer in classification and weighting. It is reasonable to compare the results of the four-system questionnaire.

As shown in Fig. 5, the four system vendors are close to the results of Question 9 (Do you recommend using GNSS or SBAS services to provide interoperability parameters) and Question 10 (whether countries should be committed to protecting the GNSS band from harmful interference). National users have indicated the need to protect the GNSS band and wish to provide interoperability parameters.

Question 4 (considering that most GNSS vendors will transmit the L5/E5a/B2a signals, will you continue to use the E5a signal) and Question 8 (whether the increased signal bandwidth is conducive to mitigating the multipath error), small, indicates that the system users in these two issues are closer to the views.

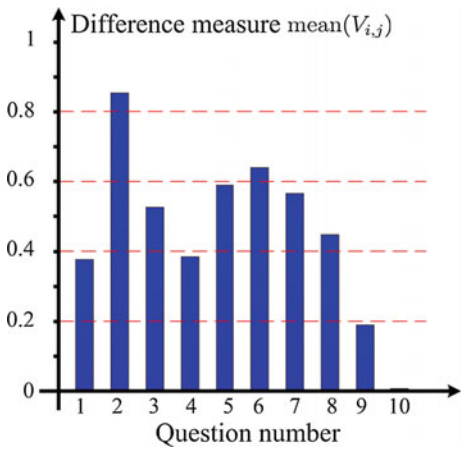

Fig. 5 Differences of common questions in questionnaire

The answers to four questions, Question 3 (Should there be commercial interest in the FDMA signal once there are a large number of good CDMA signals?), Question 5 (if the signal quality offered by the vendor is acceptable, will you be limited to some standard The number of signals), Question 6 (whether the uniform center frequency is important), Question 7 (whether you will consider future use of the third frequency interoperability), are somewhat different. For Question 3, since the FDMA signal is used by the Russian GLONASS system, no other system is involved in this type of signal, leading to differences in user viewpoints. The answer to Question 5 is itself limited by the type of user receiver, so there are large differences not only between systems but also among users. For the problem of signal frequency points 6 and 7, the users of each system are from the perspective of the continuation of their own systems, the vast majority of hope to be able to follow the existing frequency, and therefore lead to differences in user point of view. This also shows that the frequency diversity of satellite navigation system is both the status quo of GNSS, but also the needs of users.

If Question 2 (the new CDMA signal you tend to concentrate in the L1 band at 1575.42 MHz or some at other frequencies, such as 1602 MHz) is the most significant, the problem is not only an interoperability problem, but also a compatibility issue.

In addition, the user in the navigation frequency point of view also shows the satellite navigation system frequency diversity GNSS status, but also reflects the user's demand for frequency diversity.

5 Summary and Proposal

This paper mainly introduces the interoperability research activities and results of each GNSS system under the ICG framework. Through the data mining method, the paper analyzes the common questions in the questionnaire and the system questionnaires, respectively. According to the analysis results, we have the following conclusions and recommendations.

1. In the case of Beidou users, the main demand for interoperation lies in the information level, which not only solves the "information difference" between the systems, but also includes how to reduce the influence of the system time difference on the solution of the positioning equation: the necessity and feasibility of coordinate transformation the realization of the method.
2. From the point of view of the diversity of public systems, the users of each system now pay close attention to two interoperability problems, one is tend to technology (Question 9) and the other is related to national policy (Question 10).
3. The user requirement of interoperability parameters is urgent. Researchers and students in the field of satellite navigation may focus on the following aspects:

(1) Clarify the detailed parameters which could unify the system differences (so-called "interoperability parameters");
(2) Distinguish the difference of influence degree in the above interoperability parameters;
(3) The method and uncertainty analysis while applying the interoperability parameters to unify the system biases;
(4) Acquisition and calculation of method interoperability parameters while the parameters should be easy to obtain for most users.

In summary, the current research results show that realization of GNSS interoperability is mostly concerned by users, and this is also the consistent point of view in GNSS user/industry.

References

1. Yang Y, Lu M, Han C (2016) Some notes on interoperability of GNSS. Acta Geodaetica Cartogr Sin. doi:10.11947/j.AGCS.2016.20150653
2. Han T (2016) Research on interoperability algorithm of global navigation satellite system. The University of Chinese Academy Sciences
3. Han T, Lu X, Wang X et al (2011) Differential equation dynamical system based assessment model in GNSS interoperability. Sci China Phys Mech Astron 54(6):P996–P1003
4. Lu X, Lu J, Wang X, Bai Y, Han T (2012) Interoperability feasibility analysis between Beidou and GPS. In: Proceedings of China satellite navigation conference, P15–P26
5. Zhang X, Lu X, Han T (2014) Quantitative analysis of improvement of availability and continuity in service performance for users under interoperable GNSS. J Time Freq 3: P173–P180
6. Tom S (2013) GNSS modernization background & questions. ICG WG-A Interoperability Workshop
7. Shen J, Lu X (2014) Chinese user/industry interoperability viewpoint. Chinese GNSS Interoperability Workshop
8. Guieford JP (1965) Fundamental statistics in psychology and education (4th ed). McGram-Hill, New York
9. Xiao X (1997) Theoretical study and reviews on the computation method of grey interconnect degree. Syst Eng-Theory Pract 17(8):P76–P81

Applicability Analyses of Intellectual Property Securitization in Beidou Enterprises

Yalan Li and Yingchun Shen

Abstract Intellectual property securitization is a combination of technological development and financial innovation. The new financial instrument contributes to technological improvement and the efficient use of capital in small or medium technology-intensive enterprises. Beidou industry, as the new high-tech field in China, has good prospect in the future, and related companies are in the early stages of development that is dominated by small and medium enterprises. Based on financing conditions analysis of 27 Beidou listed companies, the paper summarizes exiting problems at present, and supplies a new financing tool, intellectual property securitization, to resolve the financing dilemma of small and medium Beidou enterprises. In order to explain applicability of Intellectual property fully, the paper discusses the current legal provisions on asset securitization, which briefly describes the experience at home and abroad. Meanwhile, aimed at Beidou industry, the paper analyzes the status of based assets, intellectual property, mainly from stock and increment, and supplies an application model that sets SPV in the whole industry.

Keywords Beidou enterprises · Intellectual property · Asset-backed securities

1 Introduction

Intellectual property-backed securitization is the innovation of asset-backed securities. Based on intellectual property assets, through real sale of basic asset to achieve bankruptcy remoteness, SPV (Special Purpose Vehicle) arranges security's structure and separates risk and income. After achieving credit enhancement, release security to solve financing demand of owners of assets.

Y. Li (✉) · Y. Shen
Beihang University, Xueyuan Road. 37, Beijing 100191, China
e-mail: liyalan99588@163.com; 1091740370@qq.com

J. Sun et al. (eds.), *China Satellite Navigation Conference (CSNC) 2017 Proceedings: Volume III*, Lecture Notes in Electrical Engineering 439,
DOI 10.1007/978-981-10-4594-3_52

Intellectual property securitization can applied in a wide range of fields, and the paper explores whether this pattern of financial innovation can contribute to the development of China's Beidou industry.

2 The Financing Situation of Beidou Enterprises

2.1 The Basic Condition of Beidou Enterprises

Satellite navigation system (GNSS) is composed of three parts: the space segment, ground control segment, and user segment. The space segment and ground control segment of Beidou system are the important infrastructures of a nation, while civilian-oriented products mainly focus on the user section. Civilian-oriented products on Beidou system can be summarized as PNT system (positioning, navigation, and timing service). From the perspective of industrial chain, products can be divided into the base product, implemented terminal, operation service system, and so on. Basic products mainly are chips, cards, antennas, and other basic components. Implemented terminals are various Beidou terminals that aimed at different industries and different areas, and the more compatible terminals that can be used in different navigation systems. Service systems include several fields, special services, such as national defense and public security, and other popular fields, such as agriculture, transportation, and outdoor sports.

By the end of 2015, China satellite navigation industry has formed a market that yielded one hundred billion Yuan every year. The number of related enterprises is more than 13,000, which provides more than 400,000 jobs opportunities. From 1993 to 2009, the output of GPS increased 130 times from the initial $510 million to $66 billion, and the compound annual growth rate was as high as 35%, and even in the initial stage of industrial development was reaching at 40–50%. Compared with GPS, we can predict that the annual compound growth rate of Beidou industry will be above 40% in the next decade and become a new growth point of economy.

However, major enterprises in the industry earn only 1 billion Yuan, and profits are only 10 million Yuan, which is a veritable infant industry compared with the PC industry that is a well-developed communications, and yielded trillion Yuan every year. Most related companies are medium and small enterprises, and even are micro-enterprises that survive with one or two technical advantages. How to make fully use of all resources, strengthen internal management, was the great subject of the related companies.

2.2 Business Analysis on Mainly Beidou Enterprises

By stock software, the paper selected the 27 listed companies of Beidou system and analyzed their financing condition. There are 20 SMEs in 27 listed companies, accounting for 74.1% of the total number of listed companies, which is consistent with the structure of Beidou industry. The business of selected typical samples in this paper covers four parts of industry chain (basic product, terminal device, application system, and operational service), having high industry visibility, and belonging to the leading enterprises. We can grasp dynamic of the field based on deep analysis.

2.2.1 BDStar Navigation

By the end of 2015, BDStar Navigation had seven wholly owned subsidiaries, four subsidiaries, and two joint stock companies, 8 s level subsidiaries, and total assets reached 3.792 billion Yuan.

1. Stock: capital stock is 293,709,494 shares, capital reserve is 2106305417.27 Yuan. Two items are about 2.3 billion Yuan, accounting for 60% of total assets, which is the main source of finance for the company.
2. Debt: no debt
3. Financial institutions: short-term borrowing is about 180 million, receiving mainly through mortgage loans, guarantee, and collateral. Collateral or guarantee assets are its own property land or physical assets such as construction in progress. The term of a loan is in less than 1 year, and the amount of a loan is less than 10 million.
4. Government grant: business operating income reached more than 1.1 billion, but net profit was only 50 million; net profit belonging to shareholders was about 770,000. Non-recurring profit accounted for 98.46% of net profit, and government subsidies account for 63.29% of non-recurring profit.
5. Own funds: retained earnings and surplus reserves amounted to 245 million, which can be seen as roughly the firm's own money that can be used relatively free, but it was too little compared with the total assets of the enterprise.
6. Intangible assets: 6% of the annual income was invested in research and development, and about 50% of investment achieved capitalization. By the end of 2015, the company achieved 165 patents and 193 software copyrights. These advantages become fundamental of enterprises in market competition and build a reliable strategy for future development resources.

2.2.2 UniStrong

At the end of 2015, Beijing UniStrong had five main subsidiaries, two joint stock companies (impacting profits above 10%), and total assets stood at 2.49 billion.

1. Stock: At the end of 2015, capital stock is 1.97 hundred million shares, and capital reserve is 12.91 hundred million Yuan. Two items are about 1.488 billion Yuan, accounting for 59.77% of total assets, which is the main source of finance for the company.
2. Debt: no debt
3. Financial institutions: short-term borrowing is about 3.1 hundred million, accounting for 12.46% of total assets, which is the important source of finance for the company.
4. Government grant: business operating income reached more than 7.57 hundred million, but net profit was only 60 million, half of them was non-recurring profit, and government subsidies accounts for 58% of non-recurring profit.
5. Own funds: retained earnings and surplus reserves amounted to 2.3 hundred million, which can be seen as roughly the firm's own money that can be used relatively free.
6. Intangible assets: By the end of 2015, the company's intangible assets amounted to 239 million, and developers accounted for nearly 40%, and the capitalization rate of research and development funds is close to 60%. The company received more than 70 international intellectual properties through merger and acquisition. By integrating overseas resources and teams, the company formed strong global competence.

2.3 Financing Problems of Beidou Enterprises

At present, the financing ways of Beidou enterprises have retained earnings, Government grants, bank financing, debt financing, and equity financing. In the initial stage, corporate owner financed, and government investment and bank financing is supplement. In the developing stage, enterprises always choose equity financing model, and the optimum is publicly traded for most mature enterprise.

Beidou enterprises lack of securities financing. On the one hand, domestic financial intermediations lack the experience and market imperfection, which lead to excessive risks. On the other hand, enterprises lack of basic assets, which is difficult to generate steady cash flow. Therefore, high-tech enterprises still cannot finance, even if they have a large number of intellectual properties.

To sum up, Beidou enterprises are facing the following financing problems:

1. High income, low profits, and insufficient retained earnings are in line with the character of infant industry. Revenues continue to grow, but the high cost and

high investments make net profits do not stand out, even with a deficit. This leads to own funds cannot meet technology upgrade requirements.

2. Government subsidies accounted for 5% in the earnings of Beidou enterprises, which was the government policy support to the industry, but granted items were mostly related to technical research and development or joint development contract. The condition indicated that in the field of technical research and development, Beidou companies also need more government funding, but it is clear that such subsidies are not a long-term solution. After all, the market is the essence of the enterprise.
3. Stock financing is listed the main fund-raising way, especially the equity premium from capital markets on the formation of Compass technology, and has become an important source of funding. But with standardization of the national stock market, listing requirements become more stringent, where making public offerings for many SMEs is very difficult.
4. Venture capital requires a detailed assessment of the firm's value. Therefore, if a company is not mature or just has single technical SME, the acquisition of venture capital requires a great time cost.
5. Beidou enterprises are supported by national policy, so it is easier to get bank loans. Good medium and large enterprises can get 50–100 million from the bank every time. But bank lending needs to set a number of barriers, such as physical asset mortgage-backed. Most small and medium enterprises survived with several core technologies, and intangible assets are their greatest asset. But it is obvious that the value is greatly undervalued when they apply a loan, which generally achieved only 20–30% of real value. Moreover, bank financing generally has shorter term than another financing ways, basically in 3 years and cannot effectively undertake technology development needs.
6. Now mergers between firms are frequent phenomenon. Small enterprises that just have a single technology are merged after they have been profitable, and form a group company gradually, which is the essential result to enhance the efficiency of resource use and optimize the industrial structure. But it will also form a trend of technological monopoly. Therefore, when we encourage the enterprises to be bigger and stronger, we should also develop small and medium enterprises, which is beneficial to promote the healthy competition of Beidou industry.

Financing ways are diverse, so companies need to select the appropriate measures according to the requirement of enterprise development. Financing of large enterprises or listed companies is splendid, and financial pressure is always small. They should make full use of their own advantages to build cooperative platform, and enhance the value space through the intellectual property portfolio and industrialization. For most small and medium enterprises, financing is difficult for them, which strengthen financial pressure, and intangible assets account a great proportion of total assets. In addition to merger and acquisitions from outside, actively trying to new financial instruments, using its own technology, and getting resources play important part of development and perfection of the SMEs.

3 Research on Applicability of Intellectual Property Securitization in Beidou Industry

3.1 Induction of China's Relevant Laws and Practice

3.1.1 Programmatic Documents

In 2006, government promulgated "the outline of the national medium- and long-term program for scientific and technological development (2006–2020)," which highlighted the "implementation of financial policies to promote innovation and entrepreneurship. In 2008, China launched "the national intellectual property strategy guidelines," which determined the basic rules for improving economic benefits of intellectual property in China and clearing legal responsibility from the creation, use, protection, and management aspects.

Those two files at the national strategic level refer to financial services support in the process of commercialization of intellectual property, which provides a basic policy environment for creating and development of new financial tools such as intellectual property securitization.

3.1.2 Framework of the Legal System

China has started a pilot implementation of asset-backed securities, and gradually established a set of rules and regulations and the implementation process in the course of practice. Securitization is a systematic project and needs lots of laws to support, such as the company law, trust law, the partnership enterprise law, contract law, intellectual property law (patent law, the trademark law and its implementing rules), the Bankruptcy Act, the guarantee law, tax law, and other legal support. In addition, government departments must also continue to introduce relevant implementation rules. The paper summarized detailed rules (Table 1).

3.1.3 Practice of Asset-Backed Securities in China

Summarizing experience, asset-backed securities in China can be divided into two parts. One is the credit assets securitization issued by state-owned banks in the interbank market. The other one is asset securitization products issued by securities companies in the bond market.

From the initial practice, the basic assets are selected mainly from receivables, because the future cash flow of that is stable and easy measurement. Compared with the intellectual property rights, the risk of securitization is lower, and the difficulty of formulation of relevant policies and regulations is also less. But with the development of computer technology, the capacity of data gathering and processing will be greatly increased, and the forecast of future earnings and the value of the

Table 1 Policies and regulations of asset securitization

Time	Enacting department	Files	Significance
2004	The State Council	State council boost revolution opening and stable development of capital market	Encourage financial innovation and create financial products according to the national context
2005.4.20	The People's Bank Of China, China Banking Regulatory Commission	Administrative measures for the securitization of credit assets	The trust law of specific initiatives in the area of asset securitization, emphasis on risk prevention, protection of investors' interests, laid the groundwork for other supporting policies
2005.5.16	Ministry of Construction	Pilot notification on change registration related issues of individual housing mortgage-backed securitization	Thinking of estate-backed securities
	Ministry of Finance	Pilot accounting provisions on credit assets securitization	Solve the problem about accounting standards that different participants use
2005.6.8	Ministry of Finance, Ministry of Human Resources and Social Security	Official letter on the investment of national social security fund on asset securitization products	Social insurance fund is agreed to invest asset-backed securities, and expand the scope of investors
2005.6	The People's Bank Of China	Information disclosure regulations of asset-backed securities	On the basis of the existing rules and regulations in the interbank bond market, set specific provisions for asset-backed securities
2005.11.7	China Banking Regulatory Commission	Supervision and administration on pilot credit assets of financial institutions	Supervise financial institutions in the process of securitization, and ensure to manage risk degree effectively; agreed with commercial banks and insurance companies invest asset-backed securities on the premise of controlling risk
2006.2.20	Ministry of finance, State Administration of Taxation	Notice on tax policy issues related to credit assets securitization	Proposed tax policy on credit assets securitization
2007.8	The People's Bank Of China	Notice on information disclosure regulations about the assets pool of credit assets	By the influence of subprime mortgage crisis in the United States, strengthen risk control

(continued)

Table 1 (continued)

Time	Enacting department	Files	Significance
2007.8.26	China Securities Regulatory Commission	Interim measures on the credit rating industry in Stock market	Decrease the risk of asset-backed securities by strict supervision
2013.2.26	China Securities Regulatory Commission	Administrative provisions on asset securitization business of securities companies	Manage the securitization that happened in stock exchange, and the SPV is established by security companies

assessment will be more precise, which will gradually eliminate the dilemma that intellectual property become the underlying basic asset. At present, possible direction makes intellectual property licensing revenue to be a continuous cash flow.

3.2 Characteristic of Beidou Industrial and Applicability of Intellectual Property Securitization

3.2.1 Basic Assets—The Development of Intellectual Property

Whether intellectual property-backed security can implement in an industry depends on its underlying assets–accumulation and development of intellectual property. In the Patent Search and Analysis of SIPO, search-related patents with "Beidou" for keyword and 6931 information can be retrieved (Fig. 1).

In 2003, the first generation of Beidou run successfully, related to civil technology developed quickly. In 2004–2012, the second generation of Beidou system started. It is expected that all second generation of Beidou satellites will be launched in 2020, and China will have passive positioning technology on a global scale.

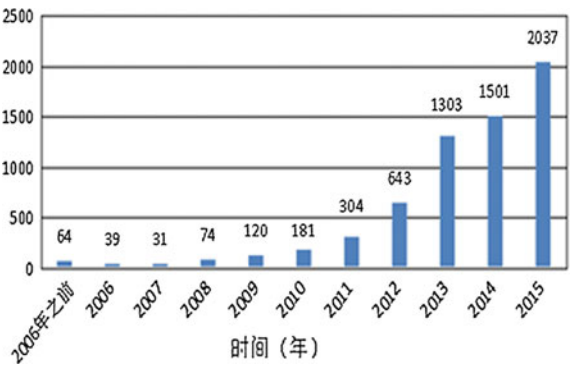

Fig. 1 The number of Beidou-related patent

During this period, the Beidou-related technology also developed quickly in the civilian field. The change of patent pending number can reflect obviously the process of rapid development and gradual maturity in Beidou industry in China.

3.2.2 The Model of Intellectual Property Securitization in Beidou Industry

The key point of achieving securitization in Beidou enterprises is the stable cash flow. Beidou enterprises are currently in the initial stages of development, which result to shortage of intellectual property in a single enterprise, and diversity is also poor. Excessive risk makes it is not possible to form an effective and stable cash flow. Meanwhile, single enterprise is too small to afford high costs of asset securitization. Therefore, it is difficult for a company to complete the Bowie bond-like securitization alone.

Securitization model proposed in this paper is cooperation in the industry. Through establishing a platform of intellectual property securitization facing to the whole industry, it can filter the member enterprise's intellectual properties, form asset pools, and establish SPV, which will pay principal and interest of security according to sales revenue of products based on important intellectual properties. Specific process is shown in Fig. 2.

First, there are n Beidou enterprises, and each one has one or more intellectual properties which are able to form a kind of product that is based on the intellectual properties. Enterprises want to raise funds to achieve large-scale production or reproduction. Intellectual properties that were applied in products and sales revenues are guaranteed to pay the securities in time.

Second, encourage Beidou enterprises to cooperate and establish industry alliance, and set up SPV together. SPV will hire a professional agency to assess value of intellectual properties that members supplied to be basic asset of securitization and estimate cash flow formed by the high-tech products in the future. After rigorous evaluation, SPV can get several products that have potential sales in the

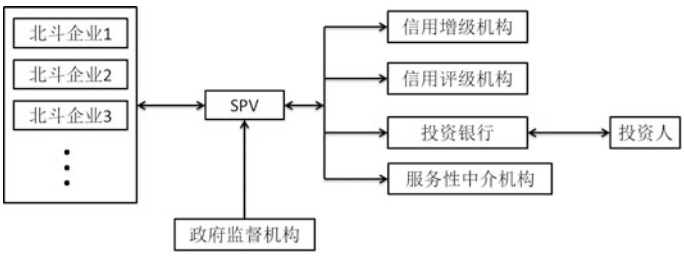

Fig. 2 Flow chart of intellectual property securitization in Beidou enterprises

future, and add them into the pool. For these selected products, the original companies need the real sale of assets to the SPV, which is the important step of achieving bankruptcy remoteness.

Third, the SPV needs to sign agreements with related agencies one by one, including managed contracts with banks, liquidity contract with insurance agencies, and underwriting equity contracts with investment banks, which will form a complete trading system. In addition, it also requires internal rating of security and determines a preliminary risk, cost, and benefit.

Fourth, SPV should use various ways to enhance credit rating of security. The main methods are division of bond rating, purchasing professional indemnity, guaranteeing from the parent companies or reputable financial institutions, announcing to purchase subordinated bonds on their own, and so on.

Fifth, after a series of internal and external risk control measures, the credit rating of security has been upgraded to the released level. SPV should hire authoritative rating agency to finish external released rating, which determines the issue price.

Sixth, the income that obtained from the issuance of the security meets the purchase cost of the underlying assets firstly. In other words, the income should meet the original Beidou enterprises' financing needs which is the original purpose of intellectual property securitization. Through the process, enterprises transform intangible assets into further production funding in the financial markets.

Seventh, the SPV, intermediary agencies, and Government-related department should record and manage the subsequent cash flow of intellectual property assets together. SPV should pay interest and principal to the investors on time and form the virtuous cycle of capital in order to protect investors' rights and interests; all income from assets will deposit in a special account and establish comprehensive monitoring mechanism in which unrelated third parties are responsible for ensuring repayment on time.

Eighth, after repayment, the interest between SPV and investors has been split clearly. At this point, the main part of the securitization process has ended. SPV pay service fees to intermediaries involved in the process and return surplus funds as an additional benefit to the sponsor, but any loss is borne by the SPV.

The advantages: ① The source of basic assets expand to full industry, which makes its number and quality has greater protection and reduces risk of securitization; ② In the process of increasing credit rating, large state-owned enterprises can provide more policy support and legal guarantees. It means that contacting the government credibility to guarantee the financial process indirectly, which is beneficial to issue successfully; ③ Stable cash flow from future sales income of products and intellectual property value form double guarantees.

Disadvantages: ① The number of participants is so many, and the structure is more complex, which leads to enhance the cost of securitization; ② Asset-backed security is market behavior. If government is involved in as a participant to support intellectual property securitization of special industries, it will result in unfair condition, so it is an important problem to choose pilot that is the result of game among several organizations.

The essence of this model is establishing unified institution that is responsible to manage intellectual property, and forming an unrelated SPV. The reason that chooses cooperation in Beidou industry is that it is beneficial to increase financial strength and diversity of assets. The isolated SPV cooperates with capital market. Meanwhile, the government finance department, department of state-owned assets, should supervise the process together. On the premise of avoiding the loss of state assets, several organizations are supposed to coordinate and achieve the securitization.

4 Conclusions

As a typical emerging technology-intensive industry, Beidou field is dominated by SMEs at present. They need large capital expenditures on technological research and development, which contributes to high cost and slim profit, so they need to search all sources of financing. When another ways are impossible or difficult to come true, intellectual property securitization, as a new financial instrument, is beneficial to finance by intangible asset for small and medium high-tech enterprises that lack of real assets. Therefore, it is necessary.

United States, Japan, and European Union had implemented dozens of successful intellectual property securitization cases and formed a mature process. Meanwhile, domestic-relevant laws and regulations continued to establish, and rules gradually enacted and explored a set of effective methods of management and supervision in pilot experiments. Its feasibility has been proved from both theory and practice.

Specific to Beidou enterprises, the stock of intellectual property has reached a high point currently and will produce a spurt of growth in the future, which creates a good basis for the assets pool. The establishment of SPV can choose industry joint. With the enhancement of market concentration, gradually defining property rights, enterprises should improve ability of management and operation for intellectual properties. In the aspects of risk control and construction of the supporting system, the Beidou industry, as sunrise industry promoting by the whole country, will get more beneficial policies and facilities. These supports help the industry achieves cooperation with international renowned financing institutions and enjoys more preferential tax policies, which will promote Beidou enterprises to go further on the road of innovation.

References

1. Li J (2006) Intellectual property securitization: theoretical analysis and applied research. Intellect Property 16(91):33–39
2. Li W (2007) Financing study on intellectual property securitization. University of International Business and Economics, Beijing

3. Tang S, Chen L (2006) Explore on intellectual property securitization. Sci Manag Res 24(4):53–56
4. Xiao Y (2007) Research on finance supported system of intellectual property securitization—fusion between technological innovation and financial innovation. Intellect Property 17(99):12–19
5. Tang S, Chen L (2006) Practice and prospect of American patent securitization. Electron Intellect Property 04:32–36
6. Yuan X (2006) Research on Japonic patent securitization. Electron Intellect Property 07: 42–46
7. Gao X (2007) Research on Sinitic intellectual property securitization. Graduate school of Chinese academy of social sciences, Beijing
8. Zhang M (2009) Application and development of Beidou navigation system. Space Int 11: 27–31
9. Cao C (2014) Research on situation and prospects of Beidou industry. Satell Appl 02:49–51
10. Wu H, Li Z, Zhang Y (2013) Development status analysis of Beidou industry. Satell Appl 04:8–11
11. Liu W, Zhu J (2007) The development of Beidou satellite navigation system. Surveying Mapp Geol Mineral Resour 23(03):29–32
12. Zhou L, Li S, Yang S (2015) Analysis and suggestions on patents of Beidou satellite navigation industry. China Invention Patent 09:44–48
13. Xing L, Tie Z, Wang Y (2013) Thinking of Beidou application and industrialization. Digit Commun World 12:29–31
14. Hao H (2013) Consideration and suggestion of Beidou intellectual property. Digit Commun World (12):12—15; (79):56—59
15. Yan Z (2014) Development ideas of China's Beidou navigation satellite application industry. Satell Appl 4:7–10
16. Medium and long term development planning of national satellite navigation industry. General Office of the State Council, 09 Oct 2013
17. Dong T (2009) Research on intellectual property securitization system. Tsinghua University Press, Beijing (Version 1)
18. Kuang Y, Zhai X (2014) Reason and policy of "national Defense patent sleeping soundly". Sci Technol Prog Policy 31(23):138–142
19. Hu M (2015) Analysis financing problem of military enterprise. Contemp Econ 32:48–49
20. Ren L, Li C, Zhang X (2014) Research on transaction structure of military enterprises' intellectual property securitization. Sci Technol Prog Policy 31(14):103–107
21. Xu Z, Guo X, Ren L, Li C (2014) Asset selection and SPV model design in. J Ind Technol Econ 6:93–101
22. Zhang R (2011) Existing problems and countermeasures analysis on financing of China's military enterprises. Jilin University, Jilin
23. Liu J, Shi X, Zhang X, Xie W (2014) Research on financing model of military industrial enterprises in China. Ind Econ Rev 4:118–126
24. BDStar Navigation 2015 Annual report
25. Beijing Unistrong Science & Technology Co., Ltd 2015 Annual report